ASME
SETTING THE STANDARD

Editor, **YOGESH JALURIA** (2010)
Assistant to the Editor, **S. PATEL**

Associate Editors
Yutaka Asako, Tokyo Metropolitan University, Japan (2010)
Gautam Biswas, Indian Inst. of Tech., Kanpur (2009)
Cho Lik Chan, The University of Arizona (2010)
Louis C. Chow, University of Central Florida (2010)
Minking Chyu, Univ. of Pittsburgh (2009)
Frank J. Cunha, Pratt & Whitney (2011)
Ali Ebadian, Florida International Univ. (2011)
Ofodike A. Ezekoye, Univ. of Texas-Austin (2011)
Satish G. Kandlikar, Rochester Inst. of Tech. (2010)
Sung Jin Kim, KAIST, Korea (2010)
Sai C. Lau, Texas A&M Univ. (2009)
Ben Q. Li, Univ. of Michigan, Dearborn (2009)
Raj M. Manglik, Univ. of Cincinnati (2009)
Jayanthi Y. Murthy, Purdue University (2010)
Pamela M. Norris, Univ. of Virginia (2011)
Patrick E. Phelan, Arizona State Univ. (2011)
Roger R. Schmidt, IBM Corporation (2010)
S. A. Sherif, University of Florida (2010)
Heping Tan, Harbin Institute of Technology (2011)
Peter Vadasz, Northern Arizona University (2010)
Jamal Yagoobi, Illinois Inst. of Tech. (2009)
Walter W. Yuen, Univ. of California–Santa Barbara (2011)

Past Editors
V. DHIR
J. R. HOWELL
R. VISKANTA
G. M. FAETH
K. T. YANG
E. M. SPARROW

HEAT TRANSFER DIVISION
Chair, **C. OH**
Vice Chair, **V. CAREY**
Past Chair, **T. TONG**

PUBLICATIONS COMMITTEE
Chair, **BAHRAM RAVANI**

OFFICERS OF THE ASME
President,
THOMAS M. BARLOW
Executive Director,
THOMAS G. LOUGHLIN
Treasurer,
THOMAS D. PESTORIUS

PUBLISHING STAFF
Managing Director, Publishing
PHILIP DI VIETRO
Manager, Journals
COLIN McATEER
Production Coordinator
JUDITH SIERANT

Transactions of the ASME, Journal of Heat Transfer (ISSN 0022-1481) is published monthly by The American Society of Mechanical Engineers, Three Park Avenue, New York, NY 10016. Periodicals postage paid at New York, NY and additional mailing offices. POSTMASTER: Send address changes to Transactions of the ASME, Journal of Heat Transfer, c/o THE AMERICAN SOCIETY OF MECHANICAL ENGINEERS, 22 Law Drive, Box 2300, Fairfield, NJ 07007-2300. **CHANGES OF ADDRESS** must be received at Society headquarters seven weeks before they are to be effective. Please send old label and new address.
STATEMENT from By-Laws. The Society shall not be responsible for statements or opinions advanced in papers or ... printed in its publications (B7.1, Para. 3). **COPYRIGHT © 2009** by The American Society of Mechanical Engineers. For authorization to photocopy material for internal or personal use under those circumstances not falling within the fair use provisions of the Copyright Act, contact the Copyright Clearance Center (CCC), 222 Rosewood Drive, Danvers, MA 01923, tel: 978-750-8400, www.copyright.com. Request for special permission or bulk copying should be addressed to Reprints/Permission Department. Canadian Goods & Services Tax Registration #126148048

Journal of Heat Transfer

Published Monthly by ASME

VOLUME 131 • NUMBER 2 • FEBRUARY 2009, pp. 021301-025503

RESEARCH PAPERS

(Contents continued on inside back cover)

This journal is printed on acid-free paper, which exceeds the ANSI Z39.48-1992 specification for permanence of paper and library materials. ♾™
♻ 85% recycled content, including 10% post-consumer fibers.

TECHNICAL BRIEFS

DISCUSSIONS

The ASME Journal of Heat Transfer is abstracted and indexed in the following:

Applied Science and Technology Index, Chemical Abstracts, Chemical Engineering and Biotechnology Abstracts (Electronic equivalent of Process and Chemical Engineering), Civil Engineering Abstracts, Compendex (The electronic equivalent of Engineering Index), Corrosion Abstracts, Current Contents, E & P Health, Safety, and Environment, Ei EncompassLit, Engineered Materials Abstracts, Engineering Index, Enviroline (The electronic equivalent of Environment Abstracts), Environment Abstracts, Environmental Engineering Abstracts, Environmental Science and Pollution Management, Fluidex, Fuel and Energy Abstracts, Index to Scientific Reviews, INSPEC, International Building Services Abstracts, Mechanical & Transportation Engineering Abstracts, Mechanical Engineering Abstracts, METADEX (The electronic equivalent of Metals Abstracts and Alloys Index), Petroleum Abstracts, Process and Chemical Engineering, Referativnyi Zhurnal, Science Citation Index, SciSearch (The electronic equivalent of Science Citation Index), Theoretical Chemical Engineering

An Algorithm Study on Inverse Identification of Interfacial Configuration in a Multiple Region Domain

Chunli Fan
e-mail: c.fan@hotmail.com
e-mail: chlfan@163.com

Fengrui Sun

Li Yang

Department of Power Engineering,
Naval University of Engineering,
Wuhan 430033, P.R.C.

A two-dimensional inverse heat conduction problem to determine the interfacial configuration of a multiple region domain is solved by utilizing temperature readings on the outer surface of the whole domain. The method used is the modified one-dimensional correction method (MODCM) along with the finite element method. The MODCM is a simple but very accurate method, which first solves the multidimensional inverse heat conduction problem based on the simplified one-dimensional model, and the discrepancy in the result caused by this one-dimensional simplification is corrected afterward by an iterative process. A series of numerical experiments is conducted in order to verify the effectiveness of the algorithm. The method can identify the interfacial configuration of the multiple region domain with high accuracy. The average relative error of the identification result is not more than 10.4% when the standard deviation of the temperature measurement is less than 2.0% of the average measured temperature for the cases tested. The number of the measurement points of the inspection surface can be reduced with no obvious effect on the estimation results as long as it is still sufficient to describe the exact interfacial configuration. The method is proved to be a simple, fast, and accurate one that can solve successfully this interfacial configuration identification problem.
[DOI: 10.1115/1.2994765]

Keywords: inverse heat conduction problem, interfacial configuration, multiple region domain, inverse identification, modified one-dimensional correction method

1 Introduction

Recently, inverse geometry problems, which are commonly encountered in a number of engineering applications, constitute an important kind of inverse heat conduction problems. Their practical applications range from the cavity detection [1,2] to the shape design [3,4]. Solutions obtained in this kind of problems may significantly increase the accuracy of component design and hence may improve the performance of the whole system.

The inverse geometry problem considered in this paper involves determining the interfacial configuration of a multiple region domain based on the surface temperature measurements. This approach can be applied to many other applications, such as interfacial configuration identification for composite materials and phase change problems, ice thickness estimation in a thermal storage system, and crystal growth estimation [5].

Many numerical methods have been developed for the inverse geometry problem. Huang and Chao [6] studied a boundary identification problem of a flat plate with an irregular-shaped boundary by both the conjugate gradient method and the Levenberg–Marquardt method along with the boundary element approach. They found that the result obtained by the conjugate gradient method was better than that of the Levenberg–Marquardt method. In this inverse geometry problem the conjugate gradient method showed many advantages including the following: (i) needs very short computer time, (ii) does not require a very accurate initial guess of the boundary shape, and (iii) needs fewer sensors. Huang and Tsai [7] also extended successfully the algorithm based on the conjugate gradient method to the transient inverse geometry problem of identifying unknown irregular boundary configurations from external measurements. The steepest descent method was also used by Huang et al. [8] to solve the two-dimensional multiple cavity estimation problem.

Fan et al. [9,10] applied the Levenberg–Marquardt method, along with the finite volume method, to the identification of the two- and three-dimensional simple shaped defects in a finite body when the test piece is heated from one part of the outer boundary and inspected at the other part. Numerical experiments certified the effectiveness of the method, but the shape description parameters of the defect boundary should be defined beforehand whether the defect shape is regular or irregular. Fan et al. [11,12] also solved successfully the inner boundary identification problem of pipelines and the irregular-shaped subsurface defect detection problem by employing the conjugate gradient method along with the finite element method.

In order to simplify the algorithm, Su and Chen [13] proposed a simple noniterative approach for the identification of the inner wall geometry of a furnace based on an inverse matrix method and a virtual area concept. It was proved by the numerical examples that the proposed method has the following advantages: (i) the computation is fast, (ii) the number of the measured points needed is small, and (iii) the positions of the measured points have negligible effect on the result of estimation.

Yang et al. [14] proposed a simple iterative algorithm, the one-dimensional correction method (ODCM), for solving the inverse geometry problem. The method solves first the multidimensional inverse problem based on a one-dimensional inverse function, and then the discrepancy caused by this one-dimensional simplification is corrected by an iterative process. As concluded by Yang et al. from the numerical experiments, the largest advantage of this simple method is that the stability of the method can guarantee the convergence of the solution because the numerical method used in

Contributed by the Heat Transfer Division of ASME for publication in the JOURNAL OF HEAT TRANSFER. Manuscript received December 19, 2007; final manuscript received June 17, 2008; published online December 15, 2008. Review conducted by A. Haji-Sheikh.

 Copyright © 2009 by ASME

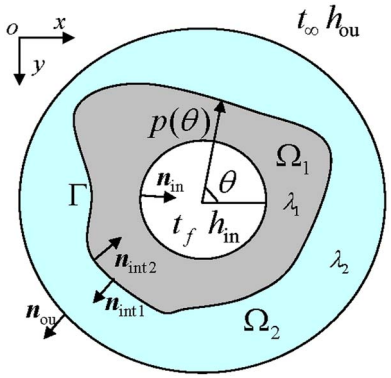

Fig. 1 Geometry of the multiple region domain

the algorithm is one of those for regular problem of differential equation. However, there are limitations in the method: One is that the final solutions are not converged completely to the original defect profiles, the other is that further refining the node interval does not improve the precision level; moreover, it may lead the iterative process to diverge. On the basis of the work of Yang et al. [14], Fan et al. [15] did some modifications to the ODCM and applied it to the inner pipe boundary identification problem. Highly accurate results are obtained for this problem, and the limitations mentioned above do not appear in the numerical examples anymore.

Up to now, as to the identification problem in a multiple region domain, little work has been done. Huang and Chen [16] extended the conjugate gradient method to a multiple region domain in estimating time- and space-varying outer boundary configurations. Huang and Shih [5] also applied the conjugate gradient method in the estimation of unknown irregular interfacial configurations in a multiple region domain. The results showed the effectiveness of the presented method. As can be seen from Ref. [5], the identification of the interfacial configuration of a multiple region domain is much more complicated than that of the single domain boundary for the identification results may be affected by much more factors such as the conductivity distribution and the temperature measurement position; therefore systematic study and discussion of this identification problem are necessary. In addition, further research is in urgent need for the simple and accurate identification algorithm.

Based on our previous work [15], this work addresses the development of the modified ODCM (MODCM) for the estimation of the unknown interfacial configuration in a multiple region domain. A series of numerical experiments is conducted to verify the effectiveness of the method. Also the effect of the factors such as the temperature measurement error and measurement point number is also investigated.

2 Temperature Distribution of Inspection Surface (Direct Problem)

To illustrate the methodology for developing the expressions to be used in determining the interfacial configuration in a multiple region domain, a two-dimensional heat conduction problem is considered. The geometry of the domain is shown in Fig. 1. The whole multiple region domain is a circle. The terms r_{in} and r_{ou} denote the inner and the outer radius of the domain, respectively. In the practical inspection work, the interfacial configuration, which is described by the distance $p(\theta)$ from the domain center up to the interface, is identified based on the temperature measurement of the inspection surface, i.e., the outer surface of the domain. The boundary conditions on both the inner and the outer surfaces of the domain are convective heat transfer.

The interface condition along Γ is continuous. The temperature and the heat flux profiles along the interface are the same on both sides of the domains Ω_1 and Ω_2.

The temperature distribution of the outer surface of the whole domain can be solved based on the following dimensionless two-dimensional heat transfer equations and boundary conditions.

For the domain Ω_1,

$$\frac{\partial^2 t_1}{\partial x^2} + \frac{\partial^2 t_1}{\partial y^2} = 0 \tag{1a}$$

$$-\lambda_1\left(\frac{\partial t_1}{\partial \boldsymbol{n}_{in}}\right) = h_{in}(t_{in} - t_f) \quad \text{on inner surface} \tag{1b}$$

For the domain Ω_2,

$$\frac{\partial^2 t_2}{\partial x^2} + \frac{\partial^2 t_2}{\partial y^2} = 0 \tag{2a}$$

$$-\lambda_2\left(\frac{\partial t_2}{\partial \boldsymbol{n}_{ou}}\right) = h_{ou}(t_{ou} - t_\infty) \quad \text{on outer surface} \tag{2b}$$

For the interface Γ,

$$t_1 = t_2 \tag{3a}$$

$$-\lambda_1\left(\frac{\partial t_1}{\partial \boldsymbol{n}_{int\,1}}\right) = -\lambda_2\left(\frac{\partial t_2}{\partial \boldsymbol{n}_{int\,2}}\right) \tag{3b}$$

where t is the temperature, λ represents the thermal conductivity, h denotes the film coefficient on the surface, subscripts 1 and 2 denote the parameters in domains Ω_1 and Ω_2, respectively, subscripts in and ou denote the parameters on the inner surface and outer surface, subscript int denotes the interface, $\boldsymbol{n}$ represents the normal vectors indicated in the figure, and t_∞ and t_f are bulk temperatures.

3 The MODCM (Inverse Problem)

3.1 Introduction of the MODCM. The MODCM is developed in our previous work [15] on the basis of the ODCM presented by Yang et al. [14] by correcting the iteration function, modifying the calculation of the correction terms, and giving the stopping criterion of the iteration. In Ref. [15] the MODCM showed better performance than the ODCM in solving the inner pipe boundary identification problem.

For the multidimensional inverse problem, the MODCM first calculates the parameters to be identified based on a one-dimensional inverse function. Then the discrepancy caused by the one-dimensional simplification is corrected by an iteration process, and the iteration function of which is deduced from Taylor's series expansion.

For the inverse problem of concern in this paper, the interfacial configuration $p(\theta)$ is described by a vector $\mathbf{P}$ formed by the element $p_i(i=1-m)$, the distance between the center of the whole domain and the ith discrete point on the interface, where m is the number of the discrete points on the interface. The term p_i is first calculated based on the discrete measured temperature value $t_{oi}(i=1-m)$ of the inspection surface, i.e., the element of the measured temperature vector $\mathbf{T}_o$, according to the one-dimensional inverse function $p_{1D}(t)$, which can be obtained easily from the one-dimensional heat conduction problem.

Based on Taylor's series expansion, the desired interfacial configuration $p_i(t_{oi})$ can be updated on the basis of the initial estimation $p_i(t_i)$ for each discrete point according to the following function:

$$p_i(t_{oi}) \approx p_i(t_i) + p_i'(t_i)(t_{oi} - t_i) + \frac{p_i''(t_i)(t_{oi} - t_i)^2}{2!} \quad (4)$$

where t_i is the corresponding precise temperature distribution of the inspection surface for the initial estimation of the interfacial configuration, which can be calculated according to the multidimensional Eqs. (1)–(3) based on the initial estimation of the interfacial configuration, and the subscript o denotes the original temperature measurement of the inspection surface.

An iteration process can then be derived for all discrete points of the interface based on Eq. (4) when the vectors formed by the elements p_i' and p_i'' are expressed as $\mathbf{P}'$ and $\mathbf{P}''$, respectively, for each iteration:

$$\mathbf{P}^{n+1} = \mathbf{P}^n + \mathbf{P}'^n * (\mathbf{T}_o - \mathbf{T}^n) + \frac{\mathbf{P}''^n}{2!} * (\mathbf{T}_o - \mathbf{T}^n) * (\mathbf{T}_o - \mathbf{T}^n) \quad (5)$$

If the last term is neglected, Eq. (5) becomes

$$\mathbf{P}^{n+1} = \mathbf{P}^n + \mathbf{P}'^n * (\mathbf{T}_o - \mathbf{T}^n) \quad (6)$$

where $\mathbf{P}^n$ is the nth estimated result of the interfacial configuration after $n-1$ iterations; $\mathbf{T}^n$ is the vector describing the temperature distribution of the inspection surface when the configuration of the interface is $\mathbf{P}^n$; $\mathbf{T}_o$ is the original measured temperature distribution at the inspection surface; $\mathbf{P}'$ and $\mathbf{P}''$ are the correction terms; the symbol "*" in Eqs. (5) and (6) denotes the Hadamard product, i.e., the element by element product, of two vectors with the same size; and the superscript n is the iteration number. It should be mentioned that the vectors $\mathbf{P}$, $\mathbf{P}'$, $\mathbf{P}''$, $\mathbf{T}$, and $\mathbf{T}_o$ in Eqs. (5) and (6) have the same size m.

3.2 Computation of Correction Terms. The elements of the two vectors $\mathbf{P}'$ and $\mathbf{P}''$ in Eq. (5) or Eq. (6) can be determined based on the following functions [14]:

$$p_i'(t_i) = 1/t_i'(p_i) \quad (7a)$$

$$p_i''(t_i) = (p_i'(t_i))' \quad (7b)$$

According to Ref. [15], the term $t_i'(p_i)$ in Eq. (7) of each iteration is computed by perturbing the element p_i of the interfacial configuration vector $\mathbf{P}$ obtained from the last iteration one by one and computing the resulting change in temperature t_i of the corresponding point of the inspection surface from the solution of the multidimensional heat conduction problem in Eqs. (1)–(3). Thereafter, $t_i'(p_i)$ is calculated by the ratio of perturbations of the two parameters: $\Delta t_i/\Delta p_i$. Then the two terms $p_i'(t_i)$ and $p_i''(t_i)$ are computed for every point to get $\mathbf{P}'$ and $\mathbf{P}''$ according to Eq. (7).

3.3 Stopping Criterion of the Iteration. For the MODCM, the stopping criterion of the iteration is given as

$$J(\mathbf{P}) = \sum_{i=1}^{m} [p_i^{n+1} - p_i^n]^2 < \varepsilon \quad (8a)$$

where ε is a small positive number, the superscript n denotes the iteration number, and m is the discrete point number of the interface. However, in the practical inspection work the observed temperature data may contain measurement errors; therefore we do not expect Eq. (8a) to be equal to zero at the final iteration step. According to Refs. [17,18], when the measurement error is considered the discrepancy principle used for the stopping criterion based on the difference of the temperature distributions calculated and measured is as follows:

$$\sum_{i=1}^{m} [t_{oi} - t_i^n]^2 < \varepsilon = m\sigma^2 \quad (8b)$$

where σ is the standard deviation of the temperature measurement. As stated in Ref. [17], such a stopping criterion gives the inverse method an iterative regularization character. According to Eq. (8b), the stopping criterion can be developed for the MODCM based on Eq. (6) as

$$J(\mathbf{P}) = \sum_{i=1}^{m} [p_i^{n+1} - p_i^n]^2 = \sum_{i=1}^{m} [p_i'^n (t_{oi} - t_i^n)]^2 = \varepsilon \le Cm\sigma^2 \quad (8c)$$

where C is a constant. The value of C can be defined based on the value of ε when it begins to fluctuate during the iteration process. As will be shown in Sec. 4, $C=1$ is good enough to get a confident identification result for the problem of concern in this paper. It should be mentioned why the stopping criterion (8b) is not used for the MODCM is that the criterion (8a) showed its advantages when solving the inverse problem based on thermographic temperature measurement [15].

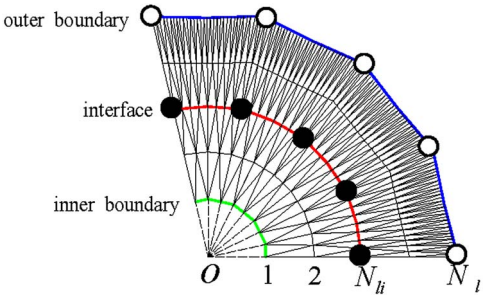

Fig. 2 Schematics of the finite element mesh for one part of the whole domain (N_l: number of the node layers of the whole domain; N_{li}: number of the node layers of domain Ω_1; and ● and ○ are the discrete points used for the inverse calculation on the interface and outer surface, respectively)

3.4 Computational Procedure of the MODCM. The iterative computational procedure for the solution of this interfacial configuration identification problem using the MODCM can be summarized as follows.

Calculate the initial interfacial configuration $\mathbf{P}^1$ based on the measured temperature distribution of the inspection surface $\mathbf{T}_o$ by using the one-dimensional inverse function $p_{1D}(t)$ to begin the iteration process. Suppose $\mathbf{P}^n$ is available after $n-1$ iterations.

(i) Calculate the temperature distribution of the inspection surface $\mathbf{T}^n$ based on the estimated configuration of the interface $\mathbf{P}^n$ according to the multidimensional heat transfer problem in Eqs. (1)–(3) by the finite element method.
(ii) Calculate the correction terms $\mathbf{P}'^n$ and $\mathbf{P}''^n$ in accordance with Eq. (7).
(iii) Calculate the new interfacial configuration $\mathbf{P}^{n+1}$ based on Eq. (5) or Eq. (6). In this paper Eq. (6) is used.
(iv) Check the stopping criterion given by Eqs. (8a)–(8c), then return to step (i) if not satisfied.

4 Results and Discussion

In order to illustrate the effectiveness of the MODCM in identifying the irregular interfacial configuration $p(\theta)$ from the knowledge of the temperature recordings at the outer surface of the whole domain, a series of numerical examples with different interfacial configurations is concerned in this section.

In all test cases considered in this paper, we have chosen $r_{ou}=0.3$, $r_{in}=0.1$, $t_f=100$, $t_\infty=10$, $h_{in}=1000$, and $h_{ou}=10$. Equations (1)–(3) are solved by the finite element method with linear triangular element. The finite element mesh of one part of the whole domain is schematically shown in Fig. 2. If not specifically mentioned, the number of the nodes or discrete points on the interface is 24 and the number of the node layers is set as $N_l=5$. The number of the node layers of domain Ω_1 is set as 3. In the numerical experiments, the measured temperature distribution $\mathbf{T}_o$ on the outer boundary of the whole domain is simulated by the solu-

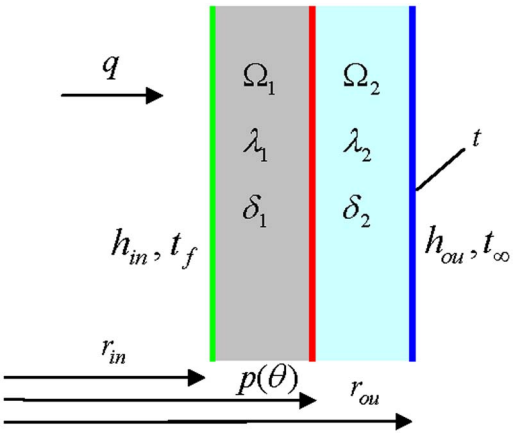

Fig. 3 Simplified one-dimensional heat transfer model of the multiple region domain

tion of the two-dimensional Eqs. (1)–(3) with known interfacial configuration, to which errors can be added to simulate the real measurement data. Based on these simulated measurement data, the identification work is conducted, and the results are compared with the known exact interfacial configuration to verify the effectiveness of the algorithm.

In order to compare the results for situations involving random measurement errors, we assume normally distributed uncorrelated errors with zero mean and constant standard deviation. The simulated inexact measurement data $\mathbf{T}_o$ can be expressed as

$$\mathbf{T}_o = \mathbf{T}_{o,\text{exact}} + \mathbf{W}\sigma \tag{9}$$

where $\mathbf{T}_{o,\text{exact}}$ is the solution of Eqs. (1)–(3) based on the known exact interfacial configuration, σ is the standard deviation of the measurements, and $\mathbf{W}$ is a vector with the same size as $\mathbf{T}_o$ formed by random numbers between −1.0 and 1.0.

In order to describe the precision level of the identification results, an average relative error (ARE) is also defined as

$$\text{ARE} = \frac{1}{m}\sum_{j=1}^{m}\left|\frac{p_i - \breve{p}_i}{\breve{p}_i}\right| \times 100\% \tag{10}$$

where p_i is the estimated result and $\breve{p}_i$ describes the exact configuration of the interface.

When the value of $r_{\text{ou}} - r_{\text{in}}$ is very small, the heat transferred from the inner surface of the whole domain to the outer surface can be deemed as of one dimension, and therefore the heat transfer analysis of the whole domain can be made based on the simplified one-dimensional physical model shown in Fig. 3. Then the inverse one-dimensional function $p_{1\text{D}}(t)$ for every measurement point of the outer surface can be derived from the following equation:

$$q = \frac{t_f - t_\infty}{\frac{1}{h_{\text{in}}} + \frac{\delta_1}{\lambda_1} + \frac{\delta_2}{\lambda_2} + \frac{1}{h_{\text{ou}}}} = \frac{t - t_\infty}{\frac{1}{h_{\text{ou}}}} \tag{11}$$

where q is the heat flux transferred from the inner surface to the outer surface of the whole domain, δ_1 and δ_2 are the thicknesses of domains Ω_1 and Ω_2, respectively, and t is the temperature of the inspection surface. Based on the above equation,

$$p_{1\text{D}}(t) = p(t) = r_{\text{ou}} - \delta_2 = r_{\text{ou}} - \left[\frac{t_f - t_\infty}{h_{\text{ou}}(t - t_\infty)} - \frac{1}{h_{\text{in}}} - \frac{1}{h_{\text{ou}}} - \frac{r_{\text{ou}} - r_{\text{in}}}{\lambda_1}\right] \Big/ \left(\frac{1}{\lambda_2} - \frac{1}{\lambda_1}\right) \tag{12}$$

or

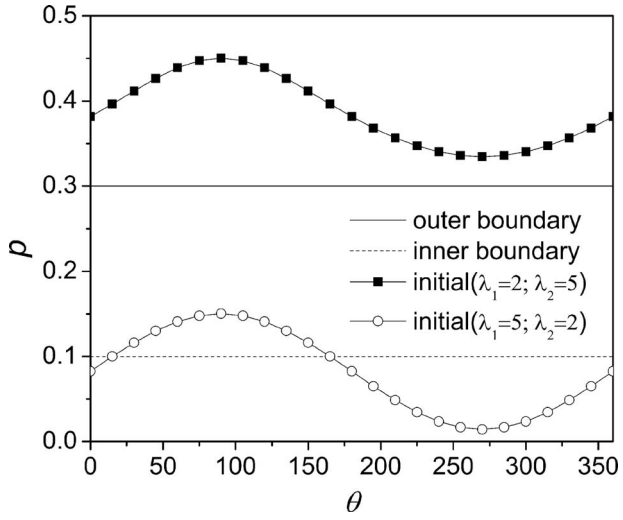

Fig. 4 Initial interfacial configurations calculated based on the one-dimensional inverse function (11) or (12) for the two conductivity distribution cases

$$p_{1\text{D}}(t) = p(t) = r_{\text{in}} + \delta_1 = r_{\text{in}} + \left[\frac{t_f - t_\infty}{h_{\text{ou}}(t - t_\infty)} - \frac{1}{h_{\text{in}}} - \frac{1}{h_{\text{ou}}} - \frac{r_{\text{ou}} - r_{\text{in}}}{\lambda_2}\right] \Big/ \left(\frac{1}{\lambda_1} - \frac{1}{\lambda_2}\right) \tag{13}$$

In order to guarantee that the initial value $\mathbf{P}^1$ falls between r_{in} and r_{ou}, a modification coefficient e ($e \geq 1$) is added to Eqs. (12) and (13), respectively, then the one-dimensional inverse function becomes

$$p_{1\text{D}}(t) = r_{\text{ou}} - \delta_2/e = r_{\text{ou}} - \left[\frac{t_f - t_\infty}{h_{\text{ou}}(t - t_\infty)} - \frac{1}{h_{\text{in}}} - \frac{1}{h_{\text{ou}}} - \frac{r_{\text{ou}} - r_{\text{in}}}{\lambda_1}\right] \Big/ \left(\frac{1}{\lambda_2} - \frac{1}{\lambda_1}\right)/e \tag{14}$$

or

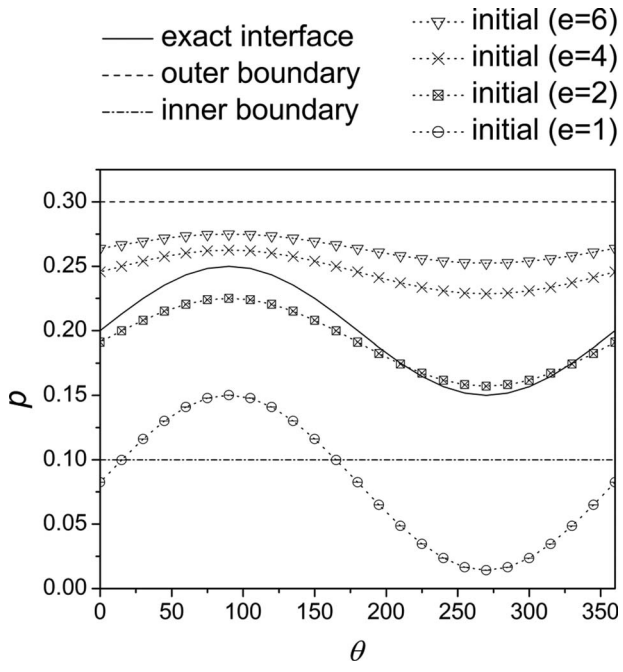

Fig. 5 Effect of coefficient *e* on the initial interfacial configurations of the iteration (λ_1=5, λ_2=2)

Table 1 AREs of identification results of the interfacial configuration with different coefficient *e*

	ARE					
	$\lambda_1=2;\ \lambda_2=5$			$\lambda_1=5;\ \lambda_2=2$		
ε	$e=2$	$e=4$	$e=6$	$e=2$	$e=4$	$e=6$
1.0	1.85%	1.85%	1.85%	0.37%	0.19%	0.24%
0.1	0.60%	0.60%	0.60%	0.06%	0.19%	0.24%
0.01	0.12%	0.12%	0.12%	0.02%	0.04%	0.05%
0.001	0.04%	0.04%	0.04%	0.004%	0.004%	0.004%

$$p_{1D}(t) = r_{in} + \delta_1/e = r_{in} + \left[\frac{t_f - t_\infty}{h_{ou}(t - t_\infty)} - \frac{1}{h_{in}} - \frac{1}{h_{ou}} - \frac{r_{ou} - r_{in}}{\lambda_2}\right] \Bigg/ \left(\frac{1}{\lambda_1} - \frac{1}{\lambda_2}\right)/e \tag{15}$$

It should be mentioned that the same initial interfacial configuration is obtained based on the one-dimensional inverse function, Eq. (12) or Eq. (13). But to restrict the initial configuration $\mathbf{P}^1$ to the range between r_i and r_o, whether Eq. (14) or Eq. (15) should be used depends on the computed result based on Eq. (12) or Eq. (13). When the calculated initial interfacial configuration falls outside the range from the boundary $p(\theta)=r_{ou}$, i.e., the calculated δ_2 is a negative value, Eq. (15) should be used in order to make $p_i^1 < r_{ou}$. For the same reason, Eq. (14) should be used when the calculated initial interfacial configuration falls outside the range from the inner boundary. For the specific test cases in this paper, this decision can be made based only on the ratio of the two conductivities λ_1 and λ_2, which will be discussed in detail in Sec. 4.1.

4.1 Numerical Test Case I. The unknown interfacial configuration is assumed to vary with θ in the form

$$p(\theta) = 0.2 + 0.05\sin(\theta), \quad 0 \text{ deg} \le \theta < 360 \text{ deg} \tag{16}$$

In order to study the effect of the conductivity distribution on the identification results, two kinds of conductivity distribution cases are first studied. One is $\lambda_1=5$, $\lambda_2=2$, the other is $\lambda_1=2$, $\lambda_2=5$.

When the coefficient e is not used, the initial interfacial configurations calculated based on the temperature recordings at the outer surface by using the one-dimensional inverse function (12) or (13) are plotted in Fig. 4. When λ_2 is larger than λ_1, the calculated initial interface configuration $\mathbf{P}^1$ falls outside the range between r_i and r_o from the side $p(\theta)=0.3$; therefore Eq. (15) should be used in order to make $p_i^1 < r_{ou}$. For the same reason, Eq. (14) should be used when λ_1 is larger. An example about the effect of the coefficient e on the calculated initial interfacial configuration when $\lambda_1=5$, $\lambda_2=2$ is shown in Fig. 5. In most cases, $e=2$ is enough. This value is used in the following test cases if not specifically mentioned.

When no measurement error is considered, the AREs of the identification results of the interfacial configurations for the two conductivity distribution cases are reported in Table 1 when the coefficient e is adopted as 2, 4, and 6, respectively. In the table, it

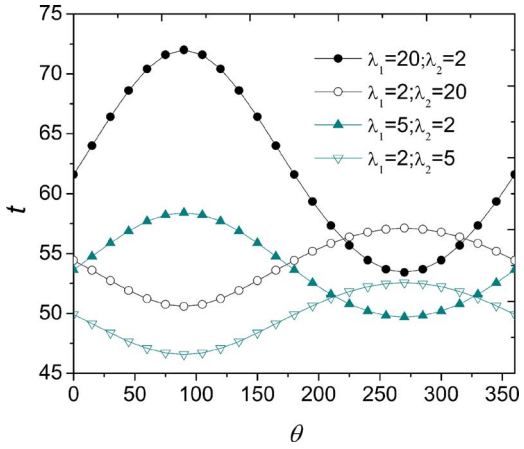

Fig. 7 Temperature distributions on the outer surface of the whole domain for different conductivity distributions

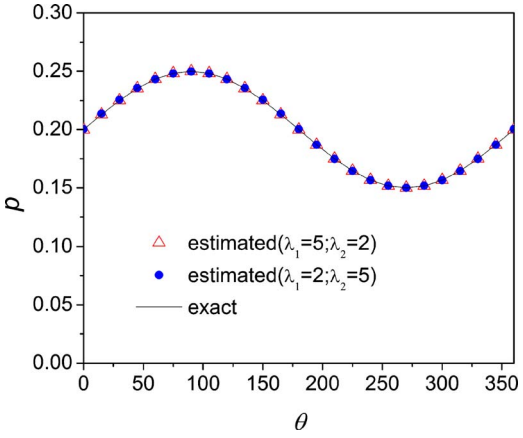

Fig. 6 Interfacial configuration identification results when no measurement error is considered ($\varepsilon=0.01$)

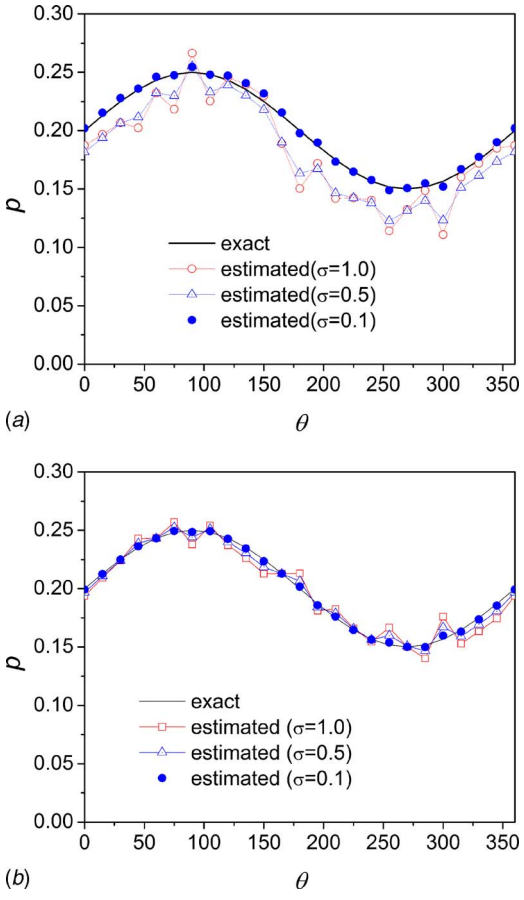

Fig. 8 Effect of measurement error on the identification results: (*a*) $\lambda_1=2$, $\lambda_2=5$ and (*b*) $\lambda_1=5$, $\lambda_2=2$

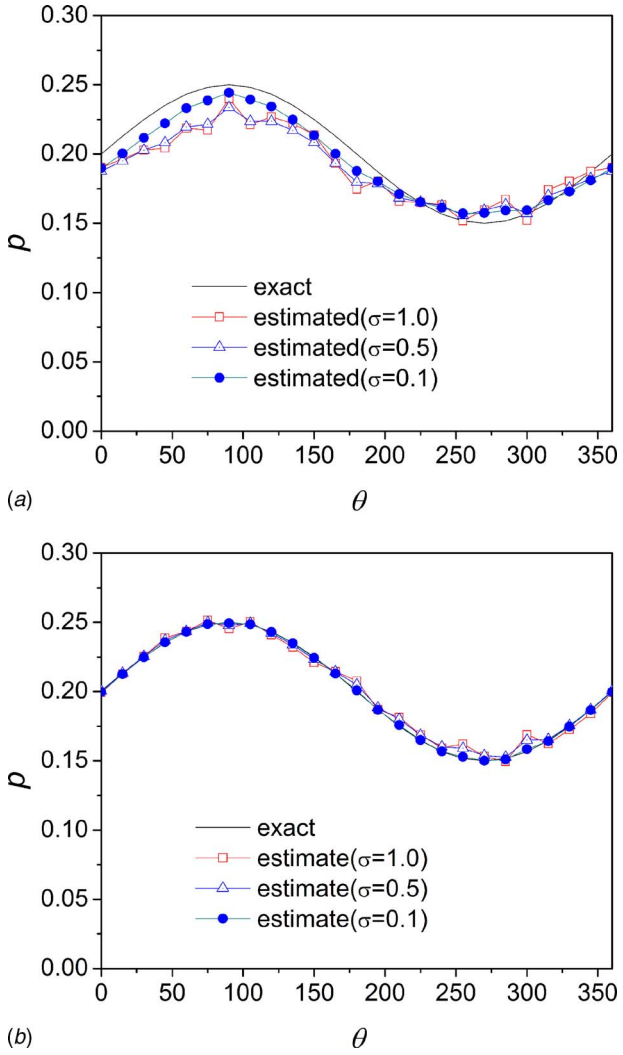

Fig. 9 Effect of measurement error on the identification results: (*a*) $\lambda_1=2$, $\lambda_2=20$ and (*b*) $\lambda_1=20$, $\lambda_2=2$

is not difficult to see that a very good agreement is obtained (the AREs are smaller than 1.0%) for both cases when the stopping criterion ε is smaller than 0.1. An example is shown in Fig. 6 for the two conductivity distribution cases when the stopping criterion is $\varepsilon=0.01$. For the studied cases in the table, when the stopping criterion ε is smaller than 0.01, the effect of the coefficient e on the accuracy of the identification result is negligible. The accuracy of the identification results is higher for cases $\lambda_1=5$, $\lambda_2=2$, i.e., $\lambda_1>\lambda_2$, when the stopping criterion is the same. This can be explained in Fig. 7 in which the temperature distributions on the outer surface of the whole domain are plotted for four conductivity distributions. In the figure, when the conductivity distributions are 2 and 5, 5 and 2, 2 and 20, and 20 and 2 for λ_1 and λ_2, the maximum temperature differences are 6, 9, 8, and 19, respectively. The larger λ_1 in the conductivity pair results in a larger maximum temperature difference on the outer surface of the whole domain, which makes the measured temperature curve easier to reflect the shape of the interface. In addition, all these identification results were obtained within 20 s.

Table 2 AREs of identification results of the interfacial configuration with measurement error considered

	ARE			
σ	$\lambda_1=2$; $\lambda_2=5$	$\lambda_1=2$; $\lambda_2=20$	$\lambda_1=5$; $\lambda_2=2$	$\lambda_1=20$; $\lambda_2=2$
0.1	1.29%	3.83%	0.54%	0.25%
0.5	9.52%	6.28%	2.08%	1.29%
1.0	9.74%	6.43%	4.06%	1.89%

Table 3 AREs of identification results when the number of measurement points is reduced to 12 and 6

		ARE			
	σ	$\lambda_1=2$; $\lambda_2=5$	$\lambda_1=2$; $\lambda_2=20$	$\lambda_1=5$; $\lambda_2=2$	$\lambda_1=20$; $\lambda_2=2$
12 points	0.1	1.1%	3.9%	0.4%	0.2%
	0.5	7.0%	7.3%	1.5%	0.7%
	1.0	8.0%	7.9%	3.1%	1.1%
6 points	0.1	1.6%	4.5%	0.3%	0.4%
	0.5	6.5%	6.9%	3.3%	0.7%
	1.0	8.1%	6.7%	3.9%	1.2%

Figures 8 and 9 show the effect of the measurement error on the identification results of the interfacial configuration. Here $\sigma=0.1$, 0.5, and 1.0 represent about 0.2%, 1.0%, and 2.0% of the average measured temperature, respectively. The stopping criterion can be obtained by the discrepancy principle given in Eq. (8*c*). The AREs of the identification results are reported in Table 2. From both the figures and the table one can see that the maximum ARE is less than 10%. The identification results are not sensitive to these mea-

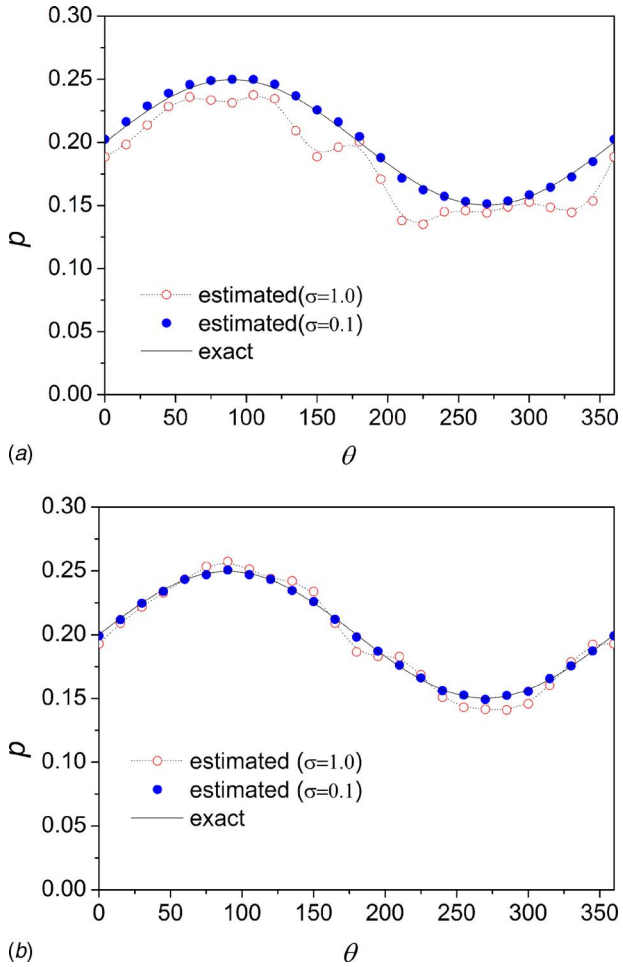

Fig. 10 Identification results of the interfacial configuration when the number of measurement points is reduced to 12: (*a*) $\lambda_1=2$, $\lambda_2=5$ and (*b*) $\lambda_1=5$, $\lambda_2=2$

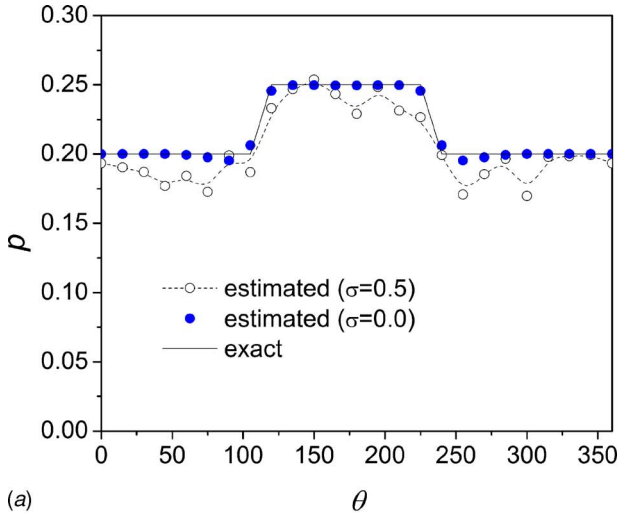

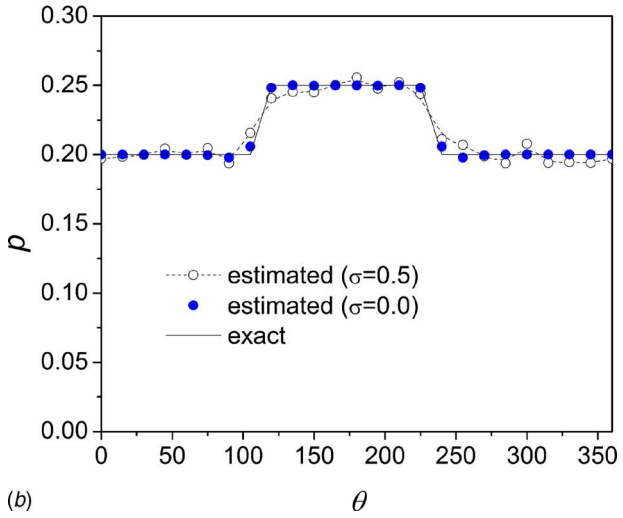

Fig. 11 Identification results of the interfacial configuration with 24 measurement points for test case II: (*a*) $\lambda_1=2$, $\lambda_2=5$ and (*b*) $\lambda_1=5$, $\lambda_2=2$

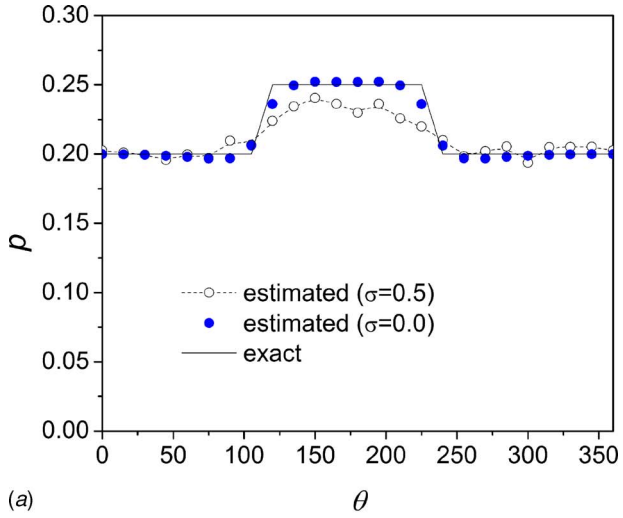

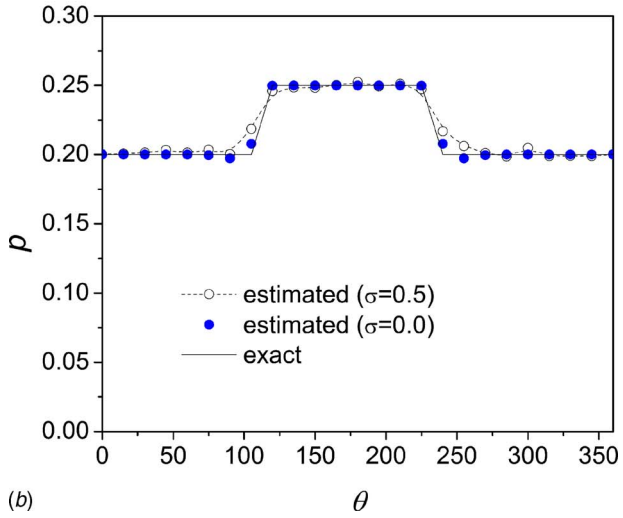

Fig. 12 Identification results of the interfacial configuration with 24 measurement points for test case II: (*a*) $\lambda_1=2$, $\lambda_2=20$ and (*b*) $\lambda_1=20$, $\lambda_2=2$

surement errors, and the solutions are good enough to be accepted as the inverse solutions of the identification problem [4,5]. From the figures, one can also see that the effect of the measurement error is relatively obvious for the case when λ_1 is smaller and that the results with higher accuracy can be obtained when the difference between λ_1 and λ_2 is increased due to the larger maximum temperature difference, as is shown in Fig. 7, on the outer surface of the domain.

The above test cases seem unrealistic since too many sensors are used in the numerical experiments. Can the number of sensors be reduced with the present approach? Table 3 answered this question, in which the number of the sensors on the outer surface of the domain is reduced to 12 and 6, respectively. In Fig. 10, both the estimated points and the *B*-spline fitting lines are also plotted for $\sigma=1.0$ and $\sigma=0.1$ when 12 temperature measurement points are used. It should be mentioned that 24 discrete points are still used to simulate the temperature measurement, and the temperature readings of the 6 and 12 points distribute uniformly along the outer boundary. In order for the convenience to compare the results with previous ones, interpolation is used to get a 24-point interfacial geometry and based on which the ARE of the identification result is calculated. From the table, one can see that the ARE of the identification result changes little when the number of temperature measurement points is reduced. This represents that the number of sensors can be reduced when the MODCM is applied.

4.2 Numerical Test Case II. In the second test case, the interfacial configuration is taken as

$$p(\theta)=\begin{cases}0.20, & 0\ \text{deg}\le\theta\le 120\ \text{deg}\\ 0.25, & 120\ \text{deg}<\theta\le 240\ \text{deg}\\ 0.20, & 240\ \text{deg}<\theta<360\ \text{deg}\end{cases} \tag{17}$$

The identification results for both conductivity pairs, i.e., 2–5 and 2–20, are plotted in Figs. 11 and 12, respectively. The stop-

Table 4 AREs of the identification results of the interfacial configuration for test case II

	ARE		
λ_1; λ_2	$\sigma=0.0$	$\sigma=0.5$	$\sigma=1.0$
2; 5	0.8%	5.6%	8.1%
5; 2	0.4%	2.4%	4.0%
2; 20	1.3%	4.0%	5.0%
20; 2	0.2%	1.5%	2.2%

Table 5 AREs of identification results when the number of measurement points is reduced to 12 and 6

		ARE			
	σ	$\lambda_1=2;\ \lambda_2=5$	$\lambda_1=5;\ \lambda_2=2$	$\lambda_1=2;\ \lambda_2=20$	$\lambda_1=20;\ \lambda_2=2$
12 points	0.1	1.5	1.3	4.0	1.3
	0.5	4.0	2.2	4.4	1.7
	1.0	5.0	3.3	5.0	2.0
6 points	0.1	3.2	3.0	5.3	2.9
	0.5	4.9	4.3	5.7	3.1
	1.0	6.2	4.8	6.3	3.3

ping criterion $\varepsilon=0.01$ is adopted for the cases when no measurement error is considered. When the measurement error is in consideration, the stopping criterion is calculated based on Eq. (8*c*). In this case, $\sigma=0.5$ and 1.0 still represent about 1.0% and 2.0% of the average measured temperature, respectively. The AREs of the identification results for a series of specific cases are reported in Table 4 when 24 temperature measurement points are used. From the figures and the table, one can see that the resultant average error of the inverse solutions is smaller than 10%, mostly 5%. Again, the identification results are not sensitive to the measurement error.

In Table 5, the AREs of identification results are reported when the number of the temperature measurement points is reduced to 12 and 6, respectively. From the table it is not difficult to see that confident identification results can still be obtained for this test case. But from the table one can see that the AREs of results with 6 points used are larger than that with 12 points used. The reason is that six points are not enough to describe exactly the interfacial configuration with sharp changes of this test case anymore though confident identification results can still be obtained for these six discrete points of the interfacial configuration, as marked by arrows in Fig. 13. This implies that more temperature measurement points should be used for the interfacial configurations with sharp changes to get more accurate identification results though the number of the measurement points affects little on the results of these specific selected discrete points.

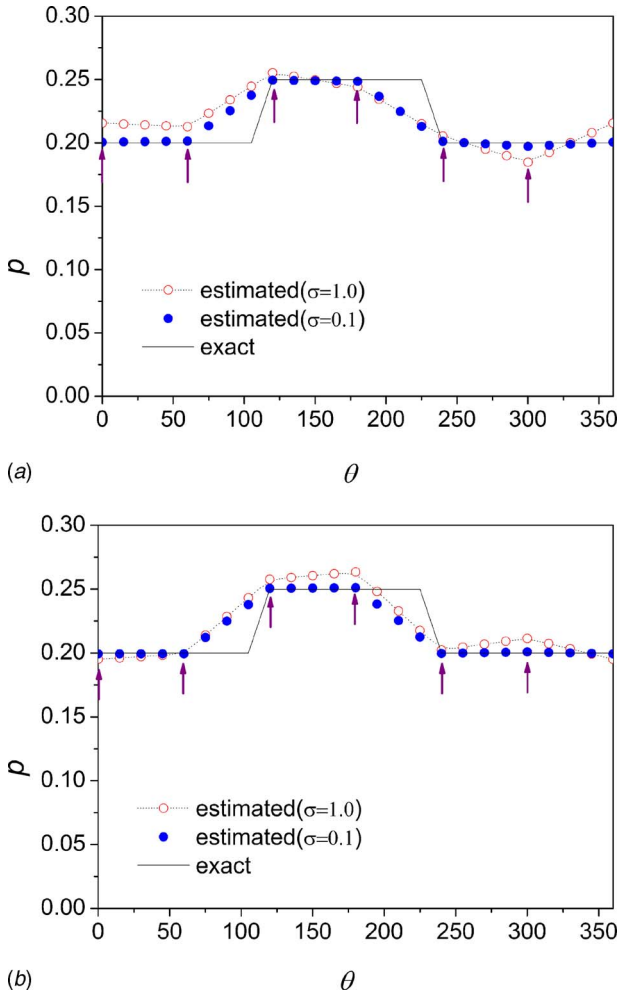

Fig. 13 Identification results of the interfacial configuration when the number of measurement points is reduced to 6: (*a*) $\lambda_1=2$, $\lambda_2=5$ and (*b*) $\lambda_1=5$, $\lambda_2=2$

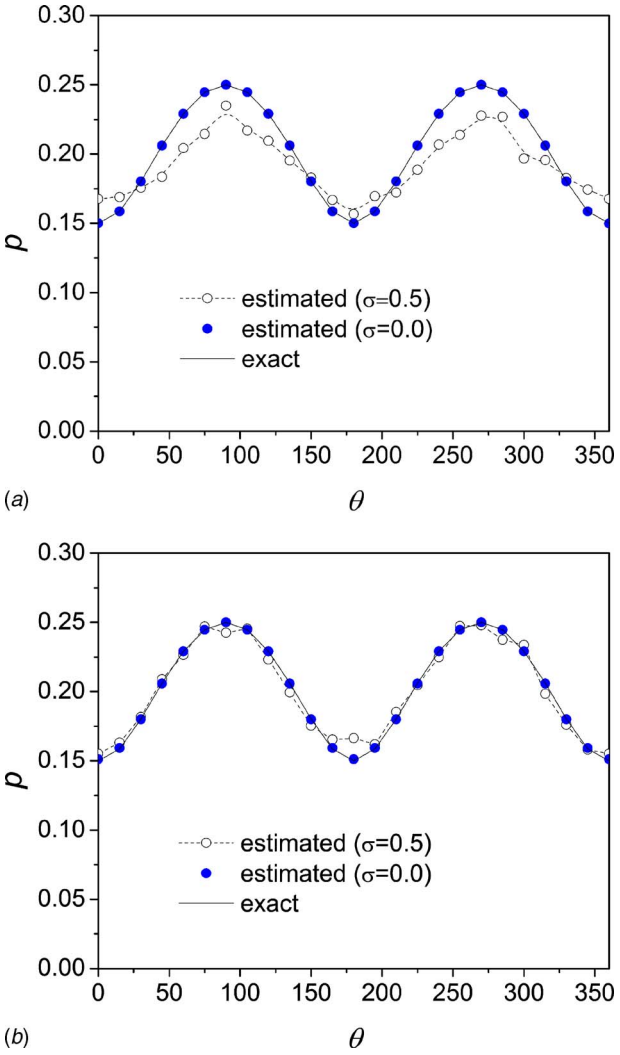

Fig. 14 Identification results of the interfacial configuration with 24 measurement points for test case III: (*a*) $\lambda_1=2$, $\lambda_2=5$ and (*b*) $\lambda_1=5$, $\lambda_2=2$

4.3 Numerical Test Case III. In the third test case, the interfacial configuration is taken as an ellipse with a long axis of 0.25 and a short one of 0.15. This can be expressed as

$$p(\theta)=\sqrt{(0.15\cos\theta)^2+(0.25\sin\theta)^2},\quad 0\ \text{deg}\le\theta<360\ \text{deg} \tag{18}$$

The estimations of the interfacial configuration with 24 temperature measurement points are plotted in Figs. 14 and 15 for

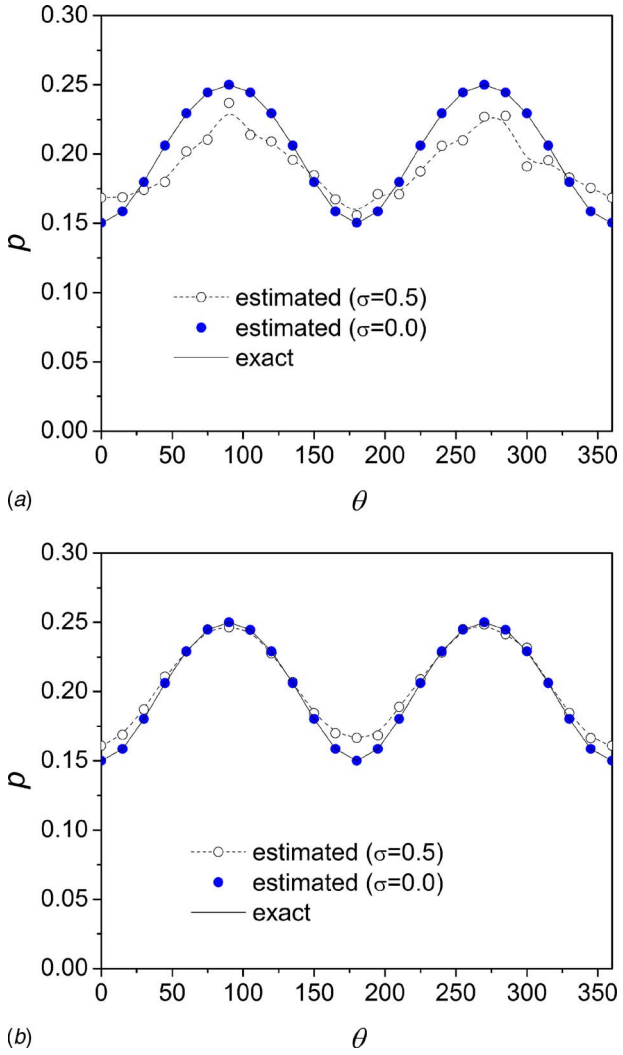

Fig. 15 Identification results of the interfacial configuration with 24 measurement points for test case III: (*a*) $\lambda_1=2$, $\lambda_2=20$ and (*b*) $\lambda_1=20$, $\lambda_2=2$

different kinds of conductivity distributions. More descriptions on the accuracy of the identification results of a series of testing cases, when 24 measurement points are used, are listed in Table 6.

In this subsection, the stopping criterion is $\varepsilon=0.0001$ when no measurement error is considered. The results show that very accurate results can be obtained as long as the stopping criterion is small enough when $\sigma=0$. Though the effect of measurement error to the identification results is relatively obvious when $\lambda_1<\lambda_2$, the results can still be accepted as very good estimations of the interfacial configuration for the AREs are less than 11%. It should also be mentioned that the iteration process is very fast since all these identification results are obtained within 1 min.

Table 6 AREs of the identification results of the interfacial configuration for test case III

	ARE		
λ_1; λ_2	$\sigma=0.0$	$\sigma=0.5$	$\sigma=1.0$
2; 5	0.02%	7.7%	8.3%
5; 2	0.01%	2.4%	3.9%
2; 20	0.1%	8.3%	10.4%
20; 2	0.003%	2.7%	2.9%

Table 7 AREs of identification results for different *C* in the stopping criterion for cases II and III

			ARE			
	λ_1; λ_2	σ	$C=10$	$C=1$	$C=0.1$	$C=0.01$
Case II	5; 2	0.1	1.1%	1.0%	1.0%	0.9%
		0.5	3.2%	2.4%	2.4%	2.7%
	2; 5	0.1	5.8%	1.5%	1.5%	9.3%
		0.5	9.3%	5.6%	5.0%	14.7%
Case III	2; 5	0.1	12.3%	1.6%	1.4%	1.3%
		0.5	15.8%	7.7%	4.4%	6.2%
	5; 2	0.1	1.8%	0.9%	0.7%	0.8%
		0.5	5.5%	2.4%	2.4%	2.5%

In Table 7, the effect of the value of the constant C on the precision level of identification results is studied for this test case and case II with sharp changes in the interfacial configuration. From the table, one can see that the value of ARE decreases when the constant C is reduced from 10 to 0.1, and then it begins to fluctuate for most examples when $C=0.01$. But for $C=1$ and $C=0.1$, the AREs have not much difference and most of them are less than 5%. This implies that it is appropriate to use $C=1$ to calculate the stopping criterion of the iteration for the test cases in this paper.

From the preceding three numerical test cases, it was concluded that the MODCM is now applied successfully in this two-dimensional inverse geometry problem for predicting the unknown interfacial configurations.

5 Conclusions

The modified one-dimensional correction method was successfully applied for the solution of the shape identification problem to determine the unknown irregular interfacial configuration by utilizing temperature readings on the outer surface of the whole domain. Several test cases involving different functional forms of the unknown interfacial configuration, different measurement errors, and different measurement point numbers were considered. The numerical testing results conclude that (i) the identification results with very high accuracy can be obtained as long as the temperature measurement is precise, (ii) a very good identification result (ARE$\leq$10.0%) of the interfacial configuration can also be obtained when the measurement error is considered, (iii) the rate of convergence is fast using the MODCM, and (iv) the number of sensors can be reduced to 12 or 6 without affecting obviously the accuracy of the inverse solution.

Acknowledgment

The authors would like to acknowledge the financial support from the Natural Science Foundation of NUE, Grant No. HGDJJ05009.

Nomenclature

- C = constant
- $\mathbf{P}$ = vector of the interfacial configuration
- $\mathbf{P}'$ = vector of the correction term
- $\mathbf{P}''$ = vector of the correction term
- $\mathbf{T}$ = vector of the temperature distribution on the outer surface
- $\mathbf{W}$ = vector of the random number
- t = temperature
- n = iteration number
- h = film coefficient
- $\boldsymbol{n}$ = normal vector
- q = heat flux

e = modification coefficient

Greek Symbols

λ = thermal conductivity
Ω = domain
δ = domain thickness in Fig. 3
ε = stopping criterion of iteration
σ = standard deviation of temperature measurement

Subscripts

in = inner surface
ou = outer surface
int = interface
f = fluid inside the inner surface
∞ = fluid outside the domain
1D = one-dimensional
o = original measured temperature
m = number of discrete points
l = node layer of the whole domain
li = node layer of the inner domain

References

[1] Hsieh, C. K., and Su, K. U., 1980, "A Methodology of Predicting Cavity Geometry Based on Scanned Surface Temperature Data-Prescribed Surface Temperature at the Cavity Side," ASME J. Heat Transfer, **102**, pp. 324–329.

[2] Hsieh, C. K., and Su, K. U., 1981, "A Methodology of Predicting Cavity Geometry Based on the Scanned Surface Temperature Data-Prescribed Heat Flux at the Cavity Side," ASME J. Heat Transfer , **103**, pp. 42–46.

[3] Cheng, C. H., Lin, H. H., and Aung, W., 2003, "Optimal Shape Design for Packaging Containing Heating Elements by Inverse Heat Transfer Method," Heat Mass Transfer, **39**, pp. 687–692.

[4] Cheng, C. H., and Chang, M. H., 2003, "Shape Design for a Cylinder With Uniform Temperature Distribution on the Outer Surface by Inverse Heat Transfer Method," Int. J. Heat Mass Transfer, **46**, pp. 101–111.

[5] Huang, C. H., and Shih, C. C., 2005, "Identify the Interfacial Configurations in a Multiple Region Domain Problem," J. Thermophys. Heat Transfer, **19**, pp. 533–541.

[6] Huang, C. H., and Chao, B. H., 1997, "An Inverse Geometry Problem in Identifying Irregular Boundary Configurations," Int. J. Heat Mass Transfer, **40**, pp. 2045–2053.

[7] Huang, C. H., and Tsai, C. C., 1998, "A Transient Inverse Two-Dimensional Geometry Problem in Estimating Time-Dependent Irregular Boundary Configurations," Int. J. Heat Mass Transfer, **41**, pp. 1707–1718.

[8] Huang, C. H., Chiang, C. C., and Chen, H. M., 1998, "Shape Identification Problem in Estimating Geometry of Multiple Cavities," J. Thermophys. Heat Transfer, **12**, pp. 270–277.

[9] Fan, C. L., Sun, F. R., and Yang, L., 2005, "A General Quantitative Identification Algorithm of Subsurface Defect for Infrared Thermography," *Proceedings of the Joint 30th International Conference on Infrared Millimeter Waves and 13th International Conference on Terahertz Electronics*, Williamsburg, VA, Vol. 2, pp. 341–342.

[10] Fan, C. L., Sun, F. R., Yang, L., and Liu, B. H., 2006, "Study on a New Quantitative Thermographic Evaluation Method of Three-Dimensional Subsurface Defect for Electric Apparatus," Proc. Chin. Soc. Electr. Eng., **26**, pp. 159–164.

[11] Fan, C. L., Sun, F. R., and Yang, L., 2007, "An Algorithm Study on the Identification of Pipe's Irregular Inner Boundary Based on Thermographic Temperature Measurement," Meas. Sci. Technol., **18**, pp. 2170–2177.

[12] Fan, C. L., Sun, F. R., and Yang, L., 2007, "An Algorithm Study on Identification of the Subsurface Defect for Infrared Thermography," J. Eng. Thermophys., **28**, pp. 304–306.

[13] Su, C. R., and Chen, C. K., 2007, "Geometry Estimation of the Furnace Inner Wall by an Inverse Approach," Int. J. Heat Mass Transfer, **50**, pp. 3767–3773.

[14] Yang, L., Geng, W., Jiang, L., Zou, L., and Hong, J., 1999, "Profile Identification in Dynamic Infrared Thermography: Adaptability and Stability," Int. J. Infrared Millim. Waves, **20**, pp. 623–634.

[15] Fan, C. L., Sun, F. R., and Yang, L., 2007, "A Modified One-Dimensional Correction Method for Multidimensional Thermographic Inner Pipe Boundary Identification," Int. J. Heat Mass Transfer, submitted.

[16] Huang, C. H., and Chen, H. M., 1999, "An Inverse Geometry Problem of Identifying Growth of Boundary Shapes in Multiple Region Domain," Numer. Heat Transfer, Part A, **35**, pp. 435–450.

[17] Ozisik, M. N., and Orlande, H. R. B., 2000, *Inverse Heat Transfer: Fundamentals and Applications*, Taylor & Francis, New York.

[18] Alifanov, O. M., 1994, *Inverse Heat Transfer Problems*, Springer-Verlag, New York.

Condensation Heat Transfer of Carbon Dioxide Inside Horizontal Smooth and Microfin Tubes at Low Temperatures

Yoon Jo Kim
The George W. Woodruff School of Mechanical Engineering,
Georgia Institute of Technology,
Atlanta, GA 30332
e-mail: yoonjo.kim@me.gatech.edu

Jeremy Jang

Predrag S. Hrnjak

Department of Mechanical Science and Engineering,
University of Illinois at Urbana-Champaign,
Urbana, IL 61801

Min Soo Kim
School of Mechanical and Aerospace Engineering,
Seoul National University,
Seoul 151-742, Korea

This paper presents heat transfer data for the condensation of CO_2 at low temperatures in horizontal smooth and microfin tubes. The test tubes included a 3.48 mm inner diameter smooth tube and a 3.51 mm melt-down diameter microfin tube. The test was performed over a mass flux range of 200–800 kg/m^2 s and at saturation temperatures of $-25°C$ and $-15°C$, respectively. The effect of various parameters—diameter, mass flux, vapor quality, and temperature difference between inner wall and refrigerant—on heat transfer coefficient and enhancement factor is analyzed. The data are compared with several correlations. The existing correlations for the smooth tube mostly overpredicted the heat transfer coefficients of the present study, which is possibly resulted from the characteristics of carbon dioxide as a "high pressure refrigerant." For the microfin tubes, due to the complexity and variety of fin geometry and flow mechanisms in microfin tubes, most of the correlations for the microfin tube were not applicable for the experimental data of the present study. The average enhancement factors and penalty factors evidenced that it was not always true that the internally finned geometry guaranteed the superior in-tube condensation performance of the microfin tube in refrigeration and air-conditioning systems. [DOI: 10.1115/1.2993139]

Keywords: carbon dioxide, microfin tube, heat transfer coefficient, low temperature, two-phase

1 Introduction

One of the most common techniques for augmenting in-tube condensation in refrigeration and air-conditioning systems is the use of microfin tubes developed at the end of 1970. However, in spite of the recent interest in CO_2, little, if any, experimental data or analysis on the condensation of CO_2 in the microfin tube has not been presented. It is mainly because in the typical operating range of refrigeration and air-conditioning systems, the "gas cooling" process usually occurs, not "condensation" process of CO_2. But some applications need a low temperature level, harmless and odorless working fluids. CO_2, as a natural refrigerant, could be a solution for this application such as a secondary loop of a "cascade system."

Typical microfin tubes available for industrial applications are made of copper and have an outside diameter from 4 mm to 15 mm, a single set of 50–70 spiral fins with a helix angle from 6 deg to 30 deg, a fin height from 0.1 mm to 0.25 mm, and triangular or trapezoidal fin shapes with an apex angle from 25 deg to 90 deg [1]. Although there are some tests showing that the local enhancement factor (EF) (ratio of the microfin tube heat transfer coefficient to the smooth tube heat transfer coefficient that is obtained from the tests with equivalent diameters at the same operating conditions) can be less than 1 at specific operating conditions and the microfin tube geometry [2], microfin tubes generally enhance the heat transfer performance by a factor of 1.5–2.8 with a slight increase in the pressure drop when compared with a smooth tube having an equivalent diameter at the same operating conditions [3]. The enhancement mechanism is generally explained by three major factors: (i) increase in the effective area, (ii) liquid drainage due to the surface tension, and (iii) turbulence induced in the liquid film by the microfins.

In this paper, the heat transfer data for the condensation of CO_2 at low temperature in horizontal smooth and microfin tubes are presented. To analyze the heat transfer performance and characteristics of microfin tubes, the condensation experiment was performed in a 3.48 mm inner diameter smooth tube and a 3.51 mm melt-down diameter microfin tube. The heat transfer coefficient data from Zilly et al. [4] are used to investigate the effect of the diameter on the heat transfer performance. The ratio of the effective heat transfer area of the microfin tube to the smooth tube is 2.84. To identify the effect of various parameters on heat transfer coefficients and EFs, experiments were performed at several test conditions listed in Table 1. There are many existing semi-empirical correlations that predict the heat transfer coefficient during condensation but a few correlations cover every flow regime during condensation. The experimental data are compared with various heat transfer coefficient correlations during condensation.

2 Literature Review

2.1 Condensation Heat Transfer in Smooth Tubes. Dobson and Chato [5] conducted an experimental study of heat transfer and flow regimes during condensation of refrigerants in horizontal tubes. Tests were performed in smooth horizontal round tubes with diameters ranging from 3.14 mm to 7.04 mm using refrigerants R22, R134a, and R410A and near-azeotropic blends of R32/R125 (50/50 and 60/40 by mass). The authors observed flow regimes and reported that the wavy to wavy-annular flow transition occurs at $Fr_{so}=7$, and the wavy-annular to annular flow transition was well predicted at the value $Fr_{so}=18$. The expression for the modified Froude number suggested by Soliman [6] is given by

Contributed by the Heat Transfer Division of ASME for publication in the JOURNAL OF HEAT TRANSFER. Manuscript received August 13, 2007; final manuscript received August 5, 2008; published online December 11, 2008. Review conducted by Raj M. Manglik.

 Copyright © 2009 by ASME

Table 1 Test conditions in the present study

Description	Present study	Zilly et al. [4]
G (kg/m^2 s)	200, 400, 800	200, 300, 400
T_s (°C)	−25, −15	−25, −15
ΔT (°C)	3, 6	3, 6

$$\mathrm{Fr}_{so} = 0.025\,\mathrm{Re}_l^{1.59}\left(\frac{1+1.09X^{0.039}}{X}\right)^{1.5}\frac{1}{\mathrm{Ga}^{0.5}} \quad \text{for } \mathrm{Re}_l \le 1250 \tag{1a}$$

$$\mathrm{Fr}_{so} = 1.26\,\mathrm{Re}_l^{1.04}\left(\frac{1+1.09X^{0.039}}{X}\right)^{1.5}\frac{1}{\mathrm{Ga}^{0.5}} \quad \text{for } \mathrm{Re}_l > 1250 \tag{1b}$$

Dobson and Chato [5] also proposed a heat transfer coefficient correlation during condensation that consists of two parts: annular flow condensation and wavy flow condensation. Cavallini et al. [7] presented a predicting model to compute the heat transfer coefficient and pressure drop during condensation. The authors stated that existing semi-empirical correlations were not able to predict the heat transfer coefficients for some fluids under extended operative conditions because of their limited validity ranges; even when the validity ranges were appropriate, quite a few procedures display acceptable discrepancies when applied with the new "high pressure" fluids. Recently, El Hajal et al. [8] developed a void fraction model and flow regime map for condensation by slightly modifying the flow pattern map of Kattan et al. [9] that is originally developed for evaporation. The authors mentioned that the homogeneous model is applicable to flows where the vapor and liquid phases travel at nearly the same velocity, such as near the critical point or at very high mass velocities where the flow regime is either bubbly flow or mist flow. They also said that no existing void fraction model is valid over the entire pressure range up to the critical pressure since none tend to approach the homogeneous model as the saturation pressure gets close to the critical pressure. This means that existing void fraction models are only valid over the typical operating range of reduced pressure, while high pressure refrigerants, which has relatively high operating pressure (or reduced pressure), cannot be predicted well by existing void fraction models. The same authors presented a heat transfer model during condensation based on a predeveloped void fraction model and flow regime map [10] as well. The database that is used for developing the correlation covers a very broad range of conditions: mass flux from 24 kg/m^2 s to 1022 kg/m^2 s, vapor qualities from 0.02 to 0.80, and tube inner diameters from 3.1 mm to 21.4 mm.

2.2 Condensation Heat Transfer in Microfin Tubes. Khanpara et al. [11] experimentally investigated the effects of several geometrical parameters (peak shape, valley shape, fin height, number of fins, and spiral angle) on single phase and condensation heat transfer and pressure drop. The authors reported that the average heat transfer coefficient is increased by 45% to 283% over the reference smooth tube value while the pressure drop increase was generally less than 100%. Schlager et al. [12] presented heat transfer and pressure drop data during evaporation and condensation of R22 in horizontal microfin tubes having 9.5 mm outer diameter and 8.9 mm maximum inner diameter. The authors reported that the EFs range from 1.4 to 1.9 for the various test conditions. The heat transfer enhancement is greater than the surface area increase due to the fins, which ranged from 1.38 to 1.55 for the microfin tubes. The same authors conducted similar experimental test with a microfin tube having 12.7 mm outer diameter and 11.7 mm maximum inner diameter [13]. They concluded that no significant differences in performance are observed between 9.52 mm and 12.7 mm microfin tubes. Comparative studies were performed by Eckels and Pate [14] on evaporation and condensation heat transfer coefficients with R134a and R12 in smooth and microfin tubes. They reported that when R134a and R12 were compared at equivalent cooling capacities, the R134a heat transfer coefficients were about 10% higher for both evaporation and condensation. They also showed that the EFs during condensation of R134a varied from 1.75 to 2.5 and that of R12 varied from 1.7 to 2.3, while the penalty factors (PFs) were less than EFs. Eckels and Tesene [15] also conducted comparative studies on the condensation heat transfer in the microfin tube with R22, R134a, R410A, and R407C. Their experimental results reveal that R134a has the highest performance in both the smooth tube and the microfin tube. R22 and R410A had similar performances that were slightly less than R134a, while R407C had the lowest performance of the refrigerants tested. Eckels and Tesene [15] also reported an interesting experimental result; heat transfer coefficients decrease at first as the mass flux increases, then heat transfer coefficients increase at the higher mass fluxes. The authors explained that the complex interactions between surface fins and fluid could contribute to this effect. Yang and Webb [16] proposed a predictive model for condensation in small hydraulic diameter tubes having axial microfins. With this analysis, they evidenced that the surface tension drainage effect on the heat transfer in microfin tubes is significant at low mass flux and high vapor quality region where the fin tip is still unflooded, while at high mass flux this effect is not as strong due to the higher vapor shear force at high vapor quality. The authors also reported that a smaller fin tip radius provides a higher surface tension force. Zilly et al. [4] conducted experimental studies on condensation of CO_2 at low temperatures in the microfin tube. The experiments were performed in a smooth tube with a diameter of 6.10 mm and a microfin tube with a melt-down diameter of 6.26 mm for mass fluxes ranging from 200 kg/m^2 s to 400 kg/m^2 s. The authors showed that the local EFs varied from 2.0 to 3.6, and the local PFs varied from 1.1 to 2.2 and from 1.1 to 1.6 for horizontal and vertical tubes, respectively. They also reported that the effect of the mass flux on microfin tube heat transfer coefficients was negligible, which is different from the general trend of heat transfer coefficients in horizontal microfin tubes. Jang and Hrnjak [17] continued and supplemented the work of Zilly et al. [4] with additional experiments and visualization. They showed that existing heat transfer coefficient correlations significantly overpredicted the experimental results. Various types of predictive models for heat transfer coefficients during condensation in microfin tubes were proposed by Luu and Bergles [18], Kaushik and Azer [19], Cavallini et al. [20], Shikazono et al. [21], Yu and Koyama [22], Kedzierski and Goncalves [2], Nozu and Honda [23], and Goto et al. [24]. Due to the complexity and variety of fin geometry and flow mechanism in microfin tubes, to the authors' knowledge, the effort to try to find a truly robust predictive model is still necessary.

3 Experimental Facility

3.1 Experimental Test Setup. Figure 1 shows a simplified sketch of the testing facility. The flow in the loop is driven by a variable speed gear pump (1). Following the pump, the refrigerant flow is measured by a Coriolis flow meter (2). A calorimeter (3) is used to bring the subcooled liquid refrigerant to the desired state at the inlet of the test section. The calorimeter has two parallel electrical heaters. Each heater is inside a copper tube with the refrigerant flowing through the spirally articulated annulus. By adjusting the power to the calorimeter the quality of CO_2 at the test section is regulated. After the calorimeter the refrigerant flows along a horizontal pipe of 1 m length to establish a flow pattern dependent on mass flux and quality. The refrigerant then enters the test section (4), which is described in detail in Sec. 3.2. After leaving the test section, CO_2 flows through a control heater (5), which evaporates liquid CO_2 in order to keep the pressure of the system at the particular level. This control heater is similar to the calorimeter. The amount of heat to the control heater is regulated

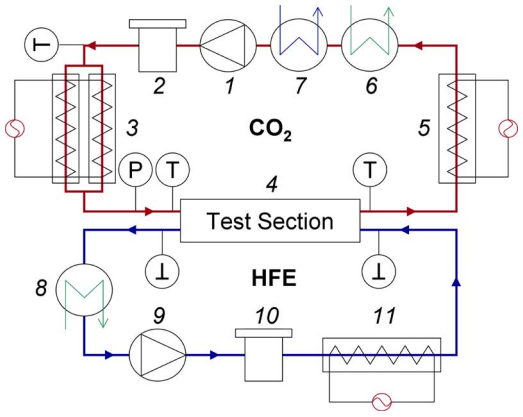

Fig. 1 Simplified schematic of the experimental facility

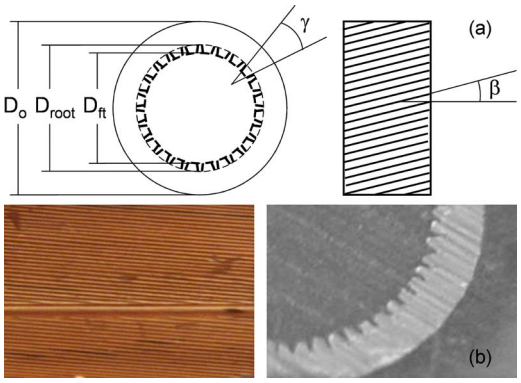

Fig. 3 (*a*) Sketches of common microfin tubes and (*b*) photos of the microfin tube used in the present study

by a PID regulator that uses the pressure measurement as an input value. The refrigerant is then condensed by the primary heat exchanger (6) with R-404A flowing on the other side and finally subcooled by the subcooling unit (7) prior to returning to the pump. Similar to the CO_2 loop, the hydrofluoroether (HFE) (HFE7100 by 3M is used as a low temperature single phase secondary coolant) starts at a plate heat exchanger (8) with R404A evaporating on the other side. The R404a loop for the HFE is independent of the R404a loop for CO_2. After the plate heat exchanger, the constant speed circulating pump (9) is placed with a bypass to control the flow and then Coriolis flow meter (10) and HFE control heater (11) are installed, which are similar to the flow meters and the heaters in the CO_2 loop, except that there is only one heater for the HFE heater (as opposed to the pair of heaters for the calorimeter). As depicted in Fig. 1, the temperatures of the calorimeter inlet and outlet (or the test section refrigerant inlet), the test section refrigerant outlet, and the test section HFE inlet and outlet are measured using T-type thermocouples. For the saturation pressure of CO_2, the absolute pressure transducer is installed at the test section inlet.

3.2 Test Section. The condenser test section consists of an inner test section tube where CO_2 flows, a two-part brass jacket that creates a uniform wall temperature at the test section tube, and outer pipes soldered around the perimeter of the brass jacket where HFE flows (see Fig. 2(*b*)). Figure 2(*a*) demonstrates the flow path of HFE. The HFE flow is first branched to the back and front of the brass jacket. The branch at the back leads to eight parallel sub-branches going over the top to the front of the brass jacket; each sub-branch then connects to a single pipe that combines the eight flows. Directly underneath this pipe is the front branch, which has eight sub-branches going from the front to the back traveling underneath the brass jacket; again, the sub-branches connect to a flow-combining pipe running along the back underneath the back branch. The two combining pipes join afterward to continue the flow. The test section tube has 12 wall thermocouples soldered into machined grooves. The physical dimensions of the condenser test tube and the locations of the thermocouples are depicted in Fig. 2(*c*). For the case of the microfin tubes and 3 mm inner diameter smooth tube, the tube is placed inside of a larger copper tube that has the same outer diameter as that of the smooth tube; the gap is then filled with tin. Figure 3 shows the sketches of common microfin tubes and photos of the microfin tube with the melt-down diameter of 3.51 mm used in the present study. Table 2 reports various dimensions of the tubes used in the experiments of the present study and Zilly et al. [4]. The outer diameter in Table 2 refers to the outer diameter of the microfin tube prior to being soldered into a larger copper tube. The melt-down diameter is the inner diameter of a hypothetical smooth tube with the same outer diameter and cross-sectional area as that of the microfin tube.

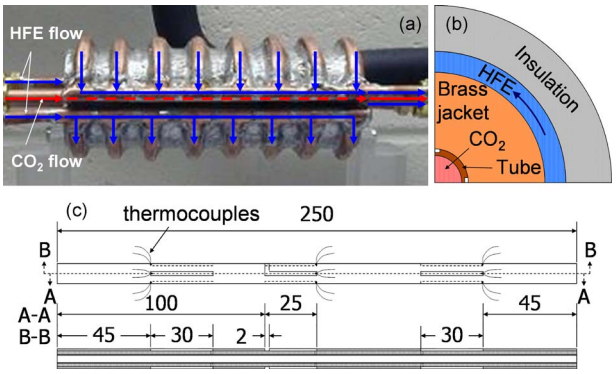

Fig. 2 (*a*) Photo and (*b*) cross-sectional view of the condenser test section and (*c*) sketch of the condenser test tube with thermocouple attachment

4 Data Reduction

The equation used to calculate the heat transfer coefficient h is given by

Table 2 Dimensions of the tubes used in the present study

	Zilly et al. [4]	Present study
Description	Microfin tubes	
Outer diameter, D_o	6.98 mm	4.34 mm
Root diameter, D_{root}	6.32 mm	3.74 mm
Fin tip diameter, D_{ft}	5.97 mm	3.30 mm
Melt-down diameter, D_{melt}	6.26 mm	3.51 mm
Hydraulic diameter, D_h	3.95 mm	1.25 mm
Fin height	0.18 mm	0.22 mm
Fin base length	0.12 mm	0.17 mm
Gap between fins	0.17 mm	0.04 mm
Perimeter, $\tilde{P}$	31.0 mm	30.9 mm
No. of fins	54	57
Helix angle, β	14 deg	6 deg
Apex angle, γ	24 deg	30 deg
Description	Smooth tubes	
Outer diameter, D_o	9.60 mm	5.00 mm
Inner diameter, D_i	6.10 mm	3.48 mm

$$\dot{Q}_{CO_2} = hA_{surf}(T_{CO_2} - T_{wall}) \quad (2)$$

where $\dot{Q}_{CO_2}$ is the heat transferred from CO_2 to the HFE, A_{surf} is the surface area inside of the test section tube (for the case of microfin tubes, the melt-down diameter was used), and T_{CO_2} is the saturation temperature of CO_2 corresponding to the measured pressure. Since T_{wall} is the average of the 12 measured wall temperatures, Eq. (2) yields the averaged local heat transfer coefficient. And $\dot{Q}_{CO_2}$ is given by the following equation:

$$\dot{Q}_{CO_2} = \dot{Q}_{HFE} - \dot{Q}_{ext,HFE} - \dot{Q}_{cond} \quad (3)$$

where $\dot{Q}_{HFE}$ is the total heat transferred to the HFE, $\dot{Q}_{ext,HFE}$ is the external heat transferred to the HFE from the environment, and $\dot{Q}_{cond}$ is the heat transferred to the HFE due to the conduction along the pipe just before and after the test section. Due to the relatively small values of heat being transferred in the test section, it is important to determine the heat transferred to the cooling fluid (HFE) by conduction along the section of the pipe before and after the test section. The details of calculating the value of $\dot{Q}_{cond}$ are described by Zilly et al. [4]. $\dot{Q}_{HFE}$ is calculated from the following equation:

$$\dot{Q}_{HFE} = \dot{m}_{HFE} c_{p,HFE}(T_{HFE,o} - T_{HFE,i}) \quad (4)$$

where $\dot{m}_{HFE}$ is the measured mass flow rate of the HFE, $T_{HFE,o}$ is the measured temperature of the HFE exiting the test section, $T_{HFE,i}$ is the measured temperature of the HFE entering the test section, and $c_{p,HFE}$ is the specific heat of HFE given by

$$c_{p,HFE} = c_{p,HFE,offset} + 0.002\frac{(T_{HFE,i}(^\circ C) + T_{HFE,o}(^\circ C))}{2} \quad (5)$$

This equation was provided by the manufacturers of HFE (3M). Note that $T_{HFE,i}$ and $T_{HFE,o}$ must be in °C for Eq. (5) to work.

$\dot{Q}_{ext,HFE}$ is calculated from the following equation:

$$\dot{Q}_{ext,HFE} = (UA)_{test}\text{LMTD} \quad (6)$$

where $(UA)_{test}$ is the UA value of the test section determined by calibration and LMTD is the log mean temperature difference between the HFE and the room air.

The quality of CO_2 at the inlet of the test section x_i is found using two other thermodynamic properties, namely, the inlet enthalpy i_i and pressure P_i. The enthalpy at the inlet i_i is controlled by a calorimeter; the equation used to calculate i_i is

$$\dot{Q}_{cal} = \dot{m}_{CO_2}(i_i - i_{cal,i}) - \dot{Q}_{ext,cal} - \dot{Q}_{ext,pipe} \quad (7)$$

where $\dot{Q}_{cal}$ is the controlled heat input from the calorimeter and $\dot{m}_{CO_2}$ is the measured mass flow rate of CO_2. $i_{cal,i}$ is the enthalpy of CO_2 at the inlet to the calorimeter; it is evaluated using two measured thermodynamic properties, namely, $T_{cal,i}$ and $P_{cal,i}$. $\dot{Q}_{ext,cal}$ and $\dot{Q}_{ext,pipe}$ are external heat inputs to the calorimeter and piping between the calorimeter and test section, respectively; both are evaluated in a similar fashion as $\dot{Q}_{ext,HFE}$. The outlet quality x_o and representative vapor quality x are calculated using the following equations:

$$\dot{Q}_{CO_2} = \dot{m}_{CO_2} i_{lv}(x_i - x_o) \quad (8a)$$

$$x = \frac{x_i + x_o}{2} \quad (8b)$$

where i_{lv} is the enthalpy of vaporization of CO_2.

EF is calculated by the following equation:

$$\text{EF} = \frac{h_{en}}{h_{sm}} \quad (9)$$

where h_{en} and h_{sm} are the heat transfer coefficients during condensation in microfin and smooth tubes having equivalent diameter at the same operating conditions.

5 Experimental Uncertainty

The experimental uncertainties of the heat transfer coefficients reported in this paper were estimated with the Taylor simplification error propagation described in Ref. [25]. All uncertainty data are based on a confidence level of 95%.

Measured parameters are temperature, mass flow rate, absolute pressure, and electrical power input. The uncertainty for temperature reading is 0.1 K for calibrated thermocouples relative to each other. One of the most important measurements at the test section is the inlet and outlet temperatures of the HFE flow. From this temperature difference the heat flow and the heat transfer coefficient are calculated. At the test section, 12 thermocouples measure the mean wall temperature. Calibration was done by using the setup of the test rig including cables, datalogger, and reference temperature. The uncertainties of these instruments are therefore included in the uncertainty of the thermocouples. The corresponding wall temperature measurement accuracy is 0.1 K. The mass flow is measured with Coriolis flow meters for both refrigerant and coolant (HFE) mass flow. The uncertainty of these meters is almost constant at 0.15% of the reading for mass flow rates above 4% of full scale. The uncertainty in the absolute pressure measurement is 0.1% of the maximum range 3446.43 kPa (500 psi). Since the saturation temperature was evaluated using the pressure measurement, considering Clasius–Clapeyron relation, the uncertainties of the saturation temperature were estimated to be almost constant at ±0.29% and ±0.39% for saturation temperatures of −25 °C and −15 °C, respectively. As a consequence, uncertainties of the temperature difference between the tube wall and the refrigerant were estimated to be ±0.47% and ±0.75% for saturation temperatures of −25 °C and −15 °C, respectively. The uncertainty differences between the 6 °C and 3 °C temperature differences are negligibly small. The uncertainty in the output value of the electrical power transducer is given as 0.2% of the measured value.

Applying error propagation analysis to Eq. (2) including all the variables used for calculating heat transfer coefficients estimates the uncertainty of the heat transfer coefficients. The estimated uncertainties range from ±7.1% to ±19.6% and from ±6.3% to ±25.6% in the smooth and microfin tubes, respectively. Also, the uncertainties of the vapor quality and EFs can be calculated with error propagation analysis using Eqs. (8*a*), (8*b*), and (9). The estimated vapor quality uncertainty ranges from ±1.8% to ±26.2% (at the lowest vapor quality) and that of EFs ranges from ±7.8% to 24.6%.

6 Results and Discussion

6.1 Heat Transfer Coefficients Inside Smooth Tube. Many researchers have given their effort to predict the heat transfer characteristics during condensation in smooth tubes, and several types of predictive models have been reported. Chato [26] and Jaster and Kosky [27] proposed correlations for the heat transfer coefficients during wavy flow condensation based on Nusselt's analysis of the filmwise condensation problem. For the annular flow condensation, Akers et al. [28], Cavallini and Zecchin [29], Shah [30], and Chen et al. [31] proposed the predictive models. Those correlations were applied to the present study with the flow regime transition criteria of Dobson and Chato [5]. The correlations of Jaster and Kosky [27] and Chen et al. [31] predicted heat transfer coefficients in the present study relatively well for the wavy flow and annular flow condensation, respectively. The correlations of Bivens and Yokozeki [32], Dobson and Chato [5], Cavallini et al. [7], and Thome et al. [10] cover every flow regime during

Table 3 The mean absolute deviations of the heat transfer coefficient predictions using several heat transfer coefficient correlations from the measured heat transfer coefficient in smooth tubes

Correlations	Zilly et al. [4]	Present study	Total
Bivens and Yokozeki [32]	22.4%	23.9%	23.0%
Dobson and Chato [5]	51.0%	56.9%	53.2%
Cavallini et al. [7]	33.5%	35.2%	34.1%
Thome et al. [10]	22.1%	20.9%	21.7%

condensation, and the mean absolute deviations of the heat transfer coefficient of the present study and Zilly et al. [4] from those correlations, defined as Eq. (10), are listed in Table 3.

$$E_{\text{abs}} = \frac{\sum \frac{|h_{\text{pred}} - h_{\text{meas}}|}{h_{\text{meas}}}}{N} \times 100\ (\%) \tag{10}$$

As evidenced by Cavallini et al. [7], when existing predictive models are applied to some of refrigerants that are operated at relatively high pressure, the predictive models usually overestimate the experimental data. Although CO_2 is not one of the refrigerants included in the comparative study of Cavallini et al. [7] and even the pressure range of the present study is significantly lower than the typical operating range, CO_2 is still the relatively high pressure refrigerant. This can be the explanation for the overpredictions of the experimental data of Zilly et al. [4] and the present study with most of the correlations. As seen in Table 3, the correlations of Bivens and Yokozeki [32] and Thome et al. [10] show higher accuracies than the others. The correlation of Bivens and Yokozeki [32] was developed by slightly modifying the correlation of Shah [30], which is only applicable to annular flow condensation and low mass flux condition. The authors introduced an empirical term, which contains mass flux and makes the predicted heat transfer coefficients smaller than that of Shah [30] over the mass flux around 170 $\text{kg/m}^2\,\text{s}$. Consequently, the degree of overprediction of the correlation by Bivens and Yokozeki [32] is smaller than the others, which makes the correlation of Bivens and Yokozeki [32] to be in relatively good agreement with the experimental data of the present study. However, as shown in the comparative study of García-Valladares [33], the predicted heat transfer coefficients by the correlation of Bivens and Yokozeki [32] have almost the same trend with that of Shah [30], of which the use needs to be essentially limited to annular flow condensation. The correlation of Thome et al. [10] shows E_{abs} of 22.1%, 20.9%, and 21.8% for the experimental data in smooth tubes of Zilly et al. [4], present study, and total, respectively. The model of Thome et al. [10] was developed based on the new void fraction model developed by El Hajal et al. [8]. The new void fraction model (the authors named it as LMε-model) is the logarithmic mean of the values of homogeneous void fraction and void fraction of Rouhani and Axelsson [34]. This simple work enabled the new void fraction model to be applicable to the refrigerants having high reduced pressure as well, which is a possible explanation for the relatively high accuracy of the correlation of Thome et al. [10].

Figure 4(*a*) shows the effect of temperature difference between tube inner wall and saturated refrigerant on heat transfer coefficients in the smooth tube. During wavy flow condensation at sufficiently low mass flux, heat is transferred in the upper portion of the tube by filmwise condensation and in the pool at the bottom of the tube by forced-convective condensation [5]. The larger the temperature difference is, the thicker the liquid film on the upper part of the tube is. Thus, the larger temperature difference results in the decrease in heat transfer coefficients during wavy flow condensation. On the other hand, during annular flow condensation, it has been known that the temperature difference has almost nothing to do with the condensation heat transfer mechanism. According to the transition criterion of Dobson and Chato [5], at low mass flux (200 $\text{kg/m}^2\,\text{s}$) in Fig. 4(*a*), the transition from wavy to annular flow occurs at the vapor quality around 0.5, while at high mass flux (800 $\text{kg/m}^2\,\text{s}$), 0.15 is the transition vapor quality, which means that the annular flow condensation is the dominant heat transfer mechanism. At low mass flux, Fig. 4(*a*) shows the effect of temperature difference on heat transfer coefficients during wavy flow condensation, i.e., the heat transfer coefficients at smaller temperature difference ($\Delta T = 3\,^\circ\text{C}$) are slightly higher than those at larger temperature difference ($\Delta T = 6\,^\circ\text{C}$). However, at high mass flux, the expected results of annular flow condensation were not observed. Instead, the heat transfer coefficient rather increases with the increase in the temperature difference at high mass flux (800 $\text{kg/m}^2\,\text{s}$). According to the early work of Dukler [35] for the condensation within a vertical tube with the consideration of interfacial shear, at sufficiently high liquid film Reynolds number and low interfacial shear, the heat transfer coefficients increase with the increase in the liquid film Reynolds number, and the trend is reversed at high interfacial shear. As expressed in Eq. (11), the liquid film Reynolds number can be increased by the increase in the temperature difference, ($T_s - T_{\text{wall}}$), or reduction in the liquid film thickness, δ, when the other properties are fixed or slightly varied.

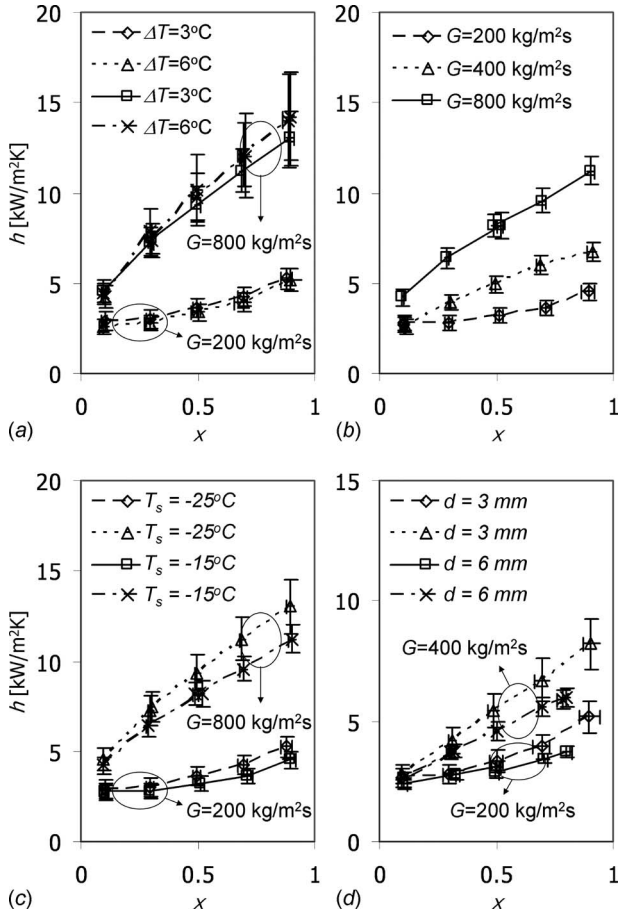

Fig. 4 Effects of (*a*) ΔT (D_i=3.48 mm and T_s=−25°C), (*b*) mass flux (D_i=3.48 mm, T_s=−15°C, and ΔT=3°C), (*c*) saturation temperature (D_i=3.48 mm and ΔT=3°C), and (d) diameter (T_s=−15°C and ΔT=6°C) on the condensation heat transfer coefficient in the smooth tube

$$\mathrm{Re}_{\text{liquid film}} = \frac{4k_l(T_s - T_{\text{wall}})z}{\delta \mu_l i_{lv}} \tag{11}$$

Therefore, at low vapor quality with the mass flux of 800 $\mathrm{kg/m^2\,s}$, it is the wavy flow condensation regime, and thus the smaller temperature difference ($\Delta T = 3\,^\circ\mathrm{C}$) has higher heat transfer coefficients due to the thinner liquid film and reduced thermal resistance. However, as the vapor quality increases, the liquid-vapor shear has more dominant effects on the heat transfer behaviors. Therefore, at the larger temperature difference, the liquid film Reynolds number and thus the heat transfer coefficients have higher values according to Dukler [35]. Moreover, as the vapor quality increases and the film thickness, δ, decreases, the heat transfer coefficients of $\Delta T = 6\,^\circ\mathrm{C}$ are further deviated from those of $\Delta T = 3\,^\circ\mathrm{C}$. It should be, however, noted that the changes in heat transfer coefficients due to the temperature difference are not much significant and even at high mass flux, the variations are less than error bar.

The increase in the vapor quality or mass flux means the increase in the vapor velocity of the refrigerant so that the forced-convective condensation becomes dominant. During forced-convective condensation, heat transfer coefficients strongly depend on the Reynolds number. As expected, in Fig. 4(*b*), the heat transfer coefficients are increased with the increase in the vapor quality and mass flux. The slight exceptional case is shown in the low vapor quality and low mass flux (200 $\mathrm{kg/m^2\,s}$) region, in which the heat transfer coefficients seem to have almost nothing to do with the vapor quality increase and even at the lowest vapor quality, the heat transfer of 200 $\mathrm{kg/m^2\,s}$ is slightly higher than that of 400 $\mathrm{kg/m^2\,s}$. This is because the flow regime of the corresponding region is the wavy flow. In the wavy flow regime, gravity is the dominant factor affecting the heat transfer behaviors so that the increase in the liquid-vapor shear due to the increase in the vapor quality and/or mass flux cannot play a meaningful role. According to Dobson and Chato [5], the transition from wavy to annular flow occurs at the vapor quality about 0.5, which is consistent with the results shown in Fig. 4(*b*). Thus, the flow regime transition can be indirectly observed using the results in Fig. 4(*b*).

The increase in the saturation temperature leads to the increase in the reduced pressure, which means that the flow loses its two-phase flow characteristics, i.e., a decrease in the difference between vapor and liquid velocity, density, viscosity, and so on. Therefore, it is evident that during the annular flow regime, heat transfer coefficients decrease with the increase in the saturation temperature, as shown in Fig. 4(*c*). In the wavy flow regime, at very low vapor velocities, the heat transfer at the bottom of the tube is much smaller than that at the top and can be readily neglected so that Nusselt's solution for external condensation on a cylinder can be used [5]. The mean heat transfer coefficient of Nusselt's theory is given by

$$\bar{h} = 0.943\left[\frac{g}{L\Delta T}\right]^{0.25}\left[\frac{\rho_l(\rho_l - \rho_v)i_{lv}k_l^3}{\mu_l}\right]^{0.25} \tag{12}$$

The last bracketed term, called the property index, depends on the saturation temperature and decreases with the increase in the saturation temperature. This can be the reason for the slight decrease in heat transfer coefficients with an increase in the saturation temperature at low vapor quality and low mass flux (200 $\mathrm{kg/m^2\,s}$).

Figure 4(*d*) shows the effect of the tube diameter on heat transfer coefficients. The heat transfer coefficient data of Zilly et al. [4] are also plotted in Fig. 4(*d*). As expected, the heat transfer coefficients decrease when the diameter of the tube is increased. It should be noted that the difference in heat transfer coefficients is mainly observed in the high quality and high mass flux region, which corresponds to the annular flow condensation. That is to say that the heat transfer in the upper portion of the tube by the film-wise condensation during the wavy flow regime has almost nothing to do with the tube diameter change. On the other hand, the tube diameter change has significant effect on the annular flow condensation, where the heat transfer mechanism is dominated by the forced-convective condensation. The predictive model of Shah [30], one of the most widely used correlations for annular flow condensation, is given by

$$h = \frac{0.023k_l}{D}\mathrm{Re}_l^{0.8}\,\mathrm{Pr}_l^{0.4}\left[1 + \frac{3.8}{P_r^{0.38}}\left(\frac{x}{1-x}\right)^{0.76}\right] \tag{13}$$

It is evident from Eq. (13) that the heat transfer coefficient is proportional to $D^{-0.2}$, which immediately shows the effect of the diameter on the heat transfer coefficient. Also, the effect of surface tension force needs to be considered. It has been well known that the surface tension of CO_2 is very low compared with other refrigerants. However, in the operating range of the present study ($-30\,^\circ\mathrm{C} \le T_{s,CO_2} \le -10\,^\circ\mathrm{C}$), the surface tension of CO_2 decreases from 0.011 N/m to 0.0065 N/m, which is considerably higher than that of the other refrigerants in the operating range of conventional refrigeration and air-conditioning systems ($30\,^\circ\mathrm{C} \le T_s \le 50\,^\circ\mathrm{C}$). The consensus of subsequent investigations is that the surface tension forces become increasingly important as the diameter is decreased and may dominate for sufficiently small tube sizes [5]. Moreover, the surface tension affects the flow regime and the cross-sectional shape of the flow, which, in turn, have an influence on the heat transfer mechanism and thermal resistance. Thus, the relatively high surface tension of CO_2 can have direct or indirect influence on the heat transfer mechanism, particularly in tubes having smaller size.

6.2 Heat Transfer Coefficients Inside Microfin Tube. Figure 5(*a*) shows the effect of the temperature difference between inner wall temperature and saturation temperature of the refrigerant on the heat transfer coefficients during condensation in microfin tubes. No significant effect of the temperature difference is observed. The helical rib of the microfin tube may delay the transition from annular flow to wavy flow [36] because the centrifugal force by the microfins spreads the liquid to the upper part of the tube. This redistribution of the liquid disturbs the appearance of the wavy or wavy-annular flow regime until the low mass flux (200 $\mathrm{kg/m^2\,s}$) in Fig. 5(*a*) and heat transfer coefficients seem to have nothing to do with the temperature difference.

Figure 5(*b*) shows the effect of the saturation temperature on the condensation heat transfer coefficient in the microfin tube. The heat transfer coefficients decrease with the increase in the saturation temperature. This trend is similar to the results of smooth tubes. The reduced pressure and the loss of two-phase characteristics affect the heat transfer coefficient in Fig. 5(*b*) again.

The heat transfer coefficients during condensation of the present study and Zilly et al. [4] are plotted versus vapor quality with the variations of mass flux in Figs. 5(*c*) and 5(*d*), respectively. The obtained results from Figs. 5(*c*) and 5(*d*) are not consistent with each other. The heat transfer coefficients in $D_{\text{melt}} = 3.51$ mm microfin tube strongly depend on the mass flux as expected while in $D_{\text{melt}} = 6.26$ mm microfin tube, heat transfer coefficients are nearly invariant to the variation in the mass flux. Eckels and Tesene [15] observed similar trends, i.e., the average heat transfer coefficients decrease at first when the mass flux increases, then heat transfer coefficients increase at the higher mass fluxes [15]. The authors explained that the "complex interactions" between surface fins and fluid could contribute to this effect. One of the complex interactions should be the liquid drainage effect that is driven by surface tension and contributes to heat transfer enhancement by forming a very thin liquid layer on the surface of microfins. Yang and Webb [16], however, showed that the enhancement by liquid drainage decreases as the mass flux increases. Also, at high mass fluxes, the contribution of turbulence induced by the helical fin is not much strong to stir up the liquid-vapor interface. Thus, as the mass flux increases, the heat transfer enhancement in the microfin tube is suppressed by several reasons. It should be noted that those enhancement and its suppression phenomena at high mass fluxes are strong functions of fin

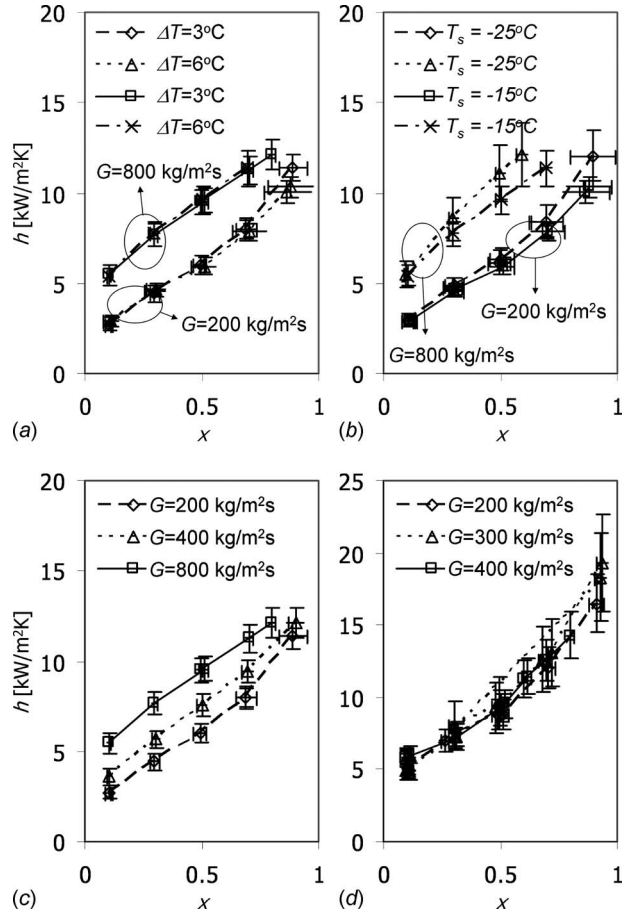

Fig. 5 Effects of (*a*) ΔT (D_{melt}=3.51 mm and T_s=−15°C), (*b*) saturation temperature (D_{melt}=3.51 mm and ΔT=6°C), (*c*) mass flux (present study, D_{melt}=3.51 mm, T_s=−15°C, and ΔT=3°C), and (*d*) mass flux (Zilly et al. [4], D_{melt}=6.26 mm, T_s=−25°C, and ΔT=3°C) on the condensation heat transfer coefficient in the microfin tube

geometry and tube diameter because those parameters have significant effects on the heat transfer mechanisms and flow regimes during condensation. In other words, in microfin tubes, the dependence of the heat transfer coefficient on the mass flux cannot be determined by the linear relations between them, and fin geometry and tube diameter play a very important role. The effects of fin geometry and/or tube diameter on the heat transfer mechanism during condensation need to be quantitatively identified for more detailed characterization of the trends in Figs. 5(*c*) and 5(*d*).

The measured heat transfer coefficients in microfin tubes of the present study and Zilly et al. [4] are compared with several correlations, and the mean absolute deviations are listed in Table 4. As shown, most of the predictive models significantly overpredict the experimental results of the present study while slightly underpredict the experimental data of Zilly et al. [4] with relatively high accuracy. These results may be attributed to the complexity and variety of fin geometry and flow mechanisms in microfin tubes again. The heat transfer mechanisms and flow regimes during condensation in microfin tubes are significantly affected by the fin geometry. However, most of the microfin tube correlations for condensation have been developed by fitting the data that are obtained from the experiment on limited variety of microfin tube fin geometries. Therefore, the unusual fin geometry of the microfin tube of the present study (small helix angle and large fin density) is beyond the applicable range of existing microfin tube correlations. Exceptionally, the correlation of Goto et al. [24] shows rather a smaller deviation from the experimental data of the present study than that of Zilly et al. [4]. The correlation of Goto et al. [24] was developed by modifying the correlation of Yu and Koyama [22] with the consideration of the various fin geometries of several microfin tubes, which may be one of the reasons for the relatively high accuracy of the correlation of Goto et al. [24]. Nevertheless, it is still necessary to give an effort to develop a robust correlation for condensation in the microfin tube.

Table 4 The mean absolute deviations of the heat transfer coefficient predictions using several heat transfer coefficient correlations from the measured heat transfer coefficient in microfin tubes

Correlations	Zilly et al. [4]	Present study	Total
Shikazono et al. [21]	24.9%	38.0%	31.3%
Yu and Koyama [22]	18.0%	44.7%	31.1%
Kedzierski and Goncalves [2]	33.4%	94.1%	63.2%
Goto et al. [24]	25.0%	16.9%	21.1%

6.3 Enhancement Factors. The ratio of the inner surface area of the microfin tube to that of the smooth tube, r_A, is defined as follows:

$$r_A = \frac{\tilde{P}_{en}}{\pi D_i} \tag{14}$$

where $\tilde{P}_{en}$ is the inner surface perimeter of the microfin tube and D_i is the inner diameter of the smooth tube. The area ratio of the microfin tube to the smooth tube is 2.84 and EFs vary from 0.92 to 2.51. On the other hand, the EFs of Zilly et al. [4]—conducted at the same test rig and similar test conditions of the present study—range from 1.82 to 3.46. Simply observed, the results show that the larger the diameter the microfin tube has, the stronger the enhancement of the heat transfer performance is. These results, however, do not coincide with the results of Schlager et al. [13]. Schlager et al. [13] reported that no significance differences in performance are observed between outer diameter of 9.52 mm and 12.7 mm microfin tubes. The helix angle β of the microfin tube in the present study is relatively small when compared with commonly used microfin tubes. Yasuda et al. [37] reported that condensation heat transfer coefficients increase with groove depth and helix angle. Chamra et al. [38] also reported that the condensation heat transfer coefficient increases as the helix angle increases. Thus, enhancement by the turbulence in the liquid film by microfins is relatively small due to the small helix angle of the microfin tube in the present study. Another possible reason for the inconsistency is that the microfin tube in the present study has 57 fins, which is similar to the number of fins (54 fins) of the D_{melt} =6.26 mm microfin tube of Zilly et al. [4], resulting in the perimeters of both microfin tubes to be almost the same, as listed in Table 2. Since the number of fins from 55 to 60 is optimal for the 9.52 mm outer diameter microfin tube [37], the number of fins of the microfin tube in the present study is not optimal for D_{melt} =3.51 mm microfin tube. Lastly, the microfin tubes used in the comparative study of Schlager et al. [13] had relatively large diameters, which is not enough to observe the significant diameter effect on the heat transfer performance of the microfin tube.

Kedzierski and Goncalves [2] reported that the EF is primarily a function of the Reynolds number and thermodynamic quality and proposed the following equation:

$$EF = 9.777\ Re_{lo,D_h}^{-0.162} x^{0.411} \tag{15}$$

According to Eq. (15), as the liquid only Reynolds number decreases and/or vapor quality increases, the EF increases. As the liquid only Reynolds number increases, the effect of liquid drainage by surface tension decreases due to the relatively high inertia force, and the effect of the turbulence induced by the fin becomes

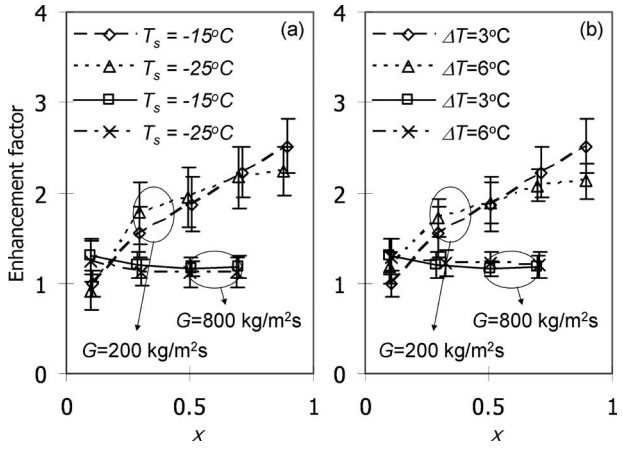

Fig. 6 Effects of (*a*) saturation temperature (D_{melt}=3.51 mm and DT=3°C) and (*b*) ΔT (D_{melt}=3.51 mm and T_s=−15°C) on the condensation heat transfer coefficient in the microfin tube

not enough to stir up the liquid-vapor interface, which results in the decrease in EF. On the other hand, as the vapor quality increases, the vapor velocity increases and the liquid film becomes thinner. This relatively thin liquid film enables both the liquid drainage by surface tension and mixing of liquid/vapor phase to be more effective so as to enhance the heat transfer performance.

The EFs measured in the present study and in Ref. [4] are compared with the correlation of Kedzierski and Goncalves [2], and the mean absolute deviations are 33.1% and 29.2% for EFs of Zilly et al. [4] and the present study, respectively. The prediction model of Kedzierski and Goncalves [2], however, significantly overpredicts the EFs of the present study while underpredicting that of Zilly et al. [4]. The primary reason for the large deviations is probably the difference of the fin geometry and the refrigerant. The hydraulic diameter in the liquid Reynolds number is the only factor to relate the various geometry effects to the correlation, which may not be sufficient. Also, the correlation was developed based on the experimental data using R134a, R410A, R125, and R32. Thus, considering the unique physical property characteristics of CO_2 at low temperatures, the prediction of CO_2 condensation behavior using the correlation is a kind of "extrapolation," which frequently brings large prediction errors. Nevertheless, the correlation is noticeable because, to the authors' best knowledge, the correlation is the only model that predicts the EF of the microfin tube and suggests underlying physical implications of condensation behavior in the microfin tube.

In Fig. 6(*a*), the aforementioned dependence of EF on vapor quality and liquid Reynolds number can be verified. The EF decreases with the increase in the mass flux and the decrease in the saturation temperature due to the increase in the liquid Reynolds number. Also, as the vapor quality increases, the EF increases at low mass flux. However, at sufficiently high liquid Reynolds number (high mass flux case, G=800 kg/m^2 s), the enhancement effects by vapor quality are largely suppressed due to the high inertia force and the turbulence. Thus, the correlation needs to be slightly modified to consider the negative dependence of EF on the vapor quality at sufficiently high mass flux, e.g., the superposition of convectively positive effect term and negative effect term. In the low vapor quality region, unusual trends are shown in Fig. 6(*a*). According to the transition criteria of Dobson and Chato [5], in smooth tubes and low mass fluxes (~200 kg/m^2 s), the transition from the annular flow to the wavy flow occurs at a vapor quality of about 0.5 in the smooth tube. In the case of high mass flux (400 kg/m^2 s and 800 kg/m^2 s), the transition occurs at a very low vapor quality. In microfin tubes, however, the transition to the wavy flow is delayed by the helical microfin effect [36]. Therefore, at the low vapor quality region, the flow regime of microfin tubes is usually the annular flow, which is different from that of smooth tubes. Thus, this flow regime change can be one of the enhancement mechanisms in microfin tubes at low vapor quality. Consequently, the steep line observed at low mass flux (200 kg/m^2 s) is because the flow regimes of a vapor quality of 0.1 still remain at the wavy flow, which means that in this region that there is no contribution to the enhancement of the flow regime change.

Table 5 Average enhancement and PFs

D_{melt} [mm]	T_{sat} [°C]	G [kg/m^2 s]	ΔT [°C]	EF	PF (Horizontal)	PF (Vertical)
	−15	200	3	2.5		
	−15	200	6	2.6	1.6	1.4
	−15	400	3	2.0		
	−15	400	6	1.9	1.4	1.3
	−25	200	3	2.8	1.5	1.1
	−25	300	3	2.4	1.4	1.3
6.26	−25	400	3	2.1		
Zilly et al. [4]	−25	400	6	2.1	1.3	1.3
	−15	200	3	1.8		
	−15	200	6	1.8	1.6	1.4
	−15	400	3	1.5		
	−15	400	6	1.5	1.5	1.3
	−15	800	3	1.2		
	−15	800	6	1.2	1.4	1.2
	−25	200	3	1.8		
	−25	200	6	1.8	1.5	1.4
	−25	400	3	1.5		
	−25	400	6	1.5	1.7	1.3
3.51	−25	800	3	1.1		
Present study	−25	800	6	1.2	1.3	1.3

The effect of the temperature difference between inner wall temperature and saturation temperature of the refrigerant on EF is shown in Fig. 6(*b*). At the high vapor quality and low mass flux (200 kg/m^2 s) region, the increased temperature difference induces the decrease in the EF while at the low vapor quality, the trend is reversed. As aforementioned, during the wavy flow regime corresponding to the low vapor quality of the low mass flux (200 kg/m^2 s) region, due to the thinner liquid film, the smaller temperature difference has a positive effect on the heat transfer coefficient in the smooth tube. However, in the microfin tube, due to the fin action, the appearance of the wavy flow regime is delayed and, therefore, the positive effect of the smaller temperature difference does not occur. Consequently, the EF increases with increasing temperature difference during wavy flow condensation. On the other hand, at the high vapor quality and low mass flux (200 kg/m^2 s) region, the heat transfer enhancement due to the liquid drainage is dominant. The enhancement mechanism due to the liquid drainage is the kind of falling film condensation on the fin tip, which results in a similar trend to the heat transfer mechanism during wavy flow condensation. However, the effect of the enhancement mechanism is weakened by high interfacial shear force induced by the high vapor velocity as the mass flux increases.

Table 5 shows the average EFs and average PFs at various operating conditions. The PF data are obtained from the experiment that was accompanied with the present heat transfer experiment by the same authors of the present study [39]. The average EFs of the present study and Zilly et al. [4] range from 1.1 to 1.8 and from 1.9 to 2.8, respectively. For the horizontal two-phase flow, the average PFs of the present study and Zilly et al. [4] range from 1.3 to 1.7 and from 1.3 to 1.6, respectively, while the vertical pressure drop PFs of the present study and Zilly et al. [4] range from 1.2 to 1.4 and from 1.1 to 1.4, respectively. Generally, the D_{melt}=6.26 mm microfin tube has better performance than the D_{melt}=3.51 mm microfin tube. When the ratio of the EF to the PF

is merely compared, at operating conditions of the saturation temperature of −25 °C, the temperature difference of 3 °C, the mass flux of 200 kg/m^2 s, and the diameter of 6 mm, the microfin tube shows the best performance.

7 Conclusion

In this study, the heat transfer data for the condensation of CO_2 at saturation temperatures of −25 °C and −15 °C in horizontal smooth and microfin tubes are presented. Qualitative analysis is discussed such as the analysis of the effect of several parameters on the heat transfer in smooth and microfin tubes with refrigerant CO_2. Generally, condensation heat transfer characteristics of refrigerant CO_2 at low temperatures are qualitatively similar to the other commonly used CFC, HCFC, and HFC refrigerants. Nevertheless, due to the different characteristics of CO_2 properties from commonly used refrigerants, existing predictive models for heat transfer coefficients, which are developed based on the experimental data using those commonly used refrigerants, have a difficulty in estimating the experimental data of the present study, even if the uniqueness of CO_2 properties is weakened at the low temperatures. Moreover, in microfin tubes, due to the complexity and variety of fin geometry and flow mechanisms, existing correlations showed significantly large deviations from the experimental data of the present study. Therefore, present CO_2 condensation data at low temperature can be used as a fundamental database for further researches on the CO_2 condensation at low temperatures, e.g., correlation development and behavior characterization. Moreover, as an extreme case of a usual refrigerant condensation, the present CO_2 data can be utilized to generalize and extend applicable ranges of existing condensation correlations.

In the smooth tube, the annular flow prevailed for all the cases. Only for the low vapor quality region below ~0.5 and ~0.15 for mass fluxes of 200 kg/m^2 s and 800 kg/m^2 s, the wavy flow characteristics were observed, which is consistent with the flow regime transition criteria of Dobson and Chato [5]. For the microfin tube, there were no available and adequate flow regime map or transition criteria. It can be only concluded that the redistribution of the liquid caused by the helical rib of the microfin tube disturbs the appearance of the wavy flow. Further researches and efforts are needed to develop the flow regime map or transition criteria.

At the wavy flow regime, the large temperature difference induced the thicker liquid film on the upper part of the tube, which leads to lower heat transfer coefficients in the smooth tube condensation, while at the annular flow regime, the trend is reversed and is attributed to the increase in interfacial shear and liquid film Reynolds number. Generally, the effects of the temperature difference, however, were relatively small. The effects of the mass flux were more complicated. At the wavy flow regime, due to the gravity dependent characteristics of the wavy flow, the increase in the liquid-vapor shear caused by the increase in the mass flux and/or vapor quality did not affect the heat transfer coefficients. On the other hand, at the annular flow regime, due to the increase in the liquid-vapor shear, the heat transfer coefficients were improved with increasing vapor quality and mass flux in the smooth tube. In the microfin tube, the mass flux seems to have nonlinear relation with the heat transfer coefficients. Even though similar trends were observed by Eckels and Tesene [15], more experimental data and analyses should be incorporated for a clearer explanation. At higher saturation temperature, due to the loss of two-phase characteristics, e.g., density, viscosity, and velocity differences between liquid and vapor phases, the heat transfer coefficients were suppressed for both smooth tube (annular flow) and microfin tube. However, at the wavy flow regime, heat transfer coefficients slightly decreased with respect to the saturation temperature increase, which can be explained by the Nusselt theory and property index. The reduction in the tube diameter positively affects the heat transfer coefficients at the annular flow regime while at the wavy flow regime the effect is considerably suppressed.

The rough comparison between the EFs and the PFs of the present study shows that it is not true that the heat transfer enhancement by the internally finned geometry always is a superior mechanism to the pressure drop penalty, which means that under specific operating conditions with unoptimized fin geometry, the microfin tube could degrade the in-tube condensation performance in the refrigeration and air-conditioning systems using CO_2 as a refrigerant. It is necessary to make a quantitative and fine investigation into the relations between the diameter of the microfin tube and its usefulness.

Acknowledgment

The authors are grateful to ACRC consortium and Wolverine for their help in the realization of this project. This work is jointly supported by the Micro Thermal System Research Center of Seoul National University and BK21 program of the Ministry of Education.

Nomenclature

A = area (m^2)
A_{surf} = effective heat transfer area (m^2)
c_p = specific heat (J/kg K)
D = diameter (m)
D_h = hydraulic diameter (m)
D_i = inner diameter of the smooth tube (m)
D_o = outer diameter (m)
E_{abs} = mean absolute deviation
Fr_{so} = modified Froude number [6] (Eqs. (1*a*) and (1*b*))
g = acceleration of gravity, 9.8 m/s^2
G = mass flux (kg/m^2 s)
Ga = Galileo number, $g\rho_l(\rho_l-\rho_v)D^3/\mu_l^2$
h = heat transfer coefficient (W/m^2 K)
$\bar{h}$ = mean heat transfer coefficient (W/m^2 K)
i = enthalpy (J/kg)
i_{lv} = latent heat (J/kg)
k = thermal conductivity (W/m K)
L = length (m)
LMTD = log mean temperature difference (K)
$\dot{m}$ = mass flow rate (kg/s)
N = the number of data
P = pressure drop (Pa)
$\tilde{P}$ = perimeter (m)
Pr = Prandtl number, $\mu c_p/k$
P_r = reduced pressure
$\dot{Q}$ = heat transfer (W)
r_A = ratio of the inner surface area of the microfin tube to that of the smooth tube
Re_l = liquid Reynolds number, $G(1-x)D/\mu_l$
Re_{lo,D_h} = liquid only Reynolds number based on the hydraulic diameter, GD/μ_l
$Re_{liquid\ film}$ = liquid film Reynolds number
T = temperature (°C)
ΔT = temperature difference between inner wall and saturated refrigerant (°C)
U = overall heat transfer coefficient (W/m^2 K)
X = Martinelli parameter, $\sqrt{(\Delta P/\Delta L)_l/(\Delta P/\Delta L)_v}$
x = vapor quality
z = distance (m)

Greek Symbols

β = helix angle
δ = film thickness (m)
γ = apex angle
μ = dynamic viscosity (kg/m s)
ρ = density (m^3/kg)

Subscripts

cal = calorimeter
CO_2 = refrigerant carbon dioxide
cond = thermal conduction
en = microfin tube
ext = external
ft = fin tip of the microfin
i = inlet
l = liquid
meas = measured
melt = melt-down
o = outlet
offset = offset
pipe = pipe between calorimeter and test section
pred = predicted
root = fin root of the microfin
s = saturated
sm = smooth tube
test = test section
v = vapor
wall = tube inner wall

References

[1] Cavallini, A., Del Col, D., Doretti, L., Longo, G. A., and Rossetto, L., 2000, "Heat Transfer and Pressure Drop During Condensation of Refrigerants Inside Horizontal Enhanced Tubes," Int. J. Refrig., **23**, pp. 4–25.

[2] Kedzierski, M. A., and Goncalves, J. M., 1999, "Horizontal Convective Condensation of Alternative Refrigerants Within a Micro-Fin Tube," J. Enhanced Heat Transfer, **6**, pp. 161–178.

[3] Cavallini, A., Censi, G., Del Col, D., Doretti, L., Longo, G. A., Rossetto, L., and Zilio, C., 2003, "Condensation Inside and Outside Smooth and Enhanced Tubes: A Review of Recent Research," Int. J. Refrig., **26**, pp. 373–392.

[4] Zilly, J., Jang, J., and Hrnjak, P. S., 2003, "Condensation of CO_2 at Low Temperatures in Micro-Fin Horizontal Tubes," University of Illinois at Urbana-Champaign, ACRC Technical Report No. 49.

[5] Dobson, M. K., and Chato, J. C., 1998, "Condensation in Smooth Horizontal Tubes," ASME J. Heat Transfer, **120**, pp. 193–213.

[6] Soliman, H. M., 1982, "On the Annular-to-Wavy Flow Pattern Transition During Condensation Inside Horizontal Tubes," Can. J. Chem. Eng., **60**, pp. 475–481.

[7] Cavallini, A., Censi, G., Del Col, D., Doretti, L., Longo, G. A., and Rossetto, L., 2002, "In-Tube Condensation of Halogenated Refrigerants," ASHRAE Trans., **108**(1), pp. 146–161.

[8] El Hajal, J., Thome, J. R., and Cavallini, A., 2003, "Condensation in Horizontal Tubes, Part I: Two-Phase Flow Pattern Map," Int. J. Heat Mass Transfer, **46**, pp. 3349–3363.

[9] Kattan, N., Thome, J. R., and Favrat, D., 1998, "Flow Boiling in Horizontal Tubes, Part I: Development of a Diabatic Tow-Phase Flow Pattern Map," ASME J. Heat Transfer, **120**, pp. 140–147.

[10] Thome, J. R., Hajal, J. E., and Cavallini, A., 2003, "Condensation in Horizontal Tubes, Part II: New Heat Transfer Model Based on Flow Regimes," Int. J. Heat Mass Transfer, **46**, pp. 3365–3387.

[11] Khanpara, J. C., Bergles, A. E., and Pate, M. B., 1986, "Augmentation of R-113 in-Tube Condensation With Micro-Fin Tubes," *Proceedings of the Heat Transfer in Air Conditioning and Refrigeration Equipment*, Vol. HTD-65, ASME, New York, pp. 21–32.

[12] Schlager, L. M., Pate, M. B., and Bergles, A. E., 1989, "Heat Transfer and Pressure Drop During Evaporation and Condensation of R22 in Horizontal Micro-Fin Tubes," Int. J. Refrig., **12**, pp. 6–14.

[13] Schlager, L. M., Pate, M. B., and Bergles, A. E., 1990, "Evaporation and Condensation Heat Transfer and Pressure Drop on Horizontal, 12.7-mm Microfin Tubes With Refrigerant 22," ASME J. Heat Transfer, **112**, pp. 1041–1047.

[14] Eckels, S. J., and Pate, M. B., 1991, "Evaporation and Condensation of HFC-134a and CFC-12 in a Smooth Tube and a Micro-Fin Tube," ASHRAE Trans., **97**(2), pp. 71–81.

[15] Eckels, S. J., and Tesene, B. A., 1999, "A Comparison of R-22, R-134a, R-410a, and R-407C Condensation Performance in Smooth and Enhanced Tubes, Part I: Heat Transfer," ASHRAE Trans., **105**(2), pp. 428–441.

[16] Yang, C.-Y., and Webb, R. L., 1997, "A Predictive Model for Condensation in Small Hydraulic Diameter Tubes Having Axial Micro-Fins," ASME J. Heat Transfer, **119**, pp. 776–782.

[17] Jang J., and Hrnjak, P. S., 2004, "Condensation of CO_2 at Low Temperatures," ACRC Technical Report No. CR-56.

[18] Luu, M., and Bergles, A. E., 1980, "Enhancement of Horizontal In-Tube Condensation of Refrigerant-113," ASHRAE Trans., **86**(1), pp. 293–312.

[19] Kaushik, N., and Azer, N. Z., 1988, "A General Heat Transfer Correlation for Condensation Inside Internally Finned Tubes," ASHRAE Trans., **94**(2), pp. 261–279.

[20] Cavallini, A., Doretti, L., Klammsteiner, N., Longo, G. A., and Rossetto, L., 1995, "Condensation of New Refrigerants Inside Smooth and Enhanced Tubes," *Proceedings of the International Congress of Refrigeration*, Vol. 4, pp. 105–114.

[21] Shikazono, N., Itoh, M., Uchida, M., Fukushima, T., and Hatada, T., 1998, "Predictive Equation Proposal for Condensation Heat Transfer Coefficient of Pure Refrigerants in Horizontal Micro-Fin Tubes," JSME Int. J., Ser. B, **64**, pp. 196–203.

[22] Yu, J., and Koyama, S., 1998, "Condensation Heat Transfer of Pure Refrigerants in Microfin Tubes," *Proceedings of the International Refrigeration Conference at Purdue*, pp. 325–330.

[23] Nozu, S., and Honda, H., 2000, "Condensation of Refrigeration in Horizontal, Spirally Grooved Microfin Tubes: Numerical Analysis of Heat Transfer in the Annular Flow Regime," ASME J. Heat Transfer, **122**, pp. 80–91.

[24] Goto, M., Inoue, N., and Yonemoto, R., 2003, "Condensation Heat Transfer of R410A Inside Internally Grooved Horizontal Tubes," Int. J. Refrig., **26**, pp. 410–416.

[25] Moffat, R. J., 1988, "Describing the Uncertainties in Experimental Results," Exp. Therm. Fluid Sci., **1**, pp. 3–17.

[26] Chato, J. C., 1962, "Laminar Condensation Inside Horizontal and Inclined Tubes," ASHRAE J., **4**, pp. 52–60.

[27] Jaster, H., and Kosky, P. G., 1976, "Condensation Heat Transfer in a Mixed Flow Regime," Int. J. Heat Mass Transfer, **19**, pp. 95–99.

[28] Akers, W. W., Deans, H. A., and Crosser, O. K., 1959, "Condensation Heat Transfer Within Horizontal Tubes," Chem. Eng. Prog., Symp. Ser., **55**, pp. 171–176.

[29] Cavallini, A., and Zecchin, R., 1974, "A Dimensionless Correlation for Heat Transfer in Forced Convection Condensation," *Proceedings of the International Heat Transfer Conference*," Tokyo, pp. 309–313.

[30] Shah, M. M., 1979, "General Correlation for Heat Transfer During Film Condensation Inside," Int. J. Heat Mass Transfer, **22**, pp. 547–556.

[31] Chen, S. L., Gerver, F. M., and Tien, C. L., 1987, "General Film Condensation Correlation," Exp. Heat Transfer, **1**, pp. 93–107.

[32] Bivens, D. B., and Yokozeki, A., 1994, "Heat Transfer Coefficient and Transport Properties for Alternative Refrigerants," *Proceedings of the International Refrigeration Conference at Purdue*, pp. 299–304.

[33] García-Valladares, O., 2003, "Review of In-Tube Condensation Heat Transfer Correlations for Smooth and Microfin Tubes," Heat Transfer Eng., **24**(4), pp. 6–24.

[34] Rouhani, Z., and Axelsson, E., 1970, "Calculation of Void Volume Fraction in the Subcooled and Quality Boiling Region," Int. J. Heat Mass Transfer, **13**, pp. 383–393.

[35] Dukler, A. E., 1960, "Fluid Mechanics and Heat Transfer in Vertical Falling Film Systems," Chem. Eng. Prog., Symp. Ser., **56**(30), pp. 1–10.

[36] Manwell, S. P., and Bergles, A. E., 1990, "Gas-Liquid Flow Patterns in Refrigerant-Oil Mixtures," ASHRAE Trans., **96**(2), pp. 456–464.

[37] Yasuda, K., Ohizumi, K., Hori, M., and Kawamata, O., 1990, "Development of Condensing Thermofin-HEX-C Tube," Hitachi Cable Review, **9**, pp. 27–30.

[38] Chamra, L. M., Webb, R. L., and Randlett, M. R., 1996, "Advanced Micro-Fin Tubes for Condensation," Int. J. Heat Mass Transfer, **39**(9), pp. 1839–1846.

[39] Kim, Y. J., Jang, J., Hrnjak, P. S., and Kim, M. S., 2008, "Adiabatic Horizontal and Vertical Pressure Drop of Carbon Dioxide Inside Smooth and Micro-Fin Tubes at Low Temperatures," ASME J. Heat Transfer, to be published.

Estimation of Unknown Boundary Heat Flux in Laminar Circular Pipe Flow Using Functional Optimization Approach: Effects of Reynolds Number

Peng Ding

Wen-Quan Tao
e-mail: wqtao@mail.xjtu.edu.cn

School of Energy and Power Engineering,
Xi'an Jiaotong University,
Xi'an 710049, China

*An inverse forced convection problem was studied in this paper. The unknown space-dependent heat flux at the outer boundary of a circular pipe was identified from the temperature measurements within the flow using the algorithm based on an improved conjugate gradient method, which is a combination of the modified inverse algorithm proposed by Ozisik et al. (Huang and Ozisik, 1992, "Inverse Problem of Determining Unknown Wall Heat Flux in Laminar Flow Through a Parallel Plate Duct," Numer. Heat Transfer, Part A **21**, pp. 2615–2618) and the general inverse algorithm based on the conjugate gradient method. The effects of the convection intensity, the number of thermocouples, the location of the thermocouples, and the measurement error on the performance of the modified inverse algorithm method and the improved inverse algorithm were studied thoroughly through three examples. It is shown that the improved inverse algorithm can greatly improve the solution accuracy in the entire computation domain. The accuracy and stability of both the modified inverse algorithm method and the improved inverse algorithm are strongly influenced by the Reynolds number and the shape of the unknown heat flux. Those functions, which contain more high-frequency components of Fourier series, are more sensitive to the increase in the Reynolds number.*
[DOI: 10.1115/1.3013825]

Keywords: conjugate gradient method, inverse convection problem, functional optimization, pipe flow, improved inverse algorithm

1 Introduction

Inverse analysis is very valuable when the direct measurements of data are impossible or the measuring process is very expensive, for example, the determination of heat transfer coefficients and the heat loads acting on the outer surface of re-entry vehicle, the estimation of unknown thermophysical properties of new materials, the prediction of the glass ribbon temperature in the float glass process, the determination of contact resistance and damage detection in the structure fields, and so on.

It is well known that the solution of inverse problems is more difficult than direct problems due to their ill-posedness nature, i.e., small error in the measurement data may deteriorate the solution significantly [1]. A lot of studies have been conducted over the past decades to improve the stability of the inverse algorithm. Generally speaking, these techniques fall into two main categories, namely, the function specification method developed by Beck et al. [2] and the iterative regularization method (also referred as conjugate gradient method) pioneered by Alifanov [3] where the regularization is inherently built in the iterative procedure. The success of the method of Beck et al. [2] depends on the choice of the future time parameter, while the iterative regularization method of Alifanov [3] appears to be one of the most efficient and universal approaches for the construction of stable algorithms for solving inverse problems.

Contributed by the Heat Transfer Division of ASME for publication in the JOURNAL OF HEAT TRANSFER. Manuscript received September 16, 2007; final manuscript received September 12, 2008; published online December 12, 2008. Review conducted by Anthony M. Jacobi.

Inverse heat conduction problems have been studied by many scientists over the past decades. A good review of the inverse heat conduction problems (IHCPs) up to the year of 1994 can be found in the book of Alifanov [3]. For the simplicity of presentation, only some related publications after 1994 are briefly review as follows. Huang and Tsai [4] adopted a boundary element method based inverse algorithm in conjunction with the iterative regularization method to solve the inverse heat conduction problem for estimating the unknown transient boundary heat flux in a multidimensional domain with arbitrary geometry. An inverse heat conduction problem was solved by using Alifanov's iterative regularization method to estimate the time-varying heat transfer coefficient of forced convection flow boiling over the outer surface of a heated tube by Su and Hewitt [5]. The estimation was based on the transient temperature measurements taken by a thermocouple on the inner surface of the circular tube on which the flow boiling occurred. Effects of the time scales of the heat transfer coefficient variation, the measurement error, and the data acquisition rates were investigated. Loulou and Scott [6] used heat flux measurement rather than temperature measurement in the object function to estimate the time-dependent blood perfusion and the thermal conductance between the probe and the tissue. The minimization procedure was achieved by using conjugate gradient method and the adjoint equations. In the work of Huang and Tsai [7], the local time-dependence of surface heat transfer coefficients for plate finned-tube heat exchangers was estimated in a three dimensional inverse heat conduction problem, and the code developed had the ability to communicate with the commercial computational fluid dynamics (CFD) code CFX4.4 by means of data transportation. Deng et al. [8] dealt with the estimation of the heat flux distribution generated by a flame gun based on the temperature

 Copyright © 2009 by ASME

measurements in a cylindrical work piece. The estimation consisted of two calculations. The first calculation was performed by solving the inverse heat problem using the conjugate gradient method. Then the results were used in the second calculation implementing an artificial neural network technique to set up correlations between the temperature of the work piece and the heat flux generated by the flame gun. Girault and Petit [9] proposed a method for solving nonlinear inverse heat conduction problems using reduced order model (ROM). The ROM was identified through a specific procedure based on the numerical optimization technique to minimize the discrepancy between the responses of the CFD model and ROM when a specific input signal was used. Then the ROM was used to solve the inverse problem through a function specification method.

In all the above examples, the heat transfer process occurred in the main body are heat conduction and either the boundary conditions, or the thermophysical properties of the main body are searched for. All such inverse problems belong to the inverse heat conduction category. The studies in the inverse convection heat transfer problems are developed more lately than the study of the inverse heat conduction problems. By the inverse convection heat transfer we mean that the process in the main body is convective. The papers published in its early stage known to the present authors were on the 1990s. Huang and Ozisik [10] used a combination of conjugate gradient method and modified conjugate gradient method to solve the inverse problem of determining the spacewise variation in an unknown wall flux for laminar flow inside a parallel plate duct. Bokar and Ozisik [11] utilized the same method to estimate the timewise variation in inlet temperature of a thermally developing, hydrodynamically developed laminar flow between parallel plates by utilizing transient temperature measurements from a single thermocouple located downstream of the entrance. In the work of Colaco and Orlande [12], the conjugate gradient method was used for the simultaneous identification of two unknown boundary heat fluxes in an irregularly shaped channels with laminar flow. The inverse convection problems in turbulent channel flow were also studied in recent years [13–15].

All the inverse convection heat transfer problems mentioned above mainly studied the effects of measurement error and the position of the thermocouples on the performance of the inverse algorithm at a single specified Reynolds number; the effects of the Reynolds number (that is, the intensity of convection itself) on the performance of the inverse algorithm have not been studied yet.

One serious defect with the conjugate gradient method is that the value of the heat flux at the final position always equals to the initial value since the normal conjugate gradient method cannot update the value of gradient at the final position. The modified conjugate gradient method proposed by Huang and Ozisik [10] has been proved an efficient method to resolve this problem in Refs. [16–18]. Its performance will be further testified in this paper, and a revision is further proposed to update the gradient both at the beginning and ending positions.

In the present study, the effects of convection on the stability and accuracy of the inverse algorithm are analyzed in terms of Reynolds number. It will be shown that Reynolds number has a significant effect on the performance of the inverse algorithm. In this paper the detailed derivation of the sets of sensitivity and adjoint equations used in the inverse algorithm will be provided first. Then numerical results about the effects of measurement error, the position of the thermocouples, and the number of thermocouples at different Reynolds number will be presented next. Finally, some brief conclusions are presented.

2 Direct Problem

The present study considers a thermally developing, hydrodynamically developed laminar forced convection of a Newtonian fluid of constant properties through a circular pipe with the outer wall subjected to a spacewise varying heat flux $Q(X)$. Fluid enters the pipe at a uniform temperature of T_0. Figure 1 presents a schematic view of the present pipe flow system, also shown in Fig. 1 is the position of thermocouples. Note that, in this study, all the thermocouples used to measure the temperature of fluid are placed along the streamwise direction at the same radial position.

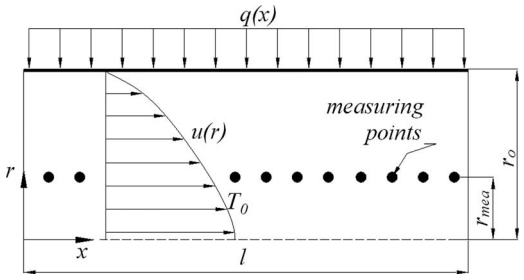

Fig. 1 Schematic view of the pipe system and position of the thermocouples. The velocity profile is fully developed and the inlet temperature is constant.

By assuming axisymmetry of the problem and neglecting axial heat conduction and viscous dissipation, the governing equation in dimensionless form for this problem is given by

$$\frac{1}{2}\mathrm{PrRe}U(R)\frac{\partial\theta(X,R)}{\partial X}=\frac{1}{R}\frac{\partial}{\partial R}\left(R\frac{\partial\theta(X,R)}{\partial R}\right) \tag{1}$$

with the boundary conditions $\partial\theta(X,0)/\partial R=0$, $\partial\theta(X,1)/\partial R=Q(X)$ and $\theta(0,R)=0$. The dimensionless variables are defined as follows:

$$X=\frac{x}{r_o},\quad R=\frac{r}{r_o},\quad U=\frac{u}{u_{\mathrm{avg}}},\quad \mathrm{Pr}=\frac{\nu}{\alpha}$$

$$\mathrm{Re}=\frac{2u_{\mathrm{avg}}r_o}{\nu},\quad \theta=\frac{k(T-T_0)}{q_{\mathrm{ref}}r_o},\quad Q=\frac{q}{q_{\mathrm{ref}}}$$

here, ν is the kinematic viscosity, α is the thermal diffusivity, k is the thermal conductivity, u_{avg} is the average inlet velocity, q_{ref} is the reference heat flux, and T_0 is the inlet temperature of fluid. The fully developed velocity profile of the fluid in the circular pipe is expressed in the dimensionless form as $U(R)=2(1-R^2)$.

In this investigation, we take the Prandtl number a constant value of 7.0 so that the working fluid can be thought of as being water. The computations were conducted at three different Reynolds numbers of Re=100, Re=1000, and Re=2000 to identify the effects of the convection on the performance of inverse algorithm. The dimensionless length in the streamwise direction, $L=\lambda/r_0$ was fixed at a value of 100. A 800×100 uniform grid system was used to discretize the space domain, and the foregoing equations are discretized by the finite volume method [19,20]. The code developed here was validated by reproducing solutions for some benchmark problems [21,22], the results were not shown here since the main subject of this paper is about the inverse problem.

3 Inverse Problem

For the inverse problem, we are going to identify the unknown dimensionless wall heat flux $Q(X)$ by using the temperature measurements taken from the pipe flow. Let the temperature measurements taken at some appropriate locations within the flow be denoted by θ^* and let the solutions of the direct problem at the thermocouples position denoted by θ, that is, the temperature corresponding to a particular value of heat flux function $Q(X)$. In the idealized situation without measurement error, the unknown heat flux $Q(X)$ can be obtained by solving an optimal problem of requiring an exact equivalency between the measured temperature θ^* and the calculated temperature θ. But in practice, the inverse

problem should be solved in a least squares way due to the ill posed nature of the inverse problem. The inverse problem treated in this paper is defined as follows.

Find a heat flux function $Q(X)$ which minimizes the object function J, defined by

$$J = \frac{1}{2}\sum_{\text{mea}=1}^{Nm} [\theta(X_{\text{mea}}, R_{\text{mea}}) - \theta^*(X_{\text{mea}}, R_{\text{mea}})]^2 \tag{2}$$

where Nm represents the total number of the measuring points, and X_{mea} and R_{mea} represent the streamwise coordinate and radial coordinate of the measuring points, respectively.

In this paper the minimization of object function J is achieved by the conjugate gradient method [16–18]. The essence of the conjugate gradient method is to decide a suitable descent direction and a suitable step size in the descent direction for the minimization of object function J [23]. The descent direction and the step size may be obtained, respectively, from the solution of two auxiliary problems known as the sensitivity problem and adjoint problem.

3.1 Sensitivity Problem. The derivation of sensitivity problem presented in this section closely follows Refs. [10,23]. We define the temperature sensitivity function $\hat{\theta}$ as the directional derivative of θ at Q in the direction of ΔQ, i.e.,

$$\hat{\theta} = D_{\Delta Q}\theta = \lim_{\varepsilon \to 0} \frac{\Delta \theta}{\varepsilon} \tag{3}$$

Based on this definition, the governing equation for the temperature sensitivity function $\hat{\theta}$ can be obtained by the following process: The formulation of direct problem given by Eq. (1) (which is written for Q) is rewritten first for $(Q+\varepsilon\Delta Q)$, and the rewritten equation is subtracted from Eq. (1). When the limiting process defined by Eq. (3) is applied to the above results, we obtain

$$\frac{1}{2}\text{PrRe}U(R)\frac{\partial \hat{\theta}(X,R)}{\partial X} = \frac{1}{R}\frac{\partial}{\partial R}\left(R\frac{\partial \hat{\theta}(X,R)}{\partial R}\right) \tag{4}$$

with the following boundary conditions $\partial\hat{\theta}(X,0)/\partial R = 0$, $\partial\hat{\theta}(X,1)/\partial R = \Delta Q(X)$, and $\hat{\theta}(0,R) = 0$

3.2 Adjoint Problem and Gradient Equation. The derivation of adjoint problem presented in this section closely follows Refs. [10,24]. We first multiply the governing equation, Eq. (1), by the Lagrange multiplier $\overleftrightarrow{\theta}(X,R)$ and integrate the production over the whole space domain. Then the resulting expression is added to the object function given by Eq. (2):

$$J = \frac{1}{2}\sum_{\text{mea}=1}^{Nm}\int_{\Omega} [\theta(X,R) - \theta^*(X,R)]^2 \delta(X - X_{\text{mea}}, R - R_{\text{mea}})d\Omega + \int_{\Omega} \overleftrightarrow{\theta}(X,R)\left[\frac{1}{2}\text{PrRe}U(R)\frac{\partial\theta(X,R)}{\partial X} - \frac{1}{R}\frac{\partial}{\partial R}\left(R\frac{\partial\theta(X,R)}{\partial R}\right)\right]d\Omega \tag{5}$$

where $\delta(\cdot)$ is the Dirac delta function. Following the same procedure with the development of the sensitivity problem, we can obtain the following equation:

$$D_{\Delta Q}J = \sum_{\text{mea}=1}^{Nm}\int_{\Omega} [\theta(X,R) - \theta^*(X,R)]\hat{\theta}(X,R)\delta(X - X_{\text{mea}}, R - R_{\text{mea}})d\Omega + \int_{\Omega} \overleftrightarrow{\theta}(X,R)\frac{1}{2}\text{PrRe}U(R)\frac{\partial(\hat{\theta}(X,R))}{\partial X}d\Omega - \int_{\Omega} \overleftrightarrow{\theta}(X,R)\frac{1}{R}\frac{\partial}{\partial R}\left(R\frac{\partial(\hat{\theta}(X,R))}{\partial R}\right)d\Omega \tag{6}$$

By employing integration by parts in the second and third terms on the right hand side of Eq. (6), using the initial and boundary conditions of the sensitivity problem and also requiring that the coefficients of $\hat{\theta}(X,R)$ vanish, we can yield the following governing equation for the adjoint function $\overleftrightarrow{\theta}(X,R)$:

$$-\frac{1}{2}\text{PrRe}U(R)\frac{\partial \overleftrightarrow{\theta}(X,R)}{\partial X} = \frac{1}{R}\frac{\partial}{\partial R}\left(R\frac{\partial \overleftrightarrow{\theta}(X,R)}{\partial R}\right) + \sum_{\text{mea}=1}^{Nm}[\theta(X,R) - \theta^*(X,R)]\delta(X - X_{\text{mea}}, R - R_{\text{mea}}) \tag{7}$$

with the boundary conditions $\partial\overleftrightarrow{\theta}(X,0)/\partial R = 0$, $\partial\overleftrightarrow{\theta}(X,1)/\partial R = \Delta Q(X)$, and $\overleftrightarrow{\theta}(L,R) = 0$. Finally, the following term is left:

$$D_{\Delta Q}J = \int_{X=0}^{L} \overleftrightarrow{\theta}(X,1)\Delta Q(X)dX \tag{8}$$

Equation (8) represents the directional derivative of object function J in the direction ΔQ; it can also be expressed in another way, i.e., the inner product of the gradient ∇J_Q with ΔQ,

$$D_{\Delta Q}J = \langle \nabla J_Q | \Delta Q \rangle = \int_{X=0}^{L} \nabla J_Q \Delta Q dX \tag{9}$$

Comparison of Eq. (8) with Eq. (9) gives that the gradient of object function J with respect to the heat flux Q is equal to the adjoint temperature at the outer surface of the tube

$$\nabla J_Q = \overleftrightarrow{\theta}(X,1) \tag{10}$$

3.3 Conjugate Gradient Method. In this investigation, the conjugate gradient method [23] was used to minimize the object function J. The iterative procedure of the conjugate gradient method to identify the unknown heat flux $Q(X)$ is given by

$$Q^{n+1}(X) = Q^n(X) + \beta^n P^n(X), \quad n = 0,1,2,\ldots,\infty \tag{11}$$

where β^n is the search step size from the nth iteration to the $(n+1)$th, and $P^n(X)$ is the search direction expressed by

$$P^n(X) = \nabla J_Q^n(X) + \gamma^n P^{n-1}(X), \quad n = 1,2,\ldots,\infty \tag{12}$$

In the adopted conjugate gradient method, the conjugate coefficient γ^n is determined from

$$\gamma^n = \int_0^L (\nabla J_Q^n)^2 dX \Big/ \int_0^L (\nabla J_Q^{n-1})^2 dX, \quad \gamma^0 = 0 \tag{13}$$

The search step size β^n is determined by

$$\beta^n = \sum_{\text{mea}=1}^{Nm}[\theta(X_{\text{mea}}, R_{\text{mea}}) - \theta^*(X_{\text{mea}}, R_{\text{mea}})]\hat{\theta}(X_{\text{mea}}, R_{\text{mea}}) \Big/ \sum_{\text{mea}=1}^{Nm}(\hat{\theta}(X_{\text{mea}}, R_{\text{mea}}))^2 \tag{14}$$

3.4 General Inverse Algorithm Based on The Conjugate Gradient Method. The general inverse algorithm based on the conjugate gradient method to identify the unknown heat flux $Q(X)$ can be arranged in the following manner:

1. solve the governing equation of the direct problem, Eq. (1), with an initial heat flux $Q^0(X)$
2. solve the adjoint problem governed by Eq. (7)
3. compute the gradient of $J, \nabla J_Q$, from Eq. (10)
4. compute the conjugate coefficient γ from Eq. (13)
5. compute the search direction P from Eq. (12)
6. solve the sensitivity problem by setting ΔQ equal to P
7. compute the search step size β from Eq. (14)
8. update the unknown heat flux Q from Eq. (11)
9. repeat above steps until convergence is reached

3.5 Modified Inverse Algorithm Based on the Conjugate Gradient Method. One serious defect of the above mentioned conjugate gradient method is that the value of the heat flux at the end of the pipe $Q(L)$ always equals to the initial value $Q^0(L)$. The reason for this can be seen from Eqs. (10)–(13). In this paper, the modified inverse algorithm proposed by Huang and Ozisik [10] was used to predict the value of heat flux $Q(L)$ at the end of the pipe. In the modified inverse algorithm, the basic steps are the same with that of the general inverse algorithm shown in the preceding section except that the search direction and the conjugate coefficient are obtained as follows.

By seeking a continuously differentiable function $Q(X)$, which is represented as

$$Q(X) = \int_{\xi=0}^{X} dQ(\xi)/d\xi d\xi \tag{15}$$

from Eqs. (9) and (10), we obtain

$$D_{\Delta Q}J = \int_{X=0}^{L} \overleftrightarrow{\theta}(X,1)\Delta Q(X)dX \tag{16}$$

Integrating Eq. (16) by parts gives

$$D_{\Delta Q}J = \int_{X=0}^{L} d\Delta Q(X)/dX \int_{X}^{L} \overleftrightarrow{\theta}(\xi,1)d\xi dX \tag{17}$$

By comparing Eqs. (16) and (17), we can conclude that the gradient of J with respect to dQ/dX can be expressed as

$$\nabla J_{dQ/dX} = \int_{X}^{L} \overleftrightarrow{\theta}(\xi,1)d\xi \tag{18}$$

According to Huang and Ozisik [10], we define

$$P^n(X) = \int_{0}^{X} (\nabla J^n_{dQ/dX} + \gamma^n P P^{n-1}(\xi))d\xi \tag{19}$$

where the conjugate coefficient γ is given by

$$\gamma^n = \int_0^L (\nabla J^n_{dQ/dX})^2 dX \Big/ \int_0^L (\nabla J^{n-1}_{dQ/dX})^2 dX, \quad \gamma^0 = 0 \tag{20}$$

Equation (20) is the expression for the conjugate coefficient for the modified conjugate gradient method.

3.6 Improved Inverse Algorithm Based on the Conjugate Gradient Method. It should be noted here that due to the same reason as the regular conjugate gradient method, the modified inverse algorithm based on the conjugate gradient method cannot identify the value of unknown heat flux $Q(0)$ at the beginning of the pipe. In this investigation, we proposed an improved inverse algorithm that includes a combination of the modified conjugate gradient method and the normal conjugate gradient method. Our improved inverse algorithm is consisted of two parts: The modified inverse algorithm is used first to obtain a reasonable value of heat flux at the end point of the pipe $Q(L)$, then the algorithm is switched to the general inverse algorithm to obtain a converged solution profile. In the following presentation, the results obtained from different inverse algorithms for three cases of outside flux distributions will be presented. The effects of the Reynolds number upon the performance of the improved inverse algorithm will also be shown.

4 Results and Discussion

In practice, the temperature measurements always contain some degree of measurement error. To simulate a set of real experimental data, in this study we generate the measurement data by adding the random error to the exact temperature T [10–15]. The simulated measurement data can be expressed in the following dimensional way:

$$T^* = T + \varpi\sigma \tag{21}$$

where T denotes the exact temperature, which is the solution of the direct problem, σ is the standard deviation of the measurement error (in °C), which takes values of 0.0, 0.10, and 0.19 in this investigation, and ϖ is a random number with normal distribution lying in the range of $-2.567 < \varpi < 2.567$ generated by a random number generator.

Two kinds of convergence criterion were used in this paper for the case of $\sigma=0$ and $\sigma\neq 0$, respectively. When $\sigma=0$, the object function J can theoretically converge to zero. It is feasible to stop the iteration after a specified iteration number since the decrease in error will become very slow as iteration goes on. But for the case of $\sigma\neq 0$, the iteration must be stopped at an appropriate number as a certain level of noise exists in the measurements. When the iteration is stopped earlier than this optimum number, a fully convergent solution can often not be reached; on the contrary, the solutions may be contaminated by high-frequency components of the noise contained in the measurement data if the iteration is stopped too late. The following condition is adopted for the case of $\sigma\neq 0$ as an estimation of the convergence criterion [10–15]:

$$J < \varepsilon \tag{22}$$

here

$$\varepsilon = \frac{1}{2}\sigma^2 Nm \tag{23}$$

According to our experience, Eq. (23) can provide a good estimation of the appropriate iteration number for stopping iteration. So in our computation, we perform computation using Eqs. (22) and (23) to get an estimated iteration number, then we conduct more iteration to determine a better solution by watching the variation trend of the smoothness of the predicted heat flux profiles.

To examine the performance of the modified inverse algorithm for the prediction of the end point heat flux $Q(L)$ and the improved inverse algorithm for the prediction of the unknown heat flux function $Q(X)$, we adopted three different shapes of heat flux function $Q(X)$, as shown in Fig. 2.

All the computations for the modified conjugate gradient method started with an initial guess of $Q^0(X)=0$, and the predicted end point value $Q(L)$ by the modified conjugate gradient method was then set as the initial heat flux of the regular conjugate gradient method.

The accuracy and robust of the inverse algorithm can be easily determined since the exact solutions were already known. The accuracy of the predicted heat flux is indicated by the parameter err, which is defined as

$$\text{err} = \|Q_{\text{estimated}} - Q_{\text{exact}}\|^2_{L_2} / \|Q_{\text{exact}}\|^2_{L_2} \tag{24}$$

where $\| \|_{L_2}$ is the usual L_2 norm.

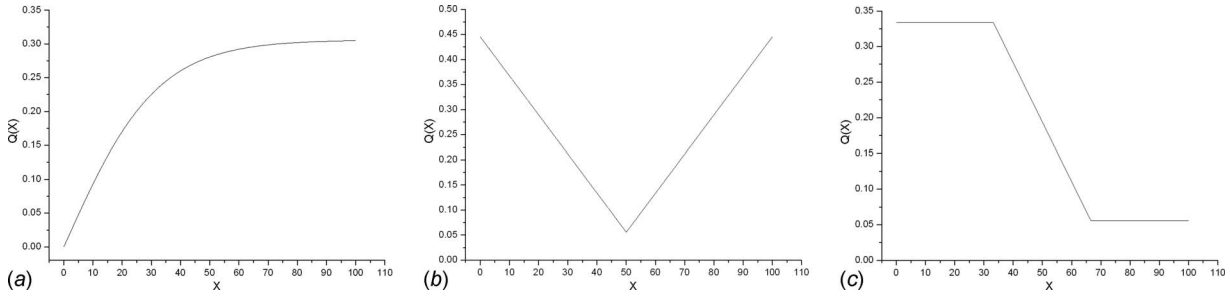

Fig. 2 Three test cases considered in this study. (*a*), (*b*), and (*c*) correspond to case (a), case (b), and case (c), respectively.

4.1 Re=100. In Fig. 3, the computational results are presented first for the most idealized situation in which there is no measurement error, i.e., $\sigma=0.0$. Figures 3(a) and 3(b) correspond to the convergence characteristics of the end point heat flux value $Q(L)$ when using the modified conjugate gradient method with all thermocouples placed at $R_{mea}=0.6R_0$. Figures 3(c) and 3(d) display the unknown wall heat flux $Q(X)$ identified by the inverse algorithm after 15 iterations. It is evident from Figs. 3(a) and 3(b) that the value of $Q(L)$ predicted by the modified conjugate gradient method seems to approach a constant value of 0.36 as iteration goes on. The convergence pattern of $Q(L)$ is different from each other according to the shape of heat flux function. This difference can be directly related to the sequential convergence characteristics [25] of the conjugate gradient (CG) method. The essence of the sequential convergence mechanism [25] of CG is that the CG iteration reveals the low-frequency components of the heat flux first, while the high-frequency components are only revealed at the latter stage. It is well known that the unknown heat flux functions can be expanded in terms of an infinite sum of Fourier series at different frequencies. For test case (a), we stop the iteration for the modified conjugate gradient method after 200 iterations. The $Q(L)$ reaches and maintains the convergence value only after 15 iterations; there are no oscillations found in the whole iteration process. While for test case (b), $Q(L)$ approaches the constant value in an oscillating way, and the iteration needed to reach the

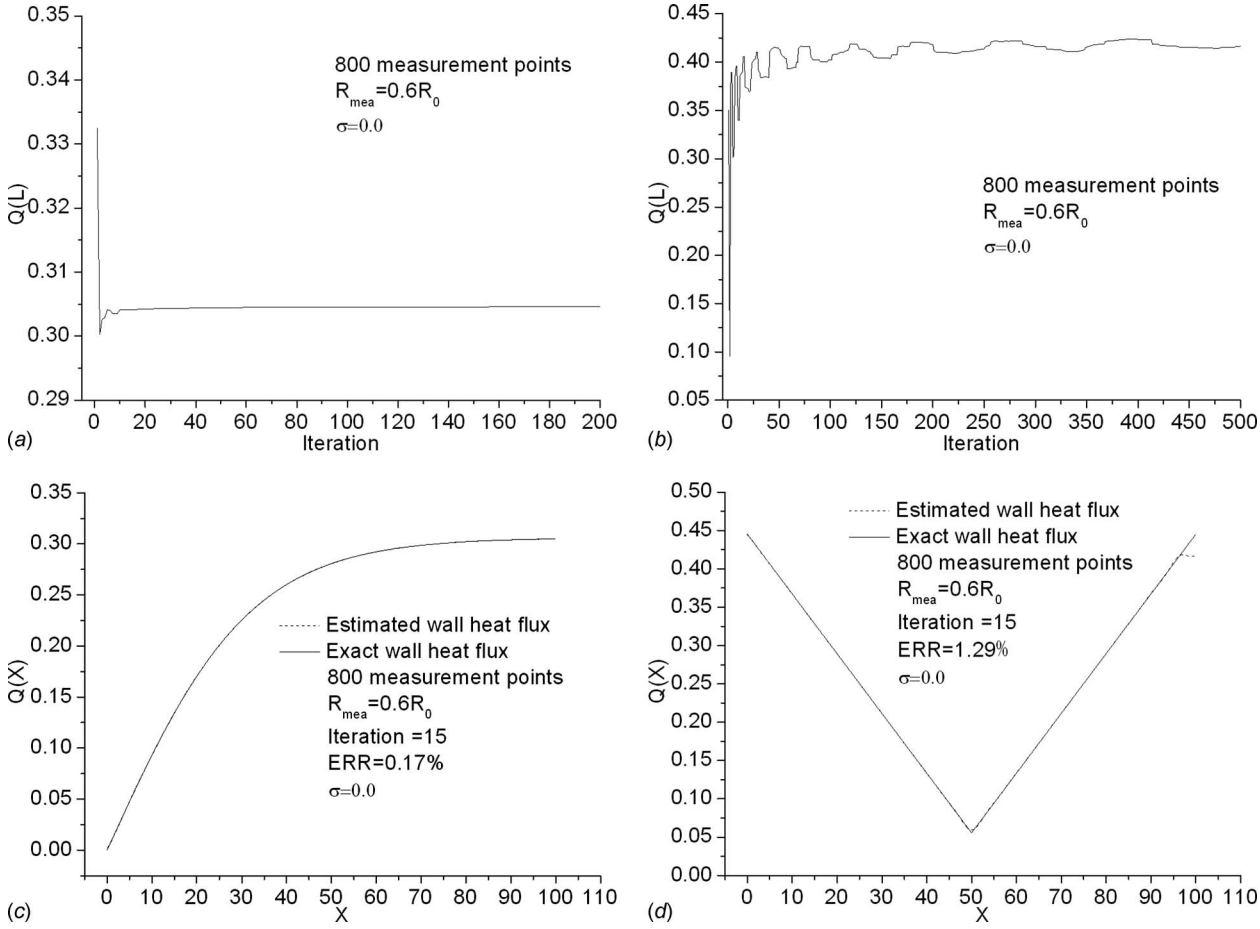

Fig. 3 Computation results for case (a) and case (b) with $R_{mea}=0.6R_0$, $\sigma=0.0$ and 800 measurement points, and Re=100. (*a*) and (*b*) correspond to the convergence characteristic of the end point value $Q(L)$ when using the modified inverse algorithm, (*c*) and (*d*) correspond to the wall heat flux $Q(X)$ identified by the improved inverse algorithm.

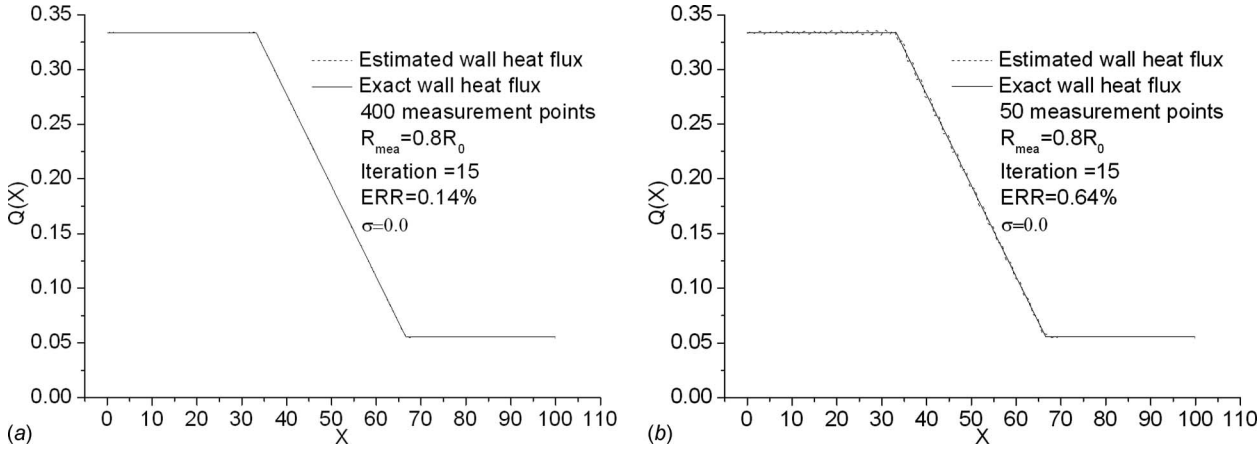

Fig. 4 The effects of the number of thermocouples on the accuracy of estimation for case (c), Re=100. (*a*) and (*b*) correspond to the wall heat flux $Q(X)$ identified by the improved inverse algorithm.

convergence is much larger than that of case (a) since the heat flux profile of case (b) includes more high-frequency Fourier components. The required iteration number is about 300 for case (b).

The estimated values of $Q(L)$ are in excellent agreement with the exact values, which is evident from Figs. 3(*c*) and 3(*d*). There is a small deviation for case (b) in Fig. 3(*d*) near the final position, at $x=100$, but the quality of the estimation can still be regarded as very good, especially when compared with the solution of the original inverse algorithm. Also shown in Figs. 3(*c*) and 3(*d*) are the prediction errors of the predicted unknown heat flux function $Q(X)$. The values of relative error err compared with the exact values are only 0.17% and 1.29% for case (a) and case (b), respectively. It is evident that the large error for case (b) is mainly caused by the inaccurate prediction of end point heat flux value $Q(L)$.

The influences of the number of thermocouples are presented in Fig. 4. It is seen from Fig. 4 that even with 50 thermocouples, at a place closer to the wall, the modified conjugate gradient method can predict the end point heat flux value very accurately. Figure 4(*a*) displays the unknown wall heat flux $Q(X)$ identified by the inverse algorithm after 15 iterations with 400 measurement points, and it can be seen that the solutions are excellent. Some problems occur when we decrease the number of measurement points from 400 to 50. Figure 4(*b*) shows the inverse solution obtained with 50 measurement points and $R_{\text{mea}}=0.8R_0$ after 15 iterations. Increasing or decreasing the number of iterations does not produce any improvement in the accuracy of solutions. It is seen from Fig. 4(*b*) that the inverse solution presents small oscillations. When we move the measurement points to the place of $R_{\text{mea}}=0.9R_0$, the oscillation is more serious. This phenomenon can be interpreted as follows. Fifty measurement points cannot provide enough constraints so as to make the inverse solution well regularized. In addition, the sensitivity with respect to the high-frequency components of the heat flux function is greater as the measurement points move closer to the outer boundary [25]. The value of err for case (c) with 50 measurement points at a place of $0.8R_0$ is 0.64%, while it is 4.38% with 50 measurement points at a place of $0.9R_0$. If the number of measurement points is enough, the movement of the measurement points to the wall will not cause so much prediction error.

Now, we turned to consider the effects of the measurement error. In Fig. 5, the computation results for case (a) with 400 thermocouples for the case of $\sigma=0.1$ and $\sigma=0.19$ are presented; also shown in Fig. 5 is the number of iteration used to obtain the value of $Q(L)$. The convergence criterion of Eqs. (22) and (23) was used to stop the iteration. An overview of Fig. 5 shows that increasing the measurement error increases the value of relative error err, but the heat flux identified by the inverse algorithm is still in a good agreement with the exact value, which demonstrates the sequential filtering mechanism built in the CG method.

4.2 Re=1000. The computation results at a Reynolds number of 1000 are shown in Figs. 6 and 7. Figure 6(*a*) shows the con-

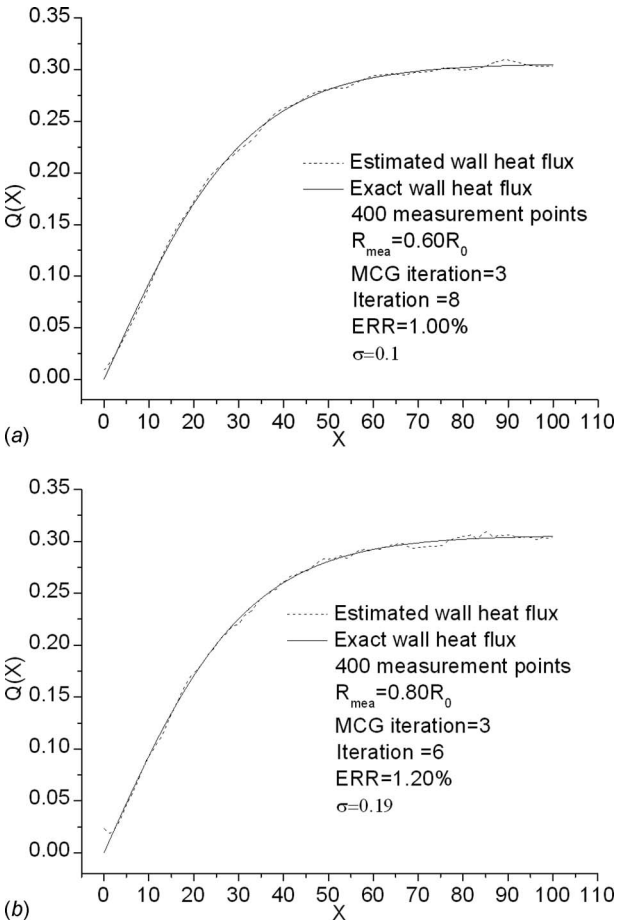

Fig. 5 Computation results for case (a) with measurement errors of $\sigma=0.1$ and $\sigma=0.19$ and Re=100. (*a*) corresponds to the wall heat flux $Q(X)$ identified by the improved inverse algorithm with $\sigma=0.1$, (*b*) corresponds to the wall heat flux $Q(X)$ identified by the improved inverse algorithm with $\sigma=0.19$.

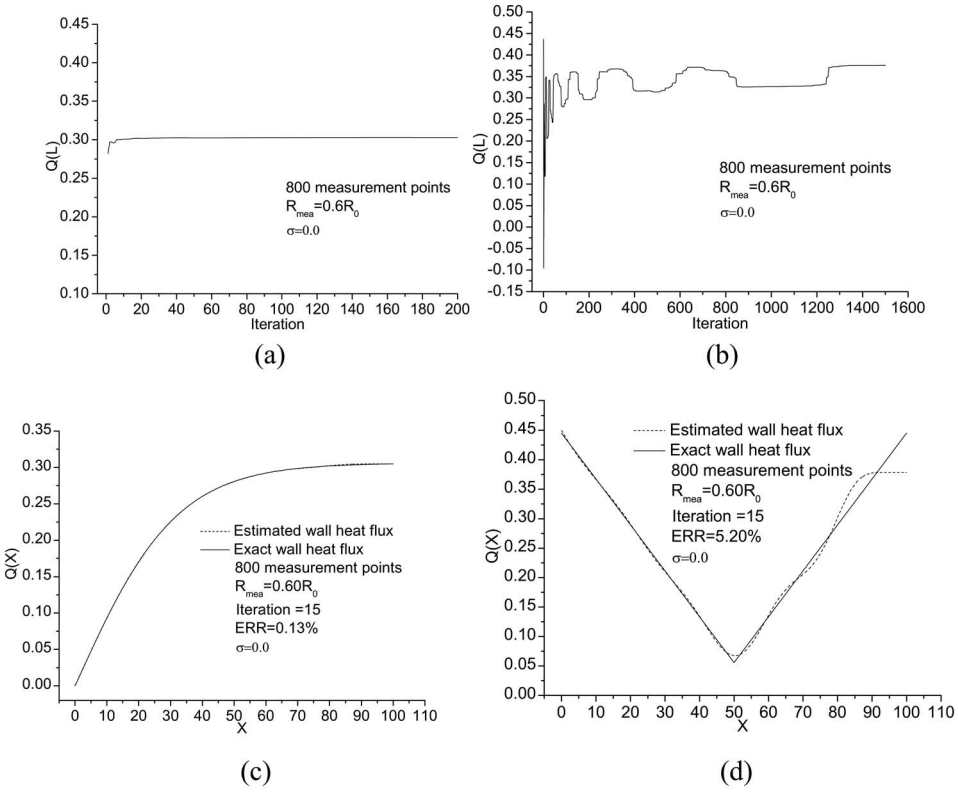

Fig. 6 Computation results for cases (a) and (b) with $R_{mea}=0.6R_0$, $\sigma=0.0$ and 800 measurement points, and Re=1000. (*a*) and (*b*) correspond to the convergence characteristic of the end point value $Q(L)$ when using the modified conjugate gradient method. (*c*) and (*d*) correspond to the wall heat flux $Q(X)$ identified by the improved inverse algorithm.

vergence characteristics of $Q(L)$ when using the modified conjugate gradient method with 800 measurement points, $R_{mea}=0.6R_0$. It is seen from Fig. 6(*a*) that increasing Reynolds number from 100 to 1000 does not influence the performance of the modified conjugate gradient method for case (a), and the convergence of $Q(L)$ can be declared after only 40 iterations. The value of $Q(L)$ predicted by the modified conjugate gradient method is in a good agreement with the exact one, which is evident from the results shown in Fig. 6(*c*). The inverse solution is very good with a relative error of err=0.13%. The convergence characteristics of $Q(L)$ for case (b) are shown in Fig. 6(*b*). Comparisons of Fig. 3(*b*) with Fig. 6(*b*) show that with the same measurement position and the same number of thermocouples, increasing Re from 100 to 1000 influences the performance of the modified conjugate gradient method significantly. The convergence history presents large oscillations at Re=1000 compared with that of Re=100, and the value of $Q(L)$ cannot approach a constant value even after 1600 iterations. The predicted unknown heat flux $Q(X)$ for case (b) was shown in Fig. 6(*d*). It is evident that there is a large error near the final position of the pipe, which is mainly caused by the inaccurate value of $Q(L)$ predicted by the modified conjugate gradient method, and this phenomenon gives a clear demonstration that the performance of the modified conjugate gradient method can be deteriorated by an increase in Re number. While at the remaining part of the pipe, the inverse algorithm can give good estimation. The relative error err for case (b) is 5.20%.

The influences of the position of measurement points and the number of measurement points at Reynolds number of 1000 were also investigated. The same conclusions with that of Re=100 can be drawn from the computation results, that is, moving the measurement points close to the wall and increasing the number of measurement points increase the accuracy and stability of the modified method of the inverse algorithm.

4.3 Re=2000. Figure 7 presents some results when the Reynolds number takes the value of 2000. It is noted that for case (a), with $R_{mea}=0.6R_0$ and 800 measurement points, the inverse solution is in a good agreement with the exact value. But for cases (b) and (c), the inverse algorithm diverges with the same measurement position. Reasonable results can be obtained when the measurement points are moved to $R_{mea}=0.7R_0$. The effects of the measurement position, the number of measurement points, and the measurement error are also studied; it was found that the same variation trend exists as for the results of Re=100 and Re=1000.

From an overview of the computation results presented in Sec. 4, we can conclude that with the same other parameters, increasing the Reynolds number will decrease the sensitivity so as to deteriorate the performance of the modified inverse algorithm and the extent of the decrease strongly depends on the shape of unknown heat flux. Those functions, which contain more high-frequency components of Fourier series, are more sensitive to the increase in the Reynolds number.

5 Concluding Remarks

An inverse forced convection problem for the determination of the unknown space-dependent wall heat flux in a circular pipe is studied in this paper. An improved inverse algorithm is proposed, which is consisted of the modified inverse algorithm of Refs. [10,11] and the general inverse algorithm based on the conjugate gradient method [23]. Three examples are illustrated by applying

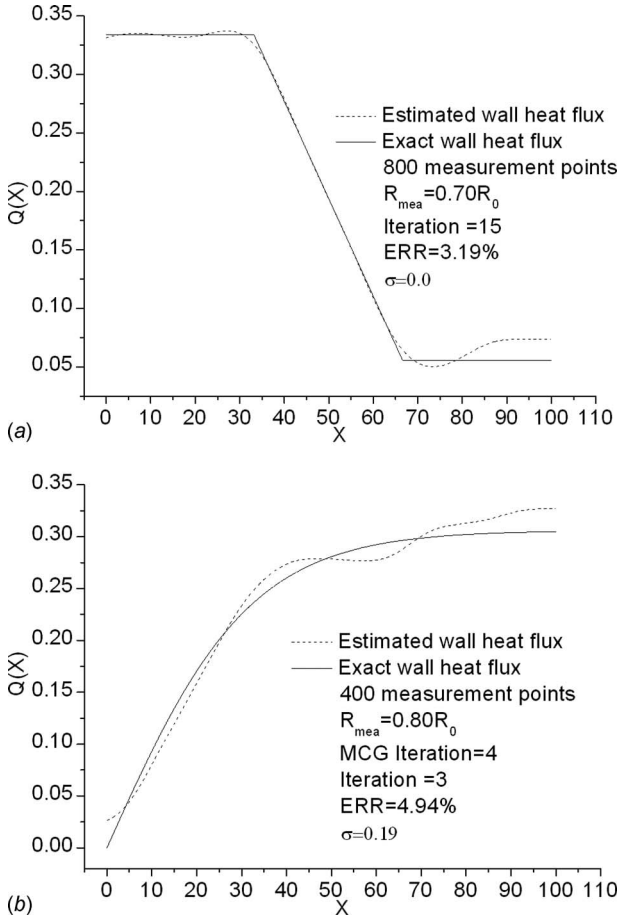

Fig. 7 Some computation results for the case of Re=2000. (*a*) corresponds to the wall heat flux $Q(X)$ identified by the improved inverse algorithm. (*b*) corresponds to the wall heat flux $Q(X)$ identified by the improved inverse algorithm with σ =0.19.

different algorithms. The effects of the convection, the number of thermocouples, the location of the thermocouples, and the measurement error on the performance of the improved inverse algorithm are studied in detail. The improved inverse algorithm has been proved to be an efficient and robust method for the solution of the inverse convection problem. When measurement error is considered, reasonable results can be obtained by stopping the iteration before the higher-frequency components of the noise are recovered and started to deteriorate the solution. An estimation method of the appropriate iteration number is proposed.

The performance of the improved inverse algorithm strongly depends on the Reynolds number, the measurement error, and the shape of the unknown heat flux. Large Reynolds number and measurement error decrease the accuracy and the stability of the improved conjugate gradient method. The performance of all the inverse algorithm can be improved greatly by moving the measurement points closer to the unknown heat flux. Those functions, which contain more high-frequency components of Fourier series, are more sensitive to the increase in the Reynolds number.

Acknowledgment

This work was supported by the National Natural Science Foundation of China (Grant No. 50636050) and the Fundamental Project of R&D in China (973 G2007CB206902).

Nomenclature

a = coefficient in the discretized equation
D = directional derivative
J = object function
q = dimensional heat flux
Q = unknown dimensionless heat flux
R = dimensionless radial coordinate
X = dimensionless streamwise coordinate
T_0 = temperature of fluid
Pr = Prandtl number
Re = Reynolds number
U = dimensionless velocity component in the X direction
$\hat{\theta}$ = temperature sensitivity function
$\ddot{\theta}$ = adjoint function
Δ = the increments between the grid interfaces
∇ = gradient
$\langle | \rangle$ = inner product of two functions

Greek Symbols

θ = dimensionless temperature
ν = kinematic viscosity
α = thermal diffusivity
κ = thermal conductivity
δ = increments between the grid lines
β = search step size
γ = conjugate coefficient
σ = standard deviation of the measurement error
ϖ = a random number

Subscripts

avg = average
o = out
mea = quantity at measurement points

Superscript

n = the nth iteration

References

[1] Hadamard, J., 1923, *Lecture on Cauchy's Problem in Linear Partial Differential Equations*, Yale University Press, New Haven, CT.
[2] Beck, J. V., Blackwell, B., and St-Clair, C. R., Jr., 1985, *Inverse Heat Conduction: Ill-Posed Problems*, Wiley Interscience, New York.
[3] Alifanov, O. M., 1994, *Inverse Heat Transfer Problems*, Springer-Verlag, Berlin.
[4] Huang, C. H., and Tsai, C. C., 1998, "An Inverse Heat Conduction Problem of Estimating Boundary Fluxes in an Irregular Domain With Conjugate Gradient Method," Heat Mass Transfer, **34**, pp. 47–54.
[5] Su, J., and Hewitt, F., 2004, "Inverse Heat Conduction Problem of Estimating Time-Varying Heat Transfer Coefficient," Numer. Heat Transfer, Part A, **45**, pp. 777–789.
[6] Loulou, T., and Scott, E. P., 2006, "An Inverse Heat Conduction Problem With Heat Flux Measurements," Int. J. Numer. Methods Eng., **67**, pp. 1587–1616.
[7] Huang, C. H., and Tsai, Y. L., 2005, "A Transient 3-D Inverse Problem in Imaging the Time-Dependent Local Heat Transfer Coefficients for Plate Fin," Appl. Therm. Eng., **25**, pp. 2478–2495.
[8] Deng, H., Guessasma, S., Montavon, G., Linao, H., Coddet, C., Benkrid, D., and Abouddi, S., 2005, "Combination of Inverse and Neural Network Methods to Estimate Heat Flux," Numer. Heat Transfer, Part A, **47**, pp. 593–607.
[9] Girault, M., and Petit, D., 2005, "Identification Methods in Nonlinear Heat Conduction. Part II: Inverse Problem Using a Reduced Model," Int. J. Heat Mass Transfer, **48**, pp. 119–133.
[10] Huang, C. H., and Ozisik, M. N., 1992, "Inverse Problem of Determining Unknown Wall Heat Flux in Laminar Flow Through a Parallel Pale Duct," Numer. Heat Transfer, Part A, **21**, pp. 2615–2618.
[11] Bokar, J. C., and Ozisik, M. N., 1995, "An Inverse Analysis for Estimating the Time-Varying Inlet Temperature in Laminar Flow Inside a Parallel Plate Duct," Int. J. Heat Mass Transfer, **38**, pp. 39–45.
[12] Colaco, M. J., and Orlande, H. R. B., 2001, "Inverse Forced Convection Problem of Simultaneous Estimation of Two Boundary Heat Flux in Irregularly Shaped Channels," Numer. Heat Transfer, Part A, **39**, pp. 737–760.
[13] Su, J., and Neto, A. J. S., 2001, "Simultaneous Estimation of Inlet Temperature and Wall Heat Flux in Turbulent Circular Pipe Flow," Numer. Heat Transfer, Part A, **40**, pp. 751–766.
[14] Li, H. Y., and Yan, W. M., 2003, "Identification of Wall Heat Flux for Turbulent Forced Convection by Inverse Analysis," Int. J. Heat Mass Transfer, **46**, pp. 1041–1048.
[15] Chen, C. K., Wu, L. W., and Yang, Y. T., 2006, "Estimation of Time-Varying Inlet Temperature and Heat Flux in Turbulent Circular Pipe Flow," ASME J.

Heat Transfer, **128**, pp. 44–52.
[16] Park, H. M., and Lee, J. H., 1998, "A Method of Solving Inverse Convection Problems by Means of Mode Reduction," Int. J. Heat Mass Transfer, **53**, pp. 1731–1744.
[17] Park, H. M., Chung, O. Y., and Lee, J. H., 1999, "On the Solution of Inverse Heat Transfer Problems Using the Karhunen-Leve Galerkin Method," Int. J. Heat Mass Transfer, **42**, pp. 127–142.
[18] Park, H. M., and Chung, O. Y., 1999, "An Inverse Natural Convection Problem of Estimating the Strength of a Heat Source," Int. J. Heat Mass Transfer, **42**, pp. 4259–4273.
[19] Patankar, S. V., 1980, *Numerical Heat Transfer and Fluid Flow*, McGraw-Hill, New York.
[20] Tao, W. Q., 2001, *Numerical Heat Transfer*, 2nd ed., Xi'an Jiaotong University, Xi'an.
[21] Shah, R. K., and London, A. L., 1978, *Laminar Forced Convection in Ducts*, Academic, New York.
[22] Kays, W. M., Crawford, M. E., and Weigand, B., 2005, *Convective Heat and Mass Transfer*, 4th ed., McGraw-Hill, Boston.
[23] Fletcher, R., and Reeves, C. M., 1964, "Function Minimization by Conjugate Gradient Method," Comput. J., **7**, pp. 149–154.
[24] Jarny, Y., Ozisik, M. N., and Bardon, J. P., 1991, "A General Optimization Method Using Adjoint Equation for Solving Multidimensional Inverse Heat Conduction," Int. J. Heat Mass Transfer, **11**, pp. 2911–2919.
[25] Prud'homme, M., and Hung Nguyen, T., 1999, "Fourier Analysis of Conjugate Gradient Method Applied to Inverse Heat Conduction Problems," Int. J. Heat Mass Transfer, **42**, pp. 4447–4460.

Optimization of Fin Performance in a Laminar Channel Flow Through Dimpled Surfaces

Carlos Silva
Doseo Park
Egidio (Ed) Marotta
Leroy (Skip) Fletcher

Department of Mechanical Engineering,
Texas A&M University,
3123 TAMU,
College Station, TX 77843-3123

The effect of the dimple shape and orientation on the heat transfer coefficient of a vertical fin surface was determined both numerically and experimentally. The investigation focused on the laminar channel flow between fins, with a Re = 500 and 1000. Numerical simulations were performed using a commercial computational fluid dynamics code to analyze optimum configurations, and then an experimental investigation was conducted on flat and dimpled surfaces for comparison purposes. Numerical results indicated that oval dimples with their "long" axis oriented perpendicular to the direction of the flow offered the best thermal improvement, hence the overall Nusselt number increased up to 10.6% for the dimpled surface. Experimental work confirmed these results with a wall-averaged temperature reduction of up to 3.7 K, which depended on the heat load and the Reynolds number. Pressure losses due to the dimple patterning were also briefly explored numerically in this work. [DOI: 10.1115/1.2994712]

Keywords: heat transfer enhancement, forced convection, dimples, dimple geometry, laminar flow, channel flow

Introduction

Over the last decade, numerical and experimental work in channel flow has shown that flow over dimpled surfaces develop vortexlike structures inside and in the wake area of the dimples, increasing the overall drag due to inertial and viscous effects in the fluid. However, dimples also increase the surface heat transfer coefficient without a substantial rise in drag penalties observed in other heat transfer enhancement devices such as rib turbulators and pin fins. Fluid motion inside dimples is self-organized: it is *induced* by the presence of the dimple with no physically protruding part projecting into the flow or deflecting it to create the vortices; therefore, dimples lack the pressure loss associated with form drag. Heat transfer is enhanced because vortex structures promote mixing, drawing cold fluid from outside the thermal boundary layer into contact with the wall and ejecting hot fluid from the near wall area into the stream, thus enhancing the overall convective heat transfer.

When a dimpled wall is used in channel flow, dimple geometry play a key role in the heat transfer and drag coefficients. The optimum configuration should provide the higher heat transfer improvement with less drag for a specific application. As of today, there exists no road map to determine the optimum dimple configuration. During the last few years, studies on turbulent flow over dimpled walls have provided some insight into the application of this technology for turbine blade and jet impingement cooling. However, application of dimples in laminar flow was scarcely explored. Microelectronic cooling and microfluids, where the flow regime is mostly laminar, are two potential fields of application for dimple technology.

Objective

The objective of this work was to determine whether or not dimpled surfaces enhance heat transfer coefficients in laminar channel flow. Emphasis was on the dimple geometry and orientation. The following tasks were performed:

- an ongoing literature review and analysis in order to identify key parameters for improved performance
- numerical modeling of novel dimple geometries and orientation relative to the flow
- fabrication and testing of model with the best-performance geometry from simulations
- validation of numerical model with experimental results

A previous numerical study presented by the authors [1] showed that dimples have the potential to improve the convective heat transfer in heat sinks for microelectronic cooling. This paper is intended to validate experimentally and extend on the investigation previously performed.

Literature Review

When a fluid goes over a dimple, the spherical shape of the well creates a pressure field within the recession that modifies the flow and generates vortex structures. Published literature have shown that the Reynolds number, the ratio of the dimple depth to the dimple diameter (relative dimple depth, δ/D), dimple spacing or relative pitch (S/D), and relative channel height (H/D) are the important parameters defining the pressure loss and heat transfer enhancements in flow over dimpled walls.

A number of experimental investigations on the use of dimples in rectangular-channel flow with Reynolds numbers ranging from 5000 to 70,000 have been published. Chyu et al. [2] focused on turbine blade cooling with circular dimples of $\delta/D=0.25$ and teardrop shaped dimples, with this publication being the only experimental work found on noncircular dimples to date. Moon et al. [3] studied dimples of $\delta/D=0.193$ and showed that the improvement on heat transfer is not significantly affected by the channel height when its value is greater than the dimple depth. Mahmood and co-workers [4–6] studied the flow and heat transfer characteristics over staggered arrays of dimples with $\delta/D=0.2$. The effects of inlet stagnation temperature, channel height, and Reynolds number were investigated. Burguess et al. [7] performed a similar study but on an array of dimples with $\delta/D=0.3$ and compared results with Mahmood. Heat transfer improvement was similar while the friction factor increased ~30–40%. Ligrani et al. [8]

Contributed by the Heat Transfer Division of ASME for publication in the JOURNAL OF HEAT TRANSFER. Manuscript received December 22, 2007; final manuscript received August 14, 2008; published online December 15, 2008. Review conducted by Anthony M. Jacobi. Paper presented at the Graduate Student Research and Innovation Conference 2007, ASME District E, Tulsa, OK.

 Copyright © 2009 by ASME

studied the influence of the combined effect of dimples and protrusions on opposite walls and showed that protrusions increased both heat transfer and friction coefficients.

Won et al. [9] and Burgess and Ligrani [10] studied the effect of the dimple's relative depth on the flow structure, Nusselt number, and friction factors on dimples with $\delta/D=0.1$, 0.2, and 0.3. Won et al. [9] performed instantaneous visualization, calculated time-averaged flow structures, and studied vortex-shedding frequencies. Burgess and Ligrani [10] developed empirical correlations for relative Nusselt numbers and friction factors as a function of δ/D in the Reynolds number range from 5000 to 80,000. The correlations showed good agreement with previously published experimental data. Ligrani et al. [11] studied the effect of the inlet turbulence level on the heat transfer improvement in walls with dimples of $\delta/D=0.1$, showing that as the turbulence level is increased the relative Nusselt number is reduced.

Experimental work on channel flow with nonrectangular geometries was performed by Bunker and Donellan [12], who studied turbulent flow in a circular pipe with dimples of $\delta/D=0.23$ and 0.4. Friction factor increment was in the range of 4–6 times that observed for a smooth pipe. Syred et al. [13] studied the effect of plane curvature, testing dimple effects in concave and convex walls. Han [14] studied the rotational effect of dimples in turbine blade cooling, concluding that dimple cooling is a good choice when the pressure drop is the main design concern. Jet impingement over a convex dimpled surface was studied by Chang et al. [15], showing increments in the relative Nusselt number of up to 1.5.

Experimental work on dimple applications for microchip cooling was presented by Small et al. [16]. On a student design competition, 27 heat sinks were tested on a mock microprocessor. The best performance was obtained by a heat sink with a staggered array of rectangular fins with dimpled surfaces. The dimpled heat sink not only showed the lower temperature difference, but also had 25% less volume than the limit set for the design contest. The effect of dimple/bump combinations was also briefly studied.

Wei et al. [17] presented a numerical study on the heat transfer inside a microchannel with one dimpled surface under laminar flow. Dimple δ/D was 0.204 and the Reynolds number, based on the hydraulic diameter, was between 100 and 900. Their results showed that the heat transfer is improved near the trailing edge of the cavities. The increment in the relative Nusselt number was approximately 1.2.

Numerical studies on dimples were performed by Isaev and co-workers [18–23], who used finite difference methods to study the effect of the dimple relative depth over a single dimple. The study showed that at relative depth of 0.22 flow becomes asymmetric and friction/heat transfer coefficients increase abruptly. They also studied the effect of the Reynolds number (both laminar and turbulent) over dimples of $\delta/D=0.22$.

Park and co-workers [24,25] used FLUENT to simulate the flow over dimples with $\delta/D=0.3$, showing a generally good agreement with the experiments from Burgess. Park also performed a numerical study on dimples with seven different geometries (spherical, cylindrical, and triangular) presenting relative Nusselt numbers, velocity, and Eddy diffusivity distributions. Spherical and tilted cylindrical dimples showed the best thermal performance. Silva et al. [1] used FLUENT to simulate the flow over dimples with $\delta/D=0.2$ showing good agreement with experiments from Mahmood. The model was used to improve the dimple spacing by increasing relative pitch (S/D), thus reducing the number of dimples and friction losses while keeping the heat transfer improvement constant.

A numerical study based on the response-surface method (RSM) was performed by Kin and Choi [26] to optimize the shape of a dimple for better turbulent heat transfer and friction losses. Using numerical simulations and the experimental results from Bunker and Donellan, Kin calculated the optimum relative depth and relative pitch to be 0.24 and 1.81, respectively. The optimum relative pitch of 1.81 is in line with the previous study of Silva et al. where the dimple overall performance was improved by increasing the relative pitch from 0.81 to 1.21. These results suggest that there is room for further improvement by increasing the dimple spacing.

Analysis

Through an examination of the published literature, key parameters and characteristics of dimple performance were identified.

- Relative to flat walls, dimpled walls can improve the heat transfer coefficient by up to ~2.5 times. This value seems independent of the Reynolds number in the 5000–70,000 range [1].
- Relative friction factor increment on dimpled walls can vary from ~1.2 to 6 times that of flat walls depending on the Reynolds number and dimple geometry.
- Relative dimple depth of 0.20–0.25 gives the best performance compromise. Higher relative depth increases friction penalties without significant heat transfer improvements; a lower relative depth gives lower heat transfer values.
- The influence of channel height on the dimple performance is negligible when the channel height is equal to or greater than twice the dimple depth [6].
- Local Nusselt number data show that heat transfer coefficients are lower on the leading edge and on the first half of the dimple, but higher on the second half, trailing edge, and flat area immediately downstream of the dimple.
- An opportunity exists for further performance improvement by carefully spacing the dimples in order to take advantage of the higher heat transfer areas while reducing the number of dimples, hence friction losses.

Based on this information some design requirements for dimpled walls were specified.

- Relative dimple depth will be 0.20.
- Relative pitch (S/D) will be specified as 1.21, based on previous numerical studies.
- High heat transfer areas will be increased while trying to reduce total number of dimples.

In order to fulfill the last requirement, the following solutions are proposed for the three high heat transfer areas in a dimpled surface.

- Second half of the dimple: Increase the area by elongating the dimple in the flow direction.
- Trailing edge of the dimple: Increase the edge by elongating the dimple in the direction perpendicular to the flow direction.
- Downstream land-area: Increase the area by adding a second smaller dimple downstream of the main dimple.

The proposed solution calls for the testing of flat surfaces and *circular* dimples as a base line, testing of *oval* dimples with the long axis aligned in both parallel and perpendicular directions relative to the fluid flow direction, and finally the testing of *double* dimples, all as potential ways to improve heat transfer performance.

Numerical Model

A model was developed using FLUENT and the geometry suggested in a previous work [2] on heat sinks. The dimensions of the vertical fin surface are shown in Table 1.

As previously stated, circular, oval, and double dimples will be tested. Oval dimples will be modeled as circular dimples split diametrically with a square section added between the two circular halves (also known as *trenched dimples*). Three midsection sizes will be changed to obtain three oval dimples with different

Table 1 Heat sink geometry

Fin height	10 mm
Fin gap	1.4 mm
Fin thickness	0.5 mm
Fin length	125 mm

aspect ratios, and the oval dimples will be tested with the long axis aligned both in the parallel and perpendicular directions with respect to the fluid flow direction. Double dimples will be modeled as circular dimples with a second smaller dimple in the wake area of every main dimple.

All dimple arrays will be staggered with relative pitch $S/D=1.21$ and a relative depth $\delta/D=0.2$. For the oval dimples, the diameter used for calculation of δ/D and S/D will be that of the circular sections halves, making it so that the oval dimples will have the same total depth and circular-edge-to-edge distance as the circular dimples. The details of the different dimple geometry and arrays used are shown in Fig. 1.

The grid used was a structured hexahedral/wedge mesh with a cylindrical array of elements within the dimples, similar to the general meshing employed in the numerical investigations performed by Isaev and co-workers [18–23]. Figure 2 shows the grid structure and array for the Oval dimple 2, defined in Fig. 1(*c*).

The domain modeled was a channel representing a single vertical fin/gap pair with symmetry boundary conditions on the fin and gap middle planes. The half-thicknesses of the fin surface and gap were 0.25 mm and 0.7 mm, respectively. The whole height of the fin was modeled, but only 20 mm of the fin length measured from the gap entrance was considered. The fin was modeled as copper, with a shroud on top to avoid fluid losses. Fluid was air as an ideal gas, with entrance conditions set at $T=300$ K and a uniform velocity of 5.6 m/s for a Reynolds number of 500 based on the channel (gap) height. The solver used was the segregated implicit, with the semi-implicit method for pressure linked equations (SIMPLE) formulation for the pressure solution and the upwind scheme for momentum and energy equations.

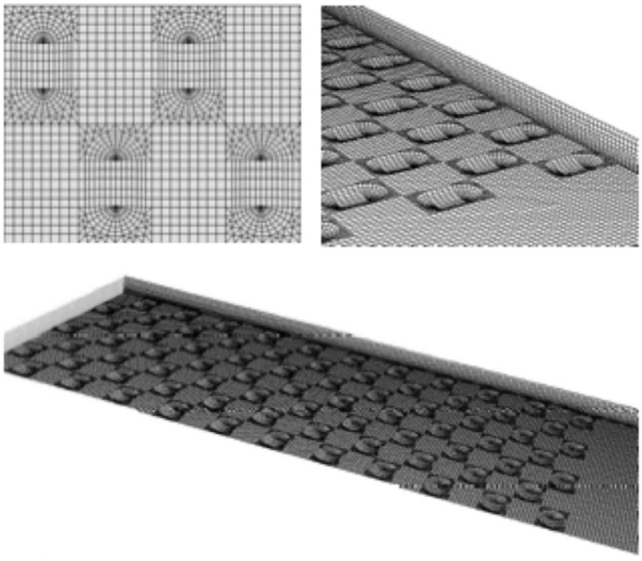

Fig. 2 Grid structure for the Oval dimple 2

Heat flux was 21,000 W/m^2 and was assumed to come from the base of the fin, not from the backside of the dimpled surfaces. This rendered a "lateral" heat flux direction relative to the plane of the dimpled surfaces, and was intended to offer a more realistic model of the fin performance in a heat sink. All other surfaces were considered thermally insulated, with the gap exit modeled as a velocity outflow at atmospheric pressure.

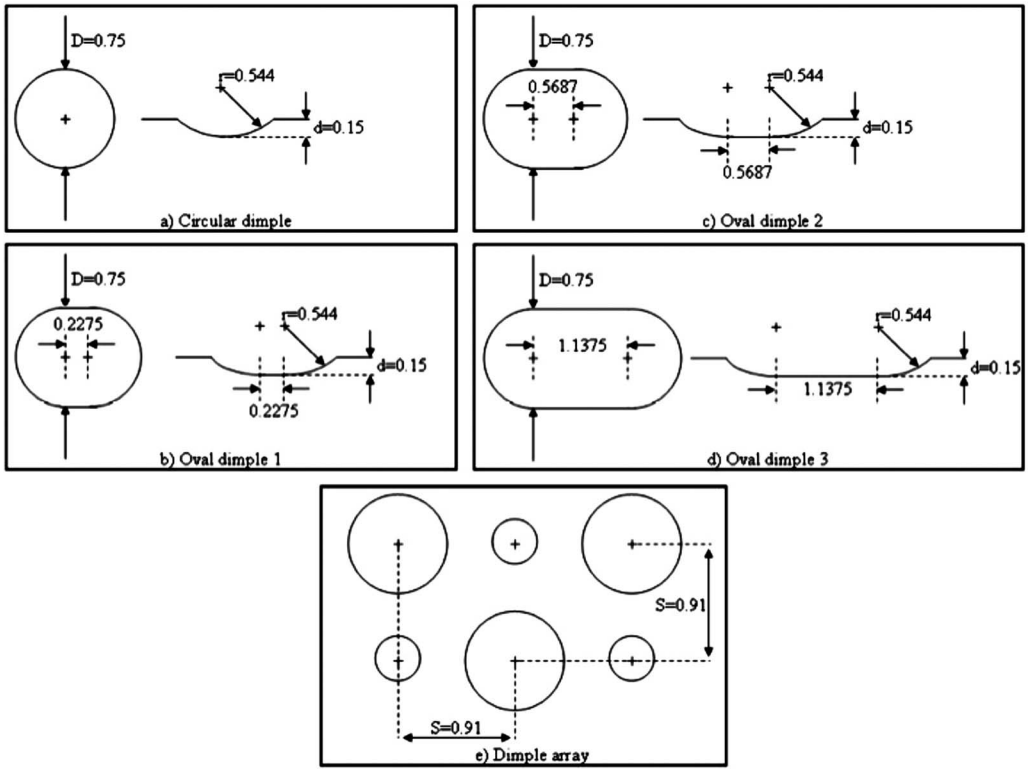

Fig. 1 Dimple geometry and array spacing. In (*e*) the smaller dimple diameter is 0.375. All dimensions are in millimeters.

Table 2 Numerical modeling results, Re=500 and heat flux=21,000 W/m^2

Model	Average wall T (K)	T-T_Flat plate (K)	Pressure drop in test area (Pa)	No. of elements total/test area (10^3)	No. of dimples	Test area size ($L\times H$, mm)
Flat	307.51	—	12.34	1209/361	—	20.02×10.01
Circular dimple	305.99	−1.52	15.39	1250/602	22×10	20.02×10.01
Oval dimple 1-horizontal[a]	307.06	−0.45	15.35	1086/497	18×10	20.47×9.1
Oval dimple 2-horizontal	307.22	−0.29	14.08	1064/475	14×10	20.70×9.1
Oval dimple 3-horizontal	307.28	−0.23	12.83	1034/445	10×10	20.47×9.1
Double dimple	305.74	−1.77	17.24	1544/896	22×10 (both)	20.02×10.01
Oval dimple 1-vertical	305.76	−1.75	16.67	1208/546	22×9	20.02×10.23
Oval dimple 2-vertical	305.64	−1.87	17.42	1192/522	22×7	20.02×10.35
Oval dimple 3-vertical	305.56	−1.95	18.27	1151/489	22×5	20.02×10.24

[a]Horizontal oval dimples have their long axis parallel to the fluid low direction. The vertical oval dimples have their long axis perpendicular to the fluid flow direction.

Grid independence was tested with numerical models of 1.22×10^6, 1.99×10^6, and 2.60×10^6 elements for the circular dimple plate. Difference in the heat transfer coefficient obtained from these three models was less than 0.2%; therefore the smaller domain was selected as the base line for all the simulations. Grid size varied from 1.03×10^6 elements to 1.54×10^6 elements depending on the number of dimples on the test section. To guarantee hydraulically developed flow at the beginning of the dimple plate, all the models had an entrance section three times the length of the test section. Calculations were performed with an IBM Regatta p690 supercomputer facility. Convergence was declared when residuals for continuity, velocity, and energy reached values of 10^{-5}, 10^{-6}, and 10^{-9}, respectively. Simulations converged after 600 iterations, taking approximately 15 h running on a single 1.3 GHz processor.

Numerical Results. Table 2 shows the area-averaged wall temperature, pressure drop, and specific characteristics of every model simulated for Re=500. Oval dimples, with their long axis aligned with the flow direction, were identified as "horizontal," while "vertical" indicated the long axis was aligned perpendicular to the flow. Only whole dimples were considered in these models; as a result, small size differences exist between models, especially in fin height, depending on the number of dimples and alignment.

Results show that circular, double, and oval vertical dimples improved the average wall temperature by up to 1.95 K when compared to the flat wall. Horizontal oval dimples offered little to no temperature improvement. Temperature distribution over the flat wall can be seen in Fig. 3, while Fig. 4 shows local temperatures for all the eight dimpled surfaces modeled. Pressure losses were calculated as the difference between the area-averaged static pressures in the inlet and outlet. Pressure loss increased in the dimpled models, with the double and vertical oval dimples showing the higher increments (up to 26%) when compared to the flat wall. There appears to be a correlation between pressure loss and the total length of trailing edges "seen" by the flow.

Figure 4(a) shows the same trend observed in published literature on dimple heat transfer improvement: Local Nusselt number is relatively lower on the leading edge and on the first half of the dimples (hence higher temperatures) but increases in the second half: trailing edge and wake area of the dimples (lower temperatures are observed). Figures 4(b)–4(d) show that in the case of the horizontal oval dimples, the higher temperature of the first half keeps constant inside of the dimples (no Nusselt number improvement inside the cavity) and it is over the trailing edge that heat transfer increases and temperature reduces. Some dimples in Figs. 4(c) and 4(d) show an area of slightly lower temperature inside the cavity, just upstream of the dimple center. This cold spot appears to be located in the place where the separated fluid from the leading edge reattaches to the bottom surface inside of the dimple. It is the authors' opinion that isolated recirculating pockets of fluid generate the high temperatures around the cold spots.

In general the average wall temperature on the channel with horizontal oval dimples increases as the dimples are elongated in the flow direction, with the Oval dimple 3-horizontal (Fig. 4(d)) having almost the same temperature profile as the flat wall (Fig. 3). Pressure drop decreases as the horizontal oval dimples are

Fig. 3 Temperature distribution in the flat surface of the heat sink fin. Fluid flow is from left to right. Heat flow is from the bottom.

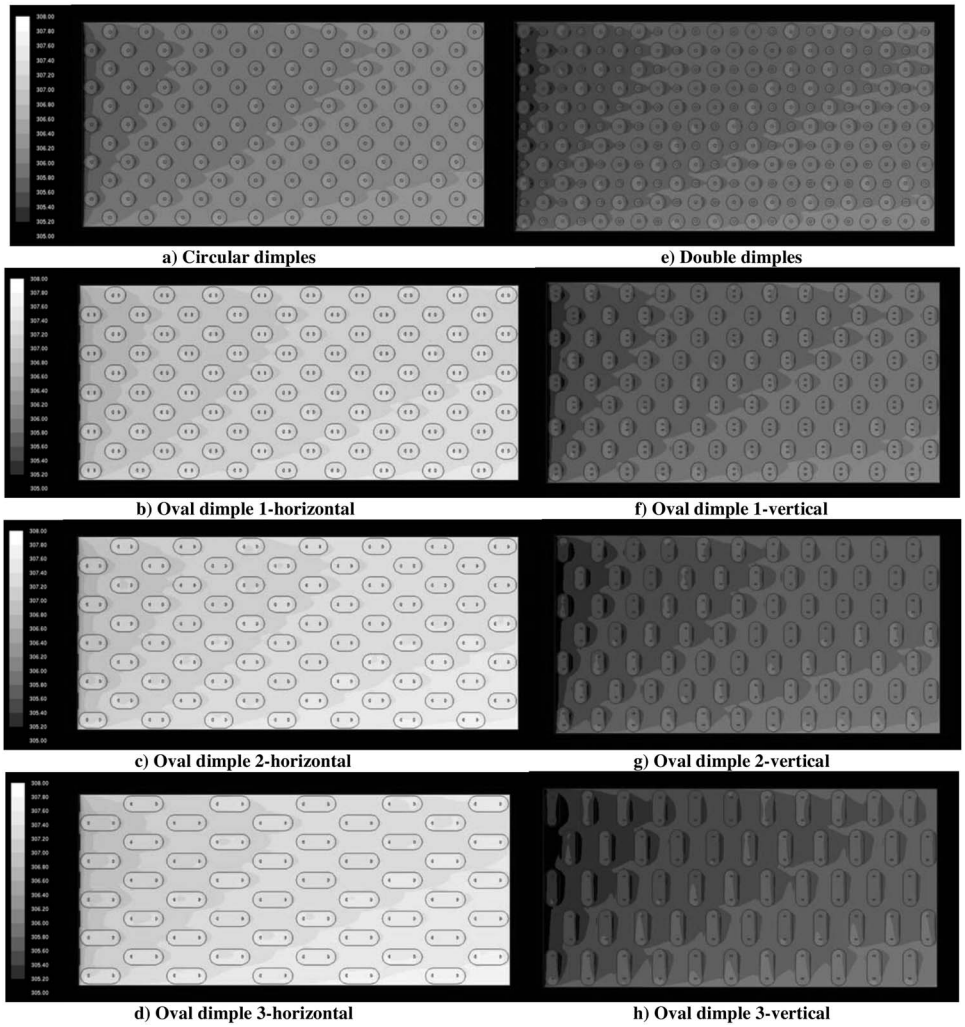

Fig. 4 Temperature distribution over the dimpled surfaces. Temperature legend is the same as in Fig. 3. Fluid flow is from the left to right. Heat flow is from the bottom to the top. (*a*) Circular dimples, (*b*) Oval dimple 1-horizontal, (*c*) Oval dimple 2-horizontal, (*d*) Oval dimple 3-horizontal, (*e*) Double dimples, (*f*) Oval dimple 1-vertical, (*g*) Oval dimple 2-vertical, and (*h*) Oval dimple 3-vertical.

elongated, with the Oval dimple 3-horizontal having similar losses as the flat plate. A reduced number of dimples seem to be the reason for this phenomenon.

Figure 4(*e*) shows the effect of double dimples, where the secondary smaller dimple increased the high Nusselt number area behind every main dimple. Small cold spots are observed after the secondary dimples, indicating that they not only increased the area, but also boosted the already improved Nusselt number downstream of the main cavities. Adding secondary dimples reduced the temperature of the circular dimpled wall by an additional 0.25 K with only a 6% increment in friction losses. One noteworthy observation is that the main dimple arrays of Figs. 4(*a*) and 4(*e*) were the same: The only difference between them was the addition of the secondary dimples in the center of the flat area between main dimples.

Figures 4(*f*)–4(*h*) show the effect of elongating the dimples perpendicularly to the fluid flow direction. The elongation increased the area with relative high Nusselt number in the trailing edge and downstream of the dimples where cold spots were present, thus reducing the average wall temperature. Temperature improvement between Oval dimples 1-vertical and 2-vertical (Figs. 4(*f*)–4(*h*)) was higher than between Oval dimple 2-vertical and 3-vertical (Figs. 4(*g*) and 4(*h*)) suggesting that there might be an optimum oval dimple size for heat transfer improvement. Models depicted in Figs. 4(*f*) and 4(*g*) showed an average wall temperature improvement of ~1.8 K and ~0.3 K over the flat and circular dimple plate, respectively. Pressure losses increased as the dimples were elongated, mainly due to the increment in length of the dimples' trailing edge where the separated fluid form the leading edge impinges generating pressure loss.

According to the numerical results and analysis, Oval dimple 2-vertical offered a good compromise between heat transfer improvement and friction losses and was therefore selected in conjunction with the flat plate and conventional dimple for the experimental work. Table 3 shows the average convective heat transfer coefficient and Nusselt number for the three selected models, calculated using energy balance, area-averaged wall, inlet and outlet temperatures, and the total area (flat and dimpled area) in each model. Thermal conductivity of air at 303 K and a channel half-height of 0.7 mm were considered for the Nusselt number calculation.

It is important to note that relative Nusselt numbers shown in Table 3 are much lower than the values previously reported in literature, typically in the range of 1.5–2.5. The authors believe the reason for this difference is (1) our model considers laminar

Table 3 Average convective heat transfer coefficient—Numerical model, Re=500 and heat flux= 21,000 W/m^2

Model	h (W/m^2 K)	Nu	Nu/Nu$_o$ (h/h_{flat})
Flat	128.12	3.465	—
Circular dimple	132.25	3.577	1.032
Oval dimple 2-vertical	141.65	3.831	1.106

Numerical model, Re=1000

Model	h (W/m^2 K)	Nu	Nu/Nu$_o$ (h/h_{flat})
Flat	185.84	5.026	—
Circular dimple	197.85	5.351	1.064
Oval dimple 2-vertical	216.00	5.842	1.162

flow while almost all previous work studied turbulent regimes with Re$\geqslant$5000 and (2) previous investigations have the heat flux coming from the backside of the dimpled wall while in our model heat flux comes from one side of the dimple wall (fin base). Previous experimental investigation of Small et al. [16] considered the same heat-flux boundary condition, and their average heat transfer improvement ranged from 1.14 to 1.45.

Experimental Work

In order to test the dimple thermal performance an experimental setup was designed and fabricated. Due to the small dimensions of surfaces and dimples modeled numerically ($\sim 20\times 10$ mm), a scale factor of 10 was used for the test plates, using similarity to maintain laminar flow conditions. Three test plates, shown in Fig. 5, were made with ASTM B152 electroless oxygen-free copper following the same geometry of the circular dimple and the Oval dimple 2-vertical shown in Figs. 1(a) and 1(c), respectively.

The plates had dimpled surfaces on both sides and were screwed onto a base made of cooper blocks. Omega electric heaters model KH-108/5-P (Kapton heater, 25.4×203.2 mm, 115 V, 40 W total power) were adhered to the top of the base. The heaters allowed a heat flux of up to 40 kW/m^2 through the 5 mm-thick test plate. Power was supplied by an Elenco Precision variable power supply model XP-800, with multimeters TENMA 72-6685A and 72-6185 used to measure voltage and current into the heater.

Each of the test plates was inserted into a channel constructed with 6.35 mm-thick transparent acrylic (k=0.16 W/m K) to facilitate the visualization of the setup and to minimize heat losses. The channel inner cross section dimensions were 33×103.5 mm, so that the test plate inside the cross section was divided into two 14 mm high channels, each corresponding to the numerical domain previously simulated.

A $300\times 300\times 450$ mm plenum and a 2500 mm long channel section was added downstream and upstream of the test section, the former to stabilize the flow drawn by the blower and the later to guarantee a uniform laminar flow over the test plate. In order to avoid fluid impingement and turbulence generation over the leading edge of the plates, a 5 mm-thick acrylic separator was added from the channel entrance to the test section. A 1.5 in. diameter polyvinyl chloride (PVC) pipe was used from the plenum to the blower, with an ASME-standard orifice plate flowmeter used to determine the volumetric air flow and to define the Reynolds number. Pressure losses in the test section were not measured in this investigation.

Temperature measurements were made using special limited error gauge-30 T-type thermocouples, with a total of 24 thermocouples distributed among the leading, trailing, and bottom edges, base, and centerline of the test section in every plate, as shown in Fig. 6. Additional thermocouples were used at the channel inlet and at the ASME orifice plate in order to obtain the air inlet temperature and the corresponding correction for the volumetric airflow. Thermocouples were connected to a National Instruments data acquisition unit model SCXI-1000 as well as a PC running LABVIEW 7.1. Channel test section was insulated with 1 in. of fiberglass wool, with the heater having a second layer of insulation both on top and between its base and the acrylic wall on top of the channel so that most of the heat flux into the channel went through the copper plates. Figure 7 depicts a schematic of the complete experimental setup.

Heat losses were estimated by measuring the steady state temperature and the electric current on the heater (heat input) during no-flow tests. In order to reduce the effect of natural convection, the channel was filled with insulation material during such tests. Maximum losses were estimated to be 26%.

Experimental Nusselt numbers were calculated by energy balance. Heat transferred to the air was obtained by

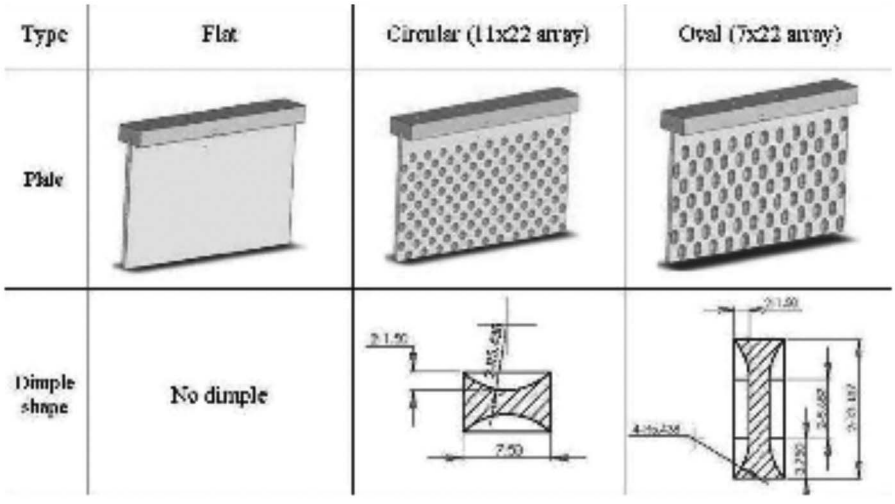

Fig. 5 Flat and dimple test plates

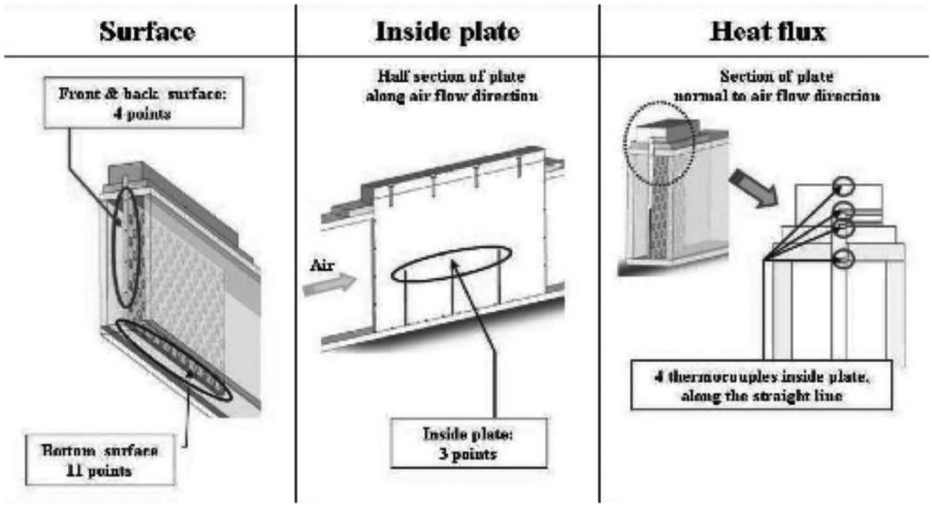

Fig. 6 Thermocouple locations in test plates

$$Q = \dot{m}C_p(T_{\text{outlet}} - T_{\text{inlet}})$$

the convective heat transfer and Nusselt number were calculated using

$$h = \frac{Q}{A_{\text{total}}(T_{\text{wall}} - T_{\text{air}})}$$

$$\text{Nu} = \frac{hl}{k}$$

with T_{wall} and T_{air} being the average of the thermocouples measurements and A_{total} being the total (not the projected) area of the test surface.

Uncertainty Analysis. Uncertainty estimates were determined using methods described by Kline and McClintock [27]. Uncertainty in temperature measurements is ± 0.5 K, while power applied has a $\pm 0.83\%$ uncertainty based on the resolution of the multimeters. The resulting heat transfer coefficient uncertainty is less than $\pm 6.8\%$.

Experimental Results. Experiments were performed for Reynolds numbers of 500 and 1000 and for a power input on the base of the fin equal to 21 kW/m^2, as in the numerical model. A second set of experiments with a lower power input of 14 kW/m^2 was also performed for comparison purposes.

Table 4 shows the power, average wall temperature, and heat transfer coefficients for Re=500 and Re=1000, respectively. Steady state was declared when all temperatures in the data acquisition system remained within ± 0.1 K for a 30 min period. Every test took approximately 8 h. The heat transfer coefficients were calculated using the *total area* and not the projected flat area of the plates; therefore any improvement in the heat transfer coefficient is additional to the increment in area (between 5% and 8%) due to the dimples.

For a Reynolds number equal to 500, Table 4 shows a definitive heat transfer improvement in the Oval dimple-2 plate over the flat plate. Enhancement of 10.4% and 11.4% were observed in the Oval dimple-2 plate for the power levels of 14 kW/m^2 and 21 kW/m^2, respectively, while the circular dimple plate showed 2.4% and no change (0.1%) for the same power levels. These heat transfer improvements follow the same trend observed in the numerical simulation and presented in Table 3, where the Oval dimple-2 surface showed a Nusselt number increase of 10.4% over the flat plate. The numerical model predicted the increment on the circular dimple plate to be 3.2%, slightly higher than the experimental value of 2.4% for the power level of 14 kW/m^2. The coefficients obtained for the circular plate are inside the uncertainty levels, and therefore cannot be regarded as conclusive.

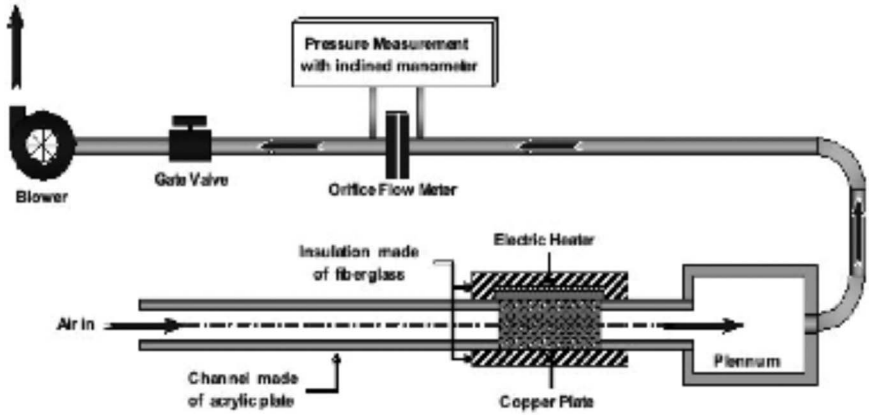

Fig. 7 Schematic of the experimental setup

Table 4 Average convective heat transfer coefficient—Experimental results, Re=500

Model	Power (W/m^2)	Average T_{wall} (K)	h (W/m^2 K)	Nu/Nu_o (h/h_{flat})
Flat	14000	324.01	8.68	—
Circular[a]	14000	322.14	8.89	1.024
Oval[a]	14000	320.77	9.58	1.104
Flat	21000	336.97	9.01	—
Circular	21000	335.88	9.00	0.999
Oval	21000	332.50	10.04	1.114

Experimental results, Re=1000

Model	Power (W/m^2)	Average T_{wall} (K)	h (W/m^2 K)	Nu/Nu_o (h/h_{flat})
Flat	14000	316.48	12.96	—
Circular[a]	14000	315.47	12.50	0.965
Oval[a]	14000	314.64	13.21	1.019
Flat	21000	327.15	12.68	—
Circular	21000	325.91	12.53	0.988
Oval	21000	323.60	13.54	1.068

[a]Circular and Oval correspond to circular dimples and Oval dimple-2 vertical models, respectively.

Experimental results for Re=1000 suggest that, for laminar regime, heat transfer on dimpled surfaces reduces as the Reynolds number increases. Heat transfer improvement on the oval-2 plate reduced from 10.4% (Re=500) to 1.9% (Re=1000) for the power level of 14 kW/m^2, while the circular plate showed a consistent reduction in heat transfer when compared to the flat wall. A possible explanation suggested by Ligrani et al. [11] for turbulent flow over dimpled surfaces is that higher turbulence levels increase diffusion and reduce the beneficial thermal effects of vortex shedding and secondary flow from the dimples. Even though the present investigation is in laminar regime, we suspect that there is an augmentation in the turbulence levels generated by the dimples as the Reynolds number is increased. The numerical simulation results shown in Table 3 indicate that the Nusselt number improvement should increase with the Reynolds number; however this simulation was based on a laminar viscous model and cannot capture any turbulence intensification effect, if present. The typical flow structure over the dimples obtained numerically for Re=500 is shown in Fig. 8. The authors believe that a more extensive experimental work with flow visualization is required to explain the physical phenomena behind the change of the heat transfer coefficient with the Reynolds number.

As a final remark on the experimental data, it can be seen in Table 4 that circular and oval-2 dimpled plates *always* showed a reduction in the average temperature, with a maximum of 3.7 K (after correction by the air inlet temperature) in the oval-2 dimple plate at Re=500 and at a power level of 21 kW/m^2. Even though there were small variations in the measured inlet temperature for every experiment (not shown), the much bigger temperature reduction associated with the dimpled plates reinforced the idea that there is an improvement on thermal performance using dimpled walls in laminar channel flow.

Findings/Conclusions

Numerical and experimental work was performed to determine the effect of dimpled surfaces on the convective heat transfer in the channel flow under a laminar regime with the Reynolds number (based on the channel height) between 500 and 1000. This study identified the best-performance dimple geometry and conducted experiments to validate the numerical results. The following findings/conclusions can be drawn from the work done:

- Dimple geometry affects heat transfer and friction coefficients:
  - Circular dimples perform—thermally—better than flat plates.
  - Double and oval dimples with the long axis aligned perpendicularly to the flow direction offered better performance than circular dimples. Thermal improvement and friction losses increased as dimples were elongated.
  - Oval dimples with their long axis aligned parallel to the flow direction showed worse performance than circular dimples (close to flat plates). Thermal improvement and friction losses decreased as dimples were elongated.
- Heat transfer coefficients were improved for dimpled surfaces; oval dimples, ranging from 11% (Re=500) to ~4.5% (Re=1000), with the lower bound of this range being under the uncertainty levels. Heat transfer coefficient for circular dimples was entirely under the uncertainty levels, and was therefore, inconclusive.
- Heat transfer improvement with dimples seems to be dependent on the Reynolds number. Coefficients measured at Re=500 were consistently higher than those at Re=1000.
- Average wall temperature of dimpled plates, after being corrected by the inlet temperature, was always equal or lower than the flat plate temperature. A maximum temperature reduction of 3.7 K was observed in the Oval dimple-2 vertical configuration, showing the potential benefits of dimples in laminar channel flow.

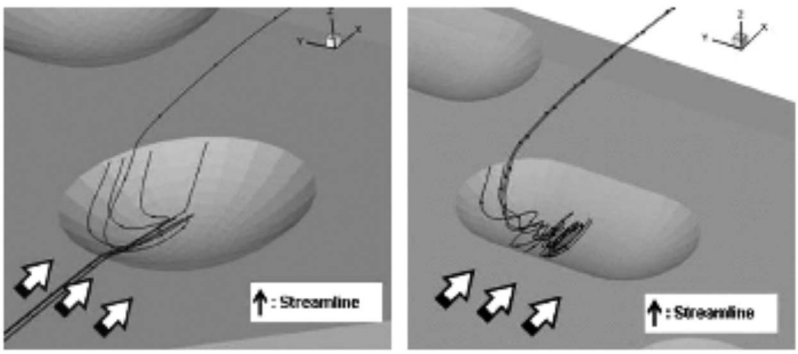

Fig. 8 Flow structure over dimples, Re=500

Acknowledgment

The authors would like to acknowledge the collaborations of Roger Schmidt from IBM for his input in the heat sink geometry used in this work and Laura Hutchinson, proofreader extraordinaire.

Nomenclature

C = internal flow friction factor
C_o = internal flow friction factor, flat channel
C_p = specific heat at constant pressure (J/g K)
D = dimple print diameter (mm)
H = channel height (mm)
h = convective heat transfer coefficient ($W/m^2 K$)
k = thermal conductivity (W/m K)
l = characteristic length (mm)
Nu = internal flow Nusselt number
Nu_o = internal flow Nusselt number, flat channel
$\dot{m}$ = mass flow (g/s)
Q = heat flow (W)
Re = Reynolds number based on channel height
S = dimple pitch (center to center distance, mm)
T = temperature (K)
T_{wall} = average wall temperature (K)
δ = dimple depth (mm)

References

[1] Silva, C., Marotta, E., and Fletcher, L., 2007, "Flow Structure and Enhanced Heat Transfer in Channel Flow With Dimpled Surfaces: Application to Heat Sinks in Microelectronic Cooling," ASME J. Electron. Packag., **129**, pp. 157–166.
[2] Chyum, M. K., Yu, Y., Ding, H., Downs, J. P., and Soechting, F. O., 1997, "Concavity Enhancement Heat Transfer in an Internal Cooling Passage," ASME Paper No. 97-GT-437.
[3] Moon, H. K., O'Connel, T., and Glezer, B., 2000, "Channel Height Effect on Heat Transfer and Friction in a Dimple Passage," ASME J. Eng. Gas Turbines Power, **122**, pp. 307–313.
[4] Mamood, G. I., Hill, M. L., Nelson, D. L., Ligrani, P. M., Moon, H. K., and Glezer, B., 2001, "Local Heat Transfer and Flow Structure on and Above a Dimpled Surface in a Channel," ASME J. Turbomach., **123**, pp. 115–123.
[5] Mamood, G. I., and Ligrani, P. M., 2002, "Heat Transfer in a Dimpled Channel: Combined Influences of Aspect Ratio, Temperature Ratio, Reynolds Number and Flow Structure," Int. J. Heat Mass Transfer, **45**, pp. 2011–2020.
[6] Mamood, G. I., Sabbagh, M. Z., and Ligrani, P. M., 2001, "Heat Transfer in a Channel With Dimples and Protrusion on Opposite Walls," J. Thermophys. Heat Transfer, **15**(3), pp. 275–283.
[7] Burguess, N. K., Oliveira, M. M., and Ligrani, P. M., 2002, "Nusselt Number Behavior on Deep Dimpled Surfaces Within a Channel," ASME Paper No. IMECE 2002–32941.
[8] Ligrani, P. M., Mahmood, G. I., Harrison, J. L., Clayton, C. M., and Nelson, D. L., 2001, "Flow Structure and Local Nusselt Number Variation in a Channel With Dimples and Protrusions on Opposite Walls," Int. J. Heat Mass Transfer, **44**, pp. 4413–4425.
[9] Won, S. Y., Zhang, Q., and Ligrani, P. M., 2005, "Comparisons of Flow Structure Above Dimpled Surfaces With Different Dimple Depths in a Channel," Phys. Fluids, **17**, p. 045105.
[10] Burgess, N. K., and Ligrani, P. M., 2005, "Effects of Dimple Depth on Channel Nusselt Numbers and Friction Factors," ASME J. Heat Transfer, **127**, pp. 839–847.
[11] Ligrani, P. M., Burgess, N. K., and Won, S. Y., 2005, "Nusselt Numbers and Flow Structure on and Above a Shallow Dimpled Surface Within a Channel Including Effects of Inlet Turbulence Intensity Level," ASME J. Turbomach., **127**, pp. 321–330.
[12] Bunker, R. S., and Donellan, K. F., 2002, "Heat Transfer and Friction Factors for Flow Inside Circular Tubes With Concavity Surfaces," ASME Paper No. GT 2003-38053.
[13] Syred, N., Khalatov, A., Kozlov, A., Shchukin, A., and Agachev, R., 2000, "Effects of Surface Curvature on Heat Transfer and Hydrodynamics Within a Single Hemispherical Dimple," ASME Paper No. 2000-GT-236.
[14] Han, J., 2006, "Turbine Blade Cooling Studies at Texas A&M University: 1980–2004," J. Thermophys. Heat Transfer, **20**(2), pp. 161–187.
[15] Chang, S. W., Jan, Y. J., and Chang, S. F., 2006, "Heat Transfer of Impinging Jet-Array Over Convex-Dimpled Surface," Int. J. Heat Mass Transfer, **49**, pp. 3045–3059.
[16] Small, E., Sadeghipour, S. M., and Asheghi, M., 2006, "Heat Sinks With Enhanced Heat Transfer Capability for Electronic Cooling Applications," ASME J. Electron. Packag., **128**, pp. 285–290.
[17] Wei, X. J., Joshi, Y. K., and Ligrani, P. M., 2007, "Numerical Simulation of Laminar Flow and Heat Transfer Inside a Micro-Channel With One Dimpled Wall," ASME J. Electron. Packag., **129**, pp. 63–70.
[18] Isaev, S. A., Leontiev, A. I., Usachev, A. E., and Frolov, D. P., 1997, "Numerical Simulation of Laminar Incompressible Three-Dimensional Flow Around a Dimple (Vortex Dynamics and Heat Transfer)," Russian Ministry of Science and Technology Institute for High-Performance Computing and Databases, preprint 6-67.
[19] Isaev, S. A., Leontiev, A. I., Metov, Kh. T., and Kharchenko, V. B., 2002, "Modeling of the Influence of Viscosity on the Tornado Heat Exchange in Turbulent Flow Around a Small Hole on the Plane," J. Eng. Phys. Thermophys., **75**(4), pp. 890–898.
[20] Isaev, S. A., Leontiev, A. I., Metov, Kh. T., and Kharchenko, V. B., 2002, "Verification of the Multiblock Computational Technology in Calculating Laminar and Turbulent Flow Around a Spherical Hole on a Channel Wall," J. Eng. Phys. Thermophys., **75**(5), pp. 1155–1158.
[21] Isaev, S. A., and Leontiev, A. I., 2003, "Numerical Simulation of Vortex Enhancement of Heat Transfer Under Conditions of Turbulent Flow Past a Spherical Dimple on the Wall of a Narrow Channel," High Temp., **41**(5), pp. 665–679.
[22] Isaev, S. A., Leontiev, A. I., Baranov, P. A., Metov, Kh. T., and Usachev, A. E., 2001, "Numerical Analysis of the Effect of Viscosity on the Vortex Dynamics in Laminar Separated Flow Past a Dimple on a Plane With Allowance for its Asymmetry," J. Eng. Phys. Thermophys., **74**(2), pp. 339–346.
[23] Isaev, S. A., Leontiev, A. I., and Baranov, P. A., 2000, "Identification of Self-Organized Vortex-Like Structures in Numerically Simulated Turbulent Flow of a Viscous Incompressible Liquid Streaming Around a Well on a Plane," Tech. Phys. Lett., **26**(1), pp. 15–18.
[24] Park, J., Desam, P. R., and Ligrani, P. M., 2004, "Numerical Predictions of Flow Structure Above a Dimpled Surface in a Channel," Numer. Heat Transfer, Part A, **45**, pp. 1–20.
[25] Park, J., and Ligrani, P. M., 2005, "Numerical Predictions of Heat Transfer and Fluid Flow Characteristics for Seven Different Dimpled Surfaces in a Channel," Numer. Heat Transfer, Part A, **47**, pp. 209–232.
[26] Kin, K. Y., and Choi, J. Y., 2005, "Shape Optimization of a Dimpled Channel to Enhance Turbulent Heat Transfer," Numer. Heat Transfer, Part A, **48**, pp. 901–915.
[27] Kline, S. J., and McClintock, F. A., 1953, "Describing Uncertainties in Single Sample Experiments," Mech. Eng. (Am. Soc. Mech. Eng.), **75**, pp. 3–8.

Air-Side Heat Transfer and Friction Correlations for Flat-Tube Louver-Fin Heat Exchangers

Young-Gil Park[1]
Post-doctoral Research Associate
e-mail: ypark5@uiuc.edu

Anthony M. Jacobi
Professor of Mechanical Engineering
e-mail: a-jacobi@uiuc.edu

Department of Mechanical Science and Engineering,
University of Illinois,
1206 West Green Street,
Urbana, IL 61801

The objective of this study is to develop an accurate, reliable, and updated predictive model for the air-side performance of flat-tube louver-fin heat exchangers. Using the most comprehensive experimental database to date—consisting of 1030 heat-transfer and 1270 pressure-drop measurements, from nine independent laboratories for 126 sample heat exchangers—j- and f-factor correlations are developed to predict the air-side performance of heat exchangers. The database is analyzed, the form of the curve fits is explored, and the predictive performance of the correlations is evaluated. The j- and f-factor correlations predict the experimental data with rms errors of 11.5% and 16.1%, respectively. Multiple regressions for a locally linearized data model were used to estimate the confidence intervals and covariances of the regression constants. A comparison to prior correlations shows the proposed correlations to provide more accurate predictions and to span a much broader parameter space than prior work. Practical utility in design and optimization, and unavoidable limitations in developing such correlations are discussed. [DOI: 10.1115/1.3000609]

Keywords: louver-fin, flat-tube, heat exchanger, heat transfer, friction, correlation, confidence interval

1 Introduction

Heat exchangers with flat tubes and louver fins are commonly used in air-cooling applications where compactness is desired, such as for automotive systems, and they are being more widely adopted in systems where energy efficiency and material-cost constraints drive heat exchanger design, such as in residential and commercial air-conditioning and heat pumping systems. Among the advantages of the flat-tube design over the round-tube design are higher compactness and reduced material costs, reduced refrigerant charge, lower fan power, and improved suitability for high tube-side operating pressures. On the other hand, flat-tube designs generally have higher manufacturing costs and can be subject to more severe performance degradation by air-side surface fouling, condensate retention, and frost accumulation. For heat-transfer surface design as well as for thermal-system design and optimization, in the context of such trade-offs, it is imperative to have reliable performance estimation for flat-tube louvered-fin heat exchangers.

A number of correlations for the thermal-hydraulic performance of flat-tube louver-fin heat exchangers can be found in the open literature [1–9]. These correlations have been reported to accurately predict the data upon which they are based, but most of them sometimes fail to provide acceptable predictions of data reported by independent laboratories, even when the heat exchanger design and operating conditions are within the parameter space spanned by the correlation. Such shortcomings seriously undermine the utility of the correlations, but they are common when a curve fit is developed from a limited database, especially when the database is from a single laboratory. Recognizing this problem and the value of a generalized performance correlation, Chang and Wang [3] compiled an extensive experimental database with 91 heat exchanger samples from related works in the literature and proposed a correlation for Colburn j-factor. Later, using the same database, Chang et al. [8] proposed a correlation for Fanning friction factor. These correlations are essentially Reynolds-number-based power-law functions modified by dimensionless geometrical parameters such as ratios of length parameters or louver angle.

The correlations of Chang and Wang [3] and Chang et al. [8] are generally considered the most reliable available, and they are recognized as providing reasonable predictions for a wide design space. Unfortunately, emerging fin designs do not fall within the parameter space of these earlier correlations, and their j and f predictions are inadequate for some new designs. Furthermore, the j-factor correlation of Chang and Wang [3] assumes a power-law form with a monotonic dependence on Reynolds number and geometric parameters, and this assumed form is not reflected by the data over the entire design and operating space of these heat exchangers. For example, data for flat-tube louver-fin heat exchangers clearly indicate the existence of a louver angle giving maximum heat transfer, but the monotonic form used by Chang and Wang [3] cannot capture this behavior nor does any other existing correlation. As another example, a low-Reynolds-number "flattening" of the j-factor was reported by Achaichia and Cowell [1], and while they provided a correlation to accommodate such a trend, Chang and Wang [3] found that correlation to significantly overpredict data by others. Chang and Wang [3] attributed the trends reported by Achaichia and Cowell to their plate-fin-and-tube geometry. Finally, it is noteworthy that the f-factor correlation by Chang et al. [8] uses of two separate equations, one for high Re and one for low Re, and the two equations predict different f-factors at moderate Reynolds numbers. Although this approach is common, the discontinuity is problematic in large-scale system optimization. Chang et al. [10] recently proposed a simple amendment addressing this issue. However, the "smoothed" discontinuity in the amended f-correlation can still manifest a reversed slope in Reynolds number for certain geometries (e.g., Ref. [11] Source 4). The amended correlation insignificantly affects the present comparison (Table 5) for which the original correlation was used.

A typical flat-tube louver-fin heat exchanger has nine or more design parameters relevant to the air-side performance, the individual and combined effects of which are apparently nonlinear

[1]Corresponding author.

Contributed by the Heat Transfer Division of ASME for publication in the JOURNAL OF HEAT TRANSFER. Manuscript received November 12, 2007; final manuscript received September 15, 2008; published online December 11, 2008. Review conducted by Sai C. Lau.

 Copyright © 2009 by ASME

and complex. Therefore, developing good air-side performance correlations requires not only large and diverse database but also insight into suitable functional forms for the j- and f-factor curves. Selecting the form of the curves to have a physical basis is preferred, because such correlations are more amenable to extrapolation. It is also important for good correlations to reflect maxima and minima if they exist and provide smooth predictions—unless a performance discontinuity truly exists—because such features make the correlations more useful in design and optimization. The correlations available in the open literature need to be improved by expanding the database used in correlation development, including specific known parametric effects such as non-power-law or nonmonotonic trends and providing a continuous prediction over the entire parameter space.

Recently, new data for the air-side performance of flat-tube louver-fin heat exchangers have been reported by Kim and Bullard [4], Kim et al. [12], Jacobi et al. [11], and Dong et al. [9]. Because these measurements included emerging fin designs beyond the extant data, they were poorly predicted by existing correlations. In the present work, an experimental database of Colburn j-and Fanning friction factors was compiled from the literature, including most of the sources used in earlier work [3] and more recent data [4,11,12]. The experimental data by Dong et al. [9] were not included for two reasons: some important parameters (louver length, number of louver banks, and tube diameter) were not available, and an inconsistent effect of fin length seems to exist within their report. Using the expanded database, new correlations have been developed to predict the air-side thermal-hydraulic performance of flat-tube louver-fin heat exchangers. The functional form of the new correlations was selected with a physical basis and captures important parametric effects. The final form of correlation has been obtained after further refinement through a statistical assessment of the regression constants as explained later. The resulting correlations provide performance predictions more accurate than prior work and span a wider design and operating space.

2 Database

Due to a paucity of experimental data for wet- or frosted-surface conditions in the open literature, only the dry air-side surface conditions are considered in the present work; nevertheless, there are many cases where dry-surface conditions prevail and design correlations are needed. It should be noted that the air-side performance of flat-tube louver-fin heat exchangers under wet conditions can be significantly different from the performance under dry conditions [11]. Also, data from numerical simulations are not included because most numerical solutions for the thermal-hydraulic performance of full-scale heat exchanger inevitably presume simplifying assumptions that are not well validated. It is difficult to find numerical data that capture flow unsteadiness, three-dimensional effects, and the influence of end walls or unlouvered fin length. The experimental data sources include Refs. [1,3,2,11,4,12,7,5,13]. In reviewing the database, we elected not to include a very small subset of data. In particular, Kim and Bullard [4] provided data for 21 heat exchangers, but measurements for six heat exchangers (those with a flow depth of 16 mm) are clearly inconsistent with their other data. The anomalous behavior of these measurements was noted but not explained by Kim and Bullard [4]; we decided to discard these data.[2] We were unable to include a small set of data because they could not be extracted from the original publication without ambiguity. When the original numerical data were not available, the data were extracted from the figures in the printed articles by scanning and digital analysis using commercial computer software. Through repeated trials using independent software packages, we established that the digitized data extraction process was typically reproducible to within 1%.[3] However, this process sometimes failed because of ambiguity in the plots, as noted in Table 1. Also as noted in the table, a few data were not used because the specimen was reported as damaged. For consistency, all performance data were cast into the form of Colburn j- factors and Fanning friction factors, with Reynolds numbers based on louver pitch. This representation follows the most common form in the literature.

The definitions of Colburn j-factor and Fanning friction factor are provided in Eqs. (1) and (2), respectively. The entrance and exit pressure-loss coefficients, K_c and K_e, were evaluated according to Kays and London [14] with an assumption of highly interrupted fin geometry (Figs. 5–3 to 5–5 in Ref. [14] when $\mathrm{Re}\rightarrow\infty$). All entries in the database include these effects, except Sunden and Svantesson [5], who neglected entrance, exit, and acceleration effects. From their data, we estimate that a 2–6% increase in their reported f-factors would result from inclusion of such effects (for $A_c/A<0.023$, $\sigma>0.8$, $K_c+K_e<0.15$, and $0.06<f<0.2$); nevertheless, we did not attempt to make a correction to their data and used their results as reported because there is a risk of generating additional error in an attempt to correct the relatively minor inconsistency.

$$j=\frac{\mathrm{Nu}}{\mathrm{Re}\,\mathrm{Pr}^{1/3}} \tag{1}$$

$$f=\frac{A_c\rho_m}{A\rho_1}\left[\frac{2\rho_1\Delta P}{G_c^2}-(K_c+1-\sigma^2)-2\left(\frac{\rho_1}{\rho_2}-1\right)+(1-\sigma^2-K_e)\frac{\rho_1}{\rho_2}\right] \tag{2}$$

In the database, all heat exchangers have a single-row of flat tubes and serpentine louver fins, except for those tested by Achaichia and Cowell [1]. Their heat exchangers have louvered plate fins and a one- or two-row flattened-tube construction. A geometrical description of a typical flat-tube heat exchanger with serpentine louver fins is provided in Fig. 1. Design parameters used in the present correlations are louver pitch, fin pitch, fin length, louver length, louver angle, flow depth, tube pitch, fin thickness, and the number of louver banks. In order to avoid overfitting[4] by including too many factors and because sometimes insufficient geometric detail was provided in the literature, other parameters that may affect the heat exchanger performance such as redirection louver geometry were omitted.

The heat exchangers in the present database are listed in Table 1 along with the geometrical parameters that characterize them. Inclusive ranges for the dimensional and dimensionless geometric parameters and Reynolds number for the database are provided in Table 2. It should be noted that satisfying the parametric ranges in Table 2 is a necessary but not a sufficient condition for a heat exchanger to be within the actual parameter space of the database. An arbitrary combination of parameters within the ranges of Table 2 may be outside the actual parameter space of the database, i.e., applying the present correlations for such a heat exchanger is, in fact, an extrapolation. However, there is generally a positive correlation between the dimensional parameters characterizing heat exchanger designs, and for this reason, it is particularly important to check the dimensionless geometric parameters. A specimen that falls within the dimensionless range of the database is more likely to be within the actual parameter space of the database.

3 Correlations

3.1 Colburn j-factor correlation. The proposed j-factor correlation is given by Eqs. (3a)–(3d). Note that louver angle (α) in

[2]We believe that these six sets of data are simply plotted with a scaling error in the Reynolds number; all the corresponding data appear to have a significant shift (27%) in Reynolds number.

[3]The digitizing uncertainty is based on a partial set of the data plotted with reasonable image quality. The increase of overall data uncertainty due to this process is insignificant.

[4]An empirically based model may yield an unreasonable fit if too many parameters are included when fitting from a limited database. Overfitted models typically show poor validation with new data.

Table 1 Geometrical description of heat exchangers in the database

Source	L_p(mm)	F_p(mm)	F_l(mm)	L_l(mm)	α(deg)	F_d(mm)	T_p(mm)	δ_f(mm)	N_{LB}
J [11] 1	1.40	1.06	7.93	6.93	27	15.9	9.86	0.102	2
J [11] 2	1.40	2.12	7.93	6.93	27	27.9	9.86	0.102	2
J [11] 3	1.40	1.06	7.93	6.93	27	27.9	9.86	0.102	2
J [11] 4	1.14	5.08	12.43	11.15	29	25.4	14.26	0.114	2
J [11] 5	1.14	2.12	12.43	11.15	29	25.4	14.26	0.114	2
J [11] 6	1.14	1.41	12.43	11.15	29	25.4	14.26	0.114	2
KB [4] 1	1.7	1.4	8.15	6.4	15	20	10.15	0.1	2
KB [4] 2	1.7	1.4	8.15	6.4	17	20	10.15	0.1	2
KB [4] 3	1.7	1.4	8.15	6.4	19	20	10.15	0.1	2
KB [4] 4	1.7	1.4	8.15	6.4	21	20	10.15	0.1	2
KB [4] 5	1.7	1.4	8.15	6.4	23	20	10.15	0.1	2
KB [4] 6	1.7	1.4	8.15	6.4	25	20	10.15	0.1	2
KB [4] 7	1.7	1.4	8.15	6.4	27	20	10.15	0.1	2
KB [4] 8	1.7	1.4	8.15	6.4	23	24	10.15	0.1	2
KB [4] 9	1.7	1.4	8.15	6.4	25	24	10.15	0.1	2
KB [4] 10	1.7	1.4	8.15	6.4	27	24	10.15	0.1	2
KB [4] 11	1.7	1.4	8.15	6.4	29	24	10.15	0.1	2
KB [4] 12	1.7	1	8.15	6.4	23	20	10.15	0.1	2
KB [4] 13	1.7	1	8.15	6.4	23	24	10.15	0.1	2
KB [4] 14	1.7	1.2	8.15	6.4	23	20	10.15	0.1	2
KB [4] 15	1.7	1.2	8.15	6.4	23	24	10.15	0.1	2
D [2] 1	3	1.55	12.7	9.5	8.4	40	14	0.075	2
D [2] 2	3	1.55	12.7	9.5	10.4	40	14	0.075	2
D [2] 3	3	1.6	12.7	9.5	16.7	40	14	0.075	2
D [2] 4	2.25	1.55	12.7	9.5	13.4	40	14	0.075	2
D [2] 5	2.25	1.56	12.7	9.5	16	40	14	0.075	2
D [2] 6	2.25	1.56	12.7	9.5	19.2	40	14	0.075	2
D [2] 7	1.8	1.55	12.7	9.5	18.8	40	14	0.075	2
D [2] 8	1.8	1.59	12.7	9.5	20.8	40	14	0.075	2
D [2] 9	1.8	1.58	12.7	9.5	27.8	40	14	0.075	2
D [2] 10	1.5	1.53	12.7	9.5	19.6	40	14	0.075	2
D [2] 11[a]	1.5	1.59	12.7	9.5	22.8	40	14	0.075	2
D [2] 12[a]	1.5	1.6	12.7	9.5	35.9	40	14	0.075	2
D [2] 13	1.8	1.63	12.7	9.5	14.2	40	14	0.075	2
D [2] 14	3	1.56	12.7	9.5	11.2	40	14	0.075	2
D [2] 15	2.25	1.68	12.7	11.7	24.1	40	14	0.075	2
D [2] 16	2.25	1.65	12.7	11	21.4	40	14	0.075	2
D [2] 17	2.25	1.65	12.7	10	21.4	40	14	0.075	2
D [2] 18	2.25	1.63	12.7	9	21.4	40	14	0.075	2
D [2] 19	2.25	1.6	12.7	8	20.3	40	14	0.075	2
D [2] 20	3	1.54	7.8	7.1	13.9	40	9.18	0.075	2
D [2] 21	2.25	1.53	7.8	7.1	13.8	40	9.17	0.075	2
D [2] 22	1.8	1.54	7.8	7.1	20.4	40	9.18	0.075	2
D [2] 23	1.5	1.55	7.8	7.1	26.1	40	9.19	0.075	2
D [2] 24	2.25	1.49	7.8	7.1	9.52	40	9.14	0.075	2
D [2] 25	2.25	1.51	7.8	7.1	16.5	40	9.16	0.075	2
D [2] 26	2.25	1.51	7.8	7.1	17.7	40	9.16	0.075	2
D [2] 27	2.25	1.23	7.8	7.1	16	40	8.93	0.075	2
D [2] 28	2.25	1.01	7.8	7.1	13.9	40	8.74	0.075	2
D [2] 29	2.25	1.54	7.8	7.1	14.2	40	9.18	0.075	2
D [2] 30	2.25	1.51	7.8	6.5	16.6	40	9.16	0.075	2
D [2] 31	2.25	1.54	7.8	6	17.6	40	9.18	0.075	2
D [2] 32	2.25	1.5	7.8	5	14.4	40	9.15	0.075	2
CW [6] 1	1.32	1.8	16	12.44	28	22	21	0.16	2
CW [6] 2	1.32	2	16	12.44	28	22	21	0.16	2
CW [6] 3	1.32	2.2	16	12.44	28	22	21	0.16	2
CW [6] 4	1.42	1.8	19	17.18	28	22	24	0.16	2
CW [6] 5[b]	1.42	2	19	17.18	28	22	24	0.16	2
CW [6] 6[b]	1.42	2.2	19	17.18	28	22	24	0.16	2
CW [6] 7	1.48	1.8	16	12.78	28	26	21	0.16	2
CW [6] 8[b]	1.48	2	16	12.78	28	26	21	0.16	2
CW [6] 9	1.48	2.2	16	12.78	28	26	21	0.16	2
CW [6] 10	1.53	1.8	19	16.07	28	26	24	0.16	2
CW [6] 11	1.53	2	19	16.07	28	26	24	0.16	2
CW [6] 12	1.53	2.2	19	16.07	28	26	24	0.16	2
CW [6] 13	1.69	1.8	16	12.15	28	32	21	0.16	2
CW [6] 14	1.69	2	16	12.15	28	32	21	0.16	2
CW [6] 15	1.69	2.2	16	12.15	28	32	21	0.16	2
CW [6] 16	1.55	1.8	19	16.17	28	32	24	0.16	4
CW [6] 17	1.55	2	19	16.17	28	32	24	0.16	4
CW [6] 18	1.55	2.2	19	16.17	28	32	24	0.16	4
CW [6] 19	1.86	1.8	19	15.25	28	38	24	0.16	4

Table 1 (***Continued.***)

Source	L_p(mm)	F_p(mm)	F_l(mm)	L_l(mm)	α(deg)	F_d(mm)	T_p(mm)	δ_f(mm)	N_{LB}
CW [6] 20	1.86	2	19	15.25	28	38	24	0.16	4
CW [6] 21	1.86	2.2	19	15.25	28	38	24	0.16	4
CW [6] 22	1.59	1.8	16	13.18	28	44	21	0.16	2
CW [6] 23	1.59	2	16	13.18	28	44	21	0.16	2
CW [6] 24	1.59	2.2	16	13.18	28	44	21	0.16	2
CW [6] 25[b]	1.53	1.8	19	16.84	28	44	24	0.16	4
CW [6] 26	1.53	2	19	16.84	28	44	24	0.16	4
CW [6] 27	1.53	2.2	19	16.84	28	44	24	0.16	4
AC [1] 1	1.4	2.02	9	8.5	25.5	41.6	11	0.05	2
AC [1] 2	1.4	3.25	9	8.5	25.5	41.6	11	0.05	2
AC [1] 3	1.4	1.65	9	8.5	25.5	41.6	11	0.05	2
AC [1] 4	1.4	2.09	9	8.5	21.5	41.6	11	0.05	2
AC [1] 5	1.4	2.03	9	8.5	28.5	41.6	11	0.05	2
AC [1] 6	1.4	2.15	9	8.5	25.5	20.8	11	0.05	1
AC [1] 7	1.4	1.7	9	8.5	25.5	20.8	11	0.05	1
AC [1] 8	0.81	2.11	9	8.5	29	41.6	11	0.05	2
AC [1] 9	0.81	1.72	9	8.5	29	41.6	11	0.05	2
AC [1] 10[c]	0.81	3.33	9	8.5	29	41.6	11	0.05	2
AC [1] 11	1.1	2.18	9	8.5	30	41.6	11	0.05	2
AC [1] 12	0.81	2.16	9	8.5	20	41.6	11	0.05	2
AC [1] 13	1.1	2.16	6	5.5	28	41.6	8	0.05	2
AC [1] 14	1.1	2.17	12	11.5	22	41.6	14	0.05	2
AC [1] 15	1.1	2.17	6	5.5	22	41.6	8	0.05	2
WJ [13] 1	1.40	2.12	18.92	16.25	30	25.4	22.99	0.158	2
WJ [13] 2	1.40	1.69	18.92	16.25	30	25.4	22.99	0.158	2
WJ [13] 3	1.40	1.41	18.92	16.25	30	25.4	22.99	0.158	2
WJ [13] 4	1.02	2.12	8.64	7.099	30	25.4	10.75[d]	0.158	2
WJ [13] 5	1.02	1.69	8.64	7.099	30	25.4	10.75[d]	0.158	2
WJ [13] 6	1.02	1.41	8.64	7.099	30	25.4	10.75[d]	0.158	2
R [7]	0.85	0.51	2.84	2.13	25	15.6	3.76[d]	0.025	2
SS [5] 1	1.4	1.5	12.5	10.2	22	57.4	14[e]	0.06	3
SS [5] 2	1.4	2	12.4	10.3	18.5	57.4	13.9[e]	0.06	2
SS [5] 3	1.3	2	12.4	10	24.5	37	13.9[e]	0.06	2
SS [5] 4	1.2	1.8	8.6	6.8	24	37	10.1[e]	0.04	2
SS [5] 5	1.1	1.8	9.6	6.8	25.5	50	11.1[e]	0.06	2
SS [5] 6	0.5	1.9	8	5	28.5	47.8	9.5[e]	0.04	4
KYL [12] 1	2.9	2.82	16.5	12.5	20	44	21.2	0.15	2
KYL [12] 2	2.9	2.42	16.5	12.5	20	44	21.2	0.15	2
KYL [12] 3	2.9	2.03	16.5	12.5	20	44	21.2	0.15	2
KYL [12] 4	2.9	2.82	16.5	12.5	25	44	21.2	0.15	2
KYL [12] 5	2.9	2.42	16.5	12.5	25	44	21.2	0.15	2
KYL [12] 6	2.9	2.03	16.5	12.5	25	44	21.2	0.15	2
KYL [12] 7	2.9	2.82	16.5	12.5	30	44	21.2	0.15	2
KYL [12] 8	2.9	2.42	16.5	12.5	30	44	21.2	0.15	2
KYL [12] 9	2.9	2.03	16.5	12.5	30	44	21.2	0.15	2
KYL [12] 10	2.9	2.82	16.5	12.5	35	44	21.2	0.15	2
KYL [12] 11	2.9	2.42	16.5	12.5	35	44	21.2	0.15	2
KYL [12] 12	2.9	2.03	16.5	12.5	35	44	21.2	0.15	2

[a]Not included in the *f*-factor database for fin damage.
[b]Not included in the *j*-factor database for ambiguous original plot.
[c]Not included in the *j*-factor database for distinct behavior.
[d]Used half tube pitch because of two fin stocks and a splitter plate between tubes.
[e]Tube minor diameter assumed to be 1.5 mm.

Eq. (3*a*) should be in radians. All numeric constants in the present *j*- and *f*-factor correlations are dimensionless and determined such that the rms relative residual of the entire database, defined by Eq. (4), is minimized—a least-squares method. The regression constants and their confidence intervals are given in Table 3. The evaluation of confidence intervals and their implications are discussed later.

$$j_{cor} = C_1 j_{Re} j_{low} j_{louver} \alpha^{C_2} N_{LB}^{C_3} \left(\frac{F_l}{L_p}\right)^{C_4} \left(\frac{F_d}{F_p}\right)^{C_5} \left(\frac{L_l}{F_l}\right)^{C_6} \left(\frac{F_l}{T_p}\right)^{C_7} \times \left(1 - \frac{\delta_f}{L_p}\right)^{C_8} \left(\frac{L_p}{F_p}\right)^{C_9} \quad (3a)$$

$$j_{Re} = \mathrm{Re}_{L_p}^{[C_{10} + C_{11}\cosh(F_P/L_P - 1)]} \quad (3b)$$

$$j_{low} = 1 - \sin\left(\frac{L_p}{F_p} \cdot \alpha\right) \left[\cosh\left(C_{12}\mathrm{Re}_{L_p} - C_{13}\frac{F_d}{N_{LB}F_p}\right)\right]^{-1} \quad (3c)$$

$$j_{louver} = 1 - C_{14}\tan(\alpha)\left(\frac{F_d}{N_{LB}F_p}\right)\cos\left[2\pi\left(\frac{F_p}{L_p\tan(\alpha)} - 1.8\right)\right] \quad (3d)$$

Minimizing

$$(\mathrm{rms}_{rel}) = \left[\frac{1}{N}\sum\left(\frac{j_{cor}}{j} - 1\right)^2\right]^{1/2}, \quad N = \text{total number of data points} \quad (4)$$

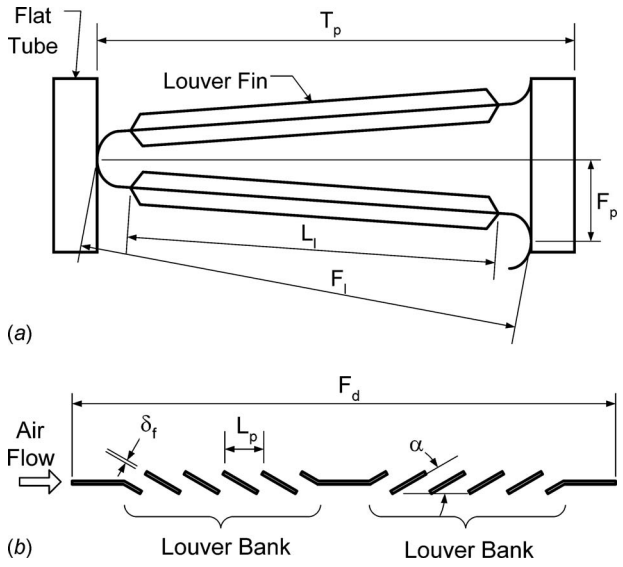

Fig. 1 Schematic of a flat-tube louver-fin heat exchanger: (*a*) close-up frontal view; (*b*) cross-sectional view of louver fin

The functional form of the fit is designed to reflect individual and combined parametric effects found in the experimental data. For example, the basic power-law form and the low-Reynolds-number flattening of the j-factor are included in Eqs. (3*b*) and (3*c*), respectively. The power-law-like behavior of j with Re and the flattening effect are consistent with boundary-layer restarting and louver-to duct-directed transitions. The louver geometry effects, embodied in Eq. (3*d*), are included through a modification to the optimal-louver-design criterion (see Eq. (5)) suggested by Suga and Aoki [15]. Equation (5) assumes that the air flow direction is aligned with the louvers (thus, the so-called flow efficiency is unity) and allows the possibility of multiple local optima in louver angle for any given fin-louver-pitch ratio. This behavior is consistent with the experimental data by Kim and Bullard [4].

$$\left[\frac{F_p}{L_p}\right]_{\text{opt}} = \frac{2m+1}{2}\tan\alpha, \quad m = 1,2,\ldots \tag{5}$$

The present j-factor correlation predicts the entire database of 1030 data points with a rms residual of 11.5% (see Table 4). In Fig. 2, j-factors predicted by the correlation are compared with the experimental data from individual sources. Data from Webb and Jung [13], Rugh et al. [7], and Davenport [2] are relatively well correlated, yielding rms errors of 7.9%, 4.9%, and 8.3%, respectively. However, the errors are larger in predicting the data from Kim and Bullard [4], Achaichia and Cowell [1], and Sunden and Svantesson [5], with rms deviations of 14.6%, 16.3%, and 16.1%, respectively (see Table 4). The veracity of an individual data source should not be evaluated by comparing that data set to the correlation, because large data sets are obviously favored by the regression (see Appendix A for further discussion).

Figures 2 and 3 also contain the distribution of errors including the maximum values in the present database by the proposed correlations and show the trends of error associated with the range of Reynolds number. The figures also illustrate that fewer geometrical varieties are represented for Reynolds numbers below 100 or above 800, as explained earlier regarding the use of inclusive ranges of parameters.

3.2 Friction Factor Correlation. An f-factor correlation for the database described in Table 1 is given in Eqs. (6*a*) and (6*b*). Note that louver angle in Eq. (6*a*) should be in radians. The first part of the correlation attempts to capture the experimental data with a slight flattening tendency at high-Reynolds numbers. This

Table 2 Inclusive range of experimental parameters for heat exchangers in the database

	Dimensional geometric parameters								
	L_p (mm)	F_p (mm)	F_l (mm)	L_l (mm)	α (deg)	F_d (mm)	T_p (mm)	δ_f (mm)	N_{LB}
From	0.5	0.51	2.84	2.13	8.4	15.6	3.76	0.0254	1
To	3	5.08	20	18.5	35.9	57.4	25	0.16	4
	Nondimensional parameters								
	F_p/L_p	F_l/L_p	L_l/F_l	α (deg)	F_d/F_p	T_p/F_l	δ_f/L_p	N_{LB}	$\text{Re}_{L_p,j}$
From	0.45	2.6	0.63	8.4	5	1.12	0.025	1	27
To	4.44	16	0.96	35.9	40	1.37	0.155	4	4132

Table 3 Regression constants and 95% confidence intervals by linear approximation

Colburn j-factor			Fanning f-factor		
Constant	Confidence interval		Constant	Confidence interval	
C_1	0.872	±0.151	D_1	3.69	±0.97
C_2	0.219	±0.038	D_2	−0.256	±0.050
C_3	−0.0881	±0.0435	D_3	0.904	±0.055
C_4	0.149	±0.044	D_4	0.200	±0.038
C_5	−0.259	±0.038	D_5	0.733	±0.047
C_6	0.540	±0.090	D_6	0.648	±0.100
C_7	−0.902	±0.186	D_7	−0.647	±0.060
C_8	2.62	±0.43	D_8	0.799	±0.062
C_9	0.301	±0.037	D_9	−0.845	±0.036
C_{10}	−0.458	±0.010	D_{10}	0.00130	±0.00023
C_{11}	−0.00874	±0.00144	D_{11}	1.26	±0.40
C_{12}	0.0490	±0.0237			
C_{13}	0.142	±0.126			
C_{14}	−0.0065	±0.0023			

Table 4 Evaluation of the predictive performance of Colburn *j*-factor correlations

Entire database predicted within	Over the entire database: Present work (%)	Chang and Wang [3] (%)	Kim and Bullard [4] (%)
±25%	95.8	93.5	94.2
±20%	92.6	84.3	85.4
±15%	83.2	74.0	75.1
±10%	64.8	55.2	58.2
±5%	34.4	27.8	29.1

	Within individual data sets: Present work		Chang and Wang [3]		Kim and Bullard [4]	
Source No. points contributed	rms[a] (%)	Mean (%)	rms (%)	Mean (%)	rms (%)	Mean (%)
Jacobi et al. [11]-36	11.7	−1.6	51.7	25.9	48.9	23.2
Kim and Bullard [4]-75	14.6	−2.9	16.4	−5.7	17.0	−7.6
Davenport [2]-311	8.3	−1.6	7.6	0.4	7.8	−2.2
Chang and Wang [6]-172	9.2	1.5	8.7	1.0	8.5	−1.3
Achaichia and Cowell [1]-126	16.3	−2.3	20.4	−6.7	20.9	−8.9
Webb and Jung [13]-35	7.9	−0.9	13.2	8.7	11.3	6.1
Rugh et al. [7]-16	4.7	2.5	4.0	−2.4	4.9	−3.7
Sunden and Svantesson [5]-87	16.1	0.7	14.8	5.4	13.7	3.0
Kim et al. [12]-172	10.8	−3.8	16.4	−12.3	17.8	−14.0
Entire data-1030	11.5	−1.3	16.2	−1.4	16.2	−3.6

[a]Root-mean-squared relative residual ($\text{rms}=\sqrt{\Sigma(j_{\text{cor}}/j-1)^2/\Sigma 1}\times 100\%$).

transition may be related to the tendency toward fully turbulent behavior of the friction factor at very high-Reynolds numbers. The regression constants and the confidence intervals are given in Table 3.

$$f_{\text{cor}} = D_1 f_{\text{Re}} N_{\text{LB}}^{D_2} \left(\frac{F_p}{L_p}\right)^{D_3} \sin(\alpha + D_4) \left(1 - \frac{F_l}{T_p}\right)^{D_5} \times \left(\frac{L_l}{F_l}\right)^{D_6} \left(\frac{\delta_f}{L_p}\right)^{D_7} \left(\frac{F_l}{F_p}\right)^{D_8} \quad (6a)$$

$$f_{\text{Re}} = \left(\text{Re}_{L_p} \cdot \frac{F_p}{L_p}\right)^{D_9} + D_{10}\, \text{Re}_{L_p}^{[D_{11}(\delta_f/F_p)]} \quad (6b)$$

The *f*-factor correlation predicts the entire database of 1270 data points with an rms residual of 16.1% (see Table 5). Experimental data from individual sources are compared with the *f*-factors predicted by the correlation in Fig. 3. In contrast to the *j*-factor correlation, there are larger scatters and biases. For example, data by Rugh et al. [7] and those by Kim et al. [12] have 37.3% and −20.1% mean residuals, respectively (see Table 5).

4 Comparison and Discussion

A typical validation of an empirical model requires comparing with an independent set of data. In this study, however, it is impossible to spare separate data for validation without a substantial loss of generality of the correlations. As discussed earlier, the performance modeling of flat-tube louver-fin heat exchangers involves a high dimensionality and demands a large database. Consequently, an independent validation of empirical correlations for such complex heat exchangers is rarely found in the literature. For this reason, any experimental data found in the open literature have been compiled into the database for fitting correlations.

Using the compiled database, the new *j*- and *f*-factor correlations are compared with other correlations for flat-tube louver-fin heat exchangers in Tables 4 and 5. We included comparisons to the correlations by Chang and Wang [3] and Chang et al. [8] as they are generally considered the current state of the art, and they are based on a large data set; we included comparisons to the correlations by Kim and Bullard [5] because they are one of the most recent correlations in the literature, and they are based on a relatively small more specialized data set. The *j*-factor comparisons in Table 4 are made in two ways. First, the percentage of the entire database predicted within prescribed rms tolerances is provided for each correlation. This comparison allows a detailed assessment of how well each correlation performs in predicting all the data. It is clear from this comparison that the new correlation provides the best predictive performance when the overall database is considered. It should be pointed out that such a comparison obviously necessitates extrapolation of earlier work, and such extrapolation is patently dubious for correlations based on small data sets. Nevertheless, such a comparison is valuable in assessing the generality of the new correlation. The second comparison in Table 4 provides an assessment of predictive performance for each correlation within a particular subset of the database (and on the entire database). The table provides rms and mean errors for each correlation in each data set, as well as for the composite database. The new *j*-factor correlation predicts the entire database with a rms residual of 11.5%, whereas the correlations by Chang and Wang [3] and Kim and Bullard [4] both yield 16.2%. The new correlation performs better than the others in a majority of the data sets, and when another correlation gives better predictions for a particular data set it is a "close call." In several cases, the new correlation predicts a data set well when other correlations fail badly. It should be noted that although the new correlation performs better than the correlation of Kim and Bullard [5] with the subset of their data used in this work, the correlation of Kim and Bullard was based on more heat exchangers (a total of 45 samples) including the data we elected to reject, as discussed earlier. Overall, the proposed *j*-factor correlation provides a better accuracy and generality than the other correlations.

The *f*-factor correlation of the present work is compared with that of Kim and Bullard [4] and Chang et al. [8] in Table 5, in the same format adopted in Table 4. However, in addition to considering the original *f*-factor correlation of Chang et al. [8], which uses separate curves for two Reynolds-number ranges, the high-Re curve ($\text{Re} > 150$) is included for comparison separately. This comparison is provided to evaluate the predictive performance of a single smooth curve (because such a curve surmounts

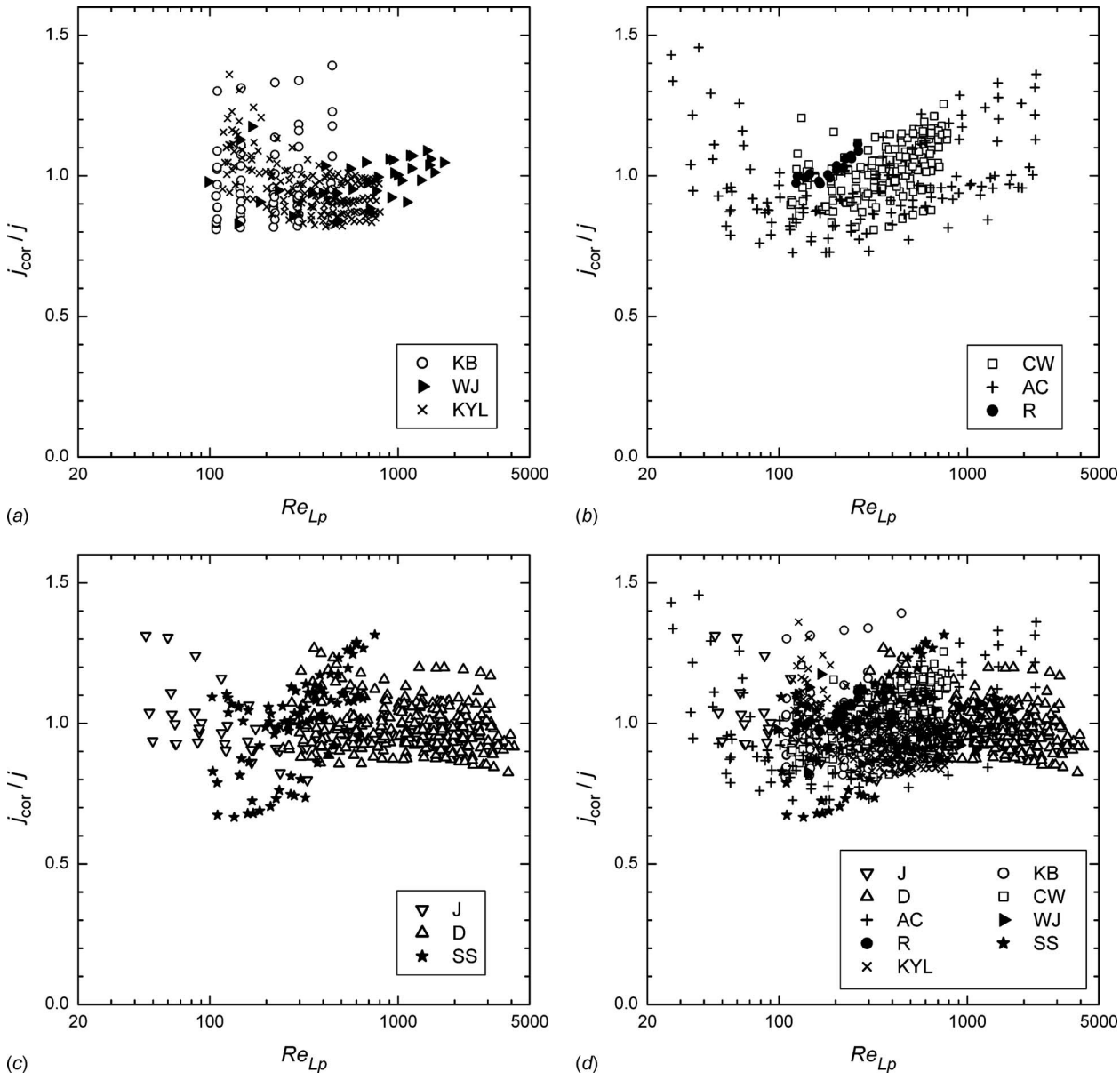

Fig. 2 Comparison of the present *j*-factor correlation and the experimental data (J, Jacobi et al. [11]; KB, Kim and Bullard [4], D, Davenport [2]; CW, Chang and Wang [6]; AC, Achaichia and Cowell [1]; WJ, Webb and Jung [13]; R, Rugh et al. [7]; SS, Sunden and Svantesson [5]; KYL, Kim et al. [12])

the difficulties associated with discontinuous curves discussed earlier). The correlation of Kim and Bullard [4] only predicts about 28% of the data to within ±25% relative error, and a comparison of the Kim and Bullard correlation to individual data sets is not provided; instead, the high-Reynolds-number correlation of Chang et al. [8] is compared with the individual data sets. Again, with extrapolation of the earlier work in mind, the new correlation provides the best prediction for the complete database: it predicts all data with a rms error of 16.1%, whereas Chang et al. [8] and Kim and Bullard [4] have rms errors of 18.1% and 92.3%, respectively. Table 5 also shows that predicting the friction factor is more challenging in general. For the data provided by Rugh et al. [7], the new correlation produces rms errors of 37%; the correlation of Chang et al. [8] produces errors of 37% with the data provided by Kim et al. [12]. Although *f*-factor predictions are more challenging, if a correlation that provides continuous predictions over the broadest possible parameter space with the smallest rms error is desired, the new correlation should be adopted.

The large rms errors associated with the correlation of Kim and Bullard [4] can be explained by their data, which are significantly underpredicted by other correlations in Table 5. The purpose of their work was not to provide a general correlation covering a large design space but rather to provide performance data for an emerging design. Their correlation reflects an unexpectedly strong dependence on air flow depth, which may be a result of overfitting. The rms residual of the entire database shows a negligible improvement when the flow depth is included in the new correlation, indicating that the *f*- factor is nearly independent of flow depth. The correlation of Kim and Bullard [5] correlates their data very well (7% rms); it only fails when applied to other data sets. Correlations developed from limited data sets are inherently limited. Chang and Wang [3] identified other correlations with similar limitations. Biases in slope can occur if the database has a narrow Reynolds-number range. Figures 2 and 3 show that individual data sources cover partial ranges of Reynolds number. Furthermore, deviations from the base function (i.e., power-law trend) are ob-

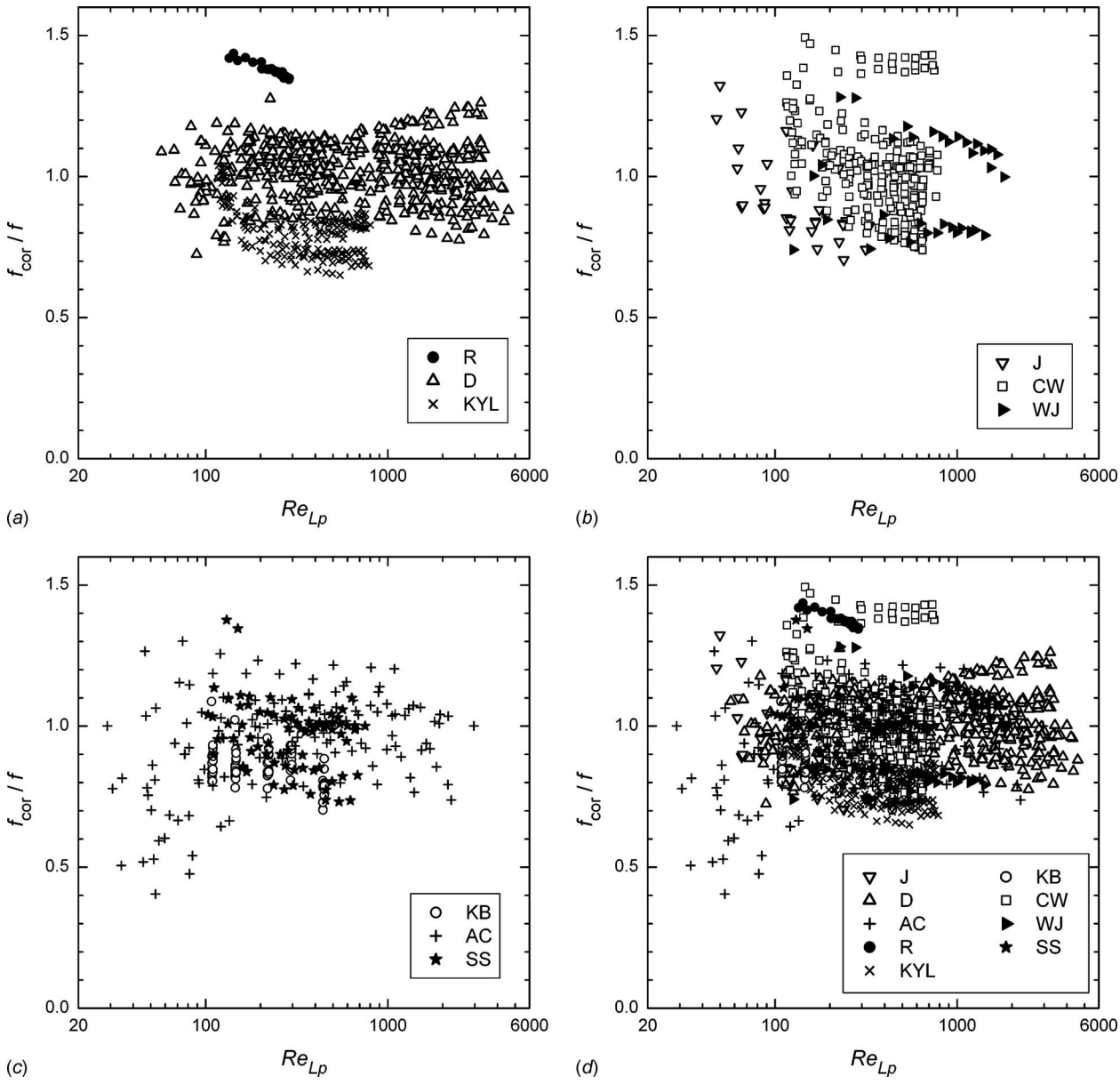

Fig. 3 Comparison of the present *f*-factor correlation and the experimental data

served more clearly from the combined database with a wide range of Reynolds number. In general, a small parameter span results in a poor representation of the parametric effect by the database. Therefore, correlations based on a limited database, even with fairly accurate data, are susceptible to biases and overfitting, and may not easily identify the efficient form of fit.

During the development of the present correlations, additional statistical assessment of the goodness of fit was made to identify an effective functional form and to reduce the risk of overfitting. Specifically, the confidence intervals of regression constants and their covariances were estimated from an approximated linear multiple regression model. For the details of local linearization, see Appendix B. In Table 3, the confidence intervals of the regression constants are presented. It can be noted that the confidence intervals of regression constants are generally much smaller than the regression constants. Errors associated with regression constants are inevitable due to the uncertainties of empirical data and the imperfect data model. Regarding empirical correlations, researchers often conclude a strong parametric dependence if the corresponding regression constant is large in magnitude. However, a more appropriate inference should be made based on the comparison of regression constants with their confidence intervals. Covariances of regression constants can be used too as an indication of redundancy in the form of fit. In the present analysis, large correlation coefficients (normalized covariances) were typically observed when the data model resulted in a significant overfitting of the database. The present correlations were obtained by repeated revision of the functional forms from the examination of confidence intervals and the covariances. Among the correlations in the literature [1–9], such an estimation of the regression constants is rare. Sunden and Svantesson [5] provided confidence intervals for the constants in their correlations, which are intrinsically linear data models. Because their correlations contained four geometrical parameters to fit a database from six geometrical variants, an overfitting may easily occur, as reflected in some of the large confidence intervals in their report. Despite the limited validity of the present linear approximation of nonlinear model, such statistical assessment is essential for the development a general correlation suitable for prediction of new data and parametric study with system modeling.

Table 5 Evaluation of the predictive performance of *f*-factor correlations

Entire database predicted within	Over the entire database: Present work (%)	Chang et al. [8] (%)	Kim and Bullard [4] (%)
±25%	88.0	83.8 (80.6)[a]	28.1
±20%	80.6	78.2 (73.5)	24.2
±15%	65.9	67.4 (63.2)	18.6
±10%	48.3	51.7 (49.0)	13.0
±5%	26.4	28.3 (27.4)	7.5

	Within individual data sets: Present work		Chang et al. [8]		Chang et al. [8][a]	
Source No. points contributed	rms[b] (%)	Mean (%)	rms (%)	Mean (%)	rms (%)	Mean (%)
Jacobi et al. [11]-33	16.8	−7.5	18.9	−10.2	25.6	0.3
Kim and Bullard [4]-75	15.8	−13.3	19.8	−16.7	23.2	−21.5
Davenport [2]-496	10.1	1.9	9.5	−4.8	8.9	−4.2
Chang and Wang [6]-227	17.8	3.5	13.3	−3.0	14.0	−1.4
Achaichia and Cowell [1]-135	18.2	−4.5	12.3	0.6	19.0	−2.2
Webb and Jung [13]-36	17.0	−2.9	15.2	−1.3	13.7	−0.3
Rugh et al. [7]-19	38.5	37.3	14.0	−0.8	6.9	−6.9
Sunden and Svantesson [5]-76	12.5	−2.7	16.9	1.4	15.6	2.6
Kim et al. [12]-173	21.8	−20.1	37.0	−34.7	38.6	−37.7
Entire database-1270	16.1	−2.4	18.1	−8.3	19.4	−8.5

[a]Entries based on high-Reynolds-number correlation ($Re_{Lp} > 150$) from Chang et al. [8].

[b]Root-mean-squared relative residual ($rms = \sqrt{\Sigma(f_{cor}/f-1)^2/\Sigma 1} \times 100\%$).

In comparison to other aforementioned works in the literature, the proposed correlations are expected to yield an improved interpolation due to the largest experimental database and parameter space, and a more reliable extrapolation from the incorporated physical effects and the smooth continuous functional form. Nevertheless, although less likely than other correlations, the present correlations are ultimately subject to the same limitation of the parameter space corresponding to the database. Also, they are affected by other challenges common for all empirical correlations.

An empirical correlation with a well-spanned database and a good functional form is not guaranteed to have small rms residuals if the heat exchanger performance data have unidentified errors. The reported uncertainties in j and f are typically less than 15% in the technical literature. However, the experimental data often reflect scatter of much greater magnitudes. For example, Fig. 4 shows an unexplained discrepancy between two heat exchangers with very similar geometry in the present database. While the j-factors are nearly the same for both heat exchangers, the f-factors have a difference as large as 50%. Practically, but unfortunately, experimental data for the performance of a heat exchanger can contain errors from a number of sources, including mistakes or inconsistencies in experimental procedure or data reduction, inaccurate geometrical data, and manufacturing defects. The energy balance between the working fluids, which is conventionally used as a measure of fidelity of the raw data, can obfuscate systematic errors through canceling effects. Systematic errors usually manifest as conflicts in a large composite database from independent sources. However, it is difficult to make a fair assessment of the veracity of data sources by comparing them against the overall behavior of the composite database. In Appendix A, how the size of an individual data set weighs data regression is discussed, and it is shown that a small set of data can exhibit magnified rms deviations from a regression to a composite data set, even when the larger contributing data sets have systematic errors of equal magnitude. In a multiple regression with complex parametric effects, it is difficult to distinguish systematic errors of individual sources from an inefficient or badly posed functional form for the curve fit.

Overcoming the practical constraints in data modeling described above requires a more rigorous standard in heat exchanger testing and data analysis. The first step toward this goal is an accurate evaluation of the experimental uncertainty. The uncertainties of Colburn j-factor and f-factor data by individual sources are shown in Table 6. Note that some sources report only one value for the uncertainty while others provide none. This lack of

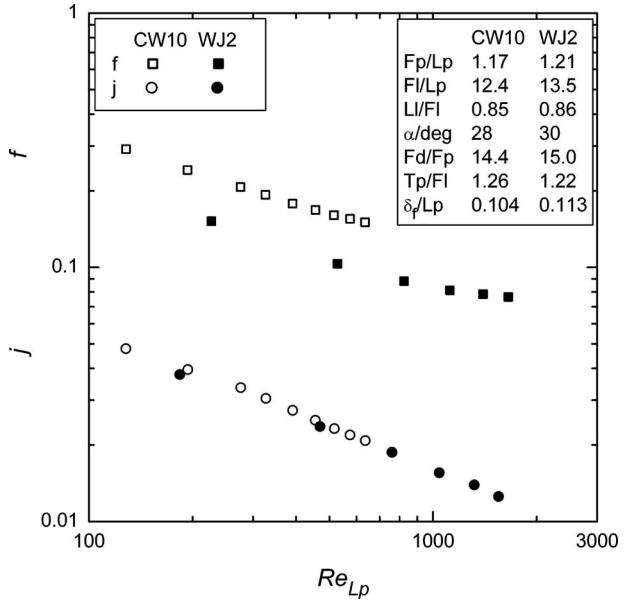

Fig. 4 Comparison of two similar heat exchangers (Chang and Wang [6] Source 10 and Webb and Jung [13] Source 2). The uncertainty of *f*-factor by Chang and Wang was 2–7% and unknown for data by Webb and Jung—it is unlikely that the discrepancy of *f*-factor is solely due to the experimental uncertainty.

Table 6 Uncertainties in Colburn *j*- and *f*-factor data per original report

Data source	Colburn *j*-factor (%)			*f*-factor (%)		
	High Re	Low Re	Mean	High Re	Low Re	Mean
Jacobi et al. [11]	2.6	14.3	5.4	4.0	10.1	4.4
Kim and Bullard [4]	-	-	12[a,b]	-	-	10[a,b]
Davenport [2]	-	-	-	-	-	-
Chang and Wang [6]	5.3	9.2	-	6.6	1.2	-
Achaichia and Cowell [1]	3.5	6.5	-	5	15	-
Webb and Jung [13]	-	-	-	-	-	-
Rugh et al. [7]	5.8	10.3	-	7.9	13.6	-
Sunden and Svantesson [5]	-	-	15[b]	-	-	6[b]
Kim et al. [12]	2.5	4.2	-	3.8	5.3	-

[a]Uncertainty of heat-transfer coefficient (h) or pressure drop (ΔP).
[b]Assumed to be mean uncertainty.

information in Table 6 prohibits the use of data uncertainty in the regression analysis (say, by χ^2 statistics). If more general and reliable correlations are to be sought, the development of these data models will almost certainly require smaller and carefully reported experimental uncertainties and a maximum-likelihood estimator that accounts for individual measurement uncertainties.

Finally, the present comparison may have limitation in comparing the effectiveness of functional forms of correlations because of differences in databases. For example, when compared with the new data [4,11,12] that are outside the parameter space of previous correlations, the proposed *j*- and *f*-factor correlations apparently yield better predictions, as shown in Tables 4 and 5. Although a minor upgrade can be attained by adjusting the same form of fit, the overall superiority of the new correlations was achieved by fundamental improvements that ensure their effectiveness in capturing the parametric trends.

5 Summary and Conclusion

New correlations for the Colburn *j*-factor and Fanning friction factor have been developed from a comprehensive experimental database for flat-tube louver-fin heat exchangers. The database represents the largest size and applicable parametric ranges in the literature. Also, the new correlations were formulated to reflect parametric effects that were not well captured by other correlations, and they provide improved predictive performance along with broader generality. While the proposed *j*-factor correlation has a significant advantage in accuracy over prior correlations, the new *f*-factor correlation improves accuracy over existing correlations to a lesser extent. However, the proposed *f*-factor correlation uses a smooth continuous functional form, as opposed to the discontinuous form of the best prior correlation, and therefore a continuous representation of the data can be obtained with advantages in design and optimization. Furthermore, based on a local linearization of the data model, important statistical assessment of the regression constants was conducted in terms of the confidence intervals and covariances. These measures were used to select an optimal form of fit and to substantiate the relative importance of the empirical parameters. A further examination of the present data modeling application indicates that the complexity of the heat exchanger design space and insufficient reporting of the experimental uncertainty pose significant challenges to the development of generalized heat exchanger performance predictions.

Acknowledgment

This work was financially supported by the U.S. Department of Energy and the Air-Conditioning and Refrigeration Technology Institute (ARTI) under 21-CR program, Elizabeth Jones project monitor. The authors gratefully acknowledge their support and technical advice from the project monitoring subcommittee: Mike Heidenreich, Shaobo Jia, Leon Tang, Ray Rite, Steve Memory, and Jim Bogart.

Nomenclature

A = total air-side heat-transfer surface area
A_c = minimum cross-sectional area for air flow
A_{front} = frontal area of the heat exchanger
f = Fanning friction factor (see Eq. (2))
f_{cor} = Fanning friction factor correlation (see Eqs. (6*a*) and (6*b*))
f_{high} = exponent of correlation factor for high-Reynolds number
f_{Re} = correlation factor for Reynolds number
F_d = air-side flow depth, or fin width
F_l = fin length
F_p = fin pitch
G_c = air mass flux at minimum cross-sectional area
h = air-side heat-transfer coefficient
j = Colburn *j* factor (see Eq. (1))
j_{cor} = Colburn *j*-factor correlation (see Eqs. (3*a*)–(3*d*))
j_{louver} = correlation factor for louver geometry effect
j_{low} = correlation factor for low-Reynolds-number effect
j_{Re} = correlation factor for Reynolds-number effect
K_c = entrance pressure-loss coefficient [14]
K_e = exit pressure-loss coefficient [14]
L_l = louver length
L_p = louver pitch
N_{LB} = number of louver banks
Nu = Nusselt number
ΔP = air-side pressure drop across heat exchanger
Pr = Prandtl number
Re = Reynolds number
Re_{L_p} = Reynolds number based on louver pitch
T_p = tube pitch

Greek Symbols

α = louver angle, rad in Eqs. (3*a*) and (6*a*)
δ_f = fin thickness
ρ = air density
σ = area contraction ratio, $\sigma = A_c/A_{\text{front}}$

Subscripts

1 = inlet
2 = outlet
m = mean
opt = optimal

Appendix A: Analysis of Database Size Effect

A composite database comprised of several subsets of heat exchanger performance data may not be well correlated, even if individual groups of data are well correlated. This failure is due to unknown systematic errors, which are not easily detected within

individual databases. However, when these self-consistent databases are combined, the systematic errors manifest and it becomes difficult to reconcile discrepancies between data from different sources. In this section, a weightlike impact of the number of data points is shown through a simple data modeling example with least-squares regression in the presence of unidentified systematic errors in the database.

Consider a composite database consisting of M subsets of data. The number of data points in the ith group is n_i. The jth data point in the ith group is $(y_{ij}, \mathrm{Re}_{ij})$. The total number of data points, N, in the composite database is

$$N = \sum_{i=1}^{M} n_i \tag{A1}$$

and for simplicity and relevance the functional form for modeling the data is selected as

$$y = a\mathrm{Re}^b \tag{A2}$$

In order to simplify the problem, random error is neglected, and each group is assumed to be self-consistent, i.e., data within a group can be perfectly fitted by a data model; thus,

$$\sum_{j=1}^{n_i} (a_i \mathrm{Re}_{ij}^{b_i} - x_{ij})^2 = 0, \quad i = 1, \ldots, M \tag{A3}$$

In order to model the entire database, constants a and b are determined such that the rms relative error or, equivalently, $F(a,b)$ is minimized:

$$(\mathrm{rms}_{\mathrm{rel}}) = \left[\frac{1}{N} \sum_{i=1}^{M} \sum_{j=1}^{n_i} \left(\frac{a\mathrm{Re}_{ij}^{b} - x_{ij}}{x_{ij}} \right)^2 \right]^{1/2} \tag{A4a}$$

$$N(\mathrm{rms}_{\mathrm{rel}})^2 = \sum_{i=1}^{M} \sum_{j=1}^{n_i} \left(\frac{a}{a_i} \mathrm{Re}_{ij}^{b-b_i} - 1 \right)^2 = F(a,b) \tag{A4b}$$

Systematic errors are assumed to be present in the individual data sets and are reflected in a_i and b_i of the data sources. These systematic errors affect the optimal values of a and b. In order to examine a simple case, assume all data sources share the same value of b_i; thus, $b_i = b$. (Imagine the j-factor data from every source to reflect the same behavior with Re, but each has a systematic bias, a shift up or down.) In this simplified case,

$$N(\mathrm{rms}_{\mathrm{rel}})^2 = F(a) = \sum_{i=1}^{M} \sum_{j=1}^{n_i} \left(\frac{a}{a_i} - 1 \right)^2 = \sum_{i=1}^{M} n_i \left(\frac{a}{a_i} - 1 \right)^2 \tag{A5}$$

When $F(a)$ is minimized,

$$\frac{dF}{da} = 0 \tag{A6}$$

which yields the following:

$$\frac{1}{a} = \sum_{i=1}^{M} \frac{n_i}{a_i^2} \Bigg/ \sum_{i=1}^{M} \frac{n_i}{a_i} \tag{A7}$$

If the systematic errors are relatively small, i.e., $|a_i/a - 1| << 1$,

$$\frac{n_i}{a_i} = \frac{n_i}{a(1 + (a_i/a - 1))} \cong \frac{n_i}{a}. \tag{A8}$$

Then, Eq. (A7) can be approximated as

$$\frac{1}{a} \cong \sum_{i=1}^{M} \left(\frac{n_i}{a} \frac{1}{a_i} \right) \Bigg/ \sum_{i=1}^{M} \frac{n_i}{a} = \sum_{i=1}^{M} \left(\frac{n_i}{a_i} \right) \Bigg/ \sum_{i=1}^{M} n_i = \frac{1}{N} \sum_{i=1}^{M} \left(\frac{n_i}{a_i} \right) \tag{A9}$$

Equation (A9) shows that the coefficient $1/a$ is the average of $1/a_i$ weighted by the size of each data group. It is also clear that the slope parameter $1/b_i$ in Eq. (A4b) will be given preference during a data regression according to the contribution of the data source.

A.1 Example. The following example clearly shows how the number of data in a subset influences the data regression and why the veracity of the subset cannot be assessed by comparison to the resulting correlation. In comparison to the true (usually unknown) values, both groups 1 and 2 below have been assigned the same magnitude of systematic error (5%). However, due to the differences in the sizes of groups, a data model for the composite set yields a rms error of 8.1% for group 1, a rms error of 1.6% for group 2, and a rms error of 3.6% for the composite database.

$$M = 2$$

$$n_1 = 10, \quad n_2 = 50$$

$$a_1 = 1.05, \quad a_2 = 0.95, \quad a_{\mathrm{true}} = 1.00 \quad \text{(true value)}$$

$$a \cong \frac{10 + 50}{10/1.05 + 50/0.95} = 0.965 \quad \text{(regression result)}$$

$$\mathrm{rms}_{\mathrm{rel},i} = \left| \frac{a}{a_i} - 1 \right| \quad \text{rms error of group } i \text{ from Eq. (A5)}$$

$$\mathrm{rms}_{\mathrm{rel},1} = \left| \frac{0.965}{1.05} - 1 \right| = 0.081$$

$$\mathrm{rms}_{\mathrm{rel},2} = \left| \frac{0.965}{0.95} - 1 \right| = 0.016$$

Appendix B: Local Linearization of Nonlinear Multivariate Data Model

Heat exchanger performance data models represented by Eqs. (3) and (6) indicate intrinsically nonlinear relations among the regression constants. While a precise statistical assessment can be difficult due to the nonlinearity, it is still desirable to evaluate the confidence intervals and the covariances of the regression constants. Confidence intervals reveal the statistical significance of the associated parametric effects. Covariances can be normalized into correlation coefficients, which indicate the degree of redundancy among the regression constants. The use of these statistics is essential toward the development of an effective and reliable data model. In this section, a locally approximated linear multiple regression method is derived for a general nonlinear model. The above statistics can be obtained easily for linear multiple regressions [16].

Consider a case when an empirical database (x,y) of size n is modeled by a multivariate function $f(x;b)$, as shown in Eq. (B1). The independent and the dependent variables are denoted by x and y, respectively. In a least-squares method, the regression constant β, a vector with m elements, is determined such that the norm of the residual $e(\beta)$ is minimized in Eq. (B2).

$$y \sim f(x;\beta) \tag{B1}$$

$$y = f(x;\beta) + e(\beta) \tag{B2}$$

A generally nonlinear function f, if continuous and differentiable in β, can be expanded linearly in $\Delta\beta$, as shown in Eq. (B3). For a small magnitude of $\Delta\beta$, function f can be approximated as linear in $\Delta\beta$, neglecting the higher order effect. Then, a linear multiple regression problem can be obtained where the residual $e(\beta)$ is fitted by $\Delta\beta$ in Eq. (B4).

$$f(x;\beta + \Delta\beta) = f(x;\beta) + \sum_{j=1}^{m} \left(\frac{\partial f}{\partial \beta_j} \right) \Delta\beta_j + \mathrm{O}(|\Delta\beta|^2) \tag{B3}$$

$$e(\beta) = y - f(x;\beta) \sim \sum_{j=1}^{m} \left(\frac{\partial f}{\partial \beta_j} \right) \Delta\beta_j \tag{B4}$$

The solution is trivial that all elements of $\Delta\beta$ should be zeros for an optimal β. On the other hand, we can extract the confidence intervals and covariances of the elements of $\Delta\beta$ for the linear multiple regression. The confidence interval of $\Delta\beta$ is considered to be equivalent to that of β, if the function f is approximately linear for that confidence interval. Although a simplified derivation is described here, it should be noted that the actual analysis used a weighted linear multiple regression to minimize the rms *relative* residual. For both j and f correlations, the solution $\Delta\beta$ was generally very small and using $\beta+\Delta\beta$ showed negligible difference in the residual, as expected.

References

[1] Achaichia, A., and Cowell, T. A., 1988, "Heat Transfer and Pressure Drop Characteristics of Flat Tube and Louvered Plate Fin Surfaces," Exp. Therm. Fluid Sci., **1**(2), pp. 147–157.

[2] Davenport, C. J., 1983, "Correlations for Heat Transfer and Flow Friction Characteristics of Louvred Fin," *Proceedings of the 21st National Heat Transfer Conference, AIChE Symposium Series* No. 225, American Institute of Chemical Engineers, New York, pp. 19–27.

[3] Chang, Y.-J., and Wang, C.-C., 1997, "A Generalized Heat Transfer Correlation for Louver Fin Geometry," Int. J. Heat Mass Transfer, **40**(3), pp. 533–544.

[4] Kim, M.-H., and Bullard, C. W., 2002, "Air-Side Thermal Hydraulic Performance of Multi-Louvered Fin Aluminum Heat Exchangers," Int. J. Refrig., **25**(3), pp. 390–400.

[5] Sunden, B., and Svantesson, J., 1992, "Correlations of J- and F-Factors for Multilouvered Heat Transfer Surfaces," *Proceedings of the Third UK National Conference Incorporating First European Conference on Thermal Sciences, Institution of Chemical Engineers Symposium Series* No. 129, Institution of Chemical Engineers, Rugby, UK, Vol. 2, pp. 805–811.

[6] Chang, Y.-J., and Wang, C.-C., 1996, "Air Side Performance of Brazed Aluminum Heat Exchangers," J. Enhanced Heat Transfer, **3**(1), pp. 15–28.

[7] Rugh, J. P., Pearson, J. T., and Ramadhyani, S., 1992, "A Study of a Very Compact Heat Exchanger Used for Passenger Compartment Heating in Automobiles," *Proceedings of the 28th National Heat Transfer Conference and Exhibition, Heat Transfer Division*, ASME, New York, HTD-Vol. 201, pp. 15–24.

[8] Chang, Y.-J., Hsu, K.-C., Lin, Y.-T., and Wang, C.-C., 2000, "A Generalized Friction Correlation for Louver Fin Geometry," Int. J. Heat Mass Transfer, **43**(12), pp. 2237–2243.

[9] Dong, J., Chen, J., Chen, Z., Zhang, W., and Zhou, Y., 2007, "Heat Transfer and Pressure Drop Correlations for the Multi-Louvered Fin Compact Heat Exchangers," Energy Convers. Manage., **48**(5), pp. 1506–1515.

[10] Chang, Y.-J., Chang, W.-J., Li, M.-C., and Wang, C.-C., 2006, "An Amendment of the Generalized Friction Correlation for Louver Fin Geometry," Int. J. Heat Mass Transfer, **49**(21–22), pp. 4250–4253.

[11] Jacobi, A. M., Park, Y., Zhong, Y., Michna, G., and Xia, Y., 2005, "High Performance Heat Exchangers for Air-Conditioning and Refrigeration Applications (Non-Circular Tubes)," University of Illinois, Phase II-Final Report No. ARTI-21CR/611-20021.

[12] Kim, J. H., Yun, J. H., and Lee, C. S., 2004, "Heat-Transfer and Friction Characteristics for the Louver-Fin Heat Exchanger," J. Thermophys. Heat Transfer, **18**(1), pp. 58–64.

[13] Webb, R. L., and Jung, S. H., 1992, "Air-Side Performance of Enhanced Brazed Aluminum Heat Exchangers," *Proceedings of the ASHRAE Transactions*, ASHRAE, Atlanta, GA, Vol. 98, Pt. 2, pp. 391–401.

[14] Kays, W. M., and London, A. L., 1984, *Compact Heat Exchangers*, 3rd ed., McGraw-Hill, New York.

[15] Suga, K., and Aoki, H., 1991, "Numerical Study on Heat Transfer and Pressure Drop in Multilouvered Fins," *Proceedings of the ASME/JSME Thermal Engineering Joint Conference*, ASME, New York, pp. 361–368.

[16] Draper, N. R., and Smith, H., 1998, *Applied Regression Analysis*, 3rd ed., Wiley, New York, p. 706.

A Microscopic Approach to Determine Electrothermal Contact Conditions During Resistance Spot Welding Process

P. Rogeon[1]
e-mail: philippe.rogeon@univ-ubs.fr

R. Raoelison

P. Carre

Laboratoire d'Études Thermiques Energétiques et Environnement,
Université de Bretagne Sud,
rue de Saint-Maudé, BP 92116,
56321 Lorient Cedex, France

F. Dechalotte
PSA Peugeot Citroën,
Centre Technique de Vélizy,
Route de Gisy,
78943 Vélizy Villacoublay Cedex, France

This study deals with resistance spot welding process modeling. Particular attention must be paid to the interfacial conditions, which strongly influence the nugget growth. Imperfect contact conditions are usually used in the macroscopic model to account for the electrical and thermal volume phenomena, which occur near a metallic interface crossed by an electric current. One approach consists in representing microconstriction phenomena by surface contact parameters: The share coefficient and the thermal and electrical contact resistances, which depend on the contact temperature. The aim of this work is to determine the share coefficient and the contact temperature through a numerical model on a microscopic scale. This surface approach does not make it possible to correctly represent the temperature profiles, with the peak temperature, observed in the immediate vicinity of the interface and thus to define, in practice, the contact temperature correctly. That is why another approach is proposed with the introduction of a low thickness layer (third body) at the level of the interface the electric and thermal resistances of which are equivalent to the electrical and thermal contact resistance values. In this case, the parameters of the model are reduced to the thickness of the arbitrarily fixed layer and equivalent electric and thermal conductivities in the thin layer, the partition coefficient and the contact temperature becoming implicit. The two types of thermoelectric contact models are tested within the framework of the numerical simulation of a spot welding test. The nugget growth development is found to be much different with each model.
[DOI: 10.1115/1.3000596]

Keywords: electro-thermal interface, heat partition coefficient, contact resistance, contact temperature, resistance spot welding

1 Introduction

Modeling and the numerical simulation can, through predictive models, effectively replace long and expensive welding tests, which are carried out to establish the weldability of the new sheet assemblies in resistance spot welding (RSW) process modeling.

A number of research works [1–12] agree on the crucial role of the interfacial conditions on the RSW process. Two approaches are considered in the different numerical models to account for the electrical and thermal contact resistances on the level of the two interface types, electrode-sheet and sheet-sheet. In the first approach [1–5], the interfacial phenomena are taken into account through a thin contact layer (third body) with very low thickness fixed a priori and with equivalent electric and thermal conductivities: The volume character of the thermoelectric interface is preserved in this approach. In the second approach [6–12], the microconstriction phenomena are replaced by a discontinuity between the two surfaces in contact through three parameters (Fig. 1): The thermal contact resistance (TCR) and the electrical contact resistance (ECR), which account for the microconstriction phenomena near the interface and the heat partition coefficient α of the heat generated by Joule effect in the ECR distributed at the boundaries of the TCR. As the contact resistances strongly depend on pressure and temperature, the contact temperature (CT) must also be determined. This technique consists in representing, in the macroscopic model, the volume phenomena of microconstriction on the scale of roughness and asperities by surface conditions. Electrical and thermal contact resistances can be determined by using theoretical approaches [8,13–18] or specific experimental devices [19–21].

The aim of this work is to define both the heat partition coefficient and the contact temperature. Only few research works deal with the determination of the heat partition coefficient [6,9,10,13] and the definition of the contact temperature in the case of electrothermal contact [13,14]. Indeed, most dealing with the heat partition coefficient concern frictional contact [22–24]. Dissipation mechanisms are different, but analogies could be found with electrothermal contact, assuming that the heat power is dissipated in the vicinity of the bulk interface. In the case of electrothermal contact, some authors suggested a definition of the heat partition coefficient as a relation depending only on the ratio of thermal effusivities [6]. First, by using a numerical approach on a microscopic scale with a thermoelectric contact model, the influence on the heat partition coefficient of the thermophysical and electric properties, as well as the microgeometrical parameters, will be studied here. Second, still dealing with the microscopic contact between the two metallic mediums partially in contact, the temperature field near the contact zone is compared with the temperature distributions obtained through the surface and the volume approaches. In the particular case where the thermal and electrical constriction functions are identical in the mediums, the contact temperature can be determined by using an analytical formula. The essential role of thermal resistance is also explained. Finally, the surface and the volume electrothermal contact models are

[1]Corresponding author.

Contributed by the Heat Transfer Division of ASME for publication in the JOURNAL OF HEAT TRANSFER. Manuscript received February 9, 2008; final manuscript received September 8, 2008; published online December 29, 2008. Review conducted by Ali Ebadian.

 Copyright © 2009 by ASME

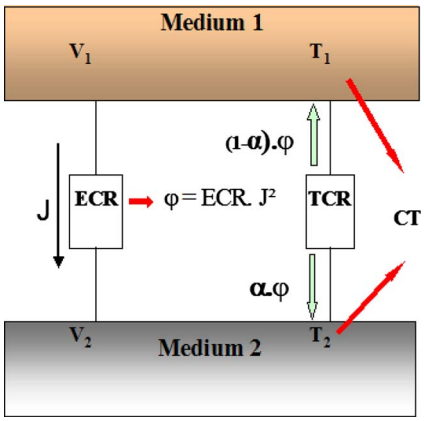

Fig. 1 Schematic of thermoelectric contact conditions in the model through surface contact parameters

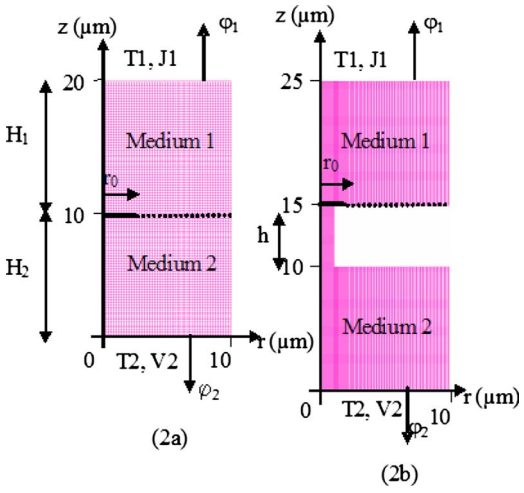

Fig. 2 Geometries and meshing of the reference model with constriction, without asperity (*h*=0) (*a*), and with asperity in the medium 2 (*h*=5 μm) (*b*)

tested in the case of a numerical simulation of a spot welding test, and their effects on the nugget growth are then compared.

2 Presentation of the Microscopic Models for Thermoelectric Contact

2.1 Definition of the Microscopic Models. Thermoelectric contact on a microscopic scale is analyzed to better understand the influence of the dissipative and diffusive phenomena within the disturbed zones on the heat partition coefficient. A numerical dimension approach at a micrometric level is used here through consideration in the micrometric contact areas of the models and micrometric volumes of mediums around them, representative of two asperities in contact at the level of a metallic interface. Three models are related to an axisymmetric elementary contact cell, which is constituted of two mediums partially in contact and subjected to thermoelectric boundary conditions. In addition, solid/solid contact is the only way considered for thermal and electric transfers. Thermal transfers and electrical conduction through interstitial medium are not dealt with here. Moreover, contact surfaces for the passage of electric and thermal currents are identical. Thus, the possible presence of oxides on contact surfaces are not considered here either, which in practice are opposed to the passage of the electrical current and not the heat flux. These reducing assumptions mean that the thermal and electrical constriction functions can be supposed identical here.

In the first model, called the reference model, the two mediums are partially in contact and the electrical and thermal constriction functions are considered identical. A methodology is developed for the determination of the heat partition coefficient. Various configurations with the reference model are tested while varying the geometrical parameters and the thermophysical properties. The model is implemented using the finite element computation software SYSWELD®, which treats electrothermal coupling. Particular attention will be paid to the analysis of the heat flux at the boundaries of the model to calculate the heat partition coefficient.

In the second and third models, called electrothermal equivalent contact (ETEC) models, there is no constriction. The schematization of the contact is simplified to the extreme and the effects of thermoelectric constrictions in the mediums are taken into account, through surface contact parameters (ECR, TCR, and α) or through equivalent electrical and thermal conductivities (σ_E and λ_E) in a thin layer whose thickness e is fixed a priori, respectively. These parameters should account for the volume phenomena, the dissipation and diffusion mechanisms, which occur, respectively, in the electrical and thermal resistance constrictions.

The models, with microconstriction and with contact parameters, will be compared in regard to the heat flux dissipated and leaving the boundaries, on the one hand, and the thermal field, on the other hand. The contact temperature will be defined in this particular thermoelectric contact configuration.

2.2 Geometries and Meshing. The reference model with constriction effect for this study is a 2D axisymmetric model, composed of two mediums (identical radius R, and heights $H1$ and $H2$) connected by thermal and electric contacts through a disk of radius r_0 (Fig. 2). Two geometrical configurations are considered. The first one has the two mediums in contact without asperity, for which various rates of contact $\tau = r_0^2/R^2$ and various dimensional ratios $H1/R$ and $H2/R$ are considered (Fig. 2(a)). In the second one, both mediums are in contact through an asperity of height h all situated in the second medium (Fig. 2(b)). Meshing is adapted to each geometrical configuration, and refinements were optimized through a numerical space convergence study. The dimensional ratios H/r_0 and R/r_0 were selected as the isotherms and the isopotentials to be plane at the exit of medium (constriction fully developed).

For the ETEC models without constriction, the contact geometries are simplified (Fig. 4). The same precautions as before have been taken for the meshes.

2.3 Equations of the Model. The electric and thermal phenomena are described by the traditional equations of conduction, with strong coupling through the source term in the heat equation, which account for the Joule effect in the microconstriction zone. Considering the very weak electric and thermal inertias of the micrometric geometries compared with the characteristic time for resistance spot welding, on a microscopic scale, the various physical phenomena can be assumed stationary. The equations of the model are as follows:

$$\mathrm{div}(\lambda \overrightarrow{\mathrm{grad}}\, T) + \overrightarrow{\mathrm{grad}}\, V \cdot (\sigma \overrightarrow{\mathrm{grad}}\, V) = 0 \tag{1}$$

$$\mathrm{div}(\sigma \overrightarrow{\mathrm{grad}}\, V) = 0 \tag{2}$$

Here, the thermophysical and electric properties (λ and σ), isotropic and constant, are also considered by choosing particular electrical and thermal conditions, which ensure weak thermal gradients in the mediums.

2.4 Boundary Conditions. From a thermal point of view, Dirichlet conditions are applied at the boundaries of the two mediums ($z=+H1 : T=T1$ and $z=-H2 : T=T2$); the other boundaries are assumed adiabatic (Figs. 2 and 4). From an electric point of view, a uniform current density ($J1$) is imposed on the surface of

Table 1 Values of the heat partition coefficient—configurations without asperity

α		$\lambda 1/\lambda 2$						
		0.1	0.25	0.5	1	2	4	10
$\sigma 1/\sigma 2$	0.1	0.50	0.56	0.62	0.71	0.79	0.85	0.91
	0.25	0.45	0.50	0.57	0.65	0.73	0.80	0.85
	0.5	0.38	0.44	0.50	0.58	0.67	0.73	0.79
	1	0.30	0.35	0.42	0.50	0.58	0.65	0.70
	2	0.21	0.27	0.33	0.42	0.50	0.56	0.62
	4	0.15	0.20	0.27	0.35	0.43	0.50	0.55
	10	0.09	0.14	0.21	0.29	0.38	0.44	0.50

medium 1 ($z=+H1$) and a zero potential ($V2=0$ V) on the surface of medium 2 ($z=-H2$); other surfaces are considered insulated (Figs. 2 and 4).

2.5 Convergence Criteria. The numerical simulations are achieved with the finite element computation software SYSWELD®. The convergence criteria retained for all the numerical simulations carried out with the three thermoelectric models were 10^{-3} (°C) for the temperatures and 10^{-5} (W) for heat flows. Furthermore, the meshes for the various models have been optimized, thanks to a numerical space convergence study to limit numerical errors.

3 Determination of the Heat Partition Coefficient

3.1 Methodology. When an electrical current crosses an interface, the heat is generated in the disturbed region where the current is constrained toward the asperities and the contact zones. The constrictions of the electrical and thermal current lines toward the contact zones increase the resistance inside the disturbed zone. In the literature [9,10], the heat partition coefficient is defined as the fraction of the total flux dissipated in constriction resistances and outgoing from the disturbed zone by the medium of reference. Constriction resistances are obtained by subtracting the resistance of mediums without constriction from the resistance of mediums with constrictions. Thus, two models should be simultaneously implemented: A model with constrictions and a second model without constriction (perfect contact) to keep only the effect of the mediums. By subtracting the heat flux φ_1' and φ_2' leaving the model without constriction only due to medium resistances, from the outgoing fluxes φ_1 and φ_2 of the model with constriction, it is possible to determine the flux only dissipated in constrictions ($\varphi_1''=\varphi_1-\varphi_1'$ and $\varphi_2''=\varphi_2-\varphi_2'$), and then, the heat partition coefficient (3):

$$\alpha=\frac{\varphi_1''}{\varphi_1''+\varphi_2''} \quad \text{and} \quad 1-\alpha=\frac{\varphi_2''}{\varphi_1''+\varphi_2''} \tag{3}$$

3.2 Results

3.2.1 Influence of Thermophysical and Electric Properties. A study is done with the geometrical configuration without asperity, with identical heights $H1$ and $H2$ (10 μm), and with radius $R=10$ μm and a contact rate τ of 1%, which allows for the full development of constriction. The thermoelectric boundary conditions applied are as follows: $T1=0$ °C, $J1=2000$ A mm^{-2}, $T2=0$ °C, $V2=0$ V. These boundary conditions ensure that heat fluxes, which leave the mediums, should proceed only from the heat dissipation by Joule effect in the electrical constriction resistances. Different ratios of thermal and electric conductivities (λ_1/λ_2 and σ_1/σ_2) are tested in order to study the influence of the properties of materials in contact on the heat partition coefficient. Some tested combinations (λ_1/λ_2) and (σ_1/σ_2) are not physical but allow the analysis to be extended. For all the considered cases, with the specific value of $J1$ (2000 (A mm^{-2})), the thermal gradients remain weak in the mediums. The calculated heat partition coefficient α corresponds to medium 1.

The ratios (λ_1/λ_2) and (σ_1/σ_2), which, respectively, account for the mechanisms of thermal diffusion and of electric dissipation, play perfect symmetrical and opposite roles (Table 1). When they are equal, the heat partition coefficient is equal to 0.5. Lemeur [9,13] proposed, using an analytical model in the case of two semi-infinite mediums partially in thermoelectric contact, an expression for the heat partition coefficient (4), which can be modified by incorporating ratios of the properties (λ_1/λ_2) and (σ_1/σ_2) (5):

$$\alpha=\frac{1}{2}\left(\frac{\rho_1}{\rho_1+\rho_2}+\frac{\lambda_1}{\lambda_1+\lambda_2}\right) \tag{4}$$

$$\alpha=\frac{1}{2}\left(\frac{1}{1+\dfrac{\sigma_1}{\sigma_2}}+\frac{1}{1+\dfrac{\lambda_2}{\lambda_1}}\right) \tag{5}$$

The values obtained with this expression are very close to those resulting from our numeric model, and for identical ratios (λ_1/λ_2) and (σ_1/σ_2), α is found to be equal to 0.5. In the case of contact between two very different metals ($\lambda_1/\lambda_2=10$ and $\sigma_1/\sigma_2=10$, case of copper-steel contact), the strongest dissipation in medium 2 (steel) is countered by a stronger thermal diffusion in medium 1 (copper): The heat partition coefficient is balanced, and α (copper side) is worth 0.5. Coupling between electric and thermal transport phenomena is expressed in the Wiedemann–Franz law (6):

$$L=\frac{\lambda_e}{\sigma T} \tag{6}$$

This formula reveals the partition of thermal conduction electronically (λ_e): In the case of metals and at low temperatures, this value is very close to the global thermal conductivity (λ), which is not always the case for all metal alloys at higher temperatures where the phonic contribution can become considerable. For contact between pure metals, the Lorenz number L remains approximately constant ($L=2.4\times10^{-8}$ (V/K)^2), which leads to $\lambda_1/\lambda_2=\sigma_1/\sigma_2$ and then $\alpha=0.5$. For contact between most metal alloys, the values of the ratios (λ_1/λ_2) and (σ_1/σ_2) still remain close generally, even at high temperatures, so that α would be close to 0.5 in these cases (Table 1).

Feulvarch et al. [6] defined the heat partition coefficient by the formula depending only on the ratio of the thermal effusivity ratio (7). This relation, which does not take the heat dissipation mechanisms into account, is inadequate to account for stationary phenomena and dissipation mechanisms in the case of electrothermal contact. In fact, thermal effusivity is the useful property in the case of fast thermal transfers occurring between two mediums abruptly put in contact:

Table 2 Values of the heat partition coefficient—configuration with asperity

α		$\lambda 1/\lambda 2$						
		0.1	0.25	0.5	1	2	4	10
$\sigma 1/\sigma 2$	0.1	0.50	0.61	0.68	0.72	0.75	0.76	0.77
	0.25	0.39	0.50	0.57	0.61	0.64	0.65	0.66
	0.5	0.32	0.43	0.50	0.54	0.57	0.58	0.59
	1	0.28	0.39	0.45	0.50	0.53	0.54	0.55
	2	0.25	0.36	0.43	0.47	0.50	0.51	0.52
	4	0.24	0.35	0.41	0.46	0.49	0.50	0.51
	10	0.23	0.34	0.40	0.45	0.48	0.49	0.50

$$\alpha = \frac{1}{1 + \dfrac{b_2}{b_1}} \quad \text{with} \quad b_1 = \sqrt{\lambda_1 \rho_1 Cp_1} \quad \text{and} \quad b_2 = \sqrt{\lambda_2 \rho_2 Cp_2} \tag{7}$$

For the dissimilar copper/steel contact, the value of α obtained with formula (7) is equal to 0.8 (copper side), instead of 0.5 with relation (5).

3.2.2 Influence of the Microgeometry. Several geometrical configurations are considered with the same thermal and electrical boundary conditions as before:

- configuration without asperity with $H1=H2=10$ μm and $\tau=1\%$ (reference case)
- configuration without asperity with $H1=10$ μm and $H2=20$ μm and $\tau=1\%$
- configuration without asperity with $H1=H2=10$ μm and $\tau=50\%$
- configuration with asperity height 5 μm with $H1=H2=10$ μm and $\tau=1\%$

The same boundary conditions as those in Sec. 3.2.1 are kept for all of the tests.

In the geometrical configuration without asperity, the three different sets of geometric parameters lead to close values of α, with relative differences remaining inferior to 0.1%. In fact, for these two geometrical modifications ($\tau=50\%$ and $H2=10$ μm), in the first case the constriction functions are identically modified in the two mediums, and in the second case they are not modified at all. That is why α remains constant despite the changes in the geometry. Thus, values and evolution of α for the latter two geometrical configurations are those that are already given in Table 1 for the reference case.

On the other hand, the model with asperity leads to different values of the heat partition coefficient (Table 2). Here, the asperity belongs to medium 2 and constitutes a real geometrical singularity, notably located in the constriction zone. Its strong electric and thermal resistances decrease the diffusion in medium 2 but reinforce dissipation there: The resistance of the asperity will thus influence the heat partition coefficient. The ratios (λ_1/λ_2) and (σ_1/σ_2) still have the symmetrical and antagonistic effects, but the extreme values of the heat partition coefficient are attenuated by the role of the asperity (Table 2).

Thus, the heat partition coefficient is related not only to the thermophysical and thermoelectric properties but more precisely to the thermal and electric constriction resistances, which obviously complicates its determination. It is, therefore, possible to generalize the formula (4) suggested by Lemeur [9,13] by expressing the heat partition coefficient with thermal and electric constriction resistances (8):

$$\alpha = \frac{1}{2}\left(\frac{1}{1 + \dfrac{\mathrm{ECR}_2}{\mathrm{ECR}_1}} + \frac{1}{1 + \dfrac{\mathrm{TCR}_1}{\mathrm{TCR}_2}} \right) \tag{8}$$

The constriction resistances can be expressed by

$$\mathrm{ECR} = \frac{1}{\sigma} F_E \quad \text{and} \quad \mathrm{TCR} = \frac{1}{\lambda} F_T \tag{9}$$

The thermal and electrical constriction functions are identical here ($F_E=F_T=F$):

$$\alpha = \frac{1}{2}\left(\frac{1}{1 + \dfrac{\dfrac{1}{\sigma_2}F_2}{\dfrac{1}{\sigma_1}F_1}} + \frac{1}{1 + \dfrac{\dfrac{1}{\lambda_1}F_1}{\dfrac{1}{\lambda_2}F_2}} \right) \tag{10}$$

While using the formula (10) with a ratio $F_2/F_1=8$, corresponding to the microgeometry with asperity considered here (Fig. 2(*b*)), the agreement between the values of α given by this formula and those of Table 2 are excellent. Moreover, differences of the values of α between the two configurations ($F_2/F_1=1$ and $F_2/F_1=8$) do not exceed 10% (Tables 1 and 2) and remain even lower than 5% for nearby ratios (λ_1/λ_2) and (σ_1/σ_2) values (which is generally the case for contact between realistic metal alloys).

4 Definition of the Contact Temperature

The comparison between the thermal fields in the reference model with constrictions and in the two ETEC models without constriction is achieved here. The geometrical configuration corresponds to the case without asperity with identical heights $H1$ and $H2$ (10 μm) and a contact rate τ equal to 1%. Two types of metallic contact are considered here: contact between two similar metals (couple steel/steel with $\lambda_1=\lambda_2=0.03$ W mm^{-1} K^{-1} and $\sigma_1=\sigma_2=8000$ Ω mm^{-1}) and contact between two different metals (couple steel/copper with $\lambda_1=0.03$ W mm^{-1} K^{-1}, $\sigma_1=8000$ Ω mm^{-1}, $\lambda_2=0.3$ W mm^{-1} K^{-1}, and $\sigma_2=80{,}000$ Ω mm^{-1}).

For the ETEC model with surface contact conditions, the calculated contact parameters, which correspond to each configuration, are for the steel/steel contact ($\mathrm{ECR}=1.6\times10^{-5}$ Ω mm^2, $\mathrm{TCR}=3.93$ K mm^2/W, and $\alpha=0.5$) and for the steel/copper contact ($\mathrm{ECR}=0.88\times10^{-5}$ Ω mm^2, $\mathrm{TCR}=2.16$ K mm^2/W, and $\alpha=0.5$). The same electric boundary conditions as those previously used are considered ($J1=2000$ A mm^{-2} and $V2=0$ V). For the thermal boundary conditions, different configurations are tested so that thermal gradients and heat fluxes in the mediums could depend not only on the heat dissipation but also on the boundary conditions: ($T1=0$°C, $T2=0$°C), ($T1=0$°C, $T2=10$°C), and ($T1=0$°C $T2=100$°C) for the steel/copper contact, and ($T1=0$°C, $T2=0$°C), ($T1=10$°C, $T2=0$°C), ($T1=100$°C, $T2=0$°C) for the steel/steel contact. The comparison more precisely concerns outgoing fluxes φ_1 and φ_2 of both mediums 1 and 2 and distributions of temperature in the mediums as well. As previously defined in Sec. 3, φ_1 and φ_2 represent the part of the total heat flux dissipated in the two mediums by Joule effect only and outgoing from mediums 1 and 2, respectively. For the different electrothermal configurations considered here, with different thermal bound-

Table 3 Comparison between heat fluxes outgoing from the models with constriction (model 1) and with surface contact parameters (model 2)—case of steel-copper contact

ECR=0.88×10^{-5} Ω mm^2 TCR=2.16 K mm^2/W α=0.5	φ_2 (W)	φ_1 (W)	Total heat flux (Joule effect) $\varphi_1+\varphi_2$ (W)	$\varphi_1/\varphi_1+\varphi_2$
Model 1: $T1=0$, $T2=0$	0.00692	0.00684	0.01376	0.5
Model 2: $T1=0$, $T2=0$	0.00628	0.00644	0.01272	0.51
Model 1: $T1=10$, $T2=0$	0.00817	0.00535	0.01353	0.4
Model 2: $T1=10$, $T2=0$	0.00756	0.00520	0.01277	0.41
Model 1: $T1=100$, $T2=0$	0.01408	0	0.01408	0
Model 2: $T1=100$, $T2=0$	0.01277	0	0.01277	0

ary conditions, good correlation is found between the heat fluxes leaving the two models (Tables 3 and 4); thanks to the spatial convergence study, good precision is ensured for the numerical results. Furthermore, the values of φ_1 and $\varphi_1/(\varphi_1+\varphi_2)$ can decrease with $T1$ (Table 3) or increase with $T2$ (Table 4); the flux dissipated in constrictions is forced in the direction opposed to the temperature gradients imposed by the boundary conditions and when the heat flux dissipated in the mediums is no longer sufficient enough to reverse the temperature gradients imposed by the boundary conditions, $\varphi_1/(\varphi_1+\varphi_2)$ can reach 0% or 100% (Tables 3 and 4). This comparison shows that the two models appear equivalent when regarding the heat fluxes φ_1 and φ_2 leaving the disturbed zone. These results also accredit the fact that the heat partition coefficient should not include the effects of thermal boundary conditions; it is really an intrinsic parameter that depends only on the thermal and electrical constriction resistances. With an adapted set of surface contact parameters (ECR, TCR, and α), it is therefore able to globally simulate the thermoelectric behavior of a metal interface crossed by an electrical current and by a heat flux. However, thermal equivalence is not perfectly checked with the model with surface contact parameters, especially when the heat dissipated in the constriction zones prevailed in the microscopic model; in this case the thermal fields in the two models are rather different (Figs. 3(*a*) and 3(*d*)) especially near the contact zone. Indeed, when the heat dissipation prevails, case $T1=T2=0\,^\circ$C (Figs. 3(*a*) and 3(*d*)) and case $T1=0\,^\circ$C, $T2=10\,^\circ$C (Fig. 3(*e*)), the modeling with the surface contact parameters in the ETEC model is not able to reproduce a thermal field sufficiently similar to that observed in the reference model. In the ETEC model, the heat dissipated in the contact resistance ECR is divided into two parts with the partition coefficient α and distributed at the boundaries of the TCR. In this manner, the heat dissipated in the ECR cannot cross the TCR, except only a small fraction, therefore preventing the TCR from assuming its function. That is the reason why the temperature is so much lower in the ETEC model. In fact, in the reference model, the heat dissipated in the electrical constriction resistances crosses the thermal constriction resistances, which generates a peak temperature in the most resistant medium (Figs. 3(*a*) and 3(*d*)). In the case of symmetrical (steel/steel) contact (Fig. 3(*d*)), the peak temperature in the reference model is equal to 45.6°C, while the temperature θ_c at both sides of the TCR in the surface contact model is equal to 11.5°C. In this particular symmetrical contact case with identical electrical and thermal constriction functions, it is possible to calculate the peak temperature in the constriction with the voltage-temperature relation expressed in Eq. (11) [13,14]:

$$\mathrm{CT}^2 = T_\infty^2 + \frac{((V_1 - V_2)/2)^2}{L} \tag{11}$$

where T_∞ is the temperature at the limit of the constriction zone. For the symmetrical steel/steel considered here, from relation (11), CT is found equal to 42.2°C, with $T_\infty=273$ K, $L=1.37\times10^{-8}$ $(\mathrm{V/K})^2$, and $V1\text{-}V2=0.0369$ V. This value is much closer to the peak temperature obtained with the reference model. However, in the general case, thermal and electrical interfacial phenomena are rather different: Heat flux can cross the interstitial dielectric medium, and oxide film can prevent the passage of the electrical current across the interface. Consequently, electrical constriction function should be much different and more important than the thermal one. Thus, it appears in practice generally difficult to calculate precisely the CT with the relation (11). However, knowing the reference CT is very important and it should be well predicted, in fact, the mechanical behavior of the asperities strongly depends on the temperature rise in the contact region and thus the contact resistances TCR and ECR evolutions as well [19,21].

In the case of a strong thermal gradient imposed by the thermal boundary conditions ($T1=0\,^\circ$C, $T2=100\,^\circ$C) or ($T1=100\,^\circ$C, $T2=0\,^\circ$C), the thermal fields in the two models are rather close (Figs. 3(*c*) and 3(*f*)). In the case of the steel/copper contact (Fig. 3(*c*)), it is possible to determine the CT, which is found to be close to the contact temperature θ_c of the medium with the greater thermal conductivity (here θ_{2c} for medium 2 corresponding to the copper). In similar cases, the CT can be calculated through the classical relation [25]

$$(\theta_{1c}\text{-CT})/(\text{CT-}\theta_{2c}) = \lambda_2/\lambda_1 \tag{12}$$

An alternative solution is proposed here, by using the ETEC model with volume contact conditions; surface contact parameters

Table 4 Comparison between heat fluxes outgoing from the models with constriction (model 1) and with surface contact parameters (model 2)—case of steel-steel contact

ECR=1.6×10^{-5} Ω mm^2 TCR=3.93 K mm^2/W α=0.5	φ_1 (W)	φ_2 (W)	Total heat flux (Joule effect) $\varphi_1+\varphi_2$ (W)	$\varphi_1/\varphi_1+\varphi_2$
Model 1: $T1=0$, $T2=0$	0.01250	0.01253	0.025	0.5
Model 2: $T1=0$, $T2=0$	0.01161	0.01161	0.0232	0.5
Model 1: $T1=0$, $T2=10$	0.01320	0.01187	0.025	0.53
Model 2: $T1=0$, $T2=10$	0.01229	0.01092	0.0232	0.53
Model 1: $T1=0$, $T2=100$	0.01936	0.006	0.025	0.77
Model 2: $T1=0$, $T2=100$	0.01844	0.0047	0.0232	0.79

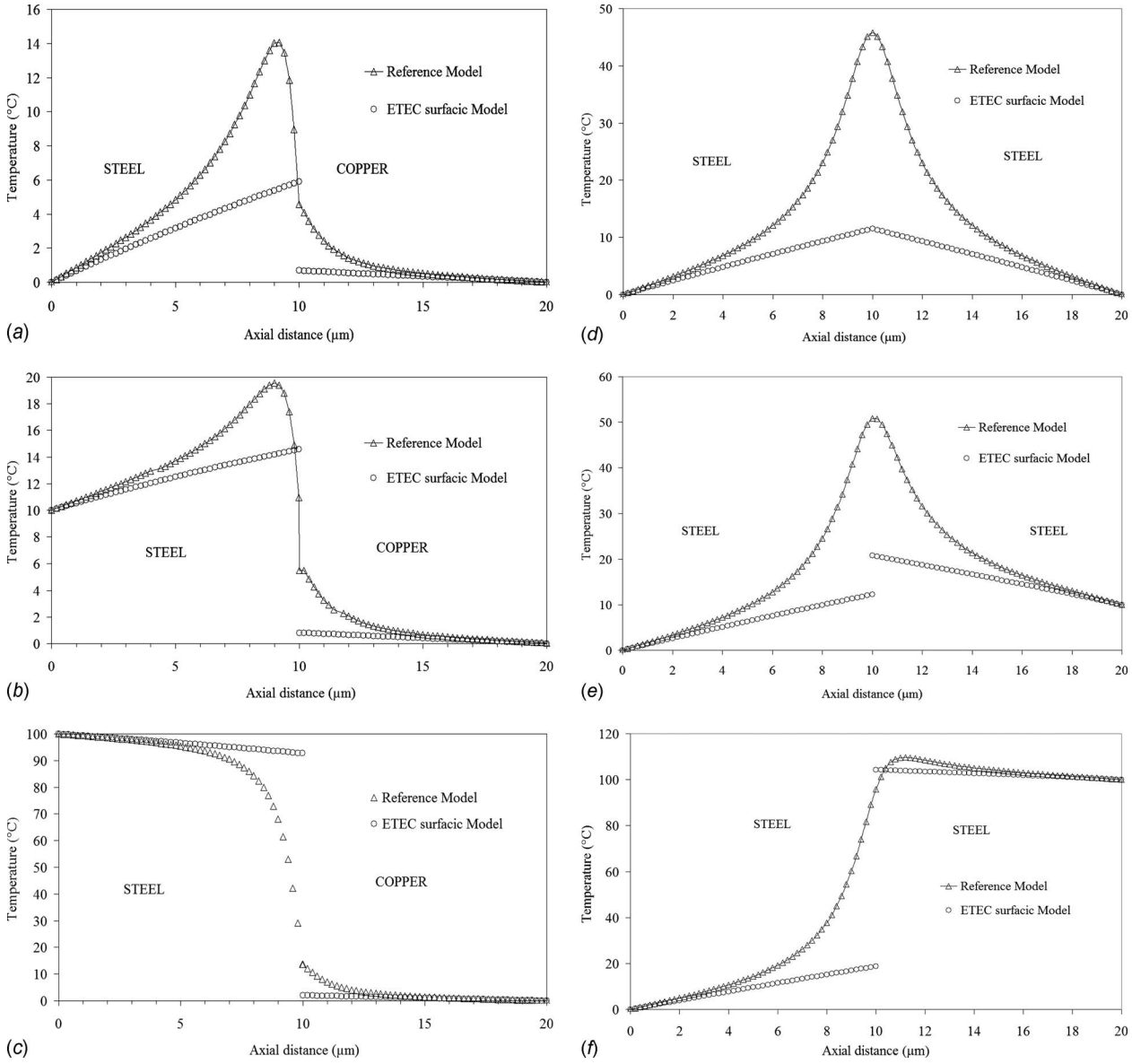

Fig. 3 Thermal fields simulated with both types (microscopic and macroscopic models) along the symmetry axis in the case of steel/copper contact (*a*) $T1 = T2 = 0\,^{\circ}\mathrm{C}$, (*b*) $T1 = 10\,^{\circ}\mathrm{C}$, $T2 = 0\,^{\circ}\mathrm{C}$, (*c*) $T1 = 100\,^{\circ}\mathrm{C}$, $T2 = 0\,^{\circ}\mathrm{C}$, and in the case of steel/steel contact (*d*) $T1 = T2 = 0\,^{\circ}\mathrm{C}$, (*e*) $T1 = 0\,^{\circ}\mathrm{C}$, $T2 = 10\,^{\circ}\mathrm{C}$), (*f*) $T1 = 0\,^{\circ}\mathrm{C}$, $T2 = 100\,^{\circ}\mathrm{C}$

(ECR, TCR, and α) are replaced by two thin layers with equivalent electrical and thermal conductivities (Fig. 4). The thickness of the two layers is arbitrarily fixed here at 1 μm. With the model with thin layers, the thermal field near the interface is found to be rather close to that observed in the reference model (Fig. 5), particularly the peak temperature in the more resistive medium. With the contact model with thin equivalent resistive layers (third body), thermal field and heat fluxes are found to be rather close to those issued from the reference model. This alternative solution allows for reducing the number of contact parameters to two equivalent conductivities σ_E and λ_E corresponding to ECR and TCR; the partition coefficient α and the reference CT are implicit. Furthermore, this solution can be applied with success in practice, depending on accurate knowledge of the electrical contact and thermal contact resistance evolutions. The demonstration is done in Sec. 5 the case of RSW numerical simulation.

5 Application to Resistance Spot Welding Numerical Simulation

The two ETEC models are successively integrated in a global model used for the numerical simulation of the spot welding process, and their effects on the nugget growth kinetic are compared. The global model has been implemented in the finite element software SYSWELD [6,7], which considers the different physical couplings between electric, thermal, metallurgic, and mechanic phenomena. The welding assembly considered here is constituted of two identical coated steel (Dual Phase DP6G) sheets of a 0.77 mm thickness and two worn electrodes (diameter of 6 mm), in Cu–Cr–Zr alloy, with flattened tips. The welding tests are achieved with the following parameters according to standard PSA Peugeot-Citroen E34.03.180.G [26]: Sinusoidal current (50 Hz, 10.1 kA), force (290 daN), 13 cycles for the welding stage, and 11 cycles for the forging stage. Welding tests are interrupted

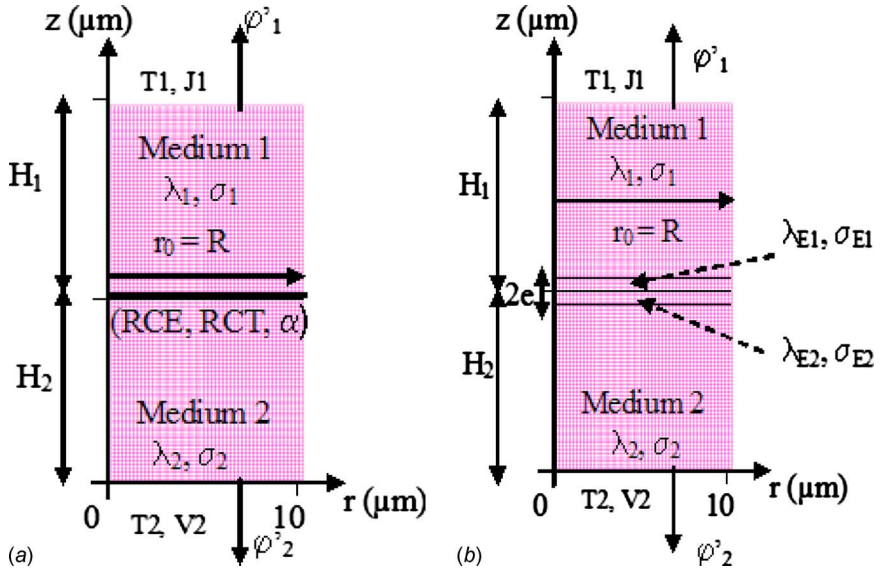

Fig. 4 Electrothermal contact conditions in the models with surface contact parameters (*a*) and with two thin contact layers and equivalent conductivities λ_E and σ_E (*b*)

at different periods and with the macrographic cuts, it is possible to reconstitute the experimental nugget growth. As the electrode tips are flat, the contact surfaces at the faying interface and at the electrode-sheet interfaces can be considered constant during the welding stage. It is thus possible to simplify the global model by considering only electrothermometallurgical couplings [6,7]. The data for the metallurgical model, the electric and thermal properties of various materials, and the electrical and thermal contact resistances (Fig. 6) were established in the framework of previous studies [6,7,21].

In the global model with the surface contact parameters ETEC model, the different parameters at the two interfaces, sheet-sheet and electrode-sheet, are as follows:

(a) the contact resistances ECR and TCR evolutions obtained on a specific device according to the temperature until 550°C under the pressure of 80 MPa (Fig. 6) [21]
(b) the heat partition coefficient taken constant and equal to 0.5
(c) the CT, considered equal to temperature on the electrode side at the interface electrode-sheet. At the faying interface, CT is taken arbitrarily equal to 1 of the temperatures of two sheet surfaces in contact.

In the global model with the third body ETEC model, the thicknesses of the thin layers on each contact surface are arbitrarily fixed to 10 μm. The electric and thermal equivalent conductivities of the thin layers σ_E and λ_E are calculated from the experimental ECR and TCR evolutions versus temperature according to

$$\sigma_E = \frac{2e}{\mathrm{ECR}} \quad \text{and} \quad \lambda_E = \frac{2e}{\mathrm{TCR}} \tag{13}$$

The thermal kinetics calculated at the faying interface reveals two different thermal regimes; the first regime, during the first welding cycle ($t < 0.01$ s), with an important heating rate (Fig. 7(*b*)) is due to heat dissipation in sheet-sheet ECR and the second regime with the slower heating rate is due to heat dissipation in the sheets (Fig. 7(*a*)). As soon as the temperature reaches 500°C, ECR becomes lower than electrical sheet resistance (Fig. 6(*b*)), and the ECR heating regime stops abruptly. With the global model with thin contact layers, the first regime is shorter; the cut temperature 500°C is reached more quickly. Thus, the energy released in sheets is weaker and the appearance of the nugget is delayed (0.18 s) versus (0.14 s) with the global model with surface contact parameters (Fig. 7(*a*)). At the end of the welding stage (0.26 s), the final nugget size calculated with the global model with surface

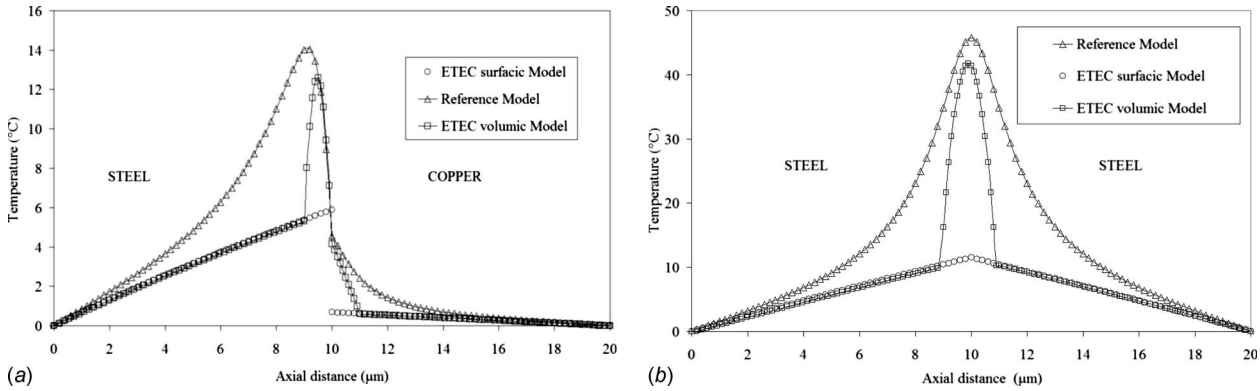

Fig. 5 Comparison between the thermal fields in the models (with contact parameters and with thin layers and equivalent conductivities) and the thermal fields in the reference model, in the case of steel/copper contact (*a*) and in the case of steel/steel contact (*b*)

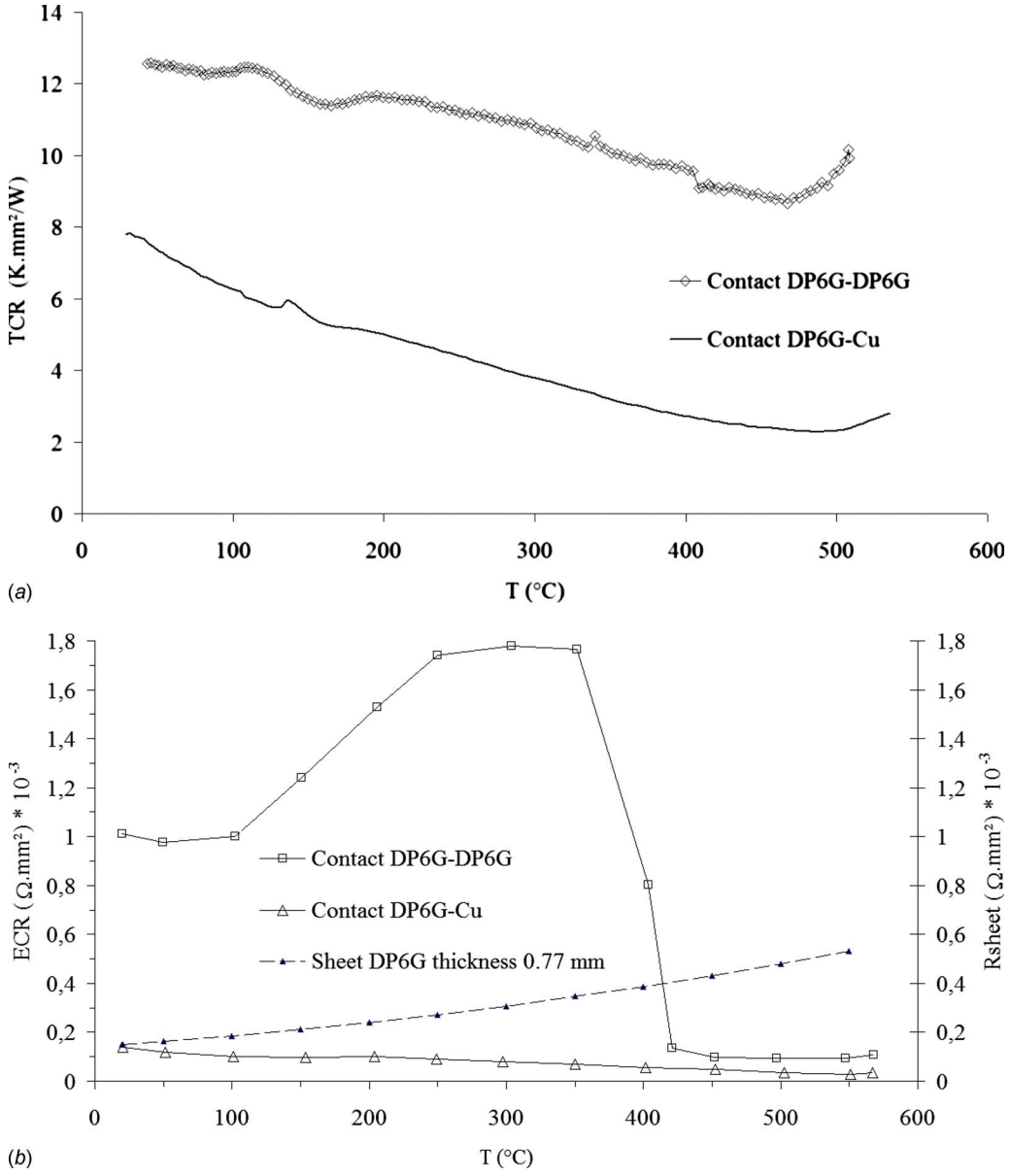

Fig. 6 Experimental evolution of TCR versus temperature under pressure of 80 MPa for the contact DP6G-Cu (*a*). Experimental evolutions of ECR versus temperature under pressure of 80 MPa for the contacts DP6G-Cu and DP6G-DP6G and comparison with the evolution of the DP6G sheet electrical resistance versus temperature (*b*).

contact parameters is definitely too big (Fig. 8(*a*)). This shows the insufficiency of the surface contact parameters ETEC model quite well; it does not at all take into account the important role of the TCR on the temperature at the faying interface. This is corrected by the third body contact ETEC model, which integrates the effect of the TCR in the equivalent thermal resistance of the thin layers and leads to a final calculated nugget size (Fig. 8(*b*)) in better adequacy with the final experimental nugget size (Fig. 9, 13th cycle).

6 Conclusion

The modeling of the electrothermal phenomena for imperfect contact between two metallic mediums constituted the aim of this work. Two finite element models of a microscopic axisymmetric contact cell between two mediums partially in contact crossed by electric current have been compared. In the reference model with volume microconstriction phenomena, mediums 1 and 2 are partially in contact. In the second model, volume electric and thermal microconstriction phenomena are replaced by a discontinuity at the interface with surface contact parameters: Electric and thermal contact resistances, the heat partition coefficient, and the contact temperature (ECR, TCR, α, and CT).

To determine α, a numerical microscopic approach was achieved with the reference model. The coefficient α appears, in fact, to depend on electrical and thermal constriction resistances and can thus be considered as an intrinsic parameter. It was found to vary symmetrically with thermal and electrical conductivity ratios in contact λ_1/λ_2 and σ_1/σ_2, respectively; diffusion and dissipation phenomena work in an opposite manner, that is why generally, for metallic contacts for which λ_1/λ_2 equal σ_1/σ_2, the heat partition coefficient value is found to be around 0.5 even for dissymmetric change of the geometry in the microconstriction zone.

The ETEC model with surface contact parameters was tested in the cases of two different metallic mediums (copper/steel) and

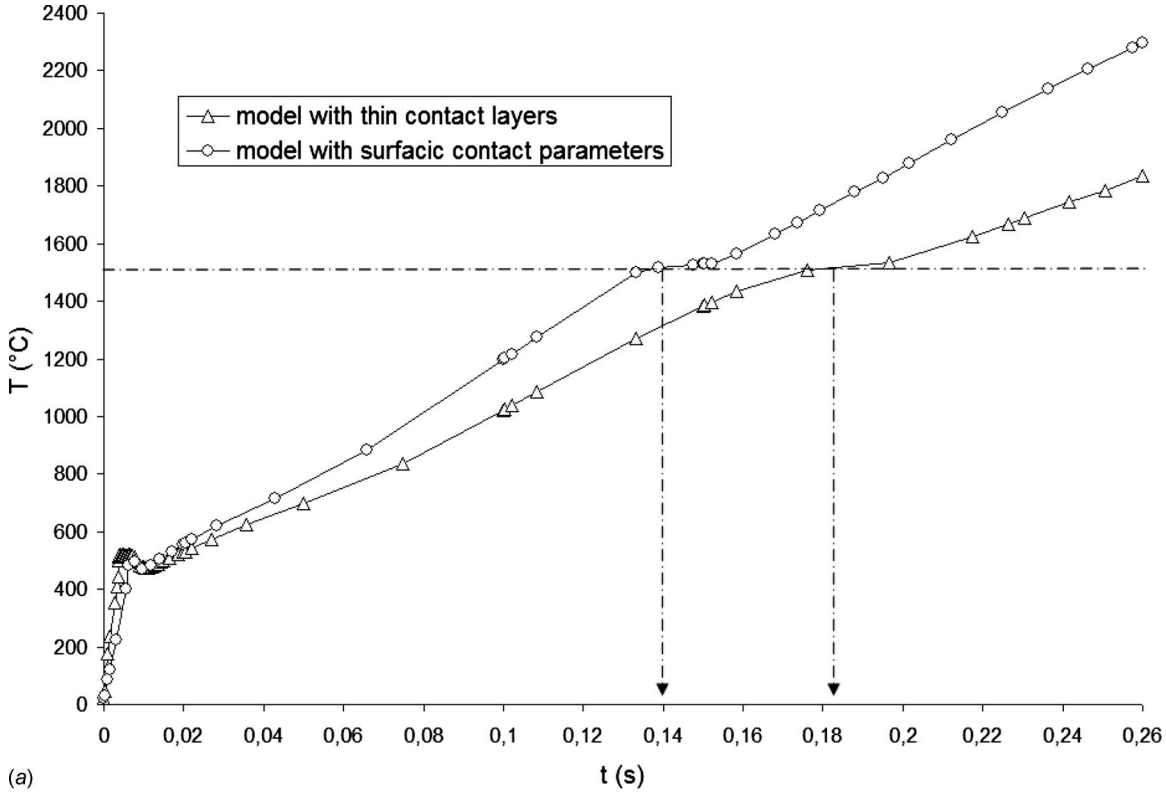

(*a*)

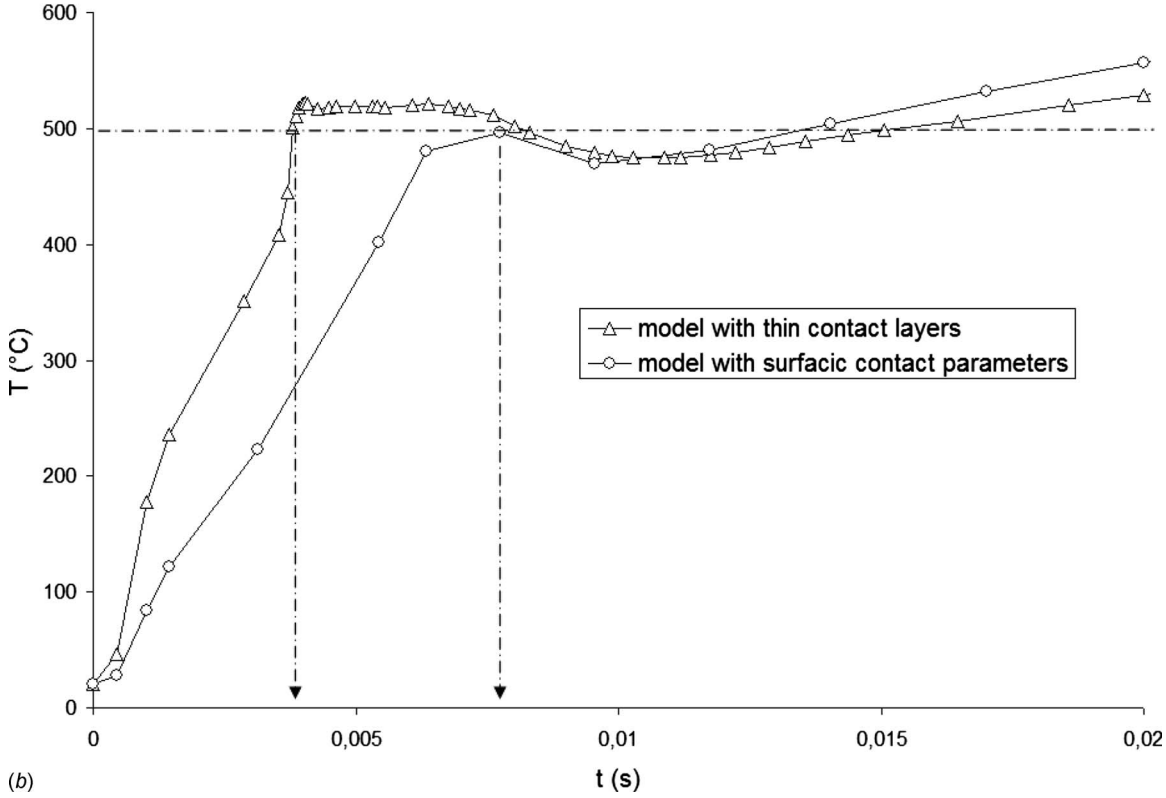

(*b*)

Fig. 7 Comparison, during the welding stage ($t<0.26$ s), between calculated temperature evolution at the faying interface with the surface contact parameters approach and with the volume contact approach (*a*) and during the first period ($t<0.02$ s) (*b*)

(steel/steel) partially in contact and compared with the reference model. Whatever the thermal boundary conditions envisaged, the boundary heat fluxes are found to be very close in the two models. However, when the heat dissipated in the electrical constriction resistances prevails, the thermal fields in the two models have been found rather different and the peak temperature observed in

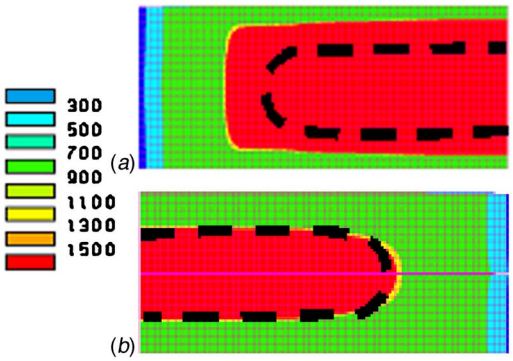

Fig. 8 Numerical nugget sizes at the end of the welding stage (13th cycle), with the surface contact parameters approach (*a*) and with the volume contact approach (*b*). Comparison with the experimental nugget size (dashed lines).

the reference model cannot be reproduced in the macroscopic model. Contrarily to what happens in the reference model, the heat flux dissipated in the ECR does not cross the TCR but is dispatched with the partition coefficient α to both sides. The thermal field near the contact zone is not sufficiently well reproduced in this ETEC model and it appears impossible in practice to define correctly the CT.

An alternative solution has been proposed here, by replacing in the ETEC model the surface contact conditions with the parameters (ECR, TCR, and α), by thin layers with equivalent electrical and thermal conductivities. With the ETEC model with thin layers, the thermal field near the interface is found to be rather close to that observed in the reference model, particularly the peak temperature in the more resistive medium. This alternative solution also allows for reducing the number of contact parameters to two equivalent conductivities σ_E and λ_E; the partition coefficient α and the reference CT become implicit in this case.

The two ETEC models have been implemented in a global model used for numerical simulation of the spot welding process and their effects on the nugget growth kinetic have been compared. With the ETEC model with surface contact parameters, which cannot be taken into account for the effect of the TCR at the faying interface, the nugget appears too early and the final nugget size is too large. This convenience disappears with the ETEC model with resistive contact layers and the numerical results are found to be much closer to the experimental one.

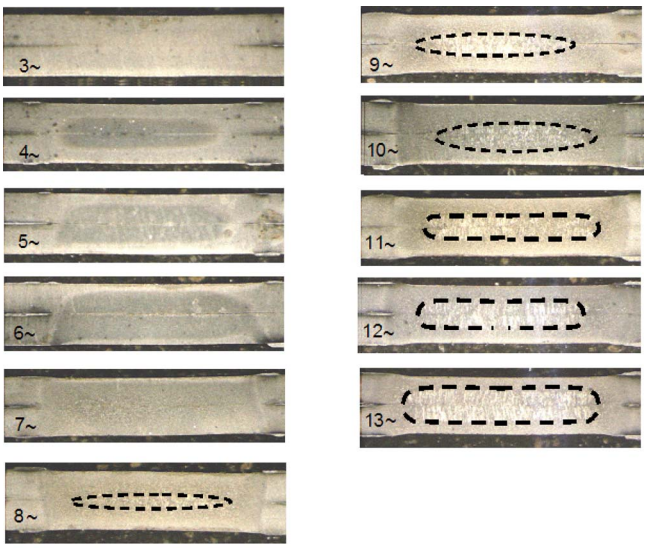

Fig. 9 Macrographic cuts at different periods presenting the experimental nugget growth (dashed lines)

Acknowledgment

We acknowledge PSA Automotive Society for their partnership with the University of South Brittany and for their technological and financial support.

Nomenclature

b = thermal effusivity (W K^{-1} m^{-2} $s^{1/2}$)
C_p = specific heat (J Kg^{-1} K^{-1})
CT = contact temperature (°C)
ECR = electrical contact resistance (Ω m^2)
e = thickness of the contact layer (m)
F = geometric constriction function
H = medium thickness (m)
h = asperity thickness (m)
J = current density (A m^{-2})
L = Lorenz number $(V/K)^2$
r_0 = contact radius (m)
R = external radius (m)
z = spatial coordinate (m)
T = temperature (°C)
T_∞ = temperature a the limit of the constriction (°C)
TCR = thermal contact resistance (K m^2 W^{-1})
V = electrical potential (V)
α = heat partition coefficient
λ = thermal conductivity (W K^{-1} m^{-1})
λ_e = electronic thermal conductivity (W K^{-1} m^{-1})
σ = electrical conductivity (W^{-1} m^{-1})
θ_c = contact temperature at the limit of the TCR (°C)
φ = heat flux (W)
τ = contact surface rate (%)

References

[1] Khan, J. A., Xu, L., Chao, Y.-J., and Broach, K., 2000, "Numerical Simulation of Resistance Spot Welding Process," Numer. Heat Transfer, Part A, **37**, pp. 425–446.
[2] De, A., Thaddeus, M. P., and Dorn, L., 2003, "Numerical Modelling of Resistance Spot Welding of Aluminium Alloy," ISIJ Int., **43**, pp. 238–244.
[3] Wang, S. C., and Wei, P. S., 2001, "Modeling Dynamic Electrical Resistance During Resistance Spot Welding," ASME J. Heat Transfer, **123**, pp. 576–585.
[4] Huh, H., and Kang, W. J., 1997, "Electrothermal Analysis of Electric Resistance Spot Welding Process by a 3-D Finite Element Method," J. Mater. Process. Technol., **63**, pp. 672–677.
[5] Sun, X., and Dong, P., 2000, "Analysis of Aluminium Resistance Spot Welding Processes Using Coupled Finite Element Procedures," Weld. Res. (Miami, FL, U. S.), **79**, pp 215.s–221.s.
[6] Feulvarch, E., Robin, V., and Bergheau, J. M., 2004, "Resistance Spot Welding Simulation—A General Finite Element Formulation of Electrothermal Contact Conditions," J. Mater. Process. Technol., **153–154**, pp. 436–441.
[7] Feulvarch, E., Rogeon, P., Carre, P., Robin, V., Sibilia, G., and Bergheau, J. M., 2006, "Resistance Spot Welding Process: Experimental and Numerical Modelling of the Weld Growth Mechanisms With Care to Contact Conditions," Numer. Heat Transfer, Part A, **49**, pp. 345–367.
[8] Feng, Z., Babu, S. S., Santella, M. L., Riemer, B. W., and Gould, J. E., 1998, "An Incrementally Coupled Electrical-Thermal-Mechanical Model for Resistance Spot Welding," *Proceedings of the Fifth International Conference on Trends in Welding Research*, Pine Mountain, June 1–5.
[9] Le Meur, G., Bourouga, B., and Bardon, J. P., 2006, "Microscopic Analysis of Interfacial Electrothermal Phenomena Definition of a Heat Generation Factor," Int. J. Heat Mass Transfer, **49**, pp. 387–401.
[10] Le Meur, G., Bourouga, B., and Dupuy, T., 2003, "Measurement of Contact Parameters at Electrode/Sheet Interface During Resistance Spot Welding Process," Sci. Technol. Weld. Joining, **8**(6), pp. 415–422.
[11] Wei, P. S., and Yeh, F. B., 1991, "Factors Affecting Nugget Growth With Mushy-Zone Phase Change During Resistance Spot Welding," ASME J. Heat Transfer, **113**, pp. 643–649.
[12] Wei, P. S., Wang, S. C., and Lin, M. S., 1996, "Transport Phenomena During Resistance Spot Welding," ASME J. Heat Transfer, **118**, pp. 762–773.
[13] Le Meur, G., 2002, "Etude de la condition de liaison thermique à une interface de contact solide—solide siège d'une dissipation par effet Joule: Application

au soudage par point," Ph.D. thesis, Ecole Polytechnique, University of Nantes, Nantes.
[14] Timsit, R. S., 2001, "The Temperature of an Electrically Heated Contact Spot," The Connector TekNote, May.
[15] Bahrami, M., Culham, J. R., and Yovanovich, M. M., 2004, "Modeling Thermal Contact Resistance: A Scale Analysis Approach," ASME J. Heat Transfer, **126**, pp. 896–905.
[16] James, P. S., Chandler, H. W., Evans, J. T., Wen, J., Browne, D. J., and Newton, C. J., 1997, "The Effect of Mechanical Loading on the Contact Resistance of Coated Aluminium," Mater. Sci. Eng., A, **230**, pp. 194–201.
[17] Jackson, R. L., Bhavnani, S. H., and Ferguson, T. P., 2008, "A Multiscale Model of Thermal Contact Resistance Between Rough Surface," ASME J. Heat Transfer, **130**(8), p. 081301.
[18] Marotta, E. E., Fletcher, L. S., and Dietz, T. A., 2001, "Thermal Contact Resistance Modeling of Non-Flat, Roughened Surfaces With Non-Metallic Coatings," ASME J. Heat Transfer, **123**(1), pp. 11–23.
[19] Vogler, M., and Sheppard, S., 1993, "Electrical Contact Resistance Under High Loads and Elevated Temperatures," Weld. J. (Miami, FL, U.S.), **72**(6), pp. 231–298.
[20] Thornton, P. H., Krause, A. R., and Davies, R. G., 1996, "Contact Resistances in Spot Welding," Weld. Res. (Miami, FL, U. S.), **75**(12), pp. 402s–412s.
[21] Rogeon, P., Carre, P., Costa, J., Sibilia, G., and Saindrenan, G., 2008, "Characterization of Electrical Contact Conditions in Spot Welding Assemblies," J. Mater. Process. Technol., **195**(1–3), pp 117–124.
[22] Bardon, J. P., 1994, "Bases Physiques des conditions de contact thermique imparfait entre deux milieux en glissement relatif," Rev. Gen. Therm., **386**, pp. 85–91.
[23] Chantrenne, P., and Raynaud, M., 1997, "A Microscopic Thermal Model for Dry Sliding Contact," Int. J. Heat Mass Transfer, **40**(5), pp. 1083–1094.
[24] Laraqi, N., 1997, "Velocity and Relative Contact Size Effects on Thermal Constriction Resistance in Sliding Solids," ASME J. Heat Transfer, **119**, pp. 173–175.
[25] Bouvier, A., 1986, "Mesure des températures par des méthodes thermoélectriques intrinsèques et semi-intrinsèques. Application à l'analyse thermique d'une opération de micro-soudure," Ph.D. thesis, Ecole Polytechnique University Nantes, Nantes.
[26] E34.03.180.G, Norme PSA Peugeot Citroën, 2001, "Soudage électrique par résistance: Techniques de Soudage—Spécifications générales," Mars.

Mixed Convection in an Impinging Laminar Single Square Jet

L. B. Y. Aldabbagh[1]
Department of Mechanical Engineering,
Eastern Mediterranean University,
Magosa, Mersin 10, Turkey
e-mail: loay.aldabagh@emu.edu.tr

A. A. Mohamad
Department of Mechanical Engineering,
Schulich School of Engineering,
The University of Calgary,
Calgary, AB, T2N 1N4, Canada

The effect of Richardson number ($Ri = Gr/Re^2 = Ra/Pr\,Re^2$) in a confined impinging laminar square jet was investigated numerically through the solution of Navier–Stokes and energy equations. The simulations were carried out for Richardson number between 0.05 and 8 and for jet Reynolds number between 50 and 300. The jet-to-target spacings were fixed to 0.25B, 0.5B, and 1.0B, respectively, where B is the jet width. The calculation results show that for the jet-to-target spacing of 0.25B, the flow structure of a square single jet impinging on a heated plate is not affected by the Richardson number. For such very small jet-to-target distances the jet is merely diverted in the transverse direction. The wall jet fills the whole gap between the plates with a very small vortex motion formed near the corners of the jet cross section close to the upper plate. In addition, the effect of the Richardson number on the variation in the local Nusselt number is found to be not significant. For higher jet-to-target spacing, the Nusselt number increased as the Richardson number increased for the same Re. In addition, the heat transfer rate increased as the jet Reynolds number increased for the same Richardson number.
[DOI: 10.1115/1.3000970]

Keywords: mixed convection in a jet, impinging jet, wall jets, laminar square jet, nozzle-to-plate spacing, jet to plate distances

1 Introduction

Impinging jets have found a large number of applications where high rates of convective heat transfer are required. Industrial uses of impinging air jets include tempering of glass, drying of paper and textiles, and cooling of the metal sheets, microelectronic components, and turbine blades. Impinging jets are generally used to increase the rate of heat transfer between a fluid and a solid and are quite often employed to produce enhanced and controlled localized cooling or heating effects on surfaces, as compared with nonimpinging flows. Although most of the applications of impinging jets are turbulent, laminar jets are also encountered when the fluid is viscous or the geometry is miniature as in microelectronics.

The heat transfer process in an impinging jet may fall in the forced- or mixed-convection regime, depending on the Richardson number, Ri, which is the ratio of the Grashof number and the Reynolds number squared. If $Ri \ll 1$, the forced-convection process is dominant, whereas for dominant natural convection, $Ri \gg 1$. In the case where Ri is of the order 1, forced and natural convection are comparable and the process falls into the mixed-convection regime. When there is a large temperature difference between the jet and the impingement surface and the velocity is not significantly high, there might be an effect of thermal buoyancy force. Therefore, it is important to understand the effects of buoyancy in the flow structure and overall heat transfer for designing the cooling system.

Numerous studies were reported in literature on the flow, heat, and mass transfer distribution under single laminar impinging jets with considering forced convection, without taking into account the buoyancy effects. Gardon and Akfirat [1] carried out an early work to measure the heat transfer coefficients between a flat plate and impinging 2D slot-jets. They focused on single jets and arrays of free air jets in laminar and turbulent flow conditions. Scholtz and Trass [2] investigated, both numerically and experimentally, the laminar impinging mass transfer with a nonuniform laminar velocity profile for nozzle-to-plate spacing ranging from 0.05 to 6 nozzle diameters. They found that the impinging mass transfer was independent of the nozzle-to-plate spacing within the range of 0.5–6.0 nozzle diameters for $500 < Re < 1970$. Chou and Hung [3] numerically investigated the effect of initial velocity profile at the nozzle exit on stagnation and local heat transfer of a confined slot-jet normally impinging on an isothermally heated surface. The range of the Reynolds number used, based on the width of the slot-jet, is from 100 to 400. Elison and Webb [4] experimentally investigated fully developed liquid jets impinging normally on a constant heat flux surface. Their study focused on the jet Reynolds number at the nozzle exit between 300 and 7000 and for jet-to-target spacing from 1.5 to 20 jet diameters. Sezai and Mohamad [5] studied numerically the flow and heat transfer characteristics of impinging laminar jets issuing from rectangular nozzles of different cross sections.

There are very few reported studies in literature considering mixed-convection effects in confined slot-jet impingement. Sparrow and Minkowycz [6] studied buoyancy-force effects on laminar forced convection over a horizontal flat plate. Hieber [7] determined buoyancy effects analytically for the laminar boundary-layer region above an isothermally heated semi-infinite horizontal surface located in a horizontal uniform stream. Yuan et al. [8] found a substantial heat transfer enhancement for high Richardson number conditions and jet offset peaks in the Nusselt number distribution. Their results also showed the relative importance of buoyancy on the flow structure for the case of two-dimensional laminar impinging jets. Wang et al. [9] investigated numerically a nonconfined circular jet impinging on a heated surface. They found that the Nusselt number is considerably influenced by natural convection only in the case of large difference between the initial gas temperature and the substrate temperature and at low Reynolds number with detrimental effects on the heat transfer at the stagnation point. Potthast et al. [10] performed mixed-

[1]Corresponding author.

Contributed by the Heat Transfer Division of ASME for publication in the JOURNAL OF HEAT TRANSFER. Manuscript received April 4, 2008; final manuscript received July 24, 2008; published online December 29, 2008. Review conducted by Ali Ebadian.

 Copyright © 2009 by ASME

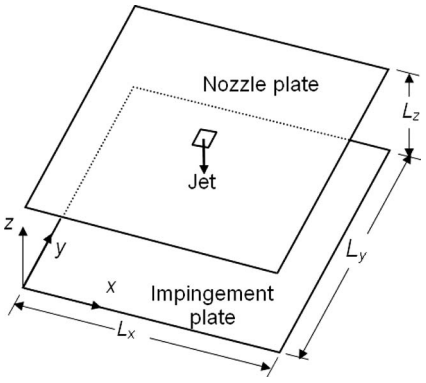

Fig. 1 Definition of geometric parameters and the coordinate system

convection simulations relative to confined axial or radial jet impingement. They found that free convection may influence the jet impingement on a horizontal plate by increasing the heat transfer and obtained periodic solution for the smallest Grashof number and a chaotic flow for the largest Grashof number. Sahoo and Sharif [11,12] investigated the associated heat transfer process in the mixed convective regime in a two-dimensional model. The ranges of the Reynolds number and jet-to-target spacings used are from 100 to 500 and from 2 to 5, respectively. The Richardson numbers vary between 0 and 10. They reported that the buoyancy effects are not very significant in the overall heat transfer process for the range of Reynolds number considered in their study. Moreover the magnitude of the local Nusselt number is reduced as the jet-to-target spacing is increased. A transient numerical analysis for fluid flow and heat transfer from a planar jet impinging on a finite thickness substrate was studied by Sarghini and Ruocco [13]. Their investigation is carried out for different geometry configuration, material coupling, and thermal-fluid driving factor. They found that for high Richardson number, Ri=5, the flow became unsteady even with very small Reynolds number used (Re =50).

The shape of the jet is very important for each application. For example, the triangular turbulent jets are used in combustion chambers of jet engines, boiler furnaces, and gas turbine plants of electric power utilities [14], while the rectangular jets may be used when more uniform cooling is needed [15]. In general, relative to the circular jets, it is found that the centerline mean velocity of noncircular jets decays more rapidly, implying increased entrainment of surrounding fluid except the square- and cross-shaped jets, which do not promote significant changes in the far-field mixing rates [16].

The numerical simulation of the single jet in laminar range with mixed convection is quite scarce. The numerical simulations of Refs. [6–13] are related to the impingement of laminar slot-jet that is two dimensional. Although the work of Sezai and Mohamad [5] is three dimensional, it is related to forced convection without taking into account the buoyancy effects. The present work deals with laminar three-dimensional analysis of a square single jet impinging on a heated flat surface (Fig. 1). The structure of the flow field and its effect on heat transfer is investigated numerically for a range of Richardson number (0.05–8). A detailed picture of the flow field is obtained and used to understand the variation in the local Nusselt number at the impingement plate.

2 Mathematical Modeling

The steady-state three-dimensional Navier–Stokes and energy equations for incompressible flows in Cartesian coordinates are used for this study. Using the following dimensionless variables: $X=x/B$, $Y=y/B$, $Z=z/B$, $P=p/\rho u_j^2$, and $\theta=(T-T_j)/(T_w-T_j)$, where B is the nozzle width, θ is the nondimensional temperature, T_j is the jet exit temperature, and T_w is the plate temperature, the equations governing the conservation of mass, momentum, and energy in nondimensional form can be written as follows:

$$\frac{\partial U}{\partial X}+\frac{\partial V}{\partial Y}+\frac{\partial W}{\partial Z}=0 \tag{1}$$

$$U\frac{\partial U}{\partial X}+V\frac{\partial U}{\partial Y}+W\frac{\partial U}{\partial Z}=-\frac{\partial P}{\partial X}+\frac{1}{\mathrm{Re}}\nabla^2 U \tag{2}$$

$$U\frac{\partial V}{\partial X}+V\frac{\partial V}{\partial Y}+W\frac{\partial V}{\partial Z}=-\frac{\partial P}{\partial Y}+\frac{1}{\mathrm{Re}}\nabla^2 V \tag{3}$$

$$U\frac{\partial W}{\partial X}+V\frac{\partial W}{\partial Y}+W\frac{\partial W}{\partial Z}=-\frac{\partial P}{\partial Z}+\frac{1}{\mathrm{Re}}\nabla^2 W+\frac{\mathrm{Ra}}{\mathrm{Pr\,Re}^2}\theta \tag{4}$$

$$U\frac{\partial \theta}{\partial X}+V\frac{\partial \theta}{\partial Y}+W\frac{\partial \theta}{\partial Z}=\frac{1}{\mathrm{Re\,Pr}}\nabla^2\theta \tag{5}$$

where the velocity is nondimensionalized by the nozzle exit velocity u_j, $\mathrm{Re}=u_jB/\nu$ is the jet Reynolds number, ν is the kinematic viscosity, $\mathrm{Pr}=\nu/a$ is the Prandtl number, α is the thermal diffusivity, $\mathrm{Ra}=g\beta\Delta TB^3/\nu a$ is the Rayleigh number, and β is the coefficient of volumetric expansion. At the exit of the flow domain the first derivative of all velocity components in the normal direction has been set to zero. All walls are stationary and impervious; therefore no slip boundary condition is used for the top and bottom solid walls except for the vertical component of velocity at the jet exit cross section at the top wall, where it is assumed to be uniform and set to be equal to unity. For the energy equation, if the fluid exits the domain the first derivative of temperature is set to zero and if the fluid flows from surroundings into the domain then the fluid temperature is set to the surrounding temperature, which is equal to the jet exit temperature, T_j. Adiabatic boundary conditions are imposed, on the top wall, except at the nozzle's exit cross section where it was set to be equal to that of ambient. The bottom wall is set to a higher temperature than the ambient.

3 Method of Solution

The governing equations are discretized by using the finite volume method in staggered nonuniform grids. The grids are generated such that denser grid clustering is obtained in the vicinity of the jets along the x- and y-directions. In the z-direction a sine function distribution is employed, yielding denser grids near the top and the impingement plate. A grid independence test was performed for Re=200 and Ri=0.05 in order to determine the effect of the number of grids on the final results. The maximum difference between the result obtained by using $101\times101\times31$ and $201\times201\times41$ grids is 1.6% for the local Nusselt number at a distance far away from the stagnation point. The corresponding difference between $251\times251\times51$ and $201\times201\times41$ grids is 0.01%. Hence, the $201\times201\times41$ grid system is used for all runs. The solution domain in the x- and y-directions has $L_x=35B$ and $L_y=35B$. Quick scheme (QUICK) [17] with ULTRA-SHARP flux limiting strategy [18,19] was used to calculate the convection of a scalar term (ϕ) at a control volume face. The extra neighboring points, resulting from the application of QUICK scheme, are written as the sum of the upwind face value plus a correction term involving the values from the previous iteration. The correction term is added to the source term in accordance with deferred correction procedure [19] so that the numerical stability is increased, while keeping the seven diagonal structures of the coefficient matrix. The strongly implicit procedure (SIP) method [20], which is extended here to handle three-dimensional problems, is used to solve the momentum equations. The conjugate gradient (CG) method [21] is used to solve the pressure correction equation. The coefficient matrix, resulting from the discretization of the energy equation, is nonsymmetric and is solved using the

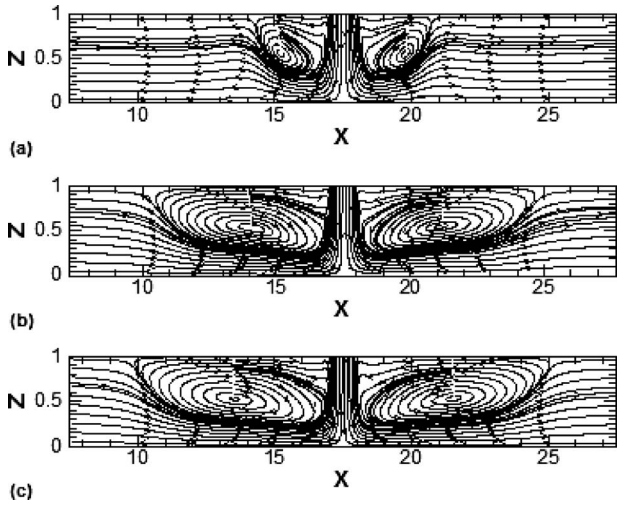

Fig. 2 Projection of flow lines on the mid-*x*-*z* plane for Re =200 and A_z=1.0 and for Richardson numbers of (*a*) Ri=0.05, (*b*) Ri=1.0, and (*c*) Ri=1.5

Bi-Conjugate gradient stabilized (Bi-CGSTAB) [22] iterative method. Symmetric successive over-relaxation (SSOR) preconditioning [23] is applied to the above iterative methods. The velocities are coupled with pressure terms using the SIMPLEC [24] algorithm.

An under-relaxation factor of 0.5 is used for momentum and energy equations in all calculations. Iterations are continued until the second norm of the residuals for all equations is reduced below 10^{-6}, where no significant variations are observed at this residual level. In the absence of experimental data under identical conditions the validation of numerical code was performed against the experimental measurements of Sparrow and Wong [25], who used a developed slot-jet flow impinging on a naphthalene plate. The results are presented in a previous publication by Aldabbagh and Sezai [26]. The agreement between the numerical results and the experimental measurements is in general good.

4 Results and Discussions

Air is used as the working fluid, having a Prandtl number of 0.71. The analysis is performed for Reynolds numbers between 50 and 300 and for the nozzle exit to plate distances between, $A_z = L_z/B$, 0.25 and 1.0. The cross section of the nozzle is taken to be a square, and the velocity distribution at the exit of the nozzles is assumed to have a flat profile.

Figure 2 shows the projection of the flow lines of the predicted velocity field on the midvertical *x*-*z* plane for Re=200, A_z=1, and Ri=0.05, 1, and 1.5. The projection of the flow lines on an *x*-*z* plane is obtained from the *x* and *z* components of the velocity vectors on that plane. At the impingement plane a wall jet is formed, spreading in the radial direction. As soon as the jet exits from the nozzle, a negative pressure is induced around the jet, which drags the fluid from the surrounding. As a result, the fluid is entrained in the flow, forming a vortex on the periphery of the jet. The vortices elongated in the radial direction far away from the jet center, where its size increased and its position changed by increasing the Richardson number. On the other hand, the thickness of the wall jet is reduced by increasing the Richardson number due to the enlargement of the vortices and elongated away from the jet axis. The evolution of the entrainment vortex and wall jets is illustrated in Fig. 3 through the projection of the flow lines of the predicted velocity field at different horizontal planes. The fluid is dragged radially toward the jet from the surrounding as soon as it exits from the nozzle. As a result a toroidal vortex is formed

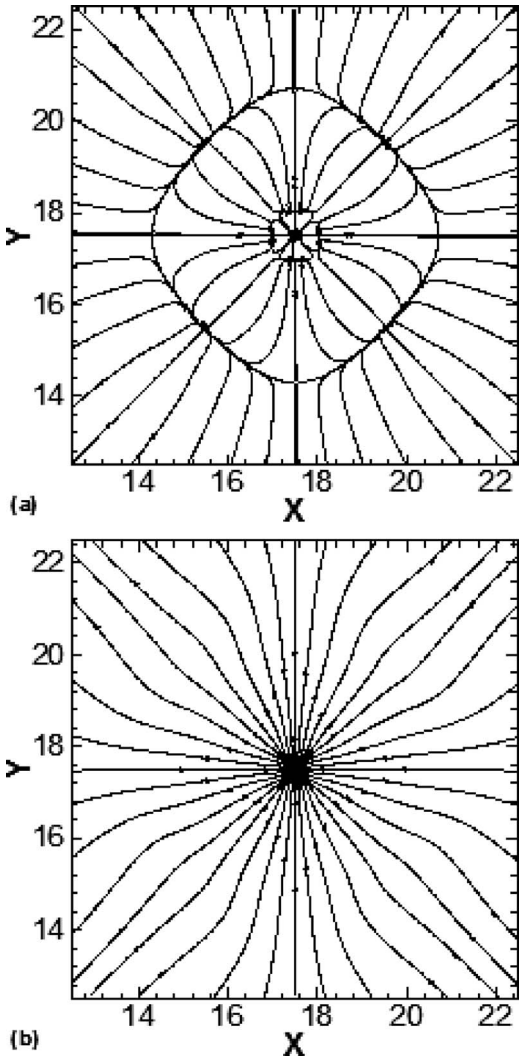

Fig. 3 Projection of flow lines for Re=200, A_z=1.0, and Ri =0.05 on the horizontal cross section at (*a*) *Z*=0.9 and (*b*) *Z* =0.3

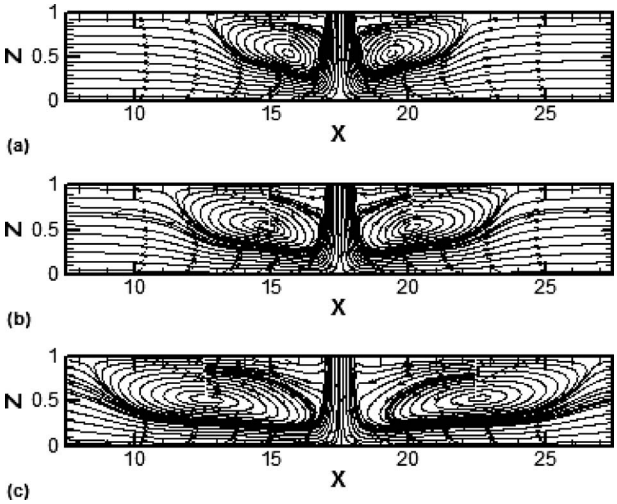

Fig. 4 Projection of flow lines on the mid-*x*-*z* plane for A_z =1.0, Ri=1.0, and (*a*) Re=100, (*b*) Re=150, and (*c*) Re=300

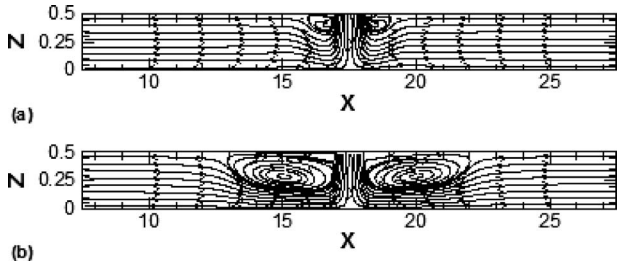

Fig. 5 Projection of flow lines on the mid-*x*-*z* plane for Re =200 and A_z=0.5 and for Richardson numbers of (*a*) Ri=0.05, (*b*) Ri=1.0, and (*c*) Ri=8.0

around the jet (Fig. 3(*a*)). At elevations closer to the bottom plate, Z=0.3, the flow pattern is characterized by the wall jets, which spreads in the radial direction.

The increases in the size of the vortices were also noticed by increasing the Reynolds number and fixing the Ri (Fig. 4), which is the case of mixed convection. The thickness of the wall jet is reduced by increasing the Reynolds number. For the cases of forced convection, the vortex became very small in size and formed very close to the upper plate near the jet exit by reducing the aspect ratio, A_z=0.5, as shown in Fig. 5. Further reducing the aspect ratio, A_z=0.25, the peripheral vortices disappeared in the

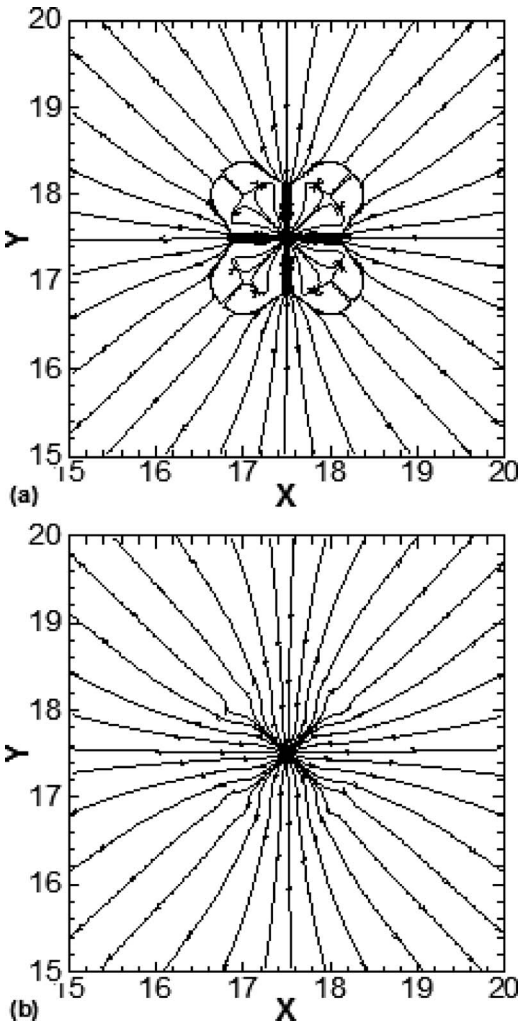

Fig. 6 Projection of flow lines for Re=200 and Ri=0.05 on the horizontal cross section at (*a*) *Z*=0.225 and (*b*) *Z*=0.175

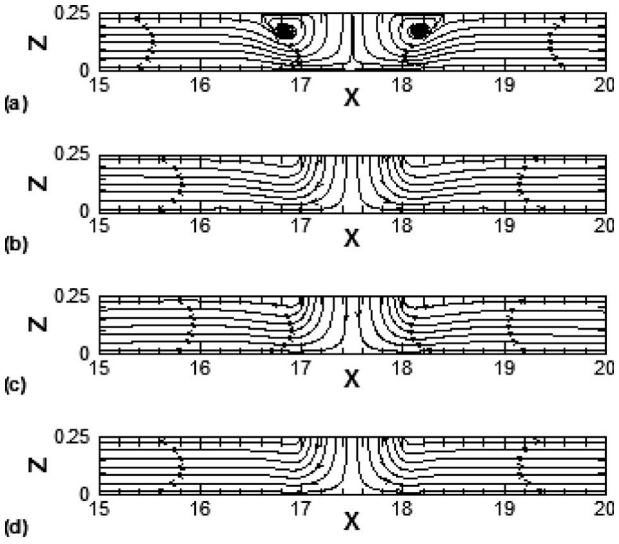

Fig. 7 Projection of flow lines on the *x*-*z* plane for (*a*) Re =200 and Ri=0.05 at *Y*=18, (*b*) Re=200 and Ri=0.05 at *Y*=17.5, (*c*) Re=200 and Ri=8.0 at *Y*=17.5, and (*d*) Re=50 and Ri=1 at *Y*=17.5

axial direction (Figs. 6 and 7(*b*)) and formed near the corners of the jet cross section close to the upper plate (Fig. 7(*a*)). At lower elevations from the jet exit section, Z=0.175, the peripheral vortices vanished (Fig. 6(*b*)). At this small aspect ratio used, the wall

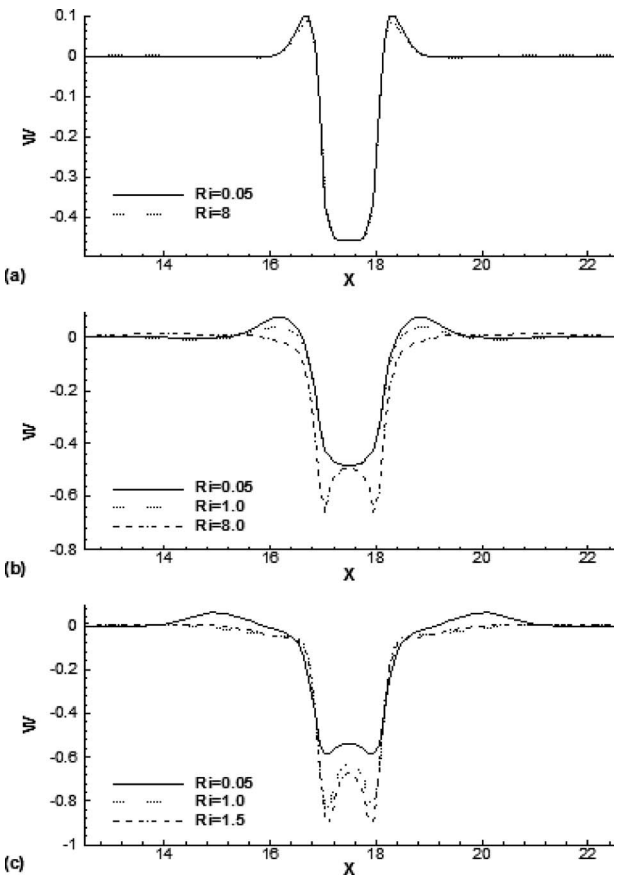

Fig. 8 Variation in the *W*-velocity with *X* at *Y*=17.5 for Re =200 and at jet-to-target spacings of (*a*) A_z=0.25 and *Z*=0.075, (*b*) A_z=0.5 and *Z*=0.15, and (*c*) A_z=1.0 and *Z*=0.3

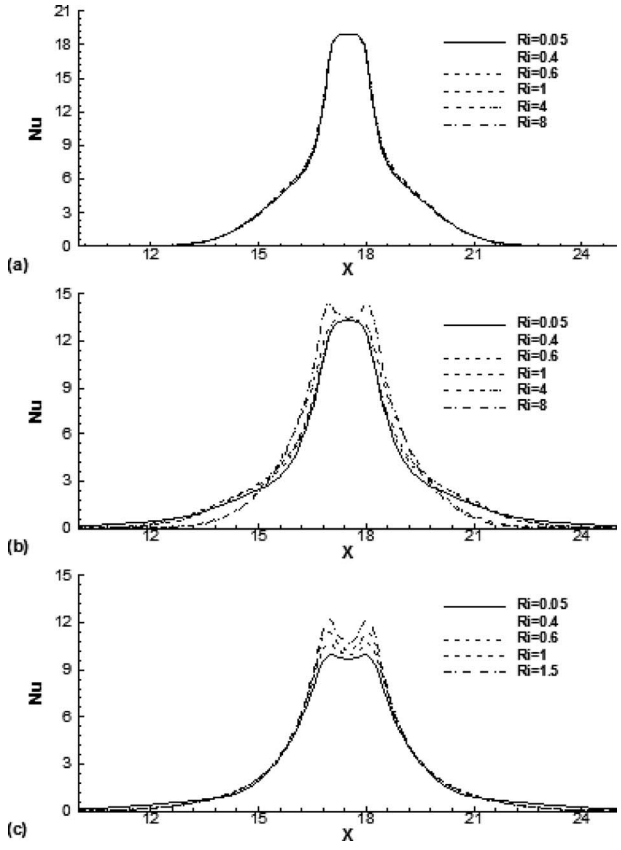

Fig. 9 Effect of Ri on the variation in the local Nusselt number for Re=200 at jet-to-target spacings of (*a*) A_z=0.25, (*b*) A_z=0.5, and (*c*) A_z=1.0

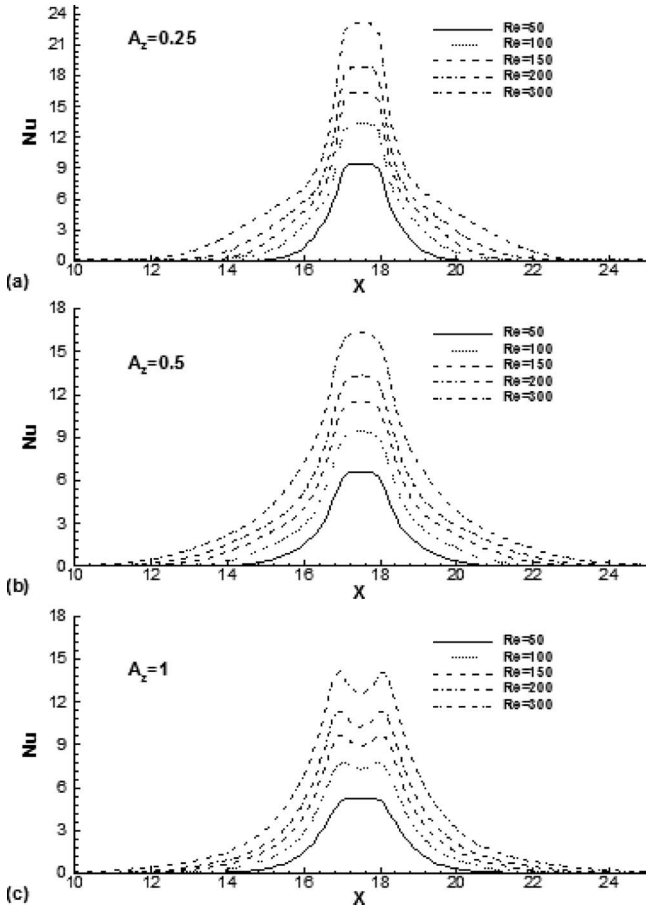

Fig. 10 Effect of Re on the variation in the local Nusselt number for Ri=1 at jet-to-target spacings of (*a*) A_z=0.25, (*b*) A_z=0.5, and (*c*) A_z=1.0

jet filled the whole gap between the plates. For such a lower aspect ratio used, the structure of the flow was not affected by the Richardson number (Figs. 7(*b*) and 7(*c*) for Re=200 and Ri=0.05 and 8, respectively) or even by reducing the Reynolds number (Fig. 7(*d*) for Re=50 and Ri=1.0). The effect of the pure forced convection (Ri=0.05) and pure natural convection (Ri=8) was only on the size of the peripheral vortices (Fig. 8(*a*)). Figure 8 shows the variation in the vertical velocity component at the horizontal cross section Z=0.075 for Re=200 and A_z=0.25, 0.5, and 1.0. The jet has one single peak at the center of the jet axis. The small change in the direction of the vertical velocity profile at X=18 is due to the formation of the peripheral vortices near the corners of the jet cross section. The variation in the vertical velocity component was also not affected by the Richardson numbers, which are not the same cases for higher aspect ratios. The variation in the vertical velocity component started to increase for A_z=0.5 and Ri>1.0. Moreover, the single peak of the jet at its center was replaced by the off-center peaks. The four peaks at the four corners of the jet cross section formed due to the interaction of the jet with the lower plate (Fig. 8(*b*)). For the case of A_z=1.0, the off-center peaks shown for all the cases run in this paper with the range of Ri used. This means that Richardson numbers play a role for the formation of the off-center peaks. We have to mention that the flow becomes transient and periodic for A_z=1.0 and Ri>1.5 and for all the cases of A_z>1.0 and Ri>0.4.

The effect of Richardson number, Ri=0.05–8, on the variation in local Nusselt numbers along the x-direction at the midsection (Y=17.5) is shown in Fig. 9 for Re=200 and A_z=0.25, 0.5, and 1.0. The local convection heat transfer coefficient is defined as

$$h = q_w''/(t_w - t_j) \tag{6}$$

where q_w'' is the local heat flux at the bottom plate and the local Nusselt number is defined in terms of the jet width, B, as

$$\mathrm{Nu} = hB/k \tag{7}$$

where B is also equal to the hydraulic diameter in the case of the square jet.

The local Nusselt number is also equal to the nondimensional heat flux and calculated as $\mathrm{Nu} = -\partial T/\partial Z|_{\mathrm{wall}}$. For A_z=0.25, the single peak of the Nusselt number was consistent with the jet velocity profile (Fig. 8(*a*)). At this small aspect ratio the heat transfer rate was not affected by the Richardson numbers. Further increasing the aspect ratio, A_z=0.5, the change in the Nusselt number was not significant for Ri≤1 (Fig. 9(*b*)). For Ri>1, the heat transfer at the stagnation point increased as the Richardson number increased. In addition, the Nusselt number decreases sharply away from the stagnation point. Moreover, the single peak of the Nusselt number was replaced by the off-center peaks, which is consistent with the jet velocity profile (Fig. 8(*b*)). The off-center peaks are also mentioned by Aldabbagh and Sezai [26–28] for the case of Ri=0.0 and A_z=1 and 2. The Nusselt number increased as the Richardson number increased for A_z=1 (Fig. 9(*c*)). In general, with all the aspect ratios used in this work, the heat transfer rate increased as the jet Reynolds number increased for the same Richardson number (Fig. 10). The increases in the heat transfer with increasing Re for the same Ri were reported in two-dimensional simulation by Sahoo and Sharif [11,12] but with higher aspect ratio (A_z=2–5). They reported that for a given domain aspect ratio and Richardson number, the average Nusselt number at the

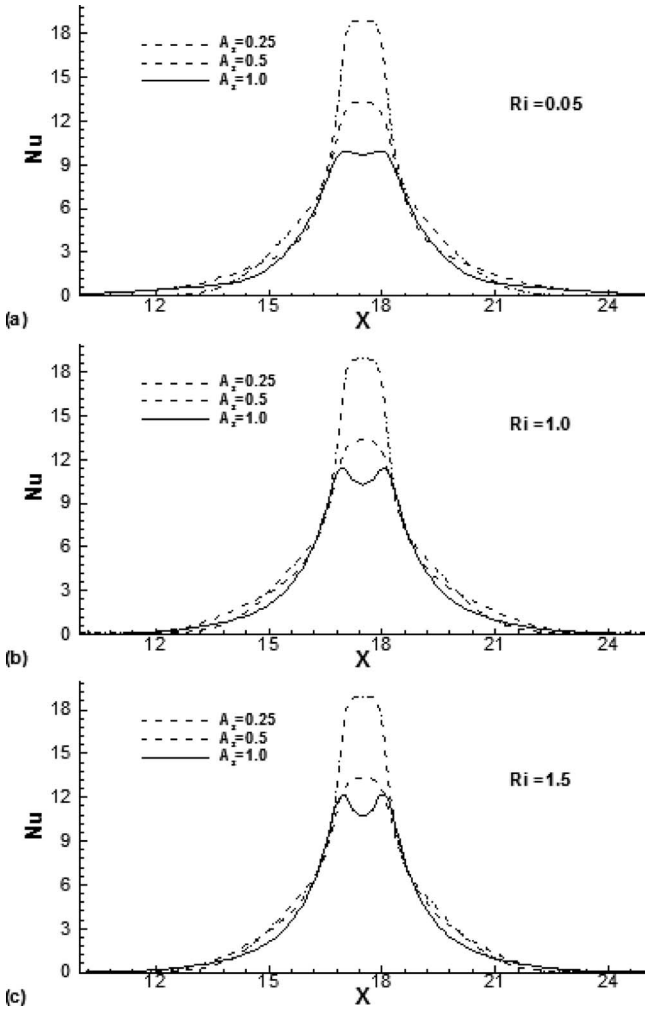

Fig. 11 Effect of jet-to-target spacing on the variation in the local Nusselt number for Richardson numbers of (*a*) Ri=0.05, (*b*) Ri=1.0, and (*c*) Ri=1.5

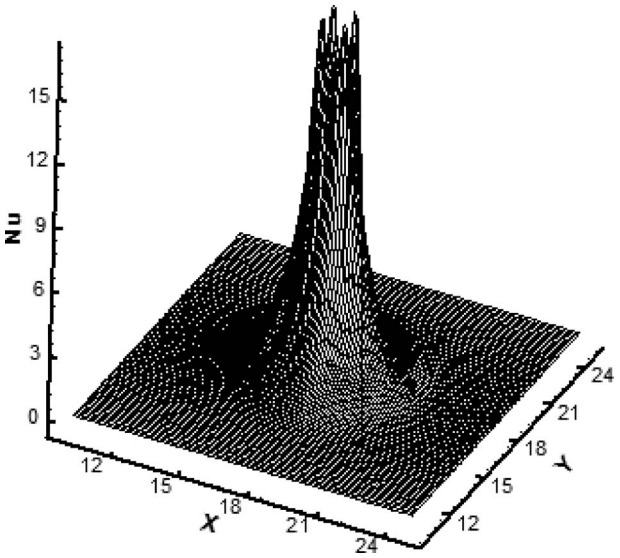

Fig. 12 The three-dimensional plot of the Nusselt number for Re=200, A_z=0.5, and Ri=8

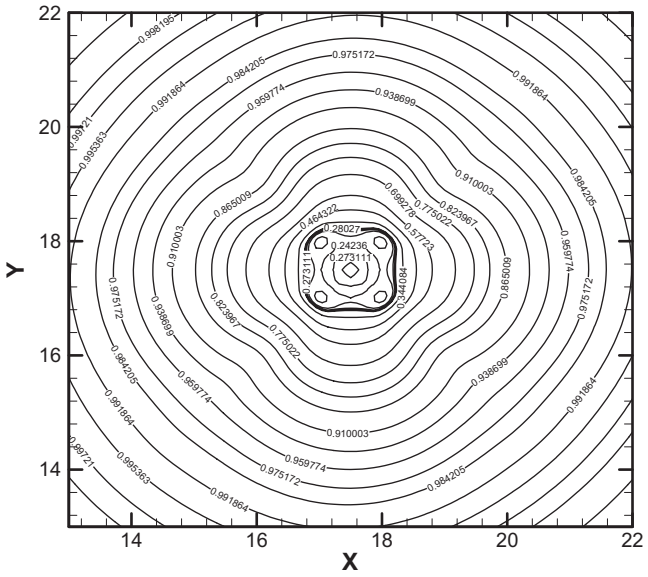

Fig. 13 The contour plots of the temperature distribution for Re=200, A_z=0.5, and Ri=8 on horizontal cross section Z=0.15

hot surface increases with increasing jet exit Reynolds number. In addition, for a given aspect ratio and Reynolds number, the average Nusselt number does not change significantly with the Richardson number, indicating that the buoyancy effects are not very significant in the overall heat transfer process for the range of the Reynolds number considered in their study. The effect of aspect ratios for the same Re and Ri is shown in Fig. 11. In general, the heat transfer increased as the aspect ratio decreased. For low A_z, the heat transfer decreases steeper away from the stagnation point. On the other hand, for high A_z, the heat transfer decreases slightly away from the stagnation point. A carpet plot of the local Nusselt number is shown in Fig. 12 for Re=200, A_z=0.5, and Ri=8. The local Nusselt number has four peaks at the four corners of the jet cross section. The four peaks at the four corners of the jet cross section are illustrated in Fig. 13 through the contour plots of the isotherm on the horizontal cross section at Z=0.15. The temperature is increased in the radial direction away from the jet axis.

5 Conclusions

The three-dimensional numerical simulation is performed to investigate the effect of mixed convection on an impinging laminar single square jet. The results indicate that for small aspect ratios of A_z=0.25 and A_z=0.5 with Ri$\leq$1.0, the structure of the flow is not affected by the Richardson number or even by reducing the Reynolds number for the range of Re used. Moreover, the heat transfer rate is not affected by increasing the Richardson numbers for the same Reynolds number used. The Nusselt number has one single peak at the stagnation point. For the cases of A_z=0.5 with Ri$>$1 and A_z=1.0, the thickness of the wall jet is reduced by increasing the Richardson number for the same Re or by increasing the Reynolds number for the same Ri due to the enlargement of the vortices and elongated away from the jet axis. The Nusselt number increased as the Richardson number increased for the same Re. In addition, the heat transfer rate increased as the jet Reynolds number increased for the same Richardson number. The local Nusselt number has four peaks at the four corners of the jet cross section. In general, the heat transfer increased as the aspect ratio decreased.

References

[1] Gardon, R., and Akfirat, J. C., 1966, "Heat Transfer Characteristics of Impinging Two Dimensional Air Jets," ASME J. Heat Transfer, **88**, pp. 101–108.
[2] Scholtz, M. T., and Trass, O., 1970, "Mass Transfer in a Nonuniform Jet: Part 2. Boundary Layer Flow Mass Transfer," AIChE J., **16**, pp. 90–96.

[3] Chou, Y. J., and Hung, Y. H., 1994, "Impingement Cooling of an Isothermally Heat Surface With a Confined Slot Jet," ASME J. Heat Transfer, **116**, pp. 479–482.
[4] Elison, B., and Webb, B. W., 1994, "Local Heat Transfer to Impinging Liquid Jets in the Initially Laminar, Transitional, and Turbulent Regimes," Int. J. Heat Mass Transfer, **37**, pp. 1207–1216.
[5] Sezai, I., and Mohamad, A. A., 1999, "3-D Simulation of Laminar Rectangular Impinging Jets, Flow Structure and Heat Transfer," ASME J. Heat Transfer, **121**, pp. 50–56.
[6] Sparrow, E. M., and Minkowycz, W. J., 1962, "Buoyancy Effects on Horizontal Boundary-Layer Flow and Heat Transfer," Int. J. Heat Mass Transfer, **5**, pp. 505–511.
[7] Hieber, C. A., 1973, "Mixed Convection Above a Heated Horizontal Surface," Int. J. Heat Mass Transfer, **16**, pp. 769–772.
[8] Yuan, T. D., Liburdy, J. A., and Wang, T., 1988, "Buoyancy Effects on Laminar Impinging Jets," ASME J. Heat Transfer, **10**(31), pp. 2137–2145.
[9] Wang, Y. B., Chaussavoine, C., and Teyssandier, F., 1993, "Two-Dimensional Modeling of a Non-Confined Circular Impinging Jet Reactor-Fluid Dynamics and Heat Transfer," Int. J. Heat Mass Transfer, **36**, pp. 857–873.
[10] Potthast, F., Laschefski, H., and Mitra, N. K., 1994, "Numerical Investigation of Flow Structure and Mixed Convection Heat Transfer of Impinging Radial and Axial Jets," Numer. Heat Transfer, Part A, **26**, pp. 123–140.
[11] Sahoo, D., and Sharif, M. A. R., 2004, "Mixed Convective Cooling of an Isothermal Hot Surface by Confined Slot Jet Impingement," Numer. Heat Transfer, Part A, **45**, pp. 887–909.
[12] Sahoo, D., and Sharif, M. A. R., 2004, "Numerical Modeling of Slot-Jet Impingement Cooling of a Constant Heat Flux Surface Confined by a Parallel Wall," Int. J. Therm. Sci., **43**, pp. 877–887.
[13] Sarghini, F., and Ruocco, G., 2004, "Enhancement and Reversal Heat Transfer by Competing Models in Jet Impingement," Int. J. Heat Mass Transfer, **47**, pp. 1711–1718.
[14] Quinn, W. R., 1990, "Mean Flow and Turbulence Measurements in a Triangular Turbulent Free Jet," Int. J. Heat Fluid Flow, **11**, pp. 220–224.
[15] Wadsworth, D. C., and Mudawar, I., 1990, "Cooling of a Multichip Electronic Module by Means of Confined Two-Dimensional Jets of Liquids," ASME J. Heat Transfer, **112**, pp. 891–898.
[16] Mi, J., Nathan, G. J., and Luxton, R. E., 2000, "Centerline Mixing Characteristics of Jets From Nine Differently Shaped Nozzles," Exp. Fluids, **28**, pp. 93–94.
[17] Leonard, B. P., 1979, "A Stable and Accurate Convective Modeling Procedure Based on Quadratic Upstream Interpolation," Comput. Methods Appl. Mech. Eng., **19**, pp. 59–98.
[18] Leonard, B. P., and Mokhtari, S., 1990, "Beyond First Order Upwinding: The ULTRA-SHARP Alternative for Nonoscillatory Steady-State Simulation of Convection," Int. J. Numer. Methods Eng., **30**, pp. 729–766.
[19] Leonard, B. P., and Drummond, J. E., 1995, "Why You Should Not Use 'Hybrid,' 'Power Law' or Related Exponential Schemes for Convective Modeling. There are Much Better Alternatives," Int. J. Numer. Methods Fluids, **20**, pp. 421–442.
[20] Stone, H. L., 1968, "Iterative Solution of Implicit Approximations of Multi-Dimensional Partial Differential Equations," SIAM (Soc. Ind. Appl. Math.) J. Numer. Anal., **5**, pp. 530–558.
[21] Hackbush, W., 1994, *Iterative Solution of Large Sparse Systems of Equations*, Springer, New York.
[22] Van der Vorst, H. A. V., 1989, "BICGSTAB: A Fast and Smoothly Converging Variant of BI-CG for the Solution of Non-Symmetric Linear Systems," SIAM (Soc. Ind. Appl. Math.) J. Sci. Stat. Comput., **10**, pp. 1174–1185.
[23] Saad, Y., 1996, *Iterative Methods for Sparse Linear Systems*, PSW, Boston.
[24] Van Doormaal, J. P., and Raithby, G. D., 1984, "Enhancements of the SIMPLE Method for Predicting Incompressible Fluid Flows," Numer. Heat Transfer, **7**, pp. 147–163.
[25] Sparrow, E. M., and Wong, T. C., 1975, "Impingement Transfer Coefficients Due to Initially Laminar Slot Jets," Int. J. Heat Mass Transfer, **18**, pp. 597–605.
[26] Aldabbagh, L. B. Y., and Sezai, I., 2004, "Three-Dimensional Numerical Simulation of an Array of Impinging Laminar Square Jets With Spent Fluid Removal," Int. J. Therm. Sci., **43**, pp. 241–247.
[27] Aldabbagh, L. B. Y., and Sezai, I., 2002, "Numerical Simulation of Three-Dimensional Laminar Square Twin-Jet Impingement on a Flat Plate, Flow Structure, and Heat Transfer," Numer. Heat Transfer, **41**, pp. 835–850.
[28] Aldabbagh, L. B. Y., and Sezai, I., 2002, "Numerical Simulation of Three-Dimensional Laminar Multiple Impinging Square Jets," Int. J. Heat Fluid Flow, **23**, pp. 509–518.

Influence of Near Hole Pressure Fluctuation on the Thermal Protection of a Film-Cooled Flat Plate

André Burdet
Gas Turbine Business,
Alstom (Switzerland) Ltd.,
CH-5242 Birr, Switzerland

Reza S. Abhari
Laboratory of Energy Conversion (LEC),
Department of Mechanical and Process Engineering,
Swiss Federal Institute of Technology (ETHZ),
CH-8092 Zürich, Switzerland

The pulsation of film cooling jets in turbines is driven by the near hole pressure fluctuation caused by the deterministic interaction of stator/rotor blade rows. Jet pulsation is characterized by the coolant near hole reduced frequency Ω^c and the pulsation amplitude coefficient Ψ. The fluctuation of the near hole pressure is simulated by setting a time-varying signal of static pressure for the outlet boundary condition of a film-cooled flat plate configuration. It is observed that the fluctuation of the near hole pressure influences the blowing ratio, hence the thermal protection downstream of the injection site. For a low mean blowing ratio ($\overline{BR}=0.75$), low-medium pulsation frequencies ($\Omega^c \leqslant 0.10$) are found to be slightly detrimental to the thermal protection versus a steady injection. On the contrary, for high pulsation frequencies ($\Omega^c \leqslant 0.17$), the thermal protection becomes better due to periodic jet disintegration into the wall surface caused by a higher level of transverse kinetic energy of the jet pulse. In addition, the overlapping of jet pulses appears to help the constant temporal spreading of coolant over the wall surface. For a higher mean blowing ratio ($\overline{BR}=1.25$), jet pulsation enhances lift-off so that the thermal protection is, in general, worse compared to a steady injection. Overall, the range of jet pulsation presented in this study affects moderately the thermal protection of the downstream surface. [DOI: 10.1115/1.2995651]

Keywords: turbine, film, cooling, coolant, jet, pulsation, pulse, fluctuation, pressure, surface, effectiveness, model, computational efficiency, thermal management

1 Introduction

Film cooling technology has successfully been applied for the heat load management of high-pressure gas turbines in the past 40 years. In some cases, more than 25% of engine mass flow can be bypassed from the compressor to the high-pressure turbine parts to be used as a coolant. The need for this low enthalpy air substantially decreases the amount of air mass flow available in the combustor, which results in less useful work per total unit of engine inlet air. Today's state of the art turbine blade cooling technology combines an advanced design of in-blade channel geometries (i.e., internal convection), material coating technology, and external film cooling. In the latter, apart from optimizing the location of the holes as well as their own geometry and the related plenum configuration, taking into account the surrounding flow unsteadiness occurring through the turbine passage with passive or, maybe in the long term, active control may help to decrease the overall coolant mass flow and thereby increase overall plant efficiency.

Different modes of unsteadiness occur in a high-pressure turbine, and they can broadly be classified into two families: deterministic (e.g., blade row interaction) and nondeterministic (e.g., impact of combustor flow). Dunn [1] presented phase-resolved heat flux data obtained in a rotating film-cooled turbine short-duration test facility. He found that at the rotor stagnation point near midspan, the periodic influence of upstream vane injection has a significant influence on the heat flux history. Abhari and Epstein [2] experimentally showed in a representative gas turbine test rig that a large-scale pressure fluctuation on the blade surface, resulting from the passing shock waves and potential interaction, leads to a 12% increase and a 5% decrease in the time-averaged surface heat transfer rate in the suction and pressure sides, respectively, compared to values with no static pressure fluctuations (isolated row). Heidmann et al. [3] experimentally found that the wake passing (or large-scale pressure fluctuation) has an impact on the blade film cooling effectiveness and blade Nusselt number level. In fact, modifications of the flow path of showerhead coolant jets were found as a function of the Strouhal number of flow pulsation. More recently, Haldeman et al. [4,5] reported the measurement of a fully cooled high-work rotating turbine stage operating in representative engine working conditions. Preliminary results (low Reynolds number case) show that the level of near hole static pressure, quantified by a pulsation amplitude coefficient Ψ, substantially varies as a function of blade location, being generally higher on the pressure side surface. As a result, the levels of surface heat flux could significantly differ from an uncooled to a film-cooled turbine configuration, the former being higher at most blade surface locations.

Detailed investigations of the impact of freestream pressure waves over film cooling performance have often been carried out in flat plate configurations. Bons et al. [6] used a loudspeaker to create freestream fluctuations; they observed the degradation of centerline effectiveness versus nonpulsated coolant jets. The research groups of University of Utah and Seoul National University have provided measured data of pulsating jets in a flat plate test section (see Ligrani et al. [7,8], Bell et al. [9], and Seo et al. [10]. A slight deterioration of film cooling protection was found when the pulsation of freestream static pressure is increased to a level where the jet behavior at the hole exit is non-quasisteady. For quasisteady freestream and coolant conditions and long cool-

Contributed by the Heat Transfer Division of ASME for publication in the JOURNAL OF HEAT TRANSFER. Manuscript received February 23, 2008; final manuscript received July 20, 2008; published online January 5, 2009. Review conducted by Frank Cunha. Paper presented at the 2007 ASME-JSME Thermal Engineering Conference and Summer Heat Transfer Conference (HT2007), Vancouver, BC, Canada, July 8–12, 2007.

 Copyright © 2009 by ASME

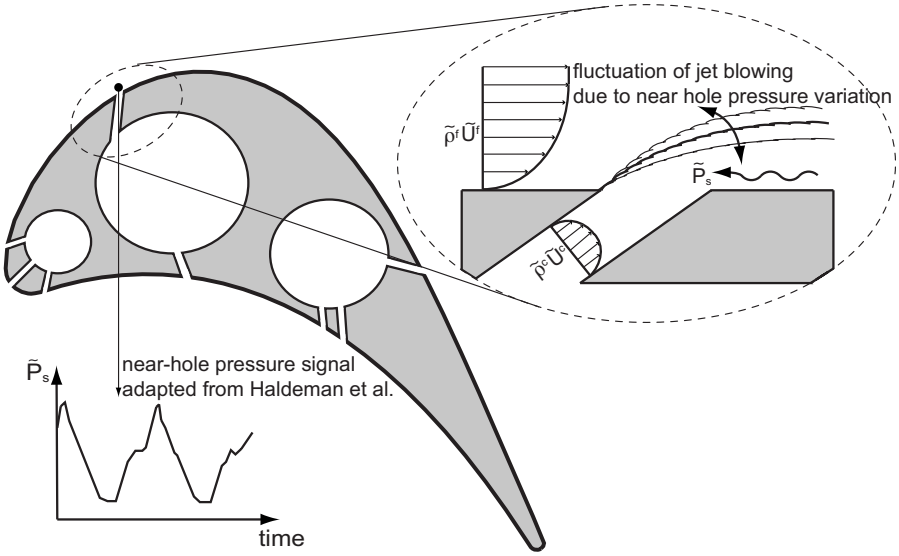

Fig. 1 Concept of large-scale pressure fluctuation in the near hole region. The pressure signal is taken from measurements of Haldeman et al. [15].

ing holes, hardly any difference in film cooling protection can be seen, compared to a steady coolant jet. Meanwhile, only low Mach number ($M^f < 0.04$), low Reynolds number ($\mathrm{Re} < 6800$), and low mean blowing ratio ($\overline{\mathrm{BR}} < 1.0$) flow regimes have been investigated. More recently, a certain number of experiments (see for instance, Coulthard et al. [11,12] were made with a forced pulsing of the jet, as opposed to inducement of pulsing by near hole pressure fluctuation. Nevertheless, it has helped to gain data and understanding of the influence of pulsation frequency and duty cycle on the thermal protection. In general, it was found that pulsation of coolant jet results in a worse thermal protection for low mean blowing ratio ($\overline{\mathrm{BR}} < 1.0$) and small to medium pulsation frequencies. For high frequencies, measurement data tend to show that thermal protection becomes better than steady injection.

The goal of this paper is to numerically investigate the influence of near hole pressure fluctuation on the thermal protection for a flat plate configuration. To proceed, a large range of pulsation frequencies and two mean blowing ratios ($\overline{\mathrm{BR}} = 0.75, 1.25$) are selected. This numerical investigation is carried out using a novel experimentally anchored feature-based jet model developed by Burdet et al. [13–15]. It has previously been validated and used for the prediction of steady film cooling flows in flat plate and turbine configurations. The similarity of the near hole jet flow structure between steady and quasisteady pulsating jets with moderate amplitudes has experimentally been observed by Bernsdorf et al. [16]. Thus, the current jet model can be proposed to be utilized for the prediction of quasisteady pulsating jets. The computational procedure for simulating a pulsating jet typical of film-cooled turbine components is presented. The simulation of near hole pressure fluctuation is explained. The predicted time-averaged effectiveness results are discussed versus a steady injection. Eventually, the investigation of the time accurate three-dimensional flow field downstream of the injection is analyzed to shed light on the time-averaged thermal protection results. This numerical study is carried out with an isotropic, algebraic turbulence model. Indeed, it is argued that the near hole kinetics of the jet pulse is predominant due to the high amplitude of fluctuation, and therefore the bulk impact of jet pulsing can be captured by the present numerical methodology.

2 Characterization of Jet Pulsation

2.1 Large-Scale Pressure Fluctuation in Turbine. A turbine large-scale fluctuation is defined as being an absolute flow fluctuation $\tilde{\phi}$ in which its first harmonic is both dominant and at the frequency level of a deterministic unsteadiness (e.g., blade passing frequency). Any flow quantity ϕ can be decomposed on a large-scale, phase-locked, fluctuation $\tilde{\phi}$ (which contains the mean amplitude $\bar{\phi}$ and its relative large-scale fluctuation $\Delta\phi$) and a small-scale fluctuation ϕ'.

$$\phi = \bar{\phi} + \Delta\phi + \phi' = \tilde{\phi} + \phi' \tag{1}$$

Abhari and Epstein [2] observed that the large-scale fluctuation of pressure $\tilde{P}_s$ at the blade surface modulates the blowing rate of coolant jets and surface heat flux (see Fig. 1). The coolant jet expansion through the hole is mainly driven by the static pressure level P_s at the hole exit [17]. Furthermore, the change in total pressure level in the plenum $\bar{P}_T^c$ for a given hole is generally negligible due to its relatively large volume and also because of a constant feeding rate of the coolant. Experimental [15] and computational studies [17] have shown at midspan section that large-scale pressure fluctuation $\tilde{P}_s$ is large all along the pressure side and substantial in the first half of the suction side. In the second half of the suction side, after the throat, the large-scale pressure fluctuation is negligible. Hence, in most regions of a turbine blade midspan section, one could argue that since large-scale pressure fluctuation is significant, the blowing of the coolant should largely be affected. In turn, substantial change in time mean and instantaneous film cooling protection may result, compared to a steady state regime.

2.2 Range of Coolant Jet Pulsation Frequency. The level of jet pulsating frequency F set by the dominant harmonic of the large-scale pressure fluctuation $\tilde{P}_s$ induces two main time scales in the near hole region. The first time scale is linked to the time required by the coolant fluid to go through the hole. It is quantified by the coolant reduced frequency Ω^c

$$\Omega^c = \frac{F \cdot l^c}{\bar{u}^c} \tag{2}$$

where l^c is the length of the hole. A coolant reduced frequency much below 1.0 means that the film cooling jet has the time to establish in the near hole region in a quasisteady mode. Meanwhile, to reach a quasisteady mode, the dominant harmonic F of large-scale pressure fluctuation should be small enough to drive

(modify) directly the coolant mass flow rate. In fact, if the frequency F is too high, the impact of the variation of the near-hole static pressure may experience an unsteady damping. To deal with this issue, the near hole static pressure reduced frequency Ω^a is introduced based on the speed of sound property,

$$\Omega^a = \frac{F \cdot l^c}{\bar{a}^c} = \bar{M}^c \cdot \Omega^c \tag{3}$$

where $\bar{a}^c$ is the speed of sound based on the coolant flow condition. Abhari and Epstein [2] measured in an engine representative film-cooled test rig that Ω^a can be about 0.06 and must be below 1.0. This demonstrates that the large-scale pressure variation $\tilde{P}_s$ indeed directly modifies the coolant flow rate. In connection to this, Ligrani et al. [7,8] proposed that typical values of Ω^a in operating turbines are in the range of

$$0.02 < \Omega^a < 0.10 \tag{4}$$

Thus, taking into account the existing range of Ω^a and the fact that the mean coolant Mach number can broadly range between $0.1 < \bar{M}^c < 1.0$, the coolant reduced frequency Ω^c should broadly range as follows:

$$0.02 < \Omega^c < 1.00 \tag{5}$$

This eventually leads to a scaling of pulsation frequencies relevant to turbine flows. It is interesting to note that the coolant reduced frequency Ω^c can be around 1.0 in some situations, so that the quasisteady assumption is not valid anymore. But this case should occur only if the coolant Mach number is low. This type of situation may especially happen at the pressure side surface. Also, a low mean coolant Mach number could reflect a very low blowing ratio, so that the flow inside the hole might already be partially or even fully reversed.

2.3 Range of Coolant Jet Pulsation Amplitude

The amplitude of the large-scale pressure fluctuation $\tilde{P}_s$ drives the magnitude of the coolant jet blowing, quantified by the pulsation amplitude coefficient Ψ [2],

$$\Psi = \frac{\tilde{P}_{s,\max} - \tilde{P}_{s,\min}}{P_T^c - \bar{P}_s} \tag{6}$$

Haldeman et al. [5] proposed that the difference in maximum and minimum instantaneous large-scale pressure fluctuations ($\tilde{P}_{s,\max}$ and $\tilde{P}_{s,\min}$) should be taken as the envelope size of all harmonic fluctuations. This pulsation amplitude coefficient Ψ can dramatically vary as a function of the location where it is observed at the blade surface. Abhari [17] calculated that in a standard industrial gas turbine rotor blade, the coefficient Ψ can vary from 0.0 up to 3.0 around the blade surface. Haldeman et al. [15] experimentally observed that Ψ can even be higher than 3.0 in some particular locations. In general, Ψ has a large value ($\Psi > 0.2$) in most regions of the pressure side and at least in the first half of the suction side.

3 Feature-Based Jet Model

3.1 Jet Model Numerical Integration. The near hole jet model is numerically immersed in the computational mesh with the use of the implicit immersed boundary method (IBM) [13]. The jet model actually delivers local boundary conditions to be fed to the computational domain. Thus, these local boundary conditions are specified at the surface of the near hole jet body, as shown in Fig. 2. The model is integrated as a separate module in the computational fluid dynamics (CFD) code. The model proceeds only in a three-dimensional grid box that is automatically extracted from the computational domain before starting the iterative procedure. This grid box contains computational cells that are located in the near hole region only.

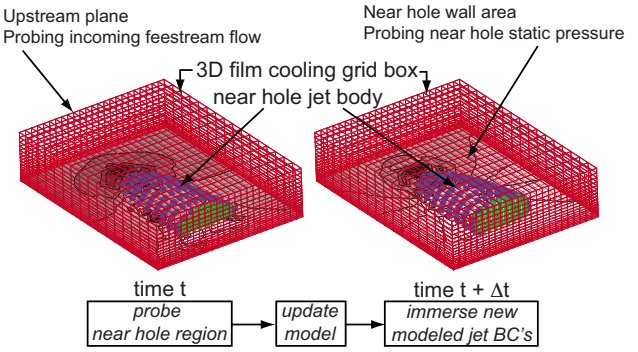

Fig. 2 Near hole jet model embedded in its three-dimensional film cooling grid box at time t (left) and later at time $t+\Delta t$ (right). Dots show the plane of injection and the jet surface. The flat plate surface area is covered by predicted contours of static pressure.

A comprehensive Reynolds-averaged Navier-Stokes (RANS)-based modeling of the near hole macroflow features, such as the jet trajectory and penetration, the counter-rotating vortex pair (CVP) as well as mixing, and the near wall wake region, is available for a broad range of turbine working conditions. The model coefficients are calibrated with a set of near hole experimental data [18] and vary as a function of the instantaneous near hole flow conditions. This high-resolution model is specified at the plane of injection (see Fig. 2). At the surface of the near hole jet, low level modeling, in the form of Dirichlet and von Neumann boundary conditions, is imposed so that a relevant representation of the near hole jet flow physics is simulated. This jet surface can be viewed as the location of the thin coolant to freestream mixing limit in the near hole region. In the current modeling, slip and isothermal coolant boundary conditions are immersed. Indeed, vorticity cannot be created at the sides of the jet, and an averaged coolant to freestream mixing temperature is assumed at the jet surface. The numerical immersion of the three-dimensional jet body allows simulating the blockage of the freestream flow. Thus, the near hole pressure field is realistically computed [14]. This is of primary importance since the near hole pressure $\tilde{P}_s$ modulates the blowing of the coolant.

3.2 Derivation of the Instantaneous Blowing Ratio. The experimentally anchored model coefficients do vary as a function of the instantaneous value of the blowing ratio $\widetilde{\mathrm{BR}}$. Furthermore, the blowing ratio level is based on the instantaneous near hole flow conditions. The instantaneous blowing ratio $\widetilde{\mathrm{BR}}$ is therefore given by

$$\widetilde{\mathrm{BR}} = \frac{\tilde{\rho}^c \tilde{u}^c}{\tilde{\rho}^f \tilde{u}^f} \quad \text{where } \tilde{\rho}^c \tilde{u}^c = \frac{4 \tilde{C}_d \tilde{m}_{\text{ideal}}}{\pi d^2}$$

$$\tilde{m}_{\text{ideal}} = P_T^c \left(\frac{\tilde{P}_s}{P_T^c} \right)^{(\gamma+1)/2\gamma} \sqrt{\left[\frac{2\gamma}{(\gamma-1) R_g T_T^c} \right] \left[\left(\frac{P_T^c}{\tilde{P}_s} \right)^{(\gamma-1)/\gamma} - 1 \right]} \tag{7}$$

where P_T^c and T_T^c are the coolant total pressure and temperature, respectively. They are assumed to stay constant in time so that they are input values for the numerical study. $\tilde{C}_d$ is the instantaneous discharge coefficient. Its numerical value is a function of the near hole pressure $\tilde{P}_s$ and the coolant plenum total pressure P_T^c. It is found by using the correlation experimentally derived by Gritsch et al. [19]. The near hole fluctuating freestream density $\tilde{\rho}^f$ and velocity $\tilde{u}^f$, as well as the near hole fluctuating static pressure

$\tilde{P}_s$, are probed in the computational domain, at a selected plane location, and at selected time steps before the jet model is updated. These numerically probed values are fed back to Eq. (7) to derive the instantaneous blowing ratio $\widetilde{\mathrm{BR}}$, eventually setting the numerical values of the model coefficients.

3.3 Computational Requirements. One of the major requirements used for the jet model is that it must behave in a quasisteady mode. To meet the quasisteady requirement, the near hole pressure reduced frequency Ω^a, as well as the coolant reduced frequency Ω^c, must be small enough, i.e., $\Omega^a < 1.0$ and $\Omega^c < 1.0$. Furthermore, on the one hand, a time criterion Δt_{upd} is required for the proper use of the jet model in such unsteady flow. This is to ensure that between two updates of the jet model, the elapsed time Δt_{upd} is bigger than the time Δt_{jet} for a fluid particle to travel in the near hole jet body. On the other hand, the time Δt_{upd} between two jet model updates should be small enough in comparison with half the dominant fluctuation time scale Δt_{per} in order to really simulate the jet movement. These computational requirements can be summarized as follows:

$$\begin{matrix}\Delta t_{\mathrm{upd}} > \Delta t_{\mathrm{jet}} \\ \Delta t_{\mathrm{upd}} < \Delta t_{\mathrm{per}}\end{matrix} \quad \text{where} \begin{cases} \Delta t_{\mathrm{upd}} = \dfrac{1}{N_{\mathrm{upd}} F} \\ \Delta t_{\mathrm{jet}} \cong \dfrac{d}{2\bar{u}^c} \\ \Delta t_{\mathrm{per}} = \dfrac{1}{2F} \end{cases} \tag{8}$$

Here N_{upd} is the number of updates of the jet model per fluctuation period. Hence, this is the value that is ultimately controlled by the user to ensure the fulfillment of the computational requirements given by Eq. (8).

4 Flow Investigation Procedure

4.1 Flat Plate Configuration and Flow Conditions. The film-cooled flat plate test case of Bernsdorf et al. [18] is selected for the current flow investigation. Unfortunately, no flat plate surface measurement data are available for this investigation yet. Meanwhile, previous extensive blind validations [13–15] of the predictive capability of the jet model in a steady environment give confidence about its utilization for the numerical simulation of quasisteady jet pulsation. The round hole diameter is $d=5$ mm, the streamwise injection angle is $\alpha_0=30$ deg, the lateral injection angle is $\beta_0=0$ deg, the flat plate length is 41 d, the hole-to-hole pitch distance is 4 d, and the hole length is 4 d. The freestream boundary layer momentum thickness is 0.051 d and the shape factor is 2.3.

The computational domain covers one hole-to-hole pitch distance and uses a periodic boundary condition at both sides. To gain computational efficiency, a slip boundary condition is specified a five hole diameter above the flat plate surface. Subsonic inlet and outlet boundary conditions are imposed where the inlet stagnation freestream pressure is $P_T^f=1.0$ bar, the inlet stagnation temperature is $T_T^f=390$ K, the inlet flow angle is strictly in the streamwise direction, and the outlet static pressure is specified such as $\bar{M}^f=0.3$ for the uncooled solution. On the flat plate surface no slip and wall adiabatic boundary conditions are specified. One density ratio ($\overline{\mathrm{DR}}=1.3$), combined with two mean blowing ratios ($\overline{\mathrm{BR}}=0.75, 1.25$), is investigated as a function of different freestream static pressure fluctuations. The coolant plenum condition is fixed to $T_T^c=300$ K and $P_T^c=0.922$ bar and 0.966 bar for $\overline{\mathrm{BR}}=0.75$ and 1.25, respectively.

4.2 Computational Methodology. The in-house RANS-based CFD code used in this investigation, MULTI3, uses a time-marching algorithm with a finite volume approach. Time discretization is based on the central vertex Ni–Lax–Wendroff second order accurate scheme. The eddy viscosity is computed using the algebraic, isotropic turbulence model Baldwin–Lomax in its low Reynolds number form. Although it is recognized that coolant jets contain significant turbulence intensity, anisotropy, and variation in the near wall Prandtl number [20], the main goal of this study is to investigate the influence of the near hole kinetics (momentum) of quasisteady jet pulsing over the global thermal protection. Previous validations of the jet model for a steady injection using Baldwin–Lomax [13–15] have shown that the predicted of laterally averaged effectiveness and Nusselt number are in good agreement with measurement data (except very near the hole for high blowing ratios) although the lateral spreading is underpredicted. The computational mesh is made of one hexahedral block with $165 \times 33 \times 53 = 288{,}585$ grid nodes in total. The first grid node above the wall is placed so that the wall stretched distance is $Y^+ \approx 1$ at this location. The grid discretization gives $N_x=5$ grid nodes per hole diameter in the axial direction and $N_y=9$ grid nodes in the lateral direction. This grid discretization has previously been shown to be optimal in terms of computational efficiency versus computational accuracy [13].

4.3 Modeling of Freestream Static Pressure Fluctuation. A fluctuating static pressure $\tilde{P}_s$ signal is introduced in the calculation in order to simulate large-scale pressure fluctuation. For this purpose, variation in time of the outlet static pressure $\tilde{P}_s^{\mathrm{out}}$ is specified as the outlet boundary condition,

$$\tilde{P}_s^{\mathrm{out}}(t) = \bar{P}_s - \Delta P_s \sin\left[\left(\frac{\pi}{2}\right) \cdot \min\left(\frac{5}{2}, 1 + 16 \cdot \mathrm{DC} \cdot F \cdot t\right)\right] \tag{9}$$

where ΔP_s is half the targeted maximum pressure amplitude fluctuation relative to the mean static pressure $\bar{P}_s$. Equation (9) is valid for $0 < t < 1/F$. DC represents the duty cycle, which is fixed to DC=0.5 in this study. The goal here is to reveal the impact of the coolant reduced frequency and the mean blowing ratio level on the surface thermal protection. With DC=0.5, the periodic passage of the wakelike signal as measured in turbine test rigs (see, for instance, Haldeman et al. [5]) can well be reproduced (see also Fig. 3).

4.4 Flow Cases Investigated and Computational Performance. The different flow cases investigated are tabulated in Table 1. It appears that, except for the two highest frequency cases ($F=1600$ Hz, 3200 Hz), all computational requirements given by Eq. (8) are fulfilled. For the two highest frequency cases, the time Δt_{upd} between two jet model updates is the same as for the time for a particle to convect inside the jet body for $\overline{\mathrm{BR}}=1.25$. This means that the handling of the near hole jet body is at the limit of its quasisteady assumption while still valid. For a low mean blowing ratio, time Δt_{upd} is too low so that a discrepancy in the modeled near hole mixing due to unsteady mixing may be present in the simulation. In addition, we note that the pulsation amplitude Ψ increases with the pulsation frequency, except for the $F=1600$ Hz case. In this case, the pulsation amplitude locally reduces. An analysis of the data has shown that at this frequency the interaction of spurious pressure waves, generated at the inlet and outlet computational domain boundaries, smooth down the fluctuation of pressure near the hole.

The computational overhead σ due to the utilization of the jet model has been calculated for all test cases. The computational overhead σ scales the temporal overhead to iterate once the CFD algorithm when using the jet model versus the simulation of the uncooled flat plate for the same grid. The envelope of the computational overhead has been found to be equal to $\sigma=4.2\%$, showing the high computational efficiency of the jet model for performing unsteady jet injection simulations. In addition, the mesh is very simple (one hexahedral block) so that the preprocessing time is largely decreased compared to the so-called complex approach,

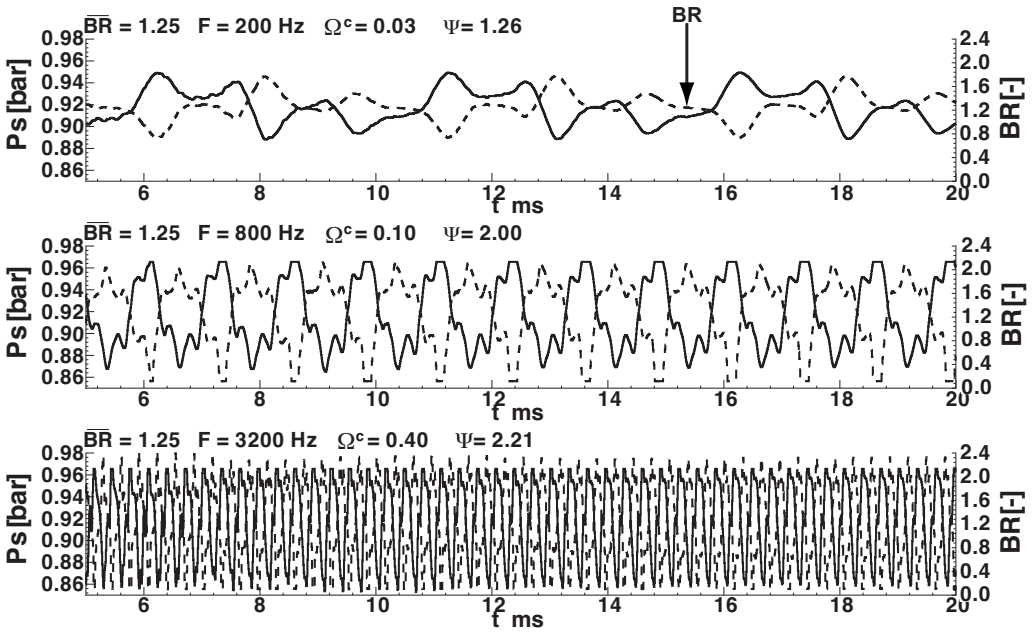

Fig. 3 Recorded near hole pressure P_s from the numerical solution and related instantaneous blowing ratio $\widetilde{BR}$ as a function of time for $\overline{BR}=1.25$

where the hole and plenum chambers are gridded. In connection to this fact, the size of the grid is also lower than that in the complex approach.

5 Near Hole Pressure Signal and Related Blowing Ratio

The recorded near hole pressure signal $\widetilde{P}_s$ obtained from the numerical solution for flow cases with pulsation frequencies of $F=[200\ \text{Hz}, 800\ \text{Hz}, 3200\ \text{Hz}]$ is plotted in Fig. 3 for $\overline{BR}=1.25$. It is superimposed with the instantaneous blowing ratio signal $\widetilde{BR}$ computed using Eq. (7). The instantaneous blowing ratio is directly used for the jet model update. The recorded pressure signal and the related blowing ratio signal for the $\overline{BR}=0.75$ case are very similar, except that the blowing ratio varies from 0.4 to 1.0. Near hole pressure signals recorded for the other frequency cases are similar to those plotted in Fig. 3. It appears that the fluctuations of the near hole pressure and instantaneous blowing ratio are relatively similar. Furthermore, the fluctuation of the probed freestream flow properties is not large enough to have a major impact on the instantaneous blowing ratio; the freestream boundary layer is established over the whole plate length so that it is less sensitive to the fluctuation of the near hole static pressure than the coolant. It is also observed that the pressure signal recorded in the near hole region does not exhibit the same amplitude for all investigated test cases. In fact, the influence of the finite computational domain length and the treatment of the boundary conditions could lead to an addition-destruction process of pressure waves as a function of the pulsation frequency. This is especially true for the $F=1600$ Hz case. Nevertheless, the range of amplitude obtained $(1.26<\Psi<2.53)$ is in good agreement with turbine flow conditions.

6 Time-Averaged Film Cooling Effectiveness

The predicted time-averaged laterally averaged wall adiabatic film cooling effectiveness $\bar{\eta}$ is plotted in Fig. 4 for the two mean blowing ratios investigated as well as for all pulsation frequencies. In addition, predicted $\bar{\eta}$ for steady injection is also plotted for comparison. It is observed in Fig. 4 that for all prediction results, there are two zones of different rates of decrease in $\bar{\eta}$ as a function of the axial distance x/d. Indeed, for axial positions x/d

Table 1 Summary of flow cases investigated and related time scales to fulfill the computational requirements of the jet model utilization

BR	F (Hz)	200	400	800	1600	3200
0.75	Ω^c	0.04	0.08	0.17	0.33	0.67
	Ψ	1.50	1.66	2.09	1.43	2.53
	N_{per}	120	60	30	30	15
	Δt_{jet}	3.7×10^{-5}	3.7×10^{-5}	3.7×10^{-5}	3.7×10^{-5}	3.7×10^{-5}
	Δt_{upd}	4.2×10^{-5}	4.2×10^{-5}	4.2×10^{-5}	2.1×10^{-5}	2.1×10^{-5}
	Δt_{per}	2.5×10^{-3}	1.3×10^{-3}	6.3×10^{-4}	3.1×10^{-4}	1.6×10^{-4}
1.25	Ω^c	0.03	0.05	0.10	0.20	0.40
	Ψ	1.26	1.35	2.00	1.33	2.21
	N_{per}	120	60	30	30	15
	Δt_{jet}	2.2×10^{-5}	2.2×10^{-5}	2.2×10^{-5}	2.2×10^{-5}	2.2×10^{-5}
	Δt_{upd}	4.2×10^{-5}	4.2×10^{-5}	4.2×10^{-5}	2.1×10^{-5}	2.1×10^{-5}
	Δt_{per}	2.5×10^{-3}	1.3×10^{-3}	6.3×10^{-4}	3.1×10^{-4}	1.6×10^{-4}

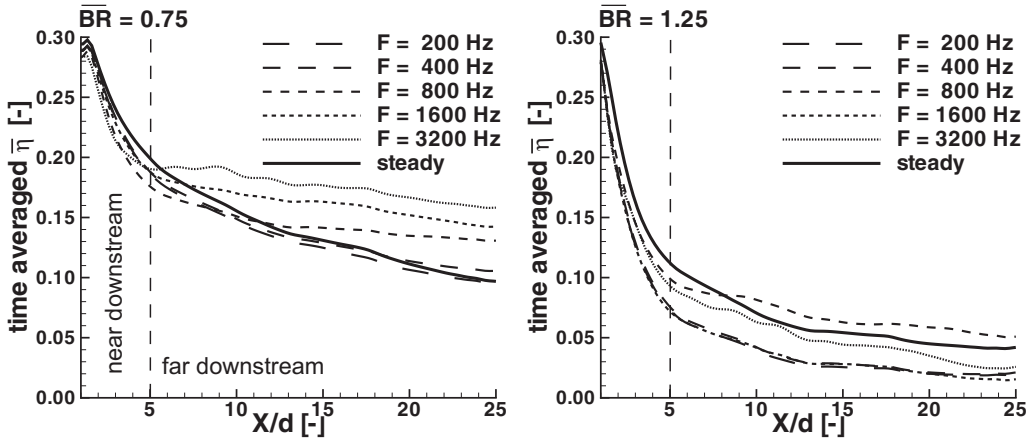

Fig. 4 Predicted time-averaged laterally averaged wall adiabatic film cooling effectiveness for all pulsation frequencies investigated. $\overline{BR}$=0.75 (left) and $\overline{BR}$=1.25 (right).

$\leqslant$5.0, the rates of decrease in $\bar{\eta}$ are higher than those further downstream and are very similar for all frequencies for a given blowing ratio. A previous experimental validation of the jet model [13] has already confirmed this flow feature; the influence of the counter-rotating vortex pair and jet penetration is dominant in the near hole downstream region but rapidly decays so that when the far downstream region is reached, mainly diffusion, combined with coolant absolute mass flux level, dominates. These experimental validations have shown that the prediction of $\bar{\eta}$ in the near downstream region is very good for the low blowing ratio case ($\overline{BR}<1.0$) but, in general, too high for the high blowing ratio case ($\overline{BR}>1.0$). Meanwhile, for high blowing ratio cases, the predicted values of $\bar{\eta}$ obtained in the far downstream region are generally in good agreement with measurement data.

Focusing next on prediction results with the low mean blowing ratio case ($\overline{BR}$=0.75) in Fig. 4 (left), it appears that the axial evolution of cooling effectiveness exhibits a different behavior between low frequencies ($\Omega^c \leqslant 0.08$ or $F \leqslant 400$ Hz) and high frequencies. In low frequency cases, the rate of decrease of $\bar{\eta}$ is very similar to the steady prediction although it exhibits a slightly gentler slope ($\Delta\bar{\eta} \cong -0.01$). For the high frequency cases ($\Omega^c \geqslant 0.17$ or $F \geqslant 800$ Hz), the rate of decrease of $\bar{\eta}$ is lower than that for the steady prediction in the far downstream region. In addition, the

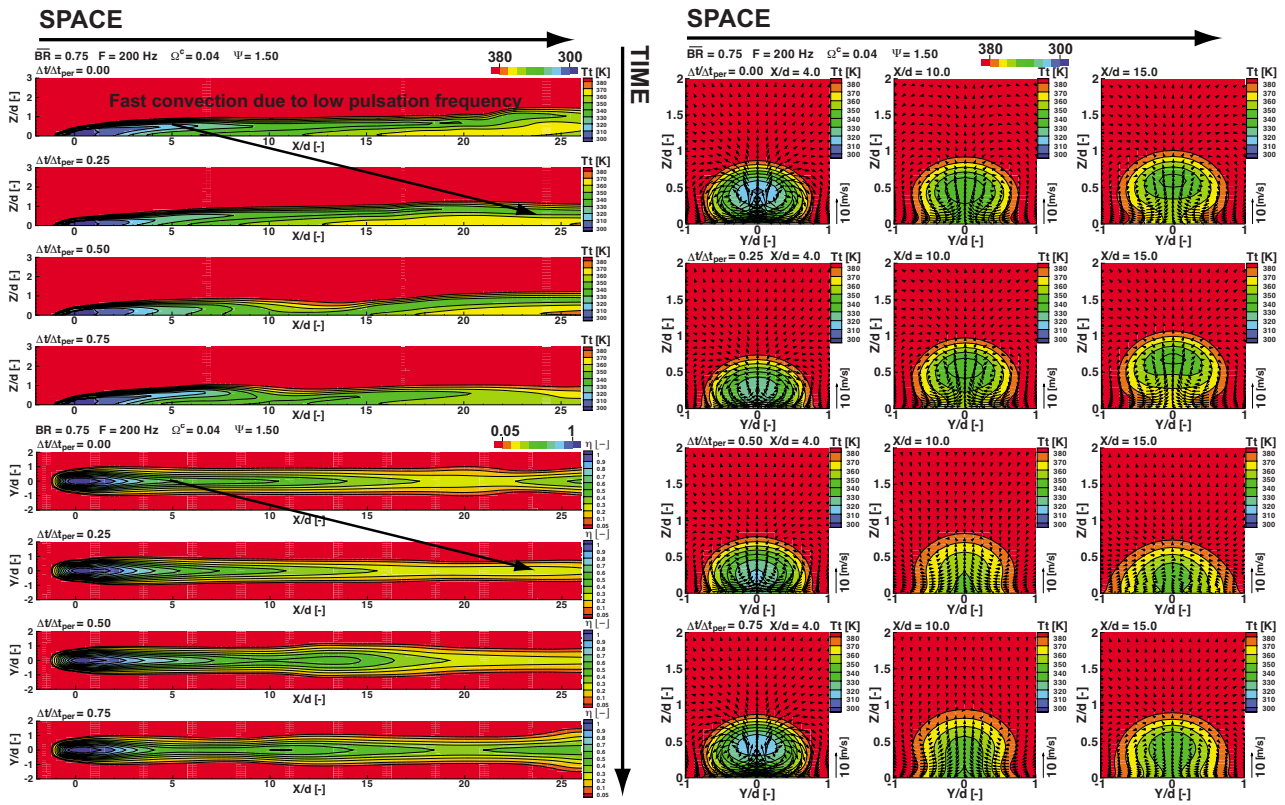

Fig. 5 Space-time diagram of the predicted total temperature T_T contours on the center plane y/d=0 (top left) on three cross planes x/d=[4,10,15] (right, with cross velocity vectors) and the predicted effectiveness η on the flat plate z/d=0 (bottom left) for four equally spaced time steps. $\overline{BR}$=0.75 and Ω^c=0.04 (F=200 Hz).

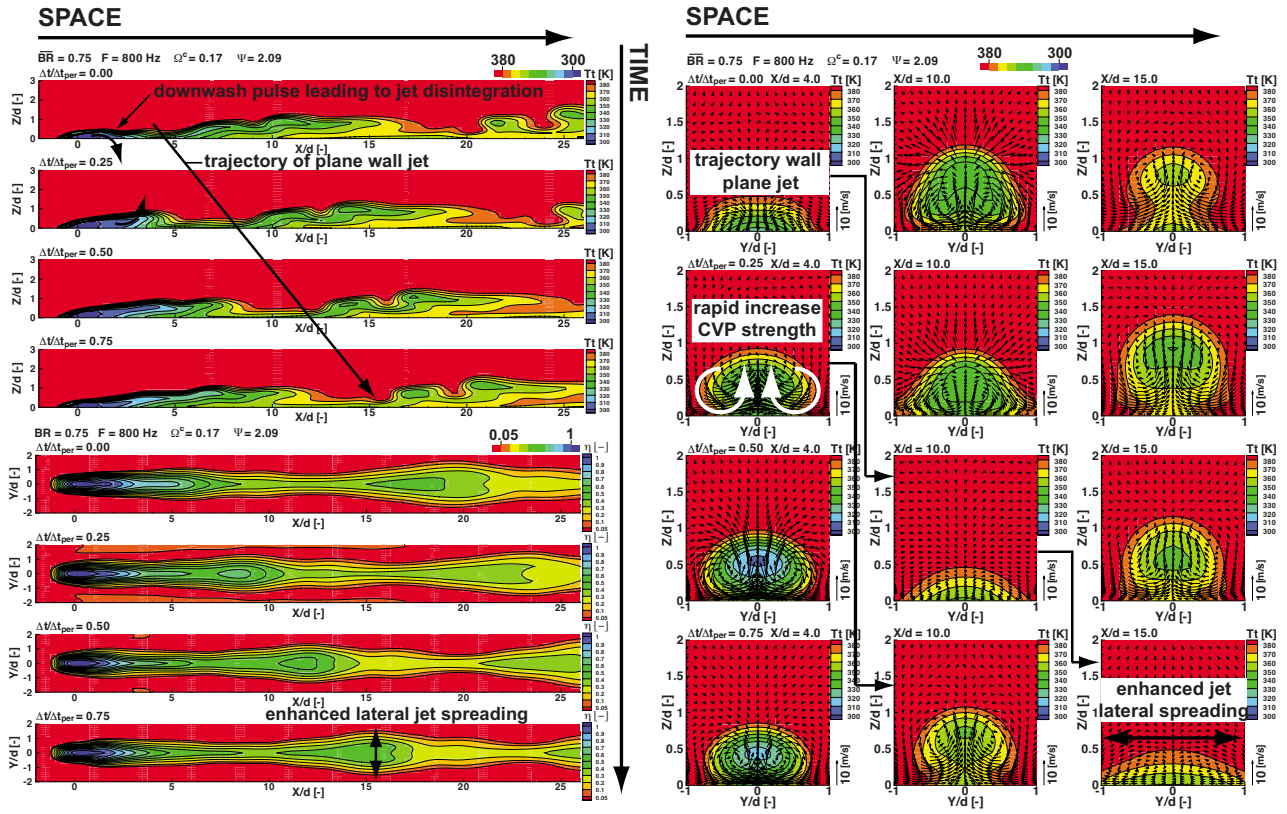

Fig. 6 Space-time diagram of the predicted total temperature T_T contours on the center plane $y/d=0$ (top left) on three cross planes $x/d=[4,10,15]$ (right, with cross velocity vectors) and the predicted effectiveness η on the flat plate $z/d=0$ (bottom left) for four equally spaced time steps. $\overline{BR}=0.75$ and $\Omega^c=0.17$ ($F=800$ Hz).

breaking point from the near hole and far hole downstream regions migrates upstream as a function of the frequency and gets sharper. Interestingly, the relative decrease of the pulsation amplitude Ψ for the F=1600 Hz case does not affect the trend. As a conclusion, for a mean low blowing ratio, low frequency pulsation ($\Omega^c \leqslant 0.08$) leads to a slightly lower cooling effectiveness than steady injection although the rate of decrease of $\bar{\eta}$ is very similar. High frequency pulsation ($\Omega^c \geqslant 0.17$) leads to a better time-averaged surface coverage due to a slower rate of decrease in $\bar{\eta}$. In particular, for these high pulsation frequencies, the switch from the near hole flow physics to the far hole flow physics is sharper. Note here that the measurement data of Coulthard et al. [11,12] have also shown that for a low mean blowing ratio ($\overline{BR}<1.0$), low to medium pulsation frequencies for the same coolant reduced frequency worsen the cooling effectiveness compared to steady injection. On the contrary, high pulsation frequencies appear to reverse this trend.

The prediction results for the high mean blowing ratio case ($\overline{BR}=1.25$, Fig. 4 (right)) appear to be somewhat different from those obtained with the low mean blowing ratio case. Indeed, the predicted axial evolution of $\bar{\eta}$ level for the steady injection case is found to be higher than all the pulsation cases, except for the medium pulsation frequency case ($\Omega^c=0.10$ or $F=800$ Hz). Here it appears, in contrast to the low mean ratio case, that the relative low pulsation amplitude Ψ in the $F=1600$ Hz case also participates in the overall decrease in cooling effectiveness $\bar{\eta}$. In addition, the rate of decay of the $\bar{\eta}$ level is similar for all injection cases. In fact, it appears that the increase of the mean blowing ratio level damps the positive influence of the frequency pulsation for spreading the coolant all over the surface.

7 Time Accurate Thermal Field

In order to better understand the influence of jet pulsation frequency and mean blowing ratio over the surface coolant effectiveness, a time accurate analysis of the predicted thermal field downstream of the injection site is carried out using a space-time diagram approach. The predicted total temperature T_T contours on the center plane ($y/d=0.0$), the predicted wall adiabatic film cooling effectiveness η on the flat plate surface ($z/d=0.0$), and the predicted total temperature contours with secondary flow vectors on three cross planes ($x/d=[4,10,15]$) for four equally spaced time steps are plotted in Figs. 5–10 for the two mean blowing ratios investigated and for pulsation frequencies $F=200$ Hz (Figs. 5 and 8), $F=800$ Hz (Figs. 6 and 9), and $F=3200$ Hz (Figs. 7 and 10).

7.1 Low Mean Blowing Ratio. The analysis of the thermal field for the low mean blowing ratio case ($\overline{BR}=0.75$) is carried out first. It is observed that for the lowest pulsation frequency case ($\Omega^c=0.03$ or $F=200$ Hz and $\Psi=1.50$) in Fig. 5, the coolant jet acts similarly to steady jet blowing. Since the pulsation frequency is relatively small, the convection of the fluid particle between two consequently plotted time steps (25% of the overall pulsation period) is fast and covers an axial distance of about $x/d \cong 19$. Unsteady mixing perpendicular to the streamwise direction is therefore unlikely to be significant. Hence, coolant protection is very similar to steady injection.

For the medium-high pulsation frequency case ($\Omega^c=0.17$ or $F=800$ Hz and $\Psi=2.09$) in Fig. 6, the thermal field gets more complicated. Firstly, the convection of the coolant jet covers an axial distance of only about $x/d=5.5$ for 25% of the pulsation period.

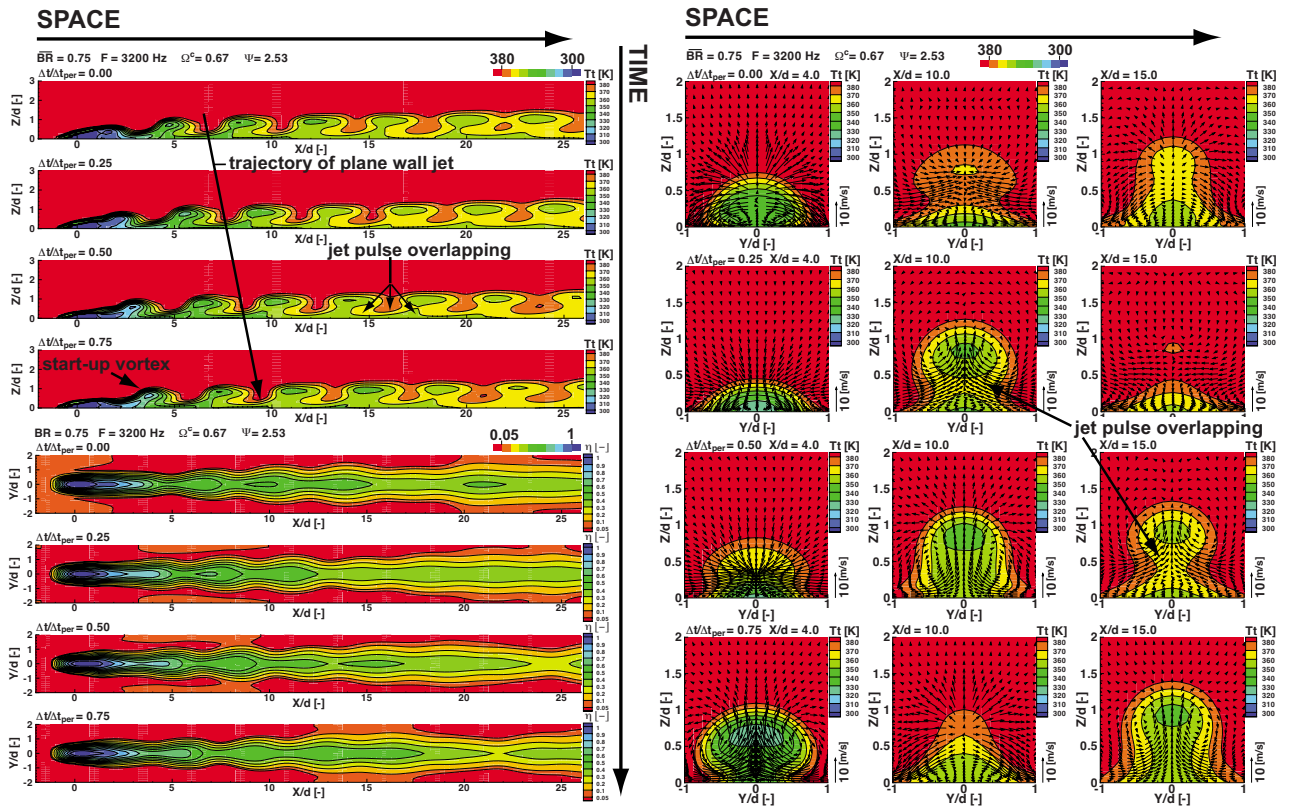

Fig. 7 Space-time diagram of the predicted total temperature T_T contours on center plane $y/d=0$ (top left) on three cross planes $x/d=[4,10,15]$ (right, with cross velocity vectors) and the predicted effectiveness η on the flat plate $z/d=0$ (bottom left) for four equally spaced time steps. $\bar{BR}=0.75$ and $\Omega^c=0.67$ ($F=3200$ Hz).

The fact that the pulsation period decreases compared to the previous case ($\Omega^c=0.03$) means that the kinetic energy of the vertical motion of the jet increases relatively to the kinetic energy in the streamwise direction. In this context, at the instant of a low blowing ratio amplitude (see, for instance, time step $\Delta t/\Delta t_{per}=0.00$), the downwash motion of the jet pulse provokes the disintegration of the jet structure because it hits the wall surface. As a result, it can be seen on different cross planes ($x/d=4$ for $\Delta t/\Delta t_{per}=0.00$, $x/d=10$ for $\Delta t/\Delta t_{per}=0.50$, and $x/d=15$ for $\Delta t/\Delta t_{per}=0.75$), the jet transforms to a wall plane jet that laterally spreads the coolant material all over the hole-to-hole pitch distance. Consequently, during the collapse of the jet structure on the flat plate surface, the CVP structure disappears. The sudden absence of the CVP structure is actually beneficial for the cooling of the surface since the entrainment of the hot freestream fluid underneath the jet is stopped. This new feature (jet disintegration) can explain the reduction of the slope of $\bar{\eta}$ observed in Fig. 4. Meanwhile, the counterbalancing effect of this jet disintegration comes shortly later in time. The blowing ratio increases again, and, helped by the upward momentum of the jet pulse, the jet structure quickly reshapes so that the strength of the CVP becomes even stronger than the one observed for steady injection (not shown here). It appears, however, that the jet does not lift off so that the coolant material always stays attached to the surface.

In the highest pulsation frequency case ($\Omega^c=0.67$ or $F=3200$ Hz and $\Psi=2.53$) in Fig. 7, the same phenomenon of repeating cycles of coolant jet structure disintegration near the wall surface and a sudden increase in the strength of the counter-rotating vortex pair is observed. In addition, a starting vortex is clearly identified when the rapid upward motion of the jet occurs. Meanwhile, in this case, it is noted that the increase in the pulsation frequency enables a continuous higher level of effectiveness all along the flat plate compared to the former jet pulsation case analyzed. In connection to this, the lateral spreading of the coolant appears to be periodically enhanced, as for the former pulsation case, but with closer repeating occurrences. Furthermore, by close inspection of cross plane prediction (Fig. 7 (right)), it appears that the rapid succession of jet pulses provokes an overlapping of the successive jet disintegration on the wall surface. Indeed, when the jet is lifting off again, there is still a trace of coolant coming from the previous wall plane jet (see, for instance, plot $x/d=10$ and $\Delta t/\Delta t_{per}=0.25$ or plot $x/d=15$ and $\Delta t/\Delta t_{per}=0.50$). Hence, this can explain why cooling effectiveness is better with the highest pulsation frequencies compared to a steady injection, as observed in Fig. 4 (left); the combination of overlapping of jet pulses attached to the wall and jet disintegration is beneficial.

7.2 High Mean Blowing Ratio. As it has been found in Fig. 4 (right), the influence of the pulsation frequency is more complicated for a higher mean blowing ratio. In order to deal with this issue, the thermal field evolution of the pulsating coolant jet at a low frequency ($\Omega^c=0.03$ or $F=200$ Hz and $\Psi=1.26$) is first analyzed in Fig. 8. As opposed to the low mean blowing ratio case, it is observed here that the coolant jet periodically detaches from the flat plate surface when the jet pulsing is near its blowing peak. Hence, periodically, cooling of the flat plate surface does not occur at all, which yields a significant detrimental impact on the overall time-averaged cooling of the surface. Furthermore, at some instants (see, for instance, cross plane $x/d=10,15$ and $\Delta t/\Delta t_{per}=0.25$), the coolant jet structure clearly breaks into two symmetrical cores of highest concentration of the coolant material. This is the mark of an enhanced strength of the CVP caused by the momentaneous high blowing. The identification of the periodic coolant jet detachment without the corresponding jet disintegration in the opposed phase explains the degradation of the time-averaged coolant protection as found in Fig. 4.

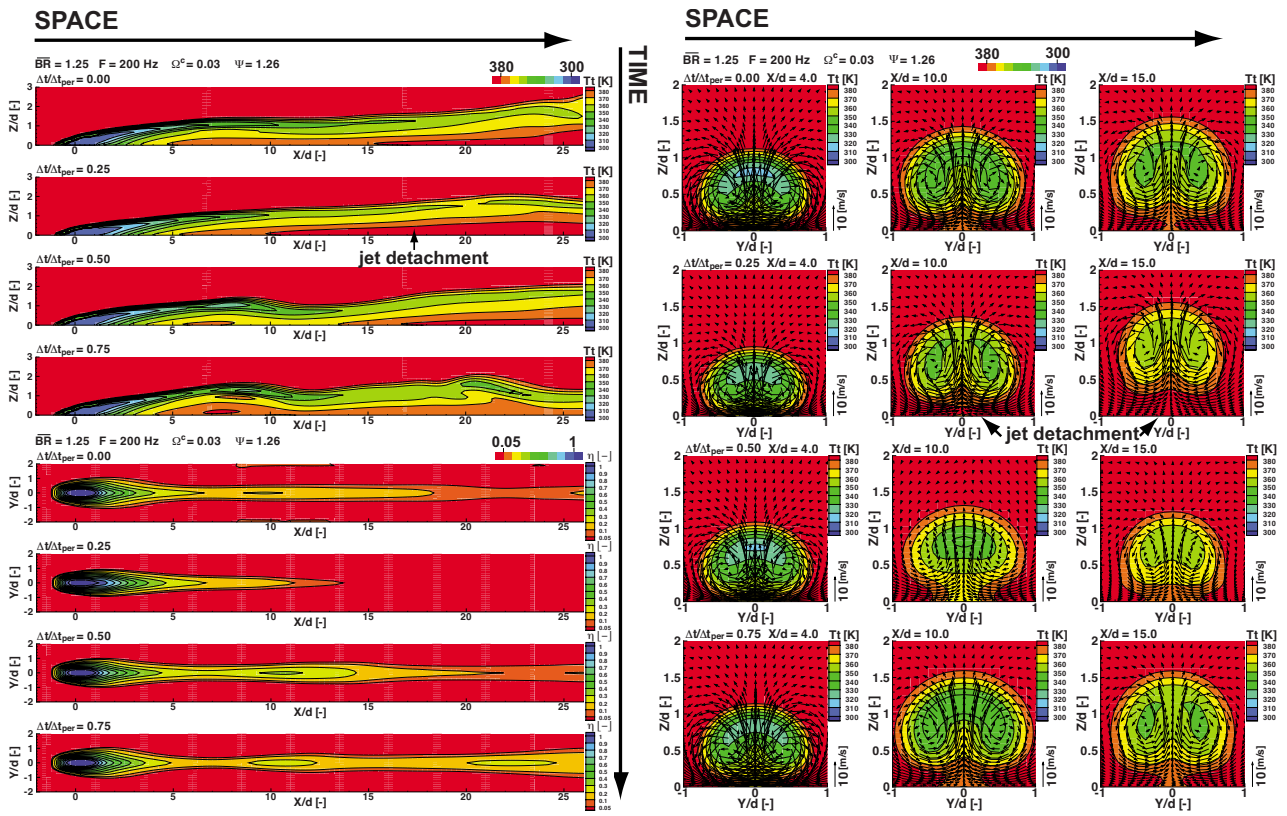

Fig. 8 Space-time diagram of the predicted total temperature T_T contours on the center plane $y/d=0$ (top left) on three cross planes $x/d=[4,10,15]$ (right, with cross velocity vectors) and the predicted effectiveness η on the flat plate $z/d=0$ (bottom left) for four equally spaced time steps. $\overline{BR}=1.25$ and $\Omega^c=0.03$ ($F=200$ Hz).

The prediction results for the medium-high frequency case ($\Omega^c=0.10$ or $F=800$ Hz and $\Psi=2.00$) shown in Fig. 9 also exhibit a complex flow structure. In observing the thermal field in the center plane in Fig. 9 (top left), at time $\Delta t/\Delta t_{per}=0.00$, the jet high momentum downwash is expected to make the jet collapsing into the flat plate surface, as it has been observed with the corresponding low mean blowing case. However, the fact that in this case the mean blowing ratio is higher leads to damp this effect; there is effectively a lateral spreading of the near wall coolant material (see, for instance, cross plane $x/d=4$ at time $\Delta t/\Delta t_{per}=0.00$), but the usual coolant jet structure remains. As a consequence, although the CVP does not disappear, the near wall region periodically experiences a weak wall plane jet, with its enhanced lateral spreading. This can be visualized in the cross plane $x/d=10$ at time $\Delta t/\Delta t_{per}=0.50$ and in the evolution of the contours of η on the flat plate surface. When the jet pulse cycle is close to maximal blowing, the jet completely detaches from the flat plate surface. This phenomenon can be observed at all cross planes. The instantaneous impact on the film cooling effectiveness is obviously its decay down to a negligible value. As a conclusion, the blended effect of the beneficial mild jet disintegration and the periodical jet detachment from the surface explains the slightly better performance of cooling relative to steady injection.

In the highest pulsation frequency case ($\Omega^c=0.40$ or $F=3200$ Hz and $\Psi=2.21$) in Fig. 10, the coolant jet appears to have vortical structures that periodically detach from the flat plate surface. The overlapping jet pulse effect, previously observed in the correspondingly low mean blowing ratio case, does also exist here. However, in this case, the trajectory of the local temperature minima is now detached from the wall. This means that although the beneficial aspect of jet pulse overlapping is observed, the spatial position of the generated temperature minima is not optimally located, i.e., it does not lie on the flat plate surface. This can clearly be observed in center plane plots as well as in cross plane plots, for instance, at $x/d=15$ and at time $\Delta t/\Delta t_{per}=0.50$. Thus, although the overlapping of the coolant jet pulse helps increasing cooling the effectiveness, it is not sufficiently high in this case to counterbalance the periodic high upwash motion (i.e., lift-off) of the jet. In addition, the observation of results for the slightly lower pulsation frequency case ($\Omega^c=0.20$ or $F=1600$ Hz and $\Psi=1.33$)—not shown here—has shown that the jet pulse overlapping is not yet fully established and, because of the smaller pulsation amplitude relative to the highest pulsation frequency case, the mild jet disintegration is not established. Hence, this can explain why $\bar{\eta}$ is particularly low for this case (see Fig. 4).

8 Conclusion

A parametric study of pulsing film cooling jets applicable to turbine flow has been carried out, thanks to the use of an experimentally anchored feature-based jet model. Using this jet model, preprocessing time to mesh the injection hole and plenum is alleviated. The processing time is also kept to a minimum value since the grid does not contain the hole and plenum. The computational overhead when using the jet model is only 4.2% compared to an uncooled prediction. The prediction results lead to the following conclusions.

- The fluctuation of the near hole static pressure as it occurs in turbines provokes a significant pulsation of the coolant jet so that the downstream thermal field is modified compared to a steady injection.
- For a low mean blowing ratio ($\overline{BR}=0.75$) and relatively low pulsation frequencies ($\Omega^c<0.08$), the time-averaged cooling effectiveness is slightly lower than that for steady injec-

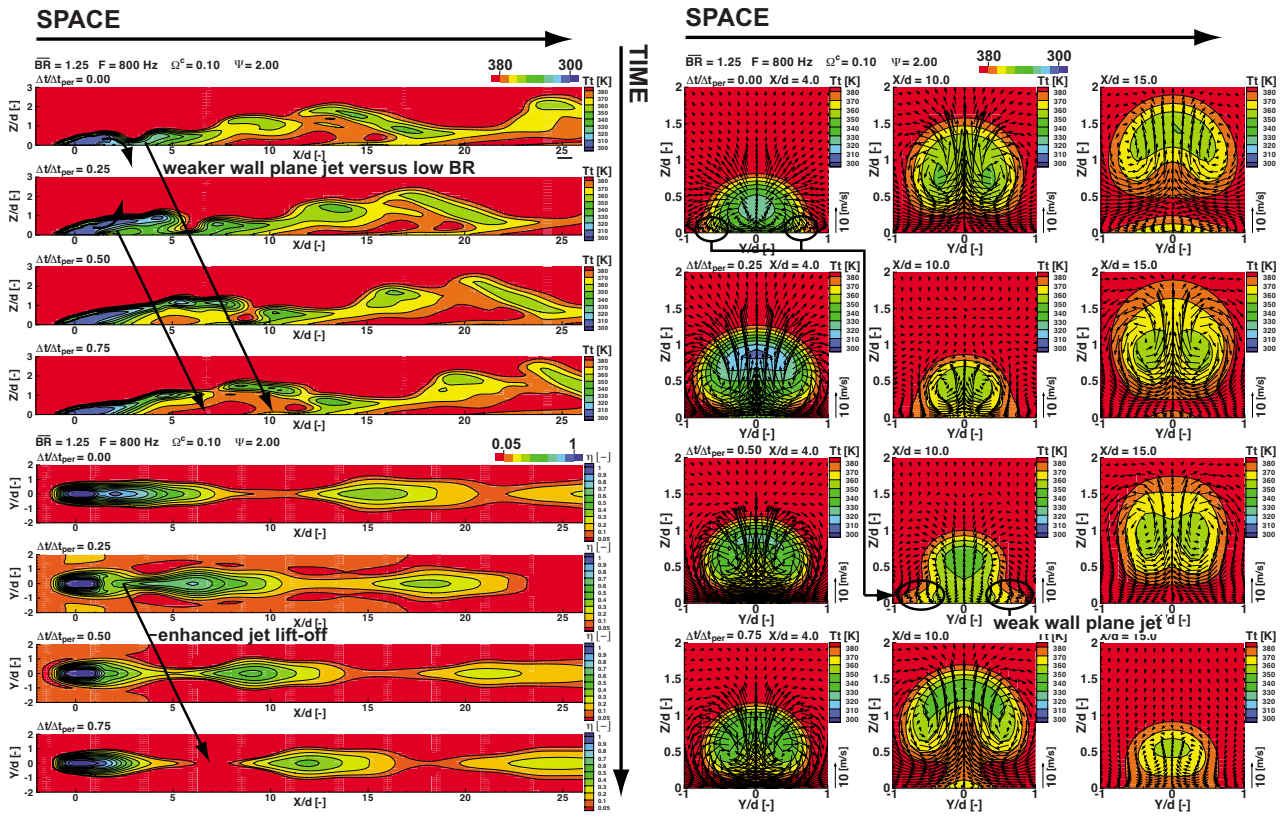

Fig. 9 Space-time diagram of the predicted total temperature T_T contours on the center plane $y/d=0$ (top left) on three cross planes $x/d=[4,10,15]$ (right, with cross velocity vectors) and the predicted effectiveness η on the flat plate $z/d=0$ (bottom left) for four equally spaced time steps. $\bar{BR}=1.25$ and $\Omega^c=0.10$ ($F=800$ Hz).

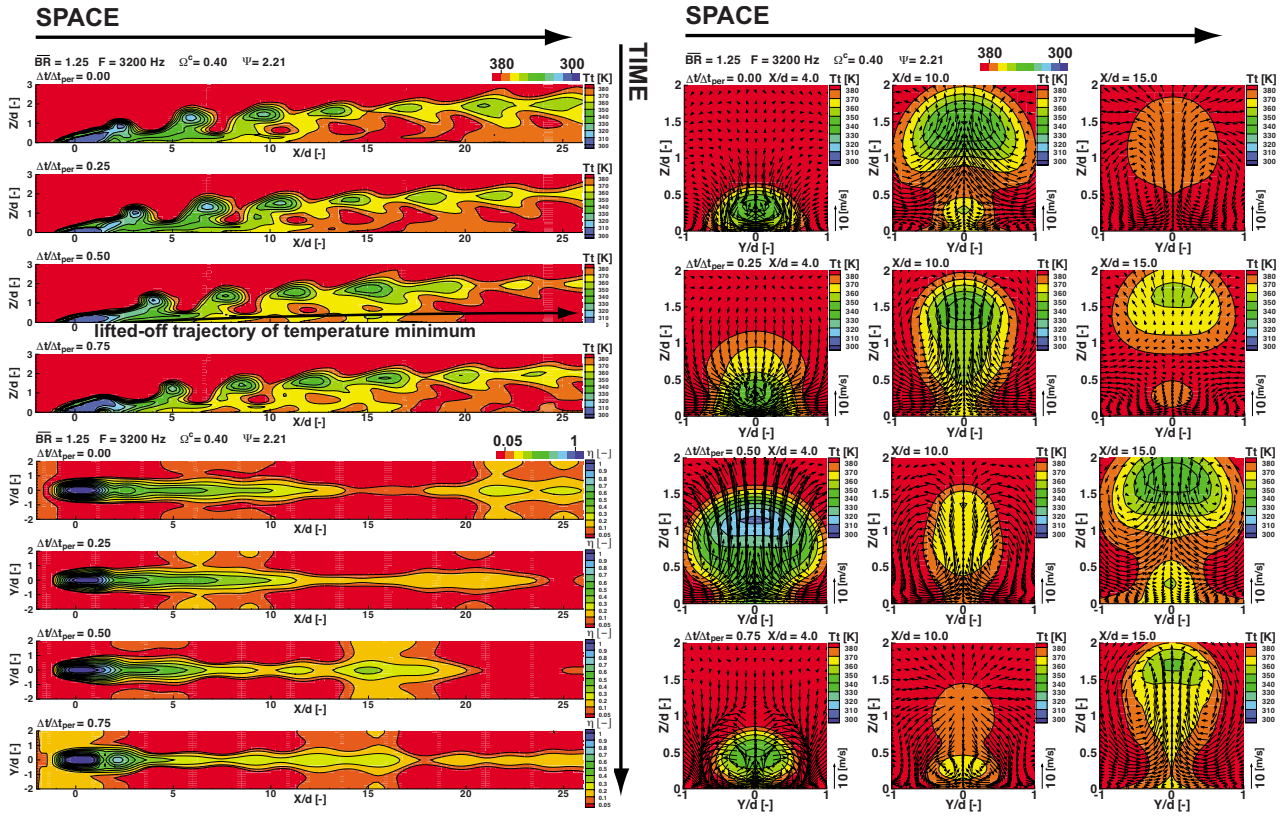

Fig. 10 Space-time diagram of the predicted total temperature T_T contours on the center plane $y/d=0$ (top left) on three cross planes $x/d=[4,10,15]$ (right, with cross velocity vectors) and the predicted effectiveness η on the flat plate $z/d=0$ (bottom left) for four equally spaced time steps. $\bar{BR}=1.25$ and $\Omega^c=0.40$ ($F=3200$ Hz).

tion and follows a similar axial evolution downstream of the injection site.

- For a low mean blowing ratio ($\overline{BR}=0.75$) and high near hole static pressure fluctuation ($\Omega^c>0.17$), the time averaged cooling effectiveness appears to be better than that for steady injection. This is due to periodic coolant jet disintegration after the injection site yielding a wall plane jet and also, for very high fluctuation ($\Omega^c=0.67$), an overlapping of the jet pulses after the injection. In addition, jet pulsation amplitude variation of the order of $1.43<\Psi<2.53$ appears not to have a significant influence on the cooling effectiveness.
- For a medium-high mean blowing ratio ($\overline{BR}=1.25$), the jet lift-off, compared to steady injection, is constantly enhanced for all frequencies. Furthermore, although the overlapping of jet pulses also occurs at high pulsation frequencies, it is detached from the surface and therefore does not optimally participate in the increase in cooling effectiveness. Hence, steady injection leads, in general, to a better coverage of coolant downstream of the hole compared with induced pulsed injection. At this mean blowing ratio level, the amplitude of the jet pulsation appears also to influence the action of the coolant onto the surface to be thermally protected.
- Overall, the near hole pressure fluctuation, typical of a film-cooled turbine flow, has a moderate impact on the thermal protection of the downstream surface.

Current limitations of the jet model, such as impact of near hole unsteady mixing and turbulence on the precise far hole thermal diffusion, are currently being addressed. Developments of the current jet model to be able to cope with unsteady multistage film-cooled turbine flows using higher-level anisotropic turbulence models are to be carried out. Furthermore, modifications of the mixing model to be imposed at the sides of the near hole jet body caused by flow unsteadiness are being developed. Eventually, companion surface and three-dimensional flow field experimental data are requested to confirm these numerical predictions.

Acknowledgment

The authors would like to acknowledge the support of the jet model development project by GE Aviation through their university strategic alliance program. The first author thanks the permission of Alstom (Switzerland) Ltd. to publish this paper.

Nomenclature

ϕ = flow quantity
x,y,z = axial, lateral, and vertical (spanwise) coordinates
u = absolute velocity magnitude
ρ = density
P = pressure
T = temperature
M = Mach number
d = hole diameter
l = geometrical feature length
$\alpha_0\beta_0$ = streamwise and lateral injection angles
DR = density ratio $=\rho^c/u^f$
BR = blowing ratio $=\rho^c u^c/\rho^f u^f$
$\dot{m}$ = mass flow
C_d = discharge coefficient
F = dominant harmonic (pulsating frequency)
R_g = gas constant for air $=287$ J/kg K
Ω = reduced frequency
Ψ = pulsation amplitude coefficient
γ = specific heat ratio for air $=1.4$
Δt = time interval
η = wall adiabatic film cooling effectiveness $=(T_{\text{recovery}}-T_{\text{adiabatic wall}})/(T_{\text{recovery}}-T_T^c)$
N_{upd} = number of jet model update per period

Subscripts/Superscripts

T = total
s = static
c = coolant fluid
f = freestream fluid
upd = between two model updates
per = half the fluctuation period
jet = travel in the near hole jet

References

[1] Dunn, M. G., 1990, "Phase and Time Resolved Measurements on the Blade of a Full Scale Rotating Turbine," ASME J. Turbomach., **112**(3), pp. 531–538.
[2] Abhari, R. S., and Epstein, A. H., 1994, "An Experimental Study of Film Cooling in a Rotating Transonic Turbine," ASME J. Turbomach., **116**(1), pp. 63–70.
[3] Heidmann, J. D., Lucci, B. L., and Reshotko, E., 1997, "An Experimental Study of the Effect of Wake Passing on Turbine Blade Film Cooling," ASME J. Turbomach., **123**(2), pp. 214–221.
[4] Haldeman, C. W., Mathison, R. M., Dunn, M. G., Southworth, S., Harral, J. W., and Heitland, G., 2006, "Aerodynamic and Heat Flux Measurements in a Single Stage Fully Cooled Turbine—Part I: Experimental Approach," ASME J. Turbomach., **130**(2), p. 021015.
[5] Haldeman, C. W., Mathison, R. M., Dunn, M. G., Southworth, S., Harral, J. W., and Heitland, G., 2006, "Aerodynamic and Heat Flux Measurements in a Single Stage Fully Cooled Turbine—Part II: Experimental Results," ASME J. Turbomach., **130**(2), p. 021016.
[6] Bons, J. P., Rivir, R. B., MacArthur, C. D., and Pestian, D. J., 1995, "The Effects of Unsteadiness on Film Cooling Effectiveness," *Proceedings of the 33rd AIAA Aerospace Sciences Meeting*, Reno, NV, Paper No. AIAA 95-0306.
[7] Ligrani, P. M., Gong, R., Cuthrell, J. M., and Lee, J. S., 1996, "Bulk Flow Pulsations and Film Cooling—I. Injectant Behavior," Int. J. Heat Mass Transfer, **39**(11), pp. 2271–2282.
[8] Ligrani, P. M., Gong, R., Cuthrell, J. M., and Lee, J. S., 1996, "Bulk Flow Pulsations and Film Cooling—II. Flow Structure and Film Effectiveness," Int. J. Heat Mass Transfer, **39**(11), pp. 2283–2292.
[9] Bell, C. M., Ligrani, P. M., Hull, W. A., and Norton, C. M., 1999, "Film Cooling Subject to Bulk Flow Pulsations: Effects of Blowing Ratio, Freestream Velocity, and Pulsation Frequency," Int. J. Heat Mass Transfer, **42**, pp. 4333–4344.
[10] Seo, H. J., Lee, J. S., and Ligrani, P. M., 1998, "The Effect of Injection Hole Length on Film Cooling With Bulk Flow Pulsations," Int. J. Heat Mass Transfer, **41**, pp. 3515–3528.
[11] Coulthard, S. M., Volino, R. J., and Flack, K. A., 2006, "Effect of Jet Pulsing on Film Cooling, Part 1: Effectiveness and Flowfield Temperature Results," ASME J. Turbomach., **129**(2), pp. 232–246.
[12] Coulthard, S. M., Volino, R. J., and Flack, K. A., 2006, "Effect of Jet Pulsing on Film Cooling, Part 2: Heat Transfer Results," ASME J. Turbomach., **129**(2), pp. 247–257.
[13] Burdet, A., 2005, "A Computationally Efficient Feature-Based Jet Model for Prediction of Film-Cooling Flows," Ph.D. thesis, ETH-Zürich, Switzerland.
[14] Burdet, A., Abhari, R. S., and Rose, M. G., 2007, "Modeling of Film Cooling—Part II: Model for Use in 3D CFD," ASME J. Turbomach., **129**(2), pp. 221–231.
[15] Burdet, A., and Abhari, R. S., 2007, "3D Flow Prediction and Improvement of Holes Arrangement of a Film-Cooled Turbine Blade Using a Feature-Based Jet Model." ASME J. Turbomach., **129**(2), pp. 258–268.
[16] Bernsdorf, S., Rose, M. G., and Abhari, R. S., 2008, "Experimental Validation of Quasi-Steady Assumption in Modeling of Unsteady Flow," ASME J. Turbomach., **130**(1), pp. 141–149.
[17] Abhari, R. S., 1996, "Impact of Rotor-Stator Interaction on Turbine Blade Film Cooling," ASME J. Turbomach., **118**(1), pp. 123–133.
[18] Bernsdorf, S., Rose, M. G., and Abhari, R. S., 2006, "Modeling of Film Cooling—Part I: Experimental Study of Flow Structure," ASME J. Turbomach., **128**(1), pp. 141–159.
[19] Gritsch, M., Schulz, A., and Wittig, S., 1998, "Method for Correlating Discharge Coefficients of Film-Cooling Holes," AIAA J., **36**(6), pp. 976–980.
[20] Kohli, A., and Bogard, D. G., 2005, "Turbulent Transport in Film Cooling Flows," ASME J. Heat Transfer, **127**(5), pp. 513–520.

Thermal Transport Characteristics of Mixed Pressure and Electro-Osmotically Driven Flow in Micro- and Nanochannels With Joule Heating

Chien-Hsin Chen
Department of Mechanical Design Engineering,
National Formosa University,
Huwei, Yunlin 632, Taiwan
e-mail: chchen@nfu.edu.tw

This study investigates convective transport phenomena of combined electro-osmotic and pressure-driven flow in a microchannel subject to constant surface heat flux, with Joule heating effect taken into account. The governing system of equations includes the electric potential field, flow field, and energy equations. Analytical solutions are obtained for constant fluid properties, while numerical solutions are presented for variable fluid properties. For constant properties, the problem is found to be governed by three ratios: the length scale ratio (the ratio of Debye length to half channel height), the velocity scale ratio (the ratio of pressure-driven velocity to electro-osmotic velocity), and the ratio of Joule heating to surface heat flux. A small length scale ratio corresponds to a microchannel, while finite length scale ratio represents a nanochannel. For electro-osmotic flow only, the momentum transport is solely a function of the length scale ratio. For combined electro-osmotic and pressure-driven flow, the velocity profile and therefore the friction factor depend on both the length scale ratio and the velocity scale ratio. Assuming a thermally fully developed flow, analytical expressions for the normalized temperature profile and Nusselt number are developed. The representative results for the friction factor, normalized temperature profile, and Nusselt number are illustrated for some typical values of the three ratios. For purely electro-osmotic flow, it is found that the Nusselt number increases with decreasing ε, approaching the value for slug flow as the length scale ratio approaches zero. For mixed flow with a given length scale ratio, the results show that the Nusselt number decreases with the velocity scale ratio, approaching the classical Poiseuille flow as the velocity scale ratio approaches infinite. When the effects of variable fluid properties are included in the analysis, numerical solutions are generated to explore the influence of thermal conductivity and viscosity variations with local temperature on the hydrodynamic and thermal characteristics of the fluid. These temperature-dependent property variations would initially develop pressure-driven flow, and correspondingly the dimensionless velocity and volume flow rate increase to account for such variations. The friction factor reduces considerably with viscosity variation, while the Nusselt number increases gently. Although the influence of thermal conductivity variation on the hydrodynamic characteristics is not impressive, it has certain impact on the heat transfer results; more specifically, increasing the conductivity variation will produce a sensible increase in Nusselt number but a small decrease in the normalized temperature. [DOI: 10.1115/1.2994720]

Keywords: electro-osmosis, microfluidics, convection heat transfer, Joule heating

1 Introduction

Transport phenomena in microchannels have recently found importance in a wide variety of practical applications, ranging from the cooling of electronic devices [1–4] to biological analysis and analytical chemistry [5–8]. Fluid delivery is crucial in the microfluidic systems because of the small size of these devices, and hence the pumping method needed for microdevices is quite different from that of macroscale devices. To meet the pumping requirements of these microdevices, various techniques have been proposed for fluid pumping, such as electrostatic [9], piezoelectric [10], electrohydrodynamic [11], magnetohydrodynamic [12], and electro-osmotic [13–15] pumping. Among them, the electro-osmotic micropump has been favored due to its many advantages over other types of micropumps. Electro-osmotic pumps need no moving parts and have much simpler design and easier fabrication. It is applicable to a wide range of conductivity of fluids, which is essential for biomedical applications. Also, precise flow control can be achieved easily by controlling the external electric field. Electro-osmosis (first discovered by Reuss in 1809 from an experimental study on porous clay diaphragms) refers to liquid flow induced by an applied external electric field along electrostatically charged surfaces, and therefore the electro-osmotic flow (EOF) is quite different from the traditional pressure-driven flow. In a steady-state flow field, the velocity profile of the pressure-driven flow assumes a parabolic shape in the fully developed region. In an electro-osmotically driven flow, an externally electric field is applied to produce a body force that then drives fluid motion. The physics of this unique mechanism has been described

Contributed by the Heat Transfer Division of ASME for publication in the JOURNAL OF HEAT TRANSFER. Manuscript received December 4, 2007; final manuscript received August 18, 2008; published online December 15, 2008. Review conducted by Satish G. Kandlikar.

 Copyright © 2009 by ASME

in detail in the literature (see, for example, Ref. [16]). The electro-osmotic flow velocity profile depends on the ratio of the Debye length to the characteristic length of the microchannel, where the Debye length characterizes the thickness of the electric double layer (EDL). When the Debye length is much smaller than the channel length scale, the velocity profile is nearly uniform (characterized by slug flow). On the other hand, the Debye length is of the same order as the channel characteristic length, while the velocity profile is practically like that of classical pressure-driven flow. Electro-osmotic flow has been used extensively in microdevices to move packets of fluid. Many applications involve either chemical separation, heterogeneous or homogeneous chemical reactions, and/or heating/cooling cycles, and some may involve combinations of forced (pressure-driven) and electro-osmotic flow. The flow rate induced by electro-osmitic force is usually small, and therefore even a small pressure gradient applied along a microchannel may cause velocity distributions and corresponding flow rates that deviate from the pure electro-osmotic flow. The pressure gradient may stem from several reasons, such as the presence of alternative pumping mechanism, placement of mechanical valve in the flow path, and the existence of variations in the wall zeta potential [17]. When electro-osmotic and traditional pressure forces are present simultaneously, the resulting velocity profile is a superposition of the electro-osmotic and pressure-driven flows [16]. It is noted that the pressure gradient may be either adverse or favorable to the electro-osmotic flow, depending on the relative signs of the potential gradient and applied pressure gradient. Since the velocity distributions of combined pressure and electro-osmotically driven flow are much different from either purely electro-osmotic flow or traditional pressure-driven flow, the thermal behavior may also be quite different.

To date, relatively less attention has been paid to the thermal behavior associated with the mixed pressure and electro-osmotically driven flow. An analysis for fully developed thermal transport was carried out by Maynes and Webb [18] for combined pressure and electro-osmotically driven flow in a circular microtube. They presented analytical results for the for fully developed Nusselt number. They also investigated the effect of viscous dissipation effect on the heat transfer of purely electro-osmotic flow in microchannels [19] and reported that viscous dissipation effect is only important at low values of the relative duct radius, and thus concluded that the influence of viscous dissipation is negligible for most practical electro-osmotic flow applications. Very recently, Das and Chakraborty [20] presented analytical solutions for the transport characteristics of a non-Newtonian power-law fluid through a parallel-plate microchannel. As an illustrative case study, they analyzed the flow behavior of a blood sample. In the present work, we deal with the problem of convective heat transfer for mixed electro-osmotic and pressure-driven flow in a microchannel subject to constant surface heat flux. The governing system of equations consists of the electric potential field, flow field, and energy equations. We first perform an analysis under the assumption of constant fluid properties (as made in the previous studies) to develop analytical expressions for velocity and temperature profiles, friction factor, and the fully developed Nusselt number. It should be noted that constant fluid properties can be justified only when the temperature change is small (less than 10 K). Well-known solutions to the Poisson–Boltzmann equation give the electrical potential distribution, the net electric charge density, and subsequently the body force due to an externally applied field. Similarly well-known solutions to the momentum equation with an electrokinetic body force yield the velocity profile of a fully developed parallel flow. The associated thermal transport problem with a constant surface heat flux boundary condition is solved to obtain the normalized temperature profiles and Nusselt number, which are shown to be dependent on the length scale ratio ε (i.e., the ratio of Debye length λ_D to half channel height H, or $\varepsilon=\lambda_D/H$), the velocity scale ratio Γ (i.e., the ratio of the pressure-driven velocity scale for Poiseuille flow to Helmholtz–Smoluchowski velocity for electro-osmotic flow, or $\Gamma=u_{PD}/u_{HS}$), and the ratio of Joule heating to surface heat flux G. It is noted from the definition of the length scale ratio that the case of $\varepsilon \ll 1$ corresponds to a microchannel, while it is the case for a nanochannel when ε is finite. Also, the velocity scale ratio can take on positive or negative values, depending on the signs of the streamwise potential and pressure gradients imposed. Representative results for temperature profiles, friction factor, and Nusselt number are presented and discussed for a range of the these three ratios.

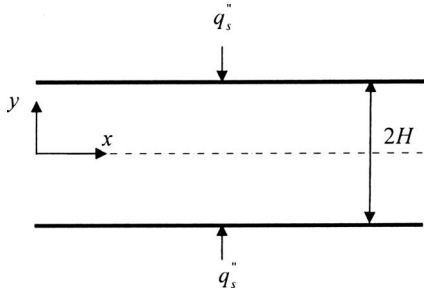

Fig. 1 Problem definition and coordinate system

In general, viscosity and thermal conductivity of fluid would vary with local temperature, and hence it is practical to investigate the effects of such variations on the heat transfer of flow caused by electro-osmotic and/or pressure forces in a microchannel. Since the flow field is coupled with the temperature field for variable fluid properties, the resulting problem is solved numerically for several representative values of the governing parameters. Numerical results reveal that variations in viscosity and thermal conductivity with local temperature initially develop pressure-driven flow, and thereby alter the hydrodynamic and thermal characteristics of the fluid. As a result, the dimensionless velocity and volume flow rate increase due to such variations. It is shown further that the friction factor decreases noticeably with viscosity variation, while the Nusselt number increases tenderly. Even though the effects of conductivity variation on velocity profile and friction factor are insignificant, it somewhat modifies the thermal characteristics of the liquid. Particularly, increasing the conductivity variation will produce a moderate increase in the Nusselt number but a small reduction in the normalized temperature.

2 Formulation and Solutions

Since electro-osmotic flows and EDL have been discussed at length in the literature, e.g., Ref. [16], here we only review the essential governing equations and controlling parameters for the comprehensive understanding of the electro-osmotically driven flow. Consider the electro-osmotic flow in a parallel-plate microchannel with one-half channel width H. An illustration of the problem is depicted in Fig. 1. It is assumed that the convective transport of ions is negligible, that the EDL does not overlap the center of the channel, and that both significant variations in cation and anion and the local electric potential occur in the normal direction to the channel walls. These assumptions yield the steady Boltzmann distribution of ions in the EDL. We also assume that the zeta potential is uniform over the channel surface. Under the above assumptions, for steady electro-osmotic flows through straight channels, it is reasonable to model the electrical potential by the following Poisson–Boltzmann equation [16,21].

$$\frac{d^2\psi}{dy^2} = -\frac{\rho_e}{\varepsilon_m} \tag{1}$$

where ε_m is the dielectric constant of the electrolyte, and ρ_e is the net electric charge density. The associated boundary conditions are $\psi=\varsigma$ (zeta potential) at the wall and $d\psi/dy=0$ at the centerline. For a symmetric dilute electrolyte (i.e., the coions and coun-

terions have the same charge valence), the electric charge density can be given by [16]

$$\rho_e = -2n_0 ez \sinh\left(\frac{ez\psi}{k_B T}\right) \tag{2}$$

where n_0 is the ion density (in molar units), e is the electron charge, z is the valence, k_B is the Boltzmann constant, and T is the absolute temperature. Invoking the Debye–Huckel linear approximation (which is appropriate for small cation and anion concentration differences [22]), the electrical potential is assumed to be small compared with the thermal energy of the ions, i.e., $|ze\psi| < |k_B T|$ so that $\sinh(ze\psi/k_B T) \approx ze\psi/k_B T$, then the electrical potential distribution is determined to be

$$\psi(y) = \frac{\varsigma \cosh(\kappa y)}{\cosh(\kappa H)} \tag{3}$$

where $\kappa = (2n_0 z^2 e^2/\varepsilon_m k_B T)^{1/2} = 1/\lambda_D$ is the Debye–Huckel parameter with λ_D denoting the Debye length. It is noted that for a symmetrical univalent electrolyte at 25°C, this approximation is found to be valid for small potentials, i.e., $\psi \leq 25.7$ mV.

In a steady-state and hydrodynamically fully developed flow, the streamwise momentum equation and the thermal energy equation are given by

$$\frac{\partial}{\partial y}\left[\mu(T)\frac{\partial u}{dy}\right] - \frac{dp}{dx} = -\rho_e E_x \tag{4}$$

$$\rho c_p u \frac{\partial T}{\partial x} = \frac{\partial}{\partial x}\left[k(T)\frac{\partial T}{\partial x}\right] + \frac{\partial}{\partial y}\left[k(T)\frac{\partial T}{\partial y}\right] + \dot{q} \tag{5}$$

where $\dot{q}$ is the volumetric heat source in the fluid, and ρ, c_p, and σ are the fluid density, specific heat, and electrical conductivity, respectively. It is noted that Eq. (4) describes the force balance among the viscous force, applied pressure gradient, and the electric body force. The electric body force can be expressed as

$$\rho_e E_x = -\frac{\varepsilon_m \varsigma E_x}{\lambda_D^2} \frac{\varsigma \cosh(y/\lambda_D)}{\cosh(H/\lambda_D)} \tag{6}$$

In general, the volumetric heat source consists of Joule heating and the viscous dissipation components. Since the electrokinetic potential in electro-osmotic flow diminishes within the effective Debye layer thickness δ over which a velocity gradient is present. Typically, δ is only few times of Debye length; accordingly, viscous dissipation term is only active within the effective EDL δ. On the other hand, Joule heating due to electric current will have effect over the whole volume. For electro-osmotic flow in a circular microtube, it has been shown that the influence of viscous dissipation is only important at low values of the relative duct radius, and thus the effect of viscous dissipation is negligible as compared with the Joule heating [18]. Now, it is instructive for the present study to examine the relative importance of viscous dissipation and Joule heating for EOF in a 2D straight channel. An order-of-magnitude analysis indicates that the thermal energy generated by viscous dissipation per channel length is of the order $2\mu W u_{\mathrm{HS}}^2/\delta$ and that due to Joule heating is of the order $2\mu^2 \sigma H W u_{\mathrm{HS}}^2/\varepsilon_m^2 \varsigma^2$, in which $u_{\mathrm{HS}} = -\varepsilon_m \varsigma E_x/\mu$ is the Helmholtz–Smoluchowski velocity. As a result, the ratio of viscous dissipation to Joule heating is of the order $\varepsilon_m^2 \varsigma^2/(\mu\sigma\lambda_D H)$. For illustration purposes, consider the typical electro-osmotic flow of an aqueous solution of a symmetrical electrolyte at 25°C ($\sigma = 10^{-3}$ S/m, $\varepsilon_m = 6.9327 \times 10^{-10}$ C^2/N m^2), and the value for zeta potential is taken as $\varsigma = -25$ mV, then viscous dissipation is comparable to Joule heating if $H \leq 5 \times 10^{-8}$ m. In other words, the Joule heating term is dominating when the channel height is larger than 0.1 μm. Thereby, viscous dissipation is comparable to Joule heating in nanoscale channels. However, we neglect viscous dissipation in the first study for the present problem. The volumetric Joule heating arising from the conduction current may be accurately modeled using Ohm's law [23]. Furthermore, for low zeta potential (as is considered here) the current density is essentially uniform across the channel height [24,25], and thus this energy generation is uniformly distributed across the microchannel cross section. According to Ohm's $i_e = \sigma E_x$, in which i_e is the current density and σ is the fluid electrical conductivity, the volumetric heat generation due to Joule heating can hence be expressed as $\dot{q} = \sigma E_x^2$.

The previous studies in the field assume viscosity and thermal conductivity to be independent of the local temperature, but this can only be justified for smaller temperature changes (less than 10 K). To account for the effects of variable viscosity and variable thermal conductivity on the flow and heat transfer, variations of the viscosity and thermal conductivity with temperature are assumed, as usual, to be in the following form:

$$\mu(T) = \mu_{\mathrm{ref}} \exp[-\gamma(T - T_{\mathrm{ref}})] \tag{7}$$

and

$$k(T) = k_{\mathrm{ref}}[1 + \beta(T - T_{\mathrm{ref}})] \tag{8}$$

where T_{ref} is a constant reference temperature. For most liquids, viscosity decreases with temperature, i.e., γ is positive. Also, β is positive for fluids such as water. For a thermally fully developed flow, it requires that

$$\frac{\partial}{\partial x}\left[\frac{T_s(x) - T(x,y)}{T_s(x) - T_m(x)}\right] = 0 \tag{9}$$

where T_s is the local wall temperature, and T_m is the bulk mean fluid temperature, respectively. The bulk mean fluid temperature is determined from

$$T_m = \frac{1}{u_m A_c}\int_{A_c} uT dA_c$$

where u_m is the mean fluid velocity, defined as

$$u_m = \frac{1}{A_c}\int_{A_c} u dA_c$$

Under an imposed constant surface heat flux condition (q_s'' = constant), after expanding Eq. (9) and solving for $\partial T/\partial x$, we have $\partial T/\partial x = dT_m/dx$ = constant and thus $\partial^2 T/\partial x^2 = 0$. Using Eqs. (6)–(8), the momentum and energy equations (4) and (5) can be rewritten as

$$\mu(T)\frac{\partial^2 u}{\partial y^2} + \frac{\partial \mu(T)}{\partial y}\frac{\partial u}{dy} - \frac{dp}{dx} - \frac{\varepsilon_m \varsigma E_x}{\lambda_D^2}\frac{\varsigma \cosh(y/\lambda_D)}{\cosh(H/\lambda_D)} = 0 \tag{10}$$

$$\rho c_p u \frac{dT_m}{dx} = k(T)\frac{\partial^2 T}{\partial y^2} + k_{\mathrm{ref}}\beta\left[\left(\frac{dT_m}{dx}\right)^2 + \left(\frac{\partial T}{\partial y}\right)^2\right] + \sigma E_x^2 \tag{11}$$

The associated boundary conditions are

$$\frac{\partial u}{\partial y} = 0 \quad \text{at } y = 0, \quad u = 0 \quad \text{at } y = H \tag{12a}$$

$$\frac{\partial T}{\partial y} = 0 \quad \text{at } y = 0, \quad q_s'' = k\frac{\partial T}{\partial y} \quad \text{at } y = H \tag{12b}$$

Since Eqs. (10) and (11) are coupled, in general, they need to be solved numerically. However, possible analytical solutions can be found for the case of constant fluid properties, i.e., both μ and k are independent of temperature.

2.1 Analytical Solution for Constant Fluid Properties. For relatively small temperature variation (less than 10 K), the fluid properties can be assumed to be independent of temperature variation. It is noted that because of the symmetry of the problem with respect to the channel axis, only one-half of the channel, i.e., the

upper portion, is considered. With μ=const and the use of Eq. (6), Eq. (4) is integrated twice to obtain the velocity distribution as

$$u(y) = u_{\mathrm{HS}}\left[1 - \frac{\cosh(\kappa y)}{\cosh(\kappa H)}\right] + u_{\mathrm{PD}}\left[1 - \left(\frac{y}{H}\right)^2\right] \tag{13}$$

In the above, the velocity scale $u_{\mathrm{HS}}=-\varepsilon_m \varsigma E_x/\mu$ is known as the Helmholtz–Smoluchowski electro-osmotic velocity, the grouping $\varepsilon_m \varsigma/\mu$ is often termed the electro-osmotic mobility of the liquid, and $u_{\mathrm{PD}}=-H^2(dp/dx)/2\mu$ is the pressure-driven velocity scale (Poiseuille flow). Consequently, the dimensionless velocity profile based on the "microfluidic scaling" can be expresses as

$$U(\eta) = \frac{u}{u_{\mathrm{HS}}} = 1 - \frac{\cosh(\eta/\varepsilon)}{\cosh(1/\varepsilon)} + \Gamma(1-\eta^2) \tag{14}$$

where $\eta=y/H$, $\varepsilon=\lambda_D/H$, and $\Gamma=u_{\mathrm{PD}}/u_{\mathrm{HS}}$ is the ratio of the two velocity scales. It is noted that Γ can also represent the ratio of pressure to electro-osmotic driving force; this can be understood by expressing this ratio as $\Gamma=(H^2/2\varepsilon_m \varsigma)\times[(dp/dx)/E_x]$. The dimensionless average velocity (or dimensionless volume flow rate) can be expressed as

$$\bar{U} = \frac{u_m}{u_{\mathrm{HS}}} = \bar{Q} = \frac{Q}{A_c u_{\mathrm{HS}}} = 1 - \varepsilon \tanh\left(\frac{1}{\varepsilon}\right) + \frac{2}{3}\Gamma \tag{15}$$

where Q is the volume flow rate, which can be obtained by integrating the velocity profile across the channel. The friction factor is defined as

$$f = \frac{\tau_w}{\rho u_m^2/2} \tag{16}$$

where $\tau_w=-\mu(du/dy)|_{y=H}$ is shear stress at the channel wall. Using Eqs. (14) and (15), we have

$$f\,\mathrm{Re} = 24\left[\frac{\frac{1}{\varepsilon}\tanh\left(\frac{1}{\varepsilon}\right) + 2\Gamma}{3 - 3\varepsilon\tanh\left(\frac{1}{\varepsilon}\right) + 2\Gamma}\right] \tag{17}$$

where $\mathrm{Re}=\rho u_m D_h/\mu$ is the Reynolds number.

In this case, the thermal conductivity is constant and the energy Eq. (11) reduces to

$$\rho c_p u \frac{dT_m}{dx} = k\frac{\partial^2 T}{\partial y^2} + \sigma E_x^2 \tag{18}$$

Performing an overall energy balance on the fluid leads to

$$\frac{dT_m}{dx} = \frac{q_s'' + H\sigma E_x^2}{\rho c_p u_m H} \tag{19}$$

Recall the thermally fully developed condition (9), the temperature distribution can be written in the form

$$T(x,y) = T_s(x) - \frac{q_s''}{h}\Phi(\eta) \tag{20}$$

In the above, Φ is a function of η only and $h=q_s''/(T_s-T_m)$ is the convective heat transfer coefficient. With the use of Eqs. (19) and (20), the energy equation (18) reduces to

$$\frac{d^2\Phi}{d\eta^2} = \frac{1}{4}\mathrm{Nu}\left[G - \frac{u}{u_m}(1+G)\right] \tag{21}$$

where Nu is the Nusselt number, and G is the ratio of energy generation due to Joule heating to the surface heat flux. They are defined as

$$\mathrm{Nu} = \frac{hD_h}{k}, \quad G = \frac{H\sigma E_x^2}{q_s''} \tag{22}$$

where D_h is the hydraulic diameter of the channel. It is noted that the parameter G can be either positive or negative. A negative value of G indicates a negative surface heat flux (i.e., surface cooling). The appropriate boundary conditions of Eq. (21) are

$$\left.\frac{\partial\Phi}{\partial\eta}\right|_{\eta=0} = 0, \quad \Phi|_{\eta=1} = 0 \tag{23}$$

Using Eqs. (14) and (15), a solution to Eq. (21) subject to boundary conditions (23) is

$$\Phi(\eta) = \mathrm{Nu}\left\{C_1(1-\eta^2) + C_2(1-\eta^4) + C_3\left[1 - \frac{\cosh(\eta/\varepsilon)}{\cosh(1/\varepsilon)}\right]\right\} \tag{24}$$

where

$$C_1 = \frac{1}{8}\left[\frac{(1+G)(1+\Gamma)}{\bar{U}} - G\right] \tag{25a}$$

$$C_2 = -\frac{\Gamma(1+G)}{48\bar{U}} \tag{25b}$$

$$C_3 = -\frac{\varepsilon^2(1+G)}{4\bar{U}} \tag{25c}$$

So far, the Nusselt number Nu in Eq. (24) is unknown. It can be determined by evaluating the bulk mean fluid temperature, which results in

$$\frac{1}{\bar{U}}\int_0^1 U(\eta)\Phi(\eta)d\eta = 1 \tag{26}$$

Substitute Eqs. (14) and (24) into Eq. (26) and integrate to get

$$\mathrm{Nu} = C_4\bar{U} \tag{27}$$

where

$$\begin{aligned} C_4^{-1} = \frac{1}{210}\{&14[10C_1 + 12C_2 + 15C_3 - 30(C_1+2C_2)\varepsilon^2 - 360C_2\varepsilon^4] \\ &+ 4[28C_1 + 32C_2 + 35C_3(1-3\varepsilon^2)]\Gamma\} + \frac{1}{2}\{C_3\,\mathrm{sech}^2(1/\varepsilon) \\ &+ \varepsilon[4\varepsilon^2(C_1 + 6C_2 + 12C_2\varepsilon^2) + C_3(-3 + 4\varepsilon^2\Gamma)]\tanh(1/\varepsilon)\} \end{aligned} \tag{28}$$

The normalized fluid temperature is also of interest, and it can be calculated from

$$\theta(\eta) = \frac{T - T_m}{Hq_s''/k} = \frac{4}{\mathrm{Nu}}[1 - \Phi(\eta)] \tag{29}$$

It is interesting to note that the dimensionless surface temperature is

$$\theta_s = \frac{4}{\mathrm{Nu}} \tag{30}$$

Also, the normalized temperature-difference distribution across the channel can be readily determined to be

$$\Delta\theta(\eta) = \theta_s - \theta = \frac{4\Phi(\eta)}{\mathrm{Nu}} \tag{31}$$

2.2 Numerical Solutions for Variable Fluid Properties. When the variations in viscosity and thermal conductivity with local temperature are taken into consideration, the flow field is coupled with the temperature field, and thus the governing equations together with the associated boundary conditions (Eqs. (10), (11), (12*a*), and (12*b*)) are solved numerically. To facilitate the analysis, we transform the set of equations into the following nondimensional form:

$$e^{A\phi}(U'' + AU'\phi') + \frac{1}{\varepsilon^2}\frac{\cosh(\eta/\varepsilon)}{\cosh(1/\varepsilon)} + 2\Gamma = 0 \tag{32}$$

$$(1 + B\phi)\phi'' + B(\phi')^2 - \left(\frac{1+G}{\bar{U}}\right)U + B\left(\frac{1+G}{\mathrm{Pe}\bar{U}}\right)^2 + G = 0 \tag{33}$$

$$U' = 0 \quad \text{at} \quad \eta = 0, \quad U = 0 \quad \text{at} \quad \eta = 1 \tag{34}$$

$$\phi' = 0 \quad \text{at} \quad \eta = 0, \quad \phi' = 1/(1 + B\phi) \quad \text{at} \quad \eta = 1 \tag{35}$$

In the above, the prime indicates differentiation with respective to η, and we have introduced the following dimensionless variables:

$$\varepsilon = \frac{\lambda_D}{H}, \quad \phi(\eta) = \frac{T - T_0}{Hq_s''/k_0}, \quad A = -\frac{\gamma H q_s''}{k_0}, \quad B = \frac{\beta H q_s''}{k_0}, \quad \mathrm{Pe} = \frac{u_{\mathrm{HS}}H}{\alpha_0} \tag{36}$$

where the reference temperature is taken as the inlet temperature T_0 for the definition of the dimensionless temperature ϕ, Pe is the Peclet number, and $\alpha = k_0/\rho c_p$. The other dimensionless variables have been defined previously. It is also noted that $A < 0$ and $B > 0$ for a positive heat flux q_s'' and vice versa.

Physical quantities of interest include the dimensionless mean velocity $\bar{U}$, friction factor f, dimensionless mean temperature, and Nusselt number. It is easy to show that

$$\bar{U} = \int_0^1 U(\eta)\, d\eta \tag{37}$$

$$f\,\mathrm{Re} = -\frac{8}{\bar{U}}(e^{A\phi}U')_{\eta=1} \tag{38}$$

$$\phi_m = \frac{T_m - T_0}{Hq_s''/k_0} = \frac{\int_0^1 U(\eta)\phi(\eta)\, d\eta}{\int_0^1 U(\eta)\, d\eta} \tag{39}$$

$$\mathrm{Nu} = \frac{hD_h}{k_0} = \frac{4}{\phi_s - \phi_m} \tag{40}$$

The normalized fluid temperature $\theta(\eta)$ defined in Eq. (29) can be related to the dimensionless temperature $\phi(\eta)$ from

$$\theta(\eta) = \phi(\eta) - \phi_s + \frac{4}{\mathrm{Nu}} \tag{41}$$

Numerical solutions for the transformed governing equations (32) and (33), subjected to the boundary conditions (34) and (35), have been generated by an implicit finite-difference method. First, the transformed differential equations were rewritten as a first-order system, which is then converted into a set of finite-difference equations using central differences. Next, we use Newton's method to solve the resulting nonlinear system of equations. The details of the solution procedure are not presented here to conserve space. It is worth noting that a step size of $\Delta\eta = 0.002$ is found to be satisfactory in obtaining sufficient accuracy within a tolerance less than 10^{-6} in nearly all cases. In order to estimate the magnitudes of various dimensionless variables, let us consider the typical electro-osmotic flow in a microchannel in which $\varsigma = -25$ mV, $\varepsilon_m = 6.9327 \times 10^{-10}$ C^2/N m^2, $H \sim 100$ μm, $E_x \sim 100$ V/mm, $\sigma \sim 10^{-3}$ S/m, and $\mu \sim 10^{-3}$ kg/m s. Then, it implies that $\mathrm{Pe} \sim \mathrm{O}(10)$ and $G \sim \mathrm{O}(1)$ for a surface heat flux of $q_s'' \sim 1$ kW/m^2. Also, the ratio of pressure to electro-osmotic driving forces is of the order $\Gamma \sim \mathrm{O}(1)$ for a pressure gradient of 1 kPa/m.

3 Results and Discussion

Although the thermally fully developed heat transfer has been analyzed for combined electro-osmotic and pressure-driven flow of constant-property fluid in a circular microtube [14], to the author's knowledge, analytical solutions for such a mixed flow in a parallel-plate microchannel with surface heat flux are not available in literature. Thereby, we first discuss the case of constant fluid properties to acquire more understanding of mixed electro-osmotic and pressure-driven flow and heat transfer in microchannels. Afterwards, the effects of thermal conductivity and viscosity variations with local temperature on hydrodynamic and thermal characteristics are examined.

3.1 Mixed Flow With Constant Fluid Properties. The dimensionless velocity profiles represented by Eq. (14) reveals that the momentum transport is dominated by electrokinetic effect as $\Gamma \to 0$, and thus the velocity profile is dependent solely on the length scale ratio ε. For $\Gamma = 0$ and $\varepsilon \to 0$, Eq. (10) is reduced to the classical Helmoltz–Smoluchowski equation $u/u_{\mathrm{HS}} = 1$. It is also noted that the momentum transport is governed by the pressure forces as $\Gamma \to \infty$ (for any value of ε), and a parabolic velocity profile of the classical Poiseuille flow can be retrieved from Eq. (14) by rescaling the velocity based on the pressure-driven velocity scale. The velocity profiles in parallel-plate microchannel exhibit similar trends to those in a circular microtube [18], and hence they are not presented here for the sake of brevity. For purely electro-osmotic flow ($\Gamma = 0$), it can be summarized that the sluglike velocity distribution is justified across the channel with a very thin boundary layer near the wall when $\varepsilon \ll 1$. On the other hand, at finite ε, say $\varepsilon \sim \mathrm{O}(1)$, the velocity distribution approximates the parabolic profile of classical pressure-driven channel flow. At intermediate values of ε, where the electrokinetic effect on momentum transport varies from a concentrated source near the channel wall (small ε) to a more dispersed source (large ε), such that the velocity distributions alter accordingly. For mixed electro-osmotic and pressure-driven flow, the resulting velocity profile is the superimposed effect of both electro-osmotic and Poiseuille flow phenomena. It is also noted that both negative and positive velocities may take place in the channel for the flow situation with an adverse pressure gradient ($\Gamma < 0$). Negative velocities occur first on the channel centerline and are found when $\Gamma < [1/\cosh(1/\varepsilon) - 1]$. Note that this criterion is valid only when Γ is negative. It can be shown from this relation that the value of Γ for which reverse flow happens in the channel core decreases from a value of $\Gamma = -0.352$ at $\varepsilon = 1$ to an asymptotic value of -1 at small ε, reaching a value of $\Gamma = -0.99$ at $\varepsilon = 0.189$. Certainly, the pressure-driven flow in the opposite direction will prevail as $-\Gamma \to \infty$. For pressure-opposed flow with small ε, the pressure gradient opposing the electro-osmotic body force is large enough to diminish the centerline velocity. Therefore, while a thin velocity boundary layer persists at the wall for this adverse pressure gradient flow, the maximum velocity occurs very close to the wall rather than on the channel centerline, and an almost stagnant central core is present. With an increase in ε, the maximum velocity decreases and occurs with a location to some extent toward the centerline. Figure 2 represents the friction factor variation as a function of ε for several values of Γ. It is evident that the friction factor decreases with increasing ε regardless of the sign of Γ. As compared with purely electro-osmotic flow ($\Gamma = 0$), the friction factor decreases with ε more rapid for pressure-assisted flow ($\Gamma > 0$), while the opposite trend is observed for pressure-opposed ($\Gamma < 0$). At the selected values of Γ, as the length scale ratio approaches zero the friction factor increases dramatically due to the strong electro-osmotic body force, i.e., the momentum transport is dominated by the electro-osmotic effect when $\varepsilon \ll 1$. At finite ε, the friction factor approaches the classical solution as Γ becomes very large, i.e., $f\,\mathrm{Re} = 24$ as $\Gamma \to \infty$ (Poiseuille flow). Consequently, the mixed flow is dominated by the pressure-driven flow

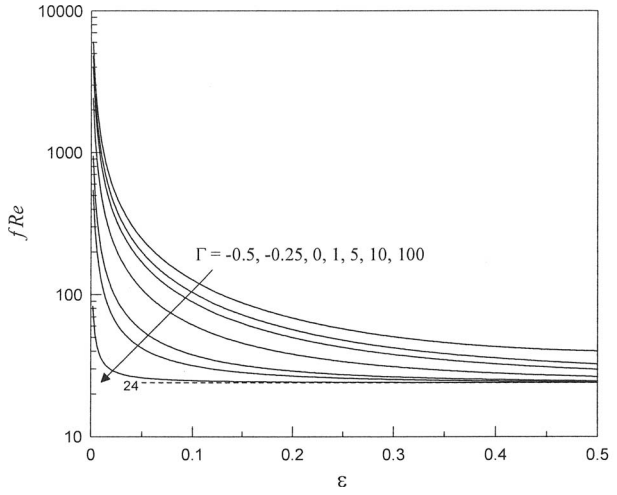

Fig. 2 Friction factor as a function of ε for various values of Γ

for a large velocity scale ratio Γ.

Figures 3(*a*)–3(*c*), respectively, show the normalized temperature profiles across the channel for values of $\Gamma=0$ (electro-osmotic flow only), $\Gamma=1$ (favorable pressure gradient flow), and $\Gamma=-1$ (adverse pressure gradient flow) for various values of ε and the ratio of Joule heating to surface heat flux G. Note from the definition of this ratio (Eq. (22)) that G can be either positive (if $q_s''>0$, i.e., surface heating) or negative (if $q_s''<0$, i.e., surface cooling). It is also interesting to note from Eq. (19) that $dT_m/dx=0$ when $G=-1$. For thermally fully developed flow in a microchannel with constant surface heat flux, the condition $q_s''=h(T_s-T_m)=$const implies that $dT_s/dx=0$. In other words, the constant surface heat flux case is also a constant surface temperature solution when $G=-1$. For the case of purely electro-osmotic flow ($\Gamma=0$), the effects of length scale ratio and the parameter G on the normalized temperature distributions are illustrated in Fig. 3(*a*). As compared with the case of $G=0$, it reveals that a positive value of G (surface heating) will result in a greater temperature variation across the microchannel, while the opposite trend is true for $G<0$ (surface cooling). The dependence of temperature on G is more significant for a larger ε, while at a small ε (e.g., $\varepsilon=0.002$) the temperature profiles are almost identical, i.e., nearly independent of G. Also, the maximum dimensionless temperature is observed at the wall ($\eta=1$), and the wall temperature increases with increasing G. Moreover, the uniform surface heat flux condition requires that the surface temperature gradient $(d\theta/d\eta)_{\eta=1}$ should be kept constant (as can be observed in the temperature distributions for all cases in the present analysis). As indicated in Eq. (29), the fully developed Nusselt number is inversely proportional to the dimensionless surface temperature, and thus an increase in G will produce a smaller Nusselt number. For mixed electro-osmotic and pressure-driven flow, the normalized temperature is a function of G for all values of ε. For the case of pressure-assisted flow, even at a very small ε the temperature profiles exhibit obvious alteration due to the change in G, as shown in Fig. 3(*b*) for $\Gamma=1$, unlike the temperature behavior shown in Fig. 3(*a*) for electro-osmotic flow only, where the dependence of θ on G disappears when $\varepsilon \ll 1$. The temperature behavior at small ε deviating from that of a pure electro-osmotic flow is more noticeable for the pressure-opposed flow, as shown in Fig. 3(*c*) for $\Gamma=-1$. It is also noted that the temperature is increased with increasing the value of ε for given values of Γ and G. Also note that the profile shape of θ shown in Fig. 3(*c*) for adverse pressure gradient flow is quite different from those of $\Gamma=0$ and $\Gamma=1$. In the absence of Joule heating ($G=0$), the normalized temperature is nearly constant in a region close to the channel core, increasing to a maxi-

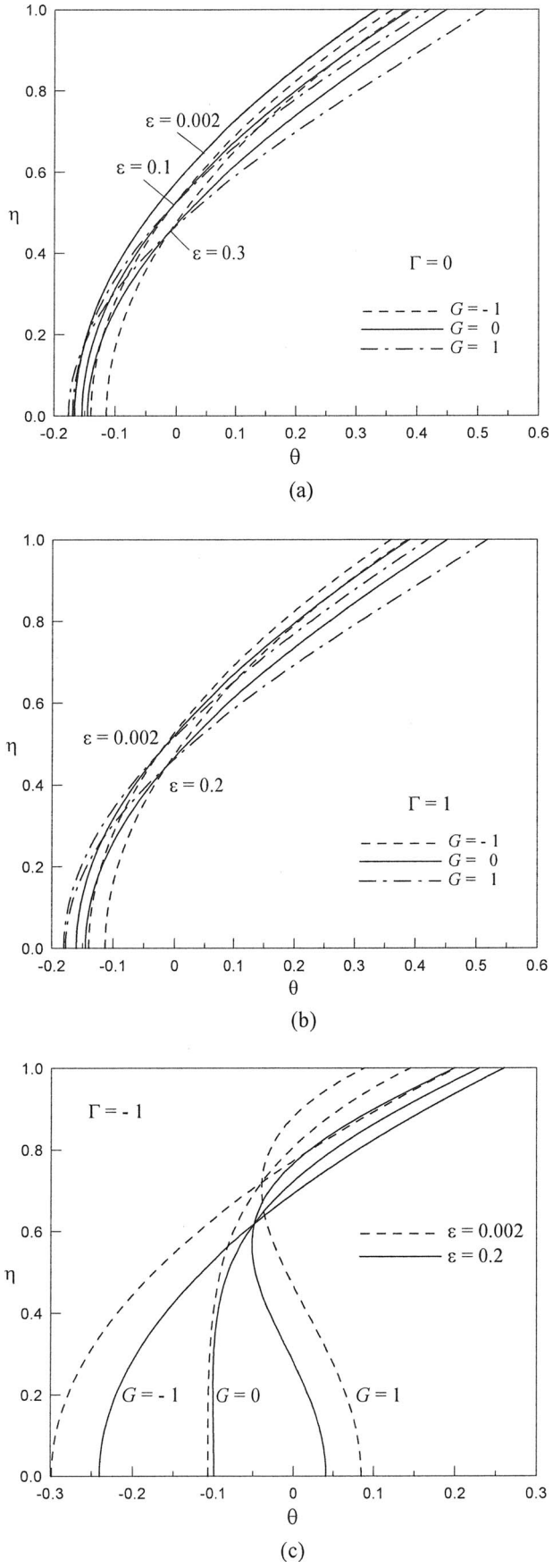

Fig. 3 Normalized temperature distributions for (*a*) electro-osmotic flow only ($\Gamma=0$), (*b*) pressure-assisted flow ($\Gamma=1$), and (*c*) pressure-opposed flow ($\Gamma=-1$)

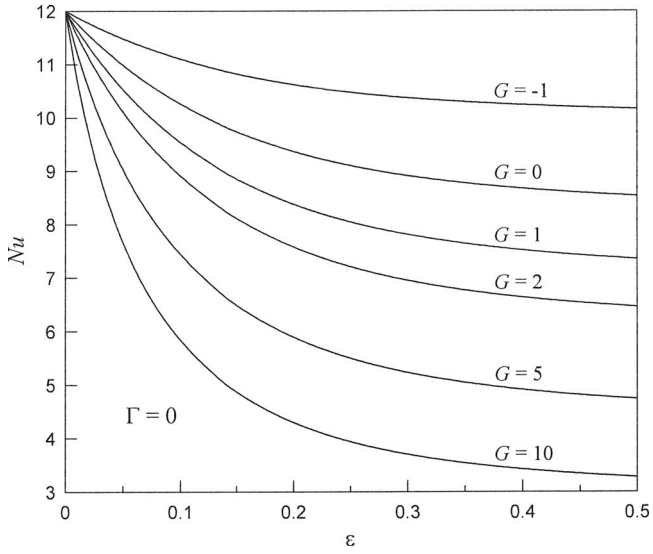

Fig. 4 Fully developed Nusselt number versus ε for electro-osmotic flow only ($\Gamma=0$) and for various values of G

mum at the wall, regardless of the magnitude of ε. For $G=1$, the temperature decreases form the centerline, attaining to a local minimum, and then increases to the wall temperature. It is also seen that for $G=-1$ the temperature increases monotonously from the channel core to the wall.

Figure 4 shows the fully developed Nusselt number as a function of length scale ratio ε for purely electro-osmotic flow ($\Gamma=0$) at selected values of G. Generally speaking, to increase G is to decrease the fully developed Nusselt number. As stated previously, the case of q''_s=const with $G=-1$ is also the constant temperature case, and the energy generated in the fluid due to Joule heating is equal to the surface heat rejection (fluid cooling); hence, the wall temperature keeps a constant value. As $\varepsilon \to 0$, for all values of G the Nusselt number approaches 12, the classical solution for slug flow [26]. The fully developed Nusselt number takes the maximum value at this limiting case and then decreases with increasing ε. This phenomenon is consistent with the wall temperature behavior presented in Fig. 3(*a*), where—at a given G-increasing ε is to increase θ_s and thus reduces the magnitude of Nu defined by Eq. (30). The variations of fully developed Nusselt number with Γ for mixed electro-osmotic and pressure-driven flow are plotted in Figs. 5(*a*)–5(*c*) for three different values of G ($G=-1,0,1$). Corresponding to the criterion for a negative velocity occurring in the channel, the minimum value of Γ in Figs. 5(*a*)–5(*c*) for a given ε is chosen as $\Gamma_{\min}=[1/\cosh(1/\varepsilon)-1]$. These figures reveal that for a specified ε the Nusselt number is a maximum when Γ is a minimum, and then it decreases with an increasing velocity scale ratio Γ. Furthermore, it can be seen that the Nusselt number is significantly influenced by ε when Γ is small in a manner that the Nusselt number is decreased due to an increase in ε at a specified Γ. As $\Gamma \to \infty$, the flow is dominated by the pressure forces, and the Nusselt number decreases asymptotically to the limit of Poiseuille flow. For example, Fig. 5(*a*) shows that the Nusselt number for no Joule heating ($G=0$) approaches the value of classical pressure-driven flow [26], i.e., Nu=8.235 as $\Gamma \to \infty$.

3.2 Effects of Variable Fluid Properties. The numerical results show that the influence of thermal conductivity variation (B) on the velocity profile is not impressive, while the velocity changes moderately with viscosity variation (A). To illustrate the influence of viscosity variation on the velocity and temperature profiles, we chose positive surface heat fluxes such that A is nega-

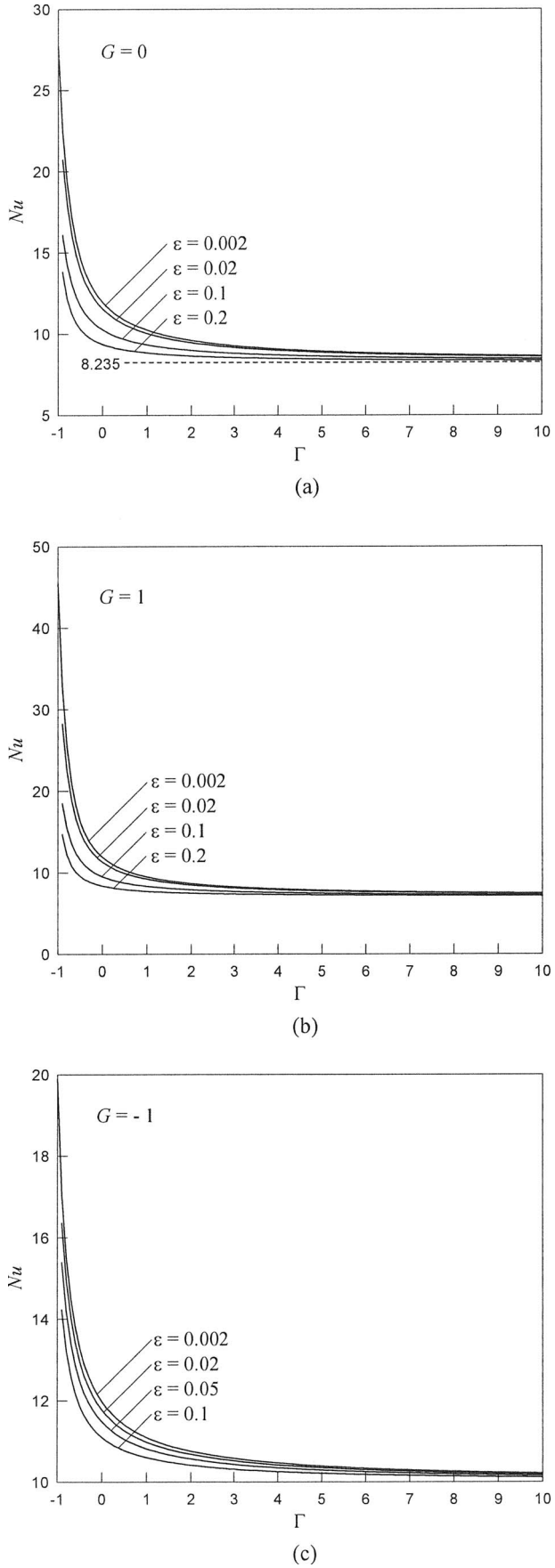

Fig. 5 Fully developed Nusselt number versus Γ at selected values of ε, (*a*) no heat generation ($G=0$), (*b*) surface heating with $G=1$, and (*c*) surface cooling with $G=-1$

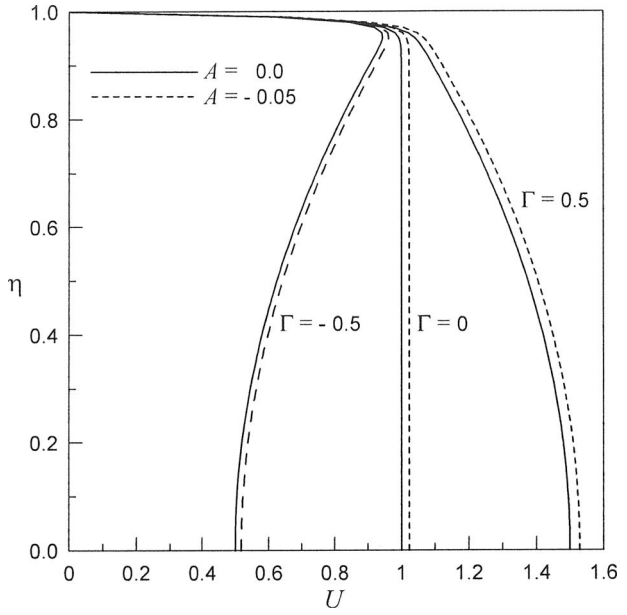

Fig. 6 Velocity distributions for $\varepsilon=0.01$, $B=0$, $G=1$, and for different values of A and Γ

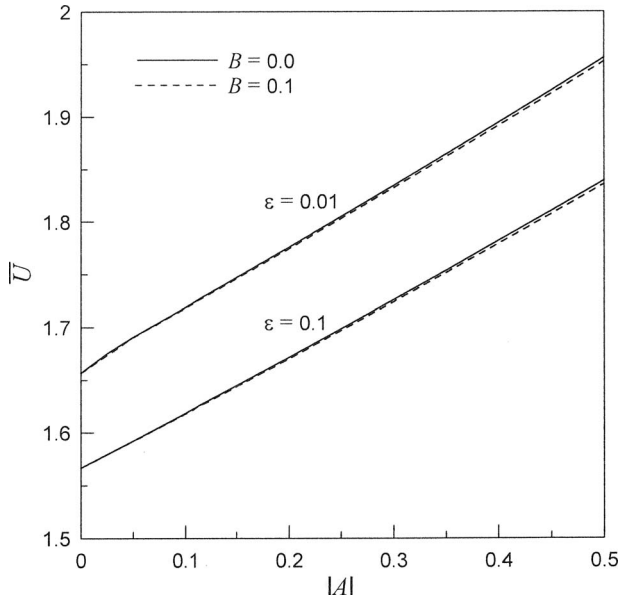

Fig. 7 Average velocity (flow rate) as a function of A for $\Gamma=1$, $G=1$, and for different values of B and ε

tive for positive γ, i.e., viscosity decreases with temperature. Figure 6 shows the effect of the viscosity variation parameter on the velocity profile $U(\eta)$ for $\varepsilon=0.01$, $B=0$, $G=1$, and for various values of Γ. For a pure electro-osmotic flow ($\Gamma=0$), it is observed that the variation in viscosity with local temperature would initially develop pressure-driven flow to account for such variation, and hence increases the dimensionless velocity. The calculation shows that the velocity at the centerline is increased by 2.4% for the given values of the governing parameters. It is also clear from this figure that the viscosity variation tends to increase the velocity profile for mixed electro-osmotic and pressure-driven flows. The centerline velocity is increased by an amount of 2% for a pressure-assisted flow with $\Gamma=0.5$, and the peak velocity is increased by 2% for a pressure-opposed flow with $\Gamma=-0.5$. The dimensionless average velocity (or volume flow rate) $\bar{U}$ is presented as a function of the viscosity variation parameter A in Fig. 7 for $\Gamma=1$, $G=1$, and for different values of length scale ratio ε and conductivity variation parameter B. For a given length scale ratio ε, this figure reveals that the average velocity increases considerably with the increase in viscosity variation, but only minor effect of conductivity variation on $\bar{U}$ is observed. This phenomenon is consistent with the results of velocity distributions shown in Fig. 6, where an increase in the local velocity is caused by viscosity variation. For specified values of parameters A and B, as the length scale ratio ε increases (such that the electric double layer becomes thicker), the average velocity decreases. In other words, the average velocity and hence the volume flow rate decreases as the Debye length increases, i.e., the excess charge distribution penetrates deeper into the core region of the channel. The influence of viscosity variation on the friction factor is depicted in Fig. 8 for $\varepsilon=0.01$, $\Gamma=1$, and two values of B. As can be seen, the friction factor decreases with the increase in viscosity variation parameter. This is readily understood for the velocity distributions shown in Fig. 6, where the velocity gradient at the wall decreases as the viscosity variation with local temperature is taken into account. Again, the influence of the conductivity variation parameter on the friction factor is not impressive.

Figure 9 represents the variation of normalized temperature profile $\theta(\eta)$ due to viscosity variation. The normalized temperature is decreased to a certain degree by viscosity variation for a very small length scale ratio (corresponding to a microchannel), whereas the temperature departure from that for constant-property viscosity diminishes when the length scale ratio becomes finite (characterizing a nanochannel). Although the influence of thermal conductivity variation on hydrodynamic characteristics is not important, this effect on the thermal characteristics, however, is more pronounced that can be readily observed from Figs. 10 and 11. Figure 10 displays the effects of thermal conductivity variation on the temperature profile for different values of ε. For both small and finite length scale ratios, the normalized temperature is found to be reduced moderately when the thermal conductivity increases with temperature, i.e., $B>0$. The increase in temperature caused by thermal conductivity variation is more obvious in the near wall region. Figure 11 illustrates the effects of viscosity and thermal conductivity variations where local temperature on the fully developed Nusselt number is depicted for $\varepsilon=0.01$, 0.1, and for sev-

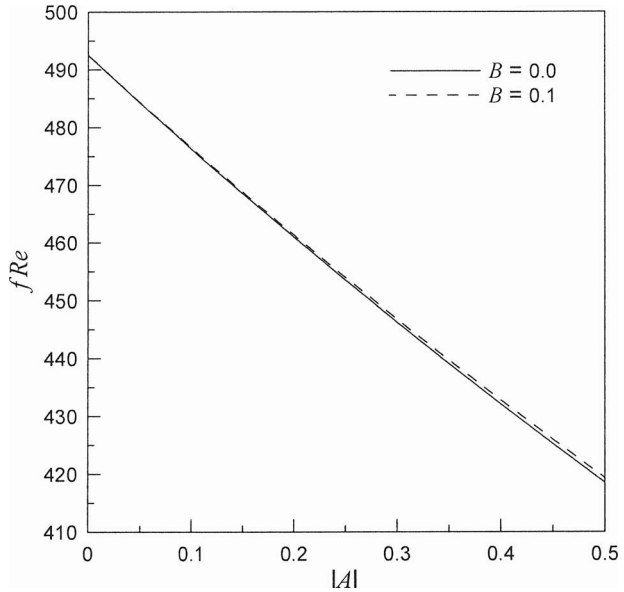

Fig. 8 Friction factor as a function of A for $\varepsilon=0.01$, $\Gamma=1$, $G=1$, and for different values of B

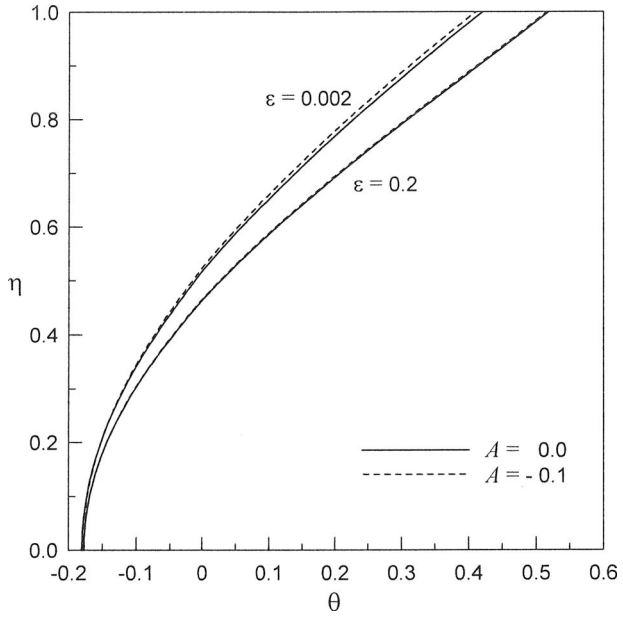

Fig. 9 Temperature distributions for *B*=0, Γ=1, *G*=1, and for different values of *A* and ε.

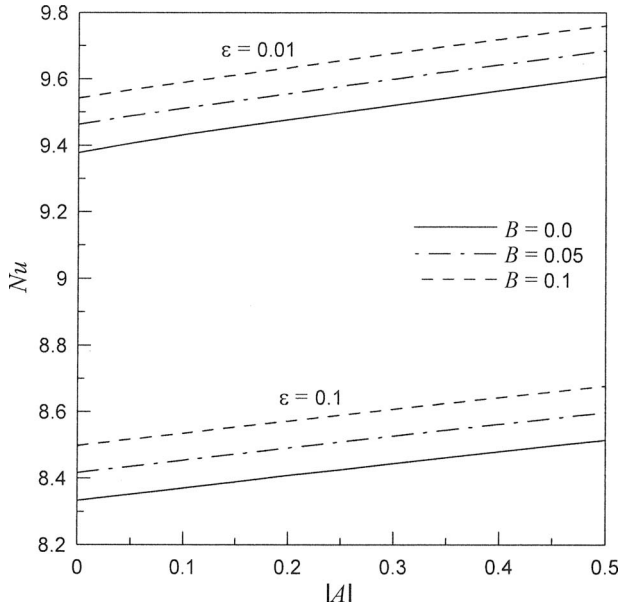

Fig. 11 Nusselt number as a function of *A* for Γ=1, *G*=1, and for different values of *B* and ε

eral values of B. For specified values of B and ε, the Nusselt number increases with the viscosity variation parameter A. Also, to increase the conductivity variation parameter B tends to increase the Nusselt number. This indicates that higher fluid thermal conductivity will produce higher heat transfer rate. The increase in Nu due to an increase in the value of B can be explained from the fact that Eq. (41) reduces to $\theta_s=4/\mathrm{Nu}$ at the channel wall, also noting that θ_s decreases with increasing B, as shown in Fig. 10, and consequently the Nusselt number increases as B increases.

4 Conclusions

An analysis is performed for the heat transfer characteristics of mixed electro-osmotic and pressure-driven flow in microchannels with Joule heating effect. Under constant surface heat flux condition and constant fluid properties, analytical solutions are obtained for the fluid flow and heat transfer characteristics. Generally speaking, the velocity distributions are strongly affected by the magnitudes of ε and Γ, and the flow rate can be increased by either increasing Γ or decreasing ε. The temperature distributions and Nusselt number in the thermally fully developed flow are shown to depend on the length scale ratio ε, the velocity scale ratio Γ, and the dimensionless source term G. For electro-osmotic flow only, the effect of heat generation on the dimensionless temperature disappears if $\varepsilon \ll 1$, while for mixed flow the dimensionless temperature profiles exhibit obvious variations caused by the change in the source term even for a very small value of ε. The fully developed Nusselt number of a purely electro-osmotic flow ($\Gamma=0$) decreases from the classical solution for slug flow with increasing the magnitude of ε. Furthermore, increasing the dimensionless source term is found to reduce the Nusselt number. For mixed electro-osmotic and pressure-driven flow, the Nusselt number decreases with increasing Γ and approaches asymptotically to the well-known Poiseuille flow limit when $\Gamma \to \infty$. The effects of thermal conductivity and viscosity variations with local temperature on the flow and temperature fields are also explored. The variation in viscosity would initially develop pressure-driven flow to account for such variation and hence increases the dimensionless velocity and flow rate. The friction factor reduces considerably with viscosity variation, while the Nusselt number increases gently due to viscosity variation. Although the variation in thermal conductivity has no impressive influence on velocity and friction, it has moderate impact on the temperature and Nusselt number, i.e., increasing the conductivity variation will produce an increase in Nusselt number but a slight decrease in the normalized temperature.

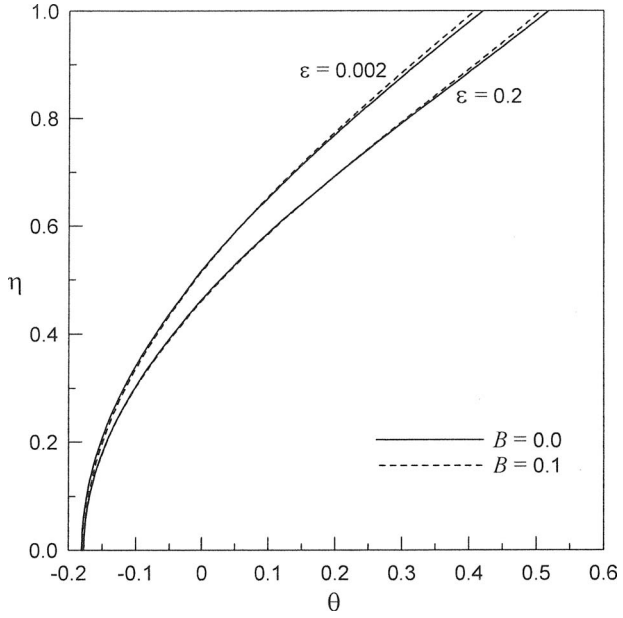

Fig. 10 Temperature distributions for *A*=0, Γ=1, *G*=1, and for different values of *B* and ε

Acknowledgment

This work was supported, in part, by the National Science Council of Taiwan through Grant No. NSC 95–2221-E-150–079.

Nomenclature

A = viscosity variation parameter
B = thermal conductivity variation parameter
c_p = fluid specific heat
D_h = hydraulic diameter

E_x = electric field component in the streamwise direction
e = electron charge
f = friction factor, $\tau_w/(\rho u_m^2/2)$
G = ratio of Joule heating to surface heat flux, $H\sigma E_x^2/q_s''$
H = half channel height
h = convective heat transfer coefficient
k = thermal conductivity
k_B = Boltzmann constant
Nu = Nusselt number, hD_h/k
n_0 = ion density
p = pressure
Q = volume flow rate
q_s'' = wall heat flux
Re = Reynolds number, $\rho u_m D_h/\mu$
T = temperature
U = dimensionless velocity
u = local fluid velocity
u_{HS} = Helmholtz–Smoluchowski velocity, $-(\varepsilon_m \varsigma/\mu)E_x$
u_{PD} = pressure-driven velocity, $-(H^2/2\mu)(dp/dx)$
x = streamwise coordinate
y = cross-stream coordinate
z = valence

Greek Symbols

α = thermal diffusivity
β = constant, Eq. (8)
Γ = velocity scale ratio, $u_{\mathrm{PD}}/u_{\mathrm{HS}}$
γ = constant, Eq. (8)
ε = length scale ratio, λ_D/H
ε_m = permittivity of the medium
ζ = wall zeta potential
η = nondimensional cross-stream coordinate
θ = normalized temperature
κ = Debye–Huckel parameter, $(2n_0 z^2 e^2/\varepsilon_m k_B T)^{1/2}$
λ_D = Debye length
μ = absolute viscosity
ρ = fluid density
σ = fluid electrical conductivity
ρ_e = net electric charge density
τ_w = wall shear stress
Φ = auxiliary function, Eq. (21)
ϕ = dimensionless temperature
ψ = electrical potential distribution

Subscripts

m = mean
ref = reference value
s = surface
0 = inlet condition

References

[1] Kim, S. J., and Kim, D., 1999, "Forced Convection in Microstructure for Electronic Equipment Cooling," ASME J. Heat Transfer, **121**, pp. 635–645.
[2] Jang, S. P., and Kim, S. J., 2005, "Fluid Flow and Thermal Characteristics of a Microchannel Heat Sink Subject to an Impinging Air Jet," ASME J. Heat Transfer, **127**, pp. 770–779.
[3] Morini, G. L., and Spiga, M., 2007, "The Role of the Viscous Dissipation in Heated Microchannels," ASME J. Heat Transfer, **129**, pp. 308–318.
[4] Chen, C.-H., 2007, "Forced Convection Heat Transfer in Microchannel Heat Sinks," Int. J. Heat Mass Transfer, **50**, pp. 2182–2189.
[5] Woolley, A. T., Hadley, D., Landre, P., deMello, A. J., Mathies, R. A., and Northrup, M. A., 1996, "Functional Integration of PCR Amplification and Capillary Electrophoresis in a Microfabricated DNA Analysis Device," Anal. Chem., **68**, pp. 4081–4086.
[6] Khandurina, J., McKnight, T. E., Jacobson, S. C., Waters, L. C., Foote, R. S., and Ramsey, J. M., 2000, "Integrated System for Rapid PCR-Based DNA Analysis in Microfluidic Devices," Anal. Chem., **72**, pp. 2995–3000.
[7] Verpoorte, E., 2002, "Microfluidic Chips for Clinical and Forensic Analysis," Electrophoresis, **23**, pp. 677–712.
[8] Taylor, M. T., Nguyen, P., Ching, J., and Petersen, K. E., 2003, "Simulation of Microfluidic Pumping in a Genomic DNA Blood-Processing Cassette," J. Micromech. Microeng., **13**, pp. 201–208.
[9] Bourouina, T., Bosseboeuf, A., and Grandchamp, J.-P., 1997, "Design and Simulation of an Electrostatic Micropump for Drug-Delivery Applications," J. Micromech. Microeng., **7**, pp. 186–188.
[10] van Lintel, H. T. G., van De Pol, F. C. M., and Bouwstra, S., 1988, "A Piezoelectric Micro Pump Based on Micromachining of Silicon," Sens. Actuators, **15**, pp. 153–167.
[11] Richter, A., Plettner, A., Hofmann, K. A., and Sandmaier, H., 1991, "A Micromachined Electrohydrodynamic (EHD) Pump," Sens. Actuators, A, **29**, pp. 159–168.
[12] Lemoff, A. V., and Lee, A. P., 2000, "An AC Magnetohydrodynamic Micropump," Sens. Actuators B, **63**, pp. 178–185.
[13] Arulanandam, S., and Li, D., 2000, "Liquid Transport in Rectangular Microchannels by Electro-Osmotic Pumping," Colloids Surf., A, **161**, pp. 89–102.
[14] Polson, N. A., and Hayes, M. A., 2000, "Electro-Osmotic Flow Control of Fluids on a Capillary Electrophoresis Microdevice Using an Applied External Voltage," Anal. Chem., **72**, pp. 1088–1092.
[15] Chen, C.-H., and Santiago, J. G., 2002, "A Planar Electro-Osmotic Micropump," J. Microelectromech. Syst., **11**, pp. 672–683.
[16] Probstein, R. F., 1994, *Physicochemical Hydrodynamics*, 2nd ed., Wiley, New York.
[17] Gleeson, J. P., 2002, "Electro-Osmotic Flows With Random Zeta Potential," J. Colloid Interface Sci., **249**, pp. 217–226.
[18] Maynes, D., and Webb, B. W., 2003, "Fully-Developed Thermal Transport in Combined Pressure and Electro-Osmotically Driven Flow in Microchannels," ASME J. Heat Transfer, **125**, pp. 889–895.
[19] Maynes, D., and Webb, B. W., 2004, "The Effect of Viscous Dissipation in Thermally Fully-Developed Electro-Osmotic Heat Transfer in Microchannels," Int. J. Heat Mass Transfer, **47**, pp. 987–999.
[20] Das, S., and Chakraborty, S., 2006, "Analytical Solutions for Velocity, Temperature and Concentration Distribution in Electro-Osmotic Microchannel Flows of a Non-Newtonian Bio-Fluid," Anal. Chim. Acta, **559**, pp. 15–24.
[21] Park, H. M., Lee, J. S., and Kim, T. W., 2007, "Comparison of the Nernst-Planck Model and the Poisson-Boltzmann Model for Electro-Osmotic Flows in Microchannels," J. Colloid Interface Sci., **315**, pp. 731–739.
[22] Conlisk, A. T., 2005, "The Debye–Huckel Approximation: Its Use in Describing Electro-Osmotic Flow in Micro- and Nano-Channels," Electrophoresis, **26**, pp. 1896–1912.
[23] Burgreen, D., and Nakache, F. R., 1964, "Electrokinetic Flow in Ultrafine Capillary Slits," J. Phys. Chem., **68**, pp. 1084–1091.
[24] Hunter, R. J., 1981, *Zeta Potential in Colloidal Science: Principles and Applications*, Academic, London.
[25] Levine, S., Marriott, J. R., Neale, G., and Epstein, N., 1975, "Theory of Electrokinetic Flow in Fine Cylindrical Capillaries at High Zeta-Potentials," J. Colloid Interface Sci., **52**, pp. 136–149.
[26] Burmeister, L. C., 1983, *Convective Heat Transfer*, Wiley, New York.

Relative Contributions of Inelastic and Elastic Diffuse Phonon Scattering to Thermal Boundary Conductance Across Solid Interfaces

Patrick E. Hopkins[1]

Pamela M. Norris[2]
e-mail: pamela@virginia.edu

Department of Mechanical and Aerospace Engineering,
University of Virginia,
P.O. Box 400746,
Charlottesville, VA 22904-4746

The accuracy of predictions of phonon thermal boundary conductance using traditional models such as the diffuse mismatch model (DMM) varies depending on the types of material comprising the interface. The DMM assumes that phonons, undergoing diffuse scattering events, are elastically scattered, which drives the energy conductance across the interface. It has been shown that at relatively high temperatures (i.e., above the Debye temperature) previously ignored inelastic scattering events can contribute substantially to interfacial transport. In this case, the predictions from the DMM become highly inaccurate. In this paper, the effects of inelastic scattering on thermal boundary conductance at metal/dielectric interfaces are studied. Experimental transient thermoreflectance data showing inelastic trends are reviewed and compared to traditional models. Using the physical assumptions in the traditional models and experimental data, the relative contributions of inelastic and elastic scattering to thermal boundary conductance are inferred. [DOI: 10.1115/1.2995623]

Keywords: thermal boundary conductance, diffuse phonon scattering, elastic scattering, inelastic scattering, nanoscale solid interfaces

Introduction

An understanding of the basic energy transport mechanisms involved in interfacial thermal transport is critical for thermal management of nanostructured devices. When the length scale of a device is comparable to or shorter than the host material's thermal diffusion length, which is often the case for modern nanoscale devices, heat transport away from the active regions is greatly affected by the interfacial properties [1]. An ever increasing challenge in the development of these devices is successfully engineering the heat transport across the interfaces to control the thermal responses experienced in the materials in the devices. This involves a fundamental understanding of the thermal boundary conductance, h_{BD}, at the specific interfaces.

This study examines the relative contributions of inelastic and elastic diffuse phonon scattering on thermal boundary conductance. Several models to predict thermal boundary conductance are discussed in detail and compared to experimental data. Based on the assumptions of these models, a new model to predict the maximum h_{BD} due to inelastic scattering is presented. Using this new model, the relative contributions of elastic and inelastic scattering on h_{BD} are examined.

Models for Phonon Thermal Boundary Conductance

In an attempt to predict thermal boundary conductance at low temperatures, Little [2] proposed the acoustic mismatch model (AMM) to account for the specular scattering of phonons at an interface between two materials. In the following derivation of the AMM and subsequent discussion, side 1 will refer to the side of the interface with the "softer" material and side 2 will refer to the side of the interface with the "stiffer" material. The softer materials are characterized by their lower phonon velocities, smaller phonon vibrational spectrum, and lower Debye temperatures compared to the stiffer materials, which have higher phonon velocities, larger phonon vibrational spectrum, and higher Debye temperatures. For example, consider a metal/dielectric system in which phonons are propagating in a metallic film such as Pb (the lower Debye temperature, softer, material) toward the interface with a dielectric substrate such as diamond (the higher Debye temperature, stiffer, material). In this case, the metallic Pb film is referred to as side 1 and the dielectric diamond substrate as side 2. Table 1 gives phonon velocities, vibrational cutoff frequencies, and Debye temperatures for several materials of interest in this work. The net heat flux occurring from side 1 to side 2 can be calculated by

$$\dot{q} = h_{BD}\Delta T \tag{1}$$

Using the analogy between photons and phonons as wavepackets of energy, the intensity of phonons [3] is used to calculate the heat flux determined from the equation of phonon radiative transfer (EPRT) [4]. The heat flux is expressed as

$$\dot{q} = \frac{1}{2}\sum_j \int_0^{\pi/2} \int_0^{\omega_{1,j}^c} D_{1,j}(\omega) n(\omega,T) \hbar\omega \nu_{1,j} \alpha_{1,j}(\phi,\omega) \times \cos(\phi)\sin(\phi) d\omega d\phi = h_{BD}\Delta T \tag{2}$$

where ω^c is the cutoff frequency, $D(\omega)$ is the density of states, $n(\omega,T)$ is the Bose–Einstein phonon distribution function, ω is the

[1]Present address: Engineering Sciences Center, Sandia National Laboratories, P.O. Box 5800, Albuquerque, NM 87185-0346.

[2]Author to whom correspondence should be addressed.

Contributed by the Heat Transfer Division of ASME for publication in the JOURNAL OF HEAT TRANSFER. Manuscript received February 13, 2008; final manuscript received August 6, 2008; published online January 5, 2009. Review conducted by Jayathi Murthy. Paper presented at the 2007 ASME International Mechanical Engineering Congress (IMECE2007), Seattle, WA, November 10–16, 2007.

 Copyright © 2009 by ASME

Table 1 Debye temperature [8,24,25], longitudinal and transverse phonon velocities [19,25], and calculated cutoff frequencies of materials of interest in this study

Material	θ_D (K)	ν_L (m s^{-1})	ν_T (m s^{-1})	$\omega_L^c \times 10^{-13}$ (s^{-1})	$\omega_T^c \times 10^{-13}$ (s^{-1})
Al_2O_3	1035	10,890	6450	12.1	7.19
AlN	1150	11,120	6267	15.8	8.89
Au	165	3390	1290	5.14	1.96
Bi	119	1543	1107	1.45	1.04
Diamond	2230	17,500	12,800	30.2	22.1
Pb	105	2350	970	2.96	1.22
Pt	240	4174	1750	6.60	2.77

phonon frequency, ν is the phonon velocity, and $\alpha(\phi,\omega)$ is the phonon transmission probability. In this analysis, a local thermodynamic equilibrium is assumed around the phonon scattering event, so local temperatures can be defined. The subscripts "1" and "j" refer to the side and the phonon mode (longitudinal or transverse), respectively. Rearranging Eq. (2) and for the limit of ΔT approaching zero, the AMM is given by

$$h_{BD} = \frac{1}{2}\sum_j \int_0^{\pi/2} \int_0^{\omega_{1,j}^c} D_{1,j}(\omega)\frac{\partial n(\omega,T)}{\partial T}\hbar\omega\nu_{1,j}\alpha_{1,j}(\phi,\omega) \times \cos(\phi)\sin(\phi)d\omega d\phi \quad (3)$$

Note, in the AMM, the transmission probability is a function of incident angle. Although Eq. (3) has been shown to predict h_{BD} relatively well at low temperatures ($T<7$ K) and at ideal interfaces where specular scattering is probable [5], this represents only a very limited population of interfaces in modern devices, which may operate at higher temperatures and have disordered regions near the interface that induce diffuse scattering.

To account for this type of phonon scattering, Swartz and Pohl [6] developed the diffuse mismatch model (DMM) to predict h_{BD} at more realistic interfaces. The DMM theory assumes elastic scattering, that is, upon scattering a phonon forgets where it came from and thus the probability of reflection from one side equals the probability of transmission from the other. The probability that a phonon will scatter into a given side of the interface is thus independent of where it came from, but rather it is proportional to the density of phonon states on that side and is restricted by the principle of detailed balance.

To apply the DMM in its simplest form, the following assumptions must be made [7]: (1) phonons are elastically scattered, i.e., a phonon from side 1 with frequency ω can only emit a phonon from the interface with the same frequency ω; (2) phonon scattering is completely diffuse, i.e., a scattered phonon has no memory of the mode (longitudinal or transverse) or direction of the incident phonon; and (3) the materials on both sides of the interface are elastically isotropic, i.e., the longitudinal and transverse acoustic velocities are constant in all crystallographic directions. Assumption (3) relaxes the angle dependence in Eq. (3), which leads to

$$h_{BD}^{\mathrm{DMM}} = \frac{1}{4}\sum_j \nu_{1,j}\int_0^{\omega_{1,j}^c} \alpha_1(\omega)\hbar\omega D_{1,j}(\omega)\frac{\partial n(\omega,T)}{\partial T}d\omega \quad (4)$$

The linear Debye approximation for the phonon dispersion will be used to calculate the phonon density of states. The cutoff frequency of each phonon mode j on side 1 can be calculated for the separate phonon modes. Assuming Debye dispersion, the cutoff frequency can be calculated by $\omega_{1,j}^c = \nu_{1,j}(6\pi^2 N_1)^{1/3}$, where N_1 is the total number of oscillators per until volume of side 1 [8]. In cubic structures (such as metal with one atom per unit cell), N_1 is simply the atomic density, calculated by $N_1 = \rho N_A / M$, where ρ is the mass density, N_A is Avogadro's number, and M is the atomic weight. However, in structures with more than one atom per unit cell (for example, diamond structures with diatomic basis such as Si or diamond), the number of primitive cells per unit volume must be divided by the number of atoms in the basis [9]. Therefore, for a diatomic basis, $N_1 = \rho N_A/(2M)$.

Due to the assumption of diffuse scattering, the probability of transmission from side 1 to side 2 is the same as the probability of reflection from side 2 to side 1, i.e., $\alpha_1(\omega) = 1 - \alpha_2(\omega)$. Therefore, according to the principle of detailed balance, the phonon transmission probability is calculated by [6]

$$\alpha_1(\omega) = \frac{\sum_j \nu_{2,j}^{-2}}{\sum_j \nu_{2,j}^{-2} + \sum_j \nu_{1,j}^{-2}} = \alpha_1 \quad (5)$$

This simplified transmission coefficient is a result of assuming a Debye density of states and elastic scattering. The transmission probability calculated with the Debye density of states agrees well with the transmission of two simple structures calculated with a more realistic density of states and molecular dynamics simulations (MDSs) [10,11]. The DMM has been shown to predict the response of higher temperature interfaces ($T>15$ K) relatively well [5,6]. However, at much higher temperatures, the DMM has been shown to do a poor job of predicting the value of h_{BD}, in some cases underpredicting [12] while in other cases overpredicting [7,12–14].

Another model for h_{BD}, the phonon radiation limit (PRL), estimates the maximum conductance for interfacial transport due to elastic scattering [15]. The development of the PRL is very similar to that of the DMM. However, the PRL assumes that all of the phonons in side 2 up below the cutoff frequency in side 1 (assuming $\omega_1^c < \omega_2^c$) contribute to thermal transport though elastic collisions ($\alpha=1$). With these assumptions, the PRL is given as

$$h_{BD}^{\mathrm{PRL}} = \frac{1}{4}\sum_j \nu_{2,j}\int_0^{\omega_{1,j}^c} \hbar\omega D_{2,j}(\omega)\frac{\partial n(\omega,T)}{\partial T}d\omega \quad (6)$$

which represents the maximum conductance due to elastic scattering.

The applicability of all of the aforementioned models is limited to interfaces in which thermal transport is dominated by elastic phonon scattering. Inelastic phonon scattering has been shown to offer an additional channel for thermal transport, which can lead to different values and trends than predicted with available models [10,16,17]. In the classical limit (for real materials $T>\theta_{D,1}$, the Debye temperature of side 1, the lower Debye temperature material), h_{BD} calculated by either the DMM or PRL is relatively independent of temperature. The only temperature dependent part of either model is in the distribution function, which at temperatures well above the Debye temperature becomes constant. Because these models do not assume any inelastic scattering, the models are independent of temperature at high temperatures (when $T>\theta_{D,1}$). To check the temperature dependence of h_{BD}, Stevens et al. [10] conducted several molecular dynamic simulations at a range of temperatures. A strong linear relationship was observed in the results of the MD calculations. This linear trend in h_{BD} when $T>\theta_{D,1}$ has been observed experimentally with transient

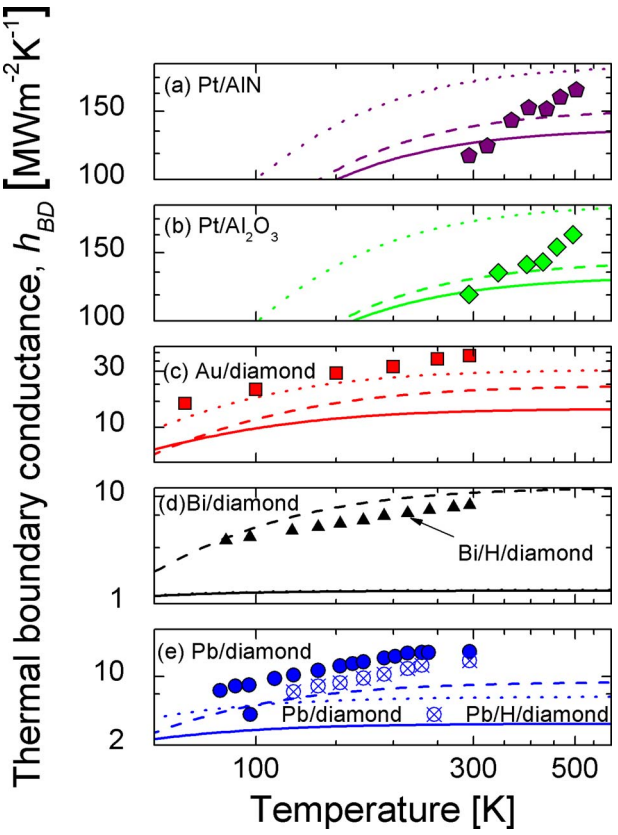

Fig. 1 DMM (solid line), PRL (dotted line), and JFDMM (dashed line) calculations compared to temperature dependent TTR data on (*a*) Pt/AlN [17], (*b*) Pt/Al_2O_3 [17], (*c*) Au/diamond [14], (*d*) Bi/H/diamond [16], and (*e*) Pb/diamond and Pb/H/diamond [16]. Note the similar temperature dependent trends of the DMM and PRL due to their assumption of elastic scattering.

thermoreflectance (TTR) pump-probe measurements. Stoner and Maris [14] have shown this linear trend for a Au film on a diamond substrate. This trend was shown on several other film substrate material systems at low temperatures by Lyeo and Cahill [16] and at high temperatures by Hopkins et al. [17]. In all cases, values and trends in the experimental data differ from those predicted by the DMM and PRL.

An underlying assumption governing the DMM and PRL is that a phonon transmits energy across an interface by emitting a phonon with the same frequency, i.e., the phonons are elastically scattered. Therefore, as the interface temperature is driven up above the Debye temperature of the softer material, h_{BD} is predicted to be relatively constant by the DMM. For example, Pb/diamond in Fig. 1 where $\theta_{D\_Pb}=105$ K and $\theta_{D\_diamond}=2200$ K [8]. This is a result of the change in phonon population with temperature predicted by the Bose–Einstein distribution function. At temperatures close to a material's Debye temperature, the change in phonon population with temperature becomes linear. The DMM is a function of the temperature derivative of the Bose–Einstein distribution, which results in the constant h_{BD} predicted at higher temperatures ($T > \theta_{D\_Pb}$). Assuming elastic scattering, the h_{BD} predictions would follow a trend relating to the change in the Pb phonon population with temperature. However, if inelastic phonon processes occur (i.e., a phonon with frequency $\omega^c_{diamond}$ scatters into several phonons with frequencies below ω^c_{Pb}), then the change in h_{BD} with temperature would be related to the change in the diamond phonon population in addition to the Pb population.

Using this approach, Hopkins and Norris [18] developed a simple correction to the DMM to account for the discrepancy between the DMM and the experimental data in the event of inelastic scattering. By blending the vibrational spectra of the film and substrate materials, an approximation was developed for the contribution of these inelastic modes with a diffuse scattering assumption, the joint frequency diffuse mismatch model (JFDMM). The JFDMM assumes the same form as the DMM (Eq. (4)) but uses a modified phonon velocity that is taken as a weighted average of the velocities of the phonons of sides 1 and 2. Consequently, this results in a weighted average of the phonon spectra used in the h_{BD} calculation, given by

$$D_{\mathrm{mod},j} = \frac{\omega^2}{2\pi^2 \nu_{\mathrm{mod},j}^{\ 3}}, \quad \omega \leqslant \omega^c_{\mathrm{mod},j} \tag{7}$$

$$\omega^c_{\mathrm{mod},j} = \nu_{\mathrm{mod},j}\{6\pi^2(\xi_1 N_1 + \xi_2 N_2)\}^{1/3} \tag{8}$$

$$\nu_{\mathrm{mod},j} = \xi_1 \nu_1 + \xi_2 \nu_2 \tag{9}$$

where the weighting factor ξ is simply a percentage of the composition of each material in the unit volume, mathematically expressed as

$$\xi_1 = \frac{\frac{N_1}{N_2} M_1}{\frac{N_1}{N_2} M_1 + M_1} \tag{10}$$

where M is the atomic mass. This approximation introduces high frequency phonons that are available in the vibrational spectrum in side 2 but not side 1 into the incident heat flux. The JFDMM increases the prediction of h_{BD} by a factor that is proportional to the side 2 vibrational spectrum, giving an approximation for inelastic scattering. The transmission coefficient for the JFDMM is still assumed to be calculated with Eq. (5); note that this relaxes the assumption of detailed balance since the JFDMM assumes a modified phonon flux.

Figure 1 compares the predictions from the DMM, PRL, and JFDMM to experimental TTR data taken on several different material systems over a wide range of temperatures. This figure compares predictive trends to data on (a) Pt/AlN (Hopkins et al.) [17], (b) Pt/Al_2O_3 (Hopkins et al.) [17], (c) Au/diamond (Stoner and Maris) [14], (d) Bi/H/diamond (Lyeo and Cahill) [16], and (e) Pb/diamond and Pb/H/diamond (Lyeo and Cahill) [16]. The model calculations use elastic constants to calculate phonon velocities and material properties to calculate the cutoff frequencies [19]. Note that the models cannot distinguish between different deposition or interface conditions [20], so the predictions by the models on the hydrogen terminated and non-hydrogen-terminated substrates are the same. In Fig. 1, the DMM is represented by the solid line, the PRL is represented by the dotted line, and the JFDMM is represented by the dashed line. Note that the JFDMM predicts a closer value and better temperature dependent trend to the experimental data than the DMM, and in most cases the PRL. Since the DMM and PRL both assume elastic scattering of frequencies only up to the side 1 cutoff frequency, these models share the same trend with temperature. The JFDMM, however, shows a different temperature dependent trend that is more in line with the experimental data since it assumes phonons with frequencies higher than the cutoff frequency in side 1 can participate in h_{BD}. These data represent material systems that show some evidence of inelastic scattering at these temperatures.

Inelastic Phonon Radiation Limit

Although the JFDMM shows improvement in h_{BD} predictions in the event that inelastic phonon scattering dominates interfacial transport, this method makes necessary assumptions about phonon transport that deserve further attention. The main assumption of the JFDMM is that a fraction of the available phonon states in the substrate are present in the film. In actuality, the atoms around the interface are vibrating at joint modes by Newton's law of motion [21]. The maximum allowable frequency for these joint modes is

the substrate cutoff frequency. However, dampening of these modes will occur due to the differing interatomic forces of the film and substrate. This prevents the joint modes from oscillating at certain frequencies. This continuum phenomenon is paralleled quantum mechanically in the JFDMM through the weighted average of two materials' phonon states in the incident flux. The weighing factor, ξ, reflects the dampening of the substrate modes, and is used to enhance the incident phonon flux to take into account the joint vibrations that are allowed after dampening effects. However, without computationally expensive computer simulations or a rigorous theoretical treatment, this weighting factor cannot be explicitly determined for every phonon mode, and therefore should be viewed as an estimation of the joint modes participating in h_{BD}. That being said, the JFDMM can be viewed as a starting point for estimating the maximum h_{BD} due to inelastic scattering.

Consider atoms vibrating at joint modes around the interface with no dampening effects. Therefore, these atoms can vibrate at all allowable frequencies up to the maximum allowed frequency in the substrate. Atoms on side 1 and side 2 will be coupled in joint vibrational modes with frequencies up to the cutoff frequency on side 2. This is paralleled in the quantum treatment by forcing $\xi_1=0$ and $\xi_2=1$, which conceptually is treating h_{BD} as a function of the incident phonon flux from side 2 transmitted into side 1. This simplifies Eqs. (7)–(9) to $D_{\mathrm{mod},j}=D_{2,j}$, $\omega^c_{\mathrm{mod},j}=\omega^c_{2,j}$, and $\nu_{\mathrm{mod},j}=\nu_{2,j}$, respectively, and redefines Eq. (4) in terms of the flux transmitted from side 2 to side 1, given as

$$h_{BD}^{\mathrm{inel}}=\frac{1}{4}\sum_j \nu_{2,j}\int_0^{\omega^c_{2,j}} \alpha_2^{\mathrm{inel}}(T)\hbar\omega D_{2,j}(\omega)\frac{\partial n(\omega,T)}{\partial T}d\omega \qquad (11)$$

From the nature of diffuse scattering, the inelastic transmission probability is $\alpha_2^{\mathrm{inel}}(T)=1-\alpha_1^{\mathrm{inel}}(T)$, which is different from the elastic transmission probability calculated with Eq. (5). Equation (11) allows for the possibility of higher frequency phonons that do not exist in the film to participate in h_{BD}. Without knowledge of the explicit temperature dependence of α_2, h_{BD} cannot be calculated. However, examining Eq. (11) along with experimental data can give important understanding of the role of inelastic phonon scattering in thermal boundary conductance.

Consider the case where all available substrate phonons are participating in h_{BD}. In this case, the probability that a phonon on side 2 is inelastically transmitted (i.e., breaks down into lower frequency phonons and transmitted into side 1) is 1. By letting $\alpha_2=1$, Eq. (11) becomes an expression for the largest allowable thermal boundary conductance due to inelastic scattering, or an inelastic phonon radiation limit (IPRL), expressed as

$$h_{BD}^{\mathrm{IPRL}}=\frac{1}{4}\sum_j \nu_{2,j}\int_0^{\omega^c_{2,j}} \hbar\omega D_{2,j}(\omega)\frac{\partial n(\omega,T)}{\partial T}d\omega \qquad (12)$$

The IPRL assumes that all side 2 phonons are transmitted into side 1, and does not explicitly take into account elastic or inelastic scattering processes. However, by allowing all frequencies of phonons in side 2 to transmit energy into side 1, which has the lower cutoff frequency, inelastic scattering is implied. Note that in this limit, similar to the JFDMM, which also takes into account some inelastic scattering, the assumption of equilibrium is relaxed and therefore the principle of detailed balance is not enforced. Also, in the case of an interface in a homogeneous material (i.e., an "imaginary" interface between two of the same materials), the IPRL does not impose any unphysical interface resistance and gives the same thermal flux across an imaginary interface in a homogeneous material as that predicted by the Fourier law. The other models discussed thus far require accurate knowledge of interface transmission probability and the use of a diffusion-transmission interface correction [22] to relax to flux predicted by the Fourier law ensuring thermal flux continuity.

Equation (12) is solely dependent on the acoustic properties of side 2, so in the IPRL, h_{BD} on any film/substrate system only depends on the stiffer material. This is apparent in Figs. 2 and 3, which compare the temperature dependent h_{BD} data from Fig. 1 to their respective IPRL and PRL calculations. The experimental data are graphed on the same plot as their PRL calculations. The IPRL calculations are shown in the lower plots of the figures since the values of the IPRL are orders of magnitude greater than the data and the PRL. However, the separate plots allow for easy comparisons of temperature trends between the models and the data.

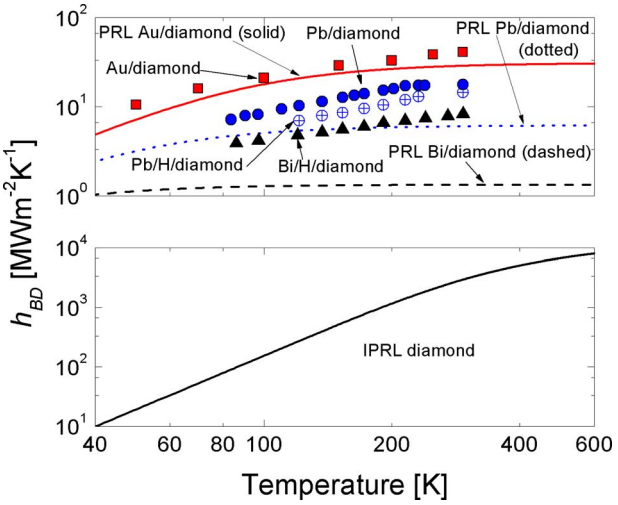

Fig. 2 (Top) Experimental measurements of h_{BD} for various interfaces (see Fig. 1) compared to their corresponding PRL. The PRL predicts a constant h_{BD} at temperatures above the Debye temperature of the lower Debye temperature material. (Bottom) Inelastic phonon radiation limit for the four material systems in the top graph. The IPRL shows a linear increase over a temperature range of 100–400 K, the same trend that is shown in the experimental data. Note, however, that the slope of the linear increase in the IPRL is much greater than the slope of the linear increase in the data.

The IPRL calculations for the three material systems in Fig. 2 are all identical, since the IPRL is only dependent on the higher

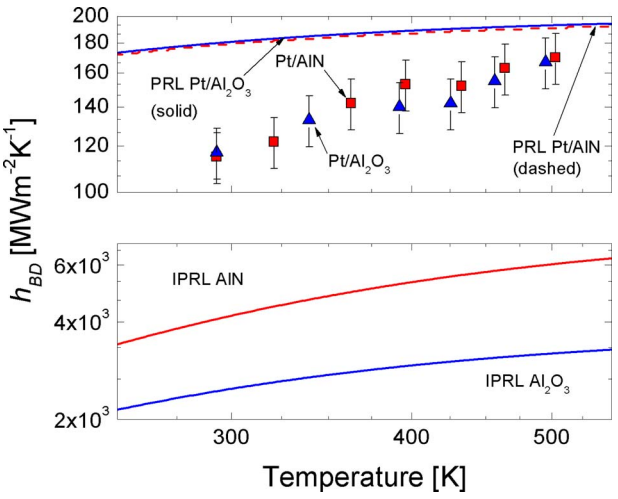

Fig. 3 (Top) Experimental measurements of h_{BD} for Pt/Al_2O_3 and Pt/AlN (see Fig. 1) compared to their corresponding PRL. (Bottom) Inelastic phonon radiation limit for the two material systems in the top graph. The increase in h_{BD} over the temperature range of interest is greater in the IPRL than in the slope of the linear increase in the data, which is greater than the increase in the PRL.

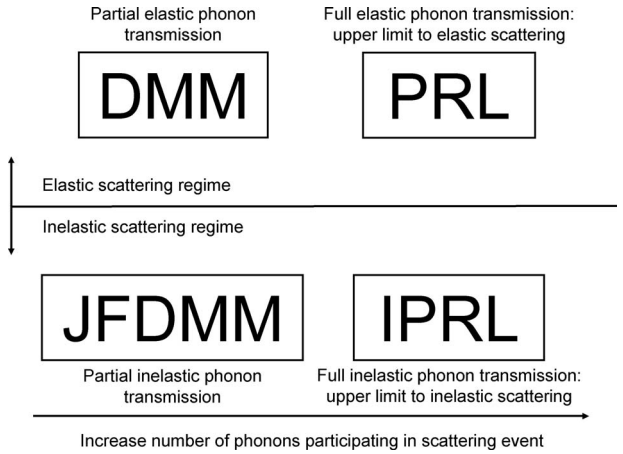

Fig. 4 Regime map of thermal boundary conductance models that takes into account various degrees of elastic and inelastic diffuse phonon scattering. The DMM and PRL, which take into account varying degrees of elastic scattering, are paralleled with the JFDMM and IPRL, which take into account varying degrees of inelastic scattering.

Debye temperature material (side 2). The PRL, on the other hand, depends on the cutoff frequency of the lower Debye temperature material (side 1), so therefore is specific for each film/substrate material system. In all cases, the IPRL is greater than the PRL, which is intuitive since the PRL assumes that only a certain fraction (up to the film cutoff frequency) of substrate phonons are participating in h_{BD} where the IPRL assumes that all available substrate phonons can participate in h_{BD}. In addition, notice that the PRL predicts h_{BD} as a constant value above the film's Debye temperature (similar to the DMM), where the IPRL predicts a linear change of h_{BD} with temperature, similar to the trends in the experimental data. In all cases, the linear change in the IPRL is much greater than the linear change in the data. Figure 3 shows the same calculations as Fig. 2 for the Pt/Al_2O_3 and Pt/AlN data. Note that the IRPL calculations for AlN and Al_2O_3 are vastly different (bottom), yet the experimental data and PRL calculations for the two samples are nearly identical (top). The measured Debye temperatures for AlN and Al_2O_3 are nearly identical, which would mean they have similar maximum cutoff frequencies. However, with a Debye approximation, the calculations of the cutoff frequencies do not match. This could be a result of assuming that these solids can be treated as Debye solids, which may not be completely accurate for complex dielectrics such as AlN or Al_2O_3. However, for the purpose of this analysis, the Debye solid is assumed for all materials since it allows for a simple calculation to elucidate important physics in interfacial phonon scattering processes.

Figure 4 shows a regime map of the four different models for thermal boundary conductance driven by diffuse phonon scattering. The DMM, which takes into account partial phonon transmissivity, is the elastic version of the JFDMM, which takes into account partial phonon transmissivity during inelastic scattering. The upper limits to the DMM and JFDMM models are the PRL and the IPRL, respectively, which assume a phonon transmissivity of unity during elastic and inelastic interfacial phonon scattering, respectively.

Relative Contributions of Inelastic and Elastic Phonon Scattering

From the trends in the IPRL as compared to the PRL and experimental data, the relative contributions of elastic and inelastic scattering can be examined. Above the film's Debye temperature, it is apparent that contributions from elastic scattering will result in a constant h_{BD}. However, inelastic scattering events will drive the linear trend in h_{BD}. Therefore, the total thermal boundary conductance in the classical limit ($T > \theta_D$) will be a blend of both the constant elastic and temperature dependent inelastic phonon scattering contributions, which can be mathematically expressed as

$$h_{BD}(T) = h_{BD}^{\text{el}} + h_{BD}^{\text{inel}}(T) \tag{13}$$

where the superscripts el and inel denote the elastic and inelastic contributions to h_{BD}. This is similar to the phenomenological observation by Stevens et al. [10] based on MD simulations. Equation (13) separates the elastic and inelastic contributions to h_{BD} by assuming that these two energy transfer mechanisms can be treated as two thermal pathways in parallel. Assuming that the elastic and inelastic scattering contributions to h_{BD} can be separated is valid since in acoustically mismatched materials such as those of interest in this work, the number of phonons at any available frequency, ω, in side 1 is much greater than the number of phonons at that same frequency ω in side 2, so phonons of frequencies ω in the side 1 vibrational spectrum can participate in both elastic and inelastic scattering events.

Since the PRL and the IPRL represent the upper limit to elastic and inelastic scattering, it is expected that the elastic and inelastic contributions to h_{BD} will be some fraction of the PRL and IPRL, respectively. Therefore, Eq. (13) can be written more explicitly as

$$h_{BD}(T) = Ah_{BD}^{\text{PRL}} + B(T)h_{BD}^{\text{IPRL}}(T) \tag{14}$$

Where h_{BD}^{PRL} is the PRL and $h_{BD}^{\text{IPRL}}(T)$ is calculated by Eq. (12). The coefficients A and $B(T)$ are coefficients representing the fraction of the maximum possible conductance due to each scattering process and will be determined from the experimental data in the next section. Although A can be estimated using Eq. (5) so that $A = 1 - \alpha_1 = \alpha_2$ and $h_{BD}^{\text{el}} = Ah_{BD}^{\text{PRL}} = [1 - \alpha_1]h_{BD}^{\text{PRL}}$ since only elastic scattering is dealt with in this case, the fundamental assumptions driving the evaluation of α are flawed, even in the elastic limit [23]. For example, in calculating Eq. (5), equilibrium is assumed (principle of detailed balance) although thermal transport is inherently a nonequilibrium process. Also, in the limit that both materials adjacent to the interface are the same, Eq. (5) becomes 50%. However, in this case, since there is no difference in the acoustic properties, phonon transmission should be 100%.

The temperature dependency of the inelastic phonon transmission coefficient, $B(T)$, arises from the fact that as temperature increases, there are proportionately more substrate phonons available to break down and scatter with lower frequency side 1 phonons. This temperature dependency is apparent from the differing linear slopes of the experimental data and the IPRL over the temperature range of interest. Therefore, Eq. (11) can be rewritten as

$$h_{BD}^{\text{inel}} = \frac{1}{4}\sum_j \nu_{2,j} \int_0^{\omega_{2,j}^c} \alpha_2^{\text{inel}}(T)\hbar\omega D_{2,j}(\omega)\frac{\partial n(\omega,T)}{\partial T}d\omega = B(T)h_{BD}^{\text{IPRL}} \tag{15}$$

where $\alpha_2^{\text{inel}}(T) = B(T)$. It is apparent in the data in Figs. 2 and 3 that the temperature dependency will be some function of the temperature dependencies of the phonon populations of both side 1 and side 2. The JFDMM takes this into account by considering a weighted average of the phonon populations of the two sides. However, this correction results in a temperature independent constant that enhances α_1, and a temperature dependent transmission coefficient should be considered to understand the relative effects of inelastic scattering. Through the principle of detailed balance invoked on the incoming phonon fluxes from sides 1 and 2, Dames and Chen [9] developed a temperature dependent transmission coefficient based on the changes of the phonon population of the two sides, given by

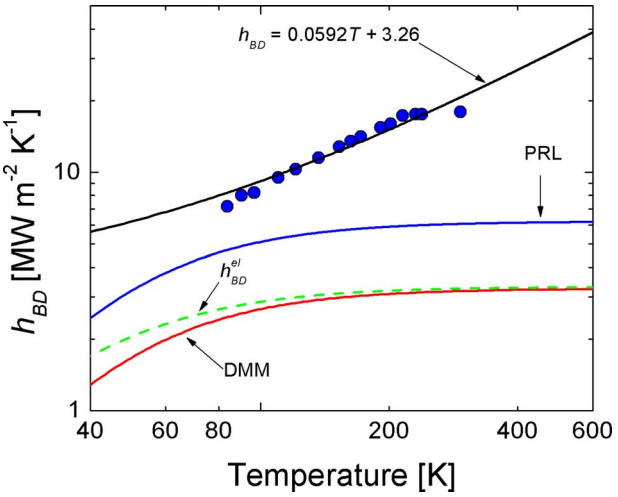

Fig. 5 Measured h_{BD} on Pb/diamond with best fit line extrapolated to determine the y-intercept at 3.26 MW m^{-2} K^{-1}, which is assumed as the elastic contribution to h_{BD} in the classical limit. This value is less than the prediction of the PRL, as expected, but agrees well with the predictions from the DMM, validating the transmission coefficient calculations in the DMM for a Pb/diamond interface.

$$\alpha_1^{\text{inel}}(T) = \frac{\sum_j \nu_{2,j} U_{2,j}(T)}{\sum_j \nu_{1,j} U_{1,j}(T) + \sum_j \nu_{2,j} U_{2,j}(T)} \tag{16}$$

where U is the internal energy of the phonon system. Although Eq. (16) gives the correct temperature dependent trend assuming that all phonon frequencies in each material available at any given temperature participate equally to energy transmission, it does not differentiate between inelastic and elastic contributions nor does it take into account the relative contributions from each phonon frequency (i.e., it assumes that all phonon frequencies have an equal probability of participating in phonon scattering events). However, there is some intrinsic frequency dependence on the transmission coefficient, which is contained in the temperature dependence of the experimental data and not contained in the assumptions of Eq. (16).

In order to determine the relative contributions from elastic and inelastic scattering, the coefficients A and $B(T)$ must be examined in greater detail, which can be accomplished by examining h_{BD} data clearly dominated by inelastic scattering. In this analysis, only temperatures in the classical limit of the metal films will be considered (i.e., temperatures above the softer material's Debye temperature). In this limit the data show the linear trend associated with inelastic scattering; however, a fraction of this h_{BD} is expected to be associated with elastic scattering, which is expected to be constant.

To determine h_{BD}^{el}, the linear fit to the data was extended to the y-axis to find the y-intercept, which is taken as the contribution of elastic scattering in the classical limit. The linear fit of the Pb/diamond data compared to h_{BD}^{PRL}, h_{BD}^{el}, and h_{BD}^{DMM} is shown in Fig. 5. The y-intercept is h_{BD}^{el}=3.26 MW m^{-2} K^{-1} where h_{BD}^{PRL} =6.17 MW m^{-2} K^{-1}. As expected, h_{BD}^{PRL} is greater than h_{BD}^{el} determined from experimental data, since not all substrate phonons will be participating in conductance. Comparing these two values yields A=0.53. In this limit, h_{BD}^{DMM}=3.32 MW m^{-2} K^{-1}, which is in excellent agreement with h_{BD}^{el}, indicating that the DMM predicts the elastic contributions to h_{BD} at the heavily mismatched Pb/diamond interface well. Table 2 compares values of h_{BD}^{el} (determined from the y-intercept), h_{BD}^{DMM}, h_{BD}^{PRL}, and the coefficient A for six samples in the classical limit. Also listed in Table 2 is the ratio of Debye temperatures of the materials comprising side 1 and side 2 for each interface. This ratio quantifies the degree of acoustic mismatch of each interface—the smaller the ratio, the greater the mismatch between phonon spectra. Note that the agreement between h_{BD}^{el} and h_{BD}^{DMM} is much better for the heavily mismatched samples than for the better matched Pt samples. This is expected since the transmission coefficient calculations become less accurate as the materials become more similar [23]. This indicates that the DMM is a good model for predicting the elastic scattering contribution to thermal boundary conductance, and the transmission coefficient calculated with Eq. (5) becomes more accurate as the adjacent phonon spectra become more dissimilar.

Now that the elastic portion of thermal boundary conductance has been determined, the inelastic contribution can be estimated from the slope of the experimental data. Rearranging Eq. (14), the coefficient representing the transmission of substrate phonons through inelastic scattering can be expressed as

$$B(T) = \frac{h_{BD}(T) - A h_{BD}^{\text{PRL}}}{h_{BD}^{\text{IPRL}}} \tag{17}$$

where $h_{BD}(T)$ is the thermal boundary conductance as a function of temperature determined from the linear fit to the experimental data, and A was determined above. Note that from the discussion of Eq. (15), $B(T)=\alpha_2^{\text{inel}}(T)$. The coefficient $B(T)$ as a function of temperature can be calculated only over the temperature range of the experimental data. However, higher temperature values were determined through a nonlinear regression extrapolation to determine $B(T)$ at all temperatures $T>\theta_D$. Due to the nature of this high temperature extrapolation, above a given temperature the slope of the IPRL decreases to a value that is less than the slope of $h_{BD}(T)$, which causes an unphysical slight linear increase in $B(T)$ resulting in a local minimum. To correct for this unphysical increase in Eq. (17), at temperatures above the local minimum temperature, $B(T)$ is fixed to a constant value of the local minimum. This gives a much more physical trend to $B(T)$ and avoids any error due to the nonlinear extrapolation routine. Figure 6 compares the temperature dependent transmission coefficient that

Table 2 High temperature limits of thermal boundary conductance and the elastic contribution to h_{BD}, the DMM, the PRL, and the predicted h_{BD} based on experimental trends [$h_{BD}(T)$] for six different interfaces. All units are in MW m^{-2} K^{-1}, except A, B, and $\theta_{D,1}/\theta_{D,2}$, which are unitless ratios.

Interface	$\theta_{D,1}/\theta_{D,2}$	h_{BD}^{el}	h_{BD}^{DMM}	h_{BD}^{PRL}	A	B	$h_{BD}(T=\infty)$
Pb/diamond	0.047	3.26	3.31	6.23	0.523	0.00436	58.7
Pb/H/diamond	0.047	1.92	3.31	6.23	0.310	0.00329	41.9
Bi/H/diamond	0.053	2.25	1.32	1.34	1.67	0.00158	22.3
Au/diamond	0.074	16.6	14.4	31.2	0.532	0.00626	96.1
Pt/Al_2O_3	0.21	51.8	130	190	0.261	0.0170	210
Pt/AlN	0.23	51.8	130	190	0.261	0.0280	200

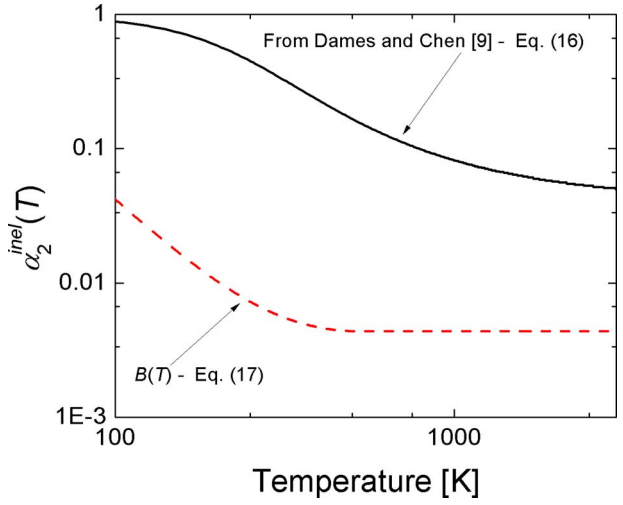

Fig. 6 Comparison of $\alpha_2^{inel}(T)$ determined by $1-\alpha_1^{inel}(T)$ where $\alpha_1^{inel}(T)$ is given by the model derived by Dames and Chen [9] and presented in Eq. (16); and $B(T)$, which is derived in this work and presented in Eq. (17). $B(T)$ decreases to a much lower constant value much more quickly than $\alpha_2^{inel}(T)$ calculated with Eq. (16). The assumption in Eq. (16) is that all phonons of all frequencies have equal probability in transmission, where Eq. (17) is based on experimental data and the IPRL. The smaller phonon transmission of side 2 phonons at higher temperatures could be due to the probability of side 2 phonons breaking down into lower frequency side 1 phonons decreasing as the side 2 phonon frequency increases.

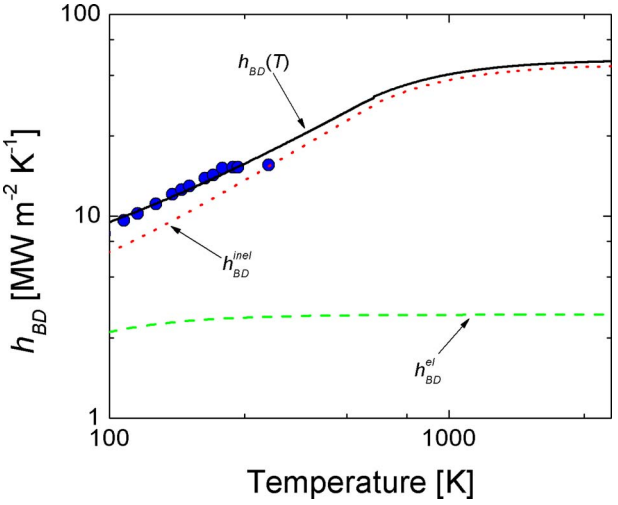

Fig. 7 Inelastic and elastic scattering contributions to h_{BD} of Pb/diamond in the classical limit. The total thermal boundary conductance, $h_{BD}(T)$, shows excellent agreement to the data at low temperatures in the classical limit, and approaches a constant value at higher temperatures that are above the Debye temperature of diamond (or at temperatures that are greater than the Debye temperature of both materials).

takes into account inelastic scattering for side 2 derived by Dames and Chen [9], $\alpha_2^{inel}(T)=1-\alpha_1^{inel}(T)$, where $\alpha_1^{inel}(T)$ is calculated with Eq. (16), to the inelastic transmission coefficient determined from Eq. (17), $B(T)$, for a Pb/diamond interface. $B(T)$ decreases to a much lower constant value much more quickly than $\alpha_2^{inel}(T)$ calculated with Eq. (16). As previously mentioned, Eq. (16) assumes that all phonon frequencies participate equally in transmission and h_{BD}. $B(T)$, however, takes into account the temperature dependent phonon scattering trends in inelastic processes by utilizing the trends encapsulated in the experimental data. The values and trends in $B(T)$ show that as temperature increases and more high frequency phonons become available in side 2 that are not available in side 1 (i.e., the phonon frequencies in side 2 that are above the side 1 cutoff frequency), the transmission of energy from side 2 to side 1 is much less than if assuming all phonon frequencies participate equally in energy transmission as assumed in Eq. (16). This suggests that phonons in side 2 with frequencies much higher than the side 1 cutoff are less likely to participate in inelastic processes than phonons with frequencies that are only slightly higher than the side 1 cutoff. A similar trend was inferred by Hopkins et al. [17], and was attributed to the probability a three-phonon process occurring, which could occur for coupling between a lower frequency side 2 phonon and two side 1 phonons, being higher than the probability of n-phonon processes occurring (where $n>3$), which would have to occur for a higher frequency side 2 phonon to couple with $n-1$ side 1 phonons.

With this, the contributions of elastic and inelastic scattering to h_{BD} were calculated based on experimental data and extended to high temperatures to determine h_{BD} in the classical limit that takes into account inelastic scattering. The inelastic and elastic contributions to h_{BD} for Pb/diamond are shown in Fig. 7, along with $h_{BD}(T)$ calculated from Eq. (14). The high temperature trends follow what is expected when temperatures are driven higher than both materials' Debye temperatures. This same agreement between Eq. (14) and the experimental data and high temperature trends are shown between Eq. (14) and the Bi/diamond, Au/diamond, Pt/Al_2O_3, and Pt/AlN data.

To demonstrate the relative magnitude of inelastic scattering on h_{BD}, the ratio $h_{BD}^{inel}/h_{BD}^{el}$ is plotted versus temperature in the classical regime in Fig. 8 for the six interfaces studied. As expected, the inelastic contribution compared to the elastic contribution to h_{BD} in Pb, Bi, and Au on diamond are more temperature dependent than the relative contribution in the Pt/Al_2O_3 and Pt/AlN samples due to the higher Debye temperature of diamond than Al_2O_3 and AlN. Also, the contribution of inelastic scattering to overall h_{BD} is greater than that of elastic scattering, and the relative contribution of inelastic scattering increases with interface

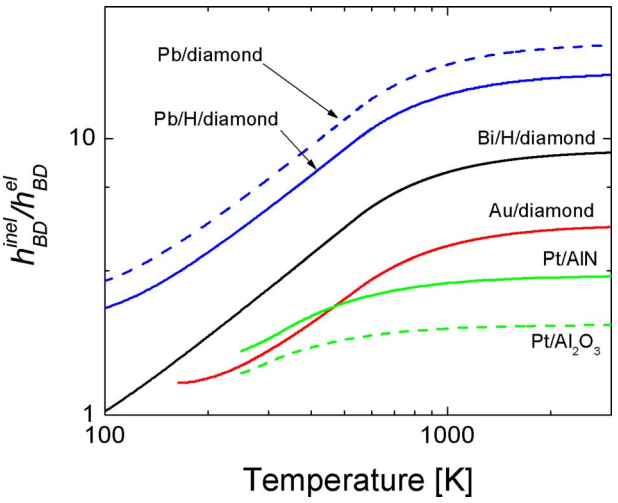

Fig. 8 Relative magnitude of inelastic scattering on h_{BD}. This ratio compares the inelastic contribution to h_{BD} to the elastic contribution as predicted via Eq. (14). The role of inelastic phonon scattering increases as the acoustic mismatch of the film and substrate becomes greater. The range in which h_{BD} should increase linearly with temperature due to inelastic scattering also increases with acoustic mismatch.

acoustic mismatch (i.e., as the film/substrate Debye temperature ratio become smaller). This also leads to the inelastic contribution becoming independent of temperature at higher temperatures in the diamond samples than in the Pt on Al_2O_3 and AlN samples. In fact, the high temperature limit of the Pb, Bi, and Au on diamond samples is not reached until the interface temperature is driven above the melting temperature of the metal, meaning that in nanostructures with Pb, Bi, and Au films adjacent to diamond structures, h_{BD} will continually increase with temperature until melting. Also, in the high temperature limit, as the mismatch between the materials adjacent to the interface grows, the contribution of inelastic phonon scattering to thermal boundary conductance increases.

Conclusions

The accuracy of h_{BD} predictions made using DMM and PRL varies depending on the types of materials comprising the interface. Due to inelastic scattering these models may not be valid at temperatures characteristic of many modern nanodevices and structures since these models do not take into account inelastic phonon scattering. Although the JFDMM provides a simple approximation of the effects of joint vibrational modes on h_{BD} using a Debye approximation, it does not specially examine the contributions due to elastic and inelastic scattering. These contributions can be extracted from the trends and values in the experimental data. To estimate the role of elastic scattering in the classical limit, the y-intercept of the linear trend in the experimental data of h_{BD} as a function of temperature is compared to the PRL in the classical limit. The resulting contribution of elastic scattering in this limit agrees well with the value of h_{BD} predicted by the DMM. This agreement increases with sample mismatch, which validates the DMM as a model to predict the contribution of elastic scattering in heavily mismatched samples. To estimate the role of inelastic scattering in the classical limit, the slope of the experimental data of h_{BD} as a function of temperature is compared to a new model, the IPRL. The IPRL predicts the maximum thermal boundary conductance assuming all substrate phonons of all frequencies are transmitted into the film. The IPRL predictions are compared to the experimental data to effectively determine what percentage of substrate phonons are participating in inelastic scattering beyond those participating in elastic scattering. The role of inelastic scattering to overall h_{BD} is shown to outweigh the role of elastic scattering at the interfaces of interest, with an increasing role of inelastic scattering with interfacial acoustic mismatch. The predictions of inelastic scattering show a linear trend at lower temperatures in the classical limit and predict a constant h_{BD} at higher temperatures, giving an upper limit to thermal boundary conductance that takes into account both elastic and inelastic scattering.

Acknowledgment

The authors would like to thank Rich Salaway, Jennifer Simmons, John Duda, Justin Smoyer, and Tom Randolph of the Microscale Heat Transfer Laboratory at U.Va. and Thomas Beechem and Samuel Graham of GA Tech for insightful discussions; Robert Stevens at RIT for insight into molecular dynamics simulations and vibrational energy transport; and Jongsoo Yoon of the Physics Department at U.Va. for critical reading of the manuscript. P.E.H. would like to thank the NSF graduate research fellowship program for funding. The authors gratefully acknowledge financial support from the Office of Naval Research MURI program, Grant No. N00014-07-1-0723.

Nomenclature

A = coefficient relating to elastic scattering in Eq. (14)
B = coefficient relating to inelastic scattering in Eq. (14)
D = phonon density of states per unit volume, s m^{-3}
$\hbar$ = Planck's constant divided by 2π, J s
h_{BD} = thermal boundary conductance, W m^{-2} K^{-1}
M = molecular weight, g mol^{-1}
N = phonon number density, m^{-3}
N_A = Avogadro's number, mol^{-1}
n = Bose–Einstein distribution function
$\dot{q}$ = heat flux, W m^{-2}
T = temperature, K
U = internal energy, J m^{-3}
ν = phonon group velocity, m s^{-1}

Greek Symbols

α = interfacial transmission probability
ϕ = incident angle
ω = angular frequency, s^{-1}
ξ = weighting factor in JFDMM

Subscripts

1 = film, or lower Debye temperature material, or softer material
2 = substrate, or higher Debye temperature material, or stiffer material
j = phonon mode (polarization)
L = longitudinal
mod = modified
T = transverse

Superscripts

c = cutoff
DMM = calculated with the diffuse mismatch model
el = elastic
inel = inelastic
IPRL = calculated with the inelastic phonon radiation limit
PRL = calculated with the phonon radiation limit

References

[1] Cahill, D. G., Ford, W. K., Goodson, K. E., Mahan, G. D., Majumdar, A., Maris, H. J., Merlin, R., and Phillpot, S. R., 2003, "Nanoscale Thermal Transport," J. Appl. Phys., **93**, pp. 793–818.
[2] Little, W. A., 1959, "The Transport of Heat Between Dissimilar Solids at Low Temperatures," Can. J. Phys., **37**, pp. 334–349.
[3] Vincenti, W. G., and Kruger, C. H., 2002, *Introduction to Physical Gas Dynamics*, Krieger, Malabar, FL.
[4] Majumdar, A., 1993, "Microscale Heat Conduction in Dielectric Thin Films," ASME J. Heat Transfer, **115**, pp. 7–16.
[5] Swartz, E. T., and Pohl, R. O., 1987, "Thermal Resistances at Interfaces," Appl. Phys. Lett., **51**, pp. 2200–2202.
[6] Swartz, E. T., and Pohl, R. O., 1989, "Thermal Boundary Resistance," Rev. Mod. Phys., **61**, pp. 605–668.
[7] Cahill, D. G., Bullen, A., and Lee, S.-M., 2000, "Interface Thermal Conductance and the Thermal Conductivity of Multilayer Thin Films," High Temp. - High Press., **32**, pp. 135–142.
[8] Kittel, C., 1996, *Introduction to Solid State Physics*, Wiley, New York.
[9] Dames, C., and Chen, G., 2004, "Theoretical Phonon Thermal Conductivity of Si/Ge Superlattice Nanowires," J. Appl. Phys., **95**, pp. 682–693.
[10] Stevens, R. J., Zhigilei, L. V., and Norris, P. M., 2007, "Effects of Temperature and Disorder on Thermal Boundary Conductance at Solid-Solid Interfaces: Nonequilibrium Molecular Dynamics Simulations," Int. J. Heat Mass Transfer, **50**, pp. 3977–3989.
[11] Schelling, P. K., Phillpot, S. R., and Keblinski, P., 2002, "Phonon Wave-Packet Dynamics at Semiconductor Interfaces by Molecular Dynamics Simulation," Appl. Phys. Lett., **80**, pp. 2484–2486.
[12] Stevens, R. J., Smith, A. N., and Norris, P. M., 2005, "Measurement of Thermal Boundary Conductance of a Series of Metal-Dielectric Interfaces by the Transient Thermoreflectance Technique," ASME J. Heat Transfer, **127**, pp. 315–322.
[13] Costescu, R. M., Wall, M. A., and Cahill, D. G., 2003, "Thermal Conductance Of Epitaxial Interfaces," Phys. Rev. B, **67**, p. 054302.
[14] Stoner, R. J., and Maris, H. J., 1993, "Kapitza Conductance and Heat Flow Between Solids at Temperatures From 50 to 300 K," Phys. Rev. B, **48**, pp. 16373–16387.
[15] Snyder, N. S., 1970, "Heat Transport Through Helium II: Kapitza Conductance," Cryogenics, **10**, pp. 89–95.
[16] Lyeo, H.-K., and Cahill, D. G., 2006, "Thermal Conductance of Interfaces

Between Highly Dissimilar Materials," Phys. Rev. B, **73**, p. 144301.
[17] Hopkins, P. E., Stevens, R. J., and Norris, P. M., 2008, "Influence of Inelastic Scattering at Metal-Dielectric Interfaces," ASME J. Heat Transfer, **130**, p. 022401.
[18] Hopkins, P. E., and Norris, P. M., 2007, "Effects of Joint Vibrational States on Thermal Boundary Conductance," Nanoscale Microscale Thermophys. Eng., **11**, pp. 247–257.
[19] Gray, D. E., 1972, *American Institute of Physics Handbook*, McGraw-Hill, New York.
[20] Hopkins, P. E., Norris, P. M., Stevens, R. J., Beechem, T., and Graham, S., 2008, "Influence of Interfacial Mixing on Thermal Boundary Conductance Across a Chromium/Silicon Interface," ASME J. Heat Transfer, **130**, p. 062402.
[21] Huberman, M. L., and Overhauser, A. W., 1994, "Electronic Kapitza Conductance at a Diamond-Pb Interface," Phys. Rev. B, **50**, pp. 2865–2873.
[22] Chen, G., 2003, "Diffusion-Transmission Interface Condition for Electron and Phonon Transport," Appl. Phys. Lett., **82**, pp. 991–993.
[23] Chen, G., 2005, *Nanoscale Energy Transport and Conversion: A Parallel Treatment of Electrons, Molecules, Phonons, and Photons*, Oxford University Press, New York.
[24] Fugate, R. Q., and Swenson, C. A., 1969, "Specific Heat of Al_2O_3 From 2 to 25 K," J. Appl. Phys., **40**, pp. 3034–3036.
[25] Levinshtein, M. E., Rumyantsev, S. L., and Shur, M. S., 2001, *Properties of Advanced Semiconductor Materials: GaN, AlN, InN, BN, SiC, SiGe*, Wiley-Interscience, New York.

Turbulent Rotating Rayleigh–Benard Convection: Spatiotemporal and Statistical Study

A. Husain

M. F. Baig[1]
e-mail: drmfbaig@yahoo.co.uk

H. Varshney

Department of Mechanical Engineering,
Aligarh Muslim University,
Aligarh 202002, India

The present study involves a 3D numerical investigation of rotating Rayleigh–Benard convection in a large aspect-ratio (8:8:1) rectangular enclosure. The rectangular cavity is rotated about a vertical axis passing through the center of the cavity. The governing equations of mass, momentum, and energy for a frame rotating with the enclosure, subject to generalized Boussinesq approximation applied to the body and centrifugal force terms, have been solved on a collocated grid using a semi-implicit finite difference technique. The simulations have been carried out for liquid metal flows having a fixed Prandtl number $Pr=0.01$ and fixed Rayleigh number $Ra=10^7$ while rotational Rayleigh number Ra_w and Taylor number Ta are varied through nondimensional rotation rate (Ω) ranging from 0 to 10^4. Generation of large-scale structures is observed at low-rotation ($\Omega=10$) rates though at higher-rotation rates ($\Omega=10^4$) the increase in magnitude of Coriolis forces leads to redistribution of buoyancy-induced vertical kinetic energy to horizontal kinetic energy. This brings about inhibition of vertical fluid transport, thereby leading to reduced vertical heat transfer. The magnitude of rms velocities remains unaffected with an increase in Coriolis forces from $\Omega=0$ to 10^4. An increase in rotational buoyancy (Ra_w), at constant rotation rate ($\Omega=10^4$), on variation in Ra_w/Ta from 10^{-3} to 10^{-2} results in enhanced breakup of large-scale structures with a consequent decrease in rms velocities but with negligible reduction in vertical heat transport.
[DOI: 10.1115/1.2993545]

Keywords: rotating convection, Coriolis forces, rotational buoyancy, low-Prandtl fluid, statistical properties

1 Introduction

Thermal convection in a horizontal fluid layer heated from below and cooled at the top finds wide application in the study of geophysical and astrophysical flows besides engineering applications in the field of crystal growth and numerous metallurgical processes. Rotation makes the flow complex and can exhibit profound influences on the convection when the different forces, viz., thermal buoyancy, Coriolis, and centrifugal, are of comparable magnitude. Low-to-moderate rotation rates have been found to stabilize the fluid layers and even its gradients and subsequently delay the onset of convection when the rotation axis is aligned with the gravity axis. But at higher-rotation rates, Nusselt number Nu surpasses the nonrotating heat transport value [1].

Many numerical and experimental works have been done until date to study the rotating Rayleigh–Benard convection (RBC) or stably stratified rotating convection with reference to spatiotemporal dynamics and heat transfer analysis. Homsy and Hudson [2] analytically studied convection in a cylinder of radius a and height $2h$ rotating about its vertical axis with a constant angular velocity. The cylinder was heated from above and was filled with homogeneous Newtonian fluid. They applied generalized Boussinesq approximation and found that horizontal Ekman layers control the flow characteristics such that the heat transfer can be considerably augmented by rotation. Elder [3] numerically simulated the RBC (at $Ra \leq 10^5$) of a horizontal fluid layer heated suddenly from below using finite difference technique. Spatial means were taken by him over the horizontal planes in order to determine the structure of mean-temperature and velocity fields. The mean-temperature field revealed that gradients were significantly larger near the horizontal boundaries while changes across the bulk of the flow were small.

Rossby [4] carried out an experimental study of Benard convection with or without rotation on a uniformly heated fluid layer of water and mercury in two separate cases. The layer of mercury showed quite different characteristics and had finite-amplitude instability for $0 < Ta < 1.8 \times 10^4$. Moreover, he found that mercury having lower-Prandtl number yielded lower Nusselt number compared with water. Lee and Lin [5] numerically showed 3D mixed convection of air assuming generalized Boussinesq approximation in a differentially heated cubical cavity with rotation about a vertical axis aligned parallel to the gravity. Convection was studied for the cases when rotational buoyancy (from centrifugal effects) was greater than the thermal buoyancy as well as when Coriolis force was greater than the thermal buoyancy.

Ker and Lin [6] performed both numerical and experimental studies for the stability of rotating flow using the same configuration as above with a difference that the cubical box was inclined at various angles. Jullien et al. [7] studied the turbulent RBC with Boussinesq approximation under the influence of rapid rotation. They assumed periodicity in the horizontal directions to approximate an infinite horizontal extent and examined the effect of both no-slip and stress-free boundary conditions on the horizontal bounding planes. In particular, they found that Nu scaling with Rayleigh number exhibited $Nu \propto Ra^{2/7}$ despite the presence of rotation.

[1]Corresponding author.

Contributed by the Heat Transfer Division of ASME for publication in the JOURNAL OF HEAT TRANSFER. Manuscript received December 3, 2007; final manuscript received August 7, 2008; published online December 12, 2008. Review conducted by Gautam Biswas.

 Copyright © 2009 by ASME

Kerr and Herring [8] carried out direct numerical simulations (DNSs) of Prandtl number dependence of Nusselt number for a convection cell of aspect-ratio $8\times8\times2$. They applied no-slip conditions on the upper and lower boundaries while free-slip condition was imposed on the insulated side-walls. They assumed Prandtl number Pr=0.07, 0.3, and 7.0 for three different cases under simulation. They concluded that there are significant changes in structure between the smallest and the largest Pr cases. At low-Prandtl number they found the flow to be dominated by thermal diffusivity and large-scale flow, whereas at high-Prandtl number individual plumes dominate the flow.

Vorobieff and Ecke [9] studied the flow structures and statistics at different depths in a fully enclosed cylindrical Rayleigh–Benard convection cell. The dimensionless rotation rate varied from 0 to 5×10^4 at $\mathrm{Ra}=3.2\times10^8$ while Rossby number Ro varied from ∞ to 0.06. They employed particle image velocimetry (PIV) to acquire instantaneous horizontal sections of velocity field and presented results characterizing cyclonic and anticyclonic vortices in terms of the eigenvalues of the velocity gradient tensor. For $\mathrm{Ro}\gg1$, the flow is dominated by sheets of thermal plumes originating from the top surface. Cold material is ejected from the top thermal boundary layer in a sheet plunging downward into the bulk of the liquid. As Ro approaches unity, the flow character changes significantly. Cyclonic vortical structures become the most prominent flow features in the flow near the top of the cell for $\mathrm{Ro}\sim1$. Finally when Ro decreases below unity, the flow pattern changes again, leading to the formation of anticyclonic structures with counterclockwise rotation.

To the best of our knowledge no previous research has studied the statistical properties of rotating RBC at moderately high Ra; hence we would like to analyze the effect of rotation on statistical properties. The main aim of our study is to explore the effect of rotational buoyancy and Coriolis forces on convection of low-Prandtl number (Pr) fluids. The present simulations have been carried out with inclusion of variable density in centrifugal force term. Furthermore, this study reports the dynamics and kinematics of low-Prandtl number rotating convection, an area of research that remains relatively less investigated.

The present work involves a numerical study of three-dimensional rotating convection in a large aspect-ratio (8:8:1) enclosure (see Fig. 1) rotating about a vertical axis passing through its center of gravity. The upper surface of the cavity is kept at lower temperature (T_c) while the lower surface is kept at a higher temperature ($T_c+\Delta T$). The side-walls of the enclosure are kept insulated with no-slip boundary conditions enforced on all the walls. Simulations are performed at different rotation rates assuming generalized Boussinesq approximation for both the gravity and centrifugal force terms [2,5,6]. Effect of rotation on the spatiotemporal dynamics is studied with reference to pattern formation and heat transfer in the cubical cavity. Statistical properties related to second-order moments of various dynamical variables have been computed.

2 Problem Formulation

We have taken a rectangular enclosure of height (H), length (L), and width (B) so that the aspect-ratio $\Gamma=L/H=B/H=8$, as shown in Fig. 1. It is filled with a fluid of kinematic viscosity ν, thermal diffusivity κ, density ρ_o, and coefficient of thermal expansion α. Generalized Boussinesq approximation, i.e., linear variation in density with small temperature difference, has been considered for both body force and centrifugal force terms [10,11], which leads to thermal, rotational (centrifugal), and Coriolis forces acting on the flow equal to $\rho_o g\alpha(T-T_o)$, $-\rho_o\alpha(T-T_o)\Omega_D\times\Omega_D\times\mathbf{r}$, and $-2\rho_o\Omega_D\times\mathbf{V}$, respectively. The mathematical formulation of the problem is carried out by expressing the mass, momentum, and energy equations in rotating frame of reference. Nondimensionalization has been performed by using length scale (H), time scale (H^2/κ), velocity scale (κ/H), pressure scale ($\rho_o\kappa^2/H^2$), temperature scale ($\Theta=(T-T_o)/\Delta T$), and (ν/H^2) scale for rotation rate. The resulting nondimensional equations take the following form.

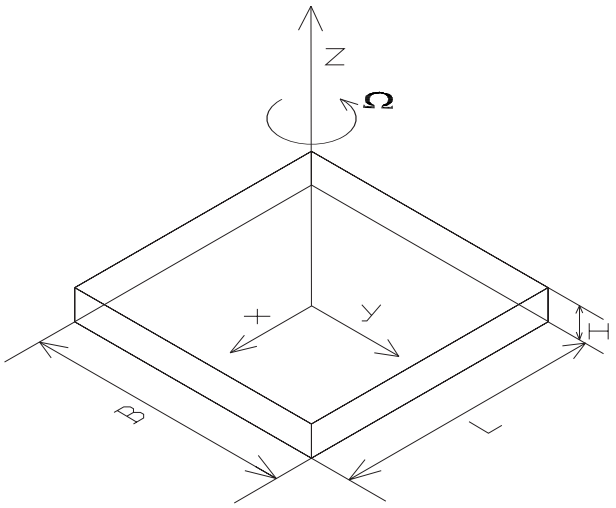

Fig. 1 Schematic of the geometry of the domain

Continuity

$$\frac{\partial u}{\partial x}+\frac{\partial v}{\partial y}+\frac{\partial w}{\partial z}=0 \tag{1}$$

x-momentum

$$\frac{\partial u}{\partial t}=-\frac{\partial p_m}{\partial x}-u\frac{\partial u}{\partial x}-v\frac{\partial u}{\partial y}-w\frac{\partial u}{\partial z}+\mathrm{Pr}\left(\frac{\partial^2u}{\partial x^2}+\frac{\partial^2u}{\partial y^2}+\frac{\partial^2u}{\partial z^2}\right)+2\ \mathrm{Ta}^{0.5}\ v\ \mathrm{Pr}-\mathrm{Ra}_w\ x\ \mathrm{Pr}\ \Theta \tag{2}$$

y-momentum

$$\frac{\partial v}{\partial t}=-\frac{\partial p_m}{\partial y}-u\frac{\partial v}{\partial x}-v\frac{\partial v}{\partial y}-w\frac{\partial v}{\partial z}+\mathrm{Pr}\left(\frac{\partial^2v}{\partial x^2}+\frac{\partial^2v}{\partial y^2}+\frac{\partial^2v}{\partial z^2}\right)-2\ \mathrm{Ta}^{0.5}\ u\ \mathrm{Pr}-\mathrm{Ra}_w\ y\ \mathrm{Pr}\ \Theta \tag{3}$$

z-momentum

$$\frac{\partial w}{\partial t}=-\frac{\partial p_m}{\partial z}-u\frac{\partial w}{\partial x}-v\frac{\partial w}{\partial y}-w\frac{\partial w}{\partial z}+\mathrm{Pr}\left(\frac{\partial^2w}{\partial x^2}+\frac{\partial^2w}{\partial y^2}+\frac{\partial^2w}{\partial z^2}\right)+\mathrm{Ra}\ \mathrm{Pr}\ \Theta \tag{4}$$

Energy

$$\frac{\partial\Theta}{\partial t}=-u\frac{\partial\Theta}{\partial x}-v\frac{\partial\Theta}{\partial y}-w\frac{\partial\Theta}{\partial z}+\left(\frac{\partial^2\Theta}{\partial x^2}+\frac{\partial^2\Theta}{\partial y^2}+\frac{\partial^2\Theta}{\partial z^2}\right) \tag{5}$$

The controlling nondimensional parameters are defined as Rayleigh number, $\mathrm{Ra}=(\alpha g\Delta TH^3)/\kappa\nu$, which is the ratio of thermal buoyancy to viscous forces, Taylor number, $\mathrm{Ta}=(\Omega_D^2H^4)/\nu^2$, which is the ratio of Coriolis to viscous forces, Prandtl number, $\mathrm{Pr}=\nu/\kappa$, which is the ratio of viscous and thermal diffusivities of the working fluid, and rotational Rayleigh number, $\mathrm{Ra}_w=(\alpha(\Omega_D^2H)\Delta TH^3)/\kappa\nu$, which is the ratio of rotational buoyancy (centrifugal) to viscous forces.

2.1 Initial and Boundary Conditions. Initially the fluid is supposed to be in the quiescent state ($u=0$, $v=0$, $w=0$) with respect to the rotating frame of reference at isothermal conditions $T=T_o$, i.e., $\Theta=0$. No-slip conditions for velocity components at the solid boundaries $u=v=w=0$ are enforced.

The thermal boundary conditions are as follows:

$$\partial\Theta/\partial x=0\ \text{ at }\ x=\pm L/2$$

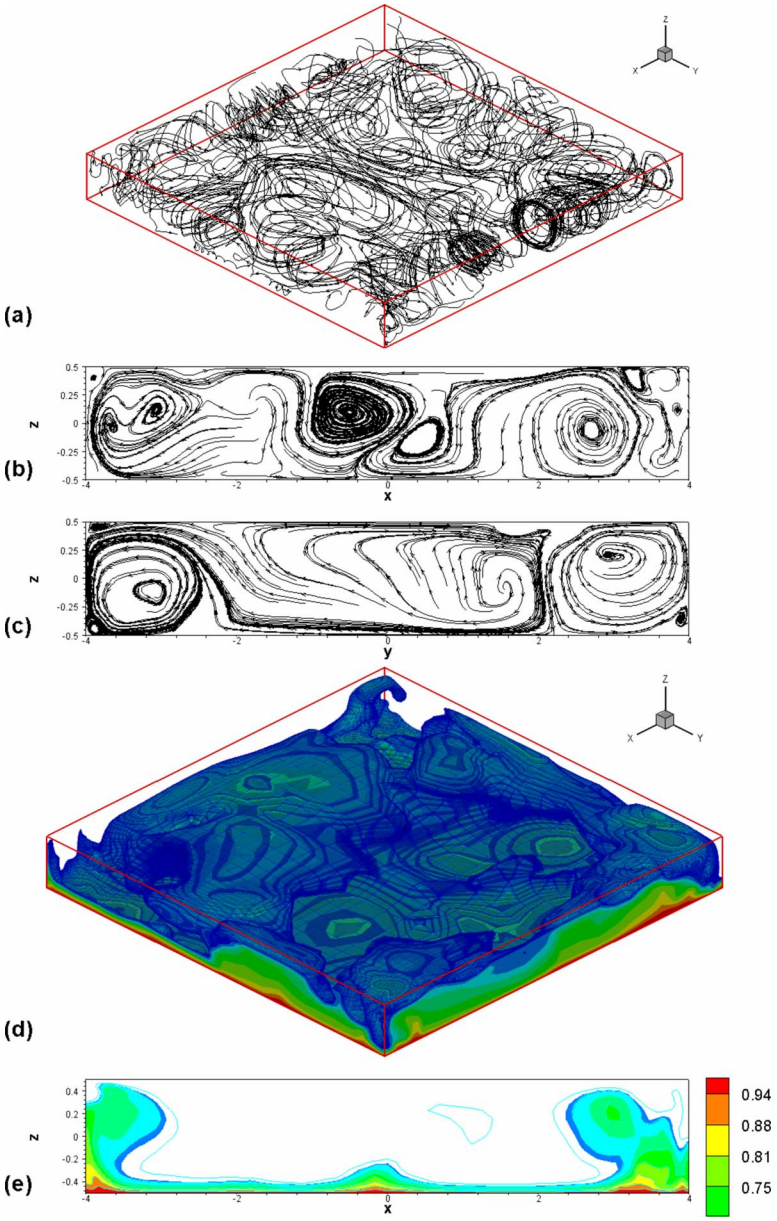

Fig. 2 (*a*) **3D streamtraces,** (*b*) **streamlines at the central *x-z* plane,** (*c*) **streamlines at the central *y-z* plane,** (*d*) **3D isotherms, and** (*e*) **isotherms in the central *x-z* plane at Ra=10^7, Ta=0, and Ra_w=0**

$$\partial\Theta/\partial y = 0 \quad \text{at} \quad y = \pm B/2$$

$$\Theta = 1 \quad \text{at} \quad z = -H/2 \quad \text{and} \quad \Theta = 0 \quad \text{at} \quad z = H/2$$

The space-averaged Nusselt number at both the cold and hot walls has been calculated using the relation

$$\mathrm{Nu} = -\frac{1}{L \times B}\int_{-L/2}^{L/2}\int_{-B/2}^{B/2}\left(\frac{\partial\Theta}{\partial z}\right)dxdy \tag{6}$$

The nonlinear convective terms are discretized using Taylor-series based upwind schemes. First-order accurate upwind scheme is used at points adjacent to the domain boundaries while second-order accurate scheme is used in the interior domain. Viscous diffusion terms and pressure terms present in the momentum and energy equations are discretized using second-order accurate central differencing scheme. Equations (1)–(5) are solved in time using second-order explicit Adam–Bashforth integration scheme. The steps of the numerical scheme can be seen in more detail from Hasan and Baig [12]. In order to verify the numerical scheme we modified the boundary conditions to compare our results with Lee and Lin [5] who studied rotating convection in a differentially heated cubical cavity of unity aspect-ratio. They tabulated the maximum global velocities at certain time instants using a grid of $30\times30\times30$ mesh points. They also presented the evaluation of the average Nusselt number at the hot-wall for Ra $=10^2$, Ta$=10^2$, Pr$=0.7$, and $Ra_w=10^6$. In another simulation they plotted the vertical component of the velocity w and temperature Θ at line $y=0$, $z=0$, and $x=-0.5$ to 0.5 for Ra$=10^6$, Ta$=10^7$, and $Ra_w=10^2$. We tried to reproduce their results using a mesh based on geometric progression from wall until the central plane and then mirroring its image. The mesh point adjacent to the wall is kept at the same distance as in Ref. [5] as the solution is very much dependent on the position of the first point adjacent to the wall. The results obtained are quite close to the one obtained by Lee and Lin [5], and more details of the verification results can be seen from Husain et al. [13].

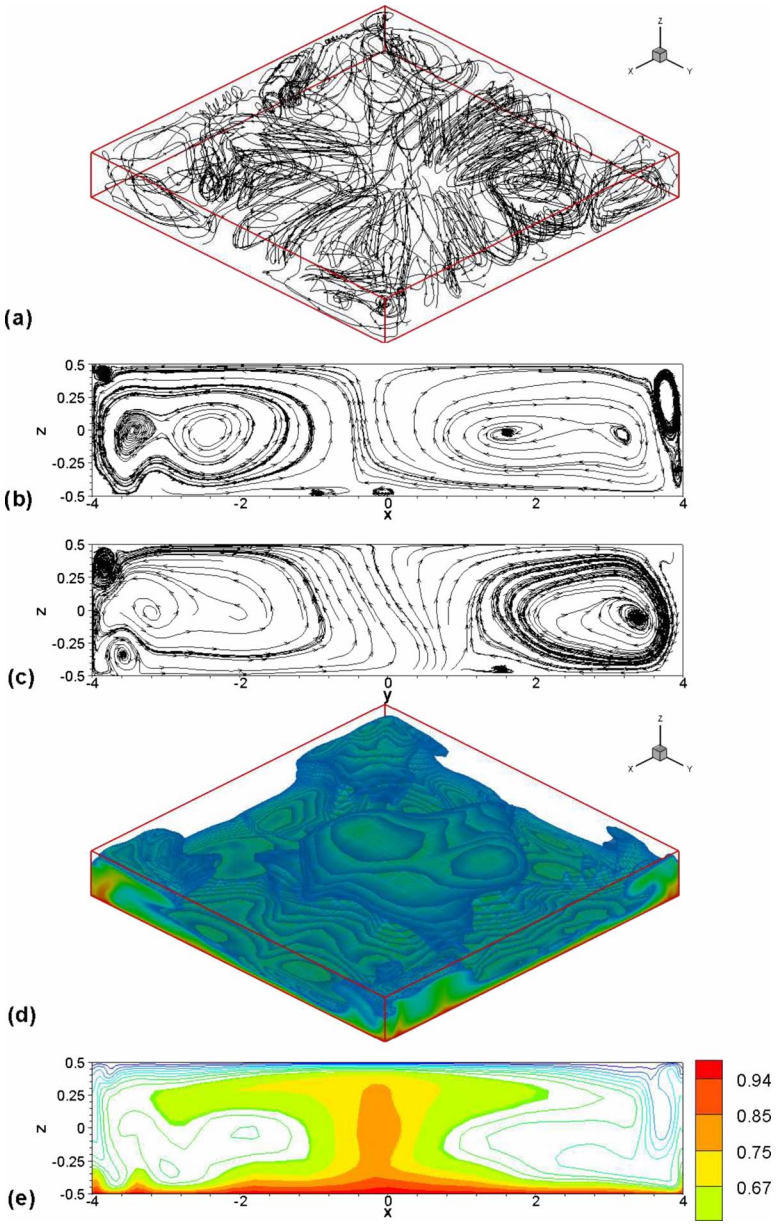

Fig. 3 (*a*) **3D streamtraces,** (*b*) **streamlines at the central *x-z* plane,** (*c*) **streamlines at the central *y-z* plane,** (*d*) **3D isotherms, and** (*e*) **isotherms in the central *x-z* plane at** $\mathbf{Ra=10^7}$, $\mathbf{Ta=10^2}$, **and** $\mathbf{Ra_w=10^{-1}}$

3 Results and Discussion

We have performed numerical simulation for six cases at nondimensional rotation rates $\Omega=0$, 10, 10^3, and 10^4. For the first four test cases Ta was computed using Ω_D while the ratio of $\mathrm{Ra}_w/\mathrm{Ta}$ was kept as 10^{-3} in order to stringently maintain Boussinesq approximation. For the next two cases at constant $\Omega=10^4$, we have kept the ratios of $\mathrm{Ra}_w/\mathrm{Ta}$ as 2×10^{-3} and 10^{-2} in order to separate out the roles played by centrifugal and Coriolis forces. In the above cases a collocated mesh of $71\times71\times31$ based on the geometric progression series was generated in order to capture the thin thermal and Ekman boundary layers especially at higher-rotation rates. The minimum grid spacing is $\Delta=0.005$ near the boundary for all the spatial directions. Regarding grid independence, we simulated RBC on a grid of $141\times141\times61$ and found that integral parameters such as mean Nu number changed by less than 4% compared with the coarse grid. Moreover, the change in global maximum velocities $u_{\max}$, $v_{\max}$, and $w_{\max}$ was less than 4%. Hence in order to cut down the computational time, we ran all our simulation cases on a coarser grid of $71\times71\times31$.

First we performed simulation for $\Omega=0$, i.e., nonrotating RBC, as this case is to serve as reference level for the other five simulations of rotating convection. The horizontal plane dimensions were taken large enough (8×8) so as to avoid the effect of sidewall modes of convection on bulk convection modes. In order to collect statistics of various dynamical variables we have performed spatial-averaging in horizontal planes and then time averaged the results. The effect of rotation on heat transfer is studied in terms of variation in Nusselt number with time and the spatial variation in isotherms.

3.1 Flow Structures. For the nonrotating Rayleigh–Benard convection at $\mathrm{Ra}=10^7$, $\mathrm{Ta}=0$, and $\mathrm{Ra}_w=0$, the thermal buoyancy is the main dominating force solely responsible for convective heat transfer. The instantaneous 3D streamtrace plots (Fig. 2(*a*))

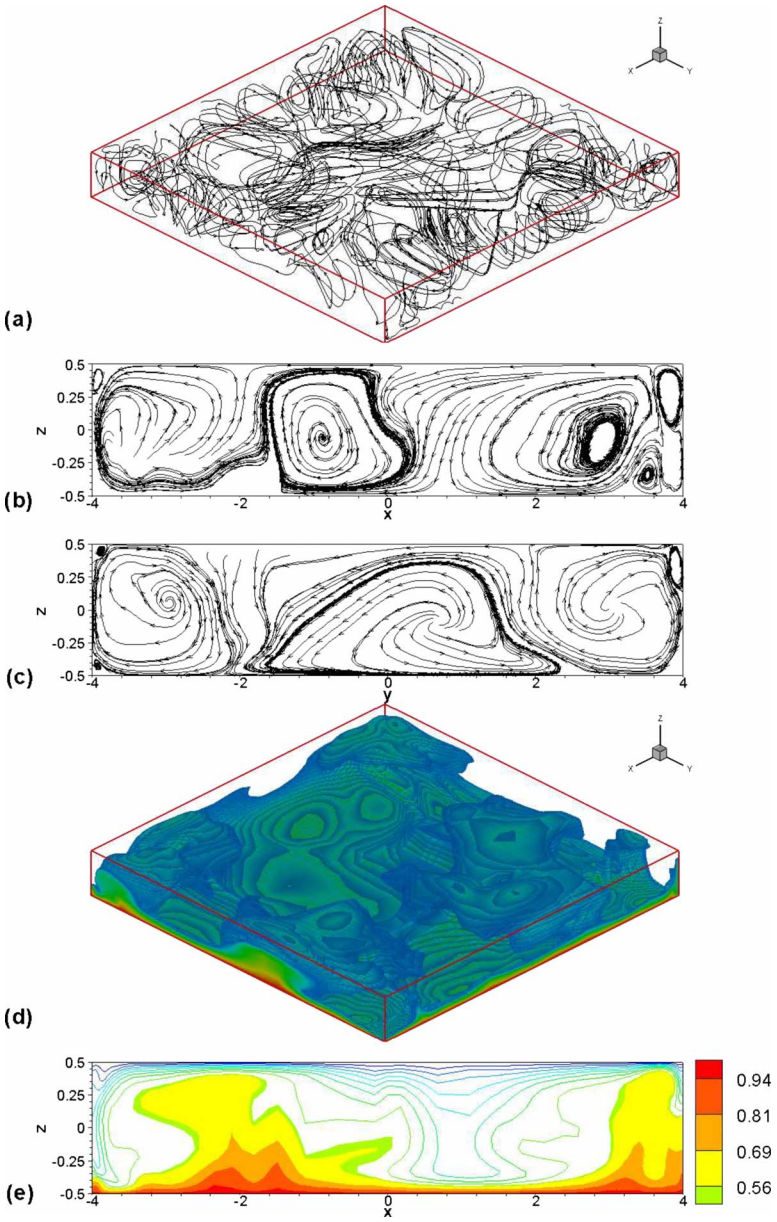

Fig. 4 (*a*) **3D streamtraces,** (*b*) **streamlines at the central *x-z* plane,** (*c*) **streamlines at the central *y-z* plane,** (*d*) **3D isotherms, and** (*e*) **isotherms in the central *x-z* plane at Ra=10^7, Ta=10^6, and Ra_w=10^3**

show multicellular rolls aligned along both x and y directions. The plots for streamtraces in the x-z and y-z central planes can be seen in Figs. 2(b) and 2(c). From these figures it is apparent that multiple large- and small-scale rolls form in both the horizontal directions. The visualization of thermal flow-field shows randomly rising and falling plumes from lower and upper walls, respectively. Their depth (or height) of penetration spans full depth of the fluid, as is evident in 3D and 2D isotherm plots of Figs. 2(d) and 2(e). The lower cutoff value of isotherms has been set as 0.55 for all the thermal flow-field plots.

For the next case, low-rotation rate ($\Omega=10$) was imparted to the cavity so that Ta=10^2 and $Ra_w=10^{-1}$ while Ra=10^7 is held constant. At this low-rotation rate, contrary to intuition, considerable dynamical changes occur, as can be seen in isotherms and streamtrace 3D plots of Figs. 3(a) and 3(d). The 2D streamtrace plots (see Figs. 3(b) and 3(c)) of central transverse planes show two large-rolls generated due to merging of multicellular rolls. Similar is the behavior observed in the 2D isotherm plot (see Fig. 3(e)), which shows a large hot plume rising from the center of the enclosure, formed by upwelling of fluid by the large-scale rolls.

For the next simulation, the rotation rate was increased hundredfold to $\Omega=10^3$ corresponding to Ta=10^6 and $Ra_w=10^3$ while keeping Ra constant. The higher-rotation rate generates 10^4 times higher rotational buoyancy, which leads to 3D plots of streamtraces and isotherms (see Figs. 4(a) and 4(d)), depicting breakup of larger structures that formed in the previous case to slightly smaller-rolls oriented in both the horizontal directions. Consequently the 2D streamtrace plots at central transverse planes (see Figs. 4(b) and 4(c)) show three large counter-rotating rolls.

With further tenfold increase in the rotation rate to $\Omega=10^4$ (Ta=10^8 and $Ra_w=10^5$) there is generation of enhanced Coriolis forces as well as rotational buoyancy. The effect of Coriolis forces redistributes the buoyancy-induced vertical kinetic energy into horizontal kinetic energy (by swirling the flow in horizontal

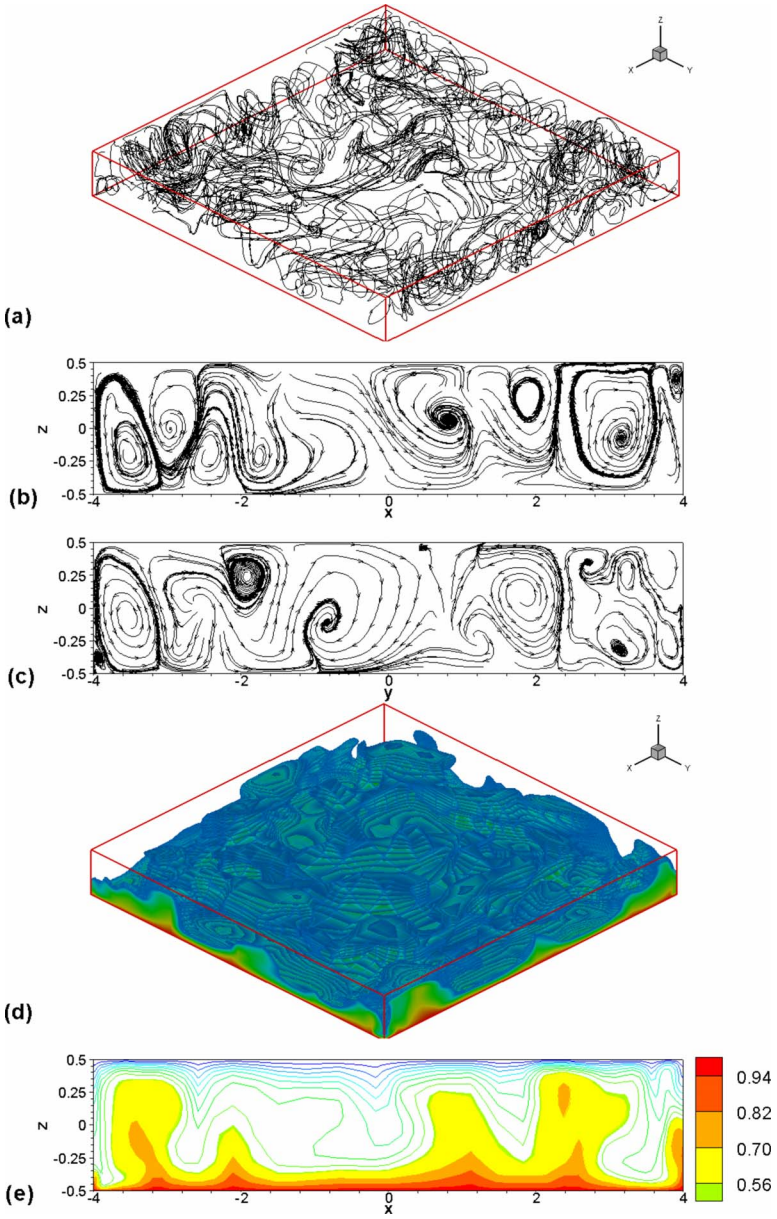

Fig. 5 (*a*) **3D streamtraces,** (*b*) **streamlines at the central *x-z* plane,** (*c*) **streamlines at the central *y-z* plane,** (*d*) **3D isotherms, and** (*e*) **isotherms in the central *x-z* plane at** $\mathbf{Ra=10^7}$, $\mathbf{Ta=10^8}$, **and** $\mathbf{Ra_w=10^5}$

planes). This phenomenon leads to inhibition of vertical transport of buoyant fluid from the bottom heated wall to the top cold wall while the simultaneous action of enhanced rotational buoyancy leads to breakup of larger-rolls. The 3D and 2D plots of streamtraces as in Figs. 5(*a*)–5(*c*) show breakup of large-rolls as present in the previous case into several smaller-rolls with no preferred orientation. The thermal flowfield (Figs. 5(*d*) and 5(*e*)) too shows randomly ascending and descending thermal plumes. Furthermore due to the generation of multiple smaller-rolls a larger number of plumes is observed.

The next two cases of simulation have been performed at constant $\Omega=10^4$ while increasing the ratio of $\mathrm{Ra}_w/\mathrm{Ta}$ from 2×10^{-3} to 10^{-2}, with the intention of separating out the roles played by centrifugal and Coriolis forces, yet maintaining the Boussinesq approximation. Since the Coriolis force remains constant for cases 4–6 (as Ra and Ta are kept constant), it is inferred that the thermal and velocity flow-fields will not show a significant change from case 4 except breakup of larger-rolls due to enhanced rotational buoyancy for cases 5 and 6. For the fifth case at constant $\Omega=10^4$, $\mathrm{Ra}_w/\mathrm{Ta}$ has been kept as 2×10^{-3} ($\mathrm{Ta}=10^8$ and $\mathrm{Ra}_w=2\times10^5$) so that the rotational buoyancy increases by a factor of 2 compared with the fourth case. The 3D and 2D plots of streamtraces as well as thermal flow-field show a picture quite akin to the previous case and hence their figures have not been included.

The sixth case corresponds to constant $\Omega=10^4$ with $\mathrm{Ra}_w/\mathrm{Ta}=10^{-2}$ (i.e., $\mathrm{Ta}=10^8$ and $\mathrm{Ra}_w=10^6$), i.e., centrifugal force increases by a factor of 10 compared with the fourth case and hence the ratio of rotational to thermal buoyancy becomes 10%. The 3D and 2D plots of streamtraces as in Figs. 6(*a*)–6(*c*) show activation of still smaller-rolls with random orientation in the three-dimensional space. The thermal flowfield (Figs. 6(*d*) and 6(*e*)) shows a picture quite similar to the previous fifth case with randomly ascending thermal plumes in the transverse central planes.

3.2 Heat Transfer Analysis. Heat transfer analysis based on

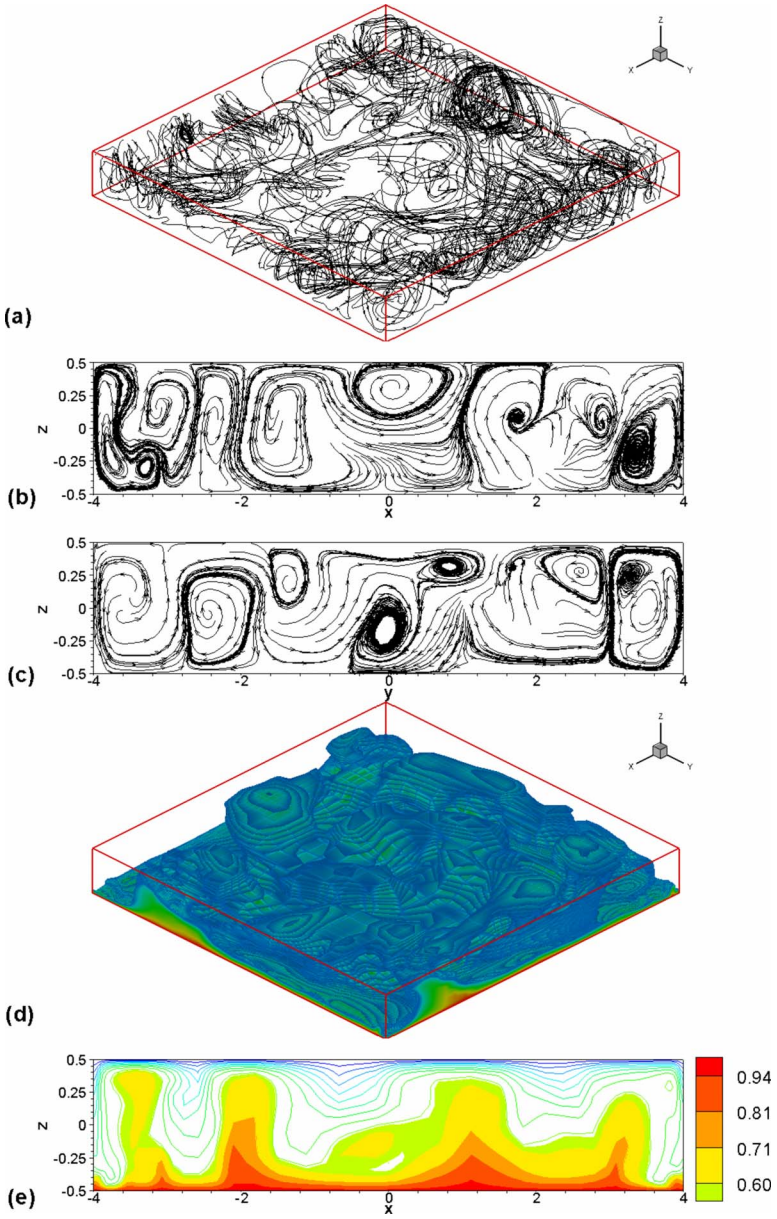

Fig. 6 (*a*) **3D streamtraces,** (*b*) **streamlines at the central *x-z* plane,** (*c*) **streamlines at the central *y-z* plane,** (*d*) **3D isotherms, and** (*e*) **isotherms in the central *x-z* plane at** $\mathbf{Ra=10^7}$, $\mathbf{Ta=10^8}$, **and** $\mathbf{Ra_w=10^6}$

temporal variation in Nusselt number is shown in Fig. 7. Spatially averaged Nusselt number $\overline{\mathrm{Nu}}$ does not change appreciably for $\Omega=0$ until $\Omega=10^3$, indicating no significant change in the heat transport due to the dominance of thermal buoyancy over the Coriolis forces. At $\Omega=10^4$, the increase in Coriolis forces leads to redistribution of kinetic energy, which in turn promotes enhanced flow in the horizontal planes, thus inhibiting buoyancy-induced vertical motion of fluid and thereby leading to reduction in vertical heat transfer from the bottom heated wall to the top cold wall. With an increase in centrifugal forces, i.e., rotational buoyancy (keeping Coriolis force constant) for the fifth and sixth cases, the thermal flow pattern exhibits a slightly larger number of thermal plumes due to activation of still smaller-rolls but this does not affect the vertical heat transfer and hence $\overline{\mathrm{Nu}}$ at both the walls remains the same as for the fourth case.

For nonrotating and low-rotation cases the values of $\overline{\mathrm{Nu}}$ at hot and cold walls are almost equal (see Figs. 7(*a*) and 7(*b*)). This is because of the almost equal thickness of the thermal boundary layers (see Fig. 9(*a*)) at the top and bottom surfaces. With an increase in rotation rate, the thickness of the thermal boundary layers at the top increases and at bottom surfaces decreases (see Fig. 9(*a*)). This results in a decrease in mean-temperature gradient $(d\bar{\Theta}/dz)$ at the top wall while the mean-temperature gradient increases at the bottom wall. At larger rotation rates, the transport of heat flux is mainly through the boundary layers as the mean-temperature gradient $(d\bar{\Theta}/dz)$ is significantly small in main bulk of the flow and this phenomenon becomes more dominant with an increase in rotation.

3.3 Statistical Properties. Statistical mean and higher-order moments of all the dynamical variables have been obtained after spatial-averaging over horizontal planes and then time-averaging until a statistically stationary state is achieved. The mean velocity profiles show small variation about a zero-mean for all the cases and their variation is less than 4% of the instantaneous values.

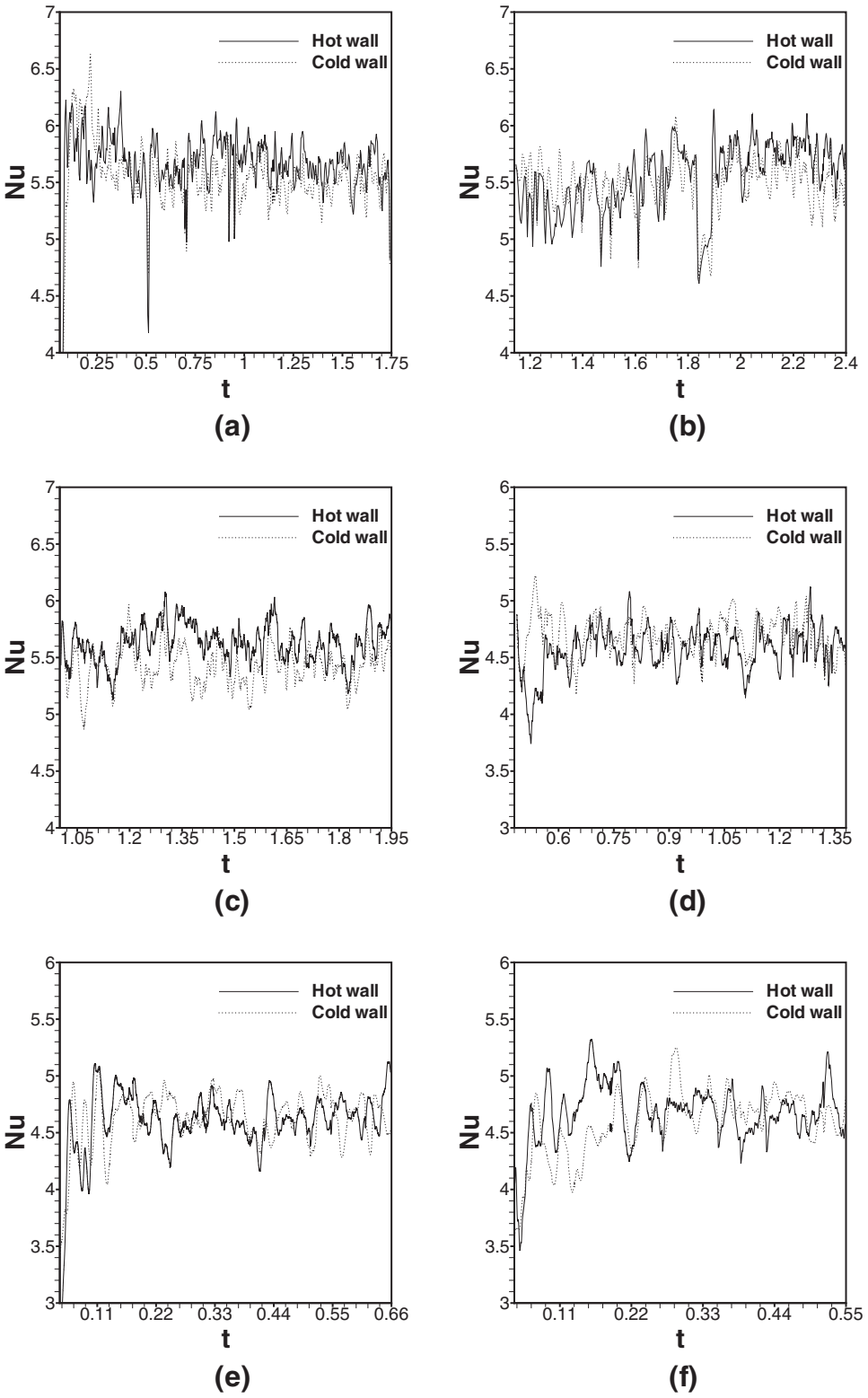

Fig. 7 Time history of the average Nusselt number on the hot and cold walls at $Ra=10^7$: (*a*) $Ta=0$ and $Ra_w=0$, (*b*) $Ta=10^2$ and $Ra_w=10^{-1}$, (*c*) $Ta=10^6$ and $Ra_w=10^3$, (*d*) $Ta=10^8$ and $Ra_w=10^5$, (*e*) $Ta=10^8$ and $Ra_w=2\times10^5$, and (*f*) $Ta=10^8$ and $Ra_w=10^6$

The root mean square velocity (u_{rms}, v_{rms}, and w_{rms}) profiles are shown in Fig. 8, and the rms temperature (Θ_{rms}) profile is shown in Fig. 9(*b*). For the nonrotating case a symmetric profile (see Fig. 8(*a*)) is obtained for all the u_{rms}, v_{rms}, and w_{rms} velocities. u_{rms} and v_{rms} have their maxima near the top and bottom *x*-*y* planes (at $z=-0.47$ and $z=0.47$) and minima at the central plane (at $z=0$). The w_{rms} profile is also symmetric but has its maxima at the central *x*-*y* plane. It is apparent from these profiles that the turbulence is anisotropic from the walls to the center of the enclosure. A similar profile is obtained at low-rotation rate $\Omega=10$, as can be seen in Fig. 8(*b*). The rms horizontal velocities show a slight variation in magnitude as the rotation rate increases from $\Omega=0$ to 10^4. A fur-

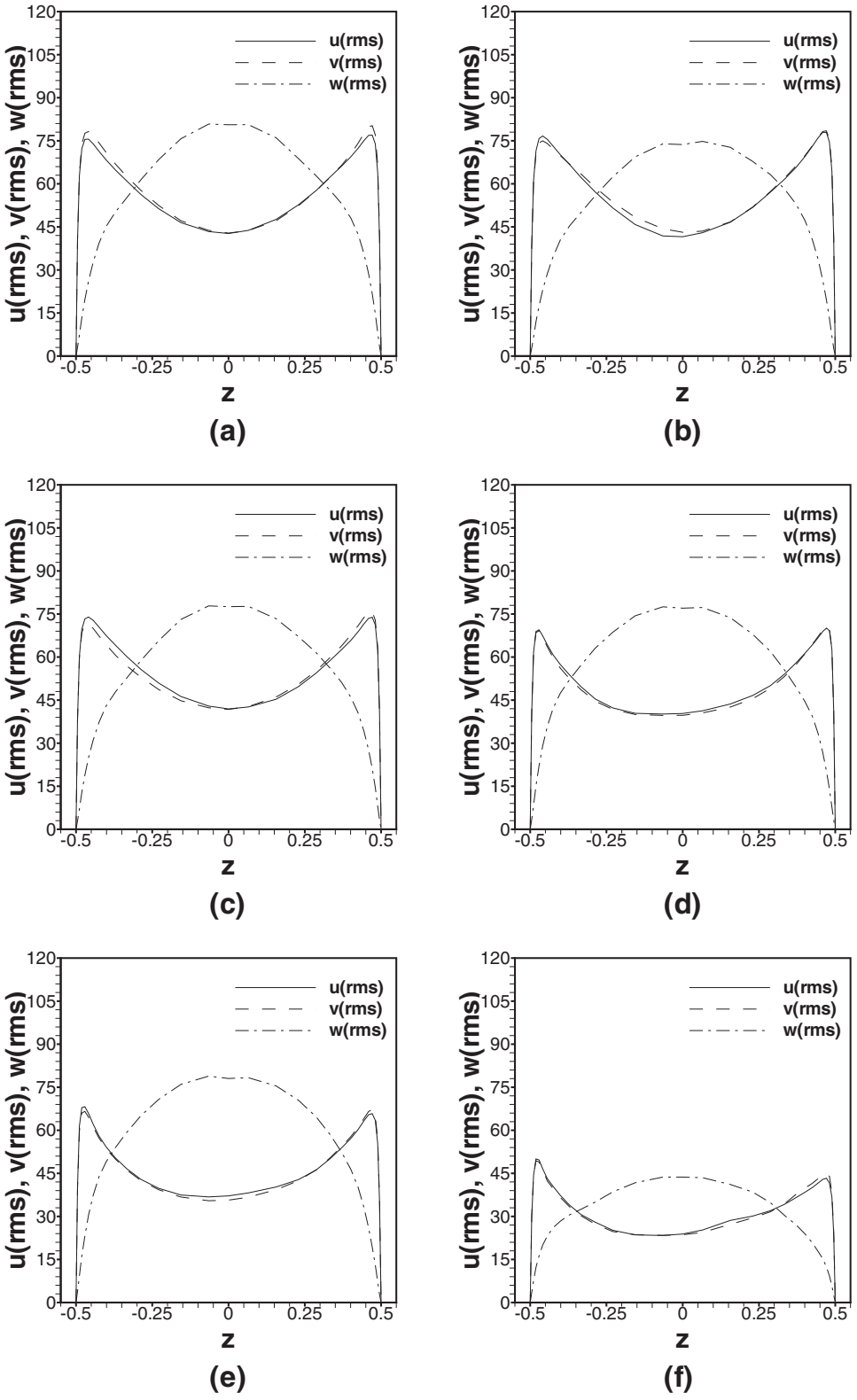

Fig. 8 Variation in the root mean square velocities u_{rms}, v_{rms}, and w_{rms} at Ra=10^7: (*a*) Ta=0 and Ra$_w$=0, (*b*) Ta=10^2 and Ra$_w$=10^{-1}, (*c*) Ta=10^6 and Ra$_w$=10^3, (*d*) Ta=10^8 and Ra$_w$=10^5, (*e*) Ta =10^8 and Ra$_w$=2×10^5, and (*f*) Ta=10^8 and Ra$_w$=10^6

ther increase in rotational buoyancy as in cases 5 and 6, keeping Coriolis forces constant, leads to a gradual decrease in horizontal as well as vertical rms velocities due to the breakup of larger structures into smaller-scales. These smaller-rolls undergo enhanced turbulent dissipation and hence the fluctuating velocities show a significant decrease in magnitude compared with cases 4 and 5. The symmetric nature of the profiles retains itself for all the cases.

The rms values for the temperature in Fig. 9(*b*) show a slight increase in magnitude of fluctuations with an increase in the rate

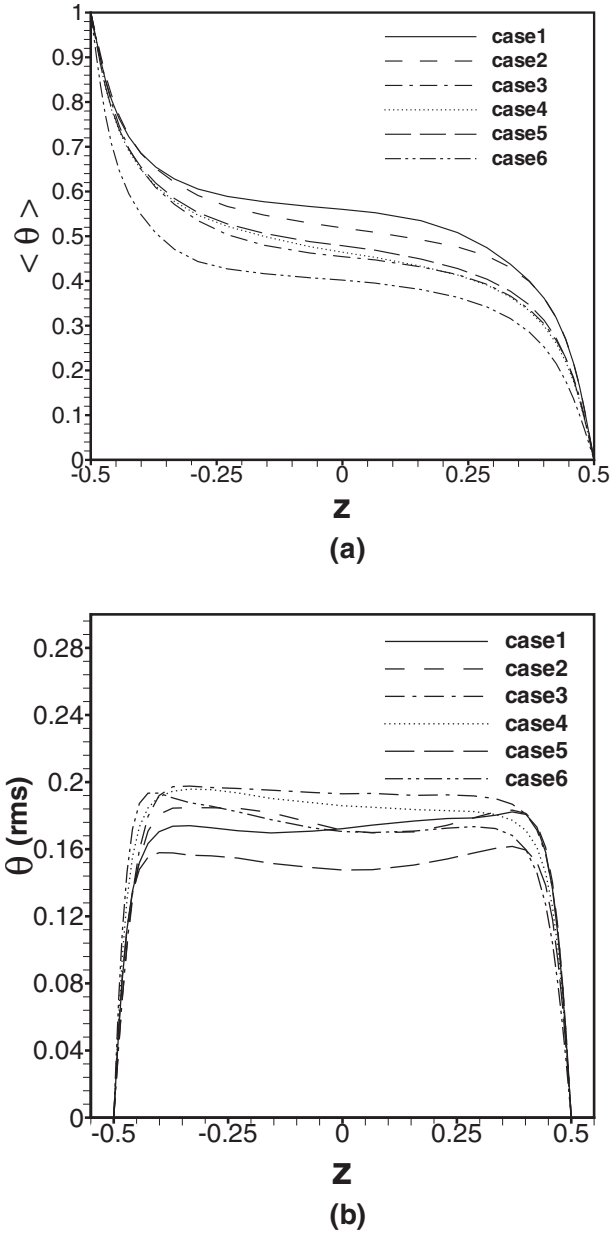

Fig. 9 Variation in the (*a*) $\bar{\Theta}$ and (*b*) Θ_{rms} at $Ra=10^7$, $Ta=0$, and $Ra_w=0$, $Ta=10^2$ and $Ra_w=10^{-1}$, $Ta=10^6$ and $Ra_w=10^3$, $Ta=10^8$ and $Ra_w=10^5$, $Ta=10^8$ and $Ra_w=2\times10^5$, and $Ta=10^8$ and $Ra_w=10^6$

of rotation beyond $\Omega=10$. From $\Omega=0$ (case 1) to $\Omega=10$ (case 2), there is a slight decrease in magnitude of thermal fluctuations due to the formation of large-scale structures but with a further increase in rotation, these structures break up, leading to slightly larger thermal fluctuations. Moreover, high gradients of fluctuations are observed within the near-wall thermal boundary layers while in the core of the cavity the temperature fluctuations Θ_{rms} are almost constant.

The mean-temperature $\bar{\Theta}$ profile shown in Fig. 9(*a*) exhibits formation of thermal boundary layers near the solid walls. The thickness of the thermal boundary layer especially near the bottom wall decreases successively as we increase the rate of rotation. This becomes more apparent with an increase in rotational buoyancy (especially for case 6 having highest Ra_w), due to which the flow experiences Ekman pumping [14], a phenomenon characterized by ascending flow being radially directed outward from the upper wall only to descend along the vertical side-walls and then pressure driven inward toward the center. This results in thicker thermal boundary layers at the top surface while thin thermal boundary layers form at the bottom wall. The mean-temperature gradient also shows a gradual reduction in magnitude in the bulk of the flow with an increase in rotation.

4 Conclusions

In light of the above results one can say that at low-rotation rates ($\Omega \leq 10^3$) there is considerable change in spatiotemporal dynamics compared with the nonrotating RBC. Basically at low-rotation rates corresponding to cases where thermal buoyancy is much larger than Coriolis forces and rotation buoyancy, there is formation of large-scale structures. With a further increase in rotation, i.e., $\Omega \geq 10^3$, the increase in rotational buoyancy leads to enhanced breakup of larger-rolls into smaller-scales.

The increase in Coriolis forces with increasing rotation (from $\Omega=10$ to $\Omega=10^4$) leads to the redistribution of vertical kinetic energy into horizontal kinetic energy, and this inhibits vertical transport of fluid, leading to an attenuation of about 16% in the magnitude of Nusselt number. An increase in rotational buoyancy (i.e., centrifugal forces) at constant $\Omega=10^4$ exhibits no significant change in magnitude of Nusselt number.

For all the rotation rates, the mean velocities in all spatial directions are considerably smaller as compared with the instantaneous velocities and exhibit a small variation about a zero-mean. With an increase in rotation rate, the rms velocities show a slight decrease while an increase in the rotational buoyancy brings about a significant decrease in rms velocities due to the enhanced breakup of larger structures into smaller-structures.

With increasing rotation rates, the mean-temperature gradient in the bulk of the flow decreases while the thermal gradients increase significantly near the bottom wall due to the formation of thinner thermal boundary layers. The top wall experiences a decrease in thermal gradients with increasing rotation rates.

An increase in centrifugal forces at constant Ω (i.e., constant Coriolis forces) with Ra_w/Ra being less than or equal to 10% leads to enhanced breakup of larger structures into smaller-scale rolls with accompanying decrease in rms velocities. The vertical heat transfer measured by $\overline{Nu}$ remains unaffected with an increase in rotational buoyancy.

References

[1] Zhong, F., Ecke, R. E., and Steinberg, V., 1993, "Rotating Rayleigh-Benard Convection: Asymmetric Modes and Vortex States," J. Fluid Mech., **249**, pp. 135–159.

[2] Homsy, G. M., and Hudson, J. L., 1969, "Centrifugally Driven Thermal Convection in a Rotating Cylinder," J. Fluid Mech., **35**, pp. 33–52.

[3] Elder, J. W., 1969, "The Temporal Development of a Model of High Rayleigh Number Convection," J. Fluid Mech., **35**, pp. 417–437.

[4] Rossby, H. T., 1969, "A Study of Benard Convection With or Without Rotation," J. Fluid Mech., **36**, pp. 309–335.

[5] Lee, T. L., and Lin, T. F., 1996, "Transient Three-Dimensional Convection of Air in a Differentially Heated Rotating Cubic Cavity," Int. J. Heat Mass Transfer, **39**, pp. 1243–1255.

[6] Ker, Y. T., and Lin, T. F., 1996, "A Combined Numerical and Experimental Study of Air Convection a Differentially Heated Cubic Cavity," Int. J. Heat Mass Transfer, **39**, pp. 3193–3210.

[7] Julien, K., Legg, S., McWilliams, J., and Werne, J., 1996, "Rapidly Rotating Turbulent Rayleigh-Benard Convection," J. Fluid Mech., **322**, pp. 243–273.

[8] Kerr, R. M., and Herring, J. R., 2000, "Prandtl Number Dependence of Nusselt Number in Direct Numerical Simulations," J. Fluid Mech., **419**, pp. 325–344.

[9] Vorobieff, P., and Ecke, R. E., 2002, "Turbulent Rotating Convection: An Experimental Study," J. Fluid Mech., **458**, pp. 191–218.

[10] Tritton, D. J., 1982, *Physical Fluid Dynamics*, Van Nostrand Reinhold, New York.

[11] Ferziger, J. H., and Peric, M., 1996, *Computational Methods for Fluid Dynamics*, Springer, Berlin, Chap. 5, pp. 95–98.

[12] Hasan, N., and Baig, F. M., 2002, "Evolution to Aperiodic Penetrative Convection in Odd Shaped Rectangular Enclosures," Int. J. Numer. Methods Heat Fluid Flow, **12**, pp. 895–915.

[13] Husain, A., Baig, M. F., and Varshney, H., 2006, "Investigation of Coherent Structures in Rotating Rayleigh-Benard Convection," Phys. Fluids, **18**, p. 125105.

[14] Davidson, P. A., 2001, *An Introduction to Magnetohydrodynamics*, Cambridge University Press, Cambridge, Chap. 3.

Mixed Convection Along a Semi-Infinite Vertical Flat Plate With Uniform Surface Heat Flux

S. Ghosh Moulic
Department of Mechanical Engineering,
Indian Institute of Technology, Kharagpur,
Kharagpur 721302, India

L. S. Yao
Department of Mechanical and Aerospace Engineering,
Arizona State University,
Tempe, AZ 85287-6106

Mixed-convection boundary-layer flow over a heated semi-infinite vertical flat plate with uniform surface heat flux, placed in a uniform isothermal upward freestream, has been investigated. Near the leading edge, the effect of natural convection can be treated as a small perturbation term. The effects of natural convection are accumulative and increase downstream. In the second region, downstream of the leading-edge region, natural convection eventually becomes as important as forced convection. The boundary-layer equations have been solved by an adaptive finite-difference marching technique. The numerical solution indicates that the series solution of the leading-edge region is included in that of the second region. This property is shared by many developing flows. However, the series solutions of local similarity or local nonsimilarity are only valid for very small distances from the leading edge. Numerical results for the local skin-friction factor, wall temperature, and local Nusselt number are presented for $Pr=1$ *for a wide range of* $Gr_x^*/Re_x^{5/2}$*, where* Gr_x^* *is a local modified Grashof number and* Re_x *is a local Reynolds number. The results indicate that* $c_{f_x}Re_x^{1/2}$ *and* $Nu_xRe_x^{-1/2}$ *increase monotonically with distance from the leading edge, where* c_{f_x} *is the local skin-friction factor and* Nu_x *is the local Nusselt number, and approach the free-convection limit at large values of* $Gr_x^*/Re_x^{5/2}$*, although the velocity distribution differs from the velocity distribution in a free-convection boundary layer.* [DOI: 10.1115/1.2995725]

Keywords: mixed convection, boundary layer, vertical flat plate, uniform surface heat flux, adaptive finite-difference marching method

1 Introduction

Mixed-convection flows, or combined free- and forced-convection flows, occur in many technological devices and in nature. Some examples include flow in electronic equipment cooled by a fan and flows in the ocean and in the atmosphere. A comprehensive review of buoyancy-induced flows is given in the monograph by Gebhart et al. [1]. Buoyancy forces induced by density gradients, due to imposed temperature differences, in a gravitational force field can have a significant effect on forced flows over heated solid surfaces. It can alter the velocity field and hence the wall shear stress and temperature distribution. It is important to understand the interaction of the free- and forced-convection modes of heat transfer in mixed-convection flows.

Perhaps, the simplest model of external mixed-convection flow is that of boundary-layer flow of a uniform stream over a heated vertical plate. Mixed-convection flows over heated vertical plates with uniform surface temperature have been studied by several workers [2–7]. Detailed description of Refs. [2–6] is given in Ref. [7]. It has been recognized that the relevant nondimensional parameter describing mixed-convection boundary-layer flows over heated vertical plates with uniform surface temperature is Gr_x/Re_x^2, where Gr_x is the local Grashof number and Re_x is the local Reynolds number. Forced convection is the dominant mode of heat transfer when $Gr_x/Re_x^2 \ll 1$. Free-convection effects become important when $Gr_x/Re_x^2 \sim 1$.

Mixed-convection flows over vertical plates with uniform surface heat flux have been investigated by Wilks [8,9] and Carey and Gebhart [10]. Wilks [8] presented results for the local Nusselt number distribution obtained using a local similarity analysis. In this analysis, the boundary-layer equations were first transformed to a suitable form. Derivatives with respect to the transformed streamwise coordinate were then neglected, and the resulting nonlinear ordinary differential equations were solved independently at discrete streamwise locations. The solution at any downstream location, predicted by this local similarity analysis, is *independent* of the solutions at upstream locations. The prediction of this approximate numerical method often has uncertain accuracy. In a later paper, Wilks [9] presented results for the local Nusselt number obtained from a numerical solution of the boundary-layer equations. He started the numerical integration of the boundary-layer equations at a point slightly downstream of the leading edge, as his iterative solution procedure failed to converge at the leading edge. Wilks [9] also presented two asymptotic series solutions, one valid in the region near the leading edge and one for the region far downstream of the leading edge. Carey and Gebhart [10] considered higher order boundary-layer effects. They also presented experimental results for the velocity and temperature profiles. Carey and Gebhart [10] pointed out that the computed results for large downstream distances, presented by Wilks [9], were based on an erroneous first-order correction equation. The asymptotic solution for the far downstream region with natural-convection dominant flow is interesting, but does not consider the influence of upstream conditions on the downstream development, as parabolic partial differential equations should; consequently, it is not physically sound.

In the present investigation, the problem of mixed-convection boundary-layer flow over a semi-infinite heated vertical flat plate with uniform surface heat flux is re-examined. A perturbation analysis has been used to identify the appropriate scaled variables for the numerical solution of the boundary-layer equations. The boundary-layer equations have been solved by an adaptive finite-difference marching method. The numerical integration of the

Contributed by the Heat Transfer Division of ASME for publication in the JOURNAL OF HEAT TRANSFER. Manuscript received March 19, 2008; final manuscript received July 26, 2008; published online January 5, 2009. Review conducted by Gautam Biswas.

 Copyright © 2009 by ASME

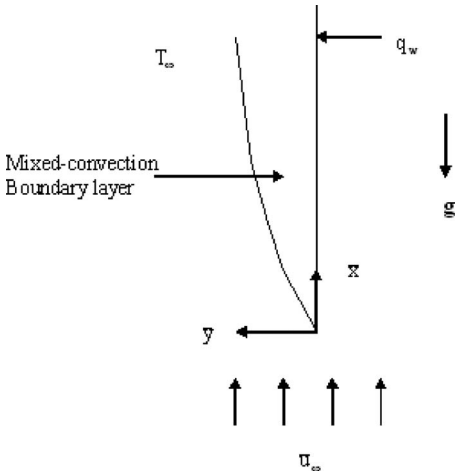

Fig. 1 Coordinates

boundary-layer equations has been started at the leading edge, using the forced-convection similarity solution for velocity and temperature as the initial condition. Results for the distribution of $c_{f_x}\mathrm{Re}_x^{1/2}$ and $\mathrm{Nu}_x\mathrm{Re}_x^{-1/2}$ have been presented for Pr=1, for a large range of $\mathrm{Gr}_x^*/\mathrm{Re}_x^{5/2}$, and compared with the solution for the limiting cases of forced and free convection. Here c_{f_x} is the local skin-friction factor, Nu_x is the local Nusselt number, Gr_x^* is the local modified Grashof number based on the wall heat flux, and Pr is the Prandtl number. Results for the variation of wall temperature, which have not been reported earlier, have also been presented.

The results indicate that, under the influence of buoyancy forces, the values of $c_{f_x}\mathrm{Re}_x^{1/2}$ and $\mathrm{Nu}_x\mathrm{Re}_x^{-1/2}$ increase monotonically with distance from the leading edge and approach the free-convection limit at large values of $\mathrm{Gr}_x^*/\mathrm{Re}_x^{5/2}$, although the velocity profile for the mixed-convection boundary layer differs from the velocity profile for a free-convection boundary layer. The wall temperature decreases with distance from the leading edge and approaches the free-convection asymptote as $\mathrm{Gr}_x^*/\mathrm{Re}_x^{5/2}\to\infty$. The results show that forced convection is the dominant mode of heat transfer in the region near the leading edge of the plate where $\mathrm{Gr}_x^*/\mathrm{Re}_x^{5/2}\ll 1$. Free-convection effects become as important as forced convection when $\mathrm{Gr}_x^*/\mathrm{Re}_x^{5/2}\sim 1$. Far downstream of the leading edge, free convection becomes the dominant mode of heat transfer, when $\mathrm{Gr}_x^*/\mathrm{Re}_x^{5/2}\gg 1$, as buoyancy forces play a significant role in the dynamics of the flow.

2 Problem Formulation

Mixed-convection boundary-layer flow along a semi-infinite heated vertical flat plate with a uniform surface heat flux, q_w, has been studied. An isothermal uniform upward flow with velocity $\bar{u}_\infty$ and temperature T_∞ is incident on the plate. The coordinate system is shown in Fig. 1. The flow is considered to be steady, laminar, and two dimensional. The equations describing the flow are the continuity, Navier–Stokes, and energy equations. Using the Boussinesq approximation, these equations may be written as

$$\frac{\partial\bar{u}}{\partial\bar{x}}+\frac{\partial\bar{v}}{\partial\bar{y}}=0 \tag{1a}$$

$$\bar{u}\frac{\partial\bar{u}}{\partial\bar{x}}+\bar{v}\frac{\partial\bar{u}}{\partial\bar{y}}=-\frac{1}{\rho_0}\frac{\partial\bar{P}}{\partial\bar{x}}+\nu\left(\frac{\partial^2\bar{u}}{\partial\bar{x}^2}+\frac{\partial^2\bar{u}}{\partial\bar{y}^2}\right)+g\beta(T-T_\infty) \tag{1b}$$

$$\bar{u}\frac{\partial\bar{v}}{\partial\bar{x}}+\bar{v}\frac{\partial\bar{v}}{\partial\bar{y}}=-\frac{1}{\rho_0}\frac{\partial\bar{P}}{\partial\bar{y}}+\nu\left(\frac{\partial^2\bar{v}}{\partial\bar{x}^2}+\frac{\partial^2\bar{v}}{\partial\bar{y}^2}\right) \tag{1c}$$

$$\bar{u}\frac{\partial T}{\partial\bar{x}}+\bar{v}\frac{\partial T}{\partial\bar{y}}=\alpha\left(\frac{\partial^2 T}{\partial\bar{x}^2}+\frac{\partial^2 T}{\partial\bar{y}^2}\right) \tag{1d}$$

Here, $\bar{x}$ is the distance along the plate, measured from the bottom (leading) edge, $\bar{y}$ is the distance measured from the plate in the normally outward direction, $\bar{u}$ and $\bar{v}$ are the velocity components in the $\bar{x}$- and $\bar{y}$-directions, T is the fluid temperature, β is the coefficient of thermal expansion, g is the gravitational acceleration, ν is the kinematic viscosity of the fluid, α is the thermal diffusivity of the fluid, T_∞ is the ambient temperature, ρ_0 is the reference density, $\bar{P}=\bar{p}+\rho_0 g\bar{x}$ is the modified pressure, and $\bar{p}$ is the pressure.

The following nondimensional variables are introduced:

$$x=\frac{\bar{x}}{l},\quad y=\frac{\bar{y}}{l}\mathrm{Re}^{1/2}\quad\text{(coordinates)} \tag{2a}$$

$$u=\frac{\bar{u}}{\bar{u}_\infty},\quad v=\frac{\bar{v}}{\bar{u}_\infty}\mathrm{Re}^{1/2}\quad\text{(velocities)} \tag{2b}$$

$$P=\frac{\bar{P}}{\rho_0\bar{u}_\infty^2},\quad \theta=\frac{T-T_\infty}{\dfrac{q_w l}{k}}\mathrm{Re}^{1/2}\quad\text{(pressure and temperature)} \tag{2c}$$

where l is the reference length, k is the thermal conductivity of the fluid, and

$$\mathrm{Re}=\frac{\bar{u}_\infty l}{\nu} \tag{3}$$

is the Reynolds number based on the reference length l. Substituting these non-dimensional variables into Eqs. (1*a*)–(1*d*), and taking the limit $\mathrm{Re}\to\infty$ with $\mathrm{Gr}^*/\mathrm{Re}^{5/2}$ finite yields

$$\frac{\partial u}{\partial x}+\frac{\partial v}{\partial y}=0 \tag{4a}$$

$$u\frac{\partial u}{\partial x}+v\frac{\partial u}{\partial y}=-\frac{\partial P}{\partial x}+\frac{\partial^2 u}{\partial y^2}+\frac{\mathrm{Gr}^*}{\mathrm{Re}^{5/2}}\theta \tag{4b}$$

$$\frac{\partial P}{\partial y}=0 \tag{4c}$$

$$u\frac{\partial\theta}{\partial x}+v\frac{\partial\theta}{\partial y}=\frac{1}{\mathrm{Pr}}\frac{\partial^2\theta}{\partial y^2} \tag{4d}$$

where

$$\mathrm{Gr}^*=\frac{g\beta q_w l^4}{k\nu^2} \tag{5}$$

is a modified Grashof number based on the wall heat flux q_w, and

$$\mathrm{Pr}=\frac{\nu}{\alpha} \tag{6}$$

is the Prandtl number of the fluid. The nondimensional variables x, y, u, v, and θ are variables of order 1 inside the boundary layer. The length scale l has been introduced for convenience, in order to show the order of magnitude of the different transport mechanisms, and the proper limiting procedures to obtain the governing equations for the mixed-convection boundary layer. Since the plate is infinite, l is not a characteristic length scale and cannot appear in the final form of the solution.

The mixed-convection boundary-layer equations (4*a*)–(4*d*) have to be solved subject to the following boundary conditions:

(i) On the surface of the plate ($y=0$):

$$u = 0 \quad \text{(no-slip condition)} \tag{7a}$$

$$v = 0 \quad \text{(no-penetration condition)} \tag{7b}$$

$$\frac{\partial \theta}{\partial y} = -1 \quad \text{(constant wall heat flux condition)} \tag{7c}$$

(ii) Matching with the isothermal uniform outer flow:

$$u \to 1 \quad \text{and} \quad \theta \to 0 \quad \text{as} \quad y \to \infty \tag{7d}$$

Equation (4*c*) indicates that the pressure inside the boundary layer is equal to the pressure in the outer region. The pressure outside the boundary layer is constant; hence, the pressure gradient, $\partial P/\partial x$, along the x-direction is zero.

2.1 Upstream Series Solution. Equation (4*b*) shows that the buoyancy force is proportional to $\mathrm{Gr}^*/\mathrm{Re}^{5/2}$. This suggests that, if $\mathrm{Gr}^*/\mathrm{Re}^{5/2} \ll 1$, an approximate analytical solution of Eqs. (4*a*)–(4*d*) may be obtained by a perturbation method. The solution of Eqs. (4*a*)–(4*d*) subject to the boundary conditions (7*a*)–(7*d*), for a forced-convection dominated flow, may be expressed as

$$u = f_0'(\eta) + \varepsilon(2x)^{3/2} f_1'(\eta) + \cdots \tag{8a}$$

$$v = \frac{1}{\sqrt{2x}}[(\eta f_0' - f_0) + \varepsilon(2x)^{3/2}(\eta f_1' - 4f_1) + \cdots] \tag{8b}$$

$$\theta = \sqrt{2x}[g_0(\eta) + \varepsilon(2x)^{3/2} g_1(\eta) + \cdots] \tag{8c}$$

where

$$\varepsilon = \mathrm{Gr}^*/\mathrm{Re}^{5/2} \tag{9}$$

is the small expansion parameter, $\eta = y/\sqrt{2x}$ is the Blasius similarity variable, and the primes denote derivatives with respect to the variable η. The equations describing the streamfunctions f_0 and f_1 and the temperature functions g_0 and g_1 are

$$(f_0)''' + f_0(f_0)'' = 0 \tag{10a}$$

$$\frac{1}{\mathrm{Pr}}(g_0)'' + f_0(g_0)' - (f_0)' g_0 = 0 \tag{10b}$$

and

$$(f_1)''' + f_0(f_1)'' - 3(f_0)'(f_1)' + 4(f_0)'' f_1 = -g_0 \tag{11a}$$

$$\frac{1}{\mathrm{Pr}}(g_1)'' + f_0(g_1)' - 4(f_0)' g_1 = (f_1)' g_0 - 4f_1(g_0)' \tag{11b}$$

The corresponding boundary conditions are

$$f_0 = (f_0)' = 0 \quad \text{and} \quad (g_0)' = -1 \quad \text{at} \quad \eta = 0 \tag{12a}$$

$$(f_0)' \to 1 \quad \text{and} \quad g_0 \to 0 \quad \text{as} \quad \eta \to \infty \tag{12b}$$

and

$$f_1 = (f_1)' = (g_1)' = 0 \quad \text{at} \quad \eta = 0, \tag{13a}$$

$$(f_1)' \to 0 \quad \text{and} \quad g_1 \to 0 \quad \text{as} \quad \eta \to \infty \tag{13b}$$

Equation (10*a*) is the Blasius equation for isothermal boundary-layer flow past a flat plate, while Eq. (10*b*) represents the similarity solution for the temperature distribution for forced-convection boundary-layer flow past a flat plate with uniform surface heat flux. Equations (11*a*) and (11*b*) represent the effect of buoyancy forces.

The local Nusselt number, based on distance from the leading edge, is given by

$$\mathrm{Nu}_x = \left[\frac{\mathrm{Re}_x}{2}\right]^{1/2} \frac{1}{g_0(0) + \varepsilon(2x)^{3/2} g_1(0) + \cdots} \tag{14}$$

where

$$\mathrm{Nu}_x = \frac{h\bar{x}}{k} \tag{15}$$

h is the local heat transfer coefficient, and

$$\mathrm{Re}_x = \frac{\bar{u}_\infty \bar{x}}{\nu} \tag{16}$$

is the local Reynolds number based on the distance from the leading edge. The local skin-friction factor defined by

$$c_{f_x} = \frac{\tau_w}{\frac{1}{2}\rho_0 \bar{u}_\infty^2} \tag{17}$$

where τ_w is the wall shear stress, may be expressed as

$$c_{f_x} = \left[\frac{2}{\mathrm{Re}_x}\right]^{1/2} [f_0''(0) + \varepsilon(2x)^{3/2} f_1''(0) + \cdots] \tag{18}$$

The first term in the series solutions (8*a*)–(8*c*) is the forced-convection solution for boundary-layer flow over a flat plate with uniform surface heat flux; the second term in the series solution represents the first-order free-convection effect. Equations (8*a*)–(8*c*), (14), and (18) indicate that the forced-convection flow exists only at the leading edge; the free-convection effect grows downstream, with an increase in distance from the leading edge, and is proportional to $\varepsilon x^{3/2}$. It may be noted that

$$\varepsilon x^{3/2} = \frac{\mathrm{Gr}_x^*}{\mathrm{Re}_x^{5/2}} \tag{19}$$

where

$$\mathrm{Gr}_x^* = \frac{g\beta q_w \bar{x}^4}{k\nu^2} \tag{20}$$

is the local modified Grashof number based on the distance from the leading edge. Thus, the actual small parameter in the perturbation series solution given by Eqs. (8*a*)–(8*c*), which determines the effect of buoyancy forces, is $\mathrm{Gr}_x^*/\mathrm{Re}_x^{5/2}$ rather than $\mathrm{Gr}^*/\mathrm{Re}^{5/2}$. The asymptotic solution given by Eqs. (8*a*)–(8*c*) is valid when $\varepsilon(2x)^{3/2}$ is small, that is, in a small region near the leading edge where $\mathrm{Gr}_x^*/\mathrm{Re}_x^{5/2} \ll 1$. The solution for $\mathrm{Gr}_x^*/\mathrm{Re}_x^{5/2} \sim 1$ has to be obtained by a numerical integration of the boundary-layer equations. Although the perturbation solution is not valid when $\mathrm{Gr}_x^*/\mathrm{Re}_x^{5/2}$ becomes $O(1)$, it reveals the analytical structure of the mixed-convection boundary layer. Knowledge of the analytical structure of the boundary layer can be exploited in the numerical solution procedure. This is described in the following section.

2.2 Downstream Mixed-Convection Boundary Layer. The following nondimensional variables, derived from the series solutions (8*a*)–(8*c*), are defined:

$$\xi = \varepsilon(2x)^{3/2} = \frac{g\beta q_w \nu^{1/2}}{k\bar{u}_\infty^{5/2}}(2\bar{x})^{3/2} = 2^{3/2}\frac{\mathrm{Gr}_x^*}{\mathrm{Re}_x^{5/2}} \tag{21a}$$

$$\eta = \frac{y}{\sqrt{2x}} = \bar{y}\sqrt{\frac{\bar{u}_\infty}{2\nu\bar{x}}} \tag{21b}$$

$$u = \frac{\bar{u}}{\bar{u}_\infty} \tag{21c}$$

$$\bar{v} = \sqrt{2x}\, v = \frac{\bar{v}}{\bar{u}_\infty}(2\mathrm{Re}_x)^{1/2} \tag{21d}$$

$$\phi = \frac{\theta}{\sqrt{2x}} = \frac{T - T_\infty}{\dfrac{q_w \bar{x}}{k}} \left(\frac{\mathrm{Re}_x}{2} \right)^{1/2} \tag{21e}$$

The axial length scale is derived from Eqs. (8*a*)–(8*c*) by noting that when $\varepsilon(2x)^{3/2}$ is $O(1)$, that is, when $\bar{x}/l \sim 1/\varepsilon^{2/3}$, the free-convection effect, represented by the second term in the series solutions (8*a*)–(8*c*), has grown to a magnitude where it cannot be treated as a perturbed quantity. In other words, the free-convection effect becomes important when the axial distance is $O(l/\varepsilon^{2/3})$. Thus, it is appropriate to use $\varepsilon(2x)^{3/2}$ and η as the independent variables in the downstream computation. The scales for the normal velocity and temperature are obtained from Eqs. (8*b*) and (8*c*) by noting that $v \sim x^{-1/2}$ and $\theta \sim x^{1/2}$ as $x \to 0$. This suggests that $vx^{1/2}$ and $\theta x^{-1/2}$ should be used as variables in the downstream computation, rather than v and θ. The constant factors, involving powers of 2, in the definition of the variables, are included for convenience in order to remove fractions from the final equations. It is worth pointing out that the variables ξ, η, u, $\tilde{v}$, and ϕ, defined in Eqs. (21*a*)–(21*e*), are independent of the reference length l.

The mixed-convection boundary layer equations (4*a*)–(4*d*) may be expressed in terms of the variables defined in Eqs. (21*a*)–(21*e*) as

$$3\xi \frac{\partial u}{\partial \xi} + \frac{\partial w}{\partial \eta} + u = 0 \tag{22a}$$

$$3\xi u \frac{\partial u}{\partial \xi} + w \frac{\partial u}{\partial \eta} = \frac{\partial^2 u}{\partial \eta^2} + \xi \phi \tag{22b}$$

$$3\xi u \frac{\partial \phi}{\partial \xi} + w \frac{\partial \phi}{\partial \eta} + u\phi = \frac{1}{\mathrm{Pr}} \frac{\partial^2 \phi}{\partial \eta^2} \tag{22c}$$

where

$$w = \tilde{v} - \eta u \tag{23}$$

The associated boundary conditions are

$$u = w = 0, \quad \frac{\partial \phi}{\partial \eta} = -1 \quad \text{at } \eta = 0 \tag{24a}$$

$$u \to 1, \quad \phi \to 0 \quad \text{as } \eta \to \infty \tag{24b}$$

It may be noted that the solution of Eqs. (4*a*)–(4*d*) depends on the independent variables x and y, and two nondimensional parameters, $\mathrm{Gr}^*/\mathrm{Re}^{5/2}$ and Pr. The solution of Eqs. (22*a*)–(22*c*), on the other hand, depends on the independent variables ξ and η and one nondimensional parameter, namely, the Prandtl number. The dependence of the solution on the parameter $\mathrm{Gr}^*/\mathrm{Re}^{5/2}$ is absorbed into the scaled axial coordinate ξ.

Equations (22*a*)–(22*c*) represent a system of parabolic partial differential equations and can be solved numerically by marching downstream in the ξ-direction, starting from the leading edge ($\xi = 0$). The initial conditions for advancing the solution forward in ξ may be determined by considering the limit of Eqs. (22*a*)–(22*c*) as $\xi \to 0$. It may be noted that all the partial derivatives with respect to ξ in Eqs. (22*a*)–(22*c*) are multiplied by ξ. Setting $\xi = 0$ in Eqs. (22*a*)–(22*c*), and assuming that all derivatives with respect to ξ remain bounded, the following differential equations are obtained:

$$\frac{\partial w}{\partial \eta} + u = 0 \tag{25a}$$

$$w \frac{\partial u}{\partial \eta} = \frac{\partial^2 u}{\partial \eta^2} \tag{25b}$$

$$w \frac{\partial \phi}{\partial \eta} + u\phi = \frac{1}{\mathrm{Pr}} \frac{\partial^2 \phi}{\partial \eta^2} \tag{25c}$$

Equations (25*a*)–(25*c*) may be viewed as ordinary differential equations with η as the independent variable, and ξ as a parameter, with value $\xi = 0$. These ordinary differential equations are solved, subject to the boundary conditions (24*a*) and (24*b*), to obtain the initial condition for u and ϕ at $\xi = 0$. The solution of Eqs. (25*a*)–(25*c*) may be expressed as

$$u(0, \eta) = f_0'(\eta) \tag{26a}$$

$$w(0, \eta) = -f_0(\eta) \tag{26b}$$

$$\phi(0, \eta) = g_0(\eta) \tag{26c}$$

Thus, the initial condition used for the numerical integration of Eqs. (22*a*)–(22*c*) is identical to the similarity solution for forced-convection boundary-layer flow past a flat plate with uniform surface heat flux.

Equation (22*b*) indicates that the magnitude of the buoyancy force increases with distance from the leading edge. This results in an acceleration of the fluid in the heated layer close to the wall. Far downstream of the leading edge, the peak of the streamwise velocity profile occurs inside the boundary layer and is much greater than the freestream velocity. The appropriate scales for the streamwise velocity, temperature, and thickness of the heated layer in this region, where buoyancy forces play a dominant role in the dynamics of the flow, may be obtained by balancing the order of magnitude of the inertia, buoyancy, and viscous forces in Eq. (4*b*) and noting that the constant surface heat flux condition implies that the order of magnitude of the temperature is the same as the order of magnitude of the boundary-layer thickness. The scale for the normal velocity can be obtained from the continuity equation. Since $\mathrm{Pr} \sim 1$, balancing the order of magnitude of the viscous and inertia forces in the streamwise momentum equation ensures that the order of magnitude of the convection and transverse conduction terms in the energy equation is also balanced. The order of magnitude analysis shows that $u \sim \varepsilon^{2/5}$, $\theta \sim y \sim 1/\varepsilon^{1/5}$, $v \sim \varepsilon^{1/5}$ inside the heated layer. Thus, it is appropriate to use the following nondimensional variables in the region far downstream of the leading edge:

$$Y = \varepsilon^{1/5} y = \frac{\bar{y}}{l} [\mathrm{Gr}^*]^{1/5} \tag{27a}$$

$$U = \frac{u}{\varepsilon^{2/5}} = \frac{\bar{u}}{\bar{u}_0} \tag{27b}$$

$$V = \frac{v}{\varepsilon^{1/5}} = \frac{\bar{v}}{\bar{u}_0} [\mathrm{Gr}^*]^{1/5} \tag{27c}$$

$$\Theta = \varepsilon^{1/5} \theta = \frac{T - T_\infty}{\dfrac{q_w l}{k}} [\mathrm{Gr}^*]^{1/5} \tag{27d}$$

where

$$\bar{u}_0 = \frac{\nu}{l} [\mathrm{Gr}^*]^{2/5} \tag{28}$$

in place of the variables y, u, v, and θ. The variables Y, U, V, and Θ, defined in Eqs. (27*a*)–(27*d*), are variables of order 1 in the region far downstream of the leading edge. It may be noted that these variables, defined in Eqs. (27*a*)–(27*d*), are the appropriate nondimensional variables for the limiting case of free-convection flow with uniform surface heat flux [11]. The boundary-layer equations for free convection along a semi-infinite vertical flat plate with uniform surface heat flux admit a similarity solution. This similarity solution shows that the thickness of the boundary

layer and the temperature vary as $x^{1/5}$, while the components of the velocity in the x and y directions vary as $x^{3/5}$ and $x^{-1/5}$, respectively [12]. In anticipation that the variables U, V, and Θ obtained by solving the mixed-convection boundary-layer equations will approach the solution of the corresponding free-convection problem when $\mathrm{Gr}_x^*/\mathrm{Re}_x^{5/2} \rangle\rangle 1$, the following transformation is introduced for computational convenience:

$$\tilde{\eta} = \frac{Y}{(5x)^{1/5}} \tag{29a}$$

$$U = (5x)^{3/5}\tilde{U}(\xi, \tilde{\eta}) \tag{29b}$$

$$V = \frac{1}{(5x)^{1/5}}\tilde{V}(\xi, \tilde{\eta}) \tag{29c}$$

$$\Theta = (5x)^{1/5}\tilde{\theta}(\xi, \tilde{\eta}) \tag{29d}$$

The mixed-convection boundary-layer equations (4*a*)–(4*d*) may be expressed in terms of the variables defined in Eqs. (29*a*)–(29*d*) as

$$\frac{15}{2}\xi\frac{\partial\tilde{U}}{\partial\xi} + \frac{\partial W}{\partial\tilde{\eta}} + 4\tilde{U} = 0 \tag{30a}$$

$$\frac{15}{2}\xi\tilde{U}\frac{\partial\tilde{U}}{\partial\xi} + W\frac{\partial\tilde{U}}{\partial\tilde{\eta}} + 3\tilde{U}^2 = \frac{\partial^2\tilde{U}}{\partial\tilde{\eta}^2} + \tilde{\theta} \tag{30b}$$

$$\frac{15}{2}\xi\tilde{U}\frac{\partial\tilde{\theta}}{\partial\xi} + W\frac{\partial\tilde{\theta}}{\partial\tilde{\eta}} + \tilde{U}\tilde{\theta} = \frac{1}{\mathrm{Pr}}\frac{\partial^2\tilde{\theta}}{\partial\tilde{\eta}^2} \tag{30c}$$

where

$$W = \tilde{V} - \tilde{\eta}\tilde{U} \tag{31}$$

The boundary conditions associated with Eqs. (30*a*)–(30*c*) are

$$\tilde{U} = W = 0, \quad \frac{\partial\tilde{\theta}}{\partial\tilde{\eta}} = -1 \quad \text{at } \tilde{\eta} = 0 \tag{32a}$$

$$\tilde{U} \to \frac{1}{\left[\left(\frac{5}{2}\right)^{3/2}\xi\right]^{2/5}}, \quad \tilde{\theta} \to 0 \quad \text{as } \tilde{\eta} \to \infty \tag{32b}$$

Equation (32*b*) shows that as $\xi \to \infty$, the value of $\tilde{U}$ at the edge of the boundary layer decreases to zero. This is because the maximum velocity inside the mixed-convection boundary layer increases as $\xi^{2/5}$, under the influence of buoyancy forces, while the freestream velocity is constant. When $\tilde{U}(\xi, \infty) = 0$, Eqs. (30*a*)–(30*c*) admit a self-similar solution of the form

$$\tilde{U} = F'(\tilde{\eta}) \tag{33a}$$

$$W = -4F(\tilde{\eta}) \tag{33b}$$

$$\tilde{\theta} = G(\tilde{\eta}) \tag{33c}$$

where F and G are solutions of the following equations:

$$F''' + 4FF'' - 3(F')^2 + G = 0 \tag{34a}$$

$$\frac{1}{\mathrm{Pr}}G'' + 4FG' - F'G = 0 \tag{34b}$$

subject to the boundary conditions

$$F(0) = F'(0) = 0, \quad G'(0) = -1 \tag{35a}$$

$$F' \to 0, \quad G \to 0 \quad \text{as } \tilde{\eta} \to \infty \tag{35b}$$

Equations (34*a*) and (34*b*) are the equations representing the similarity solution for free convection along a semi-infinite vertical plate with uniform surface heat flux. As $\xi \to \infty$, $\tilde{U}(\xi, \infty) \to 0$; thus, the solution of Eqs. (30*a*)–(30*c*) becomes independent of the coordinate ξ and asymptotically approaches the free-convection limit given by Eqs (33*a*)–(33*c*). It should be noted, however, that $\tilde{U}(\xi, \infty)$ is nonzero for finite values of ξ. Hence, the velocity distribution in a mixed-convection boundary layer differs from that of the free-convection boundary layer even at large (but finite) distances from the leading edge.

The variables defined in Eqs. (21*a*)–(21*e*) and (29*a*)–(29*d*) are related by

$$\eta = \left[\frac{5}{2\xi}\right]^{1/5}\tilde{\eta} \tag{36a}$$

$$u = \left[\left(\tfrac{5}{2}\right)^{3/2}\xi\right]^{2/5}\tilde{U} \tag{36b}$$

$$\tilde{v} = \left[\tfrac{2}{5}\xi\right]^{1/5}\tilde{V} \tag{36c}$$

$$\phi = \left[\frac{5}{2\xi}\right]^{1/5}\tilde{\theta} \tag{36d}$$

As noted earlier, the nondimensional variables ξ, η, u, $\tilde{v}$, and ϕ do not depend on the reference length l. Equations (36*a*)–(36*d*) indicate that the nondimensional variables $\tilde{\eta}$, $\tilde{U}$, $\tilde{V}$, and $\tilde{\theta}$ also do not depend on the reference length l.

Use of the transformations (29*a*)–(29*d*) minimizes the variation in the boundary-layer thickness with x and reduces the gradients of the dependent variables in the ξ-direction, in the region where $\xi \gg 1$, thereby decreasing the local discretization error associated with the numerical marching method. Consequently, the numerical prediction in the region far downstream of the leading edge is more accurate if Eqs. (30*a*)–(30*c*) are solved rather than Eqs. (22*a*)–(22*c*). For starting the numerical solution, Eqs. (22*a*)–(22*c*) are the appropriate ones to use. In this investigation, Eqs. (22*a*)–(22*c*) have been solved in the region near the leading edge, by a finite-difference marching method, from $\xi = 0$ to $\xi = 5/2$, with initial conditions obtained by solving Eqs. (25*a*)–(25*c*). The numerical solution for $\xi > 5/2$ has been obtained by solving Eqs. (30*a*)–(30*c*). The changeover from Eqs. (22*a*)–(22*c*) to Eqs. (30*a*)–(30*c*) is done most conveniently at $\xi = 5/2$, where $\tilde{\eta} = \eta$, as indicated by Eq. (36*a*). Equations (36*a*)–(36*d*) indicate that at $\xi = 5/2$,

$$\tilde{U}\left(\tfrac{5}{2}, \tilde{\eta}\right) = \tfrac{2}{5}u\left(\tfrac{5}{2}, \tilde{\eta}\right) \tag{37a}$$

$$\tilde{V}\left(\tfrac{5}{2}, \tilde{\eta}\right) = \tilde{v}\left(\tfrac{5}{2}, \tilde{\eta}\right) \tag{37b}$$

$$\tilde{\theta}\left(\tfrac{5}{2}, \tilde{\eta}\right) = \phi\left(\tfrac{5}{2}, \tilde{\eta}\right) \tag{37c}$$

The values of $\tilde{U}$ and $\tilde{\theta}$ at $\xi = 5/2$, which are used as initial conditions for integrating Eqs. (30*a*)–(30*c*), are determined using Eqs. (37*a*) and (37*c*), respectively, from the numerical solution for u and ϕ at $\xi = 5/2$ obtained by solving Eqs. (22*a*)–(22*c*).

Equations (22*a*)–(22*c*) and (30*a*)–(30*c*) were discretized using a finite-difference method. Derivatives with respect to η in the momentum and energy equations were approximated by central difference approximations on a uniform grid. Derivatives with respect to ξ were approximated by a two-point backward difference scheme. Since the equations are nonlinear and coupled, the solution at each ξ-station was obtained iteratively. The iterations were continued until the difference of successive iterates became less than a specified tolerance.

The infinite domain in the η-direction was truncated to a finite domain. The maximum value of η was fixed at $\eta_{\max} = 20$. This was found to be adequate. After several test runs, the grid size in the η-direction was set to $\Delta\eta = 0.01$. A variable step size $\Delta\xi$ was used. The step size was determined using an adaptive marching

Table 1 Coefficients for wall shear stress for Pr=1

$f_0''(0)$	$f_1''(0)$	$F''(0)$
0.46960	1.0298	0.72196

strategy similar to that used by Ghosh Moulic [13] and Ghosh Moulic and Yao [14]. The solution was advanced from ξ to $\xi+2\Delta\xi$ first in two steps with step size $\Delta\xi$, and then in one step with step size $2\Delta\xi$. The difference in the wall temperatures and the wall shear stresses predicted by the two-step integration and the one-step integration, at the location $\xi+2\Delta\xi$, was compared. If the difference was greater than 10^{-4}, the step size $\Delta\xi$ was halved and the process repeated; if the difference was less than 10^{-6}, the step size for the next step was doubled. The converged solution at $\xi+2\Delta\xi$ from the two-step integration was used as the initial guess for the single-step integration from ξ to $\xi+2\Delta\xi$. As a result, the iterations for the single-step integration converge rapidly. Using this strategy, the solution was advanced to $\xi=10^8$, with a reasonable accuracy, without using an excessive amount of computer time. The initial value of $\Delta\xi$, in the region near the leading edge, was taken to be 5×10^{-3}. The tolerance for the iterations at the leading edge was set to 10^{-12}. The tolerance for the iterations at other ξ-locations was taken to be 10^{-6}.

As a check, Eqs. (22*a*)–(22*c*) were solved for $\xi>5/2$, and the results obtained were compared with the results obtained by solving Eqs. (30*a*)–(30*c*). The difference between the two computations was found to be within the tolerance used in the computations. The step size $\Delta\xi$ selected by the adaptive marching strategy when solving Eqs. (22*a*)–(22*c*) was found to be much smaller than the step size selected by the adaptive marching scheme while solving Eqs. (30*a*)–(30*c*) in the region far downstream of the leading edge. Thus, the same degree of accuracy can be achieved with larger step sizes $\Delta\xi$, when Eqs. (30*a*)–(30*c*) are solved instead of Eqs. (22*a*)–(22*c*), for $\xi>5/2$. This results in a significant reduction in the total computing time.

3 Results and Discussion

Results have been obtained for Pr=1. The values of $f_0''(0)$, $f_1''(0)$, $g_0(0)$, and $g_1(0)$, obtained by solving Eqs. (10*a*), (10*b*), (11*a*), and (11*b*), are presented in Tables 1 and 2, respectively, for Pr=1. Table 1 indicates that both $f_0''(0)$ and $f_1''(0)$ are positive. Table 2 shows that while $g_0(0)$ is positive, $g_1(0)$ is negative. It follows from Eqs. (14) and (18) that the values of $\mathrm{Nu}_x(2/\mathrm{Re}_x)^{1/2}$ and $c_{f_x}(\mathrm{Re}_x/2)^{1/2}$ increase with x, while the wall temperature decreases. This is due to the acceleration of the fluid by buoyancy forces that aid the fluid motion. The increase in fluid velocity in the heated layer adjacent to the plate has a cooling effect; it also thins the boundary layer and increases the velocity gradients at the wall, resulting in an increase in the wall shear stress.

Typical profiles of the streamwise velocity in a mixed-convection boundary layer are plotted in Fig. 2 for $\xi=100$ and $\xi=500$. The forced-convection profile is shown in dotted lines for comparison. The figure shows that buoyancy forces accelerate the flow in the heated layer close to the plate and thin the boundary layer. At the leading edge, the maximum value of the velocity distribution occurs at the edge of the boundary layer; the effect of wall friction reduces the fluid velocity inside the boundary layer to values lower than the freestream velocity. Figure 2 shows that the

Table 2 Coefficients for wall temperature for Pr=1

$g_0(0)$	$g_1(0)$	$G(0)$
1.5406	–0.53766	1.3574

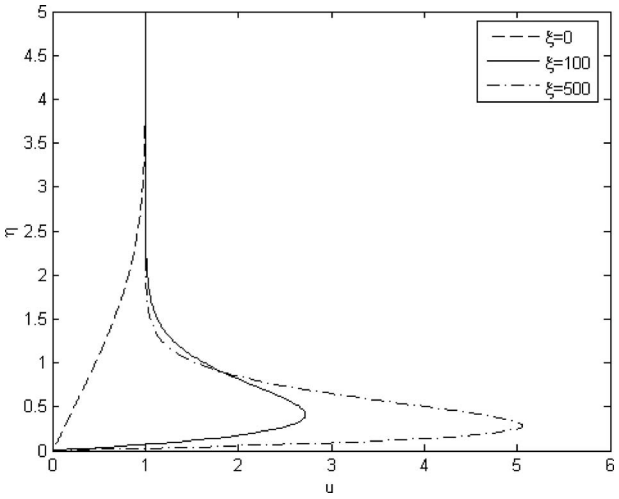

Fig. 2 Axial velocity profiles at selected locations

peak of the velocity profiles at $\xi=100$ and $\xi=500$ occurs inside the boundary layer. The maximum velocity increases with ξ under the influence of buoyancy forces. The corresponding temperature distributions are presented in Fig. 3. It can be seen that the thickness of the heated layer decreases with an increase in distance from the leading edge.

The variation in $c_{f_x}(\mathrm{Re}_x/2)^{1/2}$ with ξ is displayed in Fig. 4 for Pr=1. The local skin-friction factor is obtained using the relation

$$c_{f_x}\left(\frac{\mathrm{Re}_x}{2}\right)^{1/2}=\left(\frac{\partial u}{\partial \eta}\right)_{\eta=0} \tag{38a}$$

when $\xi\leqslant 5/2$ and the relation

$$c_{f_x}\left(\frac{\mathrm{Re}_x}{2}\right)^{1/2}=\left(\frac{5}{2}\right)^{2/5}\left(\frac{\partial \tilde{U}}{\partial \tilde{\eta}}\right)_{\tilde{\eta}=0}\xi^{3/5} \tag{38b}$$

for $\xi>5/2$ The forced-convection limit

$$c_{f_x}(\mathrm{Re}_x/2)^{1/2}=f_0''(0) \tag{39}$$

and the free-convection asymptote

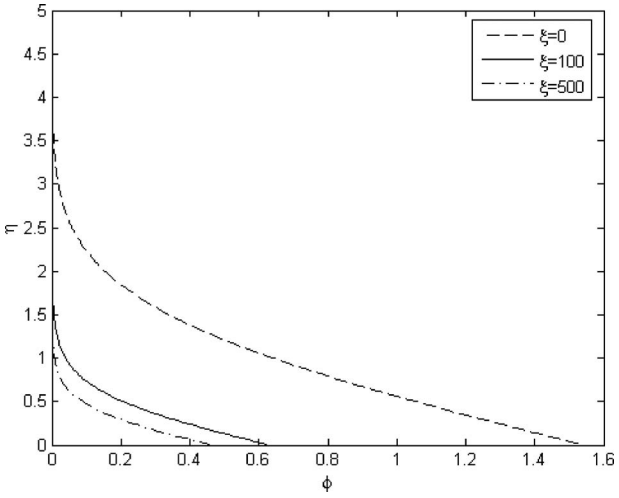

Fig. 3 Temperature distribution at selected locations

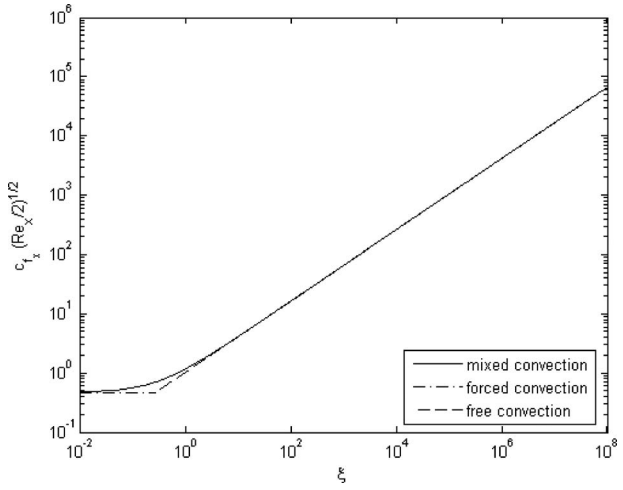

Fig. 4 Axial variation in $c_{f_x}(\mathrm{Re}_x/2)^{1/2}$

$$c_{f_x}\left(\frac{\mathrm{Re}_x}{2}\right)^{1/2} = \left(\frac{5}{2}\right)^{2/5} F''(0)\xi^{3/5} \tag{40}$$

are also plotted in Fig. 4. The values of $f_0''(0)$ and $F''(0)$ are tabulated in Table 1. It may be noted that the values of $c_{f_x}(\mathrm{Re}_x/2)^{1/2}$ depend on two nondimensional parameters, ξ and Pr, since the solution of Eqs. (22*a*)–(22*c*) and (30*a*)–(30*c*) depends on the independent variables ξ and η and the Prandtl number. Thus, for a given fluid, $c_{f_x}(\mathrm{Re}_x/2)^{1/2}$ is a sole function of ξ. For a forced-convection boundary layer, $c_{f_x}(\mathrm{Re}_x/2)^{1/2}$ is a constant with a value equal to 0.46960. Figure 4 shows that the values of $c_{f_x}(\mathrm{Re}_x/2)^{1/2}$ for the mixed-convection boundary layer increase monotonically with ξ as the boundary layer is thinned due to acceleration of the fluid by buoyancy forces. Near the leading edge, the rate of an increase in $c_{f_x}(\mathrm{Re}_x/2)^{1/2}$ with ξ is small. The value of $c_{f_x}(\mathrm{Re}_x/2)^{1/2}$ is approximately constant in the forced-convection dominated region close to the leading edge of the plate. Far downstream of the leading edge, $c_{f_x}(\mathrm{Re}_x/2)^{1/2}$ seems to merge with the free-convection limit.

The axial distribution of the wall temperature $\phi_w = \phi(\xi,0)$ is plotted in Fig. 5(*a*). The forced-convection and free-convection limits are also plotted for comparison. The figure indicates that the acceleration of the fluid by buoyancy forces leads to a cooling effect. The wall temperature starts with the forced-convection value

$$\phi_w = g_0(0) \tag{41}$$

at $\xi=0$, decreases monotonically with distance from the leading edge, and asymptotically approaches the free-convection temperature distribution

$$\phi_w = \left(\frac{5}{2\xi}\right)^{1/5} G(0) \tag{42}$$

at large values of ξ. As indicated in Table 2, the value of $G(0)$ is 1.3574 for Pr=1. Figure 5(*b*) shows the variation in the wall temperature $\tilde{\theta}_w = [2\xi/5]^{1/5}\phi_w$, on the free-convection scale. The figure indicates that $\tilde{\theta}_w$ increases with ξ initially, and then asymptotically approaches the constant value, $G(0)$, at large values of ξ.

The local Nusselt number distribution is given by the relation

$$\mathrm{Nu}_x\left(\frac{2}{\mathrm{Re}_x}\right)^{1/2} = \frac{1}{\phi_w} = \frac{1}{\phi(\xi,0)} \tag{43}$$

Equation (43) indicates that the value of $\mathrm{Nu}_x(2/\mathrm{Re}_x)^{1/2}$ depends on ξ and Pr. The variation in $\mathrm{Nu}_x(2/\mathrm{Re}_x)^{1/2}$ with ξ is displayed in Fig. 6 for Pr=1. The figure indicates that $\mathrm{Nu}_x(2/\mathrm{Re}_x)^{1/2}$ increases with ξ as the wall temperature ϕ_w decreases and asymptotically approaches the free-convection limit.

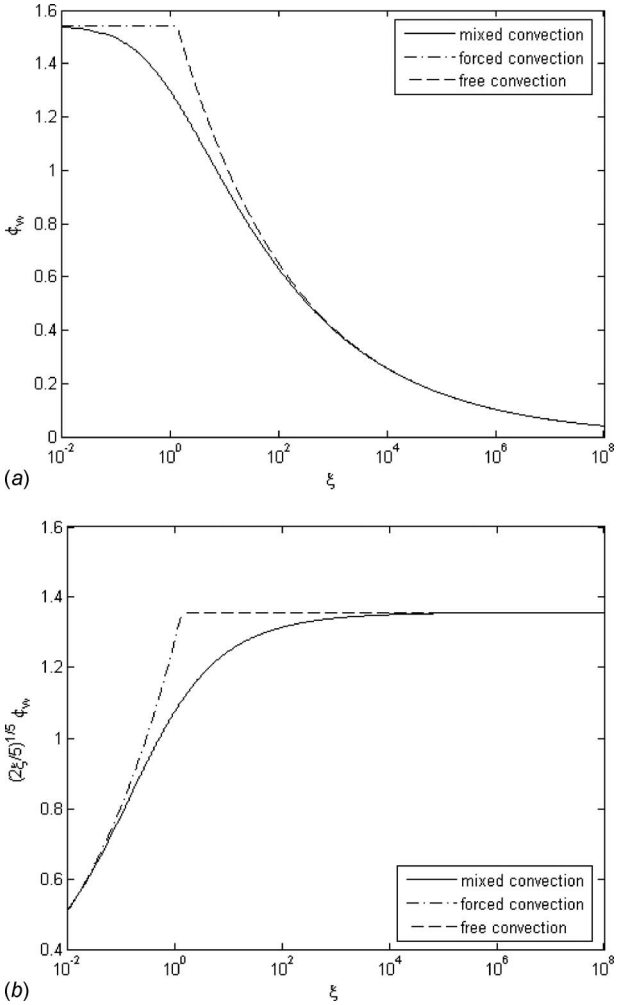

Fig. 5 Axial variation in wall temperature (*a*) on forced-convection scale and (*b*) on free-convection scale

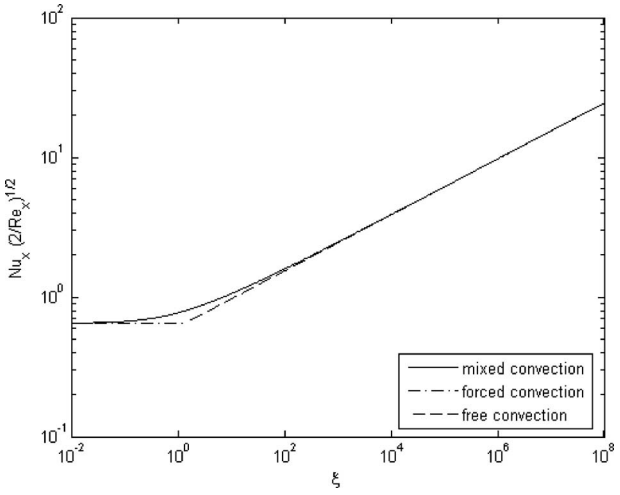

Fig. 6 Axial variation in $\mathrm{Nu}_x(2/\mathrm{Re}_x)^{1/2}$

4 Conclusions

The perturbation analysis presented in Sec. 2.1 shows that buoyancy effects grow downstream as $\varepsilon x^{3/2}$. This may be contrasted with the case of mixed convection along a vertical flat plate with uniform surface temperature, where buoyancy effects grow linearly with x. The perturbation analysis demonstrates that the relevant nondimensional parameter describing mixed-convection boundary-layer flow along a heated vertical plate with uniform surface heat flux is $\varepsilon x^{3/2}$, which is equal to $\mathrm{Gr}_x^*/\mathrm{Re}_x^{5/2}$. The mixed-convection boundary-layer equations have been solved numerically by an accurate finite-difference marching technique. Results for the local skin-friction factor, wall temperature, and local Nusselt number distribution indicate that forced convection is the dominant mode of heat transfer near the leading edge of the plate, where $\mathrm{Gr}_x^*/\mathrm{Re}_x^{5/2} \ll 1$. Buoyancy forces begin to play an important role in the dynamics of the flow when $\mathrm{Gr}_x^*/\mathrm{Re}_x^{5/2} \sim 1$. As $\mathrm{Gr}_x^*/\mathrm{Re}_x^{5/2} \to \infty$, the flow asymptotically approaches the free-convection limit, far downstream of the leading edge.

Nomenclature

c_f = skin-friction coefficient
g = gravitational acceleration
Gr* = modified Grashof number
h = local heat transfer coefficient
k = thermal conductivity of the fluid
l = reference length
Nu = Nusselt number
Pr = Prandtl number
q_w = surface heat flux
Re = Reynolds number
T = dimensional temperature
T_∞ = ambient temperature
u = velocity in the x-direction
$\bar{u}_\infty$ = freestream velocity
$\bar{u}_0$ = free-convection velocity scale
v = velocity in the y-direction
w = transformed velocity
x = coordinate along the plate
y = coordinate normal to the plate

Greek Symbols

α = thermal diffusivity of the fluid
β = coefficient of thermal expansion
η = Blasius similarity variable
$\tilde{\eta}$ = free-convection similarity variable
θ = nondimensional temperature
ν = kinematic viscosity
ρ_0 = reference density
τ_w = wall shear stress
ξ = $2^{3/2}\mathrm{Gr}_x^*/\mathrm{Re}_x^{5/2}$

Subscripts

w = wall
x = local value
∞ = freestream

Superscripts

$-$ = dimensional quantities

References

[1] Gebhart, B., Jaluria, Y., Mahajan, R. L., and Sammakia, B., 1988, *Buoyancy-Induced Flows and Transport*, Hemisphere, New York.
[2] Sparrow, E. M., and Gregg, J. L., 1959, "Buoyancy Effects in Forced Convection Flow and Heat Transfer," ASME J. Appl. Mech., **26**, pp. 133–134.
[3] Eshghy, S., 1964, "Forced Flow Effects on Free Convection Flow and Heat Transfer," ASME J. Heat Transfer, **86**, pp. 290–291.
[4] Szewczyk, A. A., 1964, "Combined Forced and Free Convection Laminar Flow," ASME J. Heat Transfer, **86**, pp. 501–507.
[5] Merkin, J. H., 1969, "The Effect of Buoyancy Forces on the Boundary-Layer Flow Over a Semi-Infinite Vertical Flat Plate in a Uniform Free Stream," J. Fluid Mech., **35**, pp. 439–450.
[6] Lloyd, J. R., and Sparrow, E. M., 1970, "Combined Forced and Free Convection Flow on Vertical Surfaces," Int. J. Heat Mass Transfer, **13**, pp. 434–438.
[7] Yao, L. S., 1987, "Two-Dimensional Mixed Convection Along a Flat Plate," ASME J. Heat Transfer, **109**, pp. 440–445.
[8] Wilks, G., 1973, "Combined Forced and Free Convection Flow on Vertical Surfaces," Int. J. Heat Mass Transfer, **16**, pp. 1958–1964.
[9] Wilks, G., 1974, "The Flow of a Uniform Stream Over a Semi-Infinite Vertical Flat Plate With Uniform Surface Heat Flux," Int. J. Heat Mass Transfer, **17**, pp. 743–753.
[10] Carey, V. P., and Gebhart, B., 1982, "Transport at Large Downstream Distances in Mixed Convection Flow Adjacent to a Vertical Uniform-Heat-Flux Surface," Int. J. Heat Mass Transfer, **25**, pp. 255–266.
[11] Ghosh Moulic, S., and Yao, L. S., 1989, "Natural Convection Along a Vertical Wavy Surface With Uniform Heat Flux," ASME J. Heat Transfer, **111**, pp. 1106–1108.
[12] Sparrow, E. M., and Gregg, J. L., 1956, "Laminar Free Convection From a Vertical Plate With Uniform Surface Heat Flux," Trans. ASME, **78**, pp. 435–440.
[13] Ghosh Moulic, S., 1988, "Mixed Convection Along a Wavy Surface," MS thesis, Arizona State University, Tempe, AZ.
[14] Ghosh Moulic, S., and Yao, L. S., 1989, "Mixed Convection Along a Wavy Surface," ASME J. Heat Transfer, **111**, pp. 974–979.

Natural Convection Reduction in a Composite Air/Porous Annular Region With Horizontal Orientation

M. Ait saada

S. Chikh

Faculté de Génie Mécanique et de Génie des Procédés,
Université des Sciences et de la Technologie Houari Boumediene,
B.P. 32, El Alia,
Bab Ezzouar 16111, Algeria

A. Campo[1]
Department of Mechanical Engineering,
The University of Vermont,
Burlington, VT 05405
e-mail: campanto@yahoo.com

This paper deals with a numerical investigation on natural convection heat transfer in a long horizontal annular region formed with a heated inner cylinder and a cooled outer cylinder. Identifying the annular region geometrically by its radius ratio, it is divided into two subregions: a thicker outer subregion is filled with a porous material saturated by air, whereas a thinner inner subregion is clear. Based on the general Darcy–Brinkman–Forchheimer model for flow in porous media, numerical calculations with the control volume method produce the velocity and temperature fields of the air motion in the two subregions. The baseline case corresponds to an annular region of same dimensions, but filled completely with a porous material saturated by air. Upon articulating the physical properties of a porous material with the clear gap size, the analyst will be able to tune those conditions that are conducive to heat transfer reduction across the concentric two-cylinder configuration. The outcome of this paper is equivalent to the determination of superior thermal insulation performance using lesser porous material. In other words, this paper boils down to beneficial energy conservation together with money savings in the purchase of the thermal insulation. [DOI: 10.1115/1.2993544]

Keywords: heat transfer reduction, long horizontal annulus, air natural convection, porous material, improved thermal insulation

1 Introduction

Convective heat transfer through porous media has gained considerable attention in recent decades due to its relevance in a multitude of technological applications such as advanced thermal insulation, compact cryogenic devices, underground cable systems, grain storage in silos, nuclear waste repositories, thermal energy storage, etc. Interestingly, a subset of these technological applications pertains to buoyancy-driven flows in a variety of configurations that bring forth natural convective heat transfer.

The pioneering work concerning annular enclosures filled with a porous medium was done by Caltagirone [1,2] who performed numerical simulations and experimental measurements with a horizontal annulus of fixed radius ratio, $R=2$. With the help of the Christiansen effect, this researcher observed a steady two-dimensional (2D) flow regime with two symmetric convective cells[2] for a modified Rayleigh number Ra^* that stayed below 65 ± 4. For higher Ra^*, fluctuating three-dimensional (3D) effects appeared in the upper part of the porous zone, although the lower zone remained two dimensional. The visualization experiments in Refs. [1,2] were reconducted by Charrier-Mojtabi et al. [3] who confirmed the existence of the two-dimensional unicellular steady structures. When Ra^* was increased up to 250, the unicellular flow patterns became three dimensional in the upper part occupied by the porous material, while still remained two dimensional in the lower part. During the cooling phase, the confined flow turned two dimensional again, being bicellular first and unicellular later when the modified Rayleigh number Ra^* dropped below 69. Collectively, either 2D unicellular flow or 2D bicellular flow was manifested for the same value of $Ra^* > 65 \pm 4$, but both cases possessed stability. Barbosa Mota and Saatdjian [4,5] reproduced numerically the hysteresis phenomenon in an annular cavity filled with a porous material, owing a moderate radius ratio $R > 1.7$. The functional relationship between the average Nusselt number and the modified Rayleigh number followed a closed hysteresis loop, which was tied up to a transition from a flow with two cells (unicellular regime) to a more complex flow with four cells (bicellular regime). For smaller $R < 1.7$, steady-state flow regimes containing two, four, six, and eight cells appeared progressively as Ra^* increased, but absent of hysteresis patterns. For a given radius ratio $R=2$, the numerical predictions were in good agreement with the experimental data reported in Ref. [1]. The two-dimensional bifurcation phenomenon was also tackled by Himasekhar and Bau [6], combining the perturbation expansion technique and the Galerkin method. Relying on an elaborate numerical procedure based on a mixed Fourier–Galerkin-collocation-Chebyshev method, Charrier-Mojtabi [7] obtained a set of representative 2D and 3D flow and temperature fields. The solution of the Boussinesq equations formulated in terms of pressure and temperature supplied the needed critical modified Rayleigh number Ra_c^* for the transition between 2D unicellular flow and 2D bicellular flow. The end result was adequately synthesized by $Ra_c^* = 61 \pm 0.5$ for $R=2$ and $Ra_c^* = 111.75 \pm 0.25$ for $R=\sqrt{2}$. The numerical findings clearly indicated the presence of complex 3D spiral flows localized at the top of the annular regions whenever the radius ratio R was contained between $\sqrt{2}$ and 2. In addition, the bifurcation point demarcating the 2D unicellular flow from the complex 3D spiral flow was determined numerically.

All publications cited previously revolve around the simple Darcy model. Conceptually, the fluid flow through a porous medium with highly permeability is subject to inertia and boundary effects that are not contemplated in the Darcy model. Based on a semi-empirical version of the momentum equation suggested by Vafai and Tien [8], the numerical computations done by Kaviany

[1]Corresponding author.
[2]Also named unicellular flow.

Contributed by the Heat Transfer Division of ASME for publication in the JOURNAL OF HEAT TRANSFER. Manuscript received October 31, 2007; final manuscript received July 10, 2008; published online December 12, 2008. Review conducted by Sung Jin Kim.

 Copyright © 2009 by ASME

[9] elucidated that the non-Darcy effects—the boundary effect being the most significant—tend to reduce the heat transfer rate. A flow diagram was elaborated by the latter author in order to classify in an orderly fashion the pseudoconduction regime, the Darcy regime, and the non-Darcy regime.

Natural convection has also been extensively studied in a horizontal annulus filled with a Newtonian fluid, mostly air and water. Grigull and Hauf [10] visualized circulatory flows and characterized them in terms of a Grashof number based on the annulus thickness, δ. This paper aptly culminated with the establishment of three regimes: the pseudoconduction ($\mathrm{Gr}_\delta < 2400$), the transition regime ($2400 \leq \mathrm{Gr}_\delta \leq 30{,}000$), and the fully developed convection ($\mathrm{Gr}_\delta > 30{,}000$). Focusing on an experimental work, Powe et al. [11] classified the flow patterns according to suitable combinations of the Rayleigh number Ra_δ and the radius ratio R. At small radius ratios ($R \leq 1.20$), the unicellular flow becomes multicellular, while remaining two dimensional when increasing the Rayleigh number in the ample range $4900 < \mathrm{Ra}_\delta < 34{,}100$. This 2D stationary flow structure was confirmed numerically by Powe et al. [12] later. For higher radius ratios inside the R-interval $1.24 \leq R \leq 1.71$, a complex 3D spiral flow develops after the first bifurcation surfaces up at the top of the annular cavity. Furthermore, an oscillating three-dimensional thermal plume was palpable in the upper part of the annular space when $R \geq 2$. Kuehn and Goldstein [13] carried out theoretical, numerical, and experimental analyses for air and water filling an annulus of fixed $R = 2.6$. At the end, they constructed empirical correlations satisfying all Ra_δ operating inside $2.1 \times 10^4 \leq \mathrm{Ra}_\delta \leq 9.8 \times 10^5$. In another work, these same authors [14] developed a laminar and turbulent model for heat transfer in concentric and eccentric circular annuli. In the extreme case connected to a narrow annular space, some investigations were initiated to decipher the instabilities created in the constrained 2D multicellular flows. The consensus was that the discrepancies found in literature [15–17] were primarily linked to pairs of flow patterns and critical Rayleigh numbers corresponding to the bifurcation points.

It should be added that turbulent thermal convection in fluids confined to horizontal concentric annuli has been investigated in Refs. [18–22], but this topic deviates from the main objective of the present paper.

Natural convection in horizontal concentric spaces partly filled with a porous matrix saturated by air has been examined in two publications, one by Aldoss et al. [23] and the other by Leong and Lai [24]. Depending on the placement of the porous matrix layer, two cases were treated in Ref. [23]. In the first case, the porous matrix layer was located adjacent to the hot inner cylinder, while in the second case was located adjacent to the cold outer cylinder. In both cases, a value of 1 was assigned to the thermal conductivity ratio $R_c = k_e/k$. It is worth pointing out that the idealized number 1 lacks physical significance because no real porous material possesses the thermal conductivity as low as the thermal conductivity of air ($k_{\mathrm{air}} = 0.026$ W/m K at $T = 20°\mathrm{C}$). Even more, since the Grashof number was applied in a small interval extending from 3.7×10^3 to 5.4×10^3, this choice means that the air motion was very weak. This situation essentially translates into dominant conduction heat transfer. As far as the presentation of results is concerned, neither streamlines nor isotherms were plotted to facilitate the visualization of the fluid/heat flow characteristics. The obtained results were directed exclusively through the dimensionless mean heat convection coefficient, that is, the mean Nu number. The tortuous airflow was treated in Ref. [24] with the Darcy–Brinkman model in the porous subdomain in contact with the heated inner cylinder. With a combination of the perturbation method and the Fourier transform, the authors determined approximate analytic velocity and temperature solutions for an ultrahigh Prandtl number fluid with 20,000 (resembling engine oil between 0°C and 20°C). A pair of extremely small Rayleigh numbers of order Ra=0.1 and 1 were associated with the thick fluid/annulus ensemble. In this regard, it may be speculated that (1) the tiny Ra values are indicative of very weak convection, (2) the tiny Ra values are not suited for real insulation purposes, and (3) the thick fluid chosen remains almost motionless at the prevalent low Ra numbers.

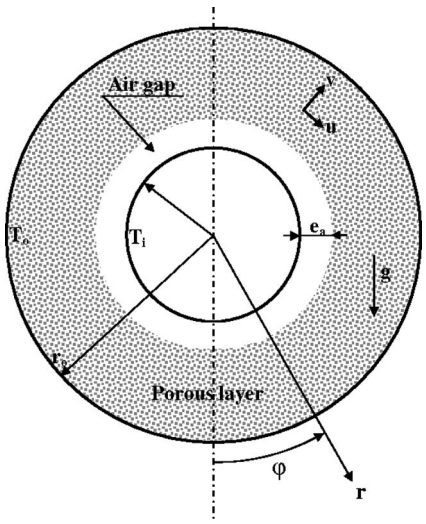

Fig. 1 Physical system and computation domain

Pipelines are used extensively in industries throughout the world to carry hot fluid streams from one location to another. The norm is that the pipelines are thermally insulated to combat the heat losses to the environment [25].

The principal motivation for undertaking the present investigation was to explore possible ways to improve the thermal insulation effectiveness of horizontal round tubes by using a smaller amount of thermal insulation material. This idea opposes radically the traditional way that pursues a larger thickness of insulation material. For this purpose, instead of analyzing the air natural convection in a horizontal annular cavity filled completely with a saturated porous medium, we analyzed instead the air natural convection in the same annular cavity partly filled with a saturated porous medium. To accomplish this goal specifically, a small clear gap is accommodated around the heated inner cylinder to exploit the poor heat conducting properties of air. The other part of the annular cavity moving outward is occupied by the saturated porous medium. The problem under study is formulated with a complete system of 2D conservation equations embracing the Darcy–Brinkman–Forchheimer model in the porous medium. The system of equations has to be solved numerically because of its severe level of complexity. Articulating the physical properties of the porous material with the air gap size in a horizontal annular cavity, the analyst will be able to tune the proper conditions that are conducive to heat transfer reduction across the concentric two-cylinder configuration. This combination of factors may render superior thermal insulation performance while using lesser porous material. In other words, this issue translates into beneficial energy conservation accompanied by money savings in the purchase of the insulating material.

2 Mathematical Formulation

Sketched in Fig. 1 is the physical system consisting in an annular geometry bounded by two long concentric impermeable solid cylinders placed in a horizontal position. The inner cylinder of radius r_i is at a hot temperature T_i, whereas the outer cylinder of radius r_o is at a cold temperature T_o. An air gap of thickness e_a is placed adjacent to the hot inner cylinder and the remaining space is filled with a porous matrix. The porous layer with porosity ε and permeability K is saturated by air with effective dynamic viscosity $\mu_e = \mu$, effective heat capacity $(\rho c_p)_e = (\rho c_p)$, and effective thermal conductivity $k_e \geq k$. The thermal-driven air flow is

presumed to be steady, incompressible, laminar, and two dimensional. The physical properties of air are taken at the average temperature $T_m=(T_i+T_o)/2$, except for the density in the buoyancy terms of the momentum equations that is allowed to vary linearly with temperature. As it is customarily done, the fluid is conceived to be in thermal equilibrium with the porous matrix.

The mathematical formulation is written in cylindrical coordinates with the origin lying at the center of the two bounding solid cylinders. The angular coordinate φ is measured from the vertical, positively counterclockwise at the bottom. The Boussinesq-approximated Navier–Stokes equations and energy equation with negligible viscous dissipation describe the buoyancy-induced airflow and temperature fields under study. The conservative equations, based on the available empirical data and the volume average principle [8], are applied in the outer porous subregion. The semi-empirical momentum equations incorporate the so-called Darcy, Brinkman, and Forchheimer terms [9]. However, the momentum equations do not account for any dispersion or spreading of momentum and thermal energy due to interpore mixing in the presence of velocity gradients. A one-domain approach with one single set of equations is used for both the fluid subregion and the porous subregion. An averaging technique is employed to handle the discontinuity of the properties at the interface. The equations of conservation of mass, momentum, and heat transport written in vector form are as follows:

$$\nabla \cdot \boldsymbol{V} = 0 \tag{1}$$

$$\rho(\boldsymbol{V}\cdot\nabla)\boldsymbol{V} = -\nabla P - \rho g\beta(T-T_m)\boldsymbol{I} + \mu\Delta\boldsymbol{V} - \frac{\varepsilon\mu}{K}\boldsymbol{V} - \frac{\rho F\varepsilon^2}{\sqrt{\mathrm{K}}}|\boldsymbol{V}|\boldsymbol{V} \tag{2}$$

$$(\boldsymbol{V}\cdot\nabla)T = \alpha_e \Delta T \tag{3}$$

where $\boldsymbol{I}=\cos\phi\boldsymbol{e_r}-\sin\phi\boldsymbol{e_\varphi}$ and $\boldsymbol{V}=v\boldsymbol{e_r}+u\boldsymbol{e_\varphi}$ ($\boldsymbol{e_r}$ and $\boldsymbol{e_\varphi}$ are unit vectors) and ρ, μ, and β are the fluid properties.

By setting the permeability K equal to infinity and the porosity ε equal to 1, the Navier–Stokes equations are recovered in the fluid subregion where the effective thermal diffusivity α_e is replaced by the air thermal diffusivity α.

The intrinsic velocity of the porous layer is obtained by way of the ratio $\boldsymbol{V}/\varepsilon$. The Darcy resistance in the momentum equation given by $(\varepsilon\mu/K)\boldsymbol{V}$ represents the influence of friction at the pore level. Non-Darcy terms are also included to capture the macroscopic and microscopic inertial effects as well as the boundary effects.

The radial coordinate r is scaled with respect to the radius r_i, the velocities u and v to α/r_i, the pressure p to $\rho(\alpha/r_i)^2$, and the temperature difference $T-T_o$ to T_i-T_o, paving the way for the definition of the dimensionless variables:

$$r^*=\frac{r}{r_i},\quad u^*=\frac{u}{\alpha/r_i},\quad v^*=\frac{v}{\alpha/r_i},\quad P^*=\frac{P}{\rho(\alpha/r_i)^2},\quad \theta=\frac{T-T_o}{T_i-T_o}$$

Thereafter, the governing equations (1)–(3) are conveniently rewritten in expanded form as

$$\frac{\partial}{\partial r^*}(r^*v^*)+\frac{\partial u^*}{\partial\varphi}=0 \tag{4}$$

$$\frac{\partial}{\partial r^*}\left(r^*v^*v^*-\mathrm{Pr}\,r^*\frac{\partial v^*}{\partial r^*}\right)+\frac{\partial}{\partial\varphi}\left(u^*v^*-\mathrm{Pr}\frac{\partial v^*}{r^*\,\partial\varphi}\right)$$
$$=-r^*\frac{\partial P^*}{\partial r^*}-\mathrm{Ra}\,\mathrm{Pr}\,\theta\cos(\varphi)r^*+\frac{u^{*2}}{r^*}r^*$$
$$-\mathrm{Pr}\left(\frac{v^*}{r^{*2}}+\frac{2}{r^{*2}}\frac{\partial u^*}{\partial\varphi}\right)r^*-\left(\frac{\mathrm{Pr}}{\mathrm{Da}}+\frac{C_f}{\sqrt{\mathrm{Da}}}|\boldsymbol{V}^*|\right)v^*r^* \tag{5}$$

$$\frac{\partial}{\partial r^*}\left(r^*v^*u^*-\mathrm{Pr}\,r^*\frac{\partial u^*}{\partial r^*}\right)+\frac{\partial}{\partial\varphi}\left(u^*u^*-\mathrm{Pr}\frac{\partial u^*}{r^*\,\partial\varphi}\right)$$
$$=-r^*\frac{\partial P^*}{\partial r^*}+\mathrm{Ra}\,\mathrm{Pr}\,\theta\sin(\varphi)r^*-\frac{v^*u^*}{r^*}r^*$$
$$-\mathrm{Pr}\left(\frac{u^*}{r^{*2}}-\frac{2}{r^{*2}}\frac{\partial v^*}{\partial\varphi}\right)r^*-\left(\frac{\mathrm{Pr}}{\mathrm{Da}}+\frac{C_f}{\sqrt{\mathrm{Da}}}|\boldsymbol{V}^*|\right)u^*r^* \tag{6}$$

$$\frac{\partial}{\partial r^*}\left(r^*v^*\theta-R_cr^*\frac{\partial\theta}{\partial r^*}\right)+\frac{\partial}{\partial\varphi}\left(u^*\theta-R_c\frac{\partial\theta}{r^*\,\partial\varphi}\right)=0 \tag{7}$$

Here the magnitude of the velocity in Eqs. (5) and (6) is related to $|\boldsymbol{V}^*|=\sqrt{u^{*2}+v^{*2}}$.

In light of the foregoing development, the following six dimensionless groups are identified as the controlling parameters of the problem:

(1) Rayleigh number $\mathrm{Ra}=g\beta(T_i-T_o)r_i^3/(\nu\alpha)$
(2) Prandtl number $\mathrm{Pr}=\nu/\alpha$
(3) Darcy number $\mathrm{Da}=\mathrm{K}/(\varepsilon r_i^2)$
(4) thermal conductivity ratio $R_c=k_e/k$
(5) radius ratio $R=r_o/r_i$
(6) dimensionless air gap thickness $e_a^*=e_a/r_i$

Three of these parameters, Ra, Da, and R_c, can be combined to deliver a composite parameter—the modified Rayleigh number $\mathrm{Ra}^*=\mathrm{Ra}\,\mathrm{Da}/R_c$—if the Boussinesq–Darcy equations are responsible for the modeling of heat/fluid flow in the porous medium.

In the fluid subregion, the Darcy number Da tends toward infinity and the thermal conductivity ratio R_c is equal to unity. In reference to the inertial coefficient $C_f=F\varepsilon^{3/2}$, its magnitude can be as small as 0.1 in the case of foam metal fibers, as indicated by Nield and Bejan [26]. Whenever $\mathrm{Ra}\le10^6$, $\mathrm{Da}\le10^{-3}$, and $R_c\le10$ hold, the microscopic inertial effects, modeled by the quadratic drag terms in Eqs. (2), (5), and (6), are very weak when compared with the Darcy effects modeled by linear drag terms. The assumption of local thermal equilibrium in the porous medium is valid for the small thermal conductivity ratios ($R_c<10$) used in the present study.

Assuming flow symmetry about the vertical plane dividing the two cylinders into two semicylinders, the computation domain is constructed in one-half of the annulus $0\le\varphi\le\pi$. The boundary conditions in dimensionless form can then be properly listed as follows:

$$u^*=v^*=0,\quad \theta=1\quad \text{at}\ r^*=1 \tag{8a}$$

$$u^*=v^*=\theta=0\quad \text{at}\ r^*=R \tag{8b}$$

$$u^*=\frac{\partial v^*}{\partial\varphi}=\frac{\partial\theta}{\partial\varphi}=0\quad \text{at}\ \varphi=0\quad \text{or}\quad \pi \tag{8c}$$

The key matching conditions at the interface between the porous subregion and the clear subregion, representative of the continuity of velocities, pressure, shear stress, temperature, and heat flux, are given by

$$\boldsymbol{V}_f^*=\boldsymbol{V}_p^*,\quad P_f^*=P_p^* \tag{9a}$$

$$\frac{\partial\boldsymbol{V}_f^*}{\partial r^*}=\frac{\partial\boldsymbol{V}_p^*}{\partial r^*} \tag{9b}$$

$$\theta_f=\theta_p \tag{9c}$$

$$\frac{\partial\theta_f}{\partial r^*}=R_c\frac{\partial\theta_p}{\partial r^*},\quad \frac{\partial\theta_f}{\partial\varphi}=R_c\frac{\partial\theta_p}{\partial\varphi} \tag{9d}$$

Table 1 Grid sensitivity analysis for Ra=10^7, Pr=0.7, and R_c=2 along with two Da; maximum relative differences are 2% for 100×120 nodes and 1.08% for 200×240 nodes

	Da=10^{-4}			Da=10^{-8}		
e_a^*	$\overline{\text{Nu}}$ 50×60 nodes	$\overline{\text{Nu}}$ 100×120 nodes	$\overline{\text{Nu}}$ 200×240 nodes	$\overline{\text{Nu}}$ 50×60 nodes	$\overline{\text{Nu}}$ 100×120 nodes	$\overline{\text{Nu}}$ 200×240 nodes
0	3.8683	3.8806	3.8821	1.0009	1.0004	1.0003
0.1	4.7132	4.7183	4.7181	1.0117	1.0099	1.0084
0.5	6.5976	6.6178	6.6326	2.2728	2.2451	2.2304
0.8	7.6781	7.7233	7.7467	4.7178	4.6233	4.5732
1	9.9714	10.0213	10.0525	–	–	–

The dimensionless heat flux from the two bounding cylinders is dependent on the temperature gradient at the wall. These two quantities are evaluated locally by

$$q_i(\varphi) = -\left.\frac{\partial\theta}{\partial r^*}\right|_{r^*=1} \quad \text{on the inner cylinder} \tag{10a}$$

$$q_o(\varphi) = -R_c\left.\frac{\partial\theta}{\partial r^*}\right|_{r^*=R} \quad \text{on the outer cylinder} \tag{10b}$$

Under steady-state conditions, the total amount of exchanged heat in the annular region is

$$Q = 2\int_0^\pi q_i d\varphi = 2\int_0^\pi q_o R d\varphi \tag{11}$$

Next, the dimensionless heat convection coefficient or the Nusselt number at the curved walls is a convenient way for expressing the heat transfer due to convective effects. In this vein, the local Nusselt numbers at the two cylinders are defined as follows:

$$\text{Nu}_i(\varphi) = -R_c^{-1}\ln[R(1+e_a^*)^{R_c-1}]\left.\frac{\partial\theta}{\partial r^*}\right|_{r^*=1} \tag{12a}$$

$$\text{Nu}_o(\varphi) = -R\ln[R(1+e_a^*)^{R_c-1}]\left.\frac{\partial\theta}{\partial r^*}\right|_{r^*=R} \tag{12b}$$

Ultimately, the mean Nusselt numbers on the inner and outer walls of the annulus are calculated by averaging the local Nusselt number on the surface area of the cylinders. For steady-state conditions, these two mean Nusselt numbers should be equal. This equality can also be considered as a physical criterion for checking the accuracy of the numerical solutions. Therefore, the mean Nusselt number defined as

$$\overline{\text{Nu}} = \frac{1}{\pi}\int_0^\pi \text{Nu}_i\, d\varphi = \frac{1}{\pi}\int_0^\pi \text{Nu}_o\, d\varphi \tag{13}$$

furnishes the ratio of the total heat transfer to the heat transfer by conduction (in the absence of natural convection, i.e., for Ra=0).

3 Numerical Procedure

Due to a superabundance of parameters controlling the present study, all numerical computations are carried out for one fluid, air (Pr=0.71) and an annular cavity with fixed radius ratio R=2.

The system of partial differential equations (4)–(7) and the imposed boundary conditions are discretized by means of the control volume method. Staggered grids and the SIMPLE (Semi Implicit Method for Pressure Linked Equations) algorithm [27] are utilized to treat the coupling between the velocity and pressure fields. A power law differencing scheme (PLDS) is used to implement the contribution of convection and diffusion in the transport phenomena. Because of the prevalent nonlinearities, the system of transformed algebraic equations is solved by employing a combination of the tridiagonal matrix algorithm (TDMA) and the Gauss–Seidel iterative method along with under-relaxation. The final flow and temperature solution is conceived to have reached convergence during the iterative process when the maximum relative error on the generic dependent variable ϕ (equivalent to the velocities u and v, the pressure p, and the temperature T),

$$\frac{1}{\phi_{\max}}\sqrt{\sum_{i=1}^{N}(\phi_i^{n+1}-\phi_i^n)^2} \le \varepsilon \tag{14}$$

is satisfied. A typical value of ε is preset at 10^{-5}. In addition, the maximum allowable absolute residue in the mass conservation equation (1) is equated to less than 10^{-10}.

For a moderate-to-high Rayleigh number of magnitude Ra=10^7 combined with a thermal conductivity ratio R_c=2, a grid sensitivity analysis was done for two contrasting Darcy numbers, a high Da=10^{-4} and a low Da=10^{-8}, while sweeping several relative air gap thicknesses e_a^*. A nonuniform grid in the radial direction is deployed having finer steps close to the inner and outer cylinders to capture the anticipated steep velocity and temperature gradients. The results reported in Table 1 served as a guidance to select a grid of 100×120 nodes in the computational domain. An additional grid refinement has shown that a finer 200×240 grid yields a maximum relative difference of 1.08% in the mean Nusselt number, $\overline{\text{Nu}}$. Actually, the first order scheme provided sufficient accuracy in the numerical solutions with this fine grid. To assess the accuracy of the numerical computations even further, a global energy balance was performed between the inner and outer solid cylinders. The quality of the results can be asserted through the excellent agreement between the inner and the outer mean Nusselt numbers $\overline{\text{Nu}_i}$ and $\overline{\text{Nu}_o}$; this parity amounts to a negligible difference of less than 0.06%.

4 Results and Discussion

From principles of heat conduction, the traditional way to improve the thermal insulation performance of a horizontal annular cavity filled with a porous material is to increase the thermal resistance by enlarging the dimension of the radius ratio R. Another possibility worth of exploring is to add thermal resistance to the annular cavity by removing a thin layer of porous material around the hot inner cylinder to create a thin air layer; this arrangement forces the air to remain stagnant in the artificially created gap. The presence of still air would facilitate the reduction in the conductive heat transfer because the thermal conductivity of air is smaller than that of typical insulation materials. In numbers, the thermal conductivity ratio usually lies inside $1 \le R_c \le 3$. With an insulating material possessing a very low permeability (Da=10^{-8}) and a small thermal conductivity ratio (R_c=2), the insertion of an air gap promotes the onset of natural convection that tends to invigorate, i.e., $\psi_{\max}$ increases with the gap size, as shown in Fig. 2(*a*). The porous layer constitutes a dynamic resistance to the thermal-driven flow in principle due to the Darcy effects and thus lessens the strength of thermal buoyancy. For Da=10^{-8}, the resistance is substantially high so that it mainly restricts the flow to the fluid subregion. For a very thin air gap, say, e_a^*=0.1, the fluid motion is very weak and may be considered nearly motion-

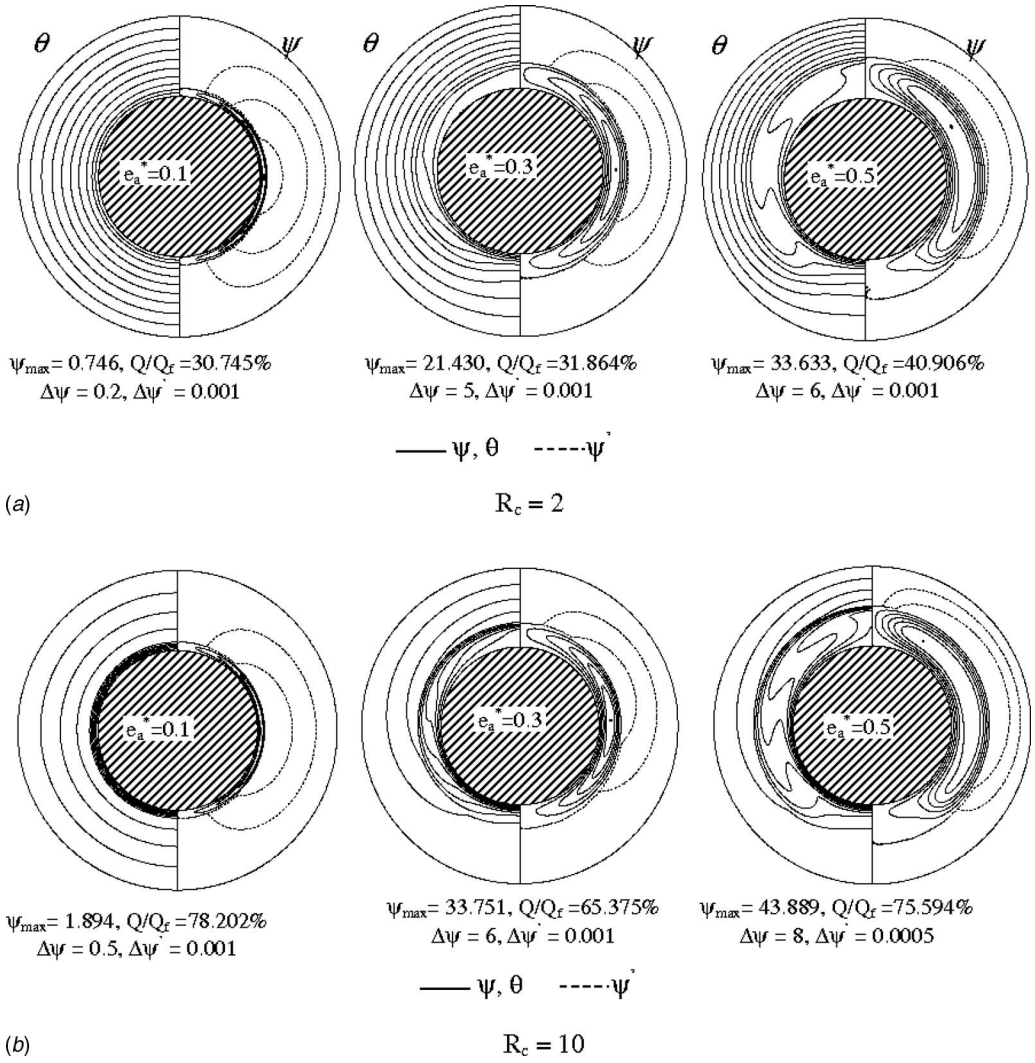

Fig. 2 Streamlines and isotherms in a partially porous annulus for Ra=10^6 and Da=10^{-8}: effect of e_a^* for (*a*) R_c=2 and (*b*) R_c=10

less. Consequently, the transfer of heat takes place by the conduction mode. On the other hand, an increment in R_c to a large value of 10 means that the temperature gradient within the porous layer diminishes to a small value. For instance, the temperature gradient applied to the air layer is substantially augmented; this augmentation yields a greater buoyancy effect that induces a more intense fluid circulation. This behavior is synonymous with higher values of $\psi_{\max}$, as reflected in Fig. 2(*b*). Furthermore, it can be recognized that the insertion of a thin air gap may lead to the minimization of heat transfer in the horizontal annular cavity. A detailed explanation of this singular feature will be given in the forthcoming figures.

The variation in the mean Nusselt number $\overline{\mathrm{Nu}}$ with the dimensionless air gap e_a^* parametrized by Da is plotted in Fig. 3 for two values of R_c. When the Darcy number is decreased, this action amplifies the viscous effects and weakens the buoyancy effect; the net result is a diminution in the mean Nusselt number. For R_c=1, the conduction resistance does not change compared with the plain fluid situation because the effective thermal conductivity of the porous material k_e is equal to that of the thermal conductivity of the fluid k. Thus, the $\overline{\mathrm{Nu}}$ value is constrained between the fully porous case typified by e_a^*=0 and Da$\leq 10^{-6}$ and the fully fluid case with e_a^*=1. The influence of e_a^* is more important whenever there is a small permeability K, in other words for a thin porous layer or a thin air gap. By increasing R_c up to 5, the heat transfer by conduction is augmented particularly for thick porous layers, i.e., this action promotes the reduction in $\overline{\mathrm{Nu}}$. On the contrary, for thin porous layers, natural convection remains the prevailing

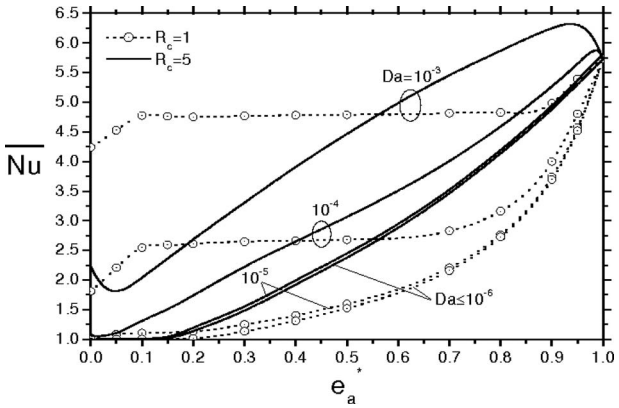

Fig. 3 Influence of e_a^* and Da on the mean Nusselt number for Ra=10^6

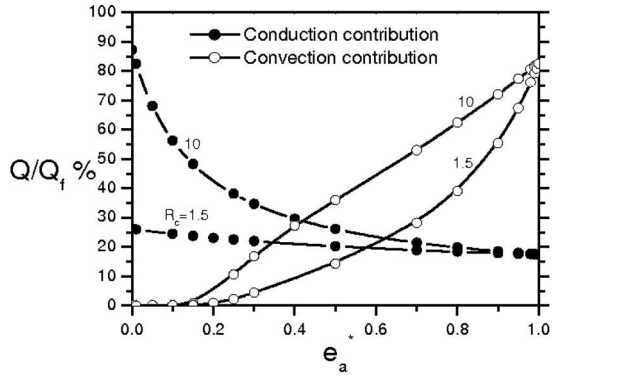

(*a*) Conduction and convection contributions to the total heat losses

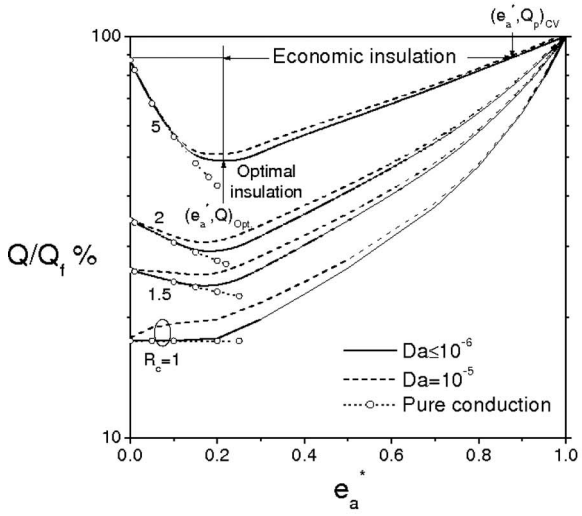

(*b*) Total heat losses

Fig. 4 Heat transfer reduction in a partly porous annulus for Ra=10^6: (*a*) conduction and convection contributions in total heat losses and (*b*) total heat losses

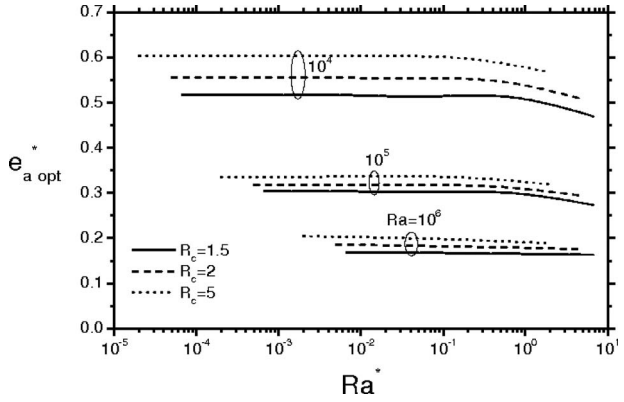

Fig. 5 Air-gap size for optimal thermal insulation

mode of heat transfer. For example, if Da=10^{-3}, the intersection point e_a^*=0.55 between the curve R_c=1 and the curve R_c=5 insinuates two regions: one subregion of highly porous annulus where the effect of R_c is substantial and another subregion of thick air gap where natural convection is dominating. The intersection point e_a^* occurs at a lower value for a smaller magnitude of the permeability K.

The forthcoming set of figures was prepared to assess the heat transfer performance in a qualitative manner. For purposes of thermal insulation as given in Fig. 4, a porous material with low or relatively moderate permeability K and low or relatively moderate thermal conductivity k_e is employed. The annular space filled completely with a porous material is then chosen as a point of reference in which the heat transfer occurs by the conduction mode. Figure 4 tries to answer the following question: Is it viable to reduce the heat losses while using lesser insulating material? In this regard, Fig. 4(*a*) illustrates the contributing parts of conduction and natural convection toward the total heat losses versus the relative air layer thickness. In fact, it is obvious that in the conduction mode, substituting part of the porous material by motionless air will increase the thermal resistance contributing to a reduction in heat losses. On the contrary, lessening the porous layer thickness or creating an artificial air gap, this reduces the hydrodynamic resistance and consequently intensifies natural convection particularly in the inner subregion of clear fluid. Certainly, the insertion of a thin air gap of approximately less than 10% of the annular space thickness does not entail to a great natural convection activity even at a moderate Da value of 10^{-5}. This statement is evidenced in Fig. 4(*b*). Therefore, conduction prevails as a heat transfer mode up to a given value of the air layer thickness e_a^*, which means that air may be considered as "quiescent" up to this point. Beyond this value of e_a^*, natural convection becomes sufficiently important to instill an increasing trend to the heat loss curve. The importance of Fig. 4 stems from the fact that it deals with the quality of thermal insulation and its potential improvement. Two points are worth defining at this point through the utilization of this figure. One, an optimal insulation corresponding to the best thermal performance given by the minimum heat losses (Q_{opt}) obtained at the thickness $e_{a,\text{opt}}^*$. The other, the upper limit of an economic insulation represented by the same heat losses (Q_p) as the reference case, but with much less insulating material ($e_{a,\text{cv}}^*$). As an example, an insulating material characterized by R_c=2 and Da$\leq 10^{-6}$ ensures an optimal insulation condition, i.e., about 17% decrement in heat losses than the fully porous annulus. In other words, this corresponds to a 13% saving in the porous material and an economic insulation, which delivers the same heat losses as the completely porous case with as much as 30% less insulating material.

In all fairness, it should be remarked that for an excellent insulating material having R_c=1 and Da$\leq 10^{-6}$, the heat losses cannot be reduced. However, the reference case can be retrieved with a less thick porous layer. To put things in perspective, a parametric study is carried out to obtain $e_{a,\text{opt}}^*$ in terms of Da, Ra, and R_c, and the computed results are plotted in Fig. 5 for further analysis. It is observable in this figure that the optimal insulation thickness varies inversely with Ra. Thus, a greater amount of insulating material is saved when the natural convection strength is small, say, around Ra=10^4.

Unlike in the previous case, highly permeable and conducting porous materials can induce a deterioration of the thermal insulation effectiveness. Generally, a porous insert with R_c=10, a small permeability K, and Ra=10^6, as illustrated in Fig. 6, would reduce the conduction resistance and increase the natural convection resistance in the same manner that was explained in Fig. 4(*a*) before. In fact, the same trend as in Fig. 4(*b*) is obtained. It is worth noting that the nearly fully porous annular cavity, indicated by the limit $e_{a,\text{HTA}}^*$, presents an interesting case of heat transfer enhancement due to the substantial reduction in conduction resistance because conduction is the prevailing heat transfer mode. As an illustrative example, for Da$\leq 10^{-6}$ the heat transferred reaches the level of the plain fluid case at $e_{a,\text{HTA}}^*$=0.06 and may exceed it by more than 77% at the fully porous limit. For a higher permeability of the porous material holding Da=10^{-3}, the natural convection resistance does not increase considerably and the thermal buoyancy becomes locally intense so that the overall heat transfer is enhanced basically due to the impact of R_c regardless of the thick-

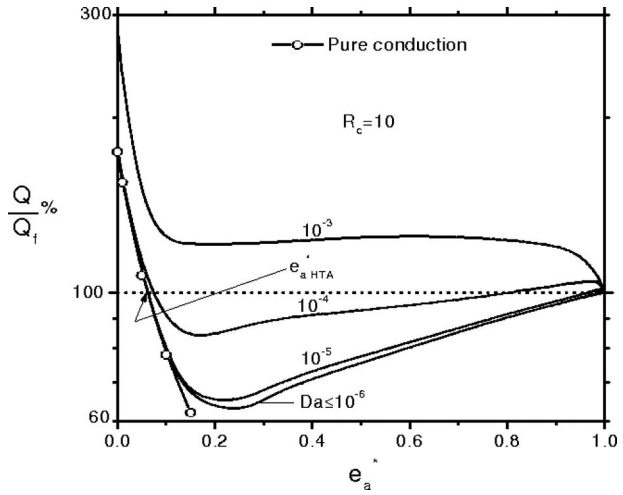

Fig. 6 Heat transfer performance in a partly porous annulus for Ra=10^6 and R_c=10

ness of the porous layer. However, one may notice immediately that the impact of R_c is much more significant for a highly porous material.

To culminate the discussion of results, we introduce a dimensionless global parameter E for the assessment of the heat transfer performance. E is defined as the ratio of the dimensionless reduced heat transfer to the dimensionless thickness of the porous layer as follows:

$$E(\%) = \frac{(Q_p - Q)/Q_f}{e_p^*} \tag{15}$$

From the standpoint of establishing an analogy, the elements in the parameter E are reminiscent of some sort of quality-to-cost ratio. In this sense, the quality corresponds to the thermal performance and the cost to the quantity of the porous material selected. Thereby, the best economical situation would be one that guarantees a maximum value of E. In harmony with this proposition, representative values for the parameter E are displayed in Fig. 7, elucidating that the best thermal insulation is close to the maximum thermal performance point ($e^*_{a,\mathrm{opt}}$). Without any doubt, this concise graphical representation is important because it will serve as a valuable guidance to thermal design engineers.

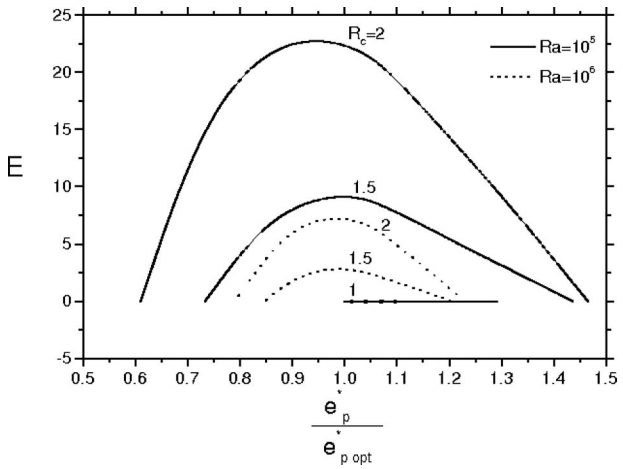

Fig. 7 Heat transfer performance for thermal insulation when Da=10^{-8}

5 Conclusion

Natural convection in a horizontal annular region partly filled with a porous material is analyzed and documented from the engineering framework of thermal insulation. Detailed numerical results convincingly demonstrate that the artificial creation of a clear gap in the annular space adjacent to the hot inner cylinder is tantamount to thermal insulation characteristics that are superior than those inherent to the standard situation of an annular region filled completely with porous material. For certain combinations of the controlling parameters, two specific thicknesses of the air gap size are obtained: one corresponds to the minimum heat loss and the other to the smallest porous material band to ensure the same amount of heat transferred as compared with the fully porous annular space.

Acknowledgment

M.A.S. and S.C. are grateful to all the staffs of IUSTI-Polytech'Marseille, France for their welcome and for the working conditions they provided during the finalization of this project.

Nomenclature

Da = Darcy number, $K/(\varepsilon r_i^2)$
e_a = air gap thickness, m
e_p = porous layer thickness, m
g = gravity acceleration, m/s^2
k = fluid thermal conductivity, W/m K
K = permeability of porous material, m^2
Nu = mean Nusselt number
p = pressure, Pa
P^* = dimensionless pressure
Pr = Prandtl number, ν/α
Q = total heat exchange, W
R = radius ratio, r_o/r_i
Ra = Rayleigh number, $g\beta(T_i-T_o)r_i^3/(\nu\alpha)$
R_c = thermal conductivity ratio, k_e/k
T = temperature, °C
u,v = tangential and radial velocities, m/s
u^*,v^* = dimensionless tangential and radial velocities
r = radial coordinate, m
r^* = dimensionless radial coordinate

Greek Symbols

α = fluid thermal diffusivity, m^2/s
β = fluid thermal dilatation coefficient, 1/K
ε = porosity
μ = fluid dynamic viscosity, kg/m s
ν = fluid kinematic viscosity, m^2/s
θ = dimensionless temperature
ψ = dimensionless stream function
ρ = fluid density, kg/m^3
φ = tangential coordinate, rad

Subscripts

a = air
e = effective
f = fluid
i = inner
o = outer
opt = optimal
p = porous
CD = conduction
cv = convection

Superscript

* = dimensionless variable

References

[1] Caltagirone, J. P., 1976, "Thermoconvective Instabilities in a Porous Medium Bounded by Two Concentric Horizontal Cylinders," J. Fluid Mech., **76**, pp. 337–362.

[2] Caltagirone, J. P., 1976, "Instabilités Themoconvectives en Milieux Poreux," These de Doctorat d'Etat , Université Pierre et Marie Curie, Paris VI, France.

[3] Charrier-Mojtabi, M. C., Mojtabi, A., Azalez, M., and Larosse, G., 1991, "Numerical and Experimental Study of Multicellular Free Convection Flows in an Annular Porous Layer," Int. J. Heat Mass Transfer, **34**, pp. 3061–3074.

[4] Barbosa Mota, J. P., and Saatdjian, E., 1994, "Natural Convection in a Porous Horizontal Cylindrical Annulus," ASME J. Heat Transfer, **116**, pp. 621–626.

[5] Barbosa Mota, J. P., and Saatdjian, E., 1995, "Natural Convection in Porous Cylindrical Annuli," Int. J. Numer. Methods Heat Fluid Flow, **5**, pp. 3–12.

[6] Himasekhar, K., and Bau, H. H., 1988, "Two-Dimensional Bifurcation Phenomena in Thermal Convection in Horizontal Concentric Annuli Containing Saturated Porous Media," J. Fluid Mech., **187**, pp. 267–300.

[7] Charrier-Mojtabi, M. C., 1997, "Numerical Simulation of Two- and Three-Dimensional Free Convection Flows in Horizontal Porous Annulus Using a Pressure and Temperature Formulation," Int. J. Heat Mass Transfer, **40**, pp. 1521–1533.

[8] Vafai, K., and Tien, C. L., 1981, "Boundary and Inertia Effects on Convective Heat Transfer in Porous Media," Int. J. Heat Mass Transfer, **34**, pp. 195–203.

[9] Kaviany, M., 1986, "Non-Darcian Effects on Natural Convection in Porous Media Confined Between Horizontal Cylinders," Int. J. Heat Mass Transfer, **29**, pp. 1513–1519.

[10] Grigull, U., and Hauf, W., 1986, "Natural Convection in Horizontal Cylindrical Annuli," *Proceedings of the 3rd International Heat Transfer Conference*, Vol. 2, pp. 182–195.

[11] Powe, R. E., Carley, C. T., and Bishop, E. H., 1969, "Free Convective Flow Patterns in Cylindrical Annuli," ASME J. Heat Transfer, **91**, pp. 310–314.

[12] Powe, R. E., Carley, C. T., and Carruth, S. L., 1971, "A Numerical Solution for Natural Convection in Cylindrical Annuli," ASME J. Heat Transfer, **93**, pp. 210–220.

[13] Kuehn, T., and Goldstein, R., 1976, "An Experimental and Theoretical Study of Natural Convection in the Annulus Between Horizontal Concentric Cylinders," J. Fluid Mech., **4**, pp. 695–719.

[14] Kuehn, T. H., and Goldstein, R. J., 1976, "Correlating Equations for Natural Convection Heat Transfer Between Horizontal Circular Cylinders," Int. J. Heat Mass Transfer, **19**, pp. 1127–1134.

[15] Fant, D. B., Rothmayer, A., and Prusa, J., 1989, "Natural Convective Flow Instability Between Horizontal Concentric Cylinders," *Numerical Methods for Laminar and Turbulent Flow*, Vol. 6, C. Taylor, ed., Pineridge, Swansea, England, pp. 1045–1065.

[16] Kim, C. J., and Ro, S. T., 1994, "Numerical Investigation on Bifurcative Natural Convection in an Air-Filled Horizontal Annulus," *Proceedings of the 10th International Heat Transfer Conference*, Vol. 7, Brighton, England, G. F. Hewitt, ed., pp. 85–90.

[17] Yoo, J. S., 1998, "Natural Convection in Narrow Horizontal Cylindrical Annulus: $Pr \leq 0.3$," Int. J. Heat Mass Transfer, **41**, pp. 3055–3073.

[18] Kuehn, T. H., and Goldstein, R. J., 1978, "An Experimental Study of Natural Convection Heat Transfer in Concentric and Eccentric Horizontal Cylindrical Annuli," ASME J. Heat Transfer, **100**, pp. 635–640.

[19] McLeod, A. E., and Bishop, E. H., 1989, "Turbulent Natural Convection of Gases in Horizontal Cylindrical Annuli at Cryogenic Temperatures," Int. J. Heat Mass Transfer, **32**, pp. 1967–1978.

[20] Desai, C. P., and Vafai, K., 1994, "An Investigation and Comparative Analysis of Two- and Three-Dimensional Turbulent Natural Convection in a Horizontal Annulus," Int. J. Heat Mass Transfer, **37**, pp. 2475–2504.

[21] Char, M., and Hsu, Y. H., 1998, "Comparative Analysis of Linear and Nonlinear Low-Reynolds-Number Eddy Viscosity Models to Turbulent Natural Convection in Horizontal Cylindrical Annuli," Numer. Heat Transfer, Part A, **33**, pp. 191–206.

[22] Padilla, E. L. M., and Silveira-Neto, A., 2008, "Large-Eddy Simulation of Transition to Turbulence in Natural Convection in a Horizontal Annular Cavity," Int. J. Heat Mass Transfer, **51**, pp. 3656–3668

[23] Aldoss, T. K., Alkam, M., and Shatarah, M., 2004, "Natural Convection From a Horizontal Annulus Partially Filled With a Porous Medium," Int. Commun. Heat Mass Transfer, **31**, pp. 441–452.

[24] Leong, J. C., and Lai, F. C., 2006, "Natural Convection in a Concentric Annulus With a Porous Sleeve," Int. J. Heat Mass Transfer, **49**, pp. 3016–3027.

[25] Hewitt, G. F., Shires, G. L., and Bott, T. R., 1994, *Process Heat Transfer*, Begell House, New York.

[26] Nield, D. A., and Bejan, A., 2006, *Convection in Porous Media*, 3rd ed., Springer, Berlin, Germany.

[27] Patankar, S. V., 1980, *Numerical Heat Transfer and Fluid Flow*, McGraw-Hill, New York/Hemisphere, Washington, DC.

Steady-State Behavior of a Two-Phase Natural Circulation Loop With Thermodynamic Nonequilibrium

Dipankar N. Basu
e-mail: dipankar@mech.iitkgp.ernet.in

Souvik Bhattacharyya
e-mail: souvik@mech.iitkgp.ernet.in

P. K. Das
e-mail: pkd@mech.iitkgp.ernet.in

Department of Mechanical Engineering,
IIT,
Kharagpur 721302, India

A model to predict the steady-state behavior of a rectangular two-phase natural circulation loop has been proposed. The analysis employs a one-dimensional two-fluid model to identify various system parameters, with particular emphasis on the subcooled boiling region. The onset of two-phase region and point of net vapor generation and associated liquid temperatures and vapor qualities have been estimated using a few widely recognized correlations. Predicted results demonstrate that the consideration of subcooled boiling may have significant effect on system behavior, particularly around the transition regions. The interaction of saturated bubbles and subcooled liquid and associated change in heat transfer and frictional forces has been discussed in detail. Fluid stream has been observed to have different combinations of flow stream conditions at boiler exit and condenser inlet. Five probable combinations have been identified and a generalized working-regime map has been proposed on $N_{sub} - N_{Zu}$ plane. Attempts have been made to identify the influence of various control parameters. A favorable sink condition (higher coolant flow rate or lower coolant entry temperature) has been found to be of particular importance to attain a wider operating range of wall heat flux and better heat transfer characteristics. A design map has been proposed to identify favorable operating condition in terms of control parameters to ensure complete condensation.
[DOI: 10.1115/1.2994721]

Keywords: natural circulation, two-phase, subcooled boiling, correlation-based model, working-regime map, design map, favorable operating condition

1 Introduction

Natural circulation loops (NCLs) provide a lucrative option of energy transfer from a high-temperature source to a low-temperature sink without employing any mechanical device and hence resulting in enhanced passive safety and highly reliable loop performance. In the case of two-phase NCLs, the circulating fluid experiences boiling at one section and condensation or phase-separation at some other section. This commonly results in two-phase mixture at one vertical arm (riser) and single-phase liquid at the other (downcomer), causing a large density difference and hence yielding very high circulation rate and large system output. Concept of two-phase NCLs has been analyzed for long, but was not applied much in industry, particularly for low-temperature appliances, even though large quantity of power can easily be transferred through such loops using a small temperature differential. Since the first significant study in two-phase thermosyphon, credited to Schmidt [1], boiling NCLs have found extensive applications in a number of very important engineering fields, such as gas turbine blade cooling [2], solar heaters [3], thermosyphon reboilers [4,5], emergency core cooling of nuclear reactors [6,7] such as Dodewaard nuclear reactor of Netherlands and economic simplified boiling water reactor designed by General Electric, geothermal energy extraction processes [8], and plenty more.

Being a self-sustaining phenomenon, NCLs call for intense analysis to ensure proper zone of operation. Because of the varying nature of the flow fields at different sections of the loop, boiling thermosyphons are always susceptible to flow fluctuations and loop instability. Considering the importance of loop reliability, particularly in applications associated with nuclear industry, it is imperative that expected system behavior is fully known. Hence, a number of research studies have been reported on two-phase NCL in the past few decades. Lee and Mital [9] predicted that, for a given operating pressure and wall temperature in the evaporator section of thermosyphon, there should be a limiting value of heat flux above which the operating pressure could not be maintained. They proposed a simple analytical model to predict the maximum heat transfer rate with the predicted trends closely matching the test data. Dobran [10] also predicted the existence of a maximum heat flux associated with flooding limits through a lumped parameter description of thermosyphon. Ramos et al. [11] presented a 1D model of two-phase thermosyphon to study the effect of vertical distance between the evaporator and the condenser. However, their work was based on sharp interface approximation, thereby neglecting the effect of two-phase zone length. That was improved by Chen and Chang [12] using a variable-area NCL based on the homogeneous model, where vapor quality in two-phase zone was assumed to be a linear function of flow distance. Rao et al. [13] analyzed a vertical rectangular NCL, with a uniform cross section and a constant heat flux along both boiling and condensing sections, employing both homogeneous and drift flux models. A large deviation was observed between the predicted results.

A meticulous survey of the available literature suggests that most of the reported research considers the system with a single-phase-separating section, typically a solitary phase-changing section in the boiler and no condensing zone. However, a number of important industrial applications, including waste heat recovery, electronic cooling, etc., comprise two distinct phase-changing sections. Hence, it is essential to study the behavior of a rectangular

Contributed by the Heat Transfer Division of ASME for publication in the JOURNAL OF HEAT TRANSFER. Manuscript received January 28, 2008; final manuscript received July 17, 2008; published online January 5, 2009. Review conducted by Sung Jin Kim.

 Copyright © 2009 by ASME

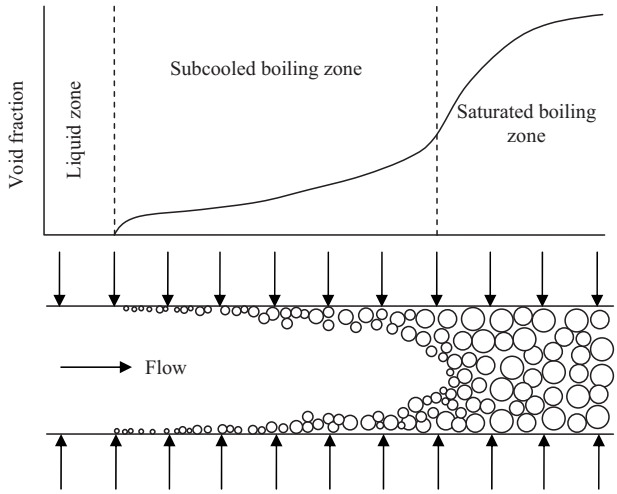

Fig. 1 Appearance of subcooled boiling zone

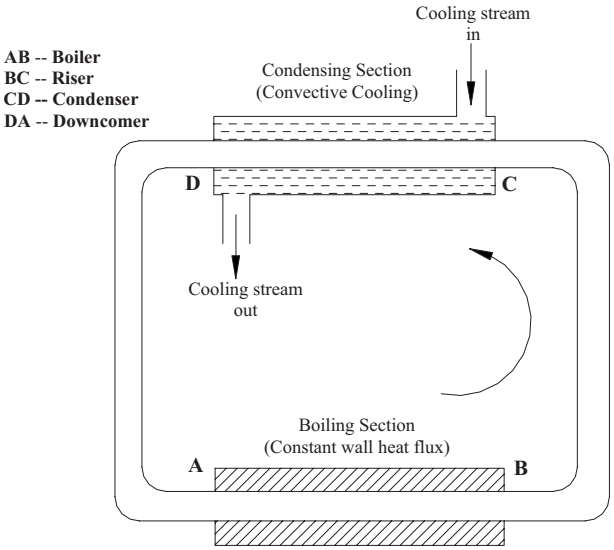

Fig. 2 Geometry of rectangular two-phase natural circulation loop

two-phase NCL with separate boiling and condensing zones. Only a few studies reported on a similar configuration [12,13] but considering the system to be always in thermal equilibrium thereby eliminating the subcooled boiling region. However, practical boiling channels invariably contain a distinct subcooled boiling zone present between fully single-phase and saturated boiling regions (Fig. 1). It is always possible to have a layer of saturated or even superheated bubbles on the wall, with subcooled liquid flowing through the pipe core. The presence of subcooled boiling increases the effective length of two-phase zone, and complex energy interactions between saturated bubbles and subcooled liquid drastically affect the heat transfer and frictional characteristics of the system. Because of bubble generation at the wall, only a fraction of the supplied wall heat flux is utilized in heating the liquid, thereby delaying the appearance of actual boiling boundary. For low power operations, this may well shift the boiling boundary outside the boiler, i.e., fluid exiting the boiling zone can be in subcooled boiling mode. For such situations, bubbles will collapse in adiabatic riser to warm the liquid and final condition will be of single-phase liquid or saturated mixture, depending on mixture enthalpy at boiler exit. That will affect the average fluid density in riser and also the frictional losses, thereby directly influencing system behavior. Hence, it is essential to ascertain the two-phase NCL performance with an appropriate analysis of the subcooled boiling region. Jeng and Pan [14] assumed a linear profile of volumetric vapor generation rate in the subcooled boiling region. But considering the detailed mechanism associated with bubble growth and departure in subcooled liquid stream [15], it is not a very justifiable assumption. Advanced subcooled boiling models are available in literature [16,17], but it is very difficult to implement such models for analysis of a complete natural circulation loop with both boiling and condensing zones, particularly as a starting point.

Hence, the purpose of the present study is to develop a simplified correlation-based model to predict steady-state behavior of a rectangular two-phase NCL containing distinct boiling and condensing sections. A one-dimensional two-fluid model has been developed for identifying boiling and condensation boundaries and obtaining profiles of liquid temperature and vapor quality throughout the loop. Particular emphasis has been exercised on the subcooled boiling zone to ascertain influence of the presence of boiling nonequilibrium. Temperature and void fraction profiles in subcooled boiling zone have been identified using well-established correlations. For cases with subcooled boiling condition at boiler exit, a condensation model has been proposed in the riser to identify the equilibrium condition. Various probable combinations of fluid stream condition have been identified and a generalized working-map has been presented. Logical parametric variation has been attempted to understand the role of different control parameters and the relative influence of different system variables has been discussed in detail to identify favorable operating conditions. A novel design map has been proposed to predict the potentially favorable zone of operation.

2 Theoretical Formulation

2.1 System Geometry and Modeling Assumptions. Schematic of the rectangular NCL is shown in Fig. 2. The present study considers a uniform diameter vertical loop. Buoyancy being the solitary driving force, it is mandatory to place the sink at an elevation higher than the source in order to utilize the gravity head. Loop fluid is supplied with a constant heat flux from outside in the boiler section (AB) along the bottom horizontal arm, and cooling effect is achieved by mounting a parallel-flow heat exchanger (CD) around the top horizontal arm. Other sections of the loop are insulated.

The following assumptions are considered for the theoretical model.

(1) One-dimensional mathematical formulation, i.e., fluid is assumed to be perfectly mixed at any cross section.
(2) Constant pressure throughout the system.
(3) Ideally insulated vertical arms, i.e., no heat leakage to the surrounding.
(4) Viscous dissipation and axial conduction effects are negligible.
(5) Effect of heat conduction through the wall is negligible.
(6) Additional pressure loss at pipe bends and fittings is negligible.
(7) Vapor superheat is negligible.

2.2 Boiler Section (AB)

2.2.1 Single-Phase Liquid Region. With the aforementioned assumptions, generalized energy equation for a single-phase liquid flowing through a heated tube can be represented as

$$\frac{\partial}{\partial t}(\rho_f h_f) + \frac{\partial}{\partial z}(\rho_f u_f h_f) = \frac{q''_w P_h}{A_{cs}} \tag{1}$$

where q''_w represents the wall heat flux, P_h represents the wetted perimeter of tube inner wall, and A_{cs} represents the pipe flow area. Under steady-state condition, the transient term vanishes yielding

a longitudinally linear profile of liquid enthalpy in the boiler.

$$\frac{d}{dz}(\rho_f u_f h_f) = \frac{q''_w P_h}{A_{cs}} \quad \Rightarrow \quad \frac{dh_f}{dz} = \left(\frac{4}{d_{in}}\right)\frac{q''_w}{G} \tag{2}$$

Here d_{in} is the pipe inner diameter and G represents the fluid mass flux.

2.2.2 Subcooled Boiling Region. The flowing stream can be considered to be single-phase liquid from boiler inlet until onset of nucleate boiling (ONB) point, where the wall superheating satisfies some requisite limit and vapor generation initiates at the heated wall. Required amount of wall superheating at ONB point has been estimated following Bergles and Rohsenow [18] as given below (with p in bars):

$$[\Delta T_{w,\text{sup}}]_{ONB} = 0.556\left[\frac{q''_w}{1082p^{1.156}}\right]^{0.463p^{0.0234}} \tag{3}$$

The corresponding value of liquid subcooling can be estimated from the heat transfer relationship as

$$q''_w = H_{1\phi}(T_w - T_f) \quad \Rightarrow \quad \Delta T_{w,\text{sup}} = \frac{q''_w}{H_{1\phi}} - \Delta T_{f,\text{sub}} \tag{4}$$

Here $H_{1\phi}$ represents the single-phase wall-to-fluid heat transfer coefficient, which has been estimated using Gnielinski relationship [19]. An enhancement factor of 30% has been used to account for the presence of bubbles following Basu et al. [17]. Location of ONB can easily be calculated by simple integration of Eq. (2) from boiler inlet to ONB point.

$$z_{ONB} = \left(\frac{Gd_{in}}{4q''_w}\right)(h_{f,ONB} - h_{f,\text{inlet}}) \tag{5}$$

Beyond the ONB point, small bubbles start growing at the heated surface. But as they infiltrate into the bulk liquid, they condense because of very high liquid subcooling; so vapor generation remains limited to discrete bubbles only on the wall, resulting in very small net vapor generation, until the fluid reaches onset of significant void (OSV). Beyond the OSV location, bubbles detach from the surface and condense slowly in slightly subcooled liquid, as they move downstream. For determining the liquid subcooling corresponding to OSV location, Saha and Zuber criterion [20], considered the most accurate [15], is employed.

$$[\Delta T_{f,\text{sub}}]_{\text{OSV}} = 0.0022\left(\frac{q''_w d_{in}}{\lambda_f}\right) \quad \text{for Pe} \le 70{,}000$$

$$= 153.8\left(\frac{q''_w}{GC_{pf}}\right) \quad \text{for Pe} > 70{,}000 \tag{6}$$

To calculate the total amount of wall vapor generation until the OSV point, Levy's model [21] has been used, which predicts OSV fraction as

$$\alpha_{\text{OSV}} = \alpha_w = \left(\frac{\pi}{6}\right)\frac{Y_B}{d_{in}} \tag{7}$$

Here $Y_B = 0.015[\sigma d_{in}/\tau_w]^{1/2}$, $\tau_w = (f/8)(G^2/\rho_f)$, and $f = 0.0055\{1 + [20{,}000(\varepsilon/d_{in}) + 10^6/\text{Re}_f]^{1/3}\}$.

The correlation proposed by Rouhani and Axelsson [22] has been used to ascertain the relationship between vapor mass fraction and void fraction. For a given void fraction, vapor quality has been estimated through iteration, whereas void fraction can be estimated directly for a given mass quality as per the following relation:

$$\alpha = \frac{x}{\rho_g}\left\{1.1\left[\frac{x}{\rho_g} + \frac{1-x}{\rho_f}\right] + \frac{1.18}{G}\left[\frac{\sigma g(\rho_f - \rho_g)}{\rho_f^2}\right]^{0.25}\right\}^{-1} \tag{8}$$

For estimation of vapor mass fraction and liquid temperature profiles in the subcooled boiling region, a simple method proposed by Levy [21] has been followed. It is assumed that actual vapor quality is related to the thermodynamic vapor quality as

$$x(z) = x(z)_{\text{eq}} - x_{\text{OSV}} \exp\left(\frac{x(z)_{\text{eq}}}{x_{\text{OSV}}} - 1\right) \tag{9}$$

Thermodynamic vapor quality at any particular location can be easily estimated applying energy balance for equilibrium flow. Equilibrium mass fraction of vapor at OSV point is negative and can be estimated as

$$x_{\text{OSV}} = -\left[\frac{C_{pf}[\Delta T_{f,\text{sub}}]_{\text{OSV}}}{h_{fg}}\right] \tag{10}$$

At the actual boiling boundary, both the real mass fraction and the thermodynamic mass fraction become identical, thereby providing a criterion to determine the location of actual boiling boundary (z_{BB}). However, an iterative procedure is required to be followed, as thermodynamic vapor quality can be evaluated only for a known length. Bowring's model (from Ref. [15]) provides an initial guess for the real boiling boundary and once vapor quality is known at any location in the subcooled boiling region, the corresponding liquid enthalpy is estimated through energy balance.

2.2.3 Saturated Boiling Region. As the fluid stream reaches the saturation temperature corresponding to system pressure, bubbles start growing from the liquid bulk. Generalized energy equation for a two-phase mixture in a heated tube can be written as

$$\frac{\partial}{\partial t}[\alpha\rho_g h_g + (1-\alpha)\rho_f h_f] + \frac{\partial}{\partial z}[\alpha\rho_g u_g h_g + (1-\alpha)\rho_f u_f h_f] = \frac{q''_w P_h}{A_{\text{cs}}} \tag{11}$$

Under steady-state condition, the transient term disappears and applying simple two-phase relations, a linearized vapor mass quality profile can be obtained as shown below:

$$\frac{d}{dz}[\alpha\rho_g u_g h_g + (1-\alpha)\rho_f u_f h_f] = \frac{q''_w P_{\text{in}}}{A_{cs}} \Rightarrow \frac{dx}{dz} = \frac{4q''_w}{Gd_{\text{in}}h_{fg}} \tag{12}$$

Vapor quality at the boiler exit can now be estimated by simple integration of Eq. (12).

$$x_{\text{bx}} = x_{\text{BB}} + \frac{4q''_w}{Gd_{\text{in}}h_{fg}}(L_{\text{boil}} - z_{\text{BB}}) \tag{13}$$

2.3 Riser Section (BC). When the fluid stream enters the adiabatic riser in single-phase liquid or saturated mixture form, in the absence of heat transfer, there is no change in any of the flow parameters. However, if the fluid stream is at subcooled boiling condition at the boiler exit because of the thermal interaction between saturated bubbles and surrounding subcooled liquid, the bubbles are inclined to condense. If the amount of heat released because of total condensation of vapor bubbles emerging from the boiler section is greater than that required for the fluid mixture to attain saturation, then a saturated mixture results. Otherwise, the fluid stream reverts to single-phase flow. In the present study, a condensation model has been incorporated following Koncar and Mavko [16] to estimate the average vapor mass condensation rate:

$$\Gamma_{\text{con}} = \frac{C_{\text{con}}H_{\text{con}}A_{\text{con}}\Delta T_{f,\text{sub}}}{h_{fg}} \tag{14}$$

Here, $\text{Nu}_{\text{con}} = H_{\text{con}}d_{\text{bub}}/\lambda_f = 0.37\,\text{Re}_{\text{bub}}^{0.6}\,\text{Pr}_f^{0.33}$, $A_{\text{con}} = 3.6\alpha/d_{\text{bub}}$, and $C_{\text{con}} = 0.4$.

Following the vapor condensation trend, the final condition of fluid mixture in the riser tube has been estimated.

2.4 Condenser Section (CD). A log mean temperature difference (LMTD) based method is used to estimate the required condensing length for the two-phase mixture. Heat transfer coefficient corresponding to the condensing stream has been estimated fol-

Table 1 Geometric dimensions of the rectangular loop

Length of horizontal arm (m)	3.0
Length of vertical arm (m)	6.0
Length of boiler section (m)	2.5
Length of condenser section (m)	2.0
Inner diameter (mm)	25.0
Wall thickness (mm)	1.0
External heat exchanger hydraulic diameter (mm)	10.0

lowing Dobson and Chato [23], where they included a stratified-wavy flow method with film condensation from the top toward the bottom of the tube and an annular flow correlation. Gnielinski correlation [19] has been used for the single-phase part, while for the coolant side, it is used along with the Petukhov and Roizen [24] correction for flow through an annular space. The overall heat transfer coefficient is thus expressed as

$$\frac{1}{U_o} = R_{\text{in}} + R_{\text{wall}} + R_{\text{out}} = \frac{1}{H_{\text{in}}(\pi d_{\text{in}})} + \frac{\ln(d_{\text{out}}/d_{\text{in}})}{2\pi\lambda_{\text{wall}}} + \frac{1}{H_{\text{out}}(\pi d_{\text{out}})} \tag{15}$$

Performing energy balance separately across the two-phase and single-phase zones of the condenser, the location of condensation boundary, vapor mass fraction profile in the two-phase zone, and liquid and coolant temperature profiles can be estimated iteratively.

In the present analysis, it has been assumed that the two-phase mixture gets completely condensed in the condenser. Under all circumstances, no vapor bubbles are allowed to the downcomer, hence always ensuring a single-phase liquid flow through the adiabatic downcomer. The presence of any bubble in the downcomer will result in a reduction in average density, thereby lowering the driving head and hence power transmission through the loop.

2.5 Pressure Drop Around the Loop. Across any section of the loop, steady-state pressure drop can be expressed as a summation of corresponding frictional, accelerational, and gravitational pressure drop, i.e.,

$$\Delta p_{\text{tot}} = \Delta p_{\text{fric}} + \Delta p_{\text{acc}} + \Delta p_{\text{grav}} \tag{16}$$

However, for a NCL, the summation of pressure drop around the loop has to be zero. Addition of the pressure losses across each small segment of the system yields an implicit equation of the loop mass flux in the form

$$f(G) = 0 \tag{17}$$

Solution of Eq. (16) along with temperature and vapor quality profiles across each segment of the loop produces the final solution for the system. Chisholm model [25] is used to estimate the frictional pressure drop in the subcooled boiling zone, while Friedel correlation [26] is employed for the fully saturated flow regime.

3 Results and Discussion

The loop wall is assumed to be fabricated of pure copper (λ_{wall}=401 $\text{Wm}^{-1}\,\text{K}^{-1}$) with geometrical details, as shown in Table 1. The working fluid, as well as the condensing fluid, is water, the thermodynamic and transport properties of which are calculated from an exclusive precision property code based on guidelines adopted by IAPWS-IF97 [27].

3.1 Typical Loop Flow Rate Characteristics. Figure 3 represents the typical loop characteristic profile in terms of the variation of loop mass flux with wall heat flux at a system pressure of 3 bars. Here, the solid line represents the profile corresponding to the present model, whereas the dotted line represents the profile for the idealized case of no subcooled boiling. For lower wall heat fluxes, mass flow rate increases moderately with single-phase flow throughout the loop. But, with elevated wall heat fluxes, two-phase flow initiates in the loop and the presence of vapor bubbles in the riser tube results in higher density difference between the two vertical arms leading to rapid increase in circulation rate However, this increases the associated frictional resistances, thereby counteracting the driving buoyancy. Beyond certain level of heat flux, the resistive forces become dominant and flow rate starts decreasing with even higher wall heat flux. Such a variation of loop circulation rate with heat flux is well established in literature [13,14].

However, as can be seen from Fig. 3, when subcooled boiling is under consideration, mass flux profile exhibits a slightly different trend. Subcooled boiling initiates for a heat flux value (point A) lower than the heat flux corresponding to saturation at the idealized case of no subcooled boiling (point D), thereby providing a longer two-phase path in the boiler. The mass flux profile becomes nearly horizontal in the immediate vicinity of point A and then decreases slightly, which is quite counterintuitive. It can be ex-

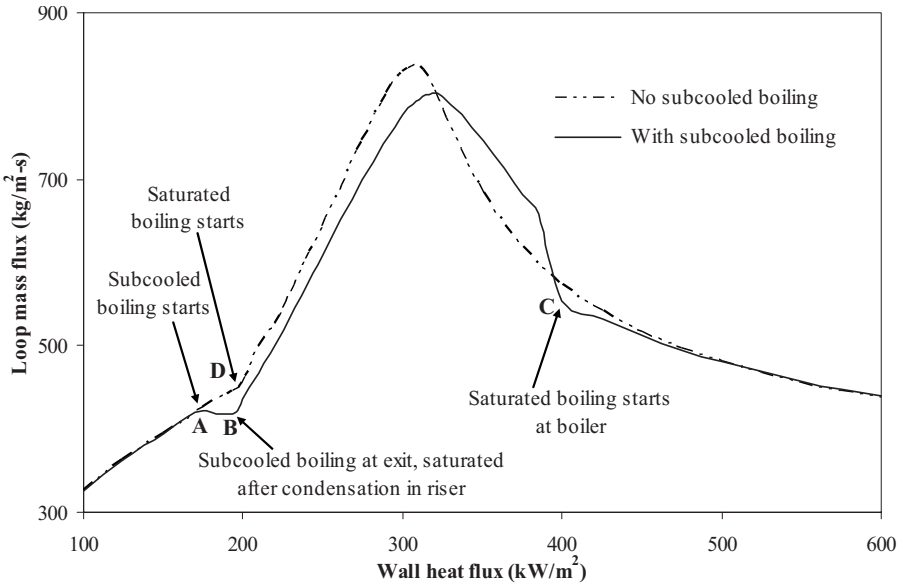

Fig. 3 Effect of wall heat flux on loop mass flux for rectangular two-phase NCL

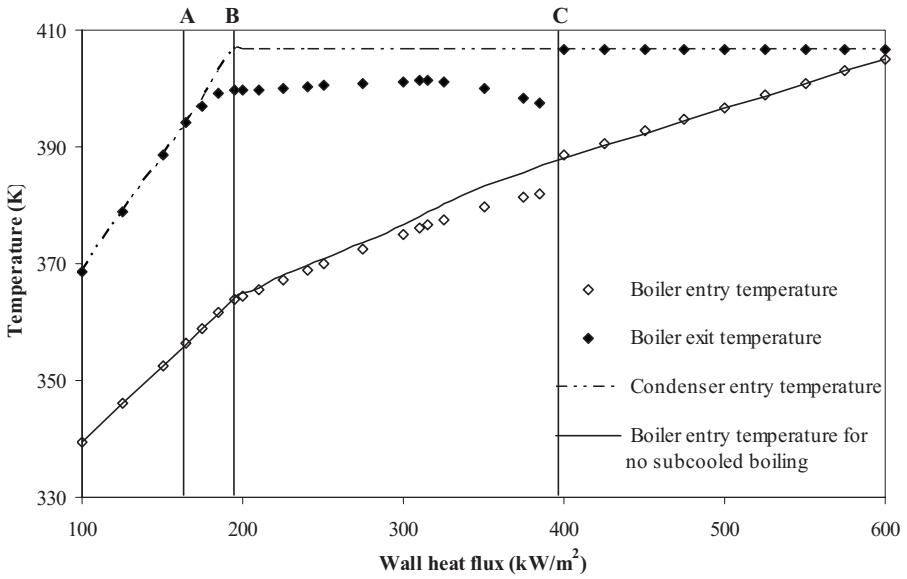

Fig. 4 Effect of wall heat flux on boiler entry and exit temperatures and condenser entry temperature

plained from the temperature profiles presented in Fig. 4. Despite net bubble growth in the boiler region, due to the highly subcooled nature of liquid at the boiler exit (for heat flux values around point A), those bubbles condense immediately after exiting the boiler, resulting in single-phase liquid flow through most part of the riser. It can be observed from Fig. 4 that the condenser entry temperature after point A is less than saturation. In fact, the profile of condenser entry temperature closely matches the boiler exit temperature profile for the idealized case, suggesting proper energy conservation. Thus, for heat flux range around 175–200 kW/m^2, most of the flow path is occupied by single-phase liquid, particularly the vertical riser tube. But two-phase situation does appear at upstream end of the boiler and early parts of the riser tube, resulting in higher frictional losses. As the operation of NCL is based on interplay between friction and buoyancy, increase in flow resistance, without much increase in driving head, instigates small decrease in flow rate. The appearance of bubble at boiler exit and full condensation in the riser tube can be amply proved from Fig. 5, which shows nonzero void fraction value at boiler exit but zero void fraction at condenser entry immediately after point A. Slightly higher rate of increase in boiler entry temperature can be noted after point A from Fig. 4, which can be attributed to enhanced fluid mixing and heat transfer with the appearance of bubbles in the boiler [17].

Beyond point A, a fraction of the supplied energy is utilized in wall vapor generation and the rest is for single-phase heating. Net vapor generation becomes quite significant at about point B and, despite having subcooled boiling situation at boiler outlet, the energy interaction in the riser tube yields a saturated mixture. It can be observed from Fig. 4 that the fluid temperature at boiler

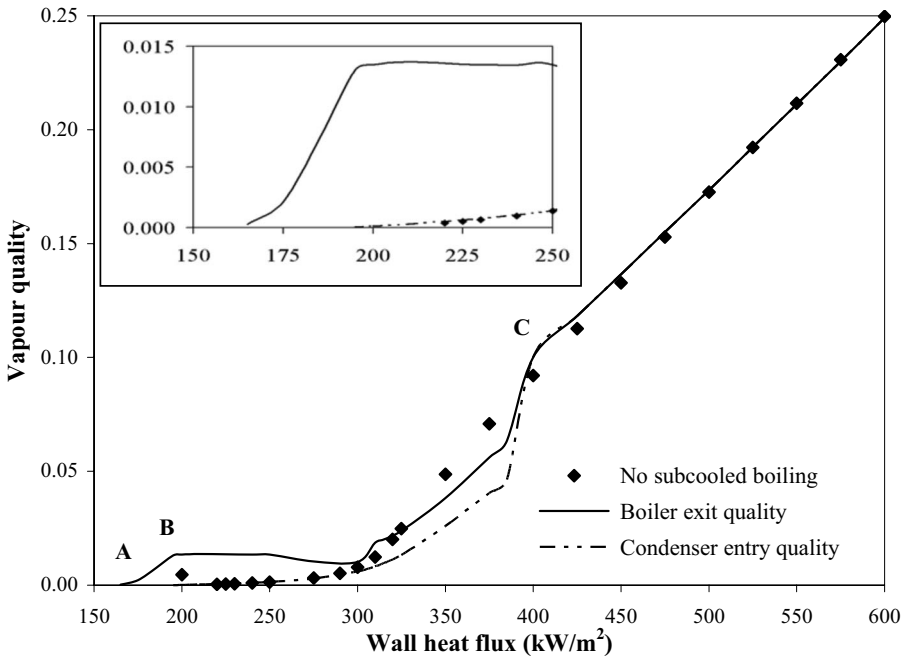

Fig. 5 Effect of wall heat flux on vapor quality

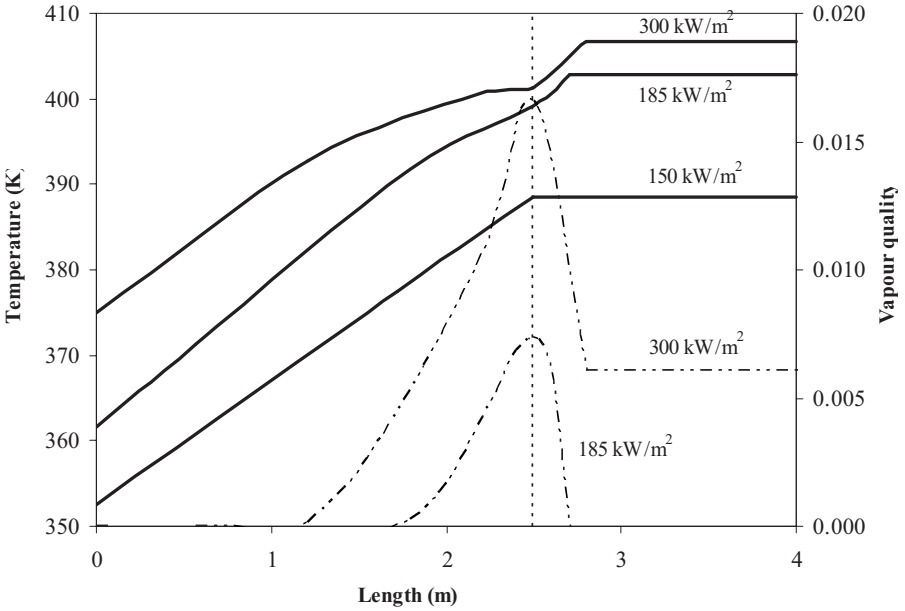

Fig. 6 Longitudinal variation of temperature and quality in and downstream of the boiler for three different cases

outlet is less than saturation, but entry to condenser is in saturated state. Also there is some change in the gradient of boiler entry temperature profile around point B, as can be seen from Fig. 4, accentuating the reduction in heat supply to the liquid phase. However, it can be noted that vapor quality at boiler exit initially increases and then starts decreasing slightly with increasing heat flux. That can be attributed to the heat transfer enhancement in the presence of bubbles as mentioned earlier.

With further increase in wall heat flux, vapor quality at boiler exit increases and condensation of vapor bubbles in the riser tube results in saturated two-phase mixture from point B onwards. The presence of two-phase mixture in riser yields a larger density difference between the vertical arms and so a rapid increase in the flow rate, until the resistive force becomes dominant. Careful observation of Fig. 3 suggests that the heat flux corresponding to the appearance of saturated mixture in riser complements well with the saturation heat flux for the idealized case (point D). The appearance of saturation in the boiler itself is found to appear for a much larger value of heat flux (point C), when the profile for mass flux is already downhill. Beyond that heat flux value, the mass flux and vapor quality profiles for both equilibrium flow (when subcooled boiling has been neglected) and the present model follow identical patterns. However, the present model predicts a slightly lower value of loop flow rate and so higher value of boiler exit quality, and that can be attributed to the longer two-phase flow zone in the loop due to subcooled boiling and hence higher frictional losses. With increase in wall heat flux, loop flow rate decreases; hence quality at boiler exit increases sharply, and the corresponding length required for condensation increases. As it is essential for the present model to have full condensation inside the condenser to avoid any vapor in the downcomer, a maximum heat flux limit is implied inherently.

A better appraisal of the operation of NCL for different conditions of the fluid stream at boiler exit may be obtained from Figs. 6 and 7. In Figs. 6 and 7, the solid lines represent the temperature profile, whereas the dash-dotted lines represent the quality profile, corresponding heat flux being inscribed therewith. Figure 6 depicts the situation where the bulk of the fluid remains below the saturation temperature at the boiler exit. Curves (a), (b), and (c) represent the operating conditions with a gradual increase in heat flux. Curve (a) represents the case that is entirely single phase, typified by continuous increase in liquid temperature in boiler, without any presence of the vapor phase. Boiler exit condition is of subcooled boiling in the other two curves. However, due to energy interaction in the riser, the fluid reverts to single phase in curve (b), whereas it becomes saturated in (c). It may be noticed from curve (b) that vapor generation starts at some intermediate part of boiler and the quality increases until the boiler exit. Thereafter, the vapor quality falls due to condensation and contributes in raising the temperature of bulk fluid. Ultimately, it becomes zero, whereas the bulk fluid temperature remains below the saturation temperature. In an elevated value of heat flux represented by curve (c), the vapor quality does not decrease to zero value outside the boiler. This situation represents the flow of a two-phase mixture through the entire length of the riser. Figure 7 depicts a case where the saturation temperature of bulk fluid is achieved within the boiler itself due to a higher value of heat flux. In this case, both the bulk temperature and vapor quality remains constant throughout the riser. It is interesting to observe the change in fluid temperature gradient to be around 0.6 m, suggesting the initiation of fully developed subcooled boiling.

3.2 Generalized Working-Regime Map. As it has been seen that a two-phase NCL can operate in different regimes depending on the operating conditions, it is prudent to develop a working-regime map based on some generalized criteria. Such a map is expected to give a broad guideline for the selection of design parameters. Considering a data set of more than 500 cases, including variations of geometry and operating conditions, a working-regime map has been prepared, as shown in Fig. 8. Two important dimensionless groups, namely, N_{sub} and N_{Zu}, have been used for the construction of the map. Here *Zuber number* (N_{Zu}) (or *phase-change number*) can be considered to be indicative of the power supplied to the system, whereas *subcooling number* (N_{sub}) may be considered to represent the degree of liquid subcooling at boiler inlet. It is clearly evident that with increase in N_{Zu} for a given liquid subcooling, fluid stream tends toward saturation inside the boiler. Similarly, with increase in N_{sub} for a given power input, the fluid stream tends toward a fully single-phase system. Such variation results in five distinct zones of boiler exit condition on the $N_{sub}-N_{Zu}$ plane, the details of which are presented in Table 2. It is possible to express all the transition criteria in a simplified linear form given by $N_{sub}=mN_{Zu}+c$ with more than 95% of the available data points satisfying the correlations, the details of m and c being

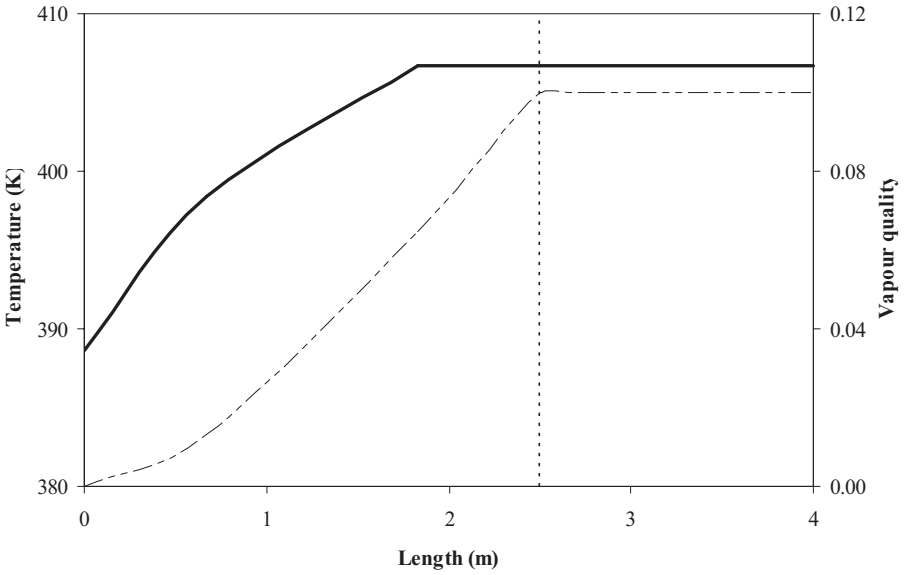

Fig. 7 Longitudinal variation of temperature and quality in and downstream of the boiler for 400 kW/m^2 heat flux

presented in Table 3.

As has been discussed by De Kruijf et al. [28], for a homogeneous equilibrium system (no subcooled boiling), the boiling boundary can be identified as

$$\frac{N_{\text{sub}}}{N_{\text{Zu}}} = \frac{z_{\text{BB}}}{L_{\text{boil}}} \tag{18}$$

Similarly, equilibrium vapor quality at boiler exit can be evaluated as

$$N_{\text{Zu}} - N_{\text{sub}} = x_{\text{bx}} \frac{(\rho_f - \rho_g)}{\rho_g} \tag{19}$$

Considering both Eqs. (18) and (19), it can be concluded that for an equilibrium system, when the Zuber number value exceeds *the* subcooling number, boiler exit quality is positive and boiling boundary appears inside the boiler, indicating the existence of saturated mixture at boiler exit. However, due to the subcooled boiling consideration in the present model, fluid stream condition at boiler exit can be of a mixture of saturated vapor and subcooled liquid. Due to further energy interaction within the riser, ultimately, a single-phase liquid or a saturated two-phase mixture may appear at the condenser inlet. It is therefore possible to have a rise in liquid temperature downstream of the boiler where there is no energy input from outside. Apparently, one may think, even if the subcooled boiling is not considered, the liquid condition at the condenser inlet remains identical due to overall energy balance. However, a more realistic picture of the circulating flow is obtained by incorporating subcooled boiling considerations. Furthermore, this has its implication on loop pressure drop, which in turn influences the circulation rate. The transition boundary between zones II and III (m is nearly equal to 1), identifying the limiting cases of having single-phase or two-phase condition at

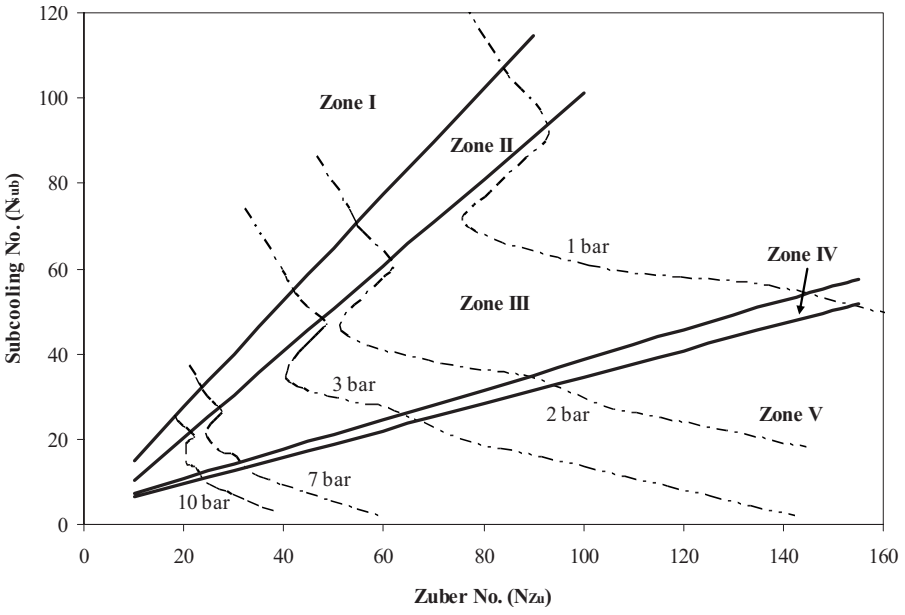

Fig. 8 Generalized flow-regime map to identify fluid stream condition at boiler exit

Table 2 Different zones of fluid exit conditions

Zone	Condition at boilerexit	Condition at condenser entry
I	Subcooled liquid	Subcooled liquid
II	Subcooled liquid + Vapor bubbles	Subcooled liquid
III	Subcooled liquid + Vapor bubbles	Saturated mixture
IV	No solution	
V	Saturated mixture	Saturated mixture

condenser inlet, closely matches the limit for equilibrium flow (where $N_{Zu}=N_{sub}$ and $z_{BB}=L_{boil}$). Mass flow rate decreases slightly around such transition locations without much change in boiler inlet temperature, thereby giving lower N_{Zu} for the N_{sub} at transition boundary. Hence the gradient of the corresponding line is slightly higher, as shown in Table 3, indicating the condenser entry condition to be saturated even when N_{Zu} is slightly less than N_{sub}.

For even higher values of N_{Zu} for a given N_{sub}, the influence of subcooled boiling is clearly evident. In fact, saturated boiling initiates in the boiler only when the value of N_{sub} is less than one-third of N_{Zu}. For intermediate values of N_{Zu}, fluid exit condition lies in zone III, that is, of subcooled boiling at boiler exit and saturated at condenser entry. Between zones III and V, a very narrow band (depicted as zone IV) is obtained. It is difficult to get a steady-state solution within this narrow band. For typical combinations of N_{Zu} and N_{sub} in this zone, the solution shifts either to zone III or to zone V. With the low-order model used in the present case, it is difficult to ascertain whether this behavior is due to the physical instability. This behavior may also be due to the condensation model used to consider energy interaction in the riser. No information is available to understand the real physical phenomenon and hence the present study incorporates the best available correlation to close the model. A few sample cases have been shown on Fig. 8 to depict the change in the nature of profile with pressure. As pressure increases, the transition lines get closer and the relative influence of subcooled boiling reduces. This is expected as with increase in system pressure, h_{fg} decreases leading to less energy requirement for fluid evaporation. The transition curves also converge toward each other for lower values of N_{Zu} and N_{sub} and are expected to merge at the critical pressure. Such a generalized working-regime map is expected to help in designing, analyzing, and understanding similar systems.

Table 3 Parameters for transition criteria

Zone	m	c
I–II	1.247	2.557
II–III	1.011	0.056
III–IV	0.347	3.833
IV–V	0.313	3.250

3.3 Influence of Sink Condition. It is now quite evident that the flow stream condition at the boiler exit and condenser inlet can be controlled by controlling the parameters N_{Zu} and N_{sub}; N_{Zu} being a linear function of the supplied wall heat flux, it is somewhat easier to regulate that. However, the degree of liquid subcooling and hence the value of N_{sub} are strongly dependent on the performance of low-temperature reservoir. In the present model, the sink is provided in the form of a parallel-flow heat exchanger, resulting in convective heat transfer between two fluid streams through a conductive wall. Hence, it is very important to ascertain system response toward different parameters associated with the coolant stream. Both coolant flow rate and inlet temperature are important control variables for a NCL. As can be seen from Fig. 9, with change in coolant flow rate, there is significant variation in system flow rate and vapor quality for any given heat flux. Maximum loop flow rate increases slightly for a higher rate of coolant flow. But for lower coolant flow rates, system attains the maximum mass flux at a much lower value of wall heat flux; e.g., for 0.5 kg/s of coolant flow rate, maximum loop mass flux appears around 250 kW/m^2, while for 1.5 kg/s of coolant flow rate, the corresponding value is about 350 kW/m^2. Consequently, the condenser entry quality for any given heat flux is much higher for a lower coolant flow rate. Hence, it is not possible to operate at very high heat fluxes with low coolant flow rates (Fig. 9). At a lower value of coolant flow rate, cooler exit temperature is high, which results in a high value of circulation rate, even at an input of low

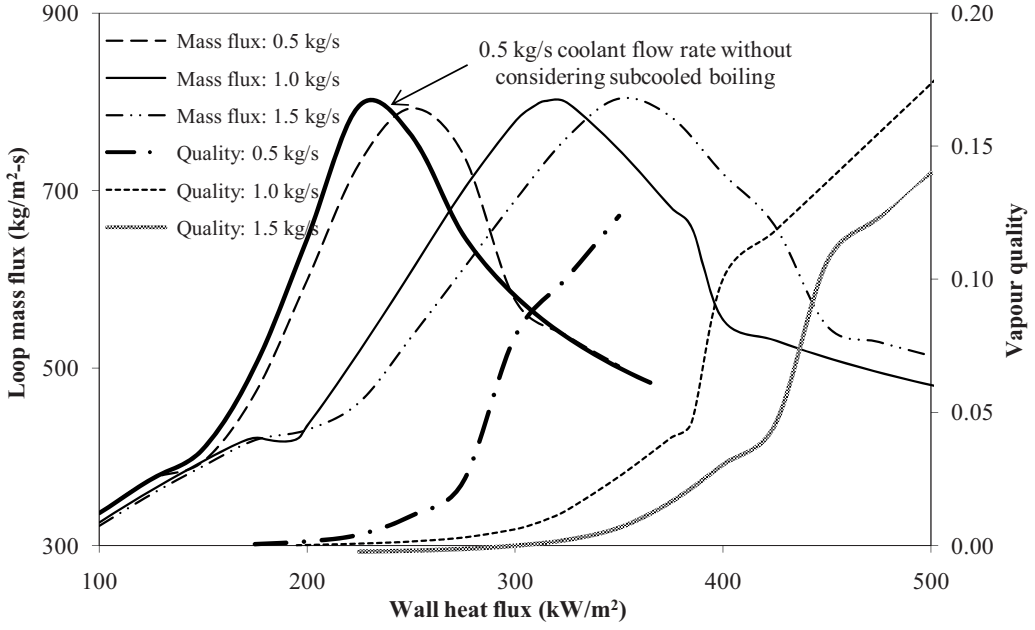

Fig. 9 Effect of coolant mass flow rate on loop mass flux and condenser entry quality

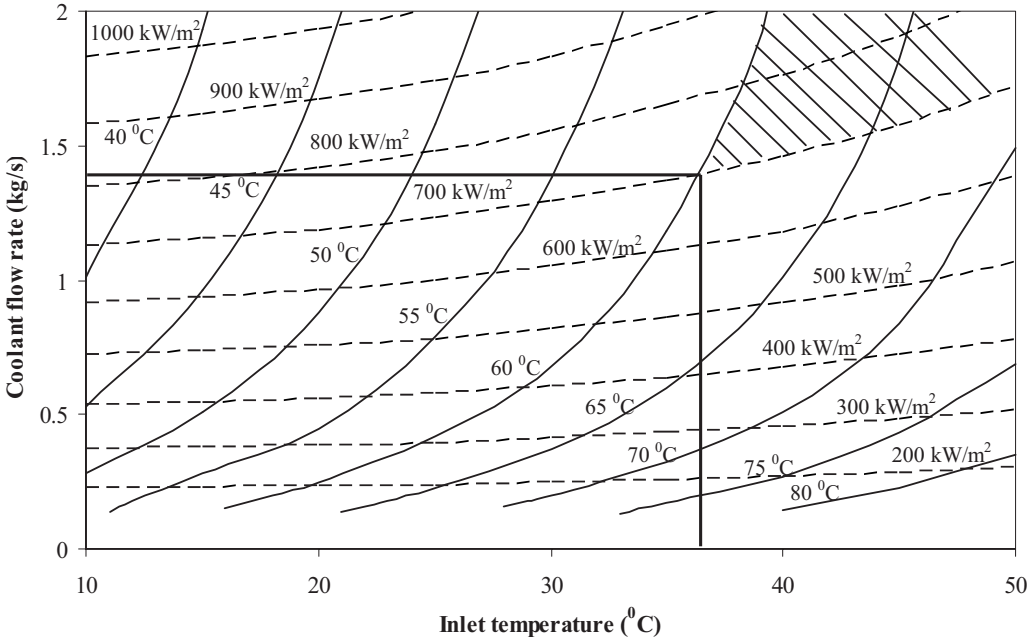

Fig. 10 Design graph for optimum coolant flow rate and inlet temperature to avoid two-phase condition at downcomer

heat flux. Furthermore, a lower coolant flow rate yields a lower value of overall heat transfer coefficient, leading to a lesser energy transfer to the coolant. It results in higher fluid temperature on the downcomer side and accordingly higher mixture enthalpy at the boiler exit, causing a sharper increase in flow rate. As the vapor quality in the riser can be very high for higher heat fluxes, there is a possibility of surface dry-out and care should be taken to avoid it. Hence, despite the requirement of larger pumping effort, it is advisable to operate with higher coolant flow rates. Moreover, the profiles for 1.0 kg/s and 1.5 kg/s coolant flow rates are much closer to each other compared with the profiles for 0.5 kg/s and 1.0 kg/s; hence, a large increase in coolant flow rate will not provide any significant gain beyond a certain limit and it is possible to optimize the pumping cost. For the sake of comparison, the mass flux profile with 0.5 kg/s coolant flow rate for the idealized case of no subcooled boiling has also been shown in Fig. 9. It predicts a higher value of limiting heat flux compared with the present model. Hence, the consideration of subcooled boiling provides a safer upper limit of operating heat flux.

Similar behavior has also been observed with an increase in coolant inlet temperature. Higher coolant inlet temperature results in smaller average temperature difference with the loop fluid, leading to lower energy transfer. Thus, for a higher coolant inlet temperature, the maximum loop mass flux appears at a lower value of wall heat flux. Hence, it can be concluded that for favorable sink conditions, i.e., high flow rate or low inlet temperature, the system can be operated through wider ranges of wall heat flux before encountering the maximum loop mass flux condition.

For satisfying the conservation of energy under steady-state condition, total supplied power must get transferred to the coolant stream, implying an implicit relationship between the wall heat flux and coolant exit condition. Depending on whether the objective of the system is to transfer a particular heat flux load or to obtain a particular coolant exit condition, the control variables, namely, the coolant flow rate and coolant inlet temperature are required to be monitored carefully. As can be observed from Fig. 9, it is not possible to operate a system with any given combination of coolant supply conditions, in order to avoid the possibility of incomplete condensation and two-phase mixture entering the downcomer. Drawing a vertical line in Fig. 9 at 350 kW/m^2 suggests that with decrease in coolant flow rate, the possibility of incomplete condensation increases, due to an increase in vapor quality at condenser entry and a decrease in overall heat transfer coefficient. A similar approach suggests that a lower coolant inlet temperature enhances condensation heat transfer, thereby reducing the possibility of two-phase mixture in downcomer. These two counterbalancing features can be combined to yield a safety limit of operation in terms of coolant supply condition for any given heat flux, which can act as a transition curve of having a favorable single-phase downcomer or potentially undesirable two-phase downcomer. Figure 10 presents a novel design curve to identify the safety limits for a number of wall heat fluxes. Here each of the broken lines represents the transition curve for a separate wall heat flux as indicated. The zone above each of them identifies the corresponding safe region, i.e., any combination of coolant flow rate and coolant inlet temperature in that region will assure complete condensation, whereas any combination below the curve will result in two-phase mixture entry into the downcomer. For any given coolant inlet temperature and wall heat flux, the curve provides the minimum allowable value of coolant flow rate to attain complete condensation. Further reduction in flow rate will reduce the overall heat transfer coefficient, resulting in two-phase mixture at downcomer inlet. With increase in wall heat flux for any given coolant inlet temperature, allowable coolant flow rate limit understandably increases to take care of the additional power. With increase in the supply temperature for any given flow rate, overall heat transfer coefficient increases slightly. However, the reduced temperature differential between the fluid and coolant causes an increase in vapor quality at condenser inlet and accordingly higher condensing length. Hence, higher coolant flow rate is required to ensure complete condensation with higher coolant supply temperature and that explains the diverging nature of the transition curves (Fig. 10).

Similar transition curves can also be generated for any desired coolant exit temperature. As the temperature rise of the cooling stream is fixed, any increase in coolant flow rate requires a proportionate increase in wall heat flux. That, in turn, causes an increase in vapor quality at condenser inlet and proportional increase in condensing length. Hence, for any given value of coolant inlet and exit temperature, it is possible to identify a maximum allowable coolant flow rate, in order to avoid incomplete condensation. With an increase in coolant supply temperature, the allow-

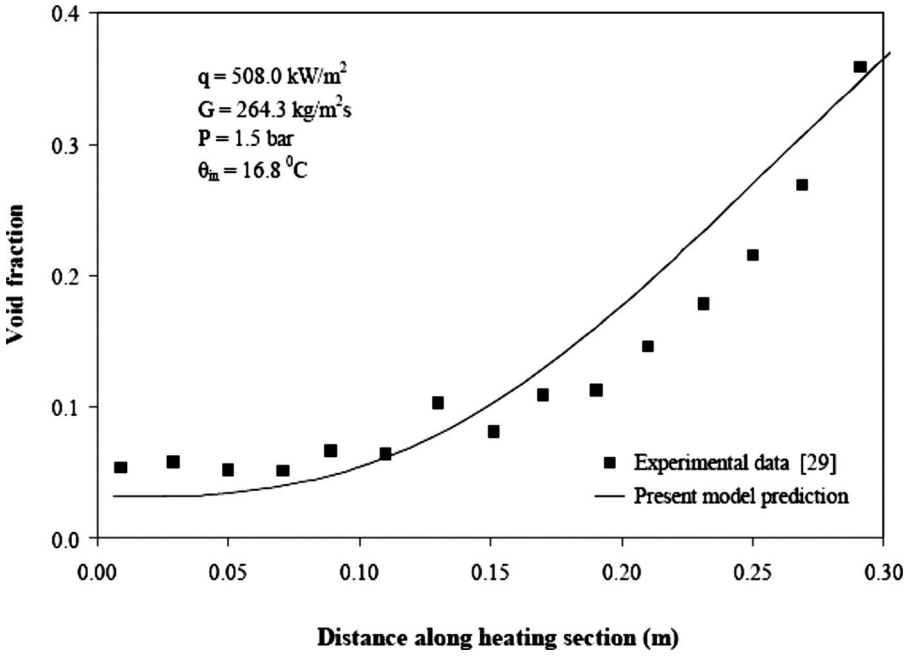

Fig. 11 Comparison of present model prediction with experimental data [29]

able flow rate limit increases, thereby generating a line of safe operation for that particular coolant exit temperature. Figure 10 represents a host of such transition curves for different coolant exit conditions using solid lines with corresponding temperatures indicated. The region to the right of each curve represents the potentially safe zone of operation. Any combination of coolant supply condition from the left of the curve will result in incomplete condensation.

Figure 10 can serve well as a design curve for the kind of system under consideration. If the objective of operation is properly defined, then the limit of operation regarding the coolant stream can easily be identified. A test case is illustrated in Fig. 10. If the system is subjected to a wall heat flux of 700 kW/m^2, with an intended coolant exit temperature of 60°C, then the limits of control parameters are as marked with dark lines. Here the limits are 1.39 kg/s coolant flow rate and 36.5°C coolant supply temperature. A number of combinations of coolant flow rate and inlet temperature are feasible as long as they satisfy the energy balance $(q''_w(\pi d L_{\text{boil}}) = \dot{m}_c C_{\text{pc}}(T_{c,\text{out}} - T_{c,\text{in}}))$, in order to achieve the given wall heat flux and coolant exit temperature. But it is essential to have the chosen combination within the hatched zone shown in Fig. 10. Any combination outside that zone will either result in incomplete condensation or deviation in the values of desired parameters. Following the same process, it is possible to identify the feasible combinations of coolant supply condition for a given wall heat flux and coolant exit temperature. In a number of practical situations, the inlet temperature may well have a constraint imposed by the application. For such cases, minimum pumping requirement can be estimated for any desired output set. It is also interesting to note that every coolant exit temperature corresponds to some minimum limit regarding the inlet condition. For example, it is not possible to have 70°C coolant exit temperature at any practicable coolant flow rate with an inlet temperature of 20°C. Hence, if the inlet temperature is fixed by the ambient, Fig. 10 is capable of identifying appropriate coolant flow rates for safe operation with a given heat flux and coolant exit temperature.

In the absence of relevant test data in the literature for a similar configuration, a complete validation of the NCL system model, incorporating subcooled boiling, was not possible. However, an attempt has been made to validate the subcooled boiling model using test data from a vertical boiling annulus, the details of which are presented in the Appendix. The comparison (Fig. 11) exhibits a reasonable agreement confirming the suitability of the model for NCL applications.

4 Conclusions

A 1D correlation-based model for steady-state analysis of a two-phase rectangular NCL has been presented here. Particular emphasis has been exercised on modeling the subcooled boiling zone. Well-established correlations have been used to determine the inception, development, and termination of subcooled boiling zone. Major observations from this study can be summarized as follows.

1. Variation of mass flux exhibits identical trend compared with that of an idealized system with perfect thermal equilibrium (no subcooled boiling), but some quantitative deviation has been observed, particularly around the transition locations. This can be attributed to the longer two-phase zone length due to the presence of subcooled boiling and corresponding higher frictional losses and thermal interactions.
2. It is possible for the fluid stream to exit the boiler under subcooled boiling condition. Following thermal interaction between vapor bubbles and subcooled liquid in riser tube, the fluid stream reverts to single-phase or saturated condition.
3. Four possible combinations of the fluid stream condition at the boiler exit and condenser inlet are predicted. A generalized working-regime map has been suggested to predict the possible combination for any given set of inputs. Transition criteria in the form of linear equations have also been proposed and more than 95% of the available data points satisfy the relations. Hence, it is possible to estimate the required degree of subcooling and so the required condensing capacity for a given power input, in order to satisfy the desired boiler exit condition, directly from the proposed map.
4. A stronger sink condition, i.e., higher coolant flow rate or lower coolant inlet temperature, has been found to result in a wider operating range of wall heat flux.
5. A methodology has been suggested to construct a design map, which will identify the favorable combinations of con-

trol variables to ensure complete condensation for any given set of wall heat flux and coolant exit temperature.

Acknowledgment

Financial support extended by the Reactor Engineering Division of Bhaba Atomic Research Centre (BARC), Mumbai, India is gratefully acknowledged.

Nomenclature

A_{cs} = cross-sectional area (m^2)
C_p = specific heat (J kg^{-1} K^{-1})
d = diameter (m)
f = friction factor
G = mass flux (kg m^{-2} s^{-1})
h = enthalpy (J kg^{-1})
h_{fg} = enthalpy of vaporization (J kg^{-1})
H = heat transfer coefficient (W m^{-2} K^{-1})
L_{boil} = boiler length (m)
$\dot{m}$ = mass flow rate (kg/s)
N_{Zu} = Zuber number $(=(4/d)(q''_w L_{boil}/G)((\rho_f-\rho_g)/\rho_g))$
N_{sub} = subcooling number $(=((h_{f-sat}-h_{f-inlet})/h_{fg})((\rho_f-\rho_g)/\rho_g))$
Nu = Nusselt number $(=Hd/\lambda)$
p = pressure (bar, Pa)
P_h = wetted perimeter (m)
Pe = Peclet number (=Re Pr)
Pr = Prandtl number $(=\mu C_p/\lambda)$
q''_w = wall heat flux (W m^{-2})
R = thermal resistance (m^2 K W^{-1})
Re = Reynolds number $(=Gd/\mu)$
T = absolute temperature (K)
u = fluid velocity (m s^{-1})
U_o = overall heat transfer coefficient (W m^{-2} K^{-1})
x = vapor quality
Y_B = distance of wall from the tip of bubble (m)
z = loop coordinate (m)

Greek symbol

α = void fraction
ΔT = temperature difference (K)
Γ_{con} = vapor condensation rate (kg m^{-3} s^{-1})
ε = surface roughness (m)
λ = thermal conductivity (W m^{-1} K^{-1})
ρ = density (kg m^{-3})
σ = surface tension (N m^{-1})
τ = wall shear stress (N m^{-2})

Subscripts

1ϕ = single-phase liquid
bub = bubble
bx = boiler exit
BB = boiling boundary
c = cooling stream
con = condensing fluid
eq = equilibrium
f = liquid
g = vapor
in = inner
out = outer
sub = subcooled
sub = superheated
w = wall

Appendix

Test results for a similar geometrical system have not been reported yet and hence a direct validation of the model was not possible. However, the novelty of the present work is in the simplified modeling of subcooled boiling and its influence on the performance of a rectangular NCL. Hence, an attempt has been made to verify the predictions from the subcooled boiling zone using the results of an experiment performed on a vertical annulus [29]. The reported tests were carried out on an electrically heated annulus of 12.7 mm inner diameter, 25.4 mm outer diameter, and a 30.6 cm long heated section, preceded and followed by unheated sections. Void fraction was measured using a single-beam gamma densitometer with ±4% average uncertainty. Predicted results and corresponding experimental data along with the operating parameters have been shown in Fig. 11. A reasonably fair agreement has been obtained over the heated range within the fully developed subcooled boiling zone with a maximum deviation of around 15%. The location of OSV (around 0.11 m) also matches quite well, as is evident from the rise in void fraction profile. It is also observed that within the fully developed subcooled boiling zone, the present model mostly overpredicts the experimental data. However, at the heated section exit, void fraction values are in close agreement. Hence, it may be concluded that the present model is capable of predicting fairly realistic values of subcooled boiling parameters and hence it is worthwhile to employ that for NCL analysis.

References

[1] Schmidt, E., 1951, *General Discussion on Heat Transfer*, Institution of Mechanical Engineers, London, Sec. IV, p. 361.
[2] Cohen, H., and Bayley, F. J., 1955, "Heat Transfer Problems of Liquid Cooled Gas Turbine Blades," Proc. Inst. Mech. Eng., **169**, pp. 1063–1080.
[3] Mertol, A., Place, W., Webster, T., and Greif, R., 1981, "Detailed Loop Model (DLM) Analysis of Liquid Solar Thermosiphons With Heat Exchangers," Sol. Energy, **27**(5), pp. 367–386.
[4] McKee, H. R., 1970, "Thermosyphon Reboilers: A Review," Ind. Eng. Chem., **62**(12), pp. 76–82.
[5] Sarma, N. V. L. A., Reddy, P. J., and Murti, P. S., 1973, "A Computer Design Method for Vertical Thermosyphon Reboilers," Ind. Eng. Chem. Process Des. Dev., **12**(3), pp. 278–290.
[6] Heisler, M. P., 1982, "Development of Scaling Requirements for Natural Convection Liquid-Metal Fast Breeder Reactor Shutdown Heat Removal Test Facilities," Nucl. Sci. Eng., **80**(3), pp. 347–359.
[7] Hsu, Y. Y., 1981, "Two-Phase Flow Problems in Pressurized Water Reactors," *Thermohydraulics of Two-Phase Systems for Industrial Design and Nuclear Engineering*, J. M. Delhaye, M. Giot, and M. L. Riethmuller, eds., Hemisphere, Washington, DC, pp. 1–10.
[8] Kreitlow, D. B., Reistad, G. M., Miles, C. R., and Culver, G. G., 1978, "Thermosyphon Models for Downhole Heat Exchanger Applications in Shallow Geothermal Systems," ASME J. Heat Transfer, **100**, pp. 713–719.
[9] Lee, Y., and Mital, U., 1972, "A Two-Phase Closed Thermosyphon," Int. J. Heat Mass Transfer, **15**(9), pp. 1695–1707.
[10] Dobran, F., 1985, "Steady-State Characteristics and Stability Thresholds of a Closed Two-Phase Thermosyphon," Int. J. Heat Mass Transfer, **28**(5), pp. 949–957.
[11] Ramos, E., Sen, M., and Trevino, C., 1985, "A Steady-State Analysis for Variable Area One- and Two-Phase Thermosyphon Loops," Int. J. Heat Mass Transfer, **28**(9), pp. 1711–1719.
[12] Chen, K. S., and Chang, Y. R., 1988, "Steady-State Analysis of Two-Phase Natural Circulation Loop," Int. J. Heat Mass Transfer, **31**(5), pp. 931–940.
[13] Rao, N. M., Chandra Sekhar, Ch., Maiti, B., and Das, P. K., 2006, "Steady-State Performance of a Two-Phase Natural Circulation Loop," Int. Commun. Heat Mass Transfer, **33**, pp. 1042–1052.
[14] Jeng, H. R., and Pan, C., 1999, "Analysis of Two-Phase Flow Characteristics in a Natural Circulation Loop Using the Drift-Flux Model Taking Flow Pattern Change and Subcooled Boiling Into Consideration," Ann. Nucl. Energy, **26**(14), pp. 1227–1251.
[15] Collier, J. G., and Thome, J. R., 1994, *Convective Boiling and Condensation*, 3rd ed., Clarendon, Oxford.
[16] Koncar, B., and Mavko, B., 2003, "Modelling of Low-Pressure Subcooled Flow Boiling Using the RELAP5 Code," Nucl. Eng. Des., **220**, pp. 255–273.
[17] Basu, N., Warrier, G. R., and Dhir, V. K., 2005, "Wall Heat Flux Partitioning During Subcooled Flow Boiling: Part I—Model Development," ASME J. Heat Transfer, **127**(2), pp. 131–140.
[18] Bergles, A. E., and Rohsenow, W. M., 1964, "The Determination of Forced-Convection Surface Boiling Heat Transfer," ASME J. Heat Transfer, **86**, pp. 365–372.
[19] Gnielinski, V., 1979, "Equations for Calculating Heat Transfer in Single Tube

Rows and Banks of Tubes in Transverse Direction," Int. Chem. Eng., **19**(3), pp. 380–391.
[20] Saha, P., and Zuber, N., 1974, "Point of Net Vapour Generation and Vapour Void Fraction in Subcooled Boiling," Proceedings of the Fifth International Heat Transfer Conference, Tokyo, Paper No. B4.7.
[21] Levy, S., 1967, "Forced Convection Subcooled Boiling: Prediction of Vapor Volumetric Fraction," Int. J. Heat Mass Transfer, **10**(7), pp. 951–965.
[22] Rouhani, S. Z., and Axelsson, E., 1970, "Calculation of Void Volume Fraction in the Subcooled and Quality Boiling Regions," Int. J. Heat Mass Transfer, **13**(2), pp. 383–393.
[23] Dobson, M. K., and Chato, J. C., 1998, "Condensation in Smooth Horizontal Tubes," ASME J. Heat Transfer, **120**(1), pp. 193–213.
[24] Petukhov, B. S., and Roizen, L. I., 1964, "Generalized Relationships for Heat Transfer in Turbulent Flow of Gas in Tubes of Annular Section," High Temp., **2**, pp. 65–68.
[25] Chisholm, D., 1973, "Pressure Gradients Due to Friction During the Flow of Evaporating Two-Phase Mixtures in Smooth Tubes and Channels," Int. J. Heat Mass Transfer, **16**(2), pp. 347–358.
[26] Friedel, L., 1979, "Improved Friction Pressure Drop Correlations for Horizontal and Vertical Two-Phase Pipe Flow," Proceedings of the European Two-Phase Flow Group Meeting, Ispra, Paper No. E2.
[27] Wagner, W., Copper, J. R., Dittmann, A., Kijima, J., Kretzschmar, H. J., Kruse, A., Mares, R., Oguchi, K., Sato, H., Stocker, I., Sifner, O., Takaishi, Y., Tanishita, I., Trubenbach, J., and Willkommen, Th., 2000, "The IAPWS Industrial Formulation 1997 for the Thermodynamic Properties of Water and Steam," ASME J. Eng. Gas Turbines Power, **122**, pp. 150–182.
[28] De Kruijf, W. J. M., Sengstag, T., De Haas, D. W., and Van Der Hagen, T. H. J. J., 2004, "Experimental Thermohydraulic Stability Map of a Freon-12 Boiling Water Reactor Facility With High Exit Friction," Nucl. Eng. Des., **229**, pp. 75–80.
[29] Zeitoun, O., and Shoukri, M., 1997, "Axial Void Fraction Profile in Low Pressure Subcooled Flow Boiling," Int. J. Heat Mass Transfer, **40**(4), pp. 869–879.

Effortless Application of the Method of Lines for the Inverse Estimation of Temperatures in a Large Slab With Two Different Surface Heating Waveforms

Antonio Campo[1]
e-mail: campanto@yahoo.com

John Ho

Mechanical Engineering Department,
The University of Vermont,
33 Colchester Avenue,
Burlington, VT 05405

The boundary inverse heat conduction problem (BIHCP) deals with the determination of the surface heat flux or the surface temperature from measured transient temperatures inside a conducting body where the initial temperature is known. This work addresses a BIHCP related to the spatiotemporal heat conduction in a large slab when a time-variable heat flux is prescribed at an exposed surface and the other surface is thermally insulated. Two different heating waveforms are studied: a constant heat flux and a time-dependent triangular heat flux. The numerical temperature-time history at the insulated surface of the large slab provides the "temperature-time measurement" with one temperature sensor. Framed in the theory of the method of lines (MOL) first and employing rudimentary concepts of numerical differentiation later, the main objective of this paper is to develop a simple computational methodology to estimate the temporal evolution of temperature at the exposed surface of the large slab receiving the two distinct heat fluxes. In the end, it is confirmed that excellent predictions of the surface temperatures versus time are achievable for the two cases tested while employing the smallest possible system of two heat conduction differential equations of first-order. [DOI: 10.1115/1.2993141]

Keywords: boundary inverse heat conduction problem (BIHCP), method of lines (MOL), numerical differentiation

1 Introduction

It has been said that inverse heat conduction problems (IHCP) are ill-posed problems and can be classified arbitrarily. However, one means of sorting them is by the type of information that is being sought in the solution procedure. A successful solution of an IHCP generally involves its reformulation as an approximate well-posed problem. New prediction methods and the availability of high-speed large scale computers have facilitated the solution of a wide variety of IHCP in a significant way. A collection of the available methods has been categorized in the specialized Refs. [1–7].

The boundary inverse heat conduction problem (BIHCP) deals with the determination of the surface heat flux or the temperature from measured transient temperatures inside a heated body where the initial temperature is known. In general, solution methods for the BIHCP can be classified into two broad categories: analytical or numerical. Regardless of the solution method, the central idea is to determine heat fluxes and temperatures on an inaccessible surface of a heated body by measuring the temperature on an accessible surface or at an interior point of the body.

Within the framework of the BIHCP, this work addresses the transient heat conduction in a large slab with a time-variable heat flux prescribed at the exposed surface while the other surface is thermally insulated. Two different heating waveforms are studied: a constant heat flux and a triangular heat flux. A single "temperature measurement" changing continually with time is taken at the insulated surface of the large slab from the exact temperature field $T(x,t)$ of the direct heat conduction problem (DHCP). The main objective here is to develop a simple systematic methodology combining the theory behind the method of lines (MOL) with elementary numerical differentiation of the tabulated temperature-time history. The secondary objective is to employ the smallest possible system of transformed heat conduction differential equations of first-order. To the authors' best knowledge, this hybrid methodology has not been developed before.

Despite that the coarsest line mesh is utilized, excellent predictions of the temperature-time histories at the exposed surface of the large slab caused by the two heating waveforms are obtained in this work.

2 Direct Formulation

Consider a one-dimensional transient heat conduction in a large slab of thickness L as sketched in Fig. 1. The slab material has constant thermal conductivity k, constant density ρ, and constant specific heat capacity c. The initial temperature distribution in the slab is $T_0(x)$. For times $t>0$, a transient heat flux is applied at the exposed left surface $x=0$, while the right surface $x=L$ is thermally insulated. The objective is to determine the temperature field $T(x,t)$ in the large slab. Correspondingly, the DHCP is modeled by the 1D heat conduction equation:

$$\rho c \frac{\partial T}{\partial t} = k \frac{\partial^2 T}{\partial x^2} \quad \text{in } 0 < x < L \tag{1}$$

subject to the initial condition,

$$T(x,0) = T_0(x) \tag{2}$$

and the two boundary conditions,

$$-k \frac{\partial T(0,t)}{\partial x} = q_s(t) \tag{3}$$

$$\frac{\partial T(L,t)}{\partial x} = 0 \tag{4}$$

3 Inverse Formulation

One type of IHCP dealing with one-dimensional transient heat conduction in a large slab of thickness L is indicated in Fig. 1. The slab material has constant thermal conductivity k, density ρ, and specific heat capacity c. The inverse problem is modeled by the 1D heat conduction in Eq. (1), the initial condition in Eq. (2), and the boundary condition at the thermally insulated surface $x=L$ in Eq. (4). For the boundary condition at the exposed surface $x=0$ in Eq. (4), the boundary condition function $q_s(t)=q(0,t)$ is the unknown or the surface temperature $T_s(t)=T(0,t)$ is the unknown. All other participating quantities, such as the three material properties k, ρ, and c, the slab thickness L, and the initial temperature distribution $T_0(x)$ are known.

Under the platform of the IHCP, the goal here is to estimate the surface heat flux $q_s(0,t)$ or the surface temperature $T_s(0,t)$ in the large slab based on the sequence of "temperature measurements"

[1]Corresponding author.

Contributed by the Heat Transfer Division of ASME for publication in the JOURNAL OF HEAT TRANSFER. Manuscript received September 7, 2007, final manuscript received July 13, 2008; published online December 11, 2008. Review conducted by A. Haji-Sheikh.

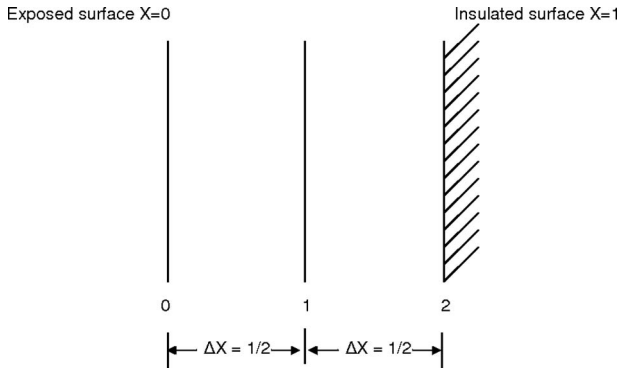

Fig. 1 Computational domain with three lines: Lines 0, 1, and 2

$$T(x_m,t_i) = T_{m,i} \tag{5}$$

taken at one location x_m and at different times t_i $(i=1,2,\ldots,I)$. In this preliminary work, it has been idealized that the "temperature measurements" with a single temperature sensor at all time are free of error or uncertainty so that there is no noise in the data.

The above-described subclass of problems is named BIHCP in Ref. [5].

4 Method of Lines

The MOL embodies a mathematical procedure for solving partial differential equations in one- or multiple dimensions. In the case of the 1D heat conduction in Eq. (1), the basic idea is to replace the spatial derivative $(\partial^2 T/\partial x^2)$ with an algebraic finite-difference approximation while holding the time derivative $(\partial T/\partial t)$ continuous [8]. This operation is done in a 1D computational domain constructed with a collection of straight lines perpendicular to the x-coordinate in the large slab. The lines are usually separated by equal spatial intervals Δx, although unequal intervals can be used. In other words, the MOL procedure transforms the parabolic partial differential equation (Eq. (1)) in x and t into a system of first-order ordinary differential equations in t that approximates the parabolic partial differential equation (Eq. (1)). An important advantage of MOL is that the errors are quantified in terms of spatial intervals Δx without the intervention of the time-interval Δt so that the errors are controllable in an easy way.

Among the various finite-difference approximations for the spatial derivative $(\partial^2 T/\partial x^2)$, we chose the central finite-difference approximation

$$\left.\frac{\partial^2 T}{\partial x^2}\right|_i \approx \frac{T_{i-1} - 2T_i + T_{i+1}}{(\Delta x)^2} + O(\Delta x)^2 \tag{6}$$

where the term $O\ (\Delta x)^2$ represents a truncation error.

Let us introduce the dimensionless variables for t, x, and T,

$$\tau = \frac{t}{L^2/\alpha}, \quad X = \frac{x}{L}, \quad \phi = \frac{T - T_0}{q_s L/k} \tag{7}$$

To commence, the application of MOL to the dimensionless version of Eq. (1)

$$\frac{\partial \phi}{\partial \tau} = \frac{\partial^2 \phi}{\partial X^2} \quad \text{in } 0 < X < 1 \tag{8}$$

supplies the following system of differential equations of first-order in τ

$$\frac{d\phi_i}{d\tau} = \frac{\phi_{i-1} - 2\phi_i + \phi_{i+1}}{(\Delta X)^2}, \quad i = 0,1,\ldots,M \tag{9}$$

Overall, this system consisting of M equations embraces the two boundary conditions in Eqs. (3) and (4) and is subject to the initial condition in Eq. (2), all rewritten in dimensionless form. Thereafter, the system may be integrated with analytical or numerical techniques. For a numerical integrator, the explicit Euler method, the implicit Euler method, or a higher order Runge–Kutta method are the most popular [9]. In principle, the solution of the partial differential equation in Eq. (8) can be provided by a solution to the approximate system of differential equations of first-order given in Eq. (9).

In retrospect, when the limit of the right hand side (RHS) of Eq. (9) is taken as $\Delta X \to 0$, the system of differential equations of first-order recovers the original partial differential equation in Eq. (8).

As a first attempt for the discretization in Eq. (9), we chose the coarsest possible line mesh with an interval $\Delta X = \frac{1}{2}$ shown in Fig. 1. In fact, this is the minimum that could be done within the scope of MOL. Thereby, the smallest possible system of two differential equations of first-order is

$$\frac{d\phi_1}{d\tau} = 4\phi_0 - 8\phi_1 + 4\phi_2 \tag{10}$$

$$\frac{d\phi_2}{d\tau} = 8\phi_1 - 8\phi_2 \tag{11}$$

whose solution is second-order accurate.

5 Test Cases

Among the four test cases proposed in Ref. [1], we selected two: a constant surface heat flux (invariant with time) and a triangular surface heat flux varying strongly with time.

5.1 First Case: Constant Surface Heat Flux. The temperature field $\phi(X,\tau)$ in the large slab taken from Ref. [1] is expressed by

$$\phi(X,\tau) = \tau + \frac{X^2}{2} - \frac{1}{6} - 2\sum_{n=1}^{\infty} \frac{(-1)^n}{(n\pi)^2} \exp[-(n\pi)^2\tau]\cos[(n\pi)X] \tag{12}$$

5.2 Second Case: Triangular Surface Heat Flux. The dimensionless variables for time t, position x, temperature T, and surface heat flux q_s are

$$\tau = \frac{t}{L^2/\alpha}, \quad X = \frac{x}{L}, \quad \phi = \frac{T - T_0}{q_N L/k}, \quad q_R = \frac{q_s}{q_N} \tag{13}$$

where q_N in the last ratio stands for the nominal surface heat flux associated with τ equal to unity in the relation

$$q_R = \tau$$

The three-part q_s function defining the triangular surface heat flux is defined as follows. Before $\tau=0$, q_s is equal to zero. For the first time subinterval between 0 and 0.6, q_s increases linearly with time, and for the second time subinterval with $\tau > 0.6$, q_s decreases linearly to zero at $\tau=1.2$; thereafter, q_s returns to zero. With regards to the two linear components of the surface heat flux q_s, the exact temperatures at the left exposed surface $X=0$ and right insulated surface $X=1$ are given by Ref. [1], as follows

(a) For the first time subinterval $0 < \tau < 0.6$,

$$\phi(0,\tau) = \frac{(\tau)^2}{2} + \frac{\tau}{3} - \frac{1}{45} + \frac{2}{\pi^4}\sum_{n=1}^{\infty} \frac{1}{n^4} \exp[-(\pi n)^2\tau] \tag{14a}$$

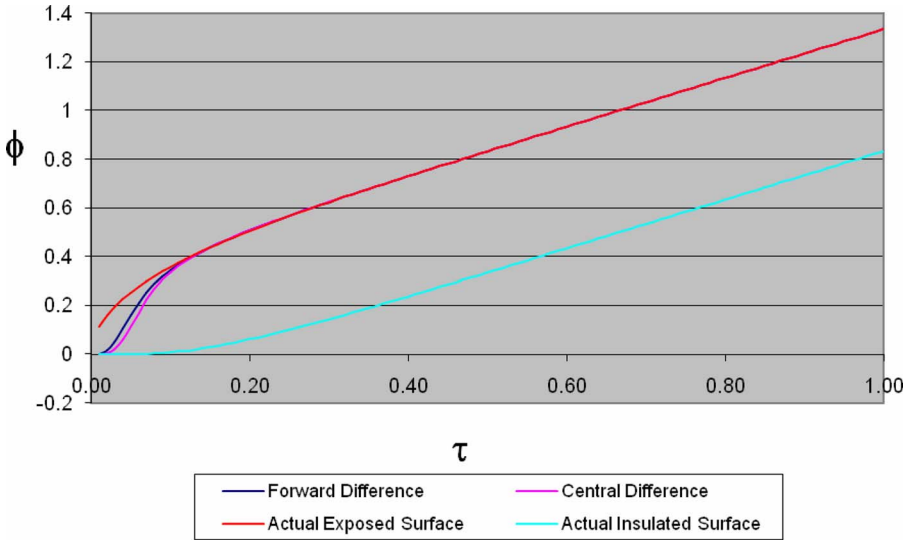

Fig. 2 Surface temperature estimates for constant surface heat flux

and

$$\phi(1,\tau) = \frac{(\tau)^2}{2} - \frac{\tau}{6} + \frac{7}{360} + \frac{2}{\pi^4}\sum_{n=1}^{\infty}\frac{(-1)^n}{n^4}\exp[-(\pi n)^2\tau] \tag{14b}$$

(b) For the second time subinterval $0.6 < \tau < 1.2$,

$$\phi(0,\tau) = \phi(1,\tau) - 2\phi(1,\tau-0.6) \tag{15a}$$

and

$$\phi(1,\tau) = \phi(1,\tau) - 2\phi(1,\tau-0.6) \tag{15b}$$

(c) For the third time subinterval $\tau > 1.2$,

$$\phi(0,\tau) = \phi(1,\tau) - 2\phi(1,\tau-0.6) + \phi(1,\tau-1.2) \tag{16a}$$

and

$$\phi(1,\tau) = \phi(1,\tau) - 2\phi(1,\tau-0.6) + \phi(1,\tau-1.2) \tag{16b}$$

6 Numerical Calculation Procedure

The calculation procedure to be delineated is common to the two heating conditions, namely, a constant surface heat flux (invariant with time) and a triangular surface heat flux varying with time.

First, isolating ϕ_1 in Eq. (11) delivers the algebraic equation,

$$\phi_1(\tau) = \phi_2(\tau) + \frac{1}{8}\frac{d\phi_2(\tau)}{d\tau} \tag{17}$$

In this two-term equation, $\phi_2(\tau)$ is the "measured temperature" at the insulated surface $X=1$ (Line 2 in Fig. 1) may be viewed as a function of time, and $(d\phi_2(\tau)/d\tau)$ is the unknown time derivative of the "temperature measurement," which is another function of time. The latter function can be calculated numerically from the tabulated data of ϕ_2 versus τ. To do this, there are two options: one is the central finite-difference approximation with a truncation error of order $(\Delta\tau)^2$ and the other is the forward finite-difference approximation with a truncation error of order $\Delta\tau$ [9].

Second, isolating ϕ_0 in Eq. (10) delivers another algebraic equation,

$$\phi_0(\tau) = \left[2\phi_1(\tau) + \frac{1}{4}\frac{d\phi_1(\tau)}{d\tau}\right] - \phi_2(\tau) \tag{18}$$

In this three-term equation, the bracketed term is associated with $X=\frac{1}{2}$ (Line 1 in Fig. 1) and the last term is connected to the insulated surface $X=1$ (Line 2 in Fig. 1). Since $\phi_1(\tau)$ is evaluated from Eq. (17), the time derivative of it $(d\phi_1(\tau)/d\tau)$ can also be calculated from the tabulated data of ϕ_1 versus τ with the central or forward finite-difference approximations [9].

In synthesis, the nature of all numerical computations turns out to be algebraic.

7 Presentation of Results

In general terms, the two extreme temperatures—one $\phi(1,\tau)$ at the insulated surface $X=1$ and the other $\phi(0,\tau)$ at the exposed surface $X=0$—are obtained from the exact temperature fields $\phi(X,\tau)$ for the two different heating wavefronts. For convergence with enhanced accuracy, a large number of terms is retained in the two exact infinite series, Eq. (12) as well as in the pair of Eqs. (14*a*) and (14*b*).

The temperature $\phi_2(\tau)$ can be conceived as a single numerical "temperature measurement" at the insulated surface $X=1$ with one temperature sensor. The numerical values of ϕ_2 at the corresponding time τ are tabulated in small intervals of size $\Delta\tau=0.01$ from $\tau=0$ to 1.

All numerical calculations for the temperatures and the time derivatives of temperatures were done with the spreadsheet software EXCEL [10].

7.1 First Case: Constant Surface Heat Flux. Figure 2 displays the exact surface temperature $\phi(0,\tau)$ from the DHCP along with the exact "measured temperature" at the insulated surface, $\phi(1,\tau)$. The former will be used for comparison purposes. Also, shown in the figure are the two estimated surface temperatures $\phi_0(\tau)$ retrieved from the MOL-based system of two differential equations of first-order coupled with the forward and the central finite-difference differentiations. Minor discrepancies are palpable for very short times before $\tau=0.1$ for the two differentiation approaches. They are attributable, as expected, to the large discretization errors of order $(0.5)^2=0.25$ for the coarsest line mesh. Thereafter, the matching of the three surface temperatures—one exact and two approximate—is perfect. Needless to say, the esti-

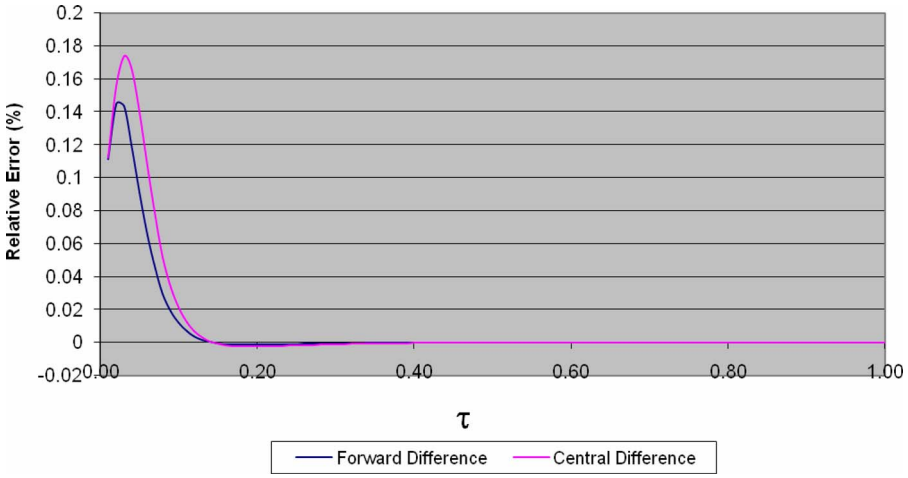

Fig. 3 Relative errors produced by the forward and central finite-difference approximations in Fig. 2

mated temperature mismatch for the very short times $\tau < 0.1$ can be eliminated with a finer mesh consisting of five lines and an interval $\Delta X = \frac{1}{4}$.

It is observable in Fig. 3 that the relative errors follow the path of a compressed bell shaped distribution near $\tau = 0$. Qualitatively speaking, the relative error reaches a maximum of 0.14 for the forward finite-difference differentiation and a maximum of 0.17 for the central finite-difference differentiation; the maximum relative errors in both cases lie around $\tau = 0.05$.

7.2 Second Case: Triangular Surface Heat Flux. Figure 4 illustrates the exact surface temperature $\phi(0,\tau)$ from the DHCP to be used for comparison purposes along with the exact "measured temperature" at the insulated surface, $\phi(1,\tau)$. Also, shown in the figure are the two estimated surface temperatures $\phi_0(\tau)$ retrieved from a MOL-based system of two differential equations of first-order articulated with the forward and the central finite-difference differentiations. It may be seen that at all times the surface temperature matching is almost perfect; the estimated surface temperatures $\phi_0(\tau)$ slightly overpredict the exact surface temperatures $\phi(0,\tau)$.

Plotted in Fig. 5 are the relative errors connected to the central finite-difference differentiation, which are confined to a thin band $e = \pm 0.01$. Similarly, those relative errors for the forward finite-difference differentiation are diminished to a thinner band $e = \pm 0.0075$.

Nomenclature

c = specific heat capacity (J/(kg K))
k = thermal conductivity (W/m K)
L = slab thickness (m)
q_s = surface heat flux (W/m^2)
t = time (s)
T_0 = initial temperature (K)
$T_{m,i}$ = temperature measurement at x_m and t_i (K)
T_s = surface temperature (K)
x = coordinate (m)
X = dimensionless coordinate, (x/L)

Greek Symbols

α = thermal diffusivity, $(k/\rho c)(m^2/s)$
ρ = density (kg/m^3)
τ = dimensionless time or Fourier number, $(t/L^2/\alpha)$
ϕ = dimensionless temperature, $(T - T_0/q_s L/k)$

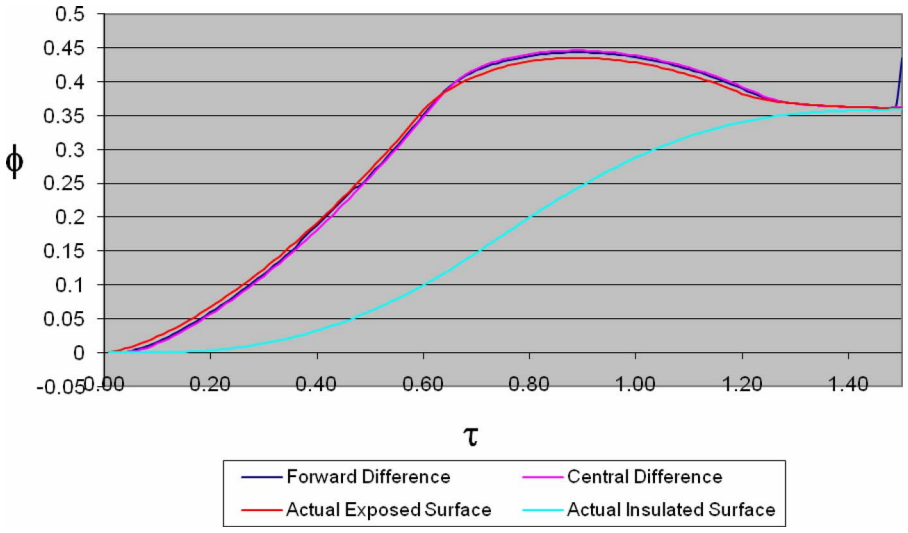

Fig. 4 Surface temperature estimates for a triangular surface heat flux

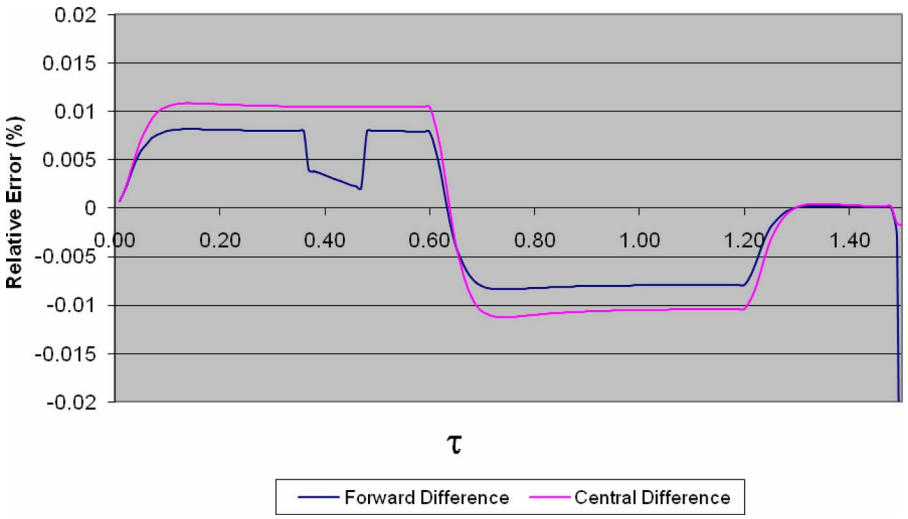

Fig. 5 Relative errors produced by the forward and central finite-difference approximations in Fig. 4

References

[1] Beck, J. V., Blackwell, B., and St. Clair, C. R., 1985, *Inverse Heat Conduction: Ill-Posed Problems*, Wiley, New York.

[2] Murio, D., 1993, *The Mollification Method and the Numerical Solution of Ill-Posed Problems*, Wiley, New York.

[3] Alifanov, O. M., 1994, *Inverse Heat Transfer Problems*, Springer-Verlag, Berlin, Germany.

[4] Hào, D. N., 1998, *Methods for Inverse Heat Conduction Problems*, Peter Lang GmbH, Berlin, Germany.

[5] Özisik, M. N., and Orlande, H. R. B., 2000, *Inverse Heat Transfer*, Taylor & Francis, New York.

[6] W. Woodbury, ed., 2002, *Inverse Engineering Handbook*, CRC, Boca Raton, FL.

[7] Taler, J., and Duda, P., 2006, *Solving Direct and Inverse Heat Conduction Problems*, Springer, Berlin, Germany.

[8] Wouwer, A. V., Saucez, P., and Schiesser, E., 2001, *Adaptive Method of Lines*, Chapman and Hall, London/CRC, Boca Raton, FL.

[9] Press, W. H., Flannery, B. P., and Teukolsky, S. A., 1992, *Numerical Recipes in FORTRAN: The Art of Scientific Computing*, 2nd ed., Cambridge University Press, London, UK, pp. 180–184.

[10] www.office.microsoft.com

Numerical and Experimental Study of Solidification in a Spherical Shell

E. Assis

G. Ziskind

R. Letan

Heat Transfer Laboratory,
Department of Mechanical Engineering,
Pearlstone Center for Aeronautical Studies,
Ben-Gurion University of the Negev,
P.O. Box 653,
Beer-Sheva 84105, Israel

The present study explores numerically and experimentally the process of a phase-change material (PCM) solidification in a spherical shell. At the initial state, the PCM liquid occupies 98.5% of the shell. The upper segment of 1.5% contains air, which flows in as the solidification progresses. In the experiments, a commercially available paraffin wax is used. Its properties are engaged in the numerical simulations. The investigation is performed for solidification in spherical shells of 20 mm, 40 mm, 60 mm, and 80 mm in diameter at the wall uniform temperature, which varied from 10°C to 40°C below the mean solidification temperature of the phase-change material. Transient numerical simulations are performed using the FLUENT 6.2 software and incorporate such phenomena as flow in the liquid phase, volumetric shrinkage due to solidification, and irregular boundary between the PCM and air. The numerical model is validated versus the experimental results. Shrinkage patterns and void formation are demonstrated. Dimensional analysis of the results is performed and presented as the PCM melt fractions versus the product of the Fourier and Stefan numbers. This analysis leads to a generalization that encompasses the cases considered herein.
[DOI: 10.1115/1.2993543]

Keywords: solidification, sphere, simulation, voids

1 Introduction

Phase change in spherical geometry is of great interest from the theoretical point of view and is of importance for the development of processes based on the use of latent heat. A considerable amount of literature on this subject exists, which reflects experimental, theoretical, and numerical investigations of melting and solidification. Theoretical studies on melting and solidification within spherical enclosures were performed by several researchers [1–8]. Advances in the field are summarized in Refs. [9,10] concerning its theoretical and practical aspects.

In the literature on solidification, a spherical shell containing a phase-change material (PCM) is usually treated as being completely filled by the molten material in the initial state. This means that the PCM touches the entire internal surface of the shell. Then, if a uniform temperature is applied to the shell, solidification would be concentric, as demonstrated recently by Chan and Tan [11]. Actually, this physical situation is commonly treated in the literature. For instance, Ismail [12] summarized the available results and compared the position of the interface reported in various investigations as a function of time. The reported deviations from concentricity are related to a nonuniform distribution of the heat-transfer coefficient on the outside of the shell, as presented in Ref. [13]. The density difference between the liquid and solid is commonly neglected in those models. This may suit water freezing in some cases. For other materials and, in particular, paraffins, the solid density is higher than that of the liquid. This means that the solid will occupy only a part of the volume initially occupied by the liquid, while the remaining fraction of the enclosed volume will be a void. In casting [14], formation of voids is recognized as a major problem, as it is also in the design of latent heat thermal energy storage (LHTES) systems based on the melting-solidification cycles [15]. For instance, the solid shape and structure will affect the rate of consequent melting [16], thus affecting the entire cycle. Also, the design of a storage system must address such questions as shell shape, strength, orientation, packaging, etc. For instance, a packed bed of spheres [10] could collapse under its own weight due to the voids in the shells.

In a completely symmetrical formulation described above, the void is formed at the center of the shell [11], and the problem remains essentially symmetrical. This makes the existing solutions applicable. However, in the other cases the location and shape of the void(s) are not known a priori, and their prediction presents a significant challenge. Following the works of Sulfredge et al. [17] for various geometries (e.g., horizontal pipes; the other works of that group are discussed in Ref. [15]), one can assume that void formation depends on the shell shape and size, material properties, cooling rate, and direction.

As mentioned above, the studies reported in the literature concern an initially completely filled spherical shell. However, it is practically impossible to have a rigid spherical shell filled 100% with liquid due to, e.g., thermal expansion. For example, if just a 0.5 mm high segment is filled with air in the upper part of a shell that is 80 mm in diameter, its volume is negligible being 0.012% of the shell volume, but its diameter is as large as 12.6 mm. As it is obvious that no solidification can occur inside the segment, its presence has a significant effect on the resulting solid shape. The profound effect of this feature has been recently demonstrated by Revankar and Croy [15].

Studies of solid-liquid phase-change are characterized by considerable difficulties encountered in both experimentation and modeling. In particular, temperature measurement inside the enclosure can affect the process itself. For this reason, visualization is widely used in melting studies. In solidification, however, visualization can be rather difficult if the solid is not transparent, hence it is rarely done [15]. Thus, it is common in the literature to report the overall results of measurements [18]. However, the overall measurements may not reflect voids or other structural features. As for the modeling, a significant effort is required to describe such features as solid-liquid volume change, natural convection in the melt, possible motion of the solid in the liquid, and, specifically in solidification, the curvilinear solid-liquid interface and formation of voids. Thus, while a pioneering work in this direction has been done back in the 1970s by Shamsundar and Sparrow [19], it is not surprising that the works that attempt at solving these problems of curvilinear geometries have started to appear only very recently [20–22].

In this study, both experiments and numerical modeling are reported. The experimental approach is similar to that employed by Glaich et al. [23] and involves thin plastic shells that are cut in halves during the process of solidification. The experimental findings serve to validate the numerical model and illustrate the essential features obtained numerically. The modeling is based on the method successfully used for melting by Assis et al. [24]

2 Modeling

2.1 Numerical Model. The numerical method has been extensively described in Ref. [24], and only the essential features are

Contributed by the Heat Transfer Division of ASME for publication in the JOURNAL OF HEAT TRANSFER. Manuscript received November 27, 2007; final manuscript received August 4, 2008; published online December 12, 2008. Review conducted by Yogendra Joshi.

 Copyright © 2009 by ASME

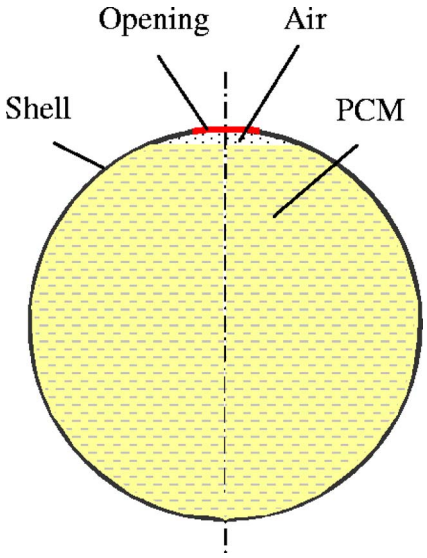

Fig. 1 Physical model

Fig. 2 Solidification with an upper void (shrinkage) for $D=70$ mm and $\Delta T=20°C$ [25]

presented here. The physical model is shown in Fig. 1. In the initial state, the liquid PCM fills 98.5% of the enclosed space. From above, the PCM is exposed to air, which is allowed to enter the shell gradually, as the process of solidification advances.

The properties of the PCM are based on a commercially available material—RT27 (Rubitherm GmbH, Berlin, Germany). As the material does not have a "sharp" melting temperature, a melting interval is used, with the solidus and liquidus temperatures set at 28°C and 30°C, respectively. The other properties are: latent heat $L=179$ kJ/kg, sensible heat capacity in liquid/solid state $c_p=2.4/1.8$ kJ/kg K, thermal conductivity in solid/liquid state $k=0.24/0.15$ W/m K, constant density of $\rho_s=870$ kg/m^3 in the solid state, and dynamic viscosity of $\mu_l=3.42\times10^{-3}$ kg/m s in the liquid state. Variable density was defined in the liquid state with $\rho_l=760$ kg/m^3 at 30°C and the volumetric expansion coefficient $\beta=0.5\times10^{-3}$ K^{-1}. In the "mushy" state, where the solid and liquid phases coexist between 28°C and 30°C, the density varies linearly from 870 kg/m^3 at 28°C to 760 kg/m^3 at 30°C. It is assumed that both solid and liquid phases are homogeneous and isotropic, and the solidification process is axisymmetric. The molten PCM and the air are incompressible Newtonian fluids, and laminar flow was assumed in both. A density-temperature relation is used for air. In the simulations, the initial temperature of the whole system is 32°C, i.e., the PCM temperature is slightly higher than its solidification temperature.

The numerical approach makes it possible to calculate the processes that occur inside the solid PCM (conduction), the liquid PCM (convection), and the air (convection) simultaneously, and to account for the phase-change and moving curvilinear boundary due to a variation in the PCM volume. Based on the axial symmetry of the physical model, a computational domain was defined as half of the model shown in Fig. 1.

In order to describe the PCM-air system with a moving internal interface but without interpenetration of these two media, a so-called "volume-of-fluid" (VOF) model has been used. For the phase-change region inside the PCM, the enthalpy-porosity approach is used, by which the porosity in each cell is set equal to the liquid fraction in that cell. Accordingly, the porosity is zero inside fully solid regions.

The numerical solution has been obtained using the FLUENT 6.2 software. The effects of time step and grid size on the solution were carefully examined in Ref. [24]. The chosen time step was as small as 0.002 s. The grid was built using the GAMBIT software, with special attention paid to the PCM-air interface in the initial state. The grid size of 3520 elements was chosen after a careful examination of the results of a grid refinement process. The convergence of the solution was checked at each time step, with the convergence criterion of 10^{-5} for the velocity components and continuity, and a criterion of 10^{-8} for energy. A Dell PowerEdge 2600 computer was used, which features two 3.20 GHz Intel Xeon processors and is scalable to 12 Gbytes of PC2100 DDR SDRAM. A typical run took from a few days to several weeks.

2.2 Experimental. In the present study, 0.1 mm thick plastic shells are used, which are cut with the PCM after the latter had solidified completely or at the intermediate stages of the process [25]. Solidification of RT27 has been conducted in a Neslab RTE 7 circulating thermostatic bath, which maintains a desired temperature within 0.1°C. The bath was kept typically at 10°C or 20°C below the mean solidification temperature of the PCM. In order to be consistent with the simulation, the shell was inserted in the bath when the PCM temperature was about 32°C, i.e., few degrees above its mean melting temperature.

Two series of the experiments were performed. The first series was conducted in shells of 30 mm and 70 mm in diameter up to complete solidification. The shells were cut in halves, and the solid shape recorded. The second series was conducted in shells of 40 mm in diameter, where each shell was withdrawn from the bath at a prescribed time. The shell was cut in halves, the remaining liquid was removed, and the solid shape was recorded.

3 Results and Analysis

3.1 Solidification Patterns. An example of the series of complete solidification of paraffin RT27 in a shell 70 mm in diameter is shown in Fig. 2. One can see in the figure that a large void is formed in the upper part of the shell. This shrinkage resembles the cavity reported in Ref. [19] and can also be compared with similar voids reported recently for spherical [15] and vertical cylindrical enclosures [20–22]. We note that its location adjacent to the initially unfilled space in the upper part of the shell is consistent with the conclusion of Sulfredge et al. [17] that "with a degassed liquid, the distribution of solidification voids is largely determined by the location and pattern of the initial shrinkage voids."

The shrinkage observed in Fig. 2 is further illustrated in Fig. 3 where the entire simulated process of solidification is presented

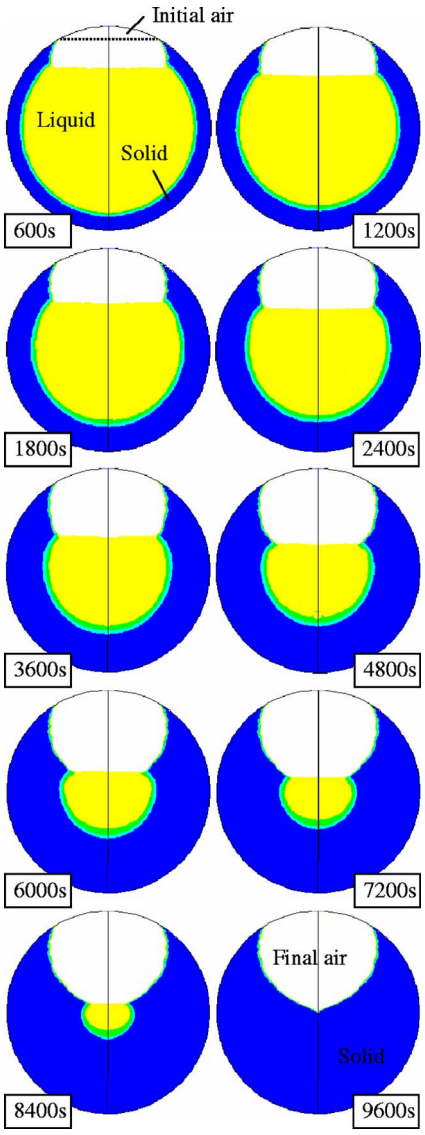

Fig. 3 Simulated solidification with upper void (D=80 mm and ΔT=20°C)

for a shell 80 mm in diameter at ΔT=20°C. The hues are shown in terms of the thermal conductivity, thus clearly separating between the solid, liquid, and air. The initial and final volumes occupied by air are denoted in the figure for the sake of clarity.

One can see from Fig. 3 that an upper shrinkage is formed, reflecting the experimental findings of Fig. 2 for a similar case. Its boundaries are defined by the initial level of the liquid PCM inside the shell. It appears that the numerical model succeeds to reflect formation of a characteristic solid phase shape up to the final state, which includes only solid and air, as shown by different colors.

The findings of Revankar and Croy [15] indicate that in some cases an additional central void can be formed when a spherical shell is not completely filled with liquid. That result was obtained for cyclohexane in a relatively small shell 2.54 cm in diameter. According to Revankar and Croy [15], "a large bubble" is formed at the top of the shell, while "several void dendrites" appear at its center. We note that the liquid-solid shrinkage of cyclohexane at 7.8% is much smaller than that of RT27, which is similar to *n*-octadecane.

Figure 4 shows our intermediate experimental and numerical results for the case of D=40 mm and ΔT=20°C. The numerical

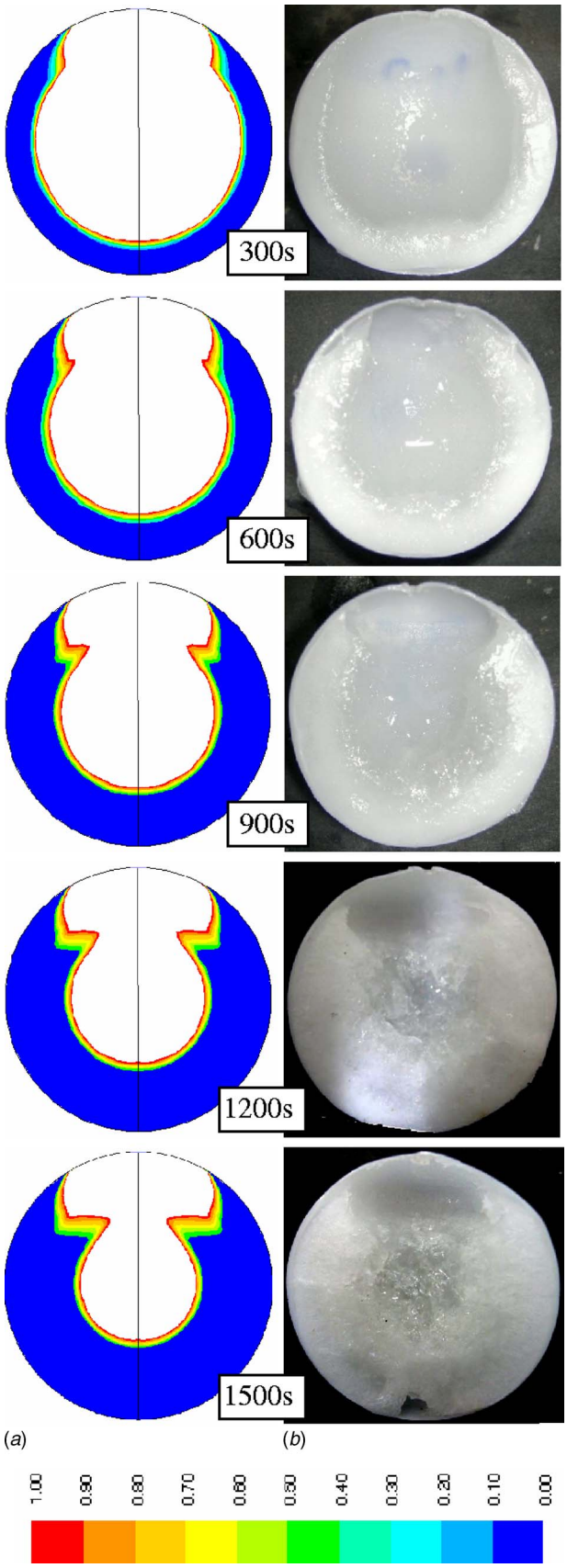

Fig. 4 Solidification with central void (D=40 mm and ΔT=20°C): (*a*) numerical, and (*b*) experimental [25]

results are shown in terms of the melt fraction (Fig. 4(*a*)) defined as the melted mass divided by the total mass of the PCM. Thus, the melt fraction is zero when solidification is complete. The experimental images are recorded immediately after the shells have been cut, and the remaining liquid has been poured out (Fig. 4(*b*)). Accordingly, the simulation results are also shown with the liquid phase "removed." It appears that a remarkable agreement is obtained between the simulation and the experiment, providing validation for the model. Actually, Fig. 4 reflects, for a relatively small shell, the process leading to the formation of a central void, similar to the experimental findings of Revankar and Croy [15]. We note that the last picture of Fig. 4(*a*) does not show complete solidification, as the numerical approach is unable at this stage to model vacuum or formation of "void dendrites" at the center. However, this picture corresponds to the situation in which about 95% of the PCM has already solidified. Thus, the process is presented almost entirely. To the best of the authors' knowledge, no simulation similar to that leading to Fig. 4 has been reported in the literature.

3.2 Melt Fraction. The melt fraction of the PCM, defined above, is shown for various cases in Fig. 5(*a*). We note here that the melt fraction reflects rather accurately the amount of heat to be removed from the system for full solidification. One can see that the full solidification time, which depends on the shell size and temperature difference, varies from 5 min to 150 min. On the other hand, the curves for various cases are similar in their shape.

3.3 Dimensional Analysis. The dimensionless parameters that define the process can be obtained from the dimensionless form of momentum and energy equations. The dimensionless energy conservation equation contains the following dimensionless groups.

(a) The Fourier number

$$\mathrm{Fo} = (k/\rho c_p)(t/R^2) \tag{1}$$

(b) The Stefan number

$$\mathrm{Ste} = c_p \Delta T/L \tag{2}$$

where ΔT is the difference between the PCM mean melting temperature T_m and the wall temperature T_w. In the present study, the Stefan number varies from about 0.1 ($\Delta T = 10°\mathrm{C}$) to 0.4 ($\Delta T = 40°\mathrm{C}$).

In order to account for the free convection contribution, the Grashof number was used in the analysis of melting [24]. However, the convective motion has been found insignificant in the solidification processes. For instance, in the process reflected in Fig. 3, i.e., for $D = 80$ mm and $\Delta T = 20°\mathrm{C}$, the velocities in the liquid phase did not exceed 1 mm/s at the beginning of the process, and 10 min later the velocities already decreased to the values below 0.1 mm/s, practically disappearing later. This result is consistent with the analysis of Viskanta and Gau [26], who established that the natural convection contribution is negligible for $\mathrm{Ste} < 1$, and with the work of Yao [27] who showed that this contribution rapidly decreases with time. It is obvious that for smaller shells, e.g., that correspond to Fig. 4, the motion is even less significant. Thus, the Grashof number has been excluded from the present analysis. We note that the Prandtl number is about 35 for the material used in the present study, i.e., $\mathrm{Pr} \gg 1$.

An application of the dimensionless groups introduced above leads to the generalized results presented in Fig. 5(*b*), where the melt fraction is shown versus the product of the Fourier and Stefan numbers FoSte for all cases considered in the present study. Thus, the analysis in the present study is consistent with that introduced by Shamsundar and Sparrow [19]. One can see that all curves practically merge into a single curve, notwithstanding the differences in void formation illustrated in Figs. 3 and 4. Thus, we conclude that the generalization is valid for $\mathrm{Ste} \leq 0.4$.

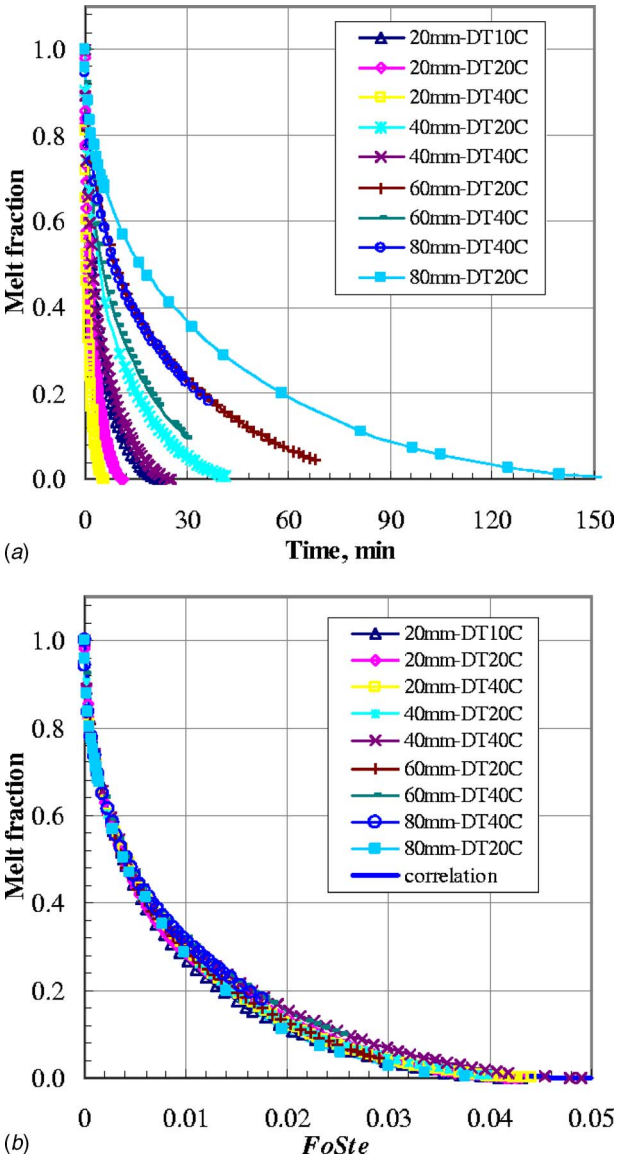

Fig. 5 Summary of the numerical results: (*a*) summary of the results for various diameters and temperature differences, and (*b*) generalized results and correlation for the melt fraction

Also, this result provides an additional indication concerning the insignificant role of convection. On the other hand, one should bear in mind that volume shrinkage due to solidification [19] does induce a local fluid motion, causing the continuously decreasing level of the liquid in the shell. Thus, the contribution of fluid motion to the phase-change process expresses itself in the irregular shapes of the resulting solid phase.

An analysis of the results of Fig. 5(*b*) yields the following expression for the melt fraction:

$$\mathrm{MF} = [1 - 4.5(\mathrm{FoSte})^{1/2}]^2 \tag{3}$$

This correlation, also shown in Fig. 5(*b*), is valid for the range of parameters explored in the present study and, in particular, for $\mathrm{Ste} \leq 0.4$ and $\mathrm{Pr} \gg 1$.

Summarizing the findings of the present study, we note that the conditions that determine the shape and structure of the voids in different cases have not been established yet. There are indications that the cooling rate and shell size are the major factors.

The results of the present investigation have been obtained for the cases in which air was allowed to flow into the shell to fill the

space formed by PCM shrinkage. In cases where the shell is sealed, the air is compressed on melting and expands on solidification, thus closing a full cycle. We assume that the trends discovered in the present study are quite general, and the results of the analysis performed herein will be valid also when additional features are taken into account.

Acknowledgment

The authors acknowledge the contribution of the undergraduate students Erez Yotvat and Shachar Zelikover, who conducted the experiments in the framework of their graduation project.

Nomenclature

c_p = specific heat at constant pressure (J/kg °C)
D = diameter (m)
Fo = Fourier number, $(k/\rho c_p)t/R^2$
k = thermal conductivity (W/m °C)
L = latent heat (J/kg)
Pr = Prandtl number, $c_p\mu/k$
R = radius (m)
Ste = Stefan number, $c_p\Delta T/L$
t = time (s)
T = temperature (°C or K)

Greek Letters

β = volumetric expansion coefficient (1/K)
Δ = difference
ρ = density (kg/m^3)

References

[1] Moore, F. E., and Bayazitoglu, Y., 1982, "Melting Within a Spherical Enclosure," ASME J. Heat Transfer, **104**, pp. 19–23.
[2] Roy, S. K., and Sengupta, S., 1987, "The Melting Process Within Spherical Enclosures," ASME J. Heat Transfer, **109**, pp. 460–462.
[3] Bahrami, P. A., and Wang, T. G., 1987, "Analysis of Gravity and Conduction-Driven Melting in a Sphere," ASME J. Heat Transfer, **109**, pp. 806–809.
[4] Tao, L. C., 1967, "Generalized Numerical Solutions of Freezing a Saturated Liquid in Cylinders and Spheres," AIChE J., **13**, pp. 165–172.
[5] Shih, Y. P., and Chou, T. C., 1971, "Analytical Solutions for Freezing a Saturated Liquid Inside or Outside Sphere," Chem. Eng. Sci., **26**, pp. 1787–1793.
[6] Pedroso, R. I., and Domoto, G. A., 1973, "Inward Spherical Solidification: Solution by the Method of Strained Coordinates," Int. J. Heat Mass Transfer, **16**, pp. 1037–1043.
[7] Riley, D. S., Smith, F. T., and Poots, G., 1974, "The Inward Solidification of Spheres and Circular Cylinders," Int. J. Heat Mass Transfer, **17**, pp. 1507–1516.
[8] Hill, J. M., and Kucera, A., 1983, "Freezing a Saturated Liquid Inside a Sphere," Int. J. Heat Mass Transfer, **26**, pp. 1631–1636.
[9] Yao, L. S., and Prusa, J., 1989, "Melting and Freezing," Adv. Heat Transfer, **19**, pp. 1–95.
[10] Regin, A. F., Solanki, S. C., and Saini, J. S., 2008, "Heat Transfer Characteristics of Thermal Energy Storage System Using PCM Capsules: A Review," Renewable Sustainable Energy Rev., **12**, pp. 2438–2458.
[11] Chan, C. W., and Tan, F. L., 2006, "Solidification Inside a Sphere: An Experimental Study," Int. Commun. Heat Mass Transfer, **33**, pp. 335–341.
[12] Ismail, K. A. R., 2002, "Heat Transfer in Phase Change in Simple and Complex Geometries," *Thermal Energy Storage Systems and Applications*, İ. Dinçer and M. A. Rosen, eds., Wiley, Chichester, Chap. 8, pp. 337–386.
[13] El Omari, K., and Dumas, J. P., 2004, "Crystallization of Supercooled Spherical Nodules in a Flow," Int. J. Therm. Sci., **43**, pp. 1171–1180.
[14] Chalmers, B., 1964, *Principles of Solidification*, Wiley, New York.
[15] Revankar, S. T., and Croy, T., 2007, "Visualization Study of the Shrinkage Void Distribution in Thermal Energy Storage Shells of Different Geometry," Exp. Therm. Fluid Sci., **31**, pp. 181–189.
[16] Ziskind, G., and Letan, R., 2007, "Phase Change Materials: Recent Advances in Modeling and Experimentation," *Proceedings of the Heat SET 2007: Heat Transfer in Components and Systems for Sustainable Energy Technologies*, Chambery, France, Apr. 18–20.
[17] Sulfredge, C. D., Chow, L. C., and Tagavi, K. A., 1992, "Void Formation in Radial Solidification of Cylinders," ASME J. Sol. Energy Eng., **114**, pp. 32–39.
[18] Cho, K., and Choi, S. H., 2000, "Thermal Characteristics of Paraffin in a Spherical Capsule During Freezing and Melting Processes," Int. J. Heat Mass Transfer, **43**, pp. 3183–3196.
[19] Shamsundar, N., and Sparrow, E. M., 1976, "Effect of Density Change on Multidimensional Conduction Phase Change," ASME J. Heat Transfer, **98**, pp. 550–557.
[20] Sun, D., Annapragada, S. R., Garimella, S. V., and Singh, S. K., 2007, "Analysis of Gap Formation in the Casting of Energetic Materials," Numer. Heat Transfer, Part A, **51**, pp. 415–444.
[21] Sun, D., and Garimella, S. V., 2007, "Numerical and Experimental Investigation of Solidification Shrinkage," Numer. Heat Transfer, Part A, **52**, pp. 145–162.
[22] Dubovsky, V., Assis, E., Kochavi, E., Ziskind, G., and Letan, R., 2008, "Study of Solidification in Vertical Cylindrical Shells," *Proceedings of the Fifth European Thermal Sciences Conference*, Eindhoven, The Netherlands.
[23] Glaich, A., Finkelshtein, L., Dubovsky, V., Ziskind, G., and Letan, R., 2003, "Experimental Investigation of Phase Change in a Spherical Enclosure," *Proceedings of the EUROTHERM Seminar 69: Heat and Mass Transfer in Solid-Liquid Phase Change Processes*, Bistra Castle, Slovenia.
[24] Assis, E., Katsman, L., Ziskind, G., and Letan, R., 2007, "Numerical and Experimental Study of Melting in a Spherical Shell," Int. J. Heat Mass Transfer, **50**, pp. 1790–1804.
[25] Yotvat, E., and Zelikover, S., 2007–2008, "Experimental Investigation of Paraffin Solidification," Graduation Project under the supervision of G. Ziskind and R. Letan, Heat Transfer Laboratory, Department of Mechanical Engineering, Ben-Gurion University of the Negev, Beer-Sheva, Israel.
[26] Viskanta, R., and Gau, C., 1982, "Inward Solidification of a Superheated Liquid in a Cooled Horizontal Tube," Waerme- Stoffuebertrag.–Thermo and Fluid Dynamics **17**(1), pp. 39–46.
[27] Yao, L. S., 1984, "Natural Convection Effects in the Continuous Casting of a Horizontal Cylinder," Int. J. Heat Mass Transfer, **27**, pp. 697–704.

Effects of a High Porous Material on Heat Transfer and Flow in a Circular Tube

Koichi Ichimiya
e-mail: ichimiya@yamanashi.ac.jp

Tetsuaki Takeda

Interdisciplinary Graduate School of Medicine and Engineering,
Mechanical Systems Engineering Division,
University of Yamanashi, Takeda-4, Kofu,
Yamanashi 400-8511, Japan

Takuya Uemura
Yamatake Co Ltd.,
Marunouchi, Chiyoda,
Tokyo 100-6419, Japan

Tetsuya Norikuni
Tekumo Co Ltd.,
Fujisawa,
Kanagawa 252-0815, Japan

This paper describes the heat transfer and flow characteristics of a heat exchanger tube filled with a high porous material. Fine copper wires (diameter: 0.5 mm) were inserted in a circular tube dominated by thermal conduction and forced convection. The porosity was from 0.98 to 1.0. The working fluid was air. The hydraulic equivalent diameter was cited as the characteristic length in the Nusselt number and the Reynolds number. The Nusselt number and the friction factor were expressed as functions of the Reynolds number and porosity. The thermal performance was evaluated by the ratio of the Nusselt number with and without a high porous material and the entropy generation. It was recognized that the high porous material was effective in low Reynolds numbers and the Reynolds number, which minimized the entropy generation existed. [DOI: 10.1115/1.2994713]

Keywords: porous medium, heat transfer enhancement, thermal performance, entropy generation

1 Introduction

Porous materials can be found in thermal engineering as a heat storage material or a heat transfer promoter, in a Stirling engine as a regenerator, in a heat engine as an exhaust gas filter, in chemical engineering as a catalyst, in fluid engineering as a filter, and so on. They are also noted as an important material in environmental problems [1]. Recently, they have been applied to improve the local heat transfer in a hydrogen production system utilizing heat from a high temperature thermal reactor (HTTR) [2]. In the hydrogen production system, the object is to keep the thermal performance and develop a compact reformer using high porous materials. Researches on porous materials have been performed on thermal radiation in fluidized bed with porosity $\varepsilon<0.8$ [3,4], and these results are applied as a transformer from thermal radiation to convection [5,6]. The porosity of heat storage materials is from $\varepsilon=0.3$ to $\varepsilon=0.4$. In porosity $\varepsilon>0.8$, heat transfer and pressure drop were investigated using a ceramic foam as a porous type turbulence promoter [7]. Pumping power of low porous materials may be higher than that of fin or roughness elements and affect economic load remarkably. To reduce the load, it is necessary to apply the high porous materials as a heat transfer promoter. A numerical basic study was reported for high Reynolds number forced convection in a channel filled with metallic fibrous materials of a high porosity ($\varepsilon=0.95$) [8]. Heat transfer to a fluid passing through a porous medium located in a parallel plate channel and in a circular tube was also estimated numerically [9]. However, the thermal performance has not been examined well in a flow passage filled with high porous materials of porosity $\varepsilon>0.98$.

In the present study, we focused on a high porous material with porosity $\varepsilon\cong 1.0$. Fine copper wires were filled in a whole circular tube and the working fluid was air. Heat and flow experiments were carried out in a high porous material with porosity $\varepsilon>0.98$. It was examined how a high porous material affects on the heat transfer and flow characteristics and the thermal performance.

2 Experimental Apparatus and Procedure

Air as a working fluid, compressed by a blower, flows into the test tube filled with fine copper wire via a flow meter and an entrance section and is heated electrically. After the air is cooled in a heat exchanger, it is released into the atmosphere. The test section is a circular tube made of stainless steel, whose inner diameter is 25 mm and length is 1000 mm. The outer surface of the tube is covered by Nichrome wire insulated and surrounded by thermal insulation material. The pressure drop is measured between the entrance and the exit. Fine copper (purity: 99.999%) wire whose diameter d_w is 0.5 mm is utilized as a porous material. Fine copper wire was uniformly inserted in the form of spirals over the whole area in a circular tube to move the fluid from the center of the flow passage to the wall along the flow direction, and the porosity was controlled by changing the wire length. Experiments of heat transfer and flow characteristics were performed with and without high porous materials.

The hydraulic equivalent diameter D_H was used as a characteristic length because the porosity is close to 1.0. D_H is expressed using tube diameter D, wire diameter d_w, and porosity ε as follows:

$$D_H = \frac{\pi D^2 \varepsilon}{\pi D + \dfrac{\pi D^2 (1-\varepsilon)}{d_w}} \tag{1}$$

D_H becomes D as the porosity approaches 1.0. Figure 1 shows the relationship between D_H and ε. There is no remarkable error even if D_H is d_w in low porosity and D_H changes rapidly near $\varepsilon\cong 0.8$ and approaches D.

Experimental conditions are as follows: Reynolds number Re $=2000-20{,}000$, wire diameter $d_w=0.5$ mm, and porosity $\varepsilon=0.98-1.0$.

3 Experimental Uncertainties

All the uncertainties were estimated by the procedure described by ANSI/ASME, PTC 19–1 [10] and Moffat [11]. The main sources of errors in Nusselt numbers and friction factors were the evaluation of the temperature, the electric input, the flow rate, the pressure drop, the size of the tube, and the thermal properties of air (specific heat, thermal conductivity, density, and kinetic viscosity). A 95% relative coverage of uncertainty for Nusselt num-

Contributed by the Heat Transfer Division of ASME for publication in the JOURNAL OF HEAT TRANSFER. Manuscript received January 9, 2008; final manuscript received July 28, 2008; published online December 29, 2008. Review conducted by Ali Ebadian. Paper presented at the 2007 ASME-JSME Thermal Engineering Conference and Summer Heat Transfer Conference (HT2007), Vancouver, BC, Canada, July 8–12, 2007.

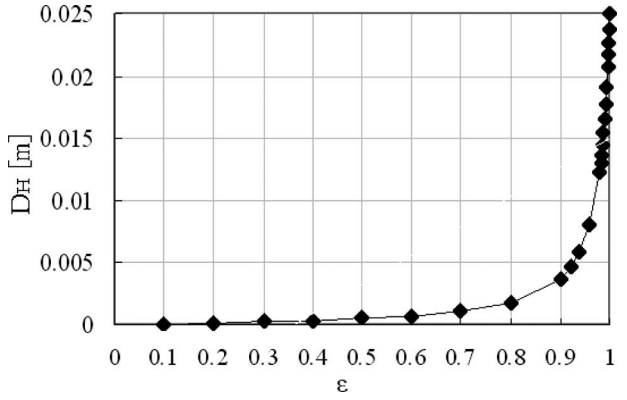

Fig. 1 Hydraulic equivalent diameter D_H (d_w=0.5 mm and D =25 mm)

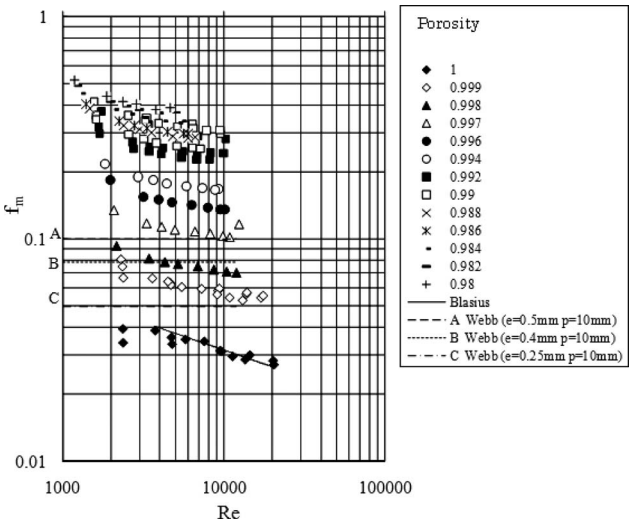

Fig. 3 Relationship between f_m and Re

bers was from 5.1% to 7.8%, depending on flow conditions. On the other hand, a 95% relative coverage of uncertainty for friction factors was from 4.2% to 6.1%.

4 Results and Discussions

4.1 Heat Transfer. The relationship between the average Nusselt number along the flow direction and the Reynolds number is presented as a parameter of porosity in Fig. 2. The solid line shows the equation in which Gnielinski [12] modified Petukov's equation [13] without porous mediums. In high Reynolds numbers, experimental values agree well. However, in comparatively low Reynolds numbers, they tend to be higher than Gnielinski's equation. This means that the transition region from laminar to turbulent flow affects heat transfer. Generally, Nusselt numbers are high at low porosities and are arranged by $Re^{0.77}$ for all porosities within present conditions. The heat transfer is improved about 2.5 times at $Re \cong 4000$. The analytical values in Refs. [8,9] are denoted by a gray triangle and a gray circle in Fig. 2. The Nusselt numbers in $Re=10^4$, $\varepsilon=0.95$ [8] and in Re=2000, Da(≡Darcy number: the ratio of permeability to characteristic length square)=10^{-4} [9] are 95 and 13, respectively, which stand on the trends of the present experimental values. In addition, the present experimental results of fine copper wire are compared with those of roughness elements by Webb et al. [14]. Nusselt numbers in height of roughness element $e=0.5$ mm (line A), $e=0.4$ mm (line B), and $e=0.25$ mm (line C) correspond to those in porosity $\varepsilon=0.982$, $\varepsilon=0.986$, and $\varepsilon=0.998$, respectively. The mechanism of heat transfer enhancement by these high porous materials is due to not only the increase in the thermal diffusion [15] and heat transfer area but also the increase in the flow mixing near the wall. Therefore, thermal resistance near the tube wall is depressed by fine wires. The enhancement rate of heat transfer tends to decrease with the increase in Reynolds number. The Nusselt number is expressed as functions of Re and ε as follows:

$$\mathrm{Nu} = 0.11\ \mathrm{Re}^{0.77}[\varepsilon(1-\varepsilon)]^{0.33} + 0.012\ \mathrm{Re}^{0.84} \tag{2}$$

The second term on the right-hand side is Nu at $\varepsilon=1.0$. The 94% of all experimental average Nusselt numbers is approximated within ±15% by Eq. (2).

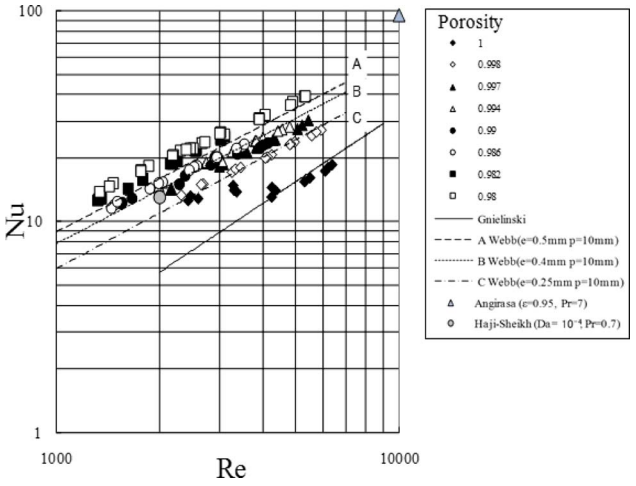

Fig. 2 Relationship between Nu and Re

4.2 Flow Resistance. The structure of the porous material is composed of square wire netting and horizontal needles. Therefore, the pressure drop is constituted in shape resistance ΔP_K and friction loss ΔP_m as follows:

$$\Delta P = \Delta P_K + \Delta P_m = K\left(\frac{\rho u^2}{2}\right)N + f_m\left(\frac{\rho u^2}{2}\right)\left(\frac{l_m}{D_H}\right) \tag{3}$$

where K is the shape factor, ρ is the air density, f_m is the friction factor, l_m is the tube length, and N is the number of wire netting. The shape factor K is expressed by Eq. (4) [16].

$$K = 6\left(\frac{d_w}{D_H}\right)^{-1/3}(1-\varepsilon)\beta^{-7/3}\ \mathrm{Re}^{-1/3} \tag{4}$$

where β is an open area ratio.

Friction loss was obtained by subtracting the shape resistance from the experimental pressure loss ΔP. The relationship between the friction factor f_m and the Reynolds number Re is denoted as a parameter of porosity ε in Fig. 3. The solid line shows Blasius's equation without porous material. The friction factor f_m increases with a decrease in porosity and depends on $Re^{-0.17}$. Present experimental data were compared with friction factors of roughness elements by Webb et al. [14]. The area contacted to air for the roughness height $e=0.25-0.5$ mm is 3–10% larger than that of the smooth tube. On the other hand, in the porous material, the contact area for porosity $\varepsilon=0.99-0.98$ increases by 50–100%. Consequently, the friction factor f_m is expressed as functions of Re and ε as follows:

$$f_m = 32.1\ \mathrm{Re}^{-0.17}\left[\frac{(1-\varepsilon)}{\varepsilon}\right]^{0.76} + 0.12\ \mathrm{Re}^{-0.15} \tag{5}$$

The second term on the right hand side is f_m in $\varepsilon=1$. The 96% of all friction factors is arranged within ±15% by Eq. (5).

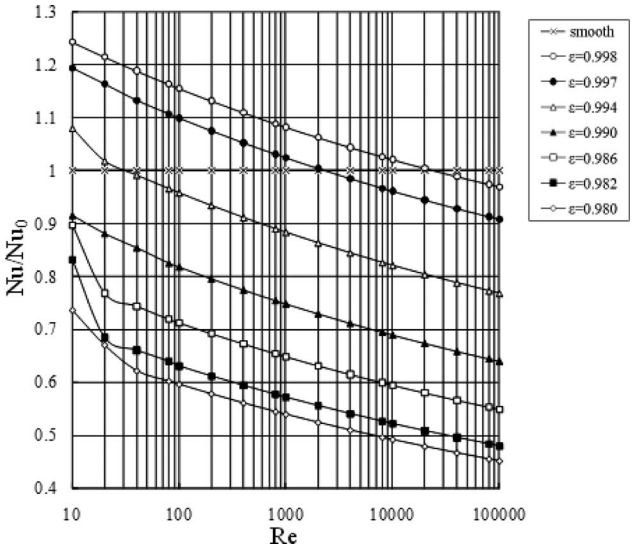

Fig. 4 Thermal performance by Nu/Nu_o; pumping power =const

4.3 Thermal Performance. Two kinds of thermal performance were evaluated for the heat transfer enhancement and the effect on the environment using heat transfer and flow characteristics. In the case of the first law of thermodynamics, evaluation is ratio of the Nusselt number with and without porous materials at (a) constant Reynolds number, (b) constant pressure drop, or (c) constant pumping power [17]. Representatively, in condition (c), heat transfer improvement can be seen in low Reynolds numbers and high porosities (Fig. 4). This means that in the field dominated by thermal conduction and convection, a small amount of the porous material is effective.

Entropy generation based on the second law of thermodynamics S_g is composed of two terms by heat transfer and flow [18] and has relation to the environmental problem. In the present case, S_g is expressed by the following equation:

$$S_g = \left(\frac{qD}{\mathrm{Nu}\,k}\right)\left(\frac{q\pi D}{T^2}\right) + \left(\frac{\pi D^2 u}{4T}\right)\left(-\frac{\Delta P_m}{l_m}\right) \tag{6}$$

The first term on heat transfer reduces with Re due to the dependency of Re on Nu in Eq. (2). On the other hand, the second term on friction increases with Re due to the dependency of Re on f_m in Eq. (5). Consequently, entropy generation cannot be avoided, but we can find a Reynolds number that minimizes entropy generation, Re_c, as an operating condition to reduce the influence to the surrounding. Figures 5(*a*) and 5(*b*) show the thermal performance by entropy generation. Figure 5(*a*) shows the relationship between S_g and Re as a parameter of porosity. In the present experiment, Re_c is about 3000 at $\varepsilon=0.98$ and $\mathrm{Re}_c \cong 10{,}000$ at $\varepsilon=0.998$. S_g behaves inversely for porosity at lower and higher Reynolds numbers than the boundary point Re_c. S_g becomes low at low Reynolds numbers for low porosity and at high Reynolds numbers for high porosity. Figure 5(*b*) presents the ratio of entropy generation with and without porous material, S_g/S_{go}. The ratio is less than 1.0 in the Reynolds number region $\mathrm{Re}<\mathrm{Re}_c$ for low porosity. S_g/S_{go} becomes higher than 1.0 at $\mathrm{Re}>\mathrm{Re}_c$. This means that a high porous material brings about an increase in entropy generation in $\mathrm{Re}>\mathrm{Re}_c$, but it is effective in $\mathrm{Re}<\mathrm{Re}_c$. When we apply the system in practical facility, we should operate in these conditions to reduce the influence of the system to the environment.

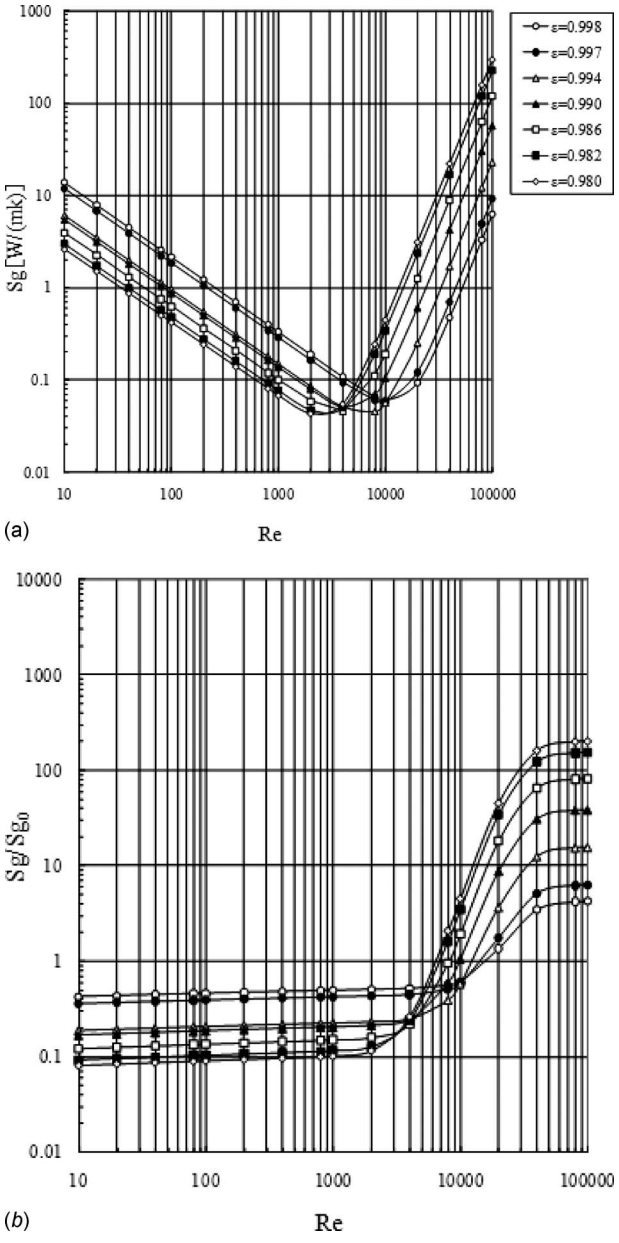

Fig. 5 Thermal performance by entropy generation: (*a*) entropy generation S_g and (*b*) entropy generation ratio S_g/S_{go}

5 Conclusions

The heat transfer and flow characteristics of a circular tube filled with fine copper wire as a high porous material ($\varepsilon>0.98$) were investigated experimentally, and the thermal performance was evaluated.

The Nusselt numbers and the friction factors were arranged by functions of the Reynolds number, based on the hydraulic equivalent diameter as a characteristic length, and the porosity, namely, Eq. (2) for Nu and Eq. (5) for f_m. For heat transfer improvement, a high porous material is useful at low Reynolds numbers. In entropy generation, a Reynolds number which minimizes entropy generation, Re_c exists for each porosity, and comparatively low porous material reduces entropy generation and is effective in lower Reynolds numbers than Re_c within the present experimental conditions.

Thermal performance depends on the evaluation based on the first law of thermodynamics for the heat transfer enhancement and

the second law of thermodynamics for effects to the environment. Therefore, when we apply the present system to practical facility, we should select the operating condition for our objectives according to the present results.

Acknowledgment

The authors thank Mr. Daiki Yamauchi for his help in their experiments.

Nomenclature

d_w = diameter of fine copper wire, mm
D = inner diameter of a tube, mm
D_H = hydraulic equivalent diameter, mm, m
f_m = friction factor
h = heat transfer coefficient, $W/(m^2\ K)$
K = shape factor
l_m = tube length, mm, m
Nu = Nusselt number in a tube with porous material $=hD_H/\lambda$
Nu_o = Nusselt number in a tube without porous material
Δp = pressure drop between entrance and exit, N/m^2
q = heat flux, W/m^2
Re = Reynolds number$=uD_H/\nu$
Re_c = Reynolds number that minimizes the entropy generation
S_g = entropy generation with porous material, W/(m K)
S_{go} = entropy generation without porous material, W/(m K)
T = temperature, °C, K
u = pore velocity, m/s
x = length along the flow direction, m
β = open area ratio
ε = porosity
λ = thermal conductivity of air, W/(m K)
ν = kinetic viscosity of air, m^2/s
ρ = density of air, kg/m^3

References

[1] Kaviany, M., 1991, *Principles of Heat Transfer in Porous Media*, Springer-Verlag, New York, pp. 1–11.
[2] Shiozawa, S., Ogawa, M., Inagaki, Y., Katanishi, S., Takeda, T., Nishihara, T., Shimizu, S., and Miyamoto, Y., 2000, "Research and Development of HTTR Hydrogen Production System in Japan," *Proceedings of the 12th Pacific Basin Nuclear Conference*, Seoul, Vol. 2, pp. 1007–1018.
[3] Echigo, R., Hasegawa, S., and Nakano, S., 2000, "Simultaneous Radiative and Convective Heat Transfer in a Packed Bed With High Porosity," JSME Int. J., Ser. B, **40**(330), pp. 479–487.
[4] Kamiuto, K., 1978, "Simultaneous Radiative and Convective Heat Transfer in a Packed Bed With High Porosity (Part 2, Consideration of Two-Dimensional Propagation of Thermal Radiation)," JSME Int. J., Ser. B, **44**(388), pp.4234–4242.
[5] Echigo, R., 1982, "Effective Conversion Method Between Gas Enthalpy and Thermal Radiation and Application to Industrial Furnaces," JSME Int. J., Ser. B, **48**(435), pp.2315–2322.
[6] Yamada, J., and Ichimiya, K., 1997, "Gas Sensible Heat Radiative Energy Exchange in Fibrous Media," JSME Int. J., Ser. B, **63**(616), pp. 4036–4042.
[7] Ichimiya, K., and Mitsushiro, K., 1986, "Enhancement of the Heat Transfer of Wide Temperature Field in a Narrow Flow Passage (Part 1, Effects of Porous-Type Turbulence Promoter in Normal Temperature Field)," JSME Int. J., Ser. B, **52**(473), pp. 441–446.
[8] Angirasa, D., 2002, "Forced Convective Heat Transfer in Metallic Fibrous Materials," Trans. ASME, Ser. C: J. Heat Transfer, **124**, pp. 739–745.
[9] Haji-Sheikh, A., 2004, "Estimation of Average and Local Heat Transfer in Parallel Plates and Circular Ducts Filled With Porous Materials," Trans. ASME, Ser. C: J. Heat Transfer, **126**, pp. 400–409.
[10] ANSI/ASME PTC 19-1, 1985, *Supplement to Performance Test Coded Instrument and Apparatus, Part I: Measurement Uncertainty*, ASME, New York.
[11] Moffat, R. J., 1988, "Describing the Uncertainties in Experimental Results," Exp. Therm. Fluid Sci., **1**, pp. 3–17.
[12] Gnielinski, V., 1976, "New Equations for Heat and Mass Transfer in Turbulent Pipe and Channel Flow," Int. Chem. Eng., **16**(2), pp. 359–367.
[13] Petukov, B. S., 1970, "Heat Transfer and Friction in Turbulent Pipe Flow With Variable Physical Properties," *Advanced Heat Transfer*, Vol. 6, J. P. Hartnett and T. F. Irvine, Jr., eds., Academic, New York, pp. 521–525.
[14] Webb, R. L., Eckert, E. R. G., and Goldstein, R. J., 1971, "Heat Transfer and Friction in Tubes With Repeated-Rib Roughness," Int. J. Heat Mass Transfer, **14**, pp. 610–617.
[15] Cao, Y., and Ponnapan, R., 2004, "A Liquid Cooler Module With Carbon Foam for Electronics Cooling Applications," *Proceedings of the 42nd AIAA Aerospace Sciences Meeting and Exhibit*, Reno, NV, pp. 1–7.
[16] JSME, 1986, *Handbook of Mechanical Engineering*, Fluid Engineering, Tokyo, p. 86, No. A5.
[17] Bergles, A. E., Blumenkrantz, A. R., and Taborek, J., 1974, "Performance Evaluation Criteria for Enhanced Heat Transfer Surfaces," *Proceedings of the 5th International Heat Transfer Conference*, Tokyo, Vol. 2, pp. 239–243.
[18] Bejan, A., 1982, *Entropy Generation Through Heat and Fluid Flow*, Wiley, New York, pp. 105–120.

Discussion: "The Modeling of Viscous Dissipation in a Saturated Porous Medium" (Nield, D. A., 2007, ASME J. Heat Transfer, 129, pp. 1459–1463)

V. A. F. Costa
Departamento de Engenharia Mecânica,
Universidade de Aveiro,
Campus Universitário de Santiago,
3810-193 Aveiro, Portugal
e-mail: v.costa@ua.pt

In a recent paper [1] modeling of viscous dissipation in fluid-saturated porous media is considered. This Comment concerns the energy conservation formulation of natural or mixed convection problems including viscous dissipation. For simplicity, sometimes only the clear fluid situation is treated, the main issues applying both to clear fluids and to fluid-saturated porous media.

Energy Conservation Formulation for Natural Convection in Enclosures

Energy conservation equation applied to any closed system gives [2]

$$\frac{dE}{dt} = \dot{Q} - \dot{W} \tag{1}$$

Property energy is composed by the components [2]: internal energy, U, kinetic energy, $(1/2)mV^2$, and potential (gravitational) energy, mgy, that is, $E=U+(1/2)mV^2+mgy$. For a closed system operating in steady-state $dE/dt=0$ and $\dot{Q}-\dot{W}=0$. $\dot{W}$ is the mechanical power exchanged between the closed system and its surroundings, which is null in the present case. Only if a rotating shaft or electrically energized cables cross the walls of the system, or the walls are deformable or mobile it is $\dot{W}\neq 0$. In the present case it is forcedly $\dot{Q}=0$.

If the domain is a differentially heated enclosure of rigid walls, with a hot wall and a cold wall, heat crosses it from the hot wall to the cold wall, and the overall heat input $\dot{Q}_H$ equals the overall heat output $\dot{Q}_C$, that is,

$$\dot{Q} = \underbrace{\dot{Q}_H}_{>0} + \underbrace{\dot{Q}_C}_{<0} = 0 \tag{2}$$

This result holds for any prescribed temperature or heat flux at the walls of the enclosure and for any orientation of these walls. Another way to write Eq. (2) is $|\dot{Q}_H|=|\dot{Q}_C|$.

For unsteady situations it can be $|\dot{Q}_C|>|\dot{Q}_H|$ as a result of a decrease in the potential energy or a decrease in the internal energy. However, under steady-state conditions, only $|\dot{Q}_H|=|\dot{Q}_C|$ is compatible with the energy conservation principle.

If the viscous dissipation term is taken into account

$$|\dot{Q}_C| = |\dot{Q}_H| + \int_V (\text{volumetric viscous dissipation rate})dV \tag{3}$$

violating the energy conservation principle by the reasons detailed above. Thus, if the viscous dissipation is taken into account an *additional* term needs to be taken into account. The complete thermal energy conservation equation (for a clear fluid) can be obtained from Ref. [3]; this additional term is the work of pressure forces, and as $|\dot{Q}_H|=|\dot{Q}_C|$ it is

$$\int_V (\text{volumetric viscous dissipation rate})dV + \int_V (\text{volumetric rate of work of pressure forces})dV = 0 \tag{4}$$

Locally, the volumetric viscous dissipation rate can be different from the volumetric rate of work of pressure forces, and Eq. (4) applies to the overall enclosure. Viscous dissipation is always positive, and the work of pressure forces can be positive or negative depending if the fluid is contracting or expanding, respectively [3]. Viscous dissipation results from the fluid motion, in natural convection problems fluid motion results from the expansion/contraction experienced by the fluid, and both the viscous dissipation and the work of pressure forces need to be taken into account in order to have the unique consistent energy conservation formulation.

No restrictions were made concerning the orientation of the enclosure or of the enclosure walls, and it is incorrect the claim made in Ref. [1] saying that Eq. (4) applies only to a laterally heated enclosure and not to a bottom heated enclosure. It is argued in Ref. [1] that the kinetic energy released in the bottom heated enclosure comes into play, and Eq. (4) does not apply. However, the thermal energy conservation equation is obtained subtracting the kinetic energy conservation equation from the total energy conservation equation [3], and the kinetic energy effects cannot be invoked when dealing with just the thermal energy conservation equation.

Energy Conservation Formulation for Natural or Mixed Convection

In mixed convection fluid motion is partially forced and partially buoyancy induced. For the buoyancy induced flow applies the mentioned above for natural convection. In this case, however, Eq. (4) does not apply, as there are forced flow contributions for viscous dissipation.

In Sec. 5 of Ref. [1] it is argued that the sentence in Refs. [4,5] "…the main results and conclusions apply to any natural or mixed convection problem…" is incorrect. However, the main results and conclusions of Refs. [4,5] are as follows. (i) The consistent energy conservation formulation of natural or mixed convection problems needs to consider both the viscous dissipation and the work of pressure forces. (ii) The energy formulation considering only the viscous dissipation term is inconsistent and violating the energy conservation principle. (iii) Viscous dissipation results from fluid motion, and in natural convection fluid motion results from the expansion/contraction experienced by the fluid, with the associated work of pressure forces. Results, in the form of Eq. (4), which apply to closed enclosures, are a way to explain the main question and not the main result and/or conclusion of Refs. [4,5]. Natural convection heat transfer problem is used to show the essence of the problem, and extrapolations are made to what happens in mixed convection heat transfer problems, where part of the fluid motion is buoyancy induced. This is highlighted in Conclusions of Refs. [4,5]. It is thus correct the claim in Sec. 5 of Ref. [1] saying that result expressed by Eq. (4) is not valid for mixed convection problems, but this is not claimed in Refs. [4,5].

Boussinesq Approximation

The above results were obtained *without* considering any simplifying approach, and no reference was made to the Boussinesq

Contributed by the Heat Transfer Division of ASME for publication in the JOURNAL OF HEAT TRANSFER. Manuscript received November 9, 2007; final manuscript received May 29, 2008; published online December 4, 2008. Review conducted by Jamal Seyed-Yagoobi.

 Copyright © 2009 by ASME

approximation or to the Oberbeck–Boussinesq approximation.

Use of a simplified model results on some *contamination* of the solution, and even on some inconsistencies taking in mind the strict (exact) model and that thermodynamics sets many links between variables and properties. This is also the case when the Boussinesq or the Oberbeck–Boussinesq approximation is used to solve the natural or mixed convection problems.

One thing is to start from the consistent energy conservation formulation of the problem and to use a simplified model to solve it, and inconsistencies on the energy conservation are due to the used simplified model. A different thing is to start from an inconsistent energy conservation formulation of the problem and to use a simplified model to solve it, and try to explain inconsistencies on the energy conservation as based only on the used simplified model to solve the problem.

Scale Analysis

Conclusions are obtained in Sec. 6 of Ref. [1] concerning the relevance of the viscous dissipation and of the work of pressure forces in natural convection problems, which are presented as depending on the considered scales and on the physical situation considered (laterally heated enclosure or bottom heated enclosure).

Result expressed by Eq. (4) applies to natural convection in enclosures, no matter how they are oriented or their walls are oriented. In Sec. 6 of Ref. [1] a scale analysis is conducted over the differential thermal energy conservation equation, and thus only local conclusions can be obtained in what concerns the relative magnitude of the involved terms. However, by the reasons mentioned above, viscous dissipation and work of pressure forces are strongly linked in natural or mixed convection problems, and local and integral assessments of their relevance can lead to significantly different conclusions (description after Eq. (4)).

References

[1] Nield, D. A., 2007, "The Modeling of Viscous Dissipation in a Saturated Porous Medium," ASME J. Heat Transfer, **129**, pp. 1459–1463.

[2] Bejan, A., 2006, *Advanced Engineering Thermodynamics*, 3rd ed., Wiley, Hoboken, NJ.

[3] Bird, R. B., Stewart, W. E., and Lightfoot, E. N., 1993, *Transport Phenomena*, 2nd ed., Wiley, New York.

[4] Costa, V. A. F., 2005, "Thermodynamics of Natural Convection in Enclosures with Viscous Dissipation," Int. J. Heat Mass Transfer, **48**, pp. 2333–2341 (2005).

[5] Costa, V. A. F., 2006, "On Natural Convection in Enclosures Filled with Fluid-Saturated Porous Media Including Viscous Dissipation," Int. J. Heat Mass Transfer, **49**, pp. 2215–2226.

Closure to "Discussion of 'The Modeling of Viscous Dissipation in a Saturated Porous Medium' " (2009, ASME J. Heat Transfer, 131, p. 025501)

D. A. Nield
Department of Engineering Science,
University of Auckland,
Private Bag 92019,
Auckland 1142, New Zealand
e-mail: d.nield@auckland.ac.nz

I thank Dr. Costa for his discussion on my paper [1], and I welcome the opportunity to clarify this matter.

Costa's Energy Conservation Formulation

Costa repeated the arguments that he presented in his earlier papers [2,3], and clarified his ambiguous statement in Ref. [3] that "… the main results and conclusions apply to any natural or mixed convection problem."

The author now argues that the general claim (as clarified) by Costa is incorrect. In particular, it is argued that (1) the application of the first law of thermodynamics in the way that he has applied it is not necessary, (2) he has applied it in an invalid manner, and (3) his claim is falsified by other results.

First, the first law of thermodynamics is already incorporated in the thermal energy equation. That equation expresses the fact that energy is conserved in each elementary volume of the domain, and hence it follows that it is conserved in an enclosure that is closed to mass flow. In the case of forced convection (for which a volume fixed in space is not closed with respect to mass flow), the thermal energy equation must be supplemented by a requirement of global conservation of energy, but for natural convection in an enclosure this is not required.

Second, in the case of a laterally heated box, it is not permissible to treat the heat flux at the hot wall and the heat flux at the cold wall as independent quantities once the hot wall temperature and the cold wall temperature have been specified. One cannot specify the boundary temperature and the boundary heat flux simultaneously. To do so would be to overspecify the boundary conditions in a boundary value problem. When one is setting up the physical situation with fixed wall temperatures, the wall heat fluxes adjust accordingly as energy is exchanged with the outside.

Third, the claim is falsified by known results in the case of forced convection, which is a limiting case of mixed convection. With forced convection it is well known (e.g., Ref. [4]) that it is possible to have a situation where there is substantial viscous dissipation but negligible pressure work. If Costa's claim were correct then one would have a substantial jump in the difference between global viscous dissipation and global pressure work as soon as one added some buoyancy, no matter how small the amount.

It appears to the present author that Costa assumed that buoyancy is a phenomenon that occurs in compressible fluids only, one intrinsically involving expansion and contraction, whereas, in fact, buoyancy results whenever there are density variations, no matter how caused. This is an additional reason why his result for natural convection in a laterally heated box does not generalize to all flows driven by buoyancy.

In the light of the above arguments it appears that the criticisms that Costa made of statements in Ref. [1] are based on a fallacious assumption. Contrary to Costa's claim, it is the scale analysis of the local energy balance (the differential equation) that is pertinent in estimating the relevant magnitude of the viscous dissipation and of the work of pressure forces. It is not possible to perform a legitimate scale analysis on a global scale.

It is the author's opinion that Costa has been misguided by some Computational fluid dynamics (CFD) calculations for the laterally heated square box—calculations based on a limited parameter range, a special geometry, and special boundary conditions. There is a need for more extensive calculations.

Addendum on Velocity Scales

The author now takes the opportunity to extend the discussion of velocity scales made in Ref. [1], where it was argued that the velocity scale for weak natural convection should be of order $U_c \mathrm{Ra}_D$, whereas that for strong natural convection it should be of order $U_c \mathrm{Ra}_D^{1/2}$. Here Ra_D is the Rayleigh–Darcy number and U_c is the conduction velocity scale. It is now pointed out that this is consistent with the fact that in the Horton–Rogers–Lapwood problem the Nusselt number varies as Ra_D for small supercritical values and as $\mathrm{Ra}_D^{1/2}$ for large values, together with the fact that the release of kinetic energy due to the buoyancy force is proportional to the product of the vertical velocity component and the temperature excess. This provides additional support for the view taken in Ref. [1] on the way in which the velocity scale affects the balance between viscous dissipation and pressure work. In that paper it was argued that (1) the magnitude of viscous dissipation compared with conduction can be estimated, a priori and independent of the consideration of pressure work, once an estimate is made for the velocity scale, and (2) there is a fundamental difference between the special case of a laterally heated box (in which, because of cancellation of the contributions from subdomains, there is to first order no net release of kinetic energy due to buoyancy) and a bottom heated box (in which there is a nonzero net release of kinetic energy due to buoyancy). This is a further reason why Costa's conclusions cannot be extended from those for a laterally heated box to all natural or mixed convection problems.

Acknowledgment

The author is grateful to Dr. Costa for private communications on this subject.

References

[1] Nield, D. A., 2007, "The Modeling of Viscous Dissipation in a Saturated Porous Medium," ASME J. Heat Transfer, **129**, pp. 1459–1463.
[2] Costa, V. A. F., 2005, "Thermodynamics of Natural Convection in Enclosures With Viscous Dissipation," Int. J. Heat Mass Transfer, **48**, pp. 2333–2341.
[3] Costa, V. A. F., 2006, "On Natural Convection in Enclosures Filled With Fluid-Saturated Porous Media Including Viscous Dissipation," Int. J. Heat Mass Transfer, **49**, pp. 2215–2226.
[4] Nield, D. A., Kuznetsov, A. V., and Xiong, M., 2004, "Effects of Viscous Dissipation and Flow Work on Forced Convection in a Channel Filled by a Saturated Porous Medium," Transp. Porous Media, **56**, pp. 351–367.

Contributed by the Heat Transfer Division of ASME for publication in the JOURNAL OF HEAT TRANSFER. Manuscript received April 4, 2008; final manuscript received May 20, 2008; published online December 4, 2008. Review conducted by Jamal Seyed-Yagoobi.

 Copyright © 2009 by ASME

Discussion: "Magnetohydrodynamic Flow Past a Vertical Plate With Radiative Heat Transfer" (Shateyi, S., Sibanda, P., and Motsa, S. S., 2007, ASME J. Heat Transfer, 129, pp. 1708–1713)

Asterios Pantokratoras
School of Engineering,
Democritus University of Thrace,
67100 Xanthi, Greece
e-mail: apantokr@civil.duth.gr

In the above paper (Shateyi et al. [1]) the authors treat the boundary layer flow along a vertical semi-infinite, isothermal plate of an electrically conducting fluid. The flow is influenced by a horizontal magnetic field taking into account the Hall effects. In the energy equation the radiation has been included. The boundary layer equations are transformed from the x, y coordinates into ξ, η and subsequently are solved numerically using the Blottner method. However, there are some significant errors in the above paper which are presented below:

The momentum equations used by the authors are (Eqs. 1(b) and 1(c) in their paper)

$$u\frac{\partial u}{\partial x}+v\frac{\partial u}{\partial y}=\nu\frac{\partial^2 u}{\partial y^2}+g\beta(T-T_\infty)-\frac{\sigma {B_0}^2}{\rho(1+m^2)}(mu+w) \quad (1)$$

$$u\frac{\partial w}{\partial x}+v\frac{\partial w}{\partial y}=\nu\frac{\partial^2 w}{\partial y^2}-\frac{\sigma {B_0}^2}{\rho(1+m^2)}(mw-u) \quad (2)$$

where u, v, and w are the velocity components in x, y, and z directions, T is the fluid temperature, β is the volumetric expansion coefficient, ν is the fluid kinematic viscosity, ρ is the fluid density, σ is the fluid electrical conductivity, B_0 is the magnetic induction and m is the Hall parameter. However, the last terms in the above two equations are wrong and the correct forms of Eqs. (1) and (2) are as follows (Hossain and Arbad [2], Pop and Watanabe [3], Saha et al. [4])

$$u\frac{\partial u}{\partial x}+v\frac{\partial u}{\partial y}=\nu\frac{\partial^2 u}{\partial y^2}+g\beta(T-T_\infty)-\frac{\sigma {B_0}^2}{\rho(1+m^2)}(u+mw) \quad (3)$$

$$u\frac{\partial w}{\partial x}+v\frac{\partial w}{\partial y}=\nu\frac{\partial^2 w}{\partial y^2}-\frac{\sigma {B_0}^2}{\rho(1+m^2)}(w-mu) \quad (4)$$

Taking into account that the Hall parameter m has been varied between 0.1 and 5 in the above work it is clear that the presented results and the conclusions are wrong.

Except that, there is a serious problem with some figures. The characteristics of the variation of velocity, temperature or any other substance transported inside a boundary layer are well established and known from 1950. Velocity and temperature profiles approach the ambient fluid conditions asymptotically. Asymptotically means that the velocity and temperature gradient at large distance from the plate is zero. Some velocity and temperature profiles that approach the ambient conditions correctly (asymptotically) in a boundary layer flow are shown, for example, on p. 72 by Jaluria [5]. However, this does not happen in the above work. One temperature profile in Fig. 2(a), all temperature profiles in Fig. 4(b), two temperature profiles in Fig. 5(a), one temperature profile in Fig. 5(b), two temperature profiles in Fig. 6(a), and two temperature profiles in Fig. 8(b) do not approach the horizontal axis asymptotically. Especially, the profiles in Fig. 4(b) are almost straight lines and such profiles do not exist in boundary layer flow. The above-mentioned profiles are truncated due to a small calculation domain used. The calculation domain was not sufficient to capture the real shape of all profiles and a wider calculation domain should be used. This is an error made frequently in the literature (see Pantokratoras [6]).

It is known in magnetohydrodynamics that the free convection along a vertical, isothermal plate under the action of a horizontal magnetic field with constant induction does not admit similarity solution. This is also mentioned in the above work (p. 1709). In a nonsimilar problem, like the present one, the velocity and temperature changes along the plate. However, this does not happen in the present problem. Although the transformed equations (5) are functions of the streamwise coordinate ξ, none of the figures contain any ξ. To what distance ξ correspond the presented profiles? No information is given.

Finally the captions in Figs. 6–8 are wrong.

References

[1] Shateyi, P., Sibanda, P., and Motsa, S. S., 2007, "Magnetohydrodynamic Flow Past a Vertical Plate With Radiative Heat Transfer," ASME J. Heat Transfer, **129**, pp. 1708–1713.
[2] Hossain, M. A., and Arbad, O., 1988, "A Numerical Study of the Unsteady MHD Free Convection With Hall Current," Astrophys. Space Sci., **141**, pp. 281–291.
[3] Pop, I., and Watanabe, T., 1994, "Hall Effects on Magnetohydrodynamic Free Convection About a Semi-Infinite Vertical Flat Plate," Int. J. Eng. Sci., **32**, pp. 1903–1994.
[4] Saha, L. K., Hossain, M. A., and Gorla, R. S. R., 2007, "Effect of Hall Current on the MHD Laminar Natural Convection Flow From a Vertical Permeable Flat Plate With Uniform Surface Temperature," Int. J. Therm. Sci., **46**, pp. 790–801.
[5] Jaluria, Y., 1980, *Natural Convection Heat and Mass Transfer*, Pergamon Press, Oxford.
[6] Pantokratoras, A., 2007, "A Common Error Made in Investigation of Boundary Layer Flows," Appl. Math. Model. (in press).

Manuscript received February 21, 2008; final manuscript received May 16, 2008; published online January 5, 2009. Review conducted by Gautam Biswas.

 Copyright © 2009 by ASME